TECHNISCHE UNIVERSITÄT MÜNCHEN

Lehrstuhl für Numerische Mechanik

Computational Methods for Thermo-Elasto-Plastic Contact

Alexander Seitz

Vollständiger Abdruck der von der Fakultät für Maschinenwesen der Technischen Universität München zur Erlangung des akademischen Grades eines

Doktor-Ingenieurs (Dr.-Ing.)

genehmigten Dissertation.

Vorsitzender	Prof. Dr. Markus Zimmermann
Prüfer der Dissertation:	
1.	Prof. Dr.-Ing. Wolfgang A. Wall
2.	Prof. Dr. Yves Renard Institut National des Sciences Appliquées de Lyon, Lyon / Frankreich

Die Dissertation wurde am 24.09.2018 bei der Technischen Universität München eingereicht und durch die Fakultät für Maschinenwesen am 30.01.2019 angenommen.

Abstract

This thesis deals with the numerical treatment of contact problems considering inelastic deformation and thermomechanical coupling. For this purpose, a novel finite element approach for elasto-plasticity at finite strains is developed and two different methods of numerical contact mechanics derived: the dual mortar method with a focus on isogeometric analysis and the Nitsche method for nonlinear problems. All developed methods are investigated via both isothermal and thermomechanical problems.

The new computational method for elasto-plasticity at finite deformations is based on a reformulation of the plastic material constraints of Hill's anisotropic yield criterion (with the well-known von Mises law as a special case) in terms of a non-smooth nonlinear complementarity (NCP) function. The resulting set of semi-smooth equations comprises of the discrete balance of linear momentum and the roots of the NCP functions at every quadrature point. This coupled system of equations can be solved for the displacements and plastic deformation efficiently by a non-smooth variant of Newton's method. Therein, the additionally introduced degrees of freedom describing the plastic deformation can be condensed from the global system of equations such that a linear system only consisting of the displacement degrees of freedom has to be solved in each iteration step. In contrast to classical return mapping methods for computational plasticity, the plastic constraints are not required to hold at every iteration in the nonlinear solution procedure, but only at convergence. This relaxation in the pre-asymptotic behavior results in an increased flexibility regarding the algorithm design and a potentially higher robustness compared to radial return mapping algorithms. Finally, the method is extended to account for plastic spin, visco-plasticity, as well as thermo-plastic coupling where plastic work is converted to heat and material parameters are temperature dependent.

Next, frictional contact is incorporated by the dual mortar method. Well-known from the literature, the use of biorthogonal (dual) basis functions for the contact Lagrange multiplier yields a localization of the contact constraints and allows for a trivial condensation of the the discrete Lagrange multiplier degrees of freedom from the global system of equations. Beyond established Lagrange multiplier bases, this thesis presents a piece-wise constant Lagrange multiplier basis for second order finite elements (FE). As compared to the dual mortar method for second order FE in the literature, the piece-wise constant space greatly simplifies the construction of the basis while maintaining optimal convergence properties. Aside from classical finite elements, isogeometric analysis (IGA) has received great attention in many fields of computational mechanics research. Especially for computational contact mechanics, the smooth surface representation provided by IGA is highly desirable. This thesis presents the first dual mortar method for IGA applied to both domain decomposition as well as contact problems. A very simple and commonly used element-wise construction of the dual basis functions is directly transferred to the IGA case. The resulting Lagrange multiplier interpolation satisfies discrete inf-sup stability and biorthogonality, however, the reproduction order is limited to one. In the domain decomposition case, this results in a limitation of the spatial convergence order to $\mathcal{O}(h^{3/2})$ in the energy norm, whereas for unilateral contact, due to the lower regularity of the solution, optimal convergence rates are still met. To include thermomechanical coupling, i.e. contact heat conduction and frictional heating, in dual mortar contact formulations, an additional Lagrange multiplier field representing the contact heat flux is introduced. By discretizing this thermal Lagrange mul-

tiplier with dual basis functions as well, it can also be condensed from the global system such that the final consistently linearized monolithic system consists of discrete displacements and temperatures only.

Finally, the application of Nitsche's method to frictional contact problems is explored. Only recently, Nitsche's method, which has originally been developed for the weak imposition of boundary conditions, has been extended to contact problems of small deformations. Different variations of Nitsche's method for large deformation contact problems are studied, ranging from the classical symmetric option to a penalty free variant. In contrast to the mortar method, which requires additional Lagrange multiplier degrees of freedom to enforce the contact constraints, Nitsche's method provides a stable and consistent contact discretization based on the original displacement degrees of freedom only. This is achieved by including a consistent stabilizing penalty term. As high penalty parameters are adverse to the robustness of the method, the minimal required penalty term is estimated here by the solution of local eigenvalue problems. For highly nonlinear material behavior, the penalty parameter has to be adapted to account for stiffening effects which is achieved by an adaptive re-evaluation of the estimate at the deformed state. Moreover, the proposed harmonic weighting of the contact traction allows to reduce the required penalty term significantly in the case of a large contrast in material parameters between the contacting bodies. Lastly, a special focus is put on the enforcement of the thermal constraints at the contact interface, namely heat conduction and frictional heating. Two numerical methods are presented to enforce these effects, a substitution method as well as a Nitsche-type approach. While the former is simpler to implement the latter has the advantage of remaining well-conditioned for all physical parameters. Numerical examples demonstrate competitive accuracy of Nitsche's method as compared to mortar contact formulations and demonstrate its applicability to nonlinear problems including thermal coupling and elasto-plastic material laws.

Zusammenfassung

Diese Arbeit beschäftigt sich mit der numerischen Behandlung von Kontaktproblemen unter Berücksichtigung inelastischer Deformationen und thermomechanischer Kopplung. Zu diesem Zweck wird ein neuartiger finite Elemente Ansatz für Elastoplastizität bei endlichen Dehnungen entwickelt und zwei verschiedene Methoden der numerischen Kontaktmechanik abgeleitet: die duale Mortar-Methode mit Schwerpunkt auf der isogeometrischen Analyse und die Nitsche-Methode für nichtlineare Probleme. Alle entwickelten Methoden werden sowohl anhand von isothermen als auch thermomechanischen Problemen untersucht.

Die neuartige Berechnungsmethode für Elastoplastizität bei großen Verformungen basiert auf einer Umformulierung der Nebenbedingungen plastischen Materialverhaltens als nichtglatte und nichtlineare Komplementärfunktion (NCP-Funktion). Betrachtet wird insbesondere das anisotrope Fließkriterium nach Hill worin von Mises-Plastizität als Spezialfall enthalten ist. Das resultierende System halbglatter Gleichungen besteht aus dem diskreten Kräftegleichgewicht und den Nullstellen der NCP-Funktionen an jedem Integrationspunkt. Dieses gekoppelte Gleichungssystem kann durch eine nichtglatte Variante des Newtonverfahrens effizient nach den diskreten Verschiebungen und der plastischen Verformung gelöst werden. Die zusätzlich eingeführten Freiheitsgrade, die die plastische Verformung beschreiben, können dabei aus dem globalen Gleichungssystem kondensiert werden. Das System, das letztlich in jedem Iterationsschritt gelöst werden muss, beinhaltet somit ausschließlich Verschiebungsfreiheitsgrade. Im Gegensatz zu klassichen Return-Mapping Methoden zur numerischen Behandlung plastischer Materialien müssen die plastischen Nebenbedingungen nicht in jeder Iteration des nichtlinearen Lösungsprozesses eingehalten werden, sondern nur im konvergierten Zustand. Diese Relaxation im präasymptotischen Bereich ermöglicht eine größere Flexibilität im Entwurf des Lösungsverfahrens und eine potentiell höhere Robustheit im Vergleich zu Return-Mapping Verfahren. Schließlich wird das Verfahren um plastischen Spin, Visko-Plastizität sowie thermoplastische Kopplung, bei der plastische Arbeit in Wärme umgewandelt wird und Materialparameter temperaturabhängig sind, erweitert.

Als nächstes wird reibungsbehafteter Kontakt mittels der dualen Mortar-Methode in das numerische Modell eingebracht. Die Verwendung biorthogonaler (dualer) Basisfuntkionen für den Kontakt-Lagrange-Multiplikator führt zu der aus der Literatur bekannten Lokalisierung der Kontaktbedingungen und ermöglicht eine triviale Kondensation der diskreten Lagrange-Multiplikator-Freiheitsgrade aus dem globalen Gleichungssystem. Jenseits der etablierten Lagrange-Multiplikator-Basen präsentiert diese Arbeit eine stückweise konstante Lagrange-Multiplikator-Basis für finite Elemente zweiter Ordnung. Im Vergleich zur dualen Mortar-Methode vereinfacht der stückweise konstante Ansatzraum die Konstruktion der Basisfunktionen, während optimale Konvergenzeigenschaften erhalten bleiben. Neben klassischen finiten Elementen hat die isogeometrische Analyse (IGA) in vielen Bereichen der numerischen Mechanik große Beachtung gefunden. Insbesondere für die numerische Kontaktmechanik ist die glatte Oberflächenrepresentation, die durch IGA erreicht wird, sehr wünschenswert. Diese Arbeit stellt die erste duale Mortar-Methode für IGA vor, die sowohl auf Gebietszerlegungs- als auch Kontaktprobleme angewandt wird. Eine sehr einfache und häufig verwendete elementweise Konstruktion der dualen Basisfunktionen wird direkt auf den isogeometrischen Fall übertragen. Die resultierende Lagrange-Multiplikator-Interpolation erfüllt diskrete inf-sup-Stabilität und

Biorthogonalität, besitzt jedoch nur eine reduzierte Reproduktionsordnung. Im Fall der Gebietszerlegung führt dies zu einer Beschränkung der räumlichen Konvergenzordnung auf $\mathcal{O}(h^{3/2})$ in der Energienorm, wohingegen in Kontaktproblemen aufgrund der reduzierten Regularität der Lösung nach wie vor optimale Konvergenzordnungen erreicht werden. Um die duale Mortar-Methode um thermomechanische Kopplung, also Kontaktwärmeleitung und Reibungswärme, zu erweitern, wird ein zusätzliches Lagrange-Multiplikatorfeld eingeführt, das den Kontaktwärmefluß darstellt. Durch Diskretisierung dieses thermischen Lagrange-Multiplikators mit dualen Basisfunktionen kann er ebenfalls aus dem globalen System kondensiert werden, sodass das resultierende, monolithische System nur aus diskreten Verschiebungs- und Temperaturfreiheitsgraden besteht.

Schließlich wird die Anwendung der Nitsche-Methode auf Reibkontaktprobleme untersucht. Erst kürzlich wurde die Nitsche-Methode, die ursprünglich für die schwache Aufbringung von Randbedingung entwickelt wurde, auf Kontaktprobleme kleiner Verformungen erweitert. Es werden verschiedene Variationen der Nitsche-Methode – von der klassischen, symmetrischen bis hin zu einer penalty-freien Variante – für Kontaktprobleme bei großen Verformungen untersucht. Im Gegensatz zur Mortar-Methode, die die Kontaktbedingungen mittels zusätzlicher Lagrange-Multiplikator-Freiheitsgrade aufbringt, liefert die Nitsche-Methode eine stabile und konsistente Kontaktdiskretisierung, die ausschließlich auf den ursprünglichen Verschiebungsfreiheitsgraden beruht. Dies wird durch einen konsistenten stabilisierenden Strafterm (Penaltyterm) erreicht. Da hohe Penaltyparameter die Robustheit des Verfahrens beeinträchtigen, wird der minimal erforderliche Penaltyparameter durch die Lösung von lokalen Eigenwertproblemen abgeschätzt. Für hochgradig nichtlineares Materialverhalten muss der Penaltyparameter angepasst werden, um Versteifungseffekte zu berücksichtigen, was durch eine adaptive Neuauswertung der Eigenwertprobleme erreicht wird. Darüber hinaus ermöglicht die vorgeschlagene harmonische Gewichtung der Kontaktspannung eine deutliche Reduzierung des erforderlichen Penaltyterms bei Kontaktproblemen mit großem Unterschied in den Materialparametern der beiden kontaktierenden Körper. Ein besonderes Augenmerk liegt schließlich auf der Aufbringung der thermischen Randbedingungen an der Kontaktfläche in Form von Wärmeleitung und Reibungswärme. Zwei numerische Methoden zur Einbringung dieser Effekte werden vorgestellt, eine Substitutionsmethode sowie ein Nitsche-artiger Ansatz. Während erstere einfacher zu implementieren ist, hat letzterer den Vorteil, dass er für alle physikalischen Parameter gut konditioniert bleibt. Numerische Beispiele zeigen die Konkurrenzfähigkeit der Nitsche-Methode im Vergleich zur Mortar-Methode sowie deren Anwendbarkeit auf nichtlineare Probleme, thermomechanische Kopplung und elasto-plastische Materialgesetze.

Contents

Nomenclature

Mathematical Operators

$(\cdot)^{\mathsf{T}}$	Transpose of a tensor
$(\cdot)^{-1}$	Inverse of a tensor
$(\cdot)^{-\mathsf{T}}$	Inverse transpose of a tensor
$(\cdot)^{+}$	Pseudo-inverse of a tensor
$\nabla_{\boldsymbol{X}}$, $\nabla_{\boldsymbol{x}}$	Material and spatial gradient operator
$\nabla_{\boldsymbol{X}}\cdot$, $\nabla_{\boldsymbol{x}}\cdot$	Material and spatial divergence operator
$\arg\min$	Argument of the minimizer
span	Linear span of a set
const	constant function
dev	Deviatoric part of a tensor
skew	Skew-symmetric part of a tensor
tr	Trace of a tensor
$\exp$	Exponential of a scalar or tensor
$\ln$	Natural logarithm of a scalar or tensor
$\|\cdot\|$	L^2-norm of a vector or tensor
$\|\cdot\|_{L^2(\Omega)}$	L^2-norm on Ω
$\|\cdot\|_E$	Energy norm
$\|\cdot\|_{\mathbb{H}}$	Anisotropic L^2-norm of a tensor
$I_{\Re_-}$	Indicator function of $\Re_-$
$[\![\cdot]\!]$	Jump across the contact interface in current configuration
$[\![\cdot]\!]_0$	Jump across the contact interface in reference configuration
$\{\cdot\}_\omega$	ω-weighted average across the contact interface
$\mathcal{O}(\cdot)$	Order of $(\cdot)$
$[\cdot]_-$	Negative part of $(\cdot)$
$[\cdot]_+$	Positive part of $(\cdot)$
$\mathcal{D}\boldsymbol{y}[\boldsymbol{x}]$	Directional derivative of $\boldsymbol{y}$ in direction of $\boldsymbol{x}$
$P_{B(r)}(\boldsymbol{z})$	Projection of $\boldsymbol{z}$ onto a Ball of radius r
δ_{ij}	Kronecker delta
$\mathrm{SO}(n)$	Special orthogonal group of order n

Special Tensors and Tensor Products

$\boldsymbol{I}$	Second order identity tensor
$\mathbb{I}_{\mathrm{s}}$	Fourth order symmetric identity tensor
$\mathbb{I}_{\mathrm{sk}}$	Fourth order skew-symmetric identity tensor

$\mathbb{P}_{\mathrm{dev}}$	Fourht order deviatoric projection tensor
$\cdot$	Single contraction
:	Double contraction
$\otimes$	Dyadic product
$\odot$	Alternative outer porduct of two second order tensors

Superscripts and Subscripts

$(\cdot)_h$	Spatially discretized
$(\cdot)_{\mathrm{u}}$	Structural field
$(\cdot)_{\mathrm{T}}$	Thermal field
$(\cdot)_{\mathrm{int}}$	Internal
$(\cdot)_{\mathrm{ext}}$	External
$(\cdot)_{\mathrm{mech}}$	Mechanical
$(\cdot)_{\mathrm{thr}}$	Thermal
$(\cdot)_{\mathrm{dev}}$	Deviatoric
$(\cdot)_n$, $(\cdot)_{n+1}$	At time t_n, t_{n+1}
$(\cdot)_{\mathrm{e}}$	Elastic
$(\cdot)_{\mathrm{p}}$	Plastic
$(\cdot)_{\mathrm{dyn}}$	Dynamic
$(\cdot)_{\mathrm{i}}$	Isotropic hardening
$(\cdot)_{\mathrm{k}}$	Kinematic hardening
$(\cdot)_q$	At quadrature point q
$(\cdot)_{\mathrm{tr}}$	Trial
$(\cdot)^{(1)}$	Slave
$(\cdot)^{(2)}$	Master
$(\cdot)_{\mathrm{c}}$	Contact
$(\cdot)_{\mathrm{n}}$	Normal
$(\cdot)_{\tau}$	Tangential

Configurations, Domains and Boundaries

Ω_0	Reference (material) configuration
Ω_t	Current (spatial) configuration
$\partial\Omega_0$, $\partial\Omega_t$	Boundary of Ω_0 and Ω_t
Γ_{u}	Dirichlet boundary for displacement field in reference configuration
Γ_{T}	Dirichlet boundary for temperature field in reference configuration
Γ_{σ}	Neumann boundary for displacement field in reference configuration
Γ_{q}	Neumann boundary for temperature field in reference configuration
Γ_{c}, γ_{c}	Potential contact boundary in reference and current configuration

Kinematics

n_{dim}	Number of spatial dimensions
$\boldsymbol{X}$	Coordinate in reference configuration
$\boldsymbol{x}$	Coordinate in current configuration
t	Time
φ	Motion of a body
φ_t	Mapping from reference to current configuration at time t
$\boldsymbol{u}$	Displacement field
$\boldsymbol{v}$	Velocity field
$\boldsymbol{a}$	Acceleration field
T	Temperature field
$\boldsymbol{N}$, $\boldsymbol{n}$	Unit outward normal on $\partial\Omega_0$ and $\partial\Omega_t$
$\boldsymbol{F}$	Deformation gradient
$\boldsymbol{R}$	Rotational part of the deformation gradient
$\boldsymbol{v}$, $\boldsymbol{U}$	Left and right stretch tensor
$\boldsymbol{C}$	Right Cauchy–Green deformation tensor
$\boldsymbol{E}$	Green–Lagrange strain tensor
$\boldsymbol{\epsilon}$	Logarithmic strain tensor
$\boldsymbol{\varepsilon}$	Linearized strain tensor
$\boldsymbol{L}$	Material velocity gradient
$\boldsymbol{D}$	Material rate of deformation
$\boldsymbol{W}$	Material spin tensor
$\mathrm{d}\boldsymbol{X}$, $\mathrm{d}\boldsymbol{x}$	Infinitesimal line element in material and spatial configuration
$\mathrm{d}\boldsymbol{A}$, $\mathrm{d}\boldsymbol{a}$	Infinitesimal surface element in material and spatial configuration
$\mathrm{d}V$, $\mathrm{d}v$	Infinitesimal volume element in material and spatial configuration
J	Jacobian determinant, determinant of $\boldsymbol{F}$
I_1, I_2, I_3	Principle invariants of $\boldsymbol{C}$

Stress and Heat Flux

$\boldsymbol{t}$	Cauchy traction vector
$\boldsymbol{\sigma}$	Cauchy stress tensor
$\boldsymbol{\tau}$	Kirchhoff stress tensor
$\boldsymbol{P}$	First Piola–Kirchhoff stress tensor
$\boldsymbol{S}$	Second Piola–Kirchhoff stress tensor
$\boldsymbol{M}$	Mandel stress tensor in reference configuration
$\boldsymbol{\Sigma}$	Mandel stress tensor in plastic intermediate configuration
$\mathbb{C}$	Material tangent tensor
q_{n}	Cauchy surface heat flux
$\boldsymbol{q}$	Cauchy heat flux
$\boldsymbol{Q}$	Piola–Kirchhoff heat flux

Balance equations

ρ_0, ρ	Mass density in reference and current configuration
$\boldsymbol{b}_0$, $\boldsymbol{b}$	Body force in reference and current configuration
e	Specific energy in reference configuration
R	Heat source in reference configuration
$\tilde{\boldsymbol{Q}}$	Entropy flux in reference configuration
$\tilde{R}$	Entropy source in reference configuration
η	Specific entropy in reference configuration
Ψ	Helmholtz free energy
$\mathcal{D}_{\mathrm{int}}$	Internal dissipation
$\mathcal{D}_{\mathrm{mech}}$	Mechanical dissipation
$\mathcal{D}_{\mathrm{thr}}$	Thermal dissipation
$\hat{\boldsymbol{t}}_0$	Prescirbed first Piola traction vector on Γ_σ
$\hat{Q}_{\mathrm{n}}$	Prescribed normal Piola heat flux on Γ_{q}
$\hat{\boldsymbol{u}}$	Prescribed displacement on Γ_{u}
$\hat{T}$	Prescribed temperature on Γ_{T}
t_{end}	End of time interval
$\boldsymbol{u}_0$	Initial displacement field
$\boldsymbol{v}_0$	Initial velocity field
T_0	Initial temperature field
h_{c}	Heat convection coefficient

Constitutive Models

$\boldsymbol{\kappa_0}$	Heat conductivity tensor
κ_0	Nonlinear isotropic heat conductivity
α	Scalar internal variable of state
$\boldsymbol{\alpha}$	Tensor valued internal variable of state
$\boldsymbol{\alpha}$	Set of internal variables of state
$\mathfrak{R}$	Response function
$\boldsymbol{F}_{\mathrm{e}}$, $\boldsymbol{F}_{\mathrm{p}}$	Elastic and plastic part of the deformation gradient
$\boldsymbol{C}_{\mathrm{e}}$, $\boldsymbol{C}_{\mathrm{p}}$	Elastic and plastic right Cauchy–Green deformation tensor
α_{i}, $\boldsymbol{\alpha}_{\mathrm{k}}$	Isotropic and kinematic hardening variable
Ψ_{e}	Elastic free energy
$\Psi_{\mathrm{e},0}$	Isothermal elastic free energy
Ψ_{ϑ}	Thermal free energy
Ψ_{p}	Hardening potential
$\Psi_{\mathrm{p,i}}$, $\Psi_{\mathrm{p,k}}$	Isotropic and kinematic hardening potential
$\boldsymbol{L}_{\mathrm{p}}$	Plastic velocity gradient
$\boldsymbol{D}_{\mathrm{p}}$	Plastic rate of deformation
$\boldsymbol{W}_{\mathrm{p}}$	Plastic material spin
$\boldsymbol{\Omega}_{\mathrm{p}}$	Plastic spin
A_{i}, $\boldsymbol{A}_{\mathrm{k}}$	Conjugate force to α_{i} and $\boldsymbol{\alpha}_{\mathrm{k}}$

Ξ_p	Plastic dissipation potential
ϕ_p	Yield function
$\boldsymbol{\eta}$	Effective stress
Σ_eq	Equivalent stress
Y	Effective yield stress
$\mathcal{E}$	Elastic domain in stress space
$\dot{\gamma}$	Plastic multiplier
μ	Viscosity (in Peric's visco-plasticity model)
ϵ	Rate sensitivity (in Peric's visco-plasticity model)
$\phi_\mathrm{p}^\mathrm{dyn}$	Dynamic yield function
Y^dyn	Effective dynamic yield stress

Material Parameters

c_v	Heat capacity
k_0	Isotropic heat conductivity constant
α_T	Thermal expansion coefficient
χ	Plastic dissipation factor (Taylor–Quinney factor)
η	Plastic spin constant
E	Young's modulus
ν	Poisson's ratio
μ	Shear modulus
λ	Lamé parameter
y_0	Initial yield stress
y_{ij}	Yield stress in i-direction (for $i = j$) and shear yield stress in i-j-plane (for $i \neq j$)
$\mathbb{H}$	Hill tensor
H_i, H_k	Linear isotropic and kinematic hardening modulus
y_∞	Saturation yield stress
δ	Isotropic hardening exponent
ω_0	Temperature dependent softening factor of yield stress
ω_h	Temperature dependent softening of hardening modulus

Contact Mechanics

$\gamma_\mathrm{c}^{(1)}$, $\gamma_\mathrm{c}^{(2)}$	Slave and master contact boundary in current configuration
χ_t	Contact projection from $\gamma_\mathrm{c}^{(1)}$ to $\gamma_\mathrm{c}^{(2)}$
$\hat{\boldsymbol{x}}^{(2)}$	Projection point of $\boldsymbol{x}^{(1)}$
g_n	Gap function
$\boldsymbol{v}_\tau$	Relative tangential velocity
$\boldsymbol{u}_\tau$	Relative tangential displacement
$\boldsymbol{t}_\mathrm{c}$	Contact Cauchy traction
e_c	Contact specific energy

T_c	Temperature of the contact surface
p_n	Normal contact pressure
$\boldsymbol{t}_\tau$	Tangential contact traction
q_c	Contact Cauchy heat flux
η_c	Contact specific energy
Ψ_c	Contact free energy
$\Psi_{\mathrm{c,T}}$	Thermal contact free energy
$\Psi_{\mathrm{c,pen}}$	Contact penalty potential
$\mathcal{D}_\mathrm{c}$	Contact dissipation
Ξ_c	Contact dissipation potential
ϕ_τ	Coulomb yield function
μ	Apparent coefficient of friction
ϑ_c	Maximum temperature of the contacting surfaces
μ_0	Reference coefficient of friction
T_d	Damage temperature
$\gamma^{(i)}$	Heat transfer coefficient of surface i
$\bar{\gamma}^{(i)}$	Heat transfer constant of surface i
β_c	Contact heat conductivity
δ_c	Contact dissipation split ratio

Space Discretization

$\boldsymbol{M}$	Mass matrix
$\boldsymbol{F}$	Global force vector
$\boldsymbol{f}$	Element force vector
$\boldsymbol{f}_q$	Element force vector contribution of quadrature point q
$\delta\mathcal{W}_\mathrm{u}$	Weak form of balance of linear momentum
$\delta\mathcal{W}_\mathrm{T}$	Weak form of balance of heat conduction equation
$\delta\boldsymbol{u}$	Displacement test function
δT	Temperature test function
$\boldsymbol{\mathcal{U}}_\mathrm{u}$, $\boldsymbol{\mathcal{V}}_\mathrm{u}$	Displacement trial and test space
$\mathcal{U}_\mathrm{T}$, $\mathcal{V}_\mathrm{T}$	Temperature trial and test space
N_i	Shape function of node/control point i
X_i	Reference coordinate of node/control point i
d_i, $\delta\mathsf{d}_i$	Displacement and displacement variation of node/control point i
v_i	Velocity of node/control point i
a_i	Acceleration of node/control point i
T_i, $\delta\mathsf{T}_i$	Temperature and temperature variation of node/control point i
h	Mesh size
$\bar{h}$	Normalized mesh size
$\mathcal{T}_h$	Finite element mesh of size h
$\tau_{h,i}$	Element i in $\mathcal{T}_h$
$\mathbb{Q}_p$	Set of polynomials upto degree p on a rectangle/cube

$\mathbb{T}_p$	Set of serendipity polynomials upto degree p on a rectangle/cube
$\mathbb{P}_p$	Set of polynomials upto degree p on a triangle/tetrahedron
$\Phi_{\tau_{h,i}}$	Isoparametric mapping of element $\tau_{h,i}$
B_i	B-spline function of control point i
$\boldsymbol{\Xi}$, $\boldsymbol{H}$, $\boldsymbol{Z}$	Knot vectors
$\bar{\boldsymbol{\Xi}}$, $\bar{\boldsymbol{H}}$, $\bar{\boldsymbol{Z}}$	Break point vectors
$\mathbb{S}_p(\boldsymbol{\Xi})$	Univariate spline space of degree p with knot vector $\boldsymbol{\Xi}$
$\mathscr{C}_{\mathrm{B-spline}}$	B-spline curve
$\mathscr{S}_{\mathrm{B-spline}}$	B-spline surface
$\mathscr{V}_{\mathrm{B-spline}}$	B-spline volume
w_i	NURBS weight of control point i
R_i	NURBS function of control point i
$\mathscr{C}$	NURBS curve
$\mathscr{S}$	NURBS surface
$\mathscr{V}$	NURBS volume
$\mathbb{R}_p$	NURBS space of degree p

Time Discretization

Δt	Time step size
β, γ	Parameters of Newmark's method
α_f, α_m	Parameters of generalized-α method
ρ_∞	Spectral radius of generalized-α method in the high-frequency limit
$\mathbf{d}_n$, $\mathbf{v}_n$, $\mathbf{a}_n$	Discrete nodal displacements, velocities and accelerations at t_n
$\mathbf{T}_n$, $\dot{\mathbf{T}}_n$	Discrete nodal temperatures and temperature rates at t_n

Nonlinear Solution Technique

$\boldsymbol{r}$	Discrete residual
$\mathbf{K}$	Effective stiffness matrix
$\Delta\mathbf{d}$	Newton increment of discrete nodal displacements
$\Delta\mathbf{T}$	Newton increment of discrete nodal temperatures

Computational Plasticity

$\mathbf{L}_\mathrm{p}$	Discrete plastic velocity gradient
$\Delta\mathbf{L}_\mathrm{p}$	Discrete plastic flow increment over one time step
$\Delta\mathbf{D}_\mathrm{p}$	Discret plastic deformation increment over one time step
$\Delta\mathbf{W}_\mathrm{p}$	Discrete plastic spin over one time step
M_q	Shape function of quadrature point q
$\mathcal{G}$	Set of all quadrature points
$\mathcal{G}_\mathrm{e}$, $\mathcal{G}_\mathrm{p}$	Set of all quadrature points undergoing elastic and plastic deformation

$\mathbf{F}_{\mathrm{p}}$	Discrete plastic deformation gradient
α_{i}, $\boldsymbol{\alpha}_{\mathrm{k}}$	Discrete isotropic and kinematic hardening variable
$\Delta\gamma$	Plastic multiplier increment over one time step
c_{p}	Plastic complementarity parameter
s_{p}	Shape parameter of NCP function
a_{p}	Damping parameter in quasi-Newton scheme
$\boldsymbol{G}_{\mathrm{p}}$	Plastic NCP function with $s_{\mathrm{p}} = 0$
$\boldsymbol{G}_{\mathrm{p},s_{\mathrm{p}}}$	Plastic NCP function
$\boldsymbol{H}_{\mathrm{p},s_{\mathrm{p}}}$	Plastic NCP function including plastic spin
w_q	Integration weight of quadrature point q

Mortar Methods for Contact Mechanics

$\tau_{\Gamma,h,j}^{(i)}$	Surface element j on $\gamma_{\mathrm{c},h}^{(i)}$
$\alpha_{\mathrm{f,c}}$	Generalized-α time integration factor of contact forces
$\boldsymbol{\lambda}$, $\delta\boldsymbol{\lambda}$	Lagrange multiplier trial and test function
λ_{n}, $\delta\lambda_{\mathrm{n}}$	Normal component of Lagrange multiplier trial and test function
$\boldsymbol{\lambda}_{\tau}$, $\delta\boldsymbol{\lambda}_{\tau}$	Tangential component of Lagrange multiplier trial and test function
$\boldsymbol{\mathcal{W}}$	Trace space of $\boldsymbol{\mathcal{U}}_{\mathrm{u}}^{(1)}$
$\mathcal{M}$, $\boldsymbol{\mathcal{M}}$	Scalar and vector valued dual space of $\boldsymbol{\mathcal{W}}$
$\boldsymbol{\mathcal{M}}(\boldsymbol{\lambda})$	Space of admissible Lagrange multipliers
$\boldsymbol{\lambda}_i$, $\delta\boldsymbol{\lambda}_i$	i-th discrete Lagrange multiplier and its variation
$\lambda_{\mathrm{n},i}$, $\delta\lambda_{\mathrm{n},i}$	Normal component of the i-th discrete Lagrange multiplier and its variation
$\boldsymbol{\lambda}_{\tau,i}$, $\delta\boldsymbol{\lambda}_{\tau,i}$	Tangential component of the i-th discrete Lagrange multiplier and its variation
$\bar{N}_j^{(i)}$, $\bar{R}_j^{(i)}$	Polynomial and NURBS shape function of node/control point j on $\gamma_{\mathrm{c},h}^{(i)}$
ϕ_i	i-th Lagrange multiplier shape function
$\mathcal{L}$	Set of Lagrange multipliers
$\mathcal{S}$	Set of all nodes/control points on $\gamma_{\mathrm{c},h}^{(1)}$
$\mathcal{S}_{\odot}$	Set of all nodes on $\gamma_{\mathrm{c},h}^{(1)}$ inside elements
$\mathcal{S}_{\square}$	Set of all nodes on $\gamma_{\mathrm{c},h}^{(1)}$ on the skeleton
$\mathcal{M}$	Set of all nodes/control points on $\gamma_{\mathrm{c},h}^{(2)}$
$\mathcal{N}$	Set of all nodes/control points neither on $\gamma_{\mathrm{c},h}^{(1)}$ nor $\gamma_{\mathrm{c},h}^{(2)}$
$\mathbf{D}$, $\mathbf{M}$	Mortar coupling matrices
$\mathbf{P}$	Mortar projection operator
$\tilde{g}_{\mathrm{n},i}$	Weighted gap associated with i-th Lagrange multiplier
$\tilde{\boldsymbol{u}}_{\tau,\mathrm{rel},i}$	Weighted relative tangential slip associated with the i-th Lagrange multiplier
c_{n}	Complementarity parameter in normal direction
$G_{\mathrm{n},i}$	NCP function of i-th Lagrange multiplier in normal direction
c_{τ}	Complementarity parameter in tangential direction
$\boldsymbol{G}_{\tau,i}$	NCP function of i-th Lagrange multiplier in tangential direction
$\boldsymbol{G}_{\mathrm{c},i}$	NCP function of i-th Lagrange multiplier

$\mathbf{C}_*$	Linearization of contact NCP function $\boldsymbol{G}_{\mathrm{c}}$
λ_{T}, $\delta\lambda_{\mathrm{T}}$	Thermal Lagrange multiplier trial and test function
$\lambda_{\mathrm{T},i}$, $\delta\lambda_{\mathrm{T},i}$	i-th discrete thermal Lagrange multiplier and its variation
$\mathcal{P}_{\mathrm{c},i}$	Frictional power of i-th Lagrange multiplier
$G_{\mathrm{T},i}$	Discrete thermal interface constraint of i-th thermal Lagrange multiplier
$\mathbf{E}_*$	Linearization of $\boldsymbol{G}_{\mathrm{T}}$

Nitsche Methods for Contact Mechanics

ω_{u}	Weighting factor of contact traction
$\omega_{\mathrm{u}}^{\tau_{h,i}^{(1)}\tau_{h,j}^{(2)}}$	Weighting factor of contact traction in common integration domain of $\tau_{h,i}^{(1)}$ and $\tau_{h,j}^{(2)}$
$\Delta\boldsymbol{u}_{\tau}$	Relative tangential slip increment over one time step
$\bar{\mu}$	Effective friction bound
$\theta_{\mathrm{u},1}$, $\theta_{\mathrm{u},2}$	Parameters for different Nitsche methods
γ_{n}, γ_{τ}	Penalty parameter in normal and tangential direction
$\gamma_{\mathrm{n},0}$, $\gamma_{\tau,0}$	Reference penalty parameter in normal and tangential direction
$\gamma_{\{\mathrm{n},\tau\}}^{\tau_{h,i}^{(1)}\tau_{h,j}^{(2)}}$	Normal and tangential penalty parameter in common integration domain of $\tau_{h,i}^{(1)}$ and $\tau_{h,j}^{(2)}$
$C_{\mathrm{I,u}}$	Constant resulting from mechanical trace inequality
$C_{\mathrm{I,u}}^{\tau_{h,j}^{(i)}}$	Constant resulting from mechanical trace inequality on element $\tau_{h,j}^{(i)}$
$\gamma_{\mathrm{c},h,0}^{(1)}$	Closed contact part of the $\gamma_{\mathrm{c},h}^{(1)}$
$\gamma_{\mathrm{c},h,+}^{(1)}$	Separated part of the $\gamma_{\mathrm{c},h}^{(1)}$
$\gamma_{\mathrm{c},h,\tau_0}^{(1)}$	Stick part of $\gamma_{\mathrm{c},h,0}^{(1)}$
$\gamma_{\mathrm{c},h,\tau_+}^{(1)}$	Slip part of $\gamma_{\mathrm{c},h,0}^{(1)}$
ω_{T}	Weighting factor of contact heat flux
$\omega_{\mathrm{T}}^{\tau_{h,i}^{(1)}\tau_{h,j}^{(2)}}$	Weighting factor of contact heat flux in common integration domain of $\tau_{h,i}^{(1)}$ and $\tau_{h,j}^{(2)}$
θ_{T}	Parameter for different Nitsche methods
γ_{T}	Thermal penalty parameter
$\gamma_{\mathrm{T},0}$	Reference thermal penalty parameter
$\gamma_{\mathrm{T}}^{\tau_{h,i}^{(1)}\tau_{h,j}^{(2)}}$	Thermal penalty parameter in common integration domain of $\tau_{h,i}^{(1)}$ and $\tau_{h,j}^{(2)}$
$C_{\mathrm{I,T}}$	Constant resulting from thermal trace inequality
$C_{\mathrm{I,T}}^{\tau_{h,j}^{(i)}}$	Constant resulting from thermal trace inequality on element $\tau_{h,j}^{(i)}$
$\bar{\beta}_{\mathrm{c}}$	Effective contact heat conductivity
$\mathcal{P}_{\mathrm{c}}$	Frictional dissipation power

Abbreviations

B-Spline	Basic spline
CAGD	Computer aided geometric design
EAS	Enhanced assumed strain
NCP	Nonlinear complementarity
FEM	Finite element method
FSI	Fluid-structure interaction
GPTS	Gauss point-to-segment
IBVP	Initial boundary value problem
IGA	Isogeometric analysis
NTS	Node-to-segment
NURBS	non-uniform rational B-spline
PTS	Point-to-segment
RMA	Return mapping algorithm
THB-Spline	Truncated hierarchical B-Spline

1 Introduction

Mankind's discovery of metal production and ability to form metal tools marks a pivoting point in human history: the transition from the Stone Age to the Bronze Age about 3000 BC. Forging metal offered flexibility in design unattainable by stone cutting and cleared the way for modern engineering. To this day still, metal processing is a core component in modern engineering technology. Taking a closer look at production technology, it becomes apparent that many manufacturing processes of metal parts are based on plastic, i.e. irreversible, deformation either at room temperature or pre-heated. Examples range from forging, a skill perfected over thousands of years, to wire drawing as a corner stone of electrification, and to sheet metal forming of car body panels. What all these processes have in common is that the plastic deformation of metal is induced by contact between a work piece and tools. Such elasto-plastic contact scenarios are the focus of this work.

From a perspective of modern mechanics and engineering science, the study of plastic material behavior dates back to the work of Tresca [219] and Mises [150] in the late 19th and early 20th century, respectively. Both names are still famously linked to their derived yield criteria. Later, various criteria to describe plastic yielding of metals have been derived to match experimental observations for different materials. In the 1960s, the emerging mathematical framework of nonlinear continuum mechanics lead the way for a sound mathematical description of large plastic deformations by either hypo-elasto-plastic models, e.g. in Green and Naghdi [84], or hyper-elasto-plastic models, e.g. Lee [134]. Methods derived in this thesis are based on the latter kinematic assumption.

The first successful study of contact problems by means of modern mathematics dates back to the pioneering work of Hertz [97] in the late 19th century. His analytical solutions for the contact of elastic spherical bodies are relevant and serve as reference solutions to this day. While significant progress in the mathematical analysis of contact problems have been made proving e.g. existence and uniqueness of solutions, see Kikuchi and Oden [120] and the references therein, actual closed form solutions to contact problems remain scarce, even for linearized elasticity let alone for problems of elasto-plasticity. Already for one of the most studied contact problems, the Hertzian contact problem of an elastic sphere with a rigid plane, analytical solutions are limited to the size of the contact patch and the contact pressure distribution. The analytic displacement field within the body remains unknown to date.

In practical applications, the lack of analytical solutions can be tackled by two remedies: experimental testing or computer simulation. Experiments, for instance crash tests of vehicles, are often very costly and thus limited in number of variations that can investigated. In addition, not every quantity of interest (e.g. local stresses in the material) is directly accessible to measurements. These drawbacks of experimental methods have resulted in an ever-growing importance of computational methods that provide a cost-efficient alternative to physical testing and insight to effects unamenable to experimental observation. In computational solid and structural mechanics, the predominant numerical method is the finite element method (FEM) also applied in

this work. Despite decades of active research on the treatment of (thermo-) plasticity and (thermomechanical) contact within the FEM, the development of accurate and robust solution methods remains a topic of ongoing research. While most works focus on numerical methods for either thermo-plasticity or thermomechanical contact, the present thesis strives for a combined approach to thermo-elasto-plastic contact problems. It makes, in fact, sense to investigate both elasto-plasticity and frictional contact at the same time, since both effects have more in common than one might initially think. The common thread lies in the fact that both problem classes introduce inequality constraints that are either geometrical (such as the contact non-penetration condition) or somehow limit the admissible stress as in plasticity or friction. Consequently, similar techniques can be used to tackle plasticity and frictional contact. Before discussing the novel contributions of this thesis, a brief review on the relevant state of the art methods is given in the following.

1.1 Computational Approaches to Thermoplasticity

The field of computational plasticity focuses on the inclusion of an elasto-plastic material response in a computational mechanics framework, most commonly the FEM. It started in the 1960's with Wilkins *et al.* [230] firstly introducing the radial return mapping algorithm (RMA) in the infinitesimal theory. Over the years, the RMA has become the by far most common approach in the computational treatment of plastic material laws. Still, it took over 20 years until the first applications of the return mapping to finite strains have been developed by Simo [196, 197]. Meanwhile, such algorithms for infinitesimal and finite deformation can be found in the standard textbooks of Bonet and Wood [19], de Souza Neto *et al.* [57], Simo and Hughes [200]. Most scientific research then focuses on material modeling, i.e. definition of yield functions and flow rules, of advanced materials rather than actual numerical algorithms as this thesis does. In terms of numerical methods, recent alternatives to the RMA at small strains include a sequential quadratic programming algorithm by Wieners [227] and interior point algorithms by Krabbenhoft *et al.* [123] which are both based on the variational formulation of small strain plasticity (see e.g. Han and Reddy [92]), as well as semi-smooth Newton methods using nonlinear complementarity (NCP) functions by Christensen [37], Hager and Wohlmuth [91]. However, due to the fundamentally different kinematic description of plasticity at finite strains compared to small strains (multiplicative vs. additive kinematics), these methods cannot be transferred directly to nonlinear kinematics. At finite strains, variational constitutive updates as proposed by Ortiz and Stainier [160] and more recently Bleier and Mosler [16], Fancello *et al.* [69], Mosler [154], Mosler and Bruhns [155] have been shown to offer improved efficiency compared to radial return mapping methods under certain conditions, see e.g. Bleier and Mosler [16]. Another alternative strategy worth mentioning, the so-called generalized plasticity algorithm, was proposed by Grillo *et al.* [87].

Transitioning from isothermal plasticity to thermoplasticity introduces a bidirectional coupling of the mechanical response and the temperature of a body. On the one hand, the mechanical material properties, most dominantly the yield stress, are temperature dependent. On the other hand, plastic work within a material is converted to heat influencing the temperature distribution within a body. Numerical algorithms for finite deformation thermo-plasticity go back to the seminal work by Simo [198], which is based on the isothermal radial return mapping al-

gorithm presented in Simo [196, 197]. Both partitioned and monolithic solution approaches are discussed in [198]. Several extensions to this algorithm have been presented later, e.g. a monolithic formulation in principle axes by Ibrahimbegovic and Chorfi [114] and a variant including temperature-dependent elastic material properties by Canajija and Brnić [27]. In a different line of work, a variational formulation of thermo-plasticity has been developed by Yang *et al.* [246], where the rate of plastic work converted to heat follows from a variational principle instead of being a (constant) material parameter as in Simo [198]. A comparison to experimental results is presented in Stainier and Ortiz [210] to support this variational form for certain alloys.

1.2 Computational Approaches to Contact Mechanics

Computational contact mechanics deals with the inclusion of contact constraints in a numerical method. The most intuitive of said constraints consists of the fact that bodies do not interpenetrate one another. Furthermore, frictional forces occur for contacting bodies in relative motion. When extending contact problems to thermomechanics, additional thermal effects need to be accounted for: Heat conduction appears through the contact region and frictional work is converted to heat. A vast amount of literature on computational contact mechanics exists, such that the following literature review focuses mainly on methods relevant to the ones derived in this thesis. In particular, this includes mortar finite element methods, isogeometric methods, Nitsche-type methods and methods for thermomechanical contact.

Node-to-Segment methods The earliest method to enforce contact constraints across non-matching interfaces in finite element simulations is the so-called node-to-segment (NTS) method, whereby nodes of a designated slave side are prohibited to penetrate the master surface described by line segments for two-dimensional problems or element facets in three dimensional problems. As NTS contact algorithms have been studied for over thirty years and can be found in standard textbooks, a literature review is skipped at this point, but the interested reader is rather referred to the monographs of Laursen [131], Wriggers [240] instead. However, some properties of NTS algorithms important for the course of this thesis should be mentioned. First, the collocated constraint enforcement at discrete nodes is not consistent in a variational sense, such that, for instance, a contact patch test of transmitting constant contact pressures is not passed without further modification as demonstrated by Crisfield [41], Taylor and Papadopoulos [214]. Necessary modifications to pass the patch test, e.g. the one proposed by Zavarise and De Lorenzis [248], then include information of the discretization of the master side and therefore are somewhat in conflict with the original NTS idea. A direct consequence of the lacking variational consistency is that NTS coupling schemes deteriorate spatial convergence orders of the finite element method [68]. A second drawback of the NTS method arises especially in sliding motions of two elastic bodies and stems from the faceted non-smooth surface representation of the master side. Since the discrete points, that is, the nodes of the slave side, may not penetrate this faceted surface, kinks in the master surface directly result in oscillations of the contact forces or impedes convergence of the nonlinear solution procedure entirely. To alleviate this issue, surface smoothing techniques are applied to generate a smooth surface representation from the master-sided discretization; an incomplete review on such smoothing strategies may include Hermite [162] or

Bernstein [239] polynomials as well as spline [135, 156], Gregory [135, 174] NURBS [209] or Nagata patches [157].

Mortar methods Mortar finite element methods are derived from a mixed variational formulation, in which in addition to the original primary variable (i.e. displacements in an isothermal mechanical problem) also its flux at the contact interface (i.e. the traction in an isothermal mechanical problem) is discretized. Mortar methods were initially introduced in the context of non-overlapping domain decomposition by Ben Belgacem [12], Bernardi *et al.* [14] to couple non-matching interface discretizations. Being able to consistently treat non-matching interfaces, mortar methods were soon applied to contact problems. First implementations for linearized kinematics and frictionless contact were presented by Ben Belgacem *et al.* [13], Hild [101]. In the subsequent years, limitations to small deformations and frictionless contact were gradually removed, resulting in the works of McDevitt and Laursen [147] for small deformation frictional contact, large deformation frictionless contact by, e.g., Cavalieri and Cardona [29], Fischer and Wriggers [71], Puso and Laursen [175], Puso *et al.* [177] and large deformation frictional contact by Fischer and Wriggers [72], Puso and Laursen [176], Tur *et al.* [220], Yang *et al.* [245]. Although mortar methods in the context of domain decomposition appear most natural with Lagrange multipliers for the constraint enforcement [12], most early mortar-based contact algorithms utilize a penalty regularization of the constraints [71, 72, 147, 246], potentially combined with an Uzawa-type augmentation [175, 176]. Mortar contact methods that include Lagrange multipliers to satisfy the contact constraints exactly (in an integral sense) were applied, e.g., by [101, 177, 220] and using the augmented Lagrangian functional of Alart and Curnier [3] in Cavalieri and Cardona [29]. The issue of faceted surface geometries that necessitates surface smoothing procedures for NTS contact algorithms is, to some extent, alleviated naturally as the contact constraints are no longer enforced at collocated points but in a weak, integral sense; an additional surface smoothing is still possible [221] but less beneficial compared to NTS algorithms.

Dual mortar methods Wohlmuth [233, 234] proposed an alternative, so-called *dual* or *biorthogonal*, approximation space for the discrete Lagrange multiplier in domain decomposition problems. In contrast to simply using the trace space of the finite element mesh as done in standard mortar methods, the biorthogonality results in a localization of the coupling conditions across the contact interface and allows for a simple elimination of the additional Lagrange multiplier unknowns. Corresponding contact algorithms using dual Lagrange multipliers were developed in the context of linearized kinmatics by Hüeber and Wohlmuth [106] for frictionless problems and Hüeber *et al.* [108], Hüeber *et al.* [109] for problems involving friction. These works also introduce nonlinear complementarity functions to solve the inequality nature of contact problems by means of a semi-smooth Newton scheme, which then serves as a primal-dual active set strategy, see Hintermüller *et al.* [103]. The review by Wohlmuth [235] may be consulted for the mathematics behind dual mortar contact methods. A first extenstion of dual mortar contact methods to finite deformation kinematics was presented by Hartmann *et al.* [95] and fully linearized by Popp *et al.* [168, 169] for frictionless contact and extended to Coulomb friction by Gitterle *et al.* [80]. Popp *et al.* [170], Wohlmuth *et al.* [232] extended the construction of dual basis functions to quadratic finite spaces and proved optimal convergence orders for contact prob-

lems. Cichosz and Bischoff [39], Popp *et al.* [172] improved robustness and consistency of the method in certain scenarios. Especially the works of Popp *et al.* [168, 169, 170, 172], Wohlmuth *et al.* [232] form the starting point for the mortar methods developed in this thesis.

Nitsche-type methods[1] More recently, consistent discretization schemes for contact problems based on Nitsche's method have been developed. Originally introduced for the weak imposition of boundary conditions by Nitsche [158], a first application of Nitsche's method to contact problems has been presented in Wriggers and Zavarise [237]. Later, Chouly and coauthors laid the groundwork by providing mathematical analysis for the symmetric Nitsche method for frictionless contact in Chouly and Hild [34], non-symmetric and skew-symmetric variants in Chouly *et al.* [35], and frictional contact in Chouly [33]. Moreover, time integration schemes for dynamic contact problems were analyzed in Chouly *et al.* [31, 32]. An unbiased variant, i.e. a variant indiscriminative to the two contacting surfaces, was proposed in Chouly *et al.* [36] and extended to nonlinear elasticity in Mlika *et al.* [152], which also includes some implementation details. In contrast to mortar methods with Lagrange multipliers, Nitsche's method consistently introduces the contact constraints by means of the traction vector computed from the underlying bulk stress tensor and a sufficiently large, consistent penalty term. Hence, no additional unknowns need to be introduced. Consistency and stability can be proven for sufficiently large penalty parameters or even any positive penalty parameter in case of the skew-symmetric Nitsche method [35]. In view of the penalty term in the boundary integral, Nitsche's method for contact problems bears some similarity to so-called Gauss-point-to-segment (GPTS) algorithms proposed, e.g., in Temizer *et al.* [216], which, however, lack the boundary traction term and are thus not consistent, i.e. some remaining penetration is required to enforce the contact constraints, and large penalty parameters are necessary to reduce the residual penetration. At the same time, GPTS algorithms are not stable in the case of large penalty parameters where they yield oscillatory results as shown by Sauer and De Lorenzis [188].

Isogeometric contact methods[2] Isogeometric analysis (IGA) as originally introduced by Hughes *et al.* [112] is based on the use of splines, most commonly non-uniform rational B-splines (NURBS) in an isoparametric finite element method. While finite elements based on Lagrange polynomials are limited to C^0 continuous displacement approximation across elements, NURBS of order p can be constructed with a maximum of C^{p-1} continuity. This increased continuity results in, among others, a smooth surface representation which, as already anticipated in the original proposition of IGA [112], makes the application to computational contact mechanics particularly appealing. As a consequence, in the past ten years various contact discretization techniques have been developed for IGA or transferred from finite elements to IGA. The extension of NTS algorithms resulted in the point-to-segment (PTS) method by Matzen and Bischoff [144], Matzen *et al.* [145], which, in contrast to NTS algorithms for finite elements, does not require an additional surface smoothing as the isogeometric discretization already provides a smooth surface description. However, the PTS method still lacks variational consistency and therefore optimal convergence orders cannot be expected. Further, GPTS methods are used in IGA by De Lorenzis *et al.* [50], Dimitri *et al.* [59], Dimitri [60], Lu [137], Temizer *et al.* [216].

[1] This section is adapted from the author's publication [195].

[2] This section is adapted from the author's publication [193].

However, as aforementioned, such methods are not consistent and unstable for large penalty parameters. Sauer and De Lorenzis [188] extended the isogeometric GPTS method by a two-half-pass algorithm to obtain an unbiased scheme and introduced a post-processing of the, due to the instability of the method, oscillatory contact traction. Obviously, a post-processing step cannot cure the instability, but results appear better even for larger penalty parameters. Isogeometric mortar methods can be found in Brivadis *et al.* [21] for domain decomposition problems and for contact problems in De Lorenzis *et al.* [50, 51], Dittmann *et al.* [61], Kim and Youn [121], Temizer *et al.* [216, 217], which are either combined with penalty approaches [50, 216], Uzawa-type algorithms [217], Lagrange multipliers [61, 121] or augmented Lagrangian methods [51] to enforce the contact constraints. In contrast to penalty methods, the other methods mentioned fulfill the contact constraints in a discrete sense exactly. The recent review by De Lorenzis *et al.* [53] gives a comprehensive discussion of isogeometric contact methods, including comparisons to their finite element counterparts and further references. In addition to the mentioned methods that are all based on an isogeometric Galerkin approximation, the higher inter-element continuity of NURBS basis functions allows for the use of collocation methods, see Reali and Hughes [182] for a general introduction and De Lorenzis *et al.* [52], Kruse *et al.* [125] for an application to computational contact mechanics.

Thermomechanical contact[1] First implementations of thermo-elastic contact based on node-to-segment contact formulations and linearized kinematics were published by Zavarise *et al.* [249] in combination with a penalty approach and Johansson and Klarbring [117] using Lagrange multipliers. These algorithms were extended to nonlinear elasticity in Oancea and Laursen [159], Pantuso *et al.* [163] and finite deformation elasto-plasticity in De Saracibar [54], Wriggers and Miehe [236], Xing and Makinouchi [244]. All of the publications mentioned employ a penalty regularization of the contact constraints with the exception of [117, 163] using Lagrange multipliers. Within the last decade, more sophisticated variationally consistent contact discretizations based on the mortar method have been developed. Hansen [94] and Hüeber and Wohlmuth [107] applied mortar methods to small strain thermo-elasticity introducing Lagrange multipliers for both the contact traction as well as the contact heat flux, either by means of standard [94] or dual basis [107] for the Lagrange multiplier. In the context of isogeometric mortar methods, Temizer [215] developed a method for small strain thermo-elasticity based on an augmented Lagrangian and Dittmann *et al.* [61] a Lagrange multiplier method for finite deformation thermo-elasticity. Due to an easier implementation and other benefits like symmetric operators, most of the cited works above employ some sort of partitioned solution scheme for solving the structural problem (at constant temperature) and thermal problem (at constant displacement) sequentially. Only [61, 107, 163, 249] employ monolithic solution schemes, which solve for displacements and temperatures simultaneously.

1.3 Research Objective

Based on the most robust, efficient, and accurate methods discussed in the previous section, the present work aims at developing new numerical methods of thermomechanical contact problems.

[1] This section is adapted from the author's publication [194].

To capture a wide range of engineering applications, large elastic and elasto-plastic deformations should be accounted for. Furthermore, a broad range of thermomechanical coupling effects need to be considered; from plastic work that is converted to heat and temperature dependent material parameters in the bulk material to heat conduction and frictional heating at the contact interface. Finally, to seek optimal performance in the nonlinear case, all methods employed should have a sound mathematical basis and have been tested successfully on simplified problems of infinitesimal deformation.

1.3.1 Specification of Requirements

Based on the abstract objective discussed above, a more detailed list of essential requirements for the methods devised within this work is given in the following.

Computational Plasticity

Increased robustness compared to classical methods Robust numerical methods allow for larger time/load steps and can hence reduce the overall computational cost. In computational plasticity, the main difficulty in constructing robust algorithms is the fact that the apparent material stiffness varies drastically between an elastic and a plastic material response and the transition between the two is non-smooth. During the nonlinear solution procedure, state of the art methods for computational plasticity have to apply the exact local elastic or plastic tangents at all time, even if the solution is far from converged, since no information of the convergence of the nonlinear solver is included. More robust schemes can be constructed by a more global treatment of plastic material behavior and including information of the global nonlinear solution scheme.

Applicability to practically relevant plasticity models Even without any numerics, material modeling of elasto-plasticity is an intricate field in itself and results in a large variety if yield criteria and hardening behavior each tailored to a specific metal alloy or polymeric compound. No matter how elegant, robust or efficient a numerical methods is, for it to gain practical relevance it has to be applicable to real world problems. This constrains methods of computational plasticity in a way that many mathematical tools can be applied to solve certain simple material models, but are difficult, if at all, extensible to more complex material models.

Extensibility to thermo-elasto-plasticity In many engineering applications, plastic deformation is interconnected with an elevated or even spatially and temporally varying temperature. Temperature, however, significantly influences the material response such that accurate predictions need to account for this influence. For strong interdependency of mechanical and thermal behavior considered in this work, partitioned schemes solving mechanical and thermal problems sequentially exhibit poor convergence. Hence, monolithic solution schemes solving for displacements and temperatures simultaneously are required to obtain an efficient method.

Computational Contact Mechanics

Consistent constraint enforcement To accurately represent the contact constraints, e.g. the condition of no interpenetration, they have to be introduced consistently to the discretized problem. In particular, this requirement rules out the widely used penalty approach which requires some residual penetration to generate contact forces. In consideration of the methods discussed in Section 1.2, mortar methods with Lagrange multipliers or an augmented Lagrangian approach as well as Nitsche's method meet this requirement. Although not variationally consistent, also NTS contact discretizations enforce the constraints (pointwise) exactly if combined with Lagrange multipliers.

Unaltered system size Classical Lagrange multiplier formulations for contact problems yield an increased system size by the additionally introduced Lagrange multiplier degrees of freedom and, moreover, a saddle point system is obtained. Both the increased (and potentially varying) system size as well as its indefinite character may have adverse effects on efficient linear solvers. Consequently, a formulation based on the original displacement degrees of freedom only is preferable. In view of the methods discussed in Section 1.2, penalty methods apparently meet this requirement, however lack consistent constraint enforcement discussed above. Two methods are both consistent and do not yield an increased system size: The dual mortar method intermediately introduces a Lagrange multiplier but later eliminates it from the global system of equations. Nitsche's method, on the contrary, does not require any Lagrange multiplier at all to consistently enforce the contact conditions.

Applicability to finite elements and isogeometric analysis In recent years, isogeometric analysis gained a lot of attention in computational contact mechanics due to its smooth surface representation in contrast to classical finite elements. Methods devised in this thesis should be constructed without any specific spatial discretization in mind but rather be applicable to FEM and IGA without any systemic changes.

Optimal performance for higher order elements Contact algorithms benefit from second or even higher order approximations through a smoother surface representation. Moreover, approximations of higher polynomial degrees yield improved convergence orders in FEM or IGA. All methods developed in this thesis should yield optimal convergence orders for contact problems, at least under uniform mesh refinement. A special characteristic of contact problems at this point is the reduced regularity of the exact solution which limits attainable convergence orders of uniform refinement to $\mathcal{O}(h^{3/2})$ instead of the order of the approximation. Restoration of higher order convergence requires adaptive refinement which is beyond the scope of this work.

Compatibility with elasto-plastic material behavior As the present thesis aims at (thermo-) elasto-plastic contact problems, the developed algorithms need to be compatible with nonlinear elasto-plastic material models in the bulk structure. For different numerical methods for contact constraint enforcement, this requirement is of different complexity. While mortar methods are entirely independent of the material model in the underlying bulk,

Nitsche's method relies on the stress evaluation of the underlying continuum and therefore requires special treatment for nonlinear or even elasto-plastic materials.

Consistent treatment of thermomechanical coupling Lastly, methods for computational contact mechanics derived in this thesis should include thermomechanical coupling. Beyond the thermomechanics in the bulk material, this includes contact heat conduction as well as frictional heating. All requirements stated above for isothermal contact problems should still hold and the coupled problem is to be solved in a monolithic fashion to obtain a robust solution.

1.3.2 Contribution of this Work

The methods proposed in this thesis address all requirements mentioned. The most important scientific novelties include

- **A semi-smooth Newton method for finite deformation elasto-plasticity** (see also Seitz *et al.* [192, 194]). The reformulation of the plastic material constraints in terms of nonlinear complementarity functions yields a more robust algorithm and allows for larger load steps as compared to classical methods. Applications include arbitrary hyperelasticity, plastic anisotropy, plastic spin, visco-plasticity as well as thermo-elasto-plasticity.

- **A mortar method for second order finite elements with piece-wise constant Lagrange multipliers.** The use of piece-wise constant Lagrange multiplier ansatz functions combines the advantages of standard and dual mortar methods, i.e. a simple to construct Lagrange multiplier space, the possibility to condense the discrete Lagrange multipliers from the global system of equations, and optimal convergence orders for contact problems.

- **An isogeometric dual mortar method for contact problems** (see also Seitz *et al.* [193]). The first application of the dual mortar method in isogeometric analysis transfers an element-wise construction of biorthogonal basis functions to isogeometric analysis using non-uniform rational B-splines (NURBS). As for classical finite elements, the biorthogonality yields a localized coupling and allows for an easy elimination of the discrete Lagrange multiplier. Though sub-optimal in applications of domain decomposition, the isogeometric dual mortar method yields optimal convergence orders in contact problems.

- **A mortar method for finite deformation thermomechanical contact** (see also Seitz *et al.* [194]). The mortar method is extended to fully nonlinear thermomechanical contact problems including contact heat conduction, frictional heating and thermo-elasto-plasticity in the bulk material. The contact heat flux is introduced as an additional Lagrange multiplier field and discretized by dual basis functions such that it can be easily eliminated from the global system. Thus, the final system in a monolithic scheme is solved for discrete displacement and temperature degrees of freedom only.

- **A Nitsche method for finite deformation elastic and elasto-plastic contact problems** (see also Seitz *et al.* [195]). Nitsche's method for linearized contact problems is extended to problems involving geometric and constitutive nonlinearities. A special focus is set

on the accurate estimation of the required penalty parameter by solving local eigenvalue problems. For contact problems involving a large contrast in material parameters, the introduced harmonic weighting of contact tractions allows for a significant reduction in the penalty parameter and thereby increase the robustness of the method. Finally, an adaptive scaling of the penalty parameter is developed to maintain stability in the case of highly nonlinear material behavior.

- **A Nitsche method for finite deformation thermomechanical contact problems** (see also Seitz *et al.* [195]). The first application of Nitsche's method to thermomechanical contact problems is developed. Thermomechanical coupling therein comprises of contact heat conduction, frictional heating and thermo-elasto-plasticity in the bulk material. Two strategies to include thermal effects at the interface are discussed: a Galerkin substitution method and a Nitsche-type method. While the substitution method may become ill-conditioned for some physical interface parameters, Nitsche's method remains well-conditioned for the entire range of parameters. Optimal convergence orders and the applicability to thermo-elasto-plasticity are demonstrated by numerical examples.

As indicated, parts of this thesis have been published prior to this monograph in Seitz *et al.* [192, 193, 194, 195] and are reproduced here with permission of the publisher. All numerical methods have been implemented in the parallel in-house finite element code BACI [225] developed at the Institute for Computational Mechanics. Parallelization and linear solvers are based on the open source trilinos project [96]. Wherever possible, existing functionality has been re-used; of particular relevance to the present thesis are the work of Popp [171] and Gitterle [79] on contact mechanics, and Danowski [48] on thermo-structure-interaction.

1.4 Outline

The discussed novelties can be clustered roughly into three major blocks: the numerical treatment of (thermo-) elasto-plasticity, mortar methods for (thermomechanical) contact problems and Nitsche-type methods for (thermomechanical) contact problems. Hence, the remainder of this thesis is organized as follows:

Chapter 2 recalls the continuum thermomechanical basis for the subsequent developments. Starting from the kinematic description of finitely deforming bodies, fundamental conservation laws, and constitutive laws for hyperelasticity, thermoelasticity and thermo-elasto-plasticity, the strong and weak form of the balance equations are derived. These are extended to a thermodynamically consistent formulation of thermomechanical contact. The weak form serves as the basis of the derived numerical methods and are therefore discretized in space by either the classical finite element method or NURBS-based isogeometric analysis. Lastly, the temporal discretization is discussed.

Chapter 3 introduces a novel computational method for (thermo-) elasto-plasticity. After a brief review on the classical return mapping algorithm, the novel semi-smooth Newton method is derived. The reformulation of the inequality constraints of elasto-plasticity as a non-smooth equality constraints allows for them to be solved within the same Newton loop as the global equilibrium. To preserve efficiency, the additional unknown plastic flow at every quadrature point is condensed from the global system of equations. Numerical examples demonstrate the

superior robustness as compared to the classical return mapping algorithm. To be applicable to practical problems, the method is extended to include plastic spin, visco-plasticity and thermo-elasto-plasticity.

Mortar methods for contact problems are investigated in **Chapter 4**. After a short introduction to the fundamental concept of mortar methods for isothermal contact problems, a special focus is put on the discrete Lagrange multiplier space. The well-known standard and dual Lagrange multiplier space for finite elements are only discussed briefly, before the two novel spaces are introduced: a piece-wise constant Lagrange multiplier space for second order finite elements and and a biorthogonal NURBS space for isogeometric dual mortar method. For both contributions, numerical examples are provided, ranging from convergence studies confirming optimal convergence orders to problems of large frictional sliding and elasto-plasticity. Transferring the idea of mortar methods isothermal to thermomechanical contact problems, an additional field of Lagrange multipliers representing the contact heat flux is introduced. By again employing dual basis functions for the Lagrange multiplier field, its discrete values can be condensed from the final system of equations that ultimately consists of displacement and temperature degrees of freedom only. A wide range of numerical examples underlines the versatility of the resulting method.

As an alternative to mortar methods, **Chapter 5** introduces Nitsche's method for finite deformation contact problems. Starting with isothermal contact problems, a family of Nitsche methods is derived, ranging from the classical symmetric variant to a penalty free method. Special emphasis is put on the estimate of the required penalty parameter by local eigenvalue problems. The extension to thermomechanical contact problems is done by either a substitution method or again a Nitsche-type method for the contact heat flux. In both the isothermal and the thermomechanical setting, numerical examples illustrate the differences between the various Nitsche methods.

Finally, the most important findings of this thesis are summarized in **Chapter 6** and an outlook to the application of the derived methods is given.

2 From Continuum Thermomechanics to a Finite Element Discretization

In the concept of continuum mechanics, the behavior, let it be mechanical, thermal or any other physics, of a body is modeled by macroscopic models. The body is assumed to be governed by partial differential equations of a continuous medium (hence the name), although on a microscopic level, those equations do not hold. In the case of small deformations, for instance, the mechanical behavior of polycrystalline metal may be modeled by elasticity, or, for larger deformations, by elasto-plasticity with an appropriate plasticity model (see e.g. Section 2.3.4.4). If one would "zoom in" to a smaller length scale, elasticity would be observed as lattice distortion within the distinct single crystals and plasticity as the movement of dislocations within a single crystal or across grain boundaries. These unresolved micro-mechanical effects are modeled in the continuum approach. This chapter aims at presenting the necessary foundations for the subsequent chapters, but, in itself, does not contain genuinely new results. Hence, it is streamlined towards the following numerical models rather than giving a broad overview over different aspects of continuum thermomechanics. More comprehensive introductions to various aspects can be found in the literature, for instance the textbooks Wegner and Haddow [226] for an easy to read introduction to continuum mechanics a continuum thermodynamics, Holzapfel [104] for an engineering introduction to nonlinear continuum mechanics, elasticity and visco-elasticity, Marsden and Hughes [143] for a more mathematical approach to nonlinear elasticity, Lubarda [138] and Lubliner [139] for a comprehensive introduction to the formulation of plasticity at finite deformations and finally Bertram [15] and Miehe [149] for thermo-elasto-plasticity.

2.1 Kinematics, Deformation and Strain

As a starting point, the deformation of a body is considered with the *reference* (or *material*) *configuration* (or *domain*) Ω_0, as an open set in a n_{dim}-dimensional space, $\Omega_0 \subset \Re^{n_{\text{dim}}}$, $n_{\text{dim}} \in \{2, 3\}$. Though only the deformation of *one* body is discussed subsequently, the derived descriptions can be readily extended to multiple bodies as used in contact mechanics, see Section 2.7. The *motion* $\varphi(\boldsymbol{X}, t)$ thereby maps the material point $\boldsymbol{X}$ in the reference configuration Ω_0 to its current coordinate $\boldsymbol{x}$ in the *displaced* (or *spatial* or *current*) configuration at time t. At any time, the motion $\varphi(\boldsymbol{X}, t)$ results in a smooth, time-dependent, bijective and orientation preserving mapping

$$\varphi_t : \Omega_0 \to \Omega_t, \quad \boldsymbol{X} \mapsto \boldsymbol{x}(\boldsymbol{X}, t) \quad . \tag{2.1}$$

In contrast to linear continuum mechanics restricted to infinitesimal displacements, the *displacement*

$$\boldsymbol{u}(\boldsymbol{X}, t) = \boldsymbol{x}(\boldsymbol{X}, t) - \boldsymbol{X} \tag{2.2}$$

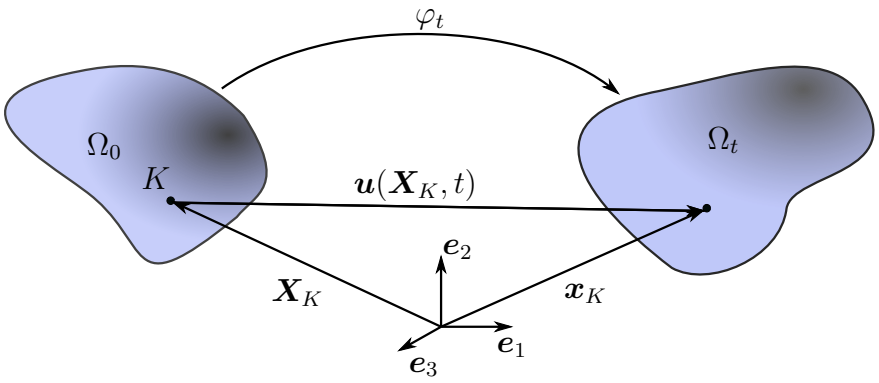

Figure 2.1: Illustration of the deformation φ_t of a body from reference configuration Ω_0 to displaced configuration Ω_t as well as reference coordinates $\boldsymbol{X}_K$ and displaced coordinates $\boldsymbol{x}_K$ of a point K.

thereby may be finite. An illustration of a mapping φ_t at a given instant in time is provided in Figure 2.1. For simplicity, the presentation is restricted to the case, where both reference and displaced configuration are described by the common Cartesian coordinate system $\{\boldsymbol{e}_1, \ldots, \boldsymbol{e}_{n_{\mathrm{dim}}}\}$. The extension to curvilinear coordinates through the concept of tensor calculus is well-known in nonlinear continuum mechanics and the reader is referred to e.g. Marsden and Hughes [143] for a thorough introduction to continuum mechanics using general curvilinear coordinate systems.

Deformation, in contrast to the motion introduced above which may include rigid body motions, describes the change of shape of the body. A first elementary measure of the local deformation at a material point is given by the *deformation gradient*

$$\boldsymbol{F} = \nabla_{\boldsymbol{X}} \boldsymbol{x} = \frac{\partial \boldsymbol{x}}{\partial \boldsymbol{X}} = \nabla_{\boldsymbol{X}} \boldsymbol{u} + \boldsymbol{I} \quad , \tag{2.3}$$

where $\nabla_{\boldsymbol{X}}$ denotes the material gradient operator and $\boldsymbol{I}$ the second order identity tensor. Being a second order tensor of which the first base vector resides in the displaced configuration, and the second one in the reference configuration, the deformation gradient is coined a two-point tensor. From its definition, the deformation gradient can also be interpreted as the mapping of infinitesimal line (vector) elements $\mathrm{d}\boldsymbol{X}$ in the reference configuration to the corresponding line element in the current configuration $\mathrm{d}\boldsymbol{x}$, viz.

$$\mathrm{d}\boldsymbol{x} = \boldsymbol{F}\mathrm{d}\boldsymbol{X} \quad . \tag{2.4}$$

Further, infinitesimal surface elements (defined as a vector in direction of the surface normal with length defined as the surface area) can be transformed from reference to displaced configuration by Nanson's formula

$$\mathrm{d}\boldsymbol{a} = J\boldsymbol{F}^{-\mathsf{T}}\mathrm{d}\boldsymbol{A} \quad , \tag{2.5}$$

where $J = \det(\boldsymbol{F})$ denotes the jacobian determinant of the mapping φ_t. Finally, infinitesimal volume elements $\mathrm{d}V$ in Ω_0 are transformed to volume elements $\mathrm{d}v$ in Ω_t by

$$\mathrm{d}v = J\mathrm{d}V \quad . \tag{2.6}$$

Due to the orientation preserving property of φ_t, it is ensured that $J > 0$ and hence no volume elements can be inverted.

Although starting point for the measurement of deformation, the deformation gradient itself is not a suitable measure for the local deformation of the body since it is contains not only of the deformation at a material point but also its rigid body rotation. More precisely, a polar decomposition of the deformation gradient yields

$$\boldsymbol{F} = \boldsymbol{R}\boldsymbol{U} = \boldsymbol{v}\boldsymbol{R} \ , \tag{2.7}$$

where $\boldsymbol{R} \in \mathrm{SO}(n_{\mathrm{dim}})$ denotes a rotation tensor, and $\boldsymbol{U}$ and $\boldsymbol{v}$ the symmetric positive definite right and left stretch tensors, respectively. As these stretch tensors do no longer include the rigid body rotation, they form the basis of objective measures of stretch and strain, such as the *right Cauchy–Green tensor* $\boldsymbol{C}$ and the *Green–Lagrange strain tensor* $\boldsymbol{E}$:

$$\boldsymbol{C} = \boldsymbol{U}^2 = \boldsymbol{F}^{\mathsf{T}}\boldsymbol{F} \ , \quad \boldsymbol{E} = \frac{1}{2}(\boldsymbol{C} - \boldsymbol{I}) \ . \tag{2.8}$$

Since $\boldsymbol{C}$ and $\boldsymbol{E}$ merely differ by a linear transformation, they essentially hold the same information, however, the Green–Lagrange strain tensor yields a zero tensor if only rigid body motions appear, i.e. when $\boldsymbol{F} \in \mathrm{SO}(n_{\mathrm{dim}})$ and therefore in fact acts as a *strain* measure. Unlike the deformation gradient, which is a two-point tensor, both the right Cauchy–Green tensor as well as the Green–Lagrange strain tensor are defined exclusively in the reference configuration. These two tensors are by no means the only viable measures of stretch and strain in the setting of nonlinear continuum mechanics. Yet, a multitude of others exist in the literature, which can be derived from the right and left stretch tensors $\boldsymbol{U}$ and $\boldsymbol{v}$. For the present thesis, however, those other strain measures are of no particular interest, such that the reader, at this point, is merely referred to the literature, e.g. Holzapfel [104].

In time dependent problems, not only the current displacement, but also its derivatives with respect to time are of interest. Velocities $\boldsymbol{v}$ and accelerations $\boldsymbol{a}$ of material points follow directly from the total time derivative of the displacement field, viz.

$$\boldsymbol{v} = \dot{\boldsymbol{u}} = \frac{\partial \boldsymbol{u}}{\partial t} = \frac{\partial \boldsymbol{x}}{\partial t} \ , \quad \boldsymbol{a} = \ddot{\boldsymbol{u}} = \frac{\partial^2 \boldsymbol{u}}{\partial t^2} = \frac{\partial^2 \boldsymbol{x}}{\partial t^2} \ . \tag{2.9}$$

Further, one can define the material and spatial velocity gradient $\dot{\boldsymbol{F}}$ and $\boldsymbol{L}$ as

$$\nabla_{\boldsymbol{X}} \boldsymbol{v} = \frac{\partial}{\partial \boldsymbol{X}} \frac{\partial \boldsymbol{x}}{\partial t} = \dot{\boldsymbol{F}} \ , \tag{2.10}$$

$$\nabla_{\boldsymbol{x}} \boldsymbol{v} = \frac{\partial}{\partial \boldsymbol{x}} \frac{\partial \boldsymbol{u}}{\partial t} = \dot{\boldsymbol{F}}\boldsymbol{F}^{-1} =: \boldsymbol{L} \ . \tag{2.11}$$

The spatial velocity gradient can be decomposed in its symmetric part, the so-called rate of deformation $\boldsymbol{D}$, and its skew symmetric part $\boldsymbol{W}$, the so-called spin, by

$$\boldsymbol{D} = \frac{1}{2}(\boldsymbol{L} + \boldsymbol{L}^{\mathsf{T}}) \ , \tag{2.12}$$

$$\boldsymbol{W} = \frac{1}{2}(\boldsymbol{L} - \boldsymbol{L}^{\mathsf{T}}) \ . \tag{2.13}$$

Finally, the rate of the right Cauchy–Green tensor and the Green–Lagrange strain can be obtained by time differentiation of (2.8) and yields

$$\dot{\boldsymbol{C}} = 2\dot{\boldsymbol{E}} = \dot{\boldsymbol{F}}^{\mathsf{T}}\boldsymbol{F} + \boldsymbol{F}^{\mathsf{T}}\dot{\boldsymbol{F}} \ , \tag{2.14}$$

which concludes the necessary kinematic description required in the following.

2.2 Conservation Laws and Entropy Inequality

The deformation of a body, as it can be described by the kinematics outlined in the previous section, needs to comply with basic physical principles such as conservation of mass, Newton's laws of motion as well as the first and second law of thermodynamics. These basic principles applied to infinitesimal volume elements within Ω_0 are the topic of the following sections.

2.2.1 Conservation of Mass

In the processes investigated in this thesis, mass is always conserved. Though, from a physical perspective, mass is conserved for any process, a mechanical model does not always have to comply with this principle as loss or gain in mass can be included in the model without specifically modeling the source or sink resulting in the change of mass. Examples for such systems with changing mass can be, for example, wear phenomena where mass at the contact interface is "lost" within the model if the debris is not explicitly handled, or conversely biological growth mechanisms where the "source" of mass, i.e. nutrients transported into the tissue, is not part of the mechanical model. Further, no convective mass transport is accounted for, such that the infinitesimal mass element of a volume element $\mathrm{d}V$ in Ω_0 needs to be conserved, i.e.

$$\frac{\mathrm{d}}{\mathrm{d}t}\mathrm{d}m = \frac{\mathrm{d}}{\mathrm{d}t}(\rho_0 \mathrm{d}V) = 0 \quad \Leftrightarrow \quad \rho_0 = \mathrm{const} \ , \tag{2.15}$$

which yields a constant reference density (since the volume element $\mathrm{d}V$ in the reference domain is constant). Analogously, the conservation of mass can be formulated for an infinitesimal volume element $\mathrm{d}v$ in the displaced configuration Ω_t. Using (2.6), one obtains

$$\frac{\mathrm{d}}{\mathrm{d}t}\mathrm{d}m = \frac{\mathrm{d}}{\mathrm{d}t}(\rho \mathrm{d}v) = \frac{\mathrm{d}}{\mathrm{d}t}(\rho J \mathrm{d}V) = 0 \quad \Leftrightarrow \quad \rho = J^{-1}\rho_0 \ , \tag{2.16}$$

i.e., to conserve mass, the density needs to transform reciprocally to the corresponding volume elements.

2.2.2 The Concept of Stress and Conservation of Linear Momentum

Before one can state the momentum balance (i.e. Newton's second law of motion) for arbitrary infinitesimal volume elements in Ω_t or Ω_0, the notion of forces needs to be extended to such a volume element. Let therefore Δa be a surface element of a fictitious surface introduced within Ω_t with the outward unit-normal $\boldsymbol{n}$ and $\Delta \boldsymbol{f}$ the resulting force on said surface. Then, following Cauchy's postulate, a surface traction $\boldsymbol{t}$ is defined via

$$\boldsymbol{t}(\boldsymbol{n}, \boldsymbol{x}, t) = \lim_{\Delta a \to 0} \frac{\Delta \boldsymbol{f}}{\Delta a} \ . \tag{2.17}$$

Since the surface Δa was introduced artificially into a body originally in equilibrium, the opposite surface, according to Newton's third law of motion, needs to be subjected to a force equal in size and pointing in opposite direction yielding

$$\boldsymbol{t}(\boldsymbol{n}, \boldsymbol{x}, t) = -\boldsymbol{t}(-\boldsymbol{n}, \boldsymbol{x}, t) \ . \tag{2.18}$$

Cauchy's postulate then states that there exists a second-order tensor $\boldsymbol{\sigma}(\boldsymbol{x}, t)$ called *Cauchy stress tensor* such that

$$\boldsymbol{t} = \boldsymbol{\sigma}\boldsymbol{n} \tag{2.19}$$

holds. Since both $\boldsymbol{t}$ and $\boldsymbol{n}$ are vectors defined in the spatial configuration, $\boldsymbol{\sigma}$ itself is a tensor with both basis vectors defined in the spatial configuration and is therefore termed a *spatial* stress tensor. In linearized kinematics (i.e. infinitesimal displacements) the reference configuration and the displaced configuration of the body coincide and therefore $\boldsymbol{\sigma}$ constitutes *the* unique measure of stress. In nonlinear continuum mechanics, a vast number of alternative stress measures can be defined, by selectively applying transformations of surface or volume elements derived above. These alternative stress measures may not have direct physical interpretation of (2.17) and (2.19), however they may be more suited for the formulation of certain balance equations or material laws. The stress measures relevant to this thesis will be briefly introduced in the following. First, there is the *Kirchhoff stress tensor*, which is obtained by scaling the Cauchy stress tensor with the Jacobian determinant:

$$\boldsymbol{\tau} = J\boldsymbol{\sigma} \quad . \tag{2.20}$$

Next, there is the *first Piola–Kirchhoff stress tensor*

$$\boldsymbol{P} = J\boldsymbol{\sigma}\boldsymbol{F}^{-\mathsf{T}} \quad , \tag{2.21}$$

which can be obtained by transforming the unit normal $\boldsymbol{n}$ in (2.17) into its counterpart in the reference configuration by means of Nanson's formula (2.5). Like the deformation gradient, the first Piola–Kirchhoff stress tensor is a two-point tensor, with the first basis vector defined in the spatial configuration and the second one defined in the reference configuration. A stress tensor completely defined in the reference configuration (and hence termed *material* stress tensor) can be obtained by

$$\boldsymbol{S} = \boldsymbol{F}^{-1}\boldsymbol{P} = J\boldsymbol{F}^{-1}\boldsymbol{\sigma}\boldsymbol{F}^{-\mathsf{T}} \tag{2.22}$$

and is called *second Piola–Kirchhoff stress*. Finally, another material stress tensor is the so-called *Mandel stress tensor* introduced by Mandel [141]

$$\boldsymbol{M} = \boldsymbol{C}\boldsymbol{S} \quad , \tag{2.23}$$

which, for elastically isotropic materials, can be interpreted as the Kirchhoff stress tensor rotated to the reference configuration, i.e. $\boldsymbol{M} = \boldsymbol{R}^{\mathsf{T}}\boldsymbol{\tau}\boldsymbol{R}$, see [116].

Shifting the focus back on balance equations, an infinitesimal volume element $\mathrm{d}v$ in the current configuration which is subjected to a distributed load (body force) $\boldsymbol{b}$ is considered. The balance of linear momentum applied to this volume element then reads

$$\nabla_{\boldsymbol{x}} \cdot \boldsymbol{\sigma} + \boldsymbol{b} = \rho\boldsymbol{a} \quad . \tag{2.24}$$

In many applications it may be more convenient not to formulate the equilibrium on a deformed infinitesimal volume element, since it is itself deformation dependent, but rather on a volume element in the reference configuration. This yields

$$\nabla_{\boldsymbol{X}} \cdot \boldsymbol{P} + \boldsymbol{b}_0 = \rho_0\boldsymbol{a} \quad , \tag{2.25}$$

where $\boldsymbol{b}_0 = J\boldsymbol{b}$ denotes the body force per unit volume in the reference domain.

2.2.3 Conservation of Angular Momentum

To be in (static or dynamic) equilibrium, not only the balance of linear momentum described by 2.24 or 2.25 need to hold, but also the balance of angular momentum. In the spatial configuration, this balance of angular momentum requires a symmetric Cauchy stress tensor (see e.g. [104]). In view of the transformation between the different stress measures introduced above, this can be stated equivalently as

$$\boldsymbol{\sigma} = \boldsymbol{\sigma}^{\mathsf{T}} \quad , \tag{2.26a}$$

$$\boldsymbol{\tau} = \boldsymbol{\tau}^{\mathsf{T}} \quad , \tag{2.26b}$$

$$\boldsymbol{P}\boldsymbol{F}^{\mathsf{T}} = \boldsymbol{F}\boldsymbol{P}^{\mathsf{T}} \quad , \tag{2.26c}$$

$$\boldsymbol{S} = \boldsymbol{S}^{\mathsf{T}} \quad , \tag{2.26d}$$

$$\boldsymbol{M}\boldsymbol{C} = \boldsymbol{C}\boldsymbol{M}^{\mathsf{T}} \quad . \tag{2.26e}$$

Since this balance of linear momentum is, in contrast to the balance of linear momentum, independent of any external loading, it will not appear explicitly in any of the numerical methods derived later but is built-in into any constitutive law such that, for instance, only symmetric second Piola–Kirchhoff stresses occur.

2.2.4 The Heat Flux and Conservation of Energy

In many applications, energy not only appears in form of elastic deformation, but also other physical effects such as thermal energy, electric or chemical potential or others. Their associated energy fluxes can be defined as the heat flux, electrical current or diffusion of chemical species. In the following, heat will be considered as the only energy flux within the system. The heat flux can be derived analogously to the concept of stress in Section 2.2.2. By introducing an fictitious surface Δa in Ω_t with the outward unit-normal $\boldsymbol{n}$, a fictitious (scalar) heat flux Δq_{n} appears across this surface with a positive sign if heat is entering the body through the surface. In the limit case of an infinitesimal surface area, one obtains the spatial surface flux

$$q_{\mathrm{n}}(\boldsymbol{n}, \boldsymbol{x}, t) = \lim_{\Delta a \to 0} \frac{\Delta q_{\mathrm{n}}}{\Delta a} \quad , \tag{2.27}$$

in analogy to Cauchy's postulate (2.17). Balance of energy across the fictitious interface Δa yields

$$q_{\mathrm{n}}(\boldsymbol{n}, \boldsymbol{x}, t) = -q_{\mathrm{n}}(-\boldsymbol{n}, \boldsymbol{x}, t) \quad , \tag{2.28}$$

which is ensured by Stokes' heat flux theorem, the thermal equivalent to Cauchy's theorem (2.19) in elasticity, which reads

$$q_{\mathrm{n}} = \boldsymbol{q} \cdot \boldsymbol{n} \quad , \tag{2.29}$$

where $\boldsymbol{q}$ is called spatial or Cauchy heat flux, a first order tensor with its basis vectors in the displaced configuration. Similar to the different stress measures defined in nonlinear continuum mechanics, also different measures of the heat flux may be defined. For instance, the corresponding material or Piola–Kirchhoff heat flux $\boldsymbol{Q}$ can be derived using the equality $\boldsymbol{q} \cdot \mathrm{d}\boldsymbol{a} = \boldsymbol{Q} \cdot \mathrm{d}\boldsymbol{A}$ and Nanson's formula (2.5) which results in

$$\boldsymbol{Q} = J\boldsymbol{F}^{-1}\boldsymbol{q} \quad . \tag{2.30}$$

With the definition of heat fluxes at hand, one can state the conservation of energy (also known as the first law of thermodynamics) for an infinitesimal volume element $\mathrm{d}V$ in Ω_0 as

$$\frac{\mathrm{d}}{\mathrm{d}t}(\frac{1}{2}\rho_0 \boldsymbol{v}^2 + e) = \nabla_{\boldsymbol{X}} \cdot (\boldsymbol{P}\boldsymbol{v}) + \boldsymbol{b}_0 \cdot \boldsymbol{v} - \nabla_{\boldsymbol{X}} \cdot \boldsymbol{Q} + R \ , \tag{2.31}$$

wherein the first term on the left hand side represents the kinetic energy and e the internal energy of the volume element $\mathrm{d}V$. On the right hand side, the first term represents the power performed by the traction on the boundary of $\mathrm{d}V$, the second one the power performed by the distributed load, the third one the thermal energy flux across the boundary of $\mathrm{d}V$ and the last one represents a heat (resp. energy) source term per unit undeformed volume. Using the identity

$$\nabla_{\boldsymbol{X}} \cdot (\boldsymbol{P}\boldsymbol{v}) = (\nabla_{\boldsymbol{X}} \cdot \boldsymbol{P}) \cdot \boldsymbol{v} + \boldsymbol{P} : \dot{\boldsymbol{F}} = (\nabla_{\boldsymbol{X}} \cdot \boldsymbol{P}) \cdot \boldsymbol{v} + \frac{1}{2}\boldsymbol{S} : \dot{\boldsymbol{C}} \ , \tag{2.32}$$

equation (2.31) can be re-arranged to the form

$$\dot{e} = \frac{1}{2}\boldsymbol{S} : \dot{\boldsymbol{C}} - \nabla_{\boldsymbol{X}} \cdot \boldsymbol{Q} + R + \underbrace{(\nabla_{\boldsymbol{X}} \cdot \boldsymbol{P} + \boldsymbol{b}_0 - \rho_0 \boldsymbol{a})}_{\overset{(2.25)}{=}0} \cdot \boldsymbol{v} \ , \tag{2.33}$$

from which the kinetic energy has been eliminated. Obviously, the conservation of energy (2.31) or (2.33) can be stated equivalently for an infinitesimal volume element $\mathrm{d}v$ in Ω_t. However, the given material form is sufficient for the subsequent derivations.

2.2.5 Entropy and the Second Law of Thermomechanics

The fist law of thermodynamics in the previous section ensures conservation of energy, however, it provides no information the direction processes proceed. For instance, from an energetic point of view, it would be admissible that, in the absence of any heat sources, an initially isothermal body heats up at on point and cools down at another as long as the total energy is conserved but apparently such a process does not occur in reality. The direction of physical processes is the main concern of the second law of thermodynamics. An additional physical quantity, the entropy, is introduced which, for any admissible process, may never decrease. The (material) entropy flux $\tilde{\boldsymbol{Q}}$ and source $\tilde{R}$ are closely related to the heat flux $\boldsymbol{Q}$ and heat source R via

$$\tilde{\boldsymbol{Q}} = \frac{\boldsymbol{Q}}{T} \ , \quad \tilde{R} = \frac{R}{T} \ , \tag{2.34}$$

where $T > 0$ denotes the absolute temperature. For an infinitesimal volume element $\mathrm{d}V$ in Ω_0 with the specific entropy η, the second law of thermodynamics then reads

$$\dot{\eta} + \nabla_{\boldsymbol{X}} \cdot \tilde{\boldsymbol{Q}} - \tilde{R} \geq 0 \ . \tag{2.35}$$

Accordingly, the local change of entropy $\dot{\eta}$ in an infinitesimal volume element $\mathrm{d}V$ is always greater or equal to the sum of the entropy flux entering $\mathrm{d}V$ across its boundary ($-\nabla_{\boldsymbol{X}} \cdot \tilde{\boldsymbol{Q}}$), and the local entropy production $\tilde{R}$. A substitution of (2.34) in (2.35), elimination of R via (2.33) and multiplying with the absolute temperature T yields the so-called Clausius–Duhem inequality

$$T\dot{\eta} - \dot{e} + \frac{1}{2}\boldsymbol{S} : \dot{\boldsymbol{C}} - \boldsymbol{Q} \cdot \nabla_{\boldsymbol{X}} T \geq 0 \ . \tag{2.36}$$

Entropy, temperature and internal energy are related to the (Helmholtz) free energy Ψ by means of the Legendre transformation

$$\Psi = e - T\eta \ , \tag{2.37}$$

which can be used to eliminate the specific energy e from (2.36) resulting in an alternative form of the Clausius-Duhem inequality

$$-\dot{T}\eta - \dot{\Psi} + \frac{1}{2}\boldsymbol{S} : \dot{\boldsymbol{C}} - \boldsymbol{Q} \cdot \nabla_{\boldsymbol{X}} T \geq 0 \ . \tag{2.38}$$

If one further introduces the physical observation, that the heat flux points in the opposite direction of the temperature gradient, i.e. heat flows, in the absence of heat sources, from hotter to cooler regions, the Clausius–Duhem inequality can be split into the heat conduction inequality and the Clausius–Planck inequality

$$\boldsymbol{Q} \cdot \nabla_{\boldsymbol{X}} T \leq 0 \ , \tag{2.39}$$

$$\mathcal{D}_{\text{int}} = -\dot{T}\eta - \dot{\Psi} + \frac{1}{2}\boldsymbol{S} : \dot{\boldsymbol{C}} \geq 0 \ , \tag{2.40}$$

which is obviously more restrictive than (2.38). Therein, $\mathcal{D}_{\text{int}}$ denotes the so-called internal dissipation.

2.3 Constitutive Relations

The balance equations derived in the previous section depend, on the one hand, on the displacement and temperature state and their rates and gradients, and, on the other hand, on the mechanical stress and the heat flux. However, the balance equations do not provide the necessary correlations, for instance how to determine stresses depending on the displacement and temperature state. This connection is introduced by means of constitutive relations which are derived from material modeling. As the term already indicates, material modeling is concerned with the derivation of models that describe, for example, the stress-strain relation of a particular material. These models may be purely phenomenological, derived from micromechanical considerations or a combination of the two.

2.3.1 State Variables and Response Functions

In thermodynamics, one usually distinguishes between *state variables* (or sometimes called independent variables) and dependent variables derived from the state variables and their temporal and spatial derivatives. Though there is no unique separation between state and dependent variables, in continuum thermomechanics usually the displacement field $\boldsymbol{u}$ and the temperature field T are considered state variables, whereas the stress $\boldsymbol{S}$, the free energy Ψ, the entropy η and the heat flux $\boldsymbol{Q}$ are considered dependent variables.[1] Displacement and temperature are so-called

[1] Also this set of dependent variables is not unique as, for instance, other stress measures may be used or the Cauchy heat flux $\boldsymbol{q}$ instead of the material heat flux $\boldsymbol{Q}$. The free energy or entropy could be replaced by the internal energy e via the Legendre transformation (2.37).

observable quantities, since they can, in principle, be measured. For purely thermo-elastic processes, knowledge of these observable quantities form a sufficient set of state variables. For inelastic processes, however, additional *internal variables of state* are required to track the local inelastic behavior of the material. These internal variables may be scalar, vector- or tensor-valued. In the abstract setting, one internal variable of state will be denoted by $\boldsymbol{\alpha}_j = \boldsymbol{\alpha}_j(\boldsymbol{X}, t)$ and all internal variables of state will be summarized in the set $\boldsymbol{\alpha} = \{\boldsymbol{\alpha}_j\}$. Most inelastic processes are associated with some form of internal dissipation (e.g. visco-elasticity or elasto-plasticity), but others are not, such as, for instance, growth and remodeling in living soft tissue [44]. While keeping the derivations as general as possible, the present work focuses on elasto-plasticity as the inelastic effect of concern; for a more general review on the concept of internal variables of state, the reader is referred to, e.g., the review article of Maugin [146]. The derived quantities then follow from the state variables trough *response functions* $\mathfrak{R}$, i.e.

$$\{\boldsymbol{S}, \Psi, \eta, \boldsymbol{Q}\} = \mathfrak{R}(\boldsymbol{F}, T, \nabla_{\boldsymbol{X}} T, \boldsymbol{\alpha}, \boldsymbol{X}) \ , \tag{2.41}$$

where, for simplicity, only material quantities are used. Other dependencies of the response functions might be conceivable, however some are in violation with the requirements specified in the following and are therefore already omitted at this point. For example, a dependency on the displacement field itself, in contrast to its derivative in the deformation gradient, contradicts the principle of material objectivity. Higher order spatial derivatives of the displacement field, on the other hand, can be used in the context of Cosserat or multipolar theory (Green and Rivlin [85], Toupin [218]) but are not considered in this work. Spatial gradients of internal variables of state are admissible as well and necessary in, for example, strain gradient plasticity (e.g. Fleck and Hutchinson [73]) and gradient damage models (e.g. Peerlings *et al.* [165]). In the classical plasticity models used in the course of this thesis, these spatial gradients are not used and therefore omitted at this point. For *homogeneous* materials, the material response depends on the state variables but is independent of the position within the body, i.e. independent of $\boldsymbol{X}$. Merely for simplicity, this thesis considers homogeneous materials only.

While there is quite some freedom in developing material models that best fit experimental data for a specific material, some basic requirements summarized in the following have to hold. For an in-depth introduction of these concepts, the interested reader is referred to the text books of Bertram [15], de Souza Neto *et al.* [57], Holzapfel [104], Marsden and Hughes [143].

Thermodynamic Determinism The axiom of determinism states that the response functions may only depend on the current state variables and past values but never on future values. In (2.41), this principle is already accounted for in an even stricter form since only state variables at the current time are involved. The dependency on the current values of the state variables only is sufficient for many materials and tracking a finite or even infinite history is impractical in numerical methods. For example, biological remodeling processes as modeled by constrained mixture models as introduced by Humphrey and Rajagopal [113] require such an infinite history, which can be overcome in more recent homogenized constrained mixture models [20, 45] which again only depend on the current state variables.

Local Action Local action requires the response function at a given point $\boldsymbol{X}$ to only depend on values of the state variables in finite neighborhood of $\boldsymbol{X}$. In the case of so-called *simple* materials, the material response at a point is determined by the state in an infinitesimal neighborhood

only, and hence, the response functions (2.41) can be formulated in terms of state variables and their gradients only.

Frame Indifference The principle of frame indifference states, that the different observers should monitor the same physical behavior. The observers thereby differ in an arbitrary relative motion. This principle can be equivalently stated as the independence of the response to superimposed rigid body motions of the displaced configuration [104]. For a motion φ_t as introduced in (2.1), a motion $\widetilde{\varphi}_t$ with a superimposed rigid body motion can be defined as

$$\widetilde{\varphi}_t : \Omega_0 \to \widetilde{\Omega_t}, \quad \boldsymbol{X} \mapsto \widetilde{\boldsymbol{x}}(\boldsymbol{X}) = \widetilde{\boldsymbol{R}}\varphi_t(\boldsymbol{X}) + \widetilde{\boldsymbol{c}} \ , \tag{2.42}$$

by a relative rotation $\widetilde{\boldsymbol{R}} \in \mathrm{SO}(n_{\mathrm{dim}})$ and a relative displacement $\widetilde{\boldsymbol{c}}$, which may depend on time but not on the material point $\boldsymbol{X}$. The motion $\widetilde{\varphi}_t$ results in a deformation gradient $\widetilde{\boldsymbol{F}} = \widetilde{\boldsymbol{R}}\boldsymbol{F}$. As the response functions in (2.41) are defined for material quantities, i.e. quantities defined in the reference configuration, they should, according to the principle of frame indifference, be unaltered by the superimposed rigid body rotation of the displaced configuration, viz.

$$\mathfrak{R}(\boldsymbol{F}, T, \nabla_{\boldsymbol{X}} T, \boldsymbol{\alpha}, \boldsymbol{X}) = \mathfrak{R}(\widetilde{\boldsymbol{R}}\boldsymbol{F}, T, \nabla_{\boldsymbol{X}} T, \boldsymbol{\alpha}, \boldsymbol{X}) \ . \tag{2.43}$$

Material Symmetry Similar to the principle of frame indifference, material symmetry requires the response to be invariant with respect to a rotation of the reference frame. Consider therefore a deformation $\breve{\varphi}_t$, in which the current configuration coincides with Ω_t, but the reference domain $\widetilde{\Omega_0}$ differs from Ω_0 by a rotation $\breve{\boldsymbol{R}} \in \mathrm{SO}(n_{\mathrm{dim}})$:

$$\breve{\varphi}_t : \widetilde{\Omega_0} \to \Omega_t, \quad \widetilde{\boldsymbol{X}} = \breve{\boldsymbol{R}}\boldsymbol{X} \mapsto \boldsymbol{x} \ . \tag{2.44}$$

The corresponding deformation gradient reads $\breve{\boldsymbol{F}} = \nabla_{\widetilde{\boldsymbol{X}}} \boldsymbol{x} = \boldsymbol{F}\breve{\boldsymbol{R}}^{\mathsf{T}}$. Moreover, the rotation $\breve{\boldsymbol{R}}$ is applied to any material direction vector $\boldsymbol{a}_i$ determining possible axes of anisotropy within the material to obtain the directions in $\widetilde{\Omega_0}$ as $\breve{\boldsymbol{a}}_i = \breve{\boldsymbol{R}}\boldsymbol{a}_i$ and any internal variable. Let therefore $\boldsymbol{\alpha} = \{\alpha_0, \boldsymbol{\alpha}_1, \boldsymbol{\alpha}_2\}$ consist of a scalar α_0, a vector $\boldsymbol{\alpha}_1$ and a second-order tensor $\boldsymbol{\alpha}_2$. The corresponding internal variables in $\widetilde{\Omega_0}$ are then obtained as

$$\breve{\boldsymbol{\alpha}} = \{\alpha_0, \breve{\boldsymbol{R}}\boldsymbol{\alpha}_1, \breve{\boldsymbol{R}}\boldsymbol{\alpha}_2\breve{\boldsymbol{R}}^{\mathsf{T}}\} \ . \tag{2.45}$$

From the principle of material symmetry it then follows, that

$$\begin{aligned} \{\boldsymbol{S}, \Psi, \eta, \boldsymbol{Q}\} = \mathfrak{R}(\boldsymbol{F}, T, \nabla_{\boldsymbol{X}} T, \boldsymbol{\alpha}, \boldsymbol{X}) \quad \Leftrightarrow \\ \{\breve{\boldsymbol{R}}\boldsymbol{S}\breve{\boldsymbol{R}}^{\mathsf{T}}, \Psi, \eta, \breve{\boldsymbol{R}}\boldsymbol{Q}\} = \mathfrak{R}(\boldsymbol{F}\breve{\boldsymbol{R}}^{\mathsf{T}}, T, \nabla_{\widetilde{\boldsymbol{X}}} T, \breve{\boldsymbol{\alpha}}, \widetilde{\boldsymbol{X}}) \ . \end{aligned} \tag{2.46}$$

Thermodynamic Consistency Finally, thermodynamic consistency (sometimes referred to as axiom of entropy production) requires any material model to satisfy the Clausius–Duhem inequality (2.38).

2.3.2 Fourier's Law of Heat Conduction

A simple phenomenological law of heat conduction that satisfies (2.39) is known as Duhamel's law of heat conduction, which, in spatial and material description, reads

$$\boldsymbol{q} = -\frac{1}{J}\boldsymbol{F}\boldsymbol{\kappa_0}\boldsymbol{F}^{\mathsf{T}}\nabla_{\boldsymbol{x}}T \ , \tag{2.47a}$$

$$\boldsymbol{Q} = -\boldsymbol{\kappa_0}\nabla_{\boldsymbol{X}}T \ , \tag{2.47b}$$

with a positive (semi-) definite second order conductivity tensor $\boldsymbol{\kappa_0}$ which may depend on displacements and temperatures. For isotropic heat conduction (in the current configuration) one further requires $\boldsymbol{F}\boldsymbol{\kappa_0}\boldsymbol{F}^{\mathsf{T}} = \kappa_0\boldsymbol{I}$ with the scalar thermal conductivity κ_0 which may still depend on displacements and temperatures. If finally this thermal conductivity is assumed to be a constant value k_0, one obtains Fourier's law of heat conduction

$$\boldsymbol{q} = -\frac{k_0}{J}\nabla_{\boldsymbol{x}}T \ , \tag{2.48a}$$

$$\boldsymbol{Q} = -k_0\boldsymbol{C}^{-1}\nabla_{\boldsymbol{X}}T \ , \tag{2.48b}$$

in the extension to nonlinear kinematics as derived e.g. in Holzapfel [104]. As the material heat flux depends on the displacement only via the right Cauchy–Green tensor, the principles of frame indifference and material symmetry stated in the previous section can easily be shown for the constitutive equation (2.48).

2.3.3 Thermo-Elasticity

For (thermo-) elastic materials, no internal variables of state are necessary, i.e. $\boldsymbol{\alpha} = \emptyset$, since an elastic response does not depend on any deformation history but can rather be determined solely by the current deformation and temperature state. Moreover, to ensure frame indifference (2.43), we assume the free energy Ψ to depend on the deformation through the right Cauchy–Green tensor $\boldsymbol{C}$ rather than the deformation gradient $\boldsymbol{F}$, and, for simplicity, homogeneous materials are considered. With these assumptions, the Clausius–Planck inequality (2.40) reads

$$\begin{aligned}\mathcal{D}_{\text{int}} = -\dot{T}\eta - \frac{\partial\Psi}{\partial\boldsymbol{C}} : \dot{\boldsymbol{C}} - \frac{\partial\Psi}{\partial T}\dot{T} - \frac{\partial\Psi}{\partial\nabla_{\boldsymbol{X}}T}\cdot\nabla_{\boldsymbol{X}}\dot{T} + \frac{1}{2}\boldsymbol{S} : \dot{\boldsymbol{C}} = \\ \left(-\eta - \frac{\partial\Psi}{\partial T}\right)\dot{T} + \left(\frac{1}{2}\boldsymbol{S} - \frac{\partial\Psi}{\partial\boldsymbol{C}}\right) : \dot{\boldsymbol{C}} - \frac{\partial\Psi}{\partial\nabla_{\boldsymbol{X}}T}\cdot\nabla_{\boldsymbol{X}}\dot{T} \geq 0 \ .\end{aligned} \tag{2.49}$$

As this inequality must hold for any $\dot{\boldsymbol{C}}$ and $\dot{T}$, the terms in parenthesis must vanish[1] which gives rise to the thermo-elastic constitutive equations for the second Piola–Kirchhoff stress, and, using (2.22), equivalently for the first Piola–Kirchhoff stress

$$\boldsymbol{S} = 2\frac{\partial\Psi}{\partial\boldsymbol{C}} \ , \quad \boldsymbol{P} = \frac{\partial\Psi}{\partial\boldsymbol{F}} \ , \tag{2.50}$$

[1] Assume a given state defined by $\boldsymbol{C}$ and T and rates $\dot{\boldsymbol{C}}$ and $\dot{T}$. Then, merely by changing loading conditions, a configuration can be achieved in which $\tilde{\dot{\boldsymbol{C}}} = -\dot{\boldsymbol{C}}$ and $\tilde{\dot{T}} = -\dot{T}$. Hence, for (2.49) to hold for both states, the terms in parenthesis must vanish.

and the specific entropy

$$\eta = -\frac{\partial \Psi}{\partial T} \ , \tag{2.51}$$

Consequently, the last term in (2.49) must vanish to ensure (2.49) to be valid for any temperature rate (or the gradient thereof). This means, that while the free energy Ψ may depend on the temperature itself, it may not depend on the temperature gradient. In summary, (thermo-) elastic materials yield no internal dissipation, i.e. $\mathcal{D}_{\text{int}} \equiv 0$, what can be seen as the fundamental concept of elasticity. The elastic response (2.50) is called isotropic, if the free energy Ψ is an isotropic tensor function of the right Cauchy–Green tensor, i.e. $\Psi(\boldsymbol{C}, T) = \Psi(\tilde{\boldsymbol{R}}^{\mathsf{T}} \boldsymbol{C} \tilde{\boldsymbol{R}}, T)$ for any rotation $\tilde{\boldsymbol{R}} \in \mathrm{SO}(n_{\text{dim}})$. this isotropy requirement can be ensured, if $\Psi = \Psi(I_1, \ldots, I_{n_{\text{dim}}}, T)$ depends on $\boldsymbol{C}$ only via its invariants

$$I_1 = \operatorname{tr} \boldsymbol{C} \ , \quad I_2 = \frac{1}{2}\left((\operatorname{tr} \boldsymbol{C})^2 - \operatorname{tr}\left(\boldsymbol{C}^2\right)\right) \ , \quad I_3 = \det \boldsymbol{C} \ , \tag{2.52}$$

which remain constant under a rotation of $\boldsymbol{C}$. IN the special case of $n_{\text{dim}} = 2$, only two of these invariants are independent and any pair of two may be chosen.

2.3.4 Thermo-Elasto-Plasticity

The concept of plasticity is related to the fact, that most material have a limited load bearing capacity. If this capacity were to be exceeded, the material limits the stress by plastic relaxation. In the following sections, first the kinematics of elasto-plastic processes is introduced and the corresponding thermodynamic implications are deduced. Finally, yield functions are introduced to determine whether a given stress state is admissible or if plastic yielding is necessary to relax the occurring stress.

2.3.4.1 Kinematics of Finite Elasto-Plasticity

At finite deformations, the kinematics of elasto-plasticity is described by a local multiplicative split of the deformation gradient

$$\boldsymbol{F}(\boldsymbol{X}, t) = \boldsymbol{F}_{\text{e}}(\boldsymbol{X}, t) \boldsymbol{F}_{\text{p}}(\boldsymbol{X}, t) \tag{2.53}$$

at every material point $\boldsymbol{X}$ into an elastic and a plastic stage as originally introduced by Lee [134]. The kinematics of this process is illustrated in Figure 2.2: By the motion φ_t, the infinitesimal volume element located at the point K with material coordinates $\boldsymbol{X}_K$ is subjected to a deformation gradient $\boldsymbol{F}$. If it were possible to extract this infinitesimal volume element from the deformed body, it would return to a relaxed state reversing any elastic deformation $\boldsymbol{F}_{\text{e}}$. A potential plastic deformation of the volume element would, however, remain present. Formally, the remaining plastic deformation after unloading can be expressed as $\boldsymbol{F}_{\text{p}} = \boldsymbol{F}_{\text{e}}^{-1} \boldsymbol{F}$.[1] In plasticity of metals, especially single crystals, this decomposition of the deformation gradient also has a micromechanical justification illustrated in Figure 2.2: The plastic deformation gradient is associated with

[1] In presence of substantial kinematic hardening, see Section 2.3.4.3, the unloaded, stress free state might actually not be admissible. Since this elastic unloading is, however, just an illustration of the multiplicative kinematics, kinematic hardening does not preclude the validity of the kinematic assumption (2.53).

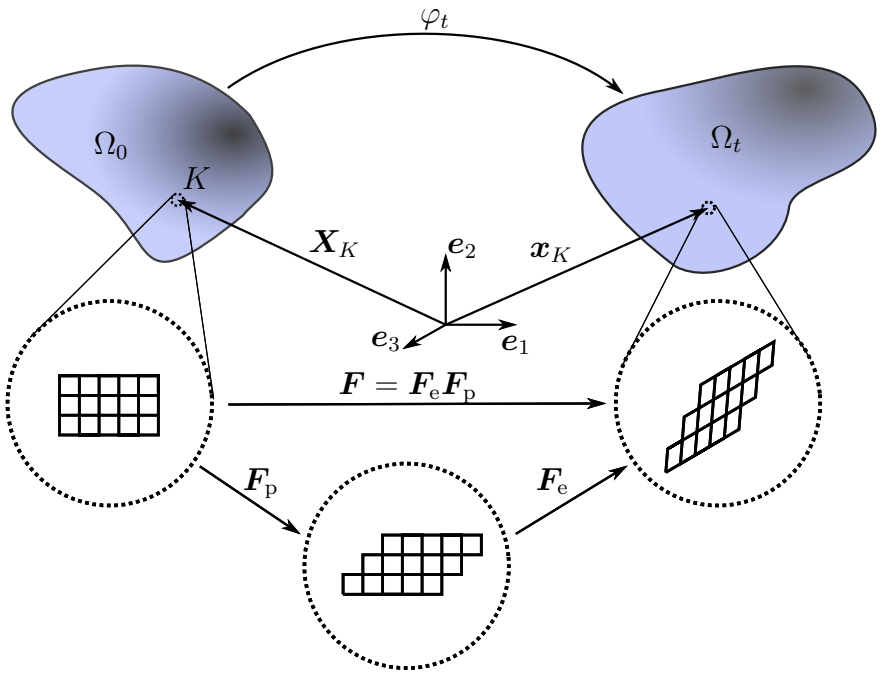

Figure 2.2: Illustration of the multiplicative decomposition of the deformation gradient at point K and time t into an elastic and plastic part as $\boldsymbol{F}(\boldsymbol{X}_K, t) = \boldsymbol{F}_\mathrm{e}(\boldsymbol{X}_K, t)\boldsymbol{F}_\mathrm{p}(\boldsymbol{X}_K, t)$. $\boldsymbol{F}_\mathrm{p}$ is associated with inelastic slip of lattice layers and $\boldsymbol{F}_\mathrm{e}$ is related to elastic lattice distortion.

the slip of atom layers or the movement of dislocations, whereas the elastic deformation is related to lattice distortion. In general, the rotational orientation of the intermediate configuration is undetermined as an equivalent split $\boldsymbol{F} = \boldsymbol{F}_\mathrm{e}\boldsymbol{F}_\mathrm{p} = (\boldsymbol{F}_\mathrm{e}\tilde{\boldsymbol{R}})(\tilde{\boldsymbol{R}}^\mathsf{T}\boldsymbol{F}_\mathrm{p}) = \tilde{\boldsymbol{F}}_\mathrm{e}\tilde{\boldsymbol{F}}_\mathrm{p}$ can be defined by a rotation of the intermediate configuration by the proper orthogonal tensor $\tilde{\boldsymbol{R}} \in \mathrm{SO}(n_\mathrm{dim})$. Therefore, the plastic deformation gradient $\boldsymbol{F}_\mathrm{p}$ cannot be chosen as an internal variable of state satisfying the material symmetry (see Section 2.3.1) if no assumption on the orientation of the intermediate configuration is made. To overcome this non-uniqueness, Mandel [142] proposed the use of a so-called *isoclinic* intermediate configuration, in which the orientation of the reference configuration is preserved (see Figure 2.2). If such an isoclinic intermediate configuration is used, the plastic deformation gradient becomes a quasi-material tensor and therefore frame indifference and material symmetry can easily be proven for $\boldsymbol{F}_\mathrm{p}$ as an internal variable.[1] Similar to the derivations in Section 2.1 several kinematic quantities can be derived from the elastic and plastic deformation gradients $\boldsymbol{F}_\mathrm{e}$ and $\boldsymbol{F}_\mathrm{p}$ such as the corresponding elastic right Cauchy–Green tensor

$$\boldsymbol{C}_\mathrm{e} = \boldsymbol{F}_\mathrm{e}^\mathsf{T}\boldsymbol{F}_\mathrm{e} = \boldsymbol{F}_\mathrm{p}^{-\mathsf{T}}\boldsymbol{C}\boldsymbol{F}_\mathrm{p}^{-1} \quad . \tag{2.54}$$

As the elastic right Cauchy–Green tensor $\boldsymbol{C}_\mathrm{e}$, which is defined in the intermediate configuration, does only depend on the elastic stretch but not on the rigid body rotation part of $\boldsymbol{F}_\mathrm{e}$, it can be used as an frame invariant measure of elastic stretch. In analogy to (2.11) - (2.13), the plastic

[1] This also holds for other internal variables defined in the intermediate configuration.

velocity gradient, plastic rate of deformation and plastic material spin can be defined as

$$\boldsymbol{L}_\mathrm{p} = \dot{\boldsymbol{F}}_\mathrm{p}\boldsymbol{F}_\mathrm{p}^{-1} \ , \tag{2.55}$$

$$\boldsymbol{D}_\mathrm{p} = \frac{1}{2}(\boldsymbol{L}_\mathrm{p} + \boldsymbol{L}_\mathrm{p}^\mathsf{T}) \ , \tag{2.56}$$

$$\boldsymbol{W}_\mathrm{p} = \frac{1}{2}(\boldsymbol{L}_\mathrm{p} - \boldsymbol{L}_\mathrm{p}^\mathsf{T}) \ . \tag{2.57}$$

Remark 2.1 (Isochoric plastic flow)**.** *A plastic flow is termed isochoric, if the plastic deformation preserves the volume of each infinitesimal volume element, i.e.* $\frac{\mathrm{d}}{\mathrm{d}t}\det\boldsymbol{F}_\mathrm{p} \equiv 0$*. According to* (2.55)*, this is equivalent to* $\operatorname{tr}\boldsymbol{L}_\mathrm{p} \equiv 0$*.*

2.3.4.2 Thermodynamics of Elasto-Plasticity

Besides this kinematic description of plastic deformation via $\boldsymbol{F}_\mathrm{p}$, additional internal variables of state might be necessary to accurately represent the micromechanical changes within the material. For instance, interaction of moving dislocations in a crystal lattice can result in hardening effects. To account for those hardening effects, a scalar α_i and a second order tensor $\boldsymbol{\alpha}_\mathrm{k}$ are introduced as internal variables of state, which will be associated with isotropic and kinematic hardening, respectively (see Section 2.3.4.3). Within the thermodynamical framework presented above, this results in the set of internal variables $\boldsymbol{\alpha} = \{\boldsymbol{F}_\mathrm{p}, \alpha_\mathrm{i}, \boldsymbol{\alpha}_\mathrm{k}\}$. Furthermore, it is assumed that the free energy Ψ decomposes into additive components associated with elastic deformation, heat and hardening effects, viz.

$$\Psi(\boldsymbol{C}, T, \boldsymbol{F}_\mathrm{p}, \alpha_\mathrm{i}, \boldsymbol{\alpha}_\mathrm{k}) = \Psi_\mathrm{e}(\boldsymbol{C}_\mathrm{e}, T) + \Psi_\vartheta(T) + \Psi_\mathrm{p}(\alpha_\mathrm{i}, \boldsymbol{\alpha}_\mathrm{k}, T) \ . \tag{2.58}$$

At any point, sufficient smoothness of Ψ with respect to all arguments is assumed. Inserting these assumptions into the Clausius–Duhem inequality (2.36) and using the heat conduction inequality (2.39) results in the Clausius–Planck inequality for elasto-plastic solids

$$\begin{aligned} \mathcal{D}_\mathrm{int} = -\dot{T}\eta - \dot{\Psi} + \frac{1}{2}\boldsymbol{S} : \dot{\boldsymbol{C}} = \\ \left(-\eta - \frac{\partial\Psi}{\partial T}\right)\dot{T} + \left(\frac{1}{2}\boldsymbol{S} - \boldsymbol{F}_\mathrm{p}^{-1}\frac{\partial\Psi_\mathrm{e}}{\partial\boldsymbol{C}_\mathrm{e}}\boldsymbol{F}_\mathrm{p}^{-\mathsf{T}}\right) : \dot{\boldsymbol{C}} \\ + \boldsymbol{\Sigma} : \boldsymbol{L}_\mathrm{p} + A_\mathrm{i}\dot{\alpha}_\mathrm{i} + \boldsymbol{A}_\mathrm{k} : \dot{\boldsymbol{\alpha}}_\mathrm{k} \geq 0 \ , \end{aligned} \tag{2.59}$$

with the Mandel stress of elasto-plasticity $\boldsymbol{\Sigma} = 2\boldsymbol{C}_\mathrm{e}\frac{\partial\Psi_\mathrm{e}}{\partial\boldsymbol{C}_\mathrm{e}}$ as introduced by Mandel [141] and the conjugate forces $A_\mathrm{i} = -\frac{\partial\Psi_\mathrm{p}}{\partial\alpha_\mathrm{i}}$ and $\boldsymbol{A}_\mathrm{k} = -\frac{\partial\Psi_\mathrm{p}}{\partial\boldsymbol{\alpha}_\mathrm{k}}$ to the internal variables α_i and $\boldsymbol{\alpha}_\mathrm{k}$. For elastically isotropic materials, the Mandel stress $\boldsymbol{\Sigma}$ can be interpreted as the Kirchhoff stress rotated to the intermediate configuration by $\boldsymbol{\Sigma} = \boldsymbol{R}_\mathrm{e}^\mathsf{T}\boldsymbol{\tau}\boldsymbol{R}_\mathrm{e}$ with the rotation tensor $\boldsymbol{R}_\mathrm{e}$ as the rotational part of $\boldsymbol{F}_\mathrm{e}$ derived by polar decomposition (2.7). As in the thermo-elastic case, (2.59) has to hold for any $\dot{T}$ and $\dot{\boldsymbol{C}}$ and therefore the terms in parenthesis must vanish. This yields the constitutive equations for the entropy η and the second Piola–Kirchhoff stress in an elasto-plastic solid

$$\eta = -\frac{\partial\Psi}{\partial T} \ , \tag{2.60}$$

$$\boldsymbol{S} = 2\boldsymbol{F}_\mathrm{p}^{-1}\frac{\partial \Psi_\mathrm{e}}{\partial \boldsymbol{C}_\mathrm{e}}\boldsymbol{F}_\mathrm{p}^{-\mathsf{T}} \quad , \quad \boldsymbol{P} = \frac{\partial \Psi}{\partial \boldsymbol{F}_\mathrm{e}}\boldsymbol{F}_\mathrm{p}^{-\mathsf{T}} \quad . \tag{2.61}$$

The equivalent form for the first Piola–Kirchhoff stress is again obtained using (2.22). With (2.60) and (2.61), the Clausius–Planck inequality (2.59) reduces to

$$\mathcal{D}_\mathrm{int} = \boldsymbol{\Sigma} : \boldsymbol{L}_\mathrm{p} + A_\mathrm{i}\dot{\alpha}_\mathrm{i} + \boldsymbol{A}_\mathrm{k} : \dot{\boldsymbol{\alpha}}_\mathrm{k} \geq 0 \quad . \tag{2.62}$$

In the following, isotropic elastic materials will be considered exclusively for which $\boldsymbol{C}_\mathrm{e}$ and $\frac{\partial \Psi_\mathrm{e}}{\partial \boldsymbol{C}_\mathrm{e}}$ commute and therefore the Mandel stress $\boldsymbol{\Sigma}$ is symmetric. As a consequence, the plastic spin $\boldsymbol{W}_\mathrm{p}$ does not contribute to the dissipation ($\boldsymbol{\Sigma} : \boldsymbol{W}_\mathrm{p} \equiv 0$) and the dissipation inequality (2.62) is equivalent to

$$\mathcal{D}_\mathrm{int} = \boldsymbol{\Sigma} : \boldsymbol{D}_\mathrm{p} + A_\mathrm{i}\dot{\alpha}_\mathrm{i} + \boldsymbol{A}_\mathrm{k} : \dot{\boldsymbol{\alpha}}_\mathrm{k} \geq 0 \quad . \tag{2.63}$$

Remark 2.2 (Internal dissipation in the presence of elastic anisotropy)**.** *For elastically anisotropic materials, the Mandel stress $\boldsymbol{\Sigma}$ is no longer symmetric, however due to the balance of angular momentum, it still has to satisfy $\boldsymbol{\Sigma}\boldsymbol{C}_\mathrm{e} = \boldsymbol{C}_\mathrm{e}\boldsymbol{\Sigma}^\mathsf{T}$ in analogy to* (2.26e)*. Though non-symmetric, $\boldsymbol{\Sigma}$ is therefore confined to a six-dimensional manifold in the nine-dimensional space of second order tensors. By an orthogonal projection onto this manifold, the plastic velocity gradient $\boldsymbol{L}_\mathrm{p}$ can then be decomposed into two parts: The one part that lies on the manifold and therefore contributes to the dissipation ($\boldsymbol{D}_\mathrm{p}$ for elastically isotropic materials) and the other part orthogonal to the manifold that does not contribute to the dissipation ($\boldsymbol{W}_\mathrm{p}$ for elastically isotropic materials).*

The requirement of a positive dissipation poses some restrictions on the otherwise, up to now, undetermined evolution of the internal variables, i.e. on $\dot{\boldsymbol{F}}_\mathrm{p}$, $\dot{\alpha}_\mathrm{i}$ and $\dot{\boldsymbol{\alpha}}_\mathrm{k}$. Following Moreau [153] (see also de Souza Neto *et al.* [57]), positive dissipation for all loading conditions can be ensured by postulating a convex[1] dissipation potential Ξ_p, from which $\boldsymbol{D}_\mathrm{p}$, $\dot{\alpha}_\mathrm{i}$ and $\dot{\boldsymbol{\alpha}}_\mathrm{k}$ follow from the (sub-) differential

$$(\boldsymbol{D}_\mathrm{p}, \dot{\alpha}_\mathrm{i}, \dot{\boldsymbol{\alpha}}_\mathrm{k}) \in \partial\Xi_\mathrm{p}\left(\boldsymbol{\Sigma}, A_\mathrm{i}, \boldsymbol{A}_\mathrm{k}\right) \quad , \tag{2.64}$$

and at the origin

$$\Xi_\mathrm{p}(\boldsymbol{0}, 0, \boldsymbol{0}) = 0 \quad \text{and} \quad (\boldsymbol{0}, 0, \boldsymbol{0}) \in \partial\Xi_\mathrm{p}(\boldsymbol{0}, 0, \boldsymbol{0}) \quad . \tag{2.65}$$

The current state may enter Ξ_p as parameters via $\boldsymbol{F}$, T, $\boldsymbol{F}_\mathrm{p}$, α_i and $\boldsymbol{\alpha}_\mathrm{k}$ as long as the Ξ_p is frame indifferent and satisfies the material symmetry.

2.3.4.3 Yield Function and Admissible Stress States

The previous section derived some requirements on the evolution of the internal variables of state, i.e. on $\dot{\boldsymbol{F}}_\mathrm{p}$, $\dot{\alpha}_\mathrm{i}$ and $\dot{\boldsymbol{\alpha}}_\mathrm{k}$, by (2.63) but does not provide any further specifications on how these temporal derivatives look like. The presented thermodynamics in Section 2.3.4.2 rather applies to any other inelastic material described by a multiplicative decomposition of the deformation gradient as well, for instance the model of visco-elasticity proposed by Reese and Govindjee [184]. In elasto-plasticity, one assumes that stresses cannot exceed a certain threshold (the yield

[1] Convexity of the dissipation potential may be relaxed to star convexity while still maintaining a positive dissipation, see Green and Naghdi [84].

limit). In the stress space, the admissible states are indicated by non-positive values of the yield function

$$\phi_{\mathrm{p}}(\boldsymbol{\Sigma}, A_{\mathrm{i}}, \boldsymbol{A}_{\mathrm{k}}; T) = \Sigma_{\mathrm{eq}}(\boldsymbol{\eta}) - (y_0 - A_{\mathrm{i}}) = \Sigma_{\mathrm{eq}}(\boldsymbol{\eta}) - Y \quad , \tag{2.66}$$

where y_0 and $Y = y_0 - A_{\mathrm{i}}$ represent the initial and effective yield stress, respectively. The scalar equivalent stress Σ_{eq} is a convex function[1] of the effective stress

$$\boldsymbol{\eta} = \boldsymbol{\Sigma} - \boldsymbol{A}_{\mathrm{k}} \tag{2.67}$$

and depends on the chosen plasticity model. The temperature may enter the yield function as a parameter. The elastic domain $\mathcal{E}$ in the stress space is then defined by the region of negative yield functions, viz.

$$\mathcal{E}(A_{\mathrm{i}}, \boldsymbol{A}_{\mathrm{k}}; T) = \left\{ \boldsymbol{\Sigma} \in \Re^{n_{\mathrm{dim}} \times n_{\mathrm{dim}}}_{\mathrm{sym}} : \phi_{\mathrm{p}} < 0 \right\} \quad . \tag{2.68}$$

The kinematic hardening force $\boldsymbol{A}_{\mathrm{k}}$ therein moves the elastic domain within the stress space, whereas A_{i} increases or decreases the size of the elastic domain. A purely elastic deformation is assumed to not alter any of the internal variables, such that

$$\phi_{\mathrm{p}} < 0 \quad \Rightarrow \quad (\boldsymbol{D}_{\mathrm{p}}, \dot{\alpha}_{\mathrm{i}}, \dot{\boldsymbol{\alpha}}_{\mathrm{k}}) = (\boldsymbol{0}, 0, \boldsymbol{0}) \quad , \tag{2.69}$$

and hence, according to (2.63), no internal dissipation takes place. On the other hand, stress states resulting in $\phi_{\mathrm{p}} > 0$ are inadmissible and plastic yielding takes place until the stress state is located on the yield surface $\phi_{\mathrm{p}} = 0$ and therefore limiting the equivalent stress to $\Sigma_{\mathrm{eq}} = Y$. Formally, the flow rules (2.64) then give

$$\phi_{\mathrm{p}} = 0 \quad \Rightarrow \quad \boldsymbol{D}_{\mathrm{p}} = \dot{\gamma} \frac{\partial \Xi_{\mathrm{p}}}{\partial \boldsymbol{\Sigma}}, \quad \dot{\alpha}_{\mathrm{i}} = \dot{\gamma} \frac{\partial \Xi_{\mathrm{p}}}{\partial A_{\mathrm{i}}}, \quad \dot{\boldsymbol{\alpha}}_{\mathrm{k}} = \dot{\gamma} \frac{\partial \Xi_{\mathrm{p}}}{\partial \boldsymbol{A}_{\mathrm{k}}} \quad , \tag{2.70}$$

with the plastic multiplier $\dot{\gamma} \geq 0$. The equations for the elastic and plastic material response (2.69) and (2.70) can be summarized in the Karush–Kuhn–Tucker complementarity (or loading/unloading) conditions

$$\phi_{\mathrm{p}} \leq 0, \quad \dot{\gamma} \geq 0, \quad \phi_{\mathrm{p}} \dot{\gamma} = 0 \quad , \tag{2.71}$$

in combination with the flow rule (2.64).

A common choice for the dissipation potential Ξ_{p} is derived from the principle of maximum plastic dissipation, i.e. maximizing (2.63) subjected to the complementarity condition (2.71). This results in the so-called associative flow rule

$$\Xi_{\mathrm{p}} = \phi_{\mathrm{p}} \quad , \tag{2.72}$$

where the direction of plastic flow is normal to the yield surface[2], see e.g. Han and Reddy [92] for the proof that this choice of the dissipation potential actually maximizes $\mathcal{D}_{\mathrm{int}}$.

[1] Convexity of the yield function applies to almost every engineering material. For a discussion on physical implications of convexity of the yield function as well as honeycomb structures as a counterexample, the reader is referred to Glüge and Bucci [81].

[2] Strictly speaking, the yield function does not satisfy the requirement (2.65) on dissipation potentials. However, the complementarity (2.71) prohibits any plastic flow for $\phi_{\mathrm{p}} < 0$, such that the dissipation potential may be chosen equivalently as $\Xi_{\mathrm{p}} = \max(0, \phi_{\mathrm{p}})$, which satisfies (2.71). Still, to be in accordance with the common literature, the following presentation sticks to the format of (2.72).

2.3.4.4 Some Examples of Yield Functions

The concrete choice of the yield function comprised of the equivalent stress Σ_{eq} as well as the hardening behavior modeled by Ψ_{p} (entering through A_{i} and $\boldsymbol{A}_{\mathrm{k}}$) depends on the material of question. It can be either purely phenomenological or include some knowledge of the microstructure as, for instance, in crystal plasticity and has to be validated by experiments. A yield function is called isotropic, if the equivalent stress $\Sigma_{\mathrm{eq}}(\boldsymbol{\eta})$ is an isotropic tensor function of $\boldsymbol{\eta}$ in which case it can be expressed in terms of the principle stresses η_1, η_2 and η_3, i.e. the eigenvalues of $\boldsymbol{\eta}$. In the following, some of the most popular yield functions are summarized.

Tresca Yield Criterion The Tresca yield criterion compares the maximal and minimal principle stress $\eta_{\max}$ and $\eta_{\min}$, respectively, using the equivalent stress

$$\Sigma_{\mathrm{eq}} = \eta_{\max} - \eta_{\min} \quad . \tag{2.73}$$

A superimposed hydrostatic pressure increases both $\eta_{\max}$ and $\eta_{\min}$ by the same value leaving Σ_{eq} unaltered. Such yield functions, that are invariant under superimposed hydrostatic pressures are called pressure insensitive.

Von Mises Yield Criterion In the von Mises yield criterion proposed by Mises [150], the equivalent stress in a three-dimensional continuum is calculated as

$$\Sigma_{\mathrm{eq}} = \sqrt{\frac{3}{2}}\sqrt{\operatorname{dev}\boldsymbol{\eta} : \operatorname{dev}\boldsymbol{\eta}} =: \sqrt{\frac{3}{2}}\|\operatorname{dev}\boldsymbol{\eta}\| \quad , \tag{2.74}$$

which only depends on the deviatoric stress $\operatorname{dev}\boldsymbol{\eta} = \mathbb{P}_{\mathrm{dev}} : \boldsymbol{\eta}$. The fourth order deviatoric projection tensor $\mathbb{P}_{\mathrm{dev}}$ is obtained from the fourth order symmetric identity tensor $\mathbb{I}_{\mathrm{s}}$ by $\mathbb{P}_{\mathrm{dev}} = \mathbb{I}_{\mathrm{s}} - {}^1\!/_{n_{\mathrm{dim}}}\boldsymbol{I}\otimes\boldsymbol{I}$. The factor of $\sqrt{{}^3\!/_2}$ is introduced such that the yield limit y_0 in (2.66) corresponds to the value measured in uniaxial tests. Since the effective stress (2.74) only depends on the deviatoric part of the stress tensor, it is insensitive to hydrostatic pressure.

Hill's Orthotropic Yield Criterion The von Mises criterion can be generalized to account for anisotropy of the yield strength as proposed by Hill [102]. In three dimensions, let therefore $\boldsymbol{n}_i$, $i \in \{1,2,3\}$ be orthogonal unit vectors in direction of the principle axes of the material and $\boldsymbol{N_i} = \boldsymbol{n}_i \otimes \boldsymbol{n}_i$ the corresponding structural tensors. In direction of $\boldsymbol{n}_i$, the normal yield stress of the material is denoted by y_{ii} and the shear yield stress in the $\boldsymbol{n}_i - \boldsymbol{n}_j$-plane ($i \neq j$) is denoted by y_{ij}. With the parameters

$$\begin{aligned} \alpha_1 &= \frac{2}{3}\frac{y_0^2}{y_{11}^2} \quad , \quad \alpha_2 = \frac{2}{3}\frac{y_0^2}{y_{22}^2} \quad , \quad \alpha_3 = \frac{2}{3}\frac{y_0^2}{y_{33}^2} \quad , \\ \alpha_7 &= \frac{1}{3}\frac{y_0^2}{y_{12}^2} \quad , \quad \alpha_8 = \frac{1}{3}\frac{y_0^2}{y_{23}^2} \quad , \quad \alpha_9 = \frac{1}{3}\frac{y_0^2}{y_{13}^2} \quad , \end{aligned} \tag{2.75}$$

the Hill tensor $\mathbb{H}$ is defined as

$$\begin{aligned} \mathbb{H} =& \alpha_1\boldsymbol{N}_1\otimes\boldsymbol{N}_1 + \alpha_2\boldsymbol{N}_2\otimes\boldsymbol{N}_2 + \alpha_3\boldsymbol{N}_3\otimes\boldsymbol{N}_3 \\ &+ {}^1\!/_2(\alpha_3-\alpha_1-\alpha_2)(\boldsymbol{N}_1\otimes\boldsymbol{N}_2 + \boldsymbol{N}_2\otimes\boldsymbol{N}_1) + \alpha_7(\boldsymbol{N}_1\odot\boldsymbol{N}_2 + \boldsymbol{N}_2\odot\boldsymbol{N}_1) \\ &+ {}^1\!/_2(\alpha_1-\alpha_2-\alpha_3)(\boldsymbol{N}_2\otimes\boldsymbol{N}_3 + \boldsymbol{N}_3\otimes\boldsymbol{N}_2) + \alpha_8(\boldsymbol{N}_2\odot\boldsymbol{N}_3 + \boldsymbol{N}_3\odot\boldsymbol{N}_2) \\ &+ {}^1\!/_2(\alpha_2-\alpha_3-\alpha_1)(\boldsymbol{N}_1\otimes\boldsymbol{N}_3 + \boldsymbol{N}_3\otimes\boldsymbol{N}_1) + \alpha_9(\boldsymbol{N}_1\odot\boldsymbol{N}_3 + \boldsymbol{N}_3\odot\boldsymbol{N}_1) \quad , \end{aligned} \tag{2.76}$$

with the outer product $\odot$ defined by $(\boldsymbol{A} \odot \boldsymbol{B}) : \boldsymbol{X} = {}^1\!/_2(\boldsymbol{A}\boldsymbol{X}\boldsymbol{B}^\mathsf{T} + \boldsymbol{B}\boldsymbol{X}^\mathsf{T}\boldsymbol{A}^\mathsf{T})$ for second order tensors $\boldsymbol{A}$, $\boldsymbol{B}$ and $\boldsymbol{X}$. From a given effective stress $\boldsymbol{\eta}$, the equivalent stress according to Hill's yield criterion is then defined as via the anisotropic quadratic norm

$$\Sigma_{\mathrm{eq}} = \sqrt{\frac{3}{2}}\sqrt{\boldsymbol{\eta} : \mathbb{H} : \boldsymbol{\eta}} =: \sqrt{\frac{3}{2}}\,\|\boldsymbol{\eta}\|_{\mathbb{H}} \quad . \tag{2.77}$$

The isotropic von Mises equivalent stress is retained for $\alpha_1 = \alpha_2 = \alpha_3 = {}^2\!/_3$ and $\alpha_7 = \alpha_8 = \alpha_9 = {}^1\!/_3$ in which case $\mathbb{H} = \mathbb{P}_{\mathrm{dev}}$. In any case, $\mathbb{H}$ includes a deviatoric projection, i.e. $\mathbb{H} = \mathbb{P}_{\mathrm{dev}} : \mathbb{H} = \mathbb{H} : \mathbb{P}_{\mathrm{dev}}$ and therefore Hill's yield criterion is also insensitive to hydrostatic pressure.

Pressure Sensitive Yield Functions Any of the above yield functions can be enhanced with a pressure term by

$$\Sigma_{\mathrm{eq}} = \widehat{\Sigma_{\mathrm{eq}}} + \beta \operatorname{tr} \boldsymbol{\eta} \quad , \tag{2.78}$$

with a material constant β and $\widehat{\Sigma_{\mathrm{eq}}}$ chosen as (2.73), (2.74) or (2.77). Based on the von Mises criterion, the resulting pressure sensitive yield function is called Drucker–Prager yield function and enhancing the Tresca yield function with a pressure sensitive term results in the so-called Mohr–Coulomb yield function.

2.3.4.5 The Plastic Spin

As discussed in Section 2.3.4.1, the rotational orientation of the unstressed intermediate configuration is set to be isoclinic, meaning that axes of the substructural material do not rotate. In the context of anisotropic Hill-type plasticity, these axes are defined by the triad $\boldsymbol{n}_i$. Let $\boldsymbol{\omega}$ denote the total spin of this triad between the reference and the intermediate configuration, also called substructural spin. This substructural spin can be decomposed into two contributions

$$\boldsymbol{\omega} = \boldsymbol{W}_{\mathrm{p}} - \boldsymbol{\Omega}_{\mathrm{p}} \quad , \tag{2.79}$$

where the sign in this decomposition is obviously arbitrary, since $\boldsymbol{\Omega}_{\mathrm{p}}$ remains undefined to this point. The minus-sign is chosen out of convention, see e.g. [46, 47, 222, 250]. While $\boldsymbol{W}_{\mathrm{p}}$ describes the spin of the macroscopic continuum, $\boldsymbol{\Omega}_{\mathrm{p}}$ represents the relative spin of the triad $\boldsymbol{n}_i$ with respect to the macroscopic continuum. Microscopically, the directions $\boldsymbol{n}_i$ may be the result of an anisotropy in the granular structure of a polycrystalline metal and finite plastic deformation can influence this microscopic texture and result in said relative spin between the triad $\boldsymbol{n}_i$ and the macroscopic continuum. A common constitutive assumption on the plastic spin used e.g. in [46, 47, 222, 250] is given by

$$\boldsymbol{\Omega}_{\mathrm{p}} = \frac{\eta}{y_0}\left(\boldsymbol{\Sigma}\boldsymbol{D}_{\mathrm{p}} - \boldsymbol{D}_{\mathrm{p}}\boldsymbol{\Sigma}\right) \quad , \tag{2.80}$$

depending on a material parameter η. According to (2.80), plastic spin occurs only in case of plastic deformation ($\boldsymbol{D}_{\mathrm{p}} \neq \boldsymbol{0}$ or equivalently $\dot{\gamma} > 0$) and if $\boldsymbol{\Sigma}$ and $\boldsymbol{D}_{\mathrm{p}}$ are not coaxial. In an isoclinic intermediate configuration, the total spin of the triad $\boldsymbol{n}_i$ vanishes ($\boldsymbol{\omega} = \boldsymbol{0}$) and therefore (2.79) gives

$$\boldsymbol{W}_{\mathrm{p}} = \boldsymbol{\Omega}_{\mathrm{p}} = \frac{\eta}{y_0}\left(\boldsymbol{\Sigma}\boldsymbol{D}_{\mathrm{p}} - \boldsymbol{D}_{\mathrm{p}}\boldsymbol{\Sigma}\right) \quad . \tag{2.81}$$

For a more detailed introduction to plastic spin including different relative spins for different tensor valued internal variables the reader is referred to the review of Dafalias [47].

2.3.4.6 Elasto-Visco-Plasticity

In the plasticity formulation derived in Sections 2.3.4.3 and 2.3.4.4, the plastic material response is independent of the loading velocity since (2.70) determines the plastic flow such that $\Sigma_{\mathrm{eq}} = Y$. Hence, time acts on the evolution of the internal variables only as a path parameter. Many materials, however, show a dependency of the resulting stress in the plastic deformations on the loading velocity; this effect is called visco-plasticity. Contrary to (2.71), visco-plastic materials allow the equivalent stress Σ_{eq} to exceed the effective yield limit Y in dynamic loading processes. Consequently, the yield function takes positive values and the plastic multiplier $\dot{\gamma}$ defining the evolution equations in (2.70) cannot be determined by the complementarity (2.71). Instead, the visco-plastic flow rule

$$\boldsymbol{D}_{\mathrm{p}} = \dot{\gamma}\frac{\partial \Xi_{\mathrm{p}}}{\partial \boldsymbol{\Sigma}}, \quad \dot{\alpha}_{\mathrm{i}} = \dot{\gamma}\frac{\partial \Xi_{\mathrm{p}}}{\partial A_{\mathrm{i}}}, \quad \dot{\boldsymbol{\alpha}}_{\mathrm{k}} = \dot{\gamma}\frac{\partial \Xi_{\mathrm{p}}}{\partial \boldsymbol{A}_{\mathrm{k}}} \quad , \tag{2.82a}$$

with

$$\dot{\gamma} = \begin{cases} 0 & \text{if } \phi_{\mathrm{p}} < 0 \\ \frac{1}{\mu}\left[\left(\frac{\Sigma_{\mathrm{eq}}}{Y}\right)^{1/\epsilon} - 1\right] & \text{if } \phi_{\mathrm{p}} \geq 0 \end{cases} \tag{2.82b}$$

replaces (2.70). The particular model (2.82) was originally proposed by Perić [166] and contains two parameters, namely the viscosity μ and the rate-sensitivity ϵ but many other models exist in the literature, see e.g. Chaboche [30] for a review. It can easily be shown[1], that (2.82b) is equivalent to enforcing the complementarity

$$\phi_{\mathrm{p}}^{\mathrm{dyn}} \leq 0, \quad \dot{\gamma} \geq 0, \quad \phi_{\mathrm{p}}^{\mathrm{dyn}}\dot{\gamma} = 0 \quad , \tag{2.83}$$

with the dynamic yield function

$$\phi_{\mathrm{p}}^{\mathrm{dyn}} = \Sigma_{\mathrm{eq}} - (1 + \mu\dot{\gamma})^{\epsilon} Y = \Sigma_{\mathrm{eq}} - Y^{\mathrm{dyn}} \tag{2.84}$$

and the dynamic effective yield stress Y^{dyn}. For a detailed discussion on dynamic yield surfaces, the interested reader is referred to Ristinmaa and Ottosen [186]. With the concept of dynamic yield functions, visco-plasticity (2.83) has formally the same complementarity structure as rate-independent plasticity (2.71) (simply by replacing ϕ_{p} with $\phi_{\mathrm{p}}^{\mathrm{dyn}}$) and therefore similar numerical techniques can be used. In the context of thermomecanics it is important to note, that viscosity μ and rate-sensitivity ϵ typically increase with increasing temperature [57].

2.4 The Heat Conduction Equation

The constitutive equations of Section 2.3 can be used to derive a simplified form of the energy balance equation (2.33) called heat conduction equation. The derivation presented in the following is based on the more general elasto-plastic constitutive relations of Section 2.3.4. The corresponding thermo-elastic formulation can easily be obtained by setting $\boldsymbol{F}_{\mathrm{p}} \equiv \boldsymbol{I}$ and neglecting all terms associated with the internal variables $\{\boldsymbol{F}_{\mathrm{p}}, \alpha_{\mathrm{i}}, \boldsymbol{\alpha}_{\mathrm{k}}\}$. In a first step, the Legendre

[1] To show equivalency of (2.83) and (2.84) with (2.82b) set $\phi_{\mathrm{p}}^{\mathrm{dyn}} = 0$ and solve for $\dot{\gamma}$.

transformation (2.37) is used to eliminate $\dot{e}$ from (2.33) to obtain

$$\dot{\Psi} + T\dot{\eta} + \dot{T}\eta = \frac{1}{2}\boldsymbol{S} : \dot{\boldsymbol{C}} - \nabla_{\boldsymbol{X}} \cdot \boldsymbol{Q} + R \quad . \tag{2.85}$$

Inserting the free energy (2.58) and making use of relations (2.60)-(2.62) results in

$$T\dot{\eta} = -\nabla_{\boldsymbol{X}} \cdot \boldsymbol{Q} + R + \mathcal{D}_{\mathrm{int}} \quad . \tag{2.86}$$

The entropy rate $\dot{\eta}$ can be expressed by the free energy Ψ through the total time derivative of the constitutive relation (2.60) to obtain

$$-T\frac{\partial^2 \Psi}{\partial T \partial T}\dot{T} = -\nabla_{\boldsymbol{X}} \cdot \boldsymbol{Q} + R + \mathcal{D}_{\mathrm{int}} + T\frac{\partial \boldsymbol{S}}{\partial T} : \dot{\boldsymbol{C}} - T\frac{\partial \mathcal{D}_{\mathrm{int}}}{\partial T} \quad . \tag{2.87}$$

In the following, it is assumed that Ψ_{e} and Ψ_{p} in (2.58) only depend linearly on the temperature and the thermal free energy Ψ_{ϑ} takes the form

$$\Psi_{\vartheta} = c_{\mathrm{v}} \left((T - T_0) - T \ln\left(\frac{T}{T_0}\right) \right) \quad , \tag{2.88}$$

with a reference temperature T_0. Finally, the heat source due to plastic work is approximated as

$$\mathcal{D}_{\mathrm{int}} - T\frac{\partial \mathcal{D}_{\mathrm{int}}}{\partial T} \approx \chi \boldsymbol{\Sigma} : \boldsymbol{D}_{\mathrm{p}} \quad , \tag{2.89}$$

using a dissipation factor χ which for metals typically is in the range of $\chi \in [0.85, 1]$. The dissipation factor χ is sometimes also termed Taylor–Quinney factor referring back to the original publication of Taylor and Quinney [213]. As in most computational methods, χ is assumed to be constant throughout this thesis although some experimental evidence in e.g. [210, 247] points at a dependency of the plastic strain. Stainier and Ortiz [210] suggest, that the heat source due to plastic deformation actually follows the variational form (2.87) for certain materials. Inserting (2.88) and (2.89) in (2.87) yields

$$c_{\mathrm{v}}\dot{T} = -\nabla_{\boldsymbol{X}} \cdot \boldsymbol{Q} + R + \chi \boldsymbol{\Sigma} : \boldsymbol{D}_{\mathrm{p}} + T\frac{\partial \boldsymbol{S}}{\partial T} : \dot{\boldsymbol{C}} \quad , \tag{2.90}$$

which is commonly referred to as the heat conduction equation.

2.5 Strong Form of the Initial Boundary Value Problem

The derivations above described the balance laws and constitutive behavior of a material point within the body defined by the reference domain Ω_0 or the displaced configuration Ω_t. Since, in practice, bodies are of finite extent, they interact with their surrounding at the boundary $\partial\Omega_0$ by so-called *boundary conditions*. To formulate boundary conditions, the boundary $\partial\Omega_0$ is split into the sets Γ_{u}, Γ_{σ}, Γ_{T} and Γ_{q} with prescribed displacements, traction, temperatures and heat fluxes. The boundaries form a partition of the entire boundary $\partial\Omega_0$ in the sense that $\overline{\Gamma_{\mathrm{u}}} \cup \overline{\Gamma_{\sigma}} = \overline{\Gamma_{\mathrm{T}}} \cup \overline{\Gamma_{\mathrm{q}}} = \partial\Omega_0$ and $\Gamma_{\mathrm{u}} \cap \Gamma_{\sigma} = \Gamma_{\mathrm{T}} \cap \Gamma_{\mathrm{q}} = \emptyset$. Not only in space, but also in time only a limited section defined by the interval $[0, t_{\mathrm{end}}]$ is investigated. When setting “boundary”

conditions on this time interval, it follows from the principle of determinism, that only values at the beginning of the time interval (chosen to zero without loss of generality) may be set by so-called initial conditions. As the balance of linear momentum (2.25) is a second order differential equation in time, initial conditions are required for both displacements and velocities. On the contrary, the heat conduction equation (2.90) is of first order in time and hence only requires initial temperatures, but no initial rates.

The *initial boundary value problem* (IBVP) of thermomechanics summarizes a set of equations to determine the motion and temperature evolution of a body over time and consists of the balance of linear momentum (2.25) and the heat conduction equation (2.90) complemented by initial and boundary conditions. Formulated in reference configuration, the strong form of the IBVP reads

$$\nabla_{\boldsymbol{X}} \cdot \boldsymbol{P} + \boldsymbol{b}_0 = \rho_0 \boldsymbol{a} \qquad \text{in } \Omega_0 \times (0, t_{\text{end}}] \ , \tag{2.91a}$$

$$-\nabla_{\boldsymbol{X}} \cdot \boldsymbol{Q} + R + \chi \boldsymbol{\Sigma} : \boldsymbol{D}_{\text{p}} + T \frac{\partial \boldsymbol{S}}{\partial T} : \dot{\boldsymbol{C}} = c_{\text{v}} \dot{T} \qquad \text{in } \Omega_0 \times (0, t_{\text{end}}] \ , \tag{2.91b}$$

$$\boldsymbol{u} = \hat{\boldsymbol{u}} \qquad \text{on } \Gamma_{\text{u}} \times (0, t_{\text{end}}] \ , \tag{2.91c}$$

$$\boldsymbol{P}\boldsymbol{N} = \hat{\boldsymbol{t}}_0 \qquad \text{on } \Gamma_{\sigma} \times (0, t_{\text{end}}] \ , \tag{2.91d}$$

$$T = \hat{T} \qquad \text{on } \Gamma_{\text{T}} \times (0, t_{\text{end}}] \ , \tag{2.91e}$$

$$\boldsymbol{Q} \cdot \boldsymbol{N} = \hat{Q}_{\text{n}} \qquad \text{on } \Gamma_{\text{q}} \times (0, t_{\text{end}}] \ , \tag{2.91f}$$

$$\boldsymbol{u} = \boldsymbol{u}_0 \qquad \text{in } \Omega_0 \times 0 \ , \tag{2.91g}$$

$$\boldsymbol{v} = \boldsymbol{v}_0 \qquad \text{in } \Omega_0 \times 0 \ , \tag{2.91h}$$

$$T = T_0 \qquad \text{in } \Omega_0 \times 0 \ , \tag{2.91i}$$

where a hat $\hat{(\cdot)}$ indicates a given boundary condition and $\boldsymbol{u}_0$, $\boldsymbol{v}_0$ and T_0 denote the given initial conditions of displacement, velocity and temperature, respectively. The boundaries Γ_{u} and Γ_{T} prescribing the state variables $\boldsymbol{u}$ and T are referred to as *Dirichlet* boundaries, whereas Γ_{σ} and Γ_{q} prescribing traction and heat flux, respectively, are referred to as *Neumann* boundaries. The conservation of mass and the balance of angular momentum are not stated explicitly, since they can easily be enforced by (2.15) and (2.26). Moreover, any constitutive relation derived in Section 2.3 can be used to link displacements and temperatures with the first Piola–Kirchhoff stress $\boldsymbol{P}$ and the heat flux $\boldsymbol{Q}$. Materials with internal variables of state such as plasticity (see Section 2.3.4) require initial data for these internal variables, from which point on their evolution is governed by evolution equations (e.g. equations (2.70) and (2.81)). Commonly, the initial plastic deformation gradient and hardening variables are set to $\boldsymbol{F}_{\text{p}}(\boldsymbol{X}, 0) = \boldsymbol{I}$, $\alpha_{\text{i}}(\boldsymbol{X}, 0) = 0$ and $\boldsymbol{\alpha}_{\text{k}}(\boldsymbol{X}, 0) = \boldsymbol{0}$.

2.6 Weak Form of the Initial Boundary Value Problem

In a first step towards a finite element method, the strong form of the IBVP (2.91) is transformed into its alternative, so-called weak form. Applying the method of weighted residuals, *weighting functions* (or *test functions*) $\delta\boldsymbol{u}$ and δT are introduced for the displacement and temperature field, respectively. In analogy to the method of virtual displacements, these quantities are sometimes

also referred to as *virtual* displacements and *virtual* temperatures. The strong form of the balance of linear momentum (2.91a) is then equivalent to finding $\boldsymbol{u}$, such that

$$\int_{\Omega_0} (\rho_0 \boldsymbol{a} - \nabla_{\boldsymbol{X}} \cdot \boldsymbol{P} + \boldsymbol{b}_0) \cdot \delta\boldsymbol{u} \, \mathrm{d}\Omega = 0 \quad \forall \delta\boldsymbol{u} \ . \tag{2.92}$$

Next, divergence theorem is applied to the stress term resulting in

$$\int_{\Omega_0} \rho_0 \boldsymbol{a} \cdot \delta\boldsymbol{u} \, \mathrm{d}\Omega + \int_{\Omega_0} \boldsymbol{P} : \nabla_{\boldsymbol{X}} \delta\boldsymbol{u} \, \mathrm{d}\Omega + \int_{\Omega_0} \boldsymbol{b}_0 \cdot \delta\boldsymbol{u} \, \mathrm{d}\Omega - \int_{\partial\Omega_0} (\boldsymbol{P}\boldsymbol{N}) \cdot \delta\boldsymbol{u} \, \mathrm{d}\Gamma = 0 \quad \forall \delta\boldsymbol{u} \ . \tag{2.93}$$

This weak form does, so far, not account for the boundary conditions (2.91c) and (2.91d). To incorporate the Dirichlet condition (2.91c), the function space $\boldsymbol{\mathcal{U}}_{\mathrm{u}}$ of admissible displacements $\boldsymbol{u}$ is set to satisfy the (2.91c), i.e.[1]

$$\boldsymbol{u}|_{\Gamma_{\mathrm{u}}} = \hat{\boldsymbol{u}} \quad \forall \boldsymbol{u} \in \boldsymbol{\mathcal{U}}_{\mathrm{u}} \ . \tag{2.94a}$$

Conversely, the admissible variations $\delta\boldsymbol{u}$ vanish at the Dirichlet boundary, as the displacement values are already set by (2.94a) resulting in the *test space* $\boldsymbol{\mathcal{V}}_{\mathrm{u}}$ with

$$\delta\boldsymbol{u}|_{\Gamma_{\mathrm{u}}} = \boldsymbol{0} \quad \forall \boldsymbol{u} \in \boldsymbol{\mathcal{V}}_{\mathrm{u}} \ . \tag{2.94b}$$

Finally, both $\boldsymbol{\mathcal{U}}_{\mathrm{u}}$ and $\boldsymbol{\mathcal{V}}_{\mathrm{u}}$ are required to be sufficiently smooth for (2.93) to make sense. In problems of linear elasticity, this would require $\boldsymbol{\mathcal{U}}_{\mathrm{u}}$ and $\boldsymbol{\mathcal{V}}_{\mathrm{u}}$ to be in the Sobolev space $[H^1(\Omega_0)]^{n_{\mathrm{dim}}}$ of square integrable functions with square integrable first derivatives. In problems of nonlinear elasticity, this is no longer a suitable space for the displacement field, but slightly stricter requirements depending on the employed hyperelastic constitutive law occur and restrict $\boldsymbol{\mathcal{U}}_{\mathrm{u}}$ to so-called Orlicz–Sobolev spaces. Since strict mathematical proofs for the derived coupled nonlinear finite element formulations derived in this thesis are beyond its scope, an exact definition of $\boldsymbol{\mathcal{U}}_{\mathrm{u}}$ and $\boldsymbol{\mathcal{V}}_{\mathrm{u}}$ is omitted here. Further discussions and exemplary spaces for certain hyperelastic materials can be found in the mathematical literature of, e.g., Ball [10], Kikuchi and Oden [120], Marsden and Hughes [143]. By (2.94b), the contribution of the Dirichlet boundary Γ_{u} to the boundary integral in the weak form (2.93) vanishes; on the remaining Neumann boundary Γ_σ, the traction $\boldsymbol{P}\boldsymbol{N}$ to be integrated is given by the Neumann data (2.91d). Replacing this given boundary value, the weak form of the structural balance equation reads: Find $\boldsymbol{u} \in \boldsymbol{\mathcal{U}}_{\mathrm{u}}$, such that

$$\delta\mathcal{W}_{\mathrm{u}} = \int_{\Omega_0} \rho_0 \boldsymbol{a} \cdot \delta\boldsymbol{u} \, \mathrm{d}\Omega + \int_{\Omega_0} \boldsymbol{P} : \nabla_{\boldsymbol{X}} \delta\boldsymbol{u} \, \mathrm{d}\Omega - \int_{\Omega_0} \boldsymbol{b}_0 \cdot \delta\boldsymbol{u} \, \mathrm{d}\Omega - \int_{\Gamma_\sigma} \hat{\boldsymbol{t}}_0 \cdot \delta\boldsymbol{u} \, \mathrm{d}\Gamma = 0 \quad \forall \delta\boldsymbol{u} \in \boldsymbol{\mathcal{V}}_{\mathrm{u}} \ . \tag{2.95}$$

It can readily be shown that any sufficiently smooth solution to the weak form (2.95) is also a solution of the strong form of the structural balance comprised of (2.91a), (2.91c), (2.91d) and vice versa (see e.g. Hughes [111]). Note, that the stress $\boldsymbol{P}$ in (2.95) is a nonlinear function of the displacement and may as well depend on the temperature and internal variables of state in the framework of Section 2.3.

[1] It is not necessary to incorporate the Dirichlet boundary condition directly into the trial and test function spaces. Alternatively, they can be included in a weak sense, see e.g. Nitsche [158].

Remark 2.3 (Principle of minimum total potential energy)**.** *The weak form* (2.95) *may alternatively be derived by minimizing the potential energy in the system. Accordingly, for an isothermal hyperelastic solid, the displacement field* $\boldsymbol{u}$ *is the minimizer*

$$\boldsymbol{u} = \underset{\boldsymbol{u},\boldsymbol{u}|_{\Gamma_\mathrm{u}}=\hat{\boldsymbol{u}}}{\arg\min} \left[\int_{\Omega_0} \Psi \,\mathrm{d}\Omega - \int_{\Omega_0} \boldsymbol{b}_0 \cdot \boldsymbol{u} \,\mathrm{d}\Omega - \int_{\Gamma_\sigma} \hat{\boldsymbol{t}}_0 \cdot \boldsymbol{u} \,\mathrm{d}\Gamma \right] \quad . \tag{2.96}$$

The weak form (2.95) *is thereby equivalent to the first variation of* (2.96) *with respect to the displacement field. However, not all mechanical problems derive from a potential especially not those including dissipative effects, with one prominent example being plasticity. In a more general setting, plasticity may be re-cast as a minimization problem of an* incremental *potential comprised of the elastic potential* (2.96) *plus the dissipation* (2.63)*. The minimization is then additionally subjected to the Karush–Kuhn–Tucker inequality constraints* (2.71)*, see, e.g., Carstensen* et al. *[28] for the isothermal case and Yang* et al. *[246] for an application to thermoplasticity.*

In complete analogy to the structural problem above, the weak form of the heat conduction (2.91b) can be derived by multiplication with a test function δT, integration over the domain and subsequent integration by parts, which results in

$$\begin{aligned} &\int_{\Omega_0} c_\mathrm{v} \dot{T} \delta T \,\mathrm{d}\Omega - \int_{\Omega_0} \boldsymbol{Q} \cdot \nabla_{\boldsymbol{X}} \delta T \,\mathrm{d}\Omega \\ &- \int_{\Omega_0} \left(R + \chi \boldsymbol{\Sigma} : \boldsymbol{D}_\mathrm{p} + T \frac{\partial \boldsymbol{S}}{\partial T} : \dot{\boldsymbol{C}} \right) \delta T \,\mathrm{d}\Omega - \int_{\partial\Omega_0} \boldsymbol{Q} \cdot \boldsymbol{N} \delta T \,\mathrm{d}\Gamma = 0 \quad \forall \delta T \quad . \end{aligned} \tag{2.97}$$

For (2.97) to make sense, the temperature T and its variation δT are chosen from sufficiently smooth spaces $\mathcal{U}_\mathrm{T}$ and $\mathcal{V}_\mathrm{T}$, respectively. Moreover, satisfaction of the Dirichlet boundary condition (2.91e) is included directly into $\mathcal{U}_\mathrm{T}$ and $\mathcal{V}_\mathrm{T}$ by

$$T|_{\Gamma_\mathrm{T}} = \hat{T} \quad \forall \; T \in \mathcal{U}_\mathrm{T} \quad , \tag{2.98a}$$

$$\delta T|_{\Gamma_\mathrm{T}} = 0 \quad \forall \delta T \in \mathcal{V}_\mathrm{T} \quad , \tag{2.98b}$$

similar to the displacement Dirichlet condition in (2.94). The remaining boundary integral in (2.97) is substituted by the given Neumann data (2.91f), which yields the weak form of the heat conduction equation: Find $T \in \mathcal{U}_\mathrm{T}$, such that

$$\begin{aligned} \delta \mathcal{W}_\mathrm{T} = &\int_{\Omega_0} c_\mathrm{v} \dot{T} \delta T \,\mathrm{d}\Omega - \int_{\Omega_0} \boldsymbol{Q} \cdot \nabla_{\boldsymbol{X}} \delta T \,\mathrm{d}\Omega \\ &- \int_{\Omega_0} \left(R + \chi \boldsymbol{\Sigma} : \boldsymbol{D}_\mathrm{p} + T \frac{\partial \boldsymbol{S}}{\partial T} : \dot{\boldsymbol{C}} \right) \delta T \,\mathrm{d}\Omega - \int_{\Gamma_\mathrm{q}} \hat{Q}_\mathrm{n} \delta T \,\mathrm{d}\Gamma = 0 \quad \forall \delta T \in \mathcal{V}_\mathrm{T} \quad . \end{aligned} \tag{2.99}$$

As for the structural problem, any sufficiently smooth solution to the weak form (2.99) is also a solution of the strong form (2.91b) in combination with the boundary conditions (2.91e) and (2.91f) and vice versa. However, the weak form has weaker differenciablity requirements on the temperature field, since only first spatial derivatives are required, compared to second derivatives in the strong form (2.91b).

2.7 Continuum Mechanics of Thermomechancial Contact

The evolution of state variables within a single body, i.e. displacement and temperature, potentially accompanied by internal variables of state, is governed by the continuum mechanical description derived in Sections 2.1 - 2.3. For systems of multiple bodies, additional contact constraints have to be satisfied to ensure that, for instance, bodies do not penetrate. Within this section, a thermodynamically consistent continuum mechanical description of contact problems is derived following the same steps as in the derivations for the bulk of a single body: First, a kinematic description of contact problems is summarized in Section 2.7.1 analogously to the kinematics of the bulk continuum derived in Section 2.1. Next, Section 2.7.2 introduces balance laws and the entropy inequality at the contact interface (cf. Section 2.2). Finally, contact constraints are incorporated in terms of contact constitutive laws in Section 2.7.3 (cf. Section 2.3). This methodology to derive contact constraints based on conservation and constitutive laws was introduced by Moreau [153] for isothermal contact problems to tackle such problems by mathematical tools of convex optimization. A more accessible introduction may be found in Curnier [42] and an extension to thermomechancial contact problems in Oancea and Laursen [159] and Laursen [131]. The thermodynamical derivation of the contact laws presented hereafter mainly follows the one originally presented by Oancea and Laursen [159].

2.7.1 Contact Kinematics

For simplicity of presentation, a two-body contact problem as depicted in Figure 2.3 is considered, however extension to multiple bodies in contact is straightforward. The body $\Omega_0^{(1)}$ will

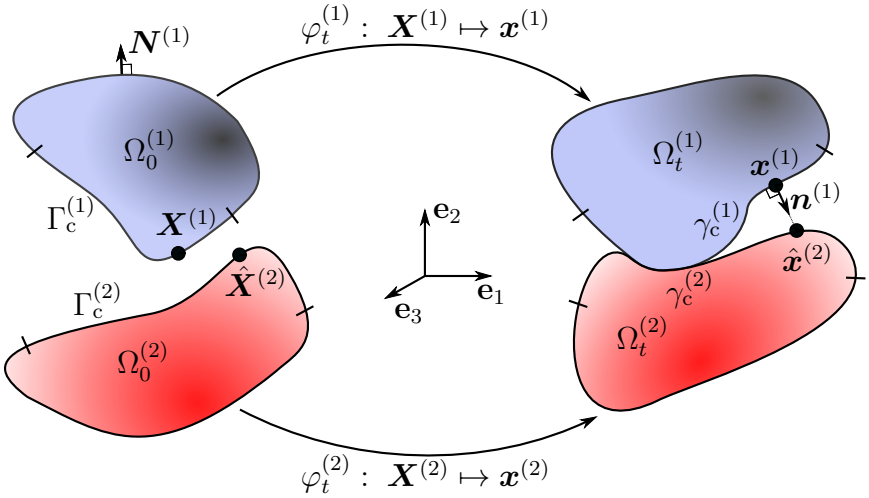

Figure 2.3: Illustration of a two-body finite deformation contact problem.

be denoted as the *slave* body and $\Omega_0^{(2)}$ as the *master* body and the same notation will be applied for coordinates, boundaries, and so on. This syntax is adopted from classical methods and literature on computational contact mechanics; its original meaning, however, may not be applicable to all methods developed within this thesis. If, for a domain, boundary or function space,

no superscript is given, the union of the respective quantity of slave and master side is used, e.g. $\Omega_0 = \Omega_0^{(1)} \cup \Omega_0^{(2)}$ or $\boldsymbol{\mathcal{U}}_\mathrm{u} = \boldsymbol{\mathcal{U}}_\mathrm{u}^{(1)} \otimes \boldsymbol{\mathcal{U}}_\mathrm{u}^{(2)}$. To account for the potential contact between the two bodies, the boundary $\partial\Omega_0^{(i)}$ is split into the Dirichlet and Neumann boundaries $\Gamma_\mathrm{u}^{(i)}$, $\Gamma_\sigma^{(i)}$, $\Gamma_\mathrm{T}^{(i)}$, $\Gamma_\mathrm{q}^{(i)}$ as introduced in Section 2.5 and the additional boundary $\Gamma_\mathrm{c}^{(i)}$ on which contact between the two bodies may occur. These boundaries form a partition of the entire boundary $\partial\Omega_0^{(i)}$ such that

$$\overline{\Gamma_\mathrm{u}^{(i)}} \cup \overline{\Gamma_\sigma^{(i)}} \cup \overline{\Gamma_\mathrm{c}^{(i)}} = \overline{\Gamma_\mathrm{T}^{(i)}} \cup \overline{\Gamma_\mathrm{q}^{(i)}} \cup \overline{\Gamma_\mathrm{c}^{(i)}} = \partial\Omega_0^{(i)} \quad , \tag{2.100a}$$

and

$$\begin{aligned} &\Gamma_\mathrm{u}^{(i)} \cap \Gamma_\sigma^{(i)} = \Gamma_\mathrm{u}^{(i)} \cap \Gamma_\mathrm{c}^{(i)} = \Gamma_\sigma^{(i)} \cap \Gamma_\mathrm{c}^{(i)} = \\ &\Gamma_\mathrm{T}^{(i)} \cap \Gamma_\mathrm{q}^{(i)} = \Gamma_\mathrm{T}^{(i)} \cap \Gamma_\mathrm{c}^{(i)} = \Gamma_\mathrm{q}^{(i)} \cap \Gamma_\mathrm{c}^{(i)} = \emptyset \quad . \end{aligned} \tag{2.100b}$$

The corresponding contact boundary in the displaced configuration is obtained via the motion $\varphi_t^{(i)}$ as $\gamma_\mathrm{c}^{(i)} = \varphi_t^{(i)}(\Gamma_\mathrm{c}^{(i)})$. To quantify relative positions and motions of the current contact boundaries at any time t, a smooth mapping

$$\chi_t : \gamma_\mathrm{c}^{(1)} \to \gamma_\mathrm{c}^{(2)}, \quad \boldsymbol{x}^{(1)} \mapsto \hat{\boldsymbol{x}}^{(2)} = \chi_t(\boldsymbol{x}^{(1)}) \quad , \tag{2.101}$$

is defined for a point on $\boldsymbol{x}^{(1)}$ on the slave surface $\gamma_\mathrm{c}^{(1)}$ by projecting $\boldsymbol{x}^{(1)}$ along its current outward normal $\boldsymbol{n}^{(1)}$ onto $\gamma_\mathrm{c}^{(2)}$, see Figure 2.3. For sufficiently smooth bodies in contact, this mapping can be assumed to exist in the zone of closed contact and a finite vicinity thereof. Vice versa, no contact may occur at $\boldsymbol{x}^{(1)}$ if $\chi_t(\boldsymbol{x}^{(1)})$ does not exist. For simplicity, χ_t is assumed to be well-defined on the entire $\gamma_\mathrm{c}^{(1)}$ in the following. Moreover, the unique contact normal $\boldsymbol{n} = \boldsymbol{n}^{(1)}(\boldsymbol{x}^{(1)})$ will be chosen as the slave-sided normal if not indicated otherwise. At any point on the potential contact surface $\gamma_\mathrm{c}^{(1)}$, the normal distance or *gap* between the two bodies is defined as

$$g_\mathrm{n}(\boldsymbol{x}^{(1)}) = -(\boldsymbol{x}^{(1)} - \hat{\boldsymbol{x}}^{(2)}) \cdot \boldsymbol{n} \quad , \tag{2.102}$$

where positive values indicate separation of the two bodies, contact yields a zero values and negative g_n values are obtained if the bodies penetrate. A frame-indifferent measure of the relative tangential velocity can be defined as

$$\boldsymbol{v}_\tau(\boldsymbol{x}^{(1)}) = -\left(\boldsymbol{I} - \boldsymbol{n} \otimes \boldsymbol{n}\right) \left[\dot{\boldsymbol{x}}^{(1)} - \dot{\hat{\boldsymbol{x}}}^{(2)} + g_\mathrm{n}(\boldsymbol{x}^{(1)})\dot{\boldsymbol{n}}\right] \quad . \tag{2.103}$$

based on the frame-indifferent relative velocity (in brackets) as proposed by Curnier *et al.* [43]. Alternatively, the relative tangential velocity may be defined in terms of convective coordinates on the contact surfaces, see e.g. Laursen [131], Schweizerhof and Konyukhov [191].

2.7.2 Conservation Laws and Entropy Inequality at the Contact Interface

On the contacting surfaces, contact tractions such as the contact pressure in normal direction occur. The spatial Cauchy contact traction $\boldsymbol{t}_\mathrm{c}^{(i)}$ can be evaluated from the Cauchy stress tensor $\boldsymbol{\sigma}^{(i)}$ within a body i and the unit outward normal $\boldsymbol{n}^{(i)}$ on $\gamma_\mathrm{c}^{(i)}$ as

$$\boldsymbol{t}_\mathrm{c}^{(i)} = \boldsymbol{\sigma}^{(i)}\boldsymbol{n}^{(i)} \tag{2.104}$$

and, for an infinitesimal surface element in the contact zone, the balance of linear momentum (cf. Section 2.2.2) reads

$$\boldsymbol{t}_{\mathrm{c}}^{(1)}(\boldsymbol{x}^{(1)}) = -\boldsymbol{t}_{\mathrm{c}}^{(2)}(\hat{\boldsymbol{x}}^{(2)}) \quad . \tag{2.105}$$

As the contact tractions only differ in sign, a unique definition of $\boldsymbol{t}_{\mathrm{c}} = \boldsymbol{t}_{\mathrm{c}}^{(1)}$ will be used hereafter, such that both the contact traction as well as the kinematic quantities in (2.102) and (2.103) are defined on the slave side. The chosen slave side has no significant implication whatsoever in the continuous setting and is merely introduced to fix notation. To be able to distinguish between the contact non-penetration condition (in normal direction) and effects of frictionless or frictional sliding (in tangential direction), the contact traction is split in its normal and tangential component, the contact pressure p_{n} and tangential traction $\boldsymbol{t}_{\tau}$, respectively:

$$p_{\mathrm{n}} = \boldsymbol{n} \cdot \boldsymbol{t}_{\mathrm{c}} \quad , \tag{2.106a}$$

$$\boldsymbol{t}_{\tau} = (\boldsymbol{I} - \boldsymbol{n} \otimes \boldsymbol{n})\, \boldsymbol{t}_{\mathrm{c}} \quad . \tag{2.106b}$$

In addition to the balance of linear momentum (2.105), the conservation of energy (cf. Section 2.2.4) needs to hold at the contact interface. For the course of the derivation it is assumed, that the contact interface may store an internal energy e_{c} per infinitesimal area $\mathrm{d}\gamma_{\mathrm{c}}^{(1)}$ at temperature T_{c}. Though it will not be used in the methods derived later on, this concept of contact surface energies is still introduced here to clarify the derivation. Mechanically, such an internal energy may include elastic deformation of asperities when modeling rough surfaces in contact or thermal energy of debris created by abrasive wear. In rate form, the conservation of energy at the contact interface then reads

$$\dot{e_{\mathrm{c}}} = p_{\mathrm{n}} \dot{g_{\mathrm{n}}} + \boldsymbol{t}_{\tau} \cdot \boldsymbol{v}_{\tau} + q_{\mathrm{c}}^{(1)} + q_{\mathrm{c}}^{(2)} \quad , \tag{2.107}$$

where the first two terms on the right hand side represent the mechanical work the contact traction in normal and tangential direction, respectively, and the third and fourth term denote the spatial contact surface heat flux

$$q_{\mathrm{c}}^{(i)} = \boldsymbol{q}^{(i)} \cdot \boldsymbol{n}^{(i)} \tag{2.108}$$

of the slave and master side according to Stokes' heat flux theorem (2.29) with a positive sign, if a heat flux appears from the body into the contact zone.

Finally, the second law of thermodynamics (cf. Section 2.2.5) should also hold at the contact interface, meaning that in analogy to (2.35), the entropy inequality reads

$$\dot{\eta_{\mathrm{c}}} + \frac{q_{\mathrm{c}}^{(1)}}{T^{(1)}} + \frac{q_{\mathrm{c}}^{(2)}}{T^{(2)}} \geq 0 \quad , \tag{2.109}$$

with the specific entropy η_{c} of an infinitesimal surface area $\mathrm{d}\gamma_{\mathrm{c}}^{(1)}$. The two fractions introduce the entropy flux into the contact surface according to (2.34). Contact energy, entropy and temperature are linked to a contact (Helmholtz) free energy Ψ_{c} via the Legendre transformation

$$\Psi_{\mathrm{c}} = e_{\mathrm{c}} - T_{\mathrm{c}} \eta_{\mathrm{c}} \quad , \tag{2.110}$$

similar to the free energy in the bulk material introduced in (2.37). Using this contact free energy, the contact entropy rate can be eliminated from (2.109) after multiplication with the positive (absolute) temperature T_{c} to obtain the contact dissipation

$$\mathcal{D}_{\mathrm{c}} = \dot{e_{\mathrm{c}}} - \dot{T_{\mathrm{c}}} \eta_{\mathrm{c}} - \dot{\Psi}_{\mathrm{c}} + \frac{q_{\mathrm{c}}^{(1)}}{T^{(1)}} T_{\mathrm{c}} + \frac{q_{\mathrm{c}}^{(2)}}{T^{(2)}} T_{\mathrm{c}} \geq 0 \quad . \tag{2.111}$$

2.7.3 Constitutive Equations at the Contact Interface

The question of contact constitutive equations is now how to define the contact free energy Ψ_{c} as well as the contact heat fluxes $q_{\mathrm{c}}^{(i)}$ such that the balance of energy (2.107) and the entropy inequality (2.111) hold. Generally, the free energy Ψ_{c}, or equivalently the internal energy e_{c}, may depend on the relative displacement of the contacting surfaces, i.e. g_{n} in normal direction and a tangential relative displacement $\boldsymbol{u}_\tau = (\boldsymbol{I} - \boldsymbol{n} \otimes \boldsymbol{n})(\boldsymbol{u}^{(1)}(\boldsymbol{X}^{(1)}) - \boldsymbol{u}^{(2)}(\hat{\boldsymbol{X}}^{(2)})$, as well as the temperature T_{c}. The relative tangential displacement $\boldsymbol{u}_\tau$ is then commonly split addititively into an "elastic" and "plastic" part, where the former is associated with elastic deformation of the asperities in contact and the latter is associated with frictional sliding, and hence only the "elastic" part enters the free energy, see e.g. Laursen [131], Wriggers [240] for a discussion on this split[1]. However, the energy stored in elastic deformation of asperities is usually negligibly small and consequently the contact free energy is assumed in the following to depend on the normal distance and contact temperature only, i.e.

$$\Psi_{\mathrm{c}} = \Psi_{\mathrm{c}}(g_{\mathrm{n}}, T_{\mathrm{c}}) \quad . \tag{2.112}$$

To avoid non-physical penetration of the two contacting bodies, any negative gap $g_{\mathrm{n}} < 0$ (i.e. penetration) can be associated with an infinite energy $\Psi_{\mathrm{c}} = \infty$; on the contrary, two separated bodies, i.e. $g_{\mathrm{n}} > 0$, are unaffected by the contact condition. This relation can be achieved by setting

$$\Psi_{\mathrm{c}} = I_{\Re-}(g_{\mathrm{n}}) + \Psi_{\mathrm{c,T}}(T_{\mathrm{c}}) \quad , \tag{2.113}$$

with the indicator function

$$I_{\Re-}(x) = \begin{cases} 0 & \text{if } x \geq 0 \\ \infty & \text{else} \end{cases} \quad . \tag{2.114}$$

Remark 2.4. *Alternatively, a regularized contact formulation can be obtained by replacing the indicator function with a penalty potential $\Psi_{\mathrm{c,pen}}$, e.g. a quadratic potential*

$$\Psi_{\mathrm{c,pen}}(g_{\mathrm{n}}) = \frac{1}{2}\epsilon_{\mathrm{c}} \left(\max\left(0, -g_{\mathrm{n}}\right)\right)^2 \quad , \tag{2.115}$$

with a penalty parameter $\epsilon_{\mathrm{c}} > 0$. Such a regularization may be physically justified by elastic compliance of asperities in contact if the penalty parameter ϵ_{c} or $\Psi_{\mathrm{c,pen}}(g_{\mathrm{n}})$ in general is well chosen, see e.g. Sitzmann et al. *[208] for a comparison with experimental data. Often, however, this argument is put forward to justify any regularized numerical method, without careful consideration of the "physical" values of the penalty parameter.*

Substituting the definition of the contact free energy (2.113) as well as the balance of energy (2.107) in the dissipation inequality (2.111) yields

$$\mathcal{D}_{\mathrm{c}} = \left(p_{\mathrm{n}} - \frac{\partial I_{\Re-}(g_{\mathrm{n}})}{\partial g_{\mathrm{n}}}\right) \dot{g}_{\mathrm{n}} + \left(-\eta_{\mathrm{c}} - \frac{\partial \Psi_{\mathrm{c,T}}}{\partial T_{\mathrm{c}}}\right) \dot{T}_{\mathrm{c}} + \boldsymbol{t}_\tau \cdot \boldsymbol{v}_\tau + \frac{q_{\mathrm{c}}^{(1)}}{T^{(1)}}\theta^{(1)} + \frac{q_{\mathrm{c}}^{(2)}}{T^{(2)}}\theta^{(2)} \geq 0 \quad , \tag{2.116}$$

[1] The terminology of "elastic" and "plastic" tangential displacement is commonly chosen in reference to elasto-plastic material behavior, whereby only a part of the displacement (the elastic one) is recovered under unloading. It should not be confused with the type of deformation, the asperities in contact undergo.

with $\theta^{(i)} = T^{(i)} - T_\mathrm{c}$. In the case of exact enforcement of the non-penetration condition by the indicator function (2.113), the derivative with respect to the gap g_n has to be interpreted as a subdifferential. Using the same arguments as in Section 2.3.3, equation (2.116) has to hold for any $\dot{g}_\mathrm{n}$ and $\dot{T}_\mathrm{c}$, such that the terms in parentheses give rise to the contact constitutive equations

$$p_\mathrm{n} \in \frac{\partial I_{\Re-}(g_\mathrm{n})}{\partial g_\mathrm{n}} \ , \tag{2.117}$$

$$\eta_\mathrm{c} = -\frac{\partial \Psi_\mathrm{c}}{\partial T_\mathrm{c}} \ . \tag{2.118}$$

Again, due to the nature of the indicator function, the constitutive equation for normal contact pressure takes the form of a subdifferential inclusion, which, as shown e.g. by Curnier [42], is equivalent to the Hertz–Signiorini–Moreau conditions

$$g_\mathrm{n} \geq 0 \ , \quad p_\mathrm{n} \leq 0 \ , \quad p_\mathrm{n} g_\mathrm{n} = 0 \ , \tag{2.119}$$

commonly enforced at the contact interface. If instead a penalty potential, e.g. (2.115), is used in normal direction, the normal contact pressure follows directly from the derivative of the penalty potential as $p_\mathrm{n} = {\partial \Psi_{\mathrm{c,pen}}}/{\partial g_\mathrm{n}}$. The remaining contact dissipation in (2.116) reads

$$\mathcal{D}_\mathrm{c} = \boldsymbol{t}_\tau \cdot \boldsymbol{v}_\tau + \frac{q_\mathrm{c}^{(1)}}{T^{(1)}}\theta^{(1)} + \frac{q_\mathrm{c}^{(2)}}{T^{(2)}}\theta^{(2)} \geq 0 \ . \tag{2.120}$$

As for the elasto-plastic material in the bulk continuum (cf. Section 2.3.4.2), non-negative dissipation can be ensured by postulating a convex dissipation potential $\Xi_\mathrm{c}(\boldsymbol{v}_\tau, \theta^{(1)}, \theta^{(2)})$ and deriving the tangential contact traction as well as the entropy fluxes via the subdifferential inclusion

$$\left(\boldsymbol{t}_\tau, \frac{q_\mathrm{c}^{(1)}}{T^{(1)}}, \frac{q_\mathrm{c}^{(2)}}{T^{(2)}} \right) \in \partial \Xi_\mathrm{c}(\boldsymbol{v}_\tau, \theta^{(1)}, \theta^{(2)}) \ . \tag{2.121}$$

Following Moreau [153], positive dissipation is ensured for a convex potential Ξ_c for which

$$\Xi_\mathrm{c}(\boldsymbol{0}, 0, 0) = 0 \quad \text{and} \quad (\boldsymbol{0}, 0, 0) \in \partial \Xi_\mathrm{p}(\boldsymbol{0}, 0, 0) \ . \tag{2.122}$$

A simple choice for the contact dissipation potential that satisfies these conditions is

$$\Xi_\mathrm{c} = \mu |p_\mathrm{n}| \|\boldsymbol{v}_\tau\| + \sum_{i=1}^{2} \frac{\gamma^{(i)}}{T^{(i)}} \left(\theta^{(i)}\right)^2 \ , \tag{2.123}$$

with a potentially temperature dependent coefficient of friction μ and commonly pressure dependent heat transfer parameters $\gamma^{(i)}$ on the slave and master side, respectively. In terms of the tangential contact traction $\boldsymbol{t}_\tau$, the subdifferential inclusion (2.121) with the dissipation potential (2.123) is equivalent (see again Moreau [153]) to Coulomb's law of friction

$$\phi_\tau := \|\boldsymbol{t}_\tau\| - \mu |p_\mathrm{n}| \leq 0 \ , \quad \boldsymbol{v}_\tau - \beta \boldsymbol{t}_\tau = \boldsymbol{0} \ , \quad \beta \geq 0 \ , \quad \phi_\tau \beta = 0 \ , \tag{2.124}$$

which bears great similarity with the material constraints of plasticity in (2.70) and (2.71). The consistency parameter β therein takes the role of the plastic multiplier $\dot{\gamma}$. In a fully thermomechanically coupled problem, the coefficient of friction may be temperature dependent; a simple dependency is given in Oancea and Laursen [159] as

$$\mu(\vartheta_\mathrm{c}) = \mu_0 \frac{(\vartheta_\mathrm{c} - T_\mathrm{d})^2}{(T_\mathrm{d} - T_0)^2} \ , \tag{2.125}$$

where the apparent coefficient of friction decreases quadratically from a reference value μ_0 at T_0 to zero at T_d depending on the the maximum of the temperatures of the two contacting surfaces $\vartheta_\mathrm{c} = \max(T^{(1)}(\boldsymbol{x}^{(1)}), T^{(2)}(\hat{\boldsymbol{x}}^{(2)}))$. The damage temperature T_d is usually chosen to be the lower melting temperature of the two contacting materials, since at this point, friction is no longer dominated by solid shearing but rather viscous effects in a thin film of molten material. The second part of (2.123) yields, via the inclusion (2.121), the contact heat fluxes

$$q_\mathrm{c}^{(i)} = \gamma^{(i)} \theta^{(i)} \ . \tag{2.126}$$

The convexity requirement of the dissipation potential to ensure positive dissipation necessitates $\gamma^{(i)} \geq 0$. Further, no heat flux at the contact interface should occur if the bodies are not in contact. Continuity of the problem formulation then depends upon $\gamma^{(i)} = 0$ if $p_\mathrm{n} = 0$, as $p_\mathrm{n} = 0$ holds for separated bodies and p_n increases continuously from there when bodies come into contact. By (2.126), then also the contact heat fluxes are zero for separated bodies and evolve continuously with p_n. Throughout this work, a simple linear function for

$$\gamma^{(i)} = |p_\mathrm{n}| \bar{\gamma}^{(i)} \ , \tag{2.127}$$

with constants $\bar{\gamma}^{(i)} \geq 0$ will be adopted for demonstration purposes, however, any nonlinear relation satisfying the requirements above may be employed as discussed at the end of this section. Lastly, it will be assumed that the thermal energy stored in the contact interface is negligible, $e_\mathrm{c} = 0$, wherefore the of energy at the contact interface reduces to[1]

$$\boldsymbol{t}_\tau \cdot \boldsymbol{v}_\tau + q_\mathrm{c}^{(1)} + q_\mathrm{c}^{(2)} = 0 \ , \tag{2.128}$$

and the temperature of the contact interface T_c can be eliminated from (2.126) to directly define the contact heat fluxes as

$$q_\mathrm{c}^{(1)} = \beta_\mathrm{c} |p_\mathrm{n}| [\![T]\!] - \delta_\mathrm{c} \boldsymbol{t}_\tau \cdot \boldsymbol{v}_\tau \ , \tag{2.129a}$$

$$q_\mathrm{c}^{(2)} = -\beta_\mathrm{c} |p_\mathrm{n}| [\![T]\!] - (1 - \delta_\mathrm{c}) \boldsymbol{t}_\tau \cdot \boldsymbol{v}_\tau \ , \tag{2.129b}$$

in terms of the temperature jump across the interface $[\![T]\!] = T^{(1)} - (T^{(2)} \circ \chi_t)$ and the two constants

$$\beta_\mathrm{c} = \frac{\bar{\gamma}^{(1)} \bar{\gamma}^{(2)}}{\bar{\gamma}^{(1)} + \bar{\gamma}^{(2)}} \geq 0 \ , \quad \delta_\mathrm{c} = \frac{\bar{\gamma}^{(1)}}{\bar{\gamma}^{(1)} + \bar{\gamma}^{(2)}} \in [0, 1] \ , \tag{2.130}$$

as defined by Oancea and Laursen [159]. The first one, β_c, represents a contact heat conductivity resulting in a heat flux from the hotter to the cooler contacting body driven by the temperature

[1] The term $p_\mathrm{n} \dot{g}_\mathrm{n}$ in (2.107) drops out due to the complementarity (2.119).

difference. Due to the linear law (2.127), this part of the heat flux is linear not only in the temperature difference $[\![T]\!]$ but also the contact pressure $|p_\mathrm{n}|$. Yet, more sophisticated models of interface heat conductivity may be found in the literature. For instance, Wriggers [240] distinguishes three sources of heat conduction across rough surfaces: conduction through contacting asperities, heat conduction in enclosed gas and radiation. In that case, the product $\beta_\mathrm{c}|p_\mathrm{n}|$ in (2.129) needs to be replaced by a nonlinear function $\tilde{\beta}_\mathrm{c}(|p_\mathrm{n}|) \geq 0$ with $\tilde{\beta}_\mathrm{c}(0) = 0$. For the numerical methods derived Chapters 4 and 5, this nonlinearity does not induce significant difficulties and is therefore omitted in the following. The second parameter in (2.129), δ_c, distributes the heat generated by frictional work to the two bodies in contact. In the limit cases of $\delta_\mathrm{c} = 0$ or $\delta_\mathrm{c} = 1$ the entire frictional dissipation is converted to heat in on the master or slave side, respectively.

2.7.4 Weak Forms including Contact

Starting point for the derivation of weak forms is again the strong form of the initial boundary value problem. The local balance of linear momentum and heat conduction equation as well as the Dirichlet and Neumann boundary conditions and initial data remain unaltered to the definition in (2.91). As done in Section 2.6, multiplication of (2.91a) with a test function and subsequent integration by parts yields the weak form of the balance of linear momentum as: Find $\boldsymbol{u} \in \boldsymbol{\mathcal{U}}_\mathrm{u}$, such that

$$\delta\mathcal{W}_\mathrm{u} - \sum_{i=1}^{2} \int_{\gamma_\mathrm{c}^{(i)}} \boldsymbol{t}_\mathrm{c}^{(i)} \cdot \delta\boldsymbol{u}^{(i)} \,\mathrm{d}\gamma = 0 \quad \forall \delta\boldsymbol{u} \in \boldsymbol{\mathcal{V}}_\mathrm{u} \ , \tag{2.131}$$

with $\delta\mathcal{W}_\mathrm{u}$ as defined in (2.95). Note, that the contact integrals are, in contrast to the all other terms, written in the current configuration using the Cauchy traction vectors according to (2.104). However, this is only a matter of notation at this point, as the surface integral on $\gamma_\mathrm{c}^{(i)}$ could be reformulated equivalently as an integral of Piola traction $\boldsymbol{t}_{0,\mathrm{c}}^{(i)} = \boldsymbol{P}^{(i)}\boldsymbol{N}^{(i)}$ over $\Gamma_\mathrm{c}^{(i)}$ in terms by means of Nanson's formula (2.5). Exploiting the balance of linear momentum across the contact interface (2.105), the contact terms may be written as a slave-sided integral only, in which case (2.131) becomes: Find $\boldsymbol{u} \in \boldsymbol{\mathcal{U}}_\mathrm{u}$, such that

$$\delta\mathcal{W}_\mathrm{u} - \int_{\gamma_\mathrm{c}^{(1)}} \boldsymbol{t}_\mathrm{c} \cdot [\![\delta\boldsymbol{u}]\!] \,\mathrm{d}\gamma = 0 \quad \forall \delta\boldsymbol{u} \in \boldsymbol{\mathcal{V}}_\mathrm{u} \ . \tag{2.132}$$

Similarly, the weak form of the heat conduction equation (2.99) has to be extended by the contact heat fluxes $q_\mathrm{c}^{(i)}$. If the contact integrals are again written on the slave side only, the weak form reads: Find $T \in \mathcal{U}_\mathrm{T}$, such that

$$\delta\mathcal{W}_\mathrm{T} + \int_{\gamma_\mathrm{c}^{(1)}} q_\mathrm{c}^{(1)}\delta T^{(1)} + q_\mathrm{c}^{(2)}(\delta T^{(2)} \circ \chi_t) \,\mathrm{d}\gamma = 0 \quad \forall \delta T \in \mathcal{V}_\mathrm{T} \ . \tag{2.133}$$

In analogy to (2.132), in which the master-sided contact traction $\boldsymbol{t}_\mathrm{c}^{(2)}$ has been eliminated via the balance of linear momentum (2.105), the master-sided contact heat flux $q_\mathrm{c}^{(2)}$ can be eliminated by virtue of the energy balance at the contact interface (2.128) to express (2.133) in terms of the slave-sided heat flux only:

$$\delta\mathcal{W}_\mathrm{T} + \int_{\gamma_\mathrm{c}^{(1)}} q_\mathrm{c}^{(1)}[\![\delta T]\!] - \boldsymbol{t}_\tau \cdot \boldsymbol{v}_\tau(\delta T^{(2)} \circ \chi_t) \,\mathrm{d}\gamma = 0 \quad \forall \delta T \in \mathcal{V}_\mathrm{T} \ . \tag{2.134}$$

In addition to the satisfaction of the weak forms (2.132) and (2.133) (or (2.134)), the contact constraints at the interface have to be met, i.e. the Hertz–Signiorini–Moreau conditions (2.119), Coulomb's law of friction (2.124) and the heat constitutive equations for the heat fluxes (2.129) have to be satisfied.

2.8 Finite Element Discretization

Even in the absence of contact, only in very limited, simple cases the IBVP (2.91) can be solved analytically; for most practical applications, approximate solutions are constructed using numerical methods. In solid mechanics, the by far most common method to do so is the Finite Element Method (FEM), which will also be used in this thesis. The introduction of the discretization given in this section is not meant as an embracing introduction to the vast field of FEM, but to provide a consistent basis for the methods derived in the following chapters. At this point, the derivation of the FEM is restricted to thermo-elasticity without contact, as the extension to elasto-plasticity is discussed in Chapter 3 and to thermomecanical contact problems in Chapters 4 and 5. For a thorough introduction to the mathematical aspects of finite element methods, the reader is referred to, e.g., Strang and Fix [211] and to Hughes [111], Zienkiewicz *et al.* [252, 253] for an engineering perspective. In line with the scope of this thesis, an introduction to nonlinear finite element methods is given by Wriggers [241], applications to nonlinear and inelastic materials can be found in Bonet and Wood [19], de Souza Neto *et al.* [57], Simo and Hughes [200] and to contact mechanics in Laursen [131], Wriggers [240].

2.8.1 Spatial Discretization

While the weak forms derived in the previous section are still equivalent with the strong form (2.91), they form the basis of a class of numerical methods, so-called *Galerkin methods* approximating the solution $\boldsymbol{u}$ and T. Therefore, discrete, finite dimensional sub-spaces $\boldsymbol{\mathcal{U}}_{\mathrm{u},h}$, $\boldsymbol{\mathcal{V}}_{\mathrm{u},h}$, $\mathcal{U}_{\mathrm{T},h}$ and $\mathcal{V}_{\mathrm{T},h}$ of the infinite dimensional function spaces $\boldsymbol{\mathcal{U}}_{\mathrm{u}}$, $\boldsymbol{\mathcal{V}}_{\mathrm{u}}$, $\mathcal{U}_{\mathrm{T}}$ and $\mathcal{V}_{\mathrm{T}}$ are introduced and the weak forms (2.95) and (2.99) are required to hold only for these sub-spaces. For simplicity of presentation, this section assumes homogeneous Dirichlet boundary conditions for both displacements and temperatures, and consequently $\boldsymbol{\mathcal{U}}_{\mathrm{u}} = \boldsymbol{\mathcal{V}}_{\mathrm{u}}$ and $\mathcal{U}_{\mathrm{T}} = \mathcal{V}_{\mathrm{T}}$. The discrete test and trial spaces are spanned by a set of n basis functions $N_i : \Omega_0 \mapsto \Re$, such that

$$\boldsymbol{\mathcal{U}}_{\mathrm{u}} \supset \boldsymbol{\mathcal{U}}_{\mathrm{u},h} = \boldsymbol{\mathcal{V}}_{\mathrm{u},h} = \left[\operatorname*{span}_{i=1\ldots n}\{N_i\}\right]^{n_{\mathrm{dim}}} \quad , \tag{2.135a}$$

$$\mathcal{U}_{\mathrm{T}} \supset \mathcal{U}_{\mathrm{T},h} = \mathcal{V}_{\mathrm{T},h} = \operatorname*{span}_{i=1\ldots n}\{N_i\} \quad . \tag{2.135b}$$

It is, however, not mandatory to use the same discrete function spaces for both the trial as well as the test functions; if they are chosen equal, the resulting method is commonly referred to as a Bubnov–Galrekin method, otherwise as a Petrov–Galerkin method. In accordance with (2.135), the displacement and temperature field as well as their variations can be represented by linear

combinations of basis functions N_i with discrete values $\mathbf{d}_i, \delta\mathbf{d}_i \in \Re^{n_{\mathrm{dim}}}$ and $\mathsf{T}_i, \delta\mathsf{T}_i \in \Re$ by

$$\boldsymbol{u}(\boldsymbol{X},t) \approx \boldsymbol{u}_h(\boldsymbol{X},t) = \sum_i N_i(\boldsymbol{X})\mathbf{d}_i(t) \quad , \quad \delta\boldsymbol{u}(\boldsymbol{X}) \approx \delta\boldsymbol{u}_h(\boldsymbol{X}) = \sum_i N_i(\boldsymbol{X})\delta\mathbf{d}_i \quad , \tag{2.136a}$$

$$T(\boldsymbol{X},t) \approx T_h(\boldsymbol{X},t) = \sum_i N_i(\boldsymbol{X})\mathsf{T}_i(t) \quad , \quad \delta T(\boldsymbol{X}) \approx \delta T_h(\boldsymbol{X}) = \sum_i N_i(\boldsymbol{X})\delta\mathsf{T}_i \quad , \tag{2.136b}$$

where the dependency of approximate fields on space and time is split to the basis functions and discrete values, respectively. The time dependency of the discrete test test functions are dropped at this point as they are supposed to take arbitrary values in the weak form anyway. Insertion of the approximation (2.135) in the weak forms (2.95) and (2.99) results in a set of coupled nonlinear equations in the discrete values $\mathbf{d}_i$ and T_i and their temporal derivatives. Subsequently, two common methods to construct approximation spaces (2.135) are discussed.

2.8.1.1 Classical Finite Elements

The far most common numerical method for computational solid mechanics is the (continuous) finite element method, subdividing the computational domain into non-overlapping elements of simple shapes, usually triangles and quadrilaterals in two dimensions and tetrahedra or hexahedra in three dimensions, and defining polynomial basis functions on these elements which are continuous across element boundaries. To fix ideas, the following derivation assumes quadrilateral and hexahedral elements only. Let therefore $\mathcal{T}_h$ be a finite element mesh on Ω_0 with a characteristic element length h and τ_h a quadrilateral or hexahedral element within this mesh, such that

$$\overline{\Omega_0} \approx \overline{\Omega_{0,h}} = \bigcup_{k=1}^{n} \overline{\tau_{h,k}} \quad , \tag{2.137}$$

with n being the number of elements in the mesh. For any element $\tau_{h,k}$, there exists a mapping $\Phi_{\tau_{h,k}} : (-1,1)^{n_{\mathrm{dim}}} \mapsto \tau_{h,k}$ of a bi-unit cube reference element with parametric coordinates $\xi_1,\ldots,\xi_{n_{\mathrm{dim}}}$ to the actual element $\tau_{h,k}$. On the reference element, polynomial basis functions of degree p in each direction are defined to span $\mathbb{Q}_p = \mathrm{span}_{\alpha_i \le p}\{\xi_1^{\alpha_1} \cdot \ldots \cdot \xi_{n_{\mathrm{dim}}}^{\alpha_{n_{\mathrm{dim}}}}\}$. Commonly, a set of element basis functions is chosen as Lagrange polynomials interpolating a grid of $p+1$ nodes in each parametric direction; the one-dimensional basis functions of first and second order are illustrated in Figure 2.4. The basis functions on the n_{dim}-dimensional bi-unit cube follow from those by tensorization, i.e.

$$N_{\mathbf{i}}^{(\tau_h)}(\boldsymbol{\xi}) = \prod_{i=1}^{n_{\mathrm{dim}}} N_i^{(\tau_h)}(\xi_i) \quad , \tag{2.138}$$

with the multi-index $\mathbf{i}$. In the isoparametric concept, the same basis functions are used to construct the mapping $\Phi_{\tau_{h,k}}$ of reference element to the element $\tau_{h,k}$ in $\mathcal{T}_h$. Let therefore $\mathbf{X}_\mathbf{i}$ be the coordinate of the $\mathbf{i}$-th element node interpolated by the basis function $N_\mathbf{i}$; then, $\Phi_{\tau_{h,k}}$ is set as

$$\Phi_{\tau_{h,k}} : (-1,1)^{n_{\mathrm{dim}}} \to \tau_{h,k}, \quad \boldsymbol{\xi} \mapsto \sum_{\mathbf{i}} N_{\mathbf{i}}^{(\tau_h)}(\boldsymbol{\xi})\mathbf{X}_\mathbf{i} \quad . \tag{2.139}$$

With this mapping at hand, finally the global discrete trial and test spaces can be defined as

$$\boldsymbol{\mathcal{U}}_{\mathrm{u},h} = \boldsymbol{\mathcal{V}}_{\mathrm{u},h} = \left\{\boldsymbol{u}_h \in \left[C^0(\Omega_{0,h})\right]^{n_{\mathrm{dim}}} \,\middle|\, \boldsymbol{u}_h|_{\tau_{h,k}} \circ \Phi_{\tau_{h,k}} \in [\mathbb{Q}_p]^{n_{\mathrm{dim}}}, \tau_{h,k} \in \mathcal{T}_h\right\} \quad , \tag{2.140a}$$

$$\mathcal{U}_{\mathrm{T},h} = \mathcal{V}_{\mathrm{T},h} = \left\{T_h \in C^0(\Omega_{0,h}) \,\middle|\, T_h|_{\tau_{h,k}} \circ \Phi_{\tau_{h,k}} \in \mathbb{Q}_p, \quad \tau_{h,k} \in \mathcal{T}_h\right\} \quad , \tag{2.140b}$$

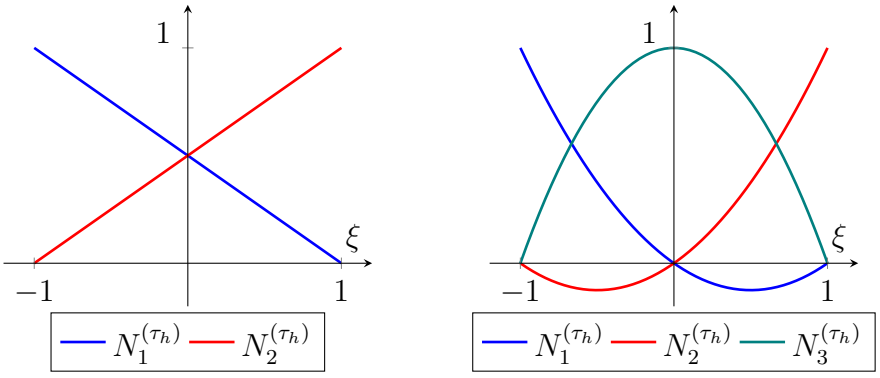

(a) $p = 1$ (b) $p = 2$

Figure 2.4: Univariate Lagrange polynomial basis functions of first and second order on the reference domain $(-1, 1)$.

where C^0 continuity across element boundaries can easily be achieved by elements sharing nodal degrees of freedom on element boundaries. To guarantee the discrete function spaces to be in sufficiently smooth, the isoparametric mapping $\Phi_{\tau_{h,k}}$ for every element $\tau_{h,k}$ has to be at least C^1-smooth, orientation preserving, invertible, and one-to-one onto $\tau_{h,k}$, see Hughes [111, Section 3.3].

Although the present thesis employs quadrilateral and hexahedral shape elements with the described tensor product structure exclusively, two other classes of elements commonly used should be commented on; a thorough introduction can be found in any textbook, e.g. the ones by Hughes [111], Quarteroni and Valli [179]. First, finite elements of quadrilateral and hexahedral shape can be constructed from the aforementioned by omitting the nodes on element faces and the element interior. This results in so-called serendipity elements with the polynomial basis $\mathbb{T}_p$ of degree p. Of course, first order elements do not contain any interior nodes, such that $\mathbb{T}_1 = \mathbb{Q}_1$. Second, finite elements of triangular and tetrahedral shape (sometimes referred to as simplex elements) in two and three dimensions, respectively, can be constructed with the basis functions in $\mathbb{P}_p$ containing all polynomials of degree p. For $p = 1$, this can be achieved using Lagrange polynomials interpolating the corners of the triangle or tetrahedron, and for higher orders, interpolatory nodes are inserted on element edges. Figure 2.5 illustrates the reference elements of tensor product finite elements, serendipity elements and simplex elements in two dimensions.

Semi-Discrete Balance of Linear Momentum The discrete function spaces (2.140), or more generally any discretization of the type (2.136), yield the semi-discrete (discretized in space, continuous in time) weak form of the balance of linear momentum (2.95) as

$$\begin{aligned}\delta\mathcal{W}_{\mathrm{u},h} = &\int_{\Omega_{0,h}} \rho_0 \boldsymbol{a}_h \cdot \delta\boldsymbol{u}_h \,\mathrm{d}\Omega + \int_{\Omega_{0,h}} \boldsymbol{P} : \nabla_{\boldsymbol{X}} \delta\boldsymbol{u}_h \,\mathrm{d}\Omega \\ &- \int_{\Omega_{0,h}} \boldsymbol{b}_0 \cdot \delta\boldsymbol{u}_h \,\mathrm{d}\Omega - \int_{\Gamma_{\sigma,h}} \hat{\boldsymbol{t}}_0 \cdot \delta\boldsymbol{u}_h \,\mathrm{d}\Gamma = 0 \quad \forall \delta\boldsymbol{u}_h \in \boldsymbol{\mathcal{V}}_{\mathrm{u},h} \ .\end{aligned} \tag{2.141}$$

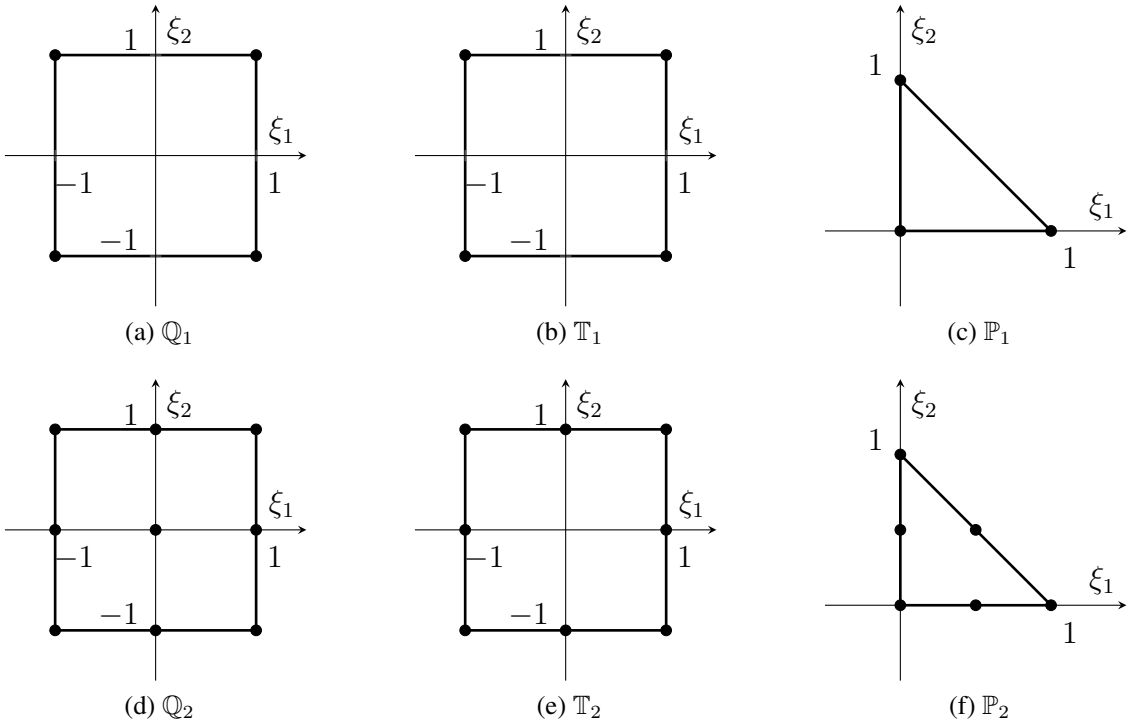

(a) $\mathbb{Q}_1$ (b) $\mathbb{T}_1$ (c) $\mathbb{P}_1$

(d) $\mathbb{Q}_2$ (e) $\mathbb{T}_2$ (f) $\mathbb{P}_2$

Figure 2.5: Two dimensional reference elements and nodes (marked as dots) for different Lagrange finite elements: First row $p = 1$, second row $p = 2$, first column tensor product elements, second column serendipity elements, third column simplex elements.

The stress $\boldsymbol{P}$ therein depend on the discrete approximation of the displacement field $\boldsymbol{u}_h$ (or the gradient thereof) as well as the discretized temperature field T_h. In the presence of internal variables of state, $\boldsymbol{P}$ additionally depends on a discretization $\boldsymbol{\alpha}_h$ of the involved internal variables, where the exact algorithmic treatment of these dependencies is the topic of Section 3. The discrete integrals, in general, cannot be evaluated analytically, but are approximated by Gaussian quadrature on each element using $p + 1$ Gauss points in each parametric direction. As the isoparametric mapping (2.139) as well as the dependency of $\boldsymbol{P}$ on discrete displacements and temperatures may be non-polynomial, Gaussian quadrature will not be exact. As the discrete weak form should hold for any discrete virtual displacement $\delta\boldsymbol{u}_h$, it can be equivalently stated as the coupled nonlinear differential equations in time

$$\boldsymbol{M}_{\mathrm{u}}\ddot{\mathbf{d}} + \boldsymbol{F}_{\mathrm{u,int}}(\mathbf{d}, \mathbf{T}, \boldsymbol{\alpha}_h) - \boldsymbol{F}_{\mathrm{u,ext}} = \mathbf{0} \quad , \tag{2.142}$$

wherein the vectors $\mathbf{d}$ and $\mathbf{T}$ contain all nodal displacement and temperature values, respectively. The first term corresponds to the first integral in (2.141) and relates to inertia forces using the constant mass matrix $\boldsymbol{M}_{\mathrm{u}}$. The second term, called internal force vector $\boldsymbol{F}_{\mathrm{u,int}}$, corresponds to the second integral in (2.141) and accounts for discrete nodal forces emanating from internal stresses, and finally the last term $\boldsymbol{F}_{\mathrm{u,ext}}$ results from external forces from the third and fourth integral in (2.141). For brevity of notation only, the external forces are assumed independent of the displacement and temperature field.

Semi-Discrete Heat Conduction Equation Analogously, the semi-discrete weak form of the heat conduction equation (2.99) is obtained introducing the discretization (2.136) and reads

$$\delta\mathcal{W}_{\mathrm{T},h} = \int_{\Omega_{0,h}} c_{\mathrm{v}}\dot{T}_h\delta T_h \,\mathrm{d}\Omega - \int_{\Omega_{0,h}} \boldsymbol{Q}\cdot\nabla_{\boldsymbol{X}}\delta T_h \,\mathrm{d}\Omega$$
$$- \int_{\Omega_{0,h}} \left(R + \chi\boldsymbol{\Sigma} : \boldsymbol{D}_{\mathrm{p},h} + T\frac{\partial \boldsymbol{S}}{\partial T} : \dot{\boldsymbol{C}}\right)\delta T_h \,\mathrm{d}\Omega - \int_{\Gamma_{\mathrm{q},h}} \hat{Q}_{\mathrm{n}}\delta T_h \,\mathrm{d}\Gamma = 0 \quad \forall \delta T_h \in \mathcal{V}_{\mathrm{T},h} \ , \tag{2.143}$$

with a discretization $\boldsymbol{D}_{\mathrm{p},h}$ of the plastic rate of deformation $\boldsymbol{D}_{\mathrm{p}}$ to be defined in Section 3.1. Other stresses, strains and heat fluxes therein are determined as functions of the discretized fields. Similar to (2.142), an equivalent coupled nonlinear differential equation can be formulated as

$$\boldsymbol{M}_{\mathrm{T}}\dot{\mathbf{T}} + \boldsymbol{F}_{\mathrm{T,int}}(\mathbf{d}, \mathbf{T}, \boldsymbol{\alpha}_h) - \boldsymbol{F}_{\mathrm{T,ext}}(\mathbf{d}, \mathbf{T}, \boldsymbol{\alpha}_h) = \mathbf{0} \ , \tag{2.144}$$

where the first term reflects the heat capacity (first integral in (2.143)) with the constant heat capacity matrix $\boldsymbol{M}_{\mathrm{T}}$, the internal force vector $\boldsymbol{F}_{\mathrm{T,int}}$ accounts for heat conduction through the second integral in (2.143) and the $\boldsymbol{F}_{\mathrm{T,ext}}$ accounts for heat sources in the bulk and on the Neumann boundary determined by the third and fourth integral in (2.143).

Locking For problems in elasticity and elasto-plasticity, it is well-known that, for low order approximations especially, solution quality may be poor for elements with high aspect ratios, trapezoidal shape or nearly incompressible materials. This phenomenon is referred to as *locking* in engineering literature. Methods to alleviate locking effects in different pathological cases are summarized as *element technology* and, to this day, constitute an active field of research. Some of meanwhile well-established methods are (selective) reduced integration introduced [251], B-bar methods [110], mixed methods [206], enhanced assumed strain (EAS) methods [202], and F-bar methods [55], where only the reference to the first appearance is given. For the course of this thesis, locking due to incompressible material behavior is of special interest as plastic deformation in metals is assumed to be volume preserving, which naturally follows from a pressure insensitive yield criterion in conjunction with an associative flow rule, see Section 2.3.4. Simply speaking, the issue of volumetric locking originates in the fact, that the displacement approximation by $\mathbb{Q}_1$ hexahedrals is not capable of representing a discrete displacement field with point-wise constant volume, i.e. $\det \boldsymbol{F} \equiv 1$. If a local change of volume is associated with large reaction forces as it is the case in incompressible elasticity or volume preserving plastic deformation, the discrete solution behaves to stiff (”locks”) underestimating displacements and overestimating forces, respectively.

To overcome this type of locking, first order F-bar elements as originally introduced by de Souza Neto *et al.* [55] for hexahedrals and extended to tetrahedrals by Andrade Pires *et al.* [4], de Souza Neto *et al.* [56] will be used in this thesis and the general concept of these elements shall be recalled briefly. Though a point-wise volume preserving deformation cannot be represented by $\mathbb{Q}_1$ elements, a constant volume evaluated at the element centers can. The idea therefore is, to first decompose the deformation gradient within an element into a purely volumetric part $\boldsymbol{F}_{\mathrm{v}} = \det[\boldsymbol{F}]^{1/3}\boldsymbol{I}$ and a deviatoric part $\boldsymbol{F}_{\mathrm{d}} = \det[\boldsymbol{F}]^{-1/3}\boldsymbol{F}$. An assumed deformation gradient $\bar{\boldsymbol{F}}$ within an element is then constructed from the deviatoric part of the deformation gradient compatible with the displacement approximation and the volumetric part from the element

center as

$$\bar{\boldsymbol{F}} = \boldsymbol{F}_{\mathrm{v},0}\boldsymbol{F}_{\mathrm{d}} = \left(\frac{\det \boldsymbol{F}_0}{\det \boldsymbol{F}}\right)^{\frac{1}{3}} \boldsymbol{F} \quad , \tag{2.145}$$

where a subscript $(\cdot)_0$ denotes a quantity evaluated at the element center. Then, the Cauchy stress $\boldsymbol{\sigma}$ is assumed to depend on $\bar{\boldsymbol{F}}$ rather than $\boldsymbol{F}$, which, in view of (2.21), yields a different approximation of the internal forces (second integral in (2.141)) as

$$\boldsymbol{F}_{\mathrm{u,int}} \cdot \delta\boldsymbol{u} = \bigcup_{\tau_h \in \mathcal{T}_h} \int_{\tau_h} \left(\frac{\det \boldsymbol{F}_0}{\det \boldsymbol{F}}\right)^{-\frac{2}{3}} \bar{\boldsymbol{P}} : \nabla_{\boldsymbol{X}} \delta\boldsymbol{u}_h \, \mathrm{d}\Omega \quad , \tag{2.146}$$

where $\bar{\boldsymbol{P}} = \boldsymbol{P}(\bar{\boldsymbol{F}})$ is calculated according to (2.50) replacing the deformation gradient $\boldsymbol{F}$ with its assumed counterpart $\bar{\boldsymbol{F}}$. For the elasto-plastic materials introduced in Section 2.3.4, the assumed deformation gradient is then split into elastic and plastic contributions $\bar{\boldsymbol{F}} = \bar{\boldsymbol{F}}_{\mathrm{e}}\bar{\boldsymbol{F}}_{\mathrm{p}}$. If additionally the plastic flow is isochoric as it is the case for pressure insensitive yield functions with an associative flow rule, one obtains $\det \boldsymbol{F}_{\mathrm{p}} \equiv 1$ and hence

$$\bar{\boldsymbol{F}} = \left(\frac{\det \boldsymbol{F}_0}{\det \boldsymbol{F}}\right)^{\frac{1}{3}} \boldsymbol{F}_{\mathrm{e}}\boldsymbol{F}_{\mathrm{p}} = \bar{\boldsymbol{F}}_{\mathrm{e}}\boldsymbol{F}_{\mathrm{p}} \quad . \tag{2.147}$$

The modification in the evaluation of stresses is therefore applied to the elastic part of the deformation gradient only, from which stresses are calculated according to (2.61).

2.8.1.2 NURBS-based Isogeometric Analysis

Since its original publication by Hughes *et al.* [112], so-called isogeometric analysis has been a very active field of research. The general idea is to use spline basis functions commonly used in computer aided geometric design (CAGD) also in numerical methods and by doing so to reduce the effort in generating computational meshes for finite element analysis. Within this work, non-uniform rational B-spline (NURBS) functions, which are one of the most frequently used approximations in CAGD, will be employed. However, most of the presented methods also transfer to more recent isogeometric methods based on trimmed NURBS [189] or T-splines [11] and locally refined discretizations based on hierarchical NURBS [224] or THB-splines [78]. Aside from the Galerkin-type approximations applied in this work, the higher continuity of NURBS basis functions allow to use collocation methods [9], which, however, require special attention in case of elasto-plasticity due to the non-smoothness of the stress-strain relation and are therefore not considered here. In the following, only a brief and far from complete introduction to the methods later used in this thesis are presented; for a thorough introduction to NURBS functions and the resulting numerical methods the reader is referred to the textbooks of Piegl and Tiller [167] and Cottrell *et al.* [40], respectively.

NURBS are, as indicated by the name, based on Basis-splines or B-splines. Starting univariate splines with the parametric coordinate ξ, a *knot-vector*

$$\boldsymbol{\Xi} = \{\xi_1, \xi_2, \ldots, \xi_{n+p+1}\} \tag{2.148}$$

is defined by a non-decreasing series of of *knots* ξ_i, where n will be the number of basis functions and p the polynomial degree. A knot-vector is called *uniform* if the knots are equally spaced and

non-uniform otherwise. In *open* knot vectors the first and last knot are repeated $(p+1)$-times such that $\xi_1 = \xi_2 = \ldots \xi_{p+1}$ and $\xi_n = \xi_{n+1} = \cdots = \xi_{n+p+1}$. Without loss of generality, it will be assumed in the following that $\xi_1 = 0$ and $\xi_{n+p+1} = 1$. Within a so-called *knot-span* $[\xi_i, \xi_{i+1})$ a B-spline of degree p is defined by the Cox–de Boor recursion formula

$$B_{i,p}(\xi) = \frac{\xi - \xi_i}{\xi_{i+p} - \xi_i} B_{i,p-1}(\xi) + \frac{\xi_{i+p+1} - \xi}{\xi_{i+p+1} - \xi_{i+1}} B_{i+1,p-1}(\xi) \quad , \tag{2.149}$$

with the initial basis of $p = 0$ defined as

$$B_{i,0}(\xi) = \begin{cases} 1 & \text{if } \xi_i \leq \xi < \xi_{i+1} \quad , \\ 0 & \text{else} \quad . \end{cases} \tag{2.150}$$

In the case of repeated knot-values, the fraction "$0/0$" is defined as 0. The B-splines $B_{i,p}$ form a partition of unity ($\sum_i B_{i,p}(\xi) = 1$), are linearly independent and form a basis of the spline space $\mathbb{S}_p(\boldsymbol{\Xi}) = \text{span}_i\{B_{i,p}(\xi)\}$. By removing all repeated entries from the knot vector, the break point vector

$$\bar{\boldsymbol{\Xi}} = \left\{\bar{\xi}_1, \bar{\xi}_2, \ldots, \bar{\xi}_{n_e+1}\right\} \tag{2.151}$$

of strictly increasing break points $\bar{\xi}_i$ is obtained. An interval $(\bar{\xi}_i, \bar{\xi}_{i+1})$ is then called *element*, as, in analogy to classical finite elements, the B-spline functions are defined as polynomials within each element. The break point vector (2.151) yields n_e elements. Any univariate spline basis function is supported on at most $p+1$ elements, and within every element $p+1$ basis functions take non-zero values. Across element boundaries, B-spline basis functions have a continuity of C^{p-m_i-1}, where m_i denotes the *multiplicity* of the break point, that is the number of repetitions of the break point $\bar{\xi}_i$ in the knot vector $\boldsymbol{\Xi}$. An exemplary B-spline basis of degree $p = 2$ is depicted in Figure 2.6. Note that, due to the varying multiplicity of break points, the basis functions are C^{-1}-continuous at the element boundaries at $\xi = 0$ and $\xi = 1$, C^0-continuous at $\xi = 3/5$ and C^1-continuous across all other element boundaries. Spline curves $\mathscr{C}_{\text{B-spline}}$ in $\Re^d$ are constructed

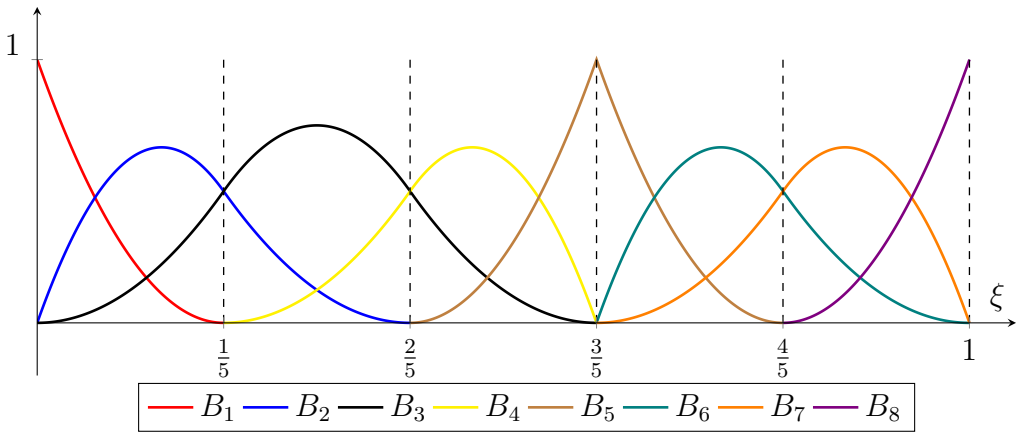

Figure 2.6: B-spline basis functions of degree $p = 2$ on the uniform knot-vector $\boldsymbol{\Xi} = \{0, 0, 0, \frac{1}{5}, \frac{2}{5}, \frac{3}{5}, \frac{3}{5}, \frac{4}{5}, 1, 1, 1\}$. Element boundaries are depicted by dashed lines.

based on a mapping of the parametric knot space

$$\mathscr{C}_{\text{B-spline}} : (0,1) \to \Re^d, \quad , \xi \mapsto \sum_i B_{i,p}(\xi) \mathbf{X}_i \quad , \tag{2.152}$$

using coordinates $\mathbf{X}_i$ of so-called *control points* which each are associated with one spline basis function. A linear interpolation of these control points froms the so-called *control polygon*. An exemplary B-spline curve employing the basis functions depicted in Figure 2.6 is given in Figure 2.7. Note that control point are in general not interpolatory, as the basis functions are not

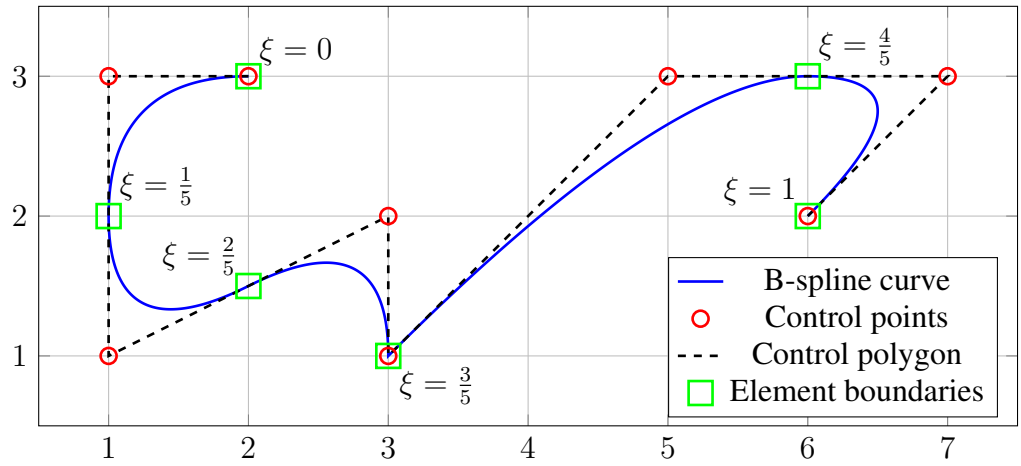

Figure 2.7: Exemplary B-spline curve employing the basis functions of Figure 2.6. Knot space coordinates of element boundaries are given for orientation.

interpolatory, however, for open knot vectors, the beginning and the end of the curve are, and, in the given case, also the control point associated with B_5 is due to the multiplicity $m = p$ of the knot $\xi = 3/5$. The resulting spline curve inherits the inter-element smoothness properties of the underlying spline basis, such that the given curve is C^1 continuous at all internal element boundaries except the one at $\xi = 3/5$, where only C^0 continuity is obtained thus representing a sharp corner.

Parametrizations of surfaces and volumes are readily obtained by forming tensor products of univariate spline bases. In three dimensions, let $\boldsymbol{\Xi}$, $\boldsymbol{H}$ and $\boldsymbol{Z}$ denote the knot vectors in the parametric directions ξ, η and ζ, and $B_{i,p}(\xi)$, $B_{j,p}(\eta)$ and $B_{k,p}(\zeta)$ the corresponding i-, j- and k-th univariate spline, respectively. For simplicity, the same polynomial order p is assumed in each direction. The multivariate basis functions

$$B_{(i,j),p}(\xi,\eta) = B_{i,p}(\xi) \cdot B_{j,p}(\eta) \quad , \tag{2.153a}$$

$$B_{(i,j,k),p}(\xi,\eta,\zeta) = B_{i,p}(\xi) \cdot B_{j,p}(\eta) \cdot B_{k,p}(\zeta) \quad , \tag{2.153b}$$

in combination with a regular mesh of control points with coordinates $\mathbf{X}_{(i,j)}$ for surfaces and $\mathbf{X}_{(i,j,k)}$ for volumes give rise to the B-spline parametrization of a surface $\mathscr{S}_{\mathrm{B-spline}}$ and $\mathscr{V}_{\mathrm{B-spline}}$ as

$$\mathscr{S}_{\mathrm{B-spline}} : (0,1)^2 \to \Re^3, \ (\xi,\eta) \quad \mapsto \sum_{i,j} \underbrace{B_{i,p}(\xi) B_{j,p}(\eta)}_{B_{(i,j),p}(\xi,\eta)} \mathbf{X}_{(i,j)} \quad , \tag{2.154a}$$

$$\mathscr{V}_{\mathrm{B-spline}} : (0,1)^3 \to \Re^3, \ (\xi,\eta,\zeta) \mapsto \sum_{i,j,k} \underbrace{B_{i,p}(\xi) B_{j,p}(\eta) B_{k,p}(\zeta)}_{B_{(i,j,k),p}(\xi,\eta,\zeta)} \mathbf{X}_{(i,j,k)} \quad . \tag{2.154b}$$

Surface and volume elements on which each multivariate B-spline basis is a polynomial, can be defined from the break point vectors $\bar{\boldsymbol{\Xi}}$, $\bar{\boldsymbol{H}}$, $\bar{\boldsymbol{Z}}$ as $(\bar{\xi}_i, \bar{\xi}_{i+1}) \times (\bar{\eta}_j, \bar{\eta}_{j+1})$ and $(\bar{\xi}_i, \bar{\xi}_{i+1}) \times (\bar{\eta}_j, \bar{\eta}_{j+1}) \times (\bar{\zeta}_k, \bar{\zeta}_{k+1})$. For surfaces (resp. volumes), each basis function is supported on at most $(p+1)^2$ (resp. $(p+1)^3$) elements and within each element exactly $(p+1)^2$ (resp. $(p+1)^3$) basis functions take non-zero values. The function spaces spanned by the multivariate B-splines are similarly obtained by the tensor product of univariate spaces, i.e. $\mathbb{S}_p(\boldsymbol{\Xi}, \boldsymbol{H}) = \operatorname{span}_{i,j}\{B_{(i,j),p}(\xi, \eta)\} = \mathbb{S}_p(\boldsymbol{\Xi}) \times \mathbb{S}_p(\boldsymbol{H})$ and $\mathbb{S}_p(\boldsymbol{\Xi}, \boldsymbol{H}, \boldsymbol{Z}) = \mathbb{S}_p(\boldsymbol{\Xi}) \times \mathbb{S}_p(\boldsymbol{H}) \times \mathbb{S}_p(\boldsymbol{Z})$.

The non-uniform B-splines described above can be generalized to non-uniform *rational* B-splines (NURBS) to enable a greater flexibility in curve representations (2.152) including, for instance, conic sections. Therefore, every control point is, in addition to its coordinates $\mathbf{X}$, given a *weight* w and a NURBS basis function is then defined from the B-spline basis via

$$R_{i,p}(\xi) = \frac{w_i B_{i,p}(\xi)}{\sum_i w_i B_{i,p}(\xi)} \quad , \tag{2.155a}$$

$$R_{(i,j),p}(\xi, \eta) = \frac{w_{(i,j)} B_{(i,j),p}(\xi, \eta)}{\sum_{i,j} w_{(i,j)} B_{(i,j),p}(\xi, \eta)} \quad , \tag{2.155b}$$

$$R_{(i,j,k),p}(\xi, \eta, \zeta) = \frac{w_{(i,j,k)} B_{(i,j,k),p}(\xi, \eta, \zeta)}{\sum_{i,j,k} w_{(i,j,k)} B_{(i,j,k),p}(\xi, \eta, \zeta)} \quad . \tag{2.155c}$$

As the B-spline basis functions form a partition of unity, the NURBS basis functions reduce to their B-spline progenitors if all weights w are chosen to one. Moreover, NURBS inherit the important properties of partition of unity as well as inter-element continuity from the underlying B-splines. The corresponding univariate, bivariate and trivariate function spaces spanned by the NURBS basis functions will be denoted as $\mathbb{R}_p(\boldsymbol{\Xi}; \boldsymbol{w})$, $\mathbb{R}_p(\boldsymbol{\Xi}, \boldsymbol{H}; \boldsymbol{w})$ and $\mathbb{R}_p(\boldsymbol{\Xi}, \boldsymbol{H}, \boldsymbol{Z}; \boldsymbol{w})$ respectively, wherein $\boldsymbol{w}$ contains the weights of all control points. Since the multivariate NURBS in (2.155b) and (2.155c) are not constructed by a tensorproduct of univariate NURBS (2.155a) also the multivariate function spaces cannot be constructed by tensorization of univariate spaces. The parametrization of a NURBS curve, surface and volume follow the same way as for a B-splines in (2.152) and (2.154) by replacing the B-spline basis functions with NURBS to obtain

$$\mathscr{C} : (0,1) \to \Re^3, \quad \xi \mapsto \sum_i R_i(\xi) \mathbf{X}_i \quad , \tag{2.156a}$$

$$\mathscr{S} : (0,1)^2 \to \Re^3, \quad (\xi, \eta) \mapsto \sum_{i,j} R_{(i,j)}(\xi, \eta) \mathbf{X}_{(i,j)} \quad , \tag{2.156b}$$

$$\mathscr{V} : (0,1)^3 \to \Re^3, \quad (\xi, \eta, \zeta) \mapsto \sum_{i,j,k} R_{(i,j,k)}(\xi, \eta, \zeta) \mathbf{X}_{(i,j,k)} \quad . \tag{2.156c}$$

In practice, most geometries may not be described as the image of a single unit cube and are instead split into several patches as illustrated, for example, in Figure 2.8.

Similar to the classical finite element approximation in Section 2.8.1.1, isogeometric analysis is based on an isoparametric principle. Hence, the basis functions used to describe the geometry in (2.156c) are used in (2.136) for the approximation of the solution fields, i.e., in the case of thermomecanics, the discrete displacement and temperature fields $\boldsymbol{u}_h$ and T_h as well as their variations. For a three-dimensional geometry consisting of n patches Ω_0^i with knot vectors $\boldsymbol{\Xi}_i, \boldsymbol{H}_i, \boldsymbol{Z}_i$

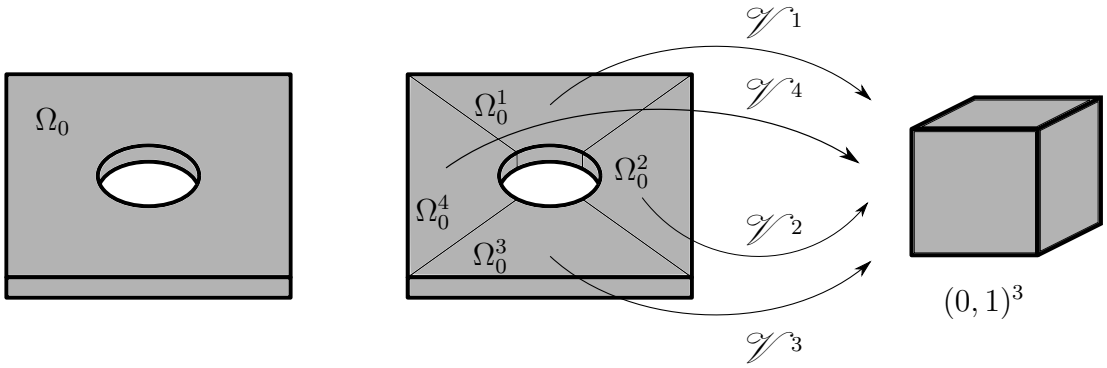

Figure 2.8: An exemplary multi-patch geometry: A square plate with a circular hole Ω_0 is split into four subdomains Ω_0^1 - Ω_0^4, which can be mapped onto a unit cube.

and weights $\boldsymbol{w}_i$, and again assuming homogeneous Dirichlet boundary conditions, the discrete trial and test spaces are therefore given as

$$\boldsymbol{\mathcal{U}}_{\mathrm{u},h} = \boldsymbol{\mathcal{V}}_{\mathrm{u},h} = \left\{ \boldsymbol{u}_h \in \left[C^0(\Omega_{0,h})\right]^3 \middle| \ \boldsymbol{u}_h|_{\Omega_0^i} \circ \ \mathscr{Y}^i \in \left[\mathbb{R}_p^i(\boldsymbol{\Xi}_i, \boldsymbol{H}_i, \boldsymbol{Z}_i; \boldsymbol{w}_i)\right]^3, \ i = 1 \dots n \right\} \ , \tag{2.157a}$$

$$\mathcal{U}_{\mathrm{T},h} = \mathcal{V}_{\mathrm{T},h} = \left\{ T_h \in C^0(\Omega_{0,h}) \quad \middle| \ T_h|_{\Omega_0^i} \circ \ \mathscr{Y}^i \in \mathbb{R}_p^i(\boldsymbol{\Xi}_i, \boldsymbol{H}_i, \boldsymbol{Z}_i; \boldsymbol{w}_i), \qquad i = 1 \dots n \right\} \ . \tag{2.157b}$$

The simplest method to ensure C^0-continuity across patches is to use a matching discretization on the interface between patches. However, due to the tensor product nature of NURBS within the patches, this requires the same discretization not only at the patch boundary but also within the patch. Methods of coupling dissimilar meshes at the interface include, among others, Nitsche's method (e.g. [6]) and mortar methods (e.g. [21]). Mortar metods and an a more convenient dual mortar method for isogeometric patch coupling are introduced in detail in Chapter 4. The definition of the discrete function spaces for finite elements (2.140) and isogeometric analysis (2.157) bear greats similarities, with the mayor difference being, that for finite elements the mapping to the parametric domain $\Phi_{\tau_{h,i}}$ is defined independently for every element $\tau_{h,i}$, whereas in isogeometric analysis the mapping $\mathscr{Y}^i$ to the parametric space is defined on each patch i containing multiple elements. As a consequence, mesh refinement within a patch, e.g. by inserting additional knots into the knot vectors[1], does not alter the geometric representation of $\Omega_{0,h}$ as the mapping $\mathscr{Y}^i$ remains unaffected. The final discrete weak forms of isogeometric analysis are the same as for classical finite elements in (2.141) and (2.143), and also the compact algebraical representations (2.142) and (2.144) remain unaltered.

2.8.2 Time Discretization[2]

To discretize the semi-discrete equilibrium (2.142) and (2.144) in time, commonly finite difference methods are applied. Therefore, a time interval of interest $[0, t_{\mathrm{end}}]$ is subdivided into n time

[1] Insertion of additional knots in the knot vector corresponds to classical h-refinement in finite elements and will be the refinement strategy exclusively used in the course of this thesis. Besides knot insertion, p- and k-refinement may be used in isogeometric analysis, see [40].

[2] This section is adapted from the author's publication [194].

intervals $[t_n, t_{n+1}]$ with the, for simplicity reasons only, constant time step size $\Delta t = t_{n+1} - t_n$. All quantities at time t_n are assumed to be known, either by initial data for $t_0 = 0$ or by solution of the previous time step, and the state at t_{n+1} is sought. Generally, time integration schemes can be classified in *explicit* and *implicit* ones with the mayor difference being whether the internal and external forces $\boldsymbol{F}_{\{\mathrm{u,T}\},\mathrm{int}}$ and $\boldsymbol{F}_{\{\mathrm{u,T}\},\mathrm{ext}}$ in (2.142) and (2.144), respectively, are evaluated solely in dependence of the known state at t_n (explicit schemes) or also depend on the unknown state at t_{n+1}. As explicit schemes are only conditionally stable (i.e. require sufficiently small time steps), they are more efficient for highly dynamic problems, as internal and external forces depend on known quantities of previous times only. On the contrary, implicit schemes can be constructed unconditionally stable and may be preferred for the simulation of low frequency responses or even quasi-static processes. The present work focuses on implicit methods exclusively.

Exemplarily for implicit methods, generalized-α schemes are presented in the following. They are of second-order accuracy, and can be formulated with the spectral radius in the high frequency limit ρ_∞ as sole parameter. For structural problems, this method has been developed by Chung and Hulbert [38]. The approximation of discrete (nodal) velocities $\mathbf{v}$ and accelerations $\mathbf{a}$ is based on the Newmark-scheme, viz.

$$\begin{aligned}
\mathbf{v}_{n+1} &= \frac{\gamma_\mathrm{u}}{\beta_\mathrm{u}\Delta t}(\mathbf{d}_{n+1} - \mathbf{d}_n) - \frac{\gamma_\mathrm{u} - \beta_\mathrm{u}}{\beta_\mathrm{u}}\mathbf{v}_n - \frac{\gamma_\mathrm{u} - 2\beta_\mathrm{u}}{2\beta_\mathrm{u}}\Delta t\mathbf{a}_n \quad , \\
\mathbf{a}_{n+1} &= \frac{1}{\beta_\mathrm{u}\Delta t^2}(\mathbf{d}_{n+1} - \mathbf{d}_n) - \frac{1}{\beta_\mathrm{u}\Delta t}\mathbf{v}_n - \frac{1 - 2\beta_\mathrm{u}}{2\beta_\mathrm{u}}\mathbf{a}_n \quad ,
\end{aligned} \tag{2.158}$$

where the subscripts $(\cdot)_n$ and $(\cdot)_{n+1}$ denote whether the respective quantity is evaluated at t_n or t_{n+1} and $\beta_\mathrm{u} \in (0, 0.5]$ and $\gamma_\mathrm{u} \in (0, 1]$ are parameters. The discrete residual $\boldsymbol{r}_\mathrm{u}$ of (2.142) is then evaluated at a generalized mid-point by introducing the parameters $\alpha_{\mathrm{f,u}}$ and $\alpha_{\mathrm{m,u}}$:

$$\boldsymbol{r}_\mathrm{u}(\mathbf{d}_{n+1}, \mathbf{T}_{n+1}) = \boldsymbol{M}_\mathrm{u}\mathbf{a}_{n+1-\alpha_{\mathrm{m,u}}} + \boldsymbol{F}_{\mathrm{u,int},n+1-\alpha_{\mathrm{f,u}}} - \boldsymbol{F}_{\mathrm{u,ext},n+1-\alpha_{\mathrm{f,u}}} = \mathbf{0} \quad . \tag{2.159}$$

The discrete forces (and accelerations) at the mid-points are eventually interpolated by the forces (and accelerations) at the end of each time step, e.g. $\boldsymbol{F}_{\mathrm{u,int},n+1-\alpha_{\mathrm{f,u}}} = (1 - \alpha_{\mathrm{f,u}})\boldsymbol{F}_{\mathrm{u,int},n+1} + \alpha_{\mathrm{f,u}}\boldsymbol{F}_{\mathrm{u,int},n}$. In [38], an optimal set of parameters is derived based on second order accuracy, unconditional stability for linear problems, maximized high frequency dissipation and minimized low frequency dissipation leaving the spectral radius in the high frequency limit $\rho_{\infty,\mathrm{u}}$ as the sole free parameter and

$$\alpha_{\mathrm{m,u}} = \frac{2\rho_{\infty,\mathrm{u}} - 1}{\rho_{\infty,\mathrm{u}} + 1} \quad , \qquad \alpha_{\mathrm{f,u}} = \frac{\rho_{\infty,\mathrm{u}}}{\rho_{\infty,\mathrm{u}} + 1} \quad , \tag{2.160}$$

$$\beta_\mathrm{u} = \frac{1}{4}(1 - \alpha_{\mathrm{m,u}} + \alpha_{\mathrm{f,u}})^2 \quad , \qquad \gamma_\mathrm{u} = \frac{1}{2} - \alpha_{\mathrm{m,u}} + \alpha_{\mathrm{f,u}} \quad . \tag{2.161}$$

The generalized-α method has been extended to systems of first order in time by Jansen *et al.* [115], which will be used for the temporal discretization of the thermal evolution (2.144). Similar to (2.158), the temperature rate is approximated by

$$\dot{\mathbf{T}}_{n+1} = \frac{1}{\gamma_\mathrm{T}\Delta t}(\mathbf{T}_{n+1} - \mathbf{T}_n) - \frac{1 - \gamma_\mathrm{T}}{\gamma_\mathrm{T}}\dot{\mathbf{T}}_n \quad . \tag{2.162}$$

with a parameter $\gamma_{\mathrm{T}} \in (0, 1]$. Again, the discrete residual $\boldsymbol{r}_{\mathrm{T}}$ of (2.144) is evaluated at a generalized mid-point defined by $\alpha_{\mathrm{m,T}}$ and $\alpha_{\mathrm{f,T}}$:

$$\boldsymbol{r}_{\mathrm{T}}(\mathbf{d}_{n+1}, \mathbf{T}_{n+1}) = \boldsymbol{M}_{\mathrm{T}} \dot{\mathbf{T}}_{n+\alpha_{\mathrm{m,T}}} + \boldsymbol{F}_{\mathrm{u,int},n+\alpha_{\mathrm{f,u}}} - \boldsymbol{F}_{\mathrm{u,ext},n+\alpha_{\mathrm{f,u}}} = \mathbf{0} \quad , \tag{2.163}$$

where the values at the mid-points are again obtained by an appropriate linear combination of the end-point values. An optimal choice of the parameters has been derived in [115] in terms of the spectral radius in the high frequency limit $\rho_{\infty,\mathrm{T}}$ as

$$\alpha_{\mathrm{f,T}} = \frac{1}{\rho_{\infty,\mathrm{T}} + 1} \quad , \quad \alpha_{\mathrm{m,T}} = \frac{1}{2} \frac{3 - \rho_{\infty,\mathrm{T}}}{\rho_{\infty,\mathrm{T}} + 1} \quad , \quad \gamma_{\mathrm{T}} = \frac{1}{2} + \alpha_{\mathrm{m,T}} - \alpha_{\mathrm{f,T}} \quad . \tag{2.164}$$

In the case of materials with internal variables of state such as presented in Section 2.3, additional time integration rules for those variables need to be defined. These time integration schemes may be tailored to fit certain characteristics of the evolution equations. For the kinematic description of elasto-plasticity derived in Section 2.3.4, such time integration schemes for the plastic deformation gradient $\boldsymbol{F}_{\mathrm{p}}$ as well as the hardening variables α_{i} and $\boldsymbol{\alpha}_{\mathrm{k}}$ will be given in Section 3.1.

Remark 2.5 (Structure preserving time integration schemes)**.** *While being relatively easy to implement and fairly robust, the presented generalized-α time integration schemes are not algorithmically energy conserving. As an alternative, so-called structure preserving time integration schemes based on the (generalized) energy momentum method have been proposed in [82, 126, 127, 203] for isothermal nonlinear elasticity. Later, those methods have been extended to isothermal contact [98], elasto-plasticity [7], thermo-elasticity [88, 99, 187] and thermo-elastic contact [61]. The combination of the cited works to a structure preserving time integration for a fully coupled thermo-elasto-plastic contact problem is beyond the scope of this thesis, but might be a worthwhile topic of future research.*

Remark 2.6 (Quasi-static processes)**.** *A process is called quasi-static, if is it "slow engough" for the system to remain in static equilibrium at all times, i.e. the right-hand-sides of* (2.91a) *and* (2.91b) *is zero. The discrete equilibria* (2.159) *and* (2.163) *then reduces to a series of equilibrium states at times t_{n+1} of the form*

$$\boldsymbol{r}_{\mathrm{u}}(\mathbf{d}_{n+1}, \mathbf{T}_{n+1}) = \boldsymbol{F}_{\mathrm{u,int},n+1} - \boldsymbol{F}_{\mathrm{u,ext},n+1} = \mathbf{0} \quad , \tag{2.165}$$

$$\boldsymbol{r}_{\mathrm{T}}(\mathbf{d}_{n+1}, \mathbf{T}_{n+1}) = \boldsymbol{F}_{\mathrm{u,int},n+1} - \boldsymbol{F}_{\mathrm{u,ext},n+1} = \mathbf{0} \quad . \tag{2.166}$$

Time therein reduces to a path variable describing the loading path of the system by, e.g., varying Dirichlet or Neumann boundary conditions.

2.8.3 Solution Scheme for Coupled Nonlinear Equations[1]

The spatial and temporal discretization results in a set of coupled nonlinear equations (2.159) and (2.163) in the discrete displacements $\mathbf{d}_{n+1}$ and $\mathbf{T}_{n+1}$. Different solution strategies for such coupled systems exist, which can generally be classified as partitioned and monolithic schemes.

[1] This section is adapted from the author's publication [195].

While partitioned schemes solve the structural and thermal field sequentially (keeping the values of the other field fixed) and iterate between the fields until convergence is achieved, monolithic approaches aim at solving the coupled system of equations within one nonlinear solution procedure. Though efficient for problems with rather weak coupling between the two fields (or a one-directional coupling only), partitioned schemes may converge slowly for strong bi-directional coupling. In such cases, monolithic approaches become more efficient, see e.g. Danowski *et al.* [49] for a comparison in the context of linear thermo-elastic problems. The current thesis solely follows the monolithic approach. The resulting coupled nonlinear system of equations is then solved using Newton's method, i.e. by solving a sequence of linearized problems of the form

$$\begin{bmatrix} \mathbf{K}_{\mathrm{uu}} & \mathbf{K}_{\mathrm{uT}} \\ \mathbf{K}_{\mathrm{Tu}} & \mathbf{K}_{\mathrm{TT}} \end{bmatrix} \Bigg|_{n+1}^{i} \begin{bmatrix} \Delta \mathbf{d}^{i} \\ \Delta \mathbf{T}^{i} \end{bmatrix} = - \begin{bmatrix} \boldsymbol{r}_{\mathrm{u}} \\ \boldsymbol{r}_{\mathrm{T}} \end{bmatrix} \Bigg|_{n+1}^{i} , \tag{2.167}$$

for increments of discrete nodal displacements $\Delta \mathbf{d}^{i}$ and $\Delta \mathbf{T}^{i}$. The right-hand-side thereby consists of blocks containing the structural and thermal residual and the tangent matrix $\mathbf{K}$, contains the respective partial derivatives of the structural and thermal residual, viz.

$$\begin{bmatrix} \boldsymbol{r}_{\mathrm{u}} \\ \boldsymbol{r}_{\mathrm{T}} \end{bmatrix} \Bigg|_{n+1}^{i} = \begin{bmatrix} \boldsymbol{r}_{\mathrm{u}}(\mathbf{d}_{n+1}^{i}, \mathbf{T}_{n+1}^{i}) \\ \boldsymbol{r}_{\mathrm{T}}(\mathbf{d}_{n+1}^{i}, \mathbf{T}_{n+1}^{i}) \end{bmatrix} , \tag{2.168}$$

$$\begin{bmatrix} \mathbf{K}_{\mathrm{uu}} & \mathbf{K}_{\mathrm{uT}} \\ \mathbf{K}_{\mathrm{Tu}} & \mathbf{K}_{\mathrm{TT}} \end{bmatrix} \Bigg|_{n+1}^{i} = \begin{bmatrix} \frac{\partial \boldsymbol{r}_{\mathrm{u}}(\mathbf{d}_{n+1}^{i}, \mathbf{T}_{n+1}^{i})}{\partial \mathbf{d}} & \frac{\partial \boldsymbol{r}_{\mathrm{u}}(\mathbf{d}_{n+1}^{i}, \mathbf{T}_{n+1}^{i})}{\partial \mathbf{T}} \\ \frac{\partial \boldsymbol{r}_{\mathrm{T}}(\mathbf{d}_{n+1}^{i}, \mathbf{T}_{n+1}^{i})}{\partial \mathbf{d}} & \frac{\partial \boldsymbol{r}_{\mathrm{T}}(\mathbf{d}_{n+1}^{i}, \mathbf{T}_{n+1}^{i})}{\partial \mathbf{T}} \end{bmatrix} . \tag{2.169}$$

After each step i displacements and temperatures are updated ($\mathbf{d}_{n+1}^{i+1} = \mathbf{d}_{n+1}^{i} + \Delta \mathbf{d}^{i}$, $\mathbf{T}_{n+1}^{i+1} = \mathbf{T}_{n+1}^{i} + \Delta \mathbf{T}^{i}$, $i \leftarrow i+1$) until convergence is achieved. In the presence of internal variables of state, as it is the case for elasto-plasticity (see Section 2.3.4), the derivatives in (2.167) are to be understood as generic operators, since the exact algorithmic treatment of the internal variables of state has not yet been specified, but is the topic of the following chapter.

For rather small problems, the linearized system (2.167) may be solved by means of direct solvers, whereas iterative linear solvers may be preferable for larger systems. For thermomecanical problems or other coupled problems of block structure similar to (2.167), efficient solvers based on block Gauss–Seidel schemes in combination with algebraic multigrid preconditioners have been presented, e.g., in Danowski *et al.* [49], Verdugo and Wall [223]. Systems with complex coupling effects such as plasticity or contact interaction, however, may require special attention in the linear solution procedure as, for the isothermal case, derived in Adams [1], Wieners [228] for elasto-plasticity and Wiesner *et al.* [229] for contact discretizations similar to the ones derived in Chapter 4. Efficient linear solvers for problems of thermo-elasto-plasticity and thermomecanical contact are beyond the scope of this thesis, such that focus on the linear solvers employed in the numerical examples is rather on robustness than on efficiency.

3 Computational Methods for Thermo-Elasto-Plasticity

The topic of computational methods for (thermo-) elasto-plasticity, or for inelastic materials in general, concerns the question of how to incorporate the evolution of internal variables (e.g. (2.70)) and potentially internal constraints (e.g. (2.71)) into the finite element discretization (2.159) and (2.163). Within this Chapter, a computational approach to finite deformation (thermo-) elasto-plasticity using nonlinear complementarity (NCP) functions is derived based on the small strain method of Hager and Wohlmuth [91] is presented. Therefore, the incremental plastic flow is introduced as additional unknowns and the constraints of elasto-plasticity are reformulated in terms of an NCP function. In contrast to the previous NCP based plasticity formulations [37, 91] using one scalar and one tensor-valued NCP function, only one tensor-valued NCP function is used here, and thus reduce the number of additional unknowns. In the final system of equations to be solved, the additionally introduced unknowns do not appear explicitly but are removed by static condensation.

The chapter is outlined as follows: first, the spatial discretization of the internal variables of state as well as the temporal discretization of their evolution equations are introduced. These discretization schemes are common to almost any numerical algorithm to treat plasticity, including the classical return mapping algorithm (RMA) as well as the newly proposed NCP function based approach. As a reference, the RMA is briefly introduced next, before the NCP function for von Mises and Hill-type plasticity is derived. Several extensions of the method are proposed including plastic spin, visco-plasticity and thermo-plasticity. Numerical examples accompany the different developments.

3.1 Discretization of Internal Variables

The internal variables of state enter the (discrete) weak form (2.141) via the first Piola–Kirchhoff stress' dependency on them. As the integrals in (2.141) are approximated by Gaussian quadrature, the stress $\boldsymbol{P}$ as a function of the discrete displacement (and potentially temperature) field is evaluated at each quadrature point. In the Lagrangian finite element formulation of continuum mechanics used for solids, quadrature points can be associated with material points directly, as the reference configuration of the mesh (and hence the location of quadrature points) does not change over time. Therefore, the natural and most common choice for the internal variables of state is to attribute independent values with each quadrature point. From a perspective of approximating the continuous fields $\boldsymbol{F}_{\mathrm{p}}$, α_{i} and $\boldsymbol{\alpha}_{\mathrm{k}}$, this means introducing a function $M_q(\boldsymbol{X})$

associated with a quadrature point q in the set of all quadrature points $\mathcal{G}$, such that

$$M_q(\boldsymbol{X}_r) = \begin{cases} 1 & \text{if } q = r \\ 0 & \text{if } q \neq r \end{cases} \quad \forall q, r \in \mathcal{G} \ , \tag{3.1}$$

where $\boldsymbol{X}_r$ denotes the material coordinate of quadrature point r. The approximate fields of the internal variables are then obtained in analogy to (2.136) by

$$\boldsymbol{F}_{\mathrm{p}}(\boldsymbol{X}, t) \approx \boldsymbol{F}_{\mathrm{p},h}(\boldsymbol{X}, t) = \sum_{q \in \mathcal{G}} M_q(\boldsymbol{X}) \mathbf{F}_{\mathrm{p},q}(t) \ , \tag{3.2a}$$

$$\alpha_{\mathrm{i}}(\boldsymbol{X}, t) \approx \alpha_{\mathrm{i},h}(\boldsymbol{X}, t) = \sum_{q \in \mathcal{G}} M_q(\boldsymbol{X}) \alpha_{\mathrm{i},q}(t) \ , \tag{3.2b}$$

$$\boldsymbol{\alpha}_{\mathrm{k}}(\boldsymbol{X}, t) \approx \boldsymbol{\alpha}_{\mathrm{k},h}(\boldsymbol{X}, t) = \sum_{q \in \mathcal{G}} M_q(\boldsymbol{X}) \boldsymbol{\alpha}_{\mathrm{k},q}(t) \ , \tag{3.2c}$$

interpolating discrete Gauss point values $\mathbf{F}_{\mathrm{p},q}$, $\alpha_{\mathrm{i},q}$ and $\boldsymbol{\alpha}_{\mathrm{k},q}$. For the sake of brevity of future notation, the vectors $\mathbf{F}_{\mathrm{p}}$, $\boldsymbol{\alpha}_{\mathrm{i}}$ and $\boldsymbol{\alpha}_{\mathrm{k}}$ shall denote the collection of all Gauss point values of the respective quantity. Since $M_q(\boldsymbol{X})$, as all other ansatz functions, are only evaluated at the quadrature points and no gradients of $M_q(\boldsymbol{X})$ are involved, the actual function $M_q(\boldsymbol{X})$ does not need to be specified explicitly. They may be seen as continuous functions within each element [183] or by splitting each element into sub-elements each containing one quadrature point and assuming $M_q = 1$ within the sub-element associated with quadrature point q and zero outside [90].

In time, the evolution of the discretized internal variables of state $\mathbf{F}_{\mathrm{p},q}$, $\alpha_{\mathrm{i},q}$ and $\boldsymbol{\alpha}_{\mathrm{k},q}$ follow the evolution equations (2.70), which are first order ordinary differential equations (ODEs) in time. As such, initial data at $t_0 = 0$ needs to be provided and is commonly chosen as

$$\mathbf{F}_{\mathrm{p},q}(t_0) = \boldsymbol{I} \ , \quad \alpha_{\mathrm{i},q}(t_0) = 0 \ , \quad \boldsymbol{\alpha}_{\mathrm{k},q}(t_0) = \mathbf{0} \ , \quad \forall q \in \mathcal{G} \ . \tag{3.3}$$

Starting from this initial data, a temporal discretization of the Gauss point local quantities $\mathbf{F}_{\mathrm{p},q}$, $\alpha_{\mathrm{i},q}$ and $\boldsymbol{\alpha}_{\mathrm{k},q}$ is necessary. As for the displacement and temperature field in Section 2.8.2, the quantities at time t_n are assumed to be given (either by initial data or the solution of the previous time step) and quantities at time t_{n+1} are sought. In computational plasticity, a first order accurate backward exponential map integrator

$$\mathbf{F}_{\mathrm{p},q,n+1} = \exp\left[\Delta \mathbf{L}_{\mathrm{p},q,n+1}\right] \mathbf{F}_{\mathrm{p},q,n} \tag{3.4}$$

is commonly applied for the plastic deformation gradient. Therein, $\Delta \mathbf{L}_{\mathrm{p},q,n+1} = \Delta \mathbf{D}_{\mathrm{p},q,n+1} + \Delta \mathbf{W}_{\mathrm{p},q,n+1} = \int_{t_n}^{t_{n+1}} \mathbf{L}_{\mathrm{p},q} \mathrm{d}t$ represents an approximation of the plastic flow within a time interval $[t_n, t_{n+1}]$ and has to be determined in such a way, that the time discrete Karush–Kuhn–Tucker conditions (see (2.71))

$$\phi_{\mathrm{p}}|_{q,n+1} \leq 0, \quad \Delta\gamma_q \geq 0 \quad \phi_{\mathrm{p}}|_{q,n+1} \, \Delta\gamma_q = 0 \tag{3.5}$$

as well as the flow rule (see (2.70))

$$\Delta \mathbf{D}_{\mathrm{p},q,n+1} = \Delta\gamma_q \left. \frac{\partial \Xi_{\mathrm{p}}}{\partial \boldsymbol{\Sigma}} \right|_{q,n+1} \tag{3.6}$$

and the discrete evolution of plastic spin (see (2.81))

$$\Delta \mathbf{W}_{\mathrm{p},q,n+1} = \frac{\eta}{y_0} \left(\boldsymbol{\Sigma}_{q,n+1} \Delta \mathbf{D}_{\mathrm{p},q,n+1} - \Delta \mathbf{D}_{\mathrm{p},q,n+1} \boldsymbol{\Sigma}_{q,n+1} \right) \tag{3.7}$$

hold. Finally, standard backward Euler schemes are applied for the hardening variables resulting in

$$\alpha_{\mathrm{i},q,n+1} = \alpha_{\mathrm{i},q,n} + \Delta\gamma_q \left. \frac{\partial \Xi_{\mathrm{p}}}{\partial A_{\mathrm{i}}} \right|_{q,n+1} , \tag{3.8}$$

$$\boldsymbol{\alpha}_{\mathrm{k},q,n+1} = \boldsymbol{\alpha}_{\mathrm{k},q,n} + \Delta\gamma_q \left. \frac{\partial \Xi_{\mathrm{p}}}{\partial \boldsymbol{A}_{\mathrm{k}}} \right|_{q,n+1} . \tag{3.9}$$

Remark 3.1 (Properties of the exponential map integrator)**.** *The exponential map integrator* (3.4) *yields at least two advantages in computational plasticity. First, though less important for the algorithm developed in this thesis, it allows, in conjunction with the use of logarithmic strain measures, to construct RMAs that preserve the algorithmic format of small strain approximations [198]. Second and more importantly, for a flow rule that is isochoric in the time-continuous setting (see Remark 2.1) this volume preserving property is maintained exactly also in the time-discrete setting. More specifically, an isochoric plastic flow is obtained for a pressure insensitive dissipation potential* Ξ_{p} *or a pressure insensitive yield function* ϕ_{p} *in conjunction with an associated flow rule. By* (3.6) *and* (3.7)*, this yields* $\operatorname{tr} \Delta \mathbf{L}_{\mathrm{p},q,n+1} \equiv 0$ *which results in an exponential map integration* (3.4) *that satisfies* $\det \mathbf{F}_{\mathrm{p},q,n+1} = \det \mathbf{F}_{\mathrm{p},q,n}$*, since* $\det[\exp \boldsymbol{A}] = \exp[\operatorname{tr} \boldsymbol{A}]$ *holds for the matrix exponential. Accordingly, the volumetric part of the plastic deformation gradient is preserved exactly.*

3.2 Classical Return Mapping Algorithms

Before the novel method is presented in the next section, a brief summary of the return mapping algorithm for finite strain plasticity as the far most popular numerical method should be given. This summary only presents the general procedure, the detailed steps as well as modifications and simplifications based on particular assumptions can be found in the textbooks of Simo and Hughes [200], Bonet and Wood [19] and especially de Souza Neto *et al.* [57]. For simplicity, the presentation is restricted to the isothermal case. Return mapping algorithms for finite deformation thermo-plasticity are commonly based on the seminal work by Simo and Miehe [201], which extends the isothermal radial return mapping algorithm presented in Simo [196, 197]. Both partitioned and monolithic solution approaches are discussed in [201]. Several extensions to this algorithm have been presented later, e.g. a monolithic formulation in principle axes by Ibrahimbegovic and Chorfi [114] and a variant including temperature-dependent elastic material properties by Canajija and Brnić [27].

The fundamental idea in the RMA is to determine the stress $\boldsymbol{P}_{n+1}$ in (2.159) at any evaluation in such a way, that the discrete Karush–Kuhn–Tucker conditions and evolution equations of the previous section hold. To abbreviate notation, the index $(\cdot)_q$ indicating a specific quadrature point is omitted in the following. At the evaluation of $\boldsymbol{P}_{n+1}$, let the current deformation state $\boldsymbol{F}_{n+1} = \nabla_{\boldsymbol{X}} \boldsymbol{u}_{h,n+1} + \boldsymbol{I}$ and the history of the internal variables $\mathbf{F}_{\mathrm{p},n}$, $\alpha_{\mathrm{i},n}$ and $\boldsymbol{\alpha}_{\mathrm{k},n}$ be given.

Then, the discrete Karusch–Kuhn–Tucker conditions (3.5) permits two mutually exclusive states: either the material reacts purely elastic if $\phi_{\mathrm{p},n+1} < 0$ such that $\Delta\gamma = 0$ or plastic deformation takes place if $\phi_{\mathrm{p},n+1} = 0$ and $\Delta\gamma \geq 0$.

The Elastic Predictor. To determine which of the cases applies, a so-called elastic predictor is introduced assuming $\Delta\gamma = 0$ to determine the trial state

$$\mathbf{F}_{\mathrm{p},n+1,\mathrm{tr}} = \mathbf{F}_{\mathrm{p},n} \quad , \quad \alpha_{\mathrm{i},n+1,\mathrm{tr}} = \alpha_{\mathrm{i},n} \quad , \quad \boldsymbol{\alpha}_{\mathrm{k},n+1,\mathrm{tr}} = \boldsymbol{\alpha}_{\mathrm{k},n} \quad , \tag{3.10}$$

indicated by a subscript $(\cdot)_{\mathrm{tr}}$. With these trial values, one obtains $\boldsymbol{F}_{\mathrm{e},n+1,\mathrm{tr}} = \boldsymbol{F}_{n+1}(\mathbf{F}_{\mathrm{p},n+1,\mathrm{tr}})^{-1}$ and by the elastic constitutive relation a corresponding Mandel stress $\boldsymbol{\Sigma}_{n+1,\mathrm{tr}}$ which gives the trial state of the yield function $\phi_{\mathrm{p},n+1,\mathrm{tr}}$. If $\phi_{\mathrm{p},n+1,\mathrm{tr}} < 0$ holds true, the assumption of $\Delta\gamma = 0$ was correct, therefore

$$\mathbf{F}_{\mathrm{p},n+1} = \mathbf{F}_{\mathrm{p},n+1,\mathrm{tr}} \quad , \quad \alpha_{\mathrm{i},n+1} = \alpha_{\mathrm{i},n+1,\mathrm{tr}} \quad , \quad \boldsymbol{\alpha}_{\mathrm{k},n+1} = \boldsymbol{\alpha}_{\mathrm{k},n+1,\mathrm{tr}} \quad , \tag{3.11}$$

and $\boldsymbol{F}_{n+1}$ in combination with $\mathbf{F}_{\mathrm{p},n+1} = \mathbf{F}_{\mathrm{p},n+1,\mathrm{tr}}$ can be used in (2.61) to determine the stress $\boldsymbol{P}_{n+1}$.

The Plastic Corrector. In the case of $\phi_{\mathrm{p},n+1,\mathrm{tr}} \geq 0$, the assumption of purely elastic deformation and $\Delta\gamma = 0$ was incorrect and plastic deformation takes place within this time step. To determine the actual values of the incremental plastic multiplier $\Delta\gamma$ and the internal variables of state $\mathbf{F}_{\mathrm{p},n+1}$, $\alpha_{\mathrm{i},n+1}$ and $\boldsymbol{\alpha}_{\mathrm{k},n+1}$, the coupled system of nonlinear equations

$$\phi_{\mathrm{p},n+1} = 0 \quad , \tag{3.12a}$$

$$\mathbf{F}_{\mathrm{p},n+1} - \exp\left[\Delta\gamma\left(\frac{\partial\Xi_{\mathrm{p}}}{\partial\boldsymbol{\Sigma}} + \frac{\eta}{y_0}\left(\left(\boldsymbol{\Sigma}\frac{\partial\Xi_{\mathrm{p}}}{\partial\boldsymbol{\Sigma}} - \frac{\partial\Xi_{\mathrm{p}}}{\partial\boldsymbol{\Sigma}}\boldsymbol{\Sigma}\right)\right)\right)\right]\mathbf{F}_{\mathrm{p},n} = \mathbf{0} \quad , \tag{3.12b}$$

$$\alpha_{\mathrm{i},n+1} - \alpha_{\mathrm{i},n} - \Delta\gamma\frac{\partial\Xi_{\mathrm{p}}}{\partial\alpha_{\mathrm{i}}} = 0 \quad , \tag{3.12c}$$

$$\boldsymbol{\alpha}_{\mathrm{k},n+1} - \boldsymbol{\alpha}_{\mathrm{k},n} - \Delta\gamma\frac{\partial\Xi_{\mathrm{p}}}{\partial\boldsymbol{\alpha}_{\mathrm{k}}} = \mathbf{0} \tag{3.12d}$$

needs to be solved at a fixed total deformation gradient $\boldsymbol{F}_{n+1}$; all quantities not indexed are evaluated at t_{n+1}. From the resulting inelastic deformation $\mathbf{F}_{\mathrm{p},n+1}$, the acting first Piola–Kirchhoff stress can then again be evaluated according to (2.61).

Remark 3.2 (Simplified RMAs)**.** *In many practical implementations, the system of nonlinear equations* (3.12) *can be reduced significantly, for instance using a formulation in logarithmic strains [57], or, for isotropic plasticity, in principle directions [19]. For a Hencky-type hyperelastic material*[1] *in particular, the return mapping* (3.12) *can even be reduced to a scalar nonlinear equation.*

In view of the global solution of the nonlinear equation (2.159), the RMA yields a hierarchy nonlinear solvers: At the global level, a Newton scheme (2.167) is applied and within each step

[1] This material constitutes a linear relation between the logarithmic strains $\boldsymbol{\varepsilon}_{\mathrm{e}} = {}^1\!/_2 \ln[\boldsymbol{F}_{\mathrm{e}}\boldsymbol{F}_{\mathrm{e}}^{\mathsf{T}}]$ and the Kirchhoff stress $\boldsymbol{\tau}$.

of this Newton scheme, the RMA solves local nonlinear problem (3.12) to convergence at every quadrature point undergoing plastic deformation. From a performance perspective it has to be noted, that this remains rather efficient as the local problems (3.12), especially if simplified (see Remark 3.2), is way smaller than (2.159) which consists of all nodal displacement degrees of freedom. A consequence of solving (3.12) to convergence at every Newton step of (2.167) is that the yield limit $\phi_{\mathrm{p}} \leq 0$ needs to be satisfied in every iterate. If the current iterate is, however, far from the converged solution, the plastic deformation obtained by (3.12) may be largely overestimated and result in divergence of the global Newton scheme. The relaxation of this constraint in the pre-asymtotic range of the global Newton scheme is one of the ideas in the subsequently derived plasticity algorithm.

3.3 Nonlinear Complementarity Functions for Finite Strain Plasticity

Nonlinear complementarity (NCP) functions originate in the field of constrained optimization and are used to convert inequality constraints into equivalent non-smooth equality constraints [212]. These can then be used as merit functions (see e.g. Geiger and Kanzow [77]) or to render inequality constrained problems amenable to numerical methods for equality constraints, e.g. semi-smooth Newton methods in Hintermüller *et al.* [103], Qi and Sun [178]. For problems of elasto-plasticity, NCP functions have been used by Christensen [37], Hager [90], Hager and Wohlmuth [91] for small strain isothermal von Mises plasticity and in Seitz *et al.* [192] for finite deformation isothermal Hill-type plasticity and extended to thermoplasticity in Seitz *et al.* [194].

In the following, the inequality-type material constraints posed by Hill's yield criterion will be recast as an equality constraint. This equality constraint can be solved simultaneously to the global equilibrium search within *one* non-smooth Newton scheme, for which the robustness is further increased by a quasi-Newton method.

3.3.1 Reformulation of the Inequality Constraints

Before the inequality constraints are reformulated as an equality constraint, the yield function and evolution equations for associative Hill-type plasticity are recalled. For the yield function and dissipation potential, (2.66) in combination with (2.67) and (2.77) yields

$$\Xi_{\mathrm{p}} = \phi_{\mathrm{p}} = \sqrt{\frac{3}{2}} \left\| \boldsymbol{\Sigma} - \boldsymbol{A}_{\mathrm{k}} \right\|_{\mathbb{H}} - (y_0 - A_{\mathrm{i}}) = \sqrt{\frac{3}{2}} \left\| \boldsymbol{\eta} \right\|_{\mathbb{H}} - Y \quad . \tag{3.13}$$

The evolution of the plastic flow (3.6) can be rewritten as

$$\Delta \mathbf{D}_{\mathrm{p}} = \Delta\gamma \sqrt{\frac{3}{2}} \frac{\mathbb{H} : \boldsymbol{\eta}}{\left\| \boldsymbol{\eta} \right\|_{\mathbb{H}}} \quad , \tag{3.14}$$

wherein, as in the following, both indices $(\cdot)_q$ denoting the quadrature point and $(\cdot)_{n+1}$ denoting the time step have been dropped. If not indicated otherwise, all quantities are evaluated at a

discrete Gauss point and at time t_{n+1}. The time discrete evolution of the hardening variables α_i and $\boldsymbol{\alpha}_\mathrm{k}$ in (3.8) and (3.9) can be reformulated in terms of $\Delta\mathbf{D}_\mathrm{p}$ as

$$\alpha_\mathrm{i} = \begin{cases} \alpha_{\mathrm{i},n} + \sqrt{\frac{2}{3}} \frac{\|\boldsymbol{\eta}\|_\mathbb{H}}{\|\mathbb{H} : \boldsymbol{\eta}\|} \|\Delta\mathbf{D}_\mathrm{p}\| & \text{(3.15a)} \\ \alpha_{\mathrm{i},n} + \max\left(0, \sqrt{\frac{2}{3}} \frac{\|\boldsymbol{\eta}\|_\mathbb{H} \boldsymbol{\eta} : \mathbb{H} : \Delta\mathbf{D}_\mathrm{p}}{\|\mathbb{H} : \boldsymbol{\eta}\|^2}\right) & \text{(3.15b)} \end{cases}$$

$$\boldsymbol{\alpha}_\mathrm{k} = \boldsymbol{\alpha}_{\mathrm{k},n} - \Delta\mathbf{D}_\mathrm{p} \quad . \tag{3.16}$$

The two variants (3.15a) and (3.15b) to define the evolution of the isotropic hardening variable α_i are equivalent, if (3.14) is satisfied, but yield slightly different numerical properties in the subsequently derived algorithm.[1] More simply, the evolution of $\boldsymbol{\alpha}_\mathrm{k}$ in terms of $\Delta\mathbf{D}_\mathrm{p}$ follows directly from the dependency of ϕ_p in (3.13) on the effective stress $\boldsymbol{\eta} = \boldsymbol{\Sigma} - \boldsymbol{A}_\mathrm{k}$, such that $\frac{\partial \Xi_\mathrm{p}}{\partial \boldsymbol{A}_\mathrm{k}} = -\frac{\partial \Xi_\mathrm{p}}{\partial \boldsymbol{\Sigma}} = -\mathbf{D}_\mathrm{p}$ and (3.16) arises from a backward Euler discretization in time.

With the evolution of the hardening variables given in terms of $\Delta\mathbf{D}_\mathrm{p}$, the discrete Karush–Kuhn–Tucker conditions (3.5) together with the evolution (3.14) for $\Delta\mathbf{D}_\mathrm{p}$ can be stated equivalently as finding the root

$$\boldsymbol{G}_\mathrm{p} = \operatorname{dev}\boldsymbol{\eta} - \min\left(1, \frac{Y}{\sqrt{3/2}\,\|\boldsymbol{\eta}_\mathrm{tr}\|_\mathbb{H}}\right)\boldsymbol{\eta}_\mathrm{tr} = \mathbf{0} \quad , \tag{3.17a}$$

$$\operatorname{tr}\Delta\mathbf{D}_\mathrm{p} = 0 \quad , \tag{3.17b}$$

with the trial effective stress

$$\boldsymbol{\eta}_\mathrm{tr} = \operatorname{dev}\boldsymbol{\eta} + c_\mathrm{p}\mathbb{H}^+ : \Delta\mathbf{D}_\mathrm{p} \quad , \quad c_\mathrm{p} > 0 \quad , \tag{3.18}$$

wherein $\mathbb{H}^+$ denotes the pseudo-inverse[2] of $\mathbb{H}$ in the sense that $\operatorname{dev}\boldsymbol{T} = \mathbb{H}^+ : \mathbb{H} : \boldsymbol{T}$. This trial stress is not to be confused with the trial state of the RMA outlined in the previous section. Here, it merely represents an abbreviation for the combination of the effective stress $\boldsymbol{\eta}$ and the plastic flow $\Delta\mathbf{D}_\mathrm{p}$.

Proof. To show equivalence of (3.17) with (3.5) in combination with (3.13) and (3.14), it is first assumed that (3.5), (3.13) and (3.14) hold true and (3.17) is verified. In the elastic case, (3.5), (3.13) and (3.14) give $\sqrt{3/2}\,\|\boldsymbol{\eta}\|_\mathbb{H} \leq Y$ and $\Delta\mathbf{D}_\mathrm{p} = \mathbf{0}$, such that by (3.18) $\boldsymbol{\eta}_\mathrm{tr} = \boldsymbol{\eta}$ and $\sqrt{3/2}\,\|\boldsymbol{\eta}_\mathrm{tr}\|_\mathbb{H} \leq Y$ and therefore (3.17) holds. In the plastic case, (3.5), (3.13) give $\sqrt{3/2}\,\|\boldsymbol{\eta}\|_\mathbb{H} = Y$ and $\Delta\gamma \geq 0$ in (3.14). In that case, the trial stress $\boldsymbol{\eta}_\mathrm{tr}$ becomes

$$\boldsymbol{\eta}_\mathrm{tr} = \left(1 + \sqrt{\frac{3}{2}}\frac{c_\mathrm{p}\Delta\gamma}{\|\boldsymbol{\eta}\|_\mathbb{H}}\right)\operatorname{dev}\boldsymbol{\eta} \quad , \tag{3.19}$$

[1] Note that for von Mises plasticity, i.e. $\mathbb{H} = \mathbb{P}_\mathrm{dev}$, (3.15b) simplifies due to the fact that $\|\mathbb{P}_\mathrm{dev} : \boldsymbol{\eta}\| = \|\boldsymbol{\eta}\|_{\mathbb{P}_\mathrm{dev}}$.

[2] Note that $\mathbb{H}$ includes a deviatoric projection $\mathbb{H} = \mathbb{P}_\mathrm{dev} : \mathbb{H} = \mathbb{H} : \mathbb{P}_\mathrm{dev}$, see Section 2.3.4.4, and hence does not have full rank.

and, as $\mathbb{H}$ includes a deviatoric projection, the semi-norm

$$\|\boldsymbol{\eta}_{\mathrm{tr}}\|_{\mathbb{H}} = \left(1 + \sqrt{\frac{3}{2}}\frac{c_{\mathrm{p}}\Delta\gamma}{\|\boldsymbol{\eta}\|_{\mathbb{H}}}\right)\|\boldsymbol{\eta}\|_{\mathbb{H}}\,. \tag{3.20}$$

Since $c_{\mathrm{p}} > 0$ and $\Delta\gamma \geq 0$ it follows that $\sqrt{3/2}\,\|\boldsymbol{\eta}_{\mathrm{tr}}\|_{\mathbb{H}} \geq \sqrt{3/2}\,\|\boldsymbol{\eta}\|_{\mathbb{H}} = Y$, which guarantees that (3.17a) holds true.

Conversely, now assume (3.17a) holds and (3.5), (3.13) and (3.14) have to be verified. In the case of $\sqrt{3/2}\,\|\boldsymbol{\eta}_{\mathrm{tr}}\|_{\mathbb{H}} \leq Y$, (3.17a) reduces to $\mathbb{H}^{+} : \Delta\mathbf{D}_{\mathrm{p}} = \mathbf{0}$, from which it follows that $\operatorname{dev}\Delta\mathbf{D}_{\mathrm{p}} = \mathbf{0}$ and finally together with (3.17b) one obtains $\Delta\mathbf{D}_{\mathrm{p}} = \mathbf{0}$. As a consequence, $\sqrt{3/2}\,\|\boldsymbol{\eta}_{\mathrm{tr}}\|_{\mathbb{H}} = \sqrt{3/2}\,\|\boldsymbol{\eta}\|_{\mathbb{H}} \leq Y$ and therefore $\sqrt{3/2}\,\|\boldsymbol{\eta}_{\mathrm{tr}}\|_{\mathbb{H}} \leq Y$ in (3.17a) recovers the elastic case of (3.5), (3.13) and (3.14). In the case of $\sqrt{3/2}\,\|\boldsymbol{\eta}_{\mathrm{tr}}\|_{\mathbb{H}} \geq Y$, (3.17a) (multiplied by $\|\boldsymbol{\eta}_{\mathrm{tr}}\|_{\mathbb{H}}$ and rearranged) becomes

$$\sqrt{3/2}\,\|\boldsymbol{\eta}_{\mathrm{tr}}\|_{\mathbb{H}}\operatorname{dev}\boldsymbol{\eta} = Y\boldsymbol{\eta}_{\mathrm{tr}}\quad. \tag{3.21}$$

Taking the $\|\cdot\|_{\mathbb{H}}$-semi-norm on both sides reveals that $\sqrt{3/2}\,\|\boldsymbol{\eta}\|_{\mathbb{H}} = Y$. Finally, we replace $\boldsymbol{\eta}_{\mathrm{tr}}$ on the right-hand-side of (3.21) by (3.18) and solve for $\Delta\mathbf{D}_{\mathrm{p}}$ to obtain

$$\operatorname{dev}\Delta\mathbf{D}_{\mathrm{p}} = \frac{\sqrt{3/2}\,\|\boldsymbol{\eta}_{\mathrm{tr}}\|_{\mathbb{H}} - Y}{c_{\mathrm{p}}}\mathbb{H} : \boldsymbol{\eta} = \Delta\gamma\mathbb{H} : \boldsymbol{\eta} \quad \text{with} \quad \Delta\gamma = \frac{\sqrt{3/2}\,\|\boldsymbol{\eta}_{\mathrm{tr}}\|_{\mathbb{H}} - Y}{c_{\mathrm{p}}} \geq 0\quad, \tag{3.22}$$

and, by using (3.17b), $\Delta\mathbf{D}_{\mathrm{p}} = \operatorname{dev}\Delta\mathbf{D}_{\mathrm{p}}$. Hence, $\sqrt{3/2}\,\|\boldsymbol{\eta}_{\mathrm{tr}}\|_{\mathbb{H}} \geq Y$ in (3.17) recovers the plastic case of (3.5), (3.13) and (3.14). □

Remark 3.3 (NCP function in the stress-free state)**.** *Technically speaking,* (3.17a) *as well as the evolution equations* (3.15a) *and* (3.15b) *are not well-defined in the stress-free case of* $\|\boldsymbol{\eta}_{\mathrm{tr}}\|_{\mathbb{H}} = 0$ *and* $\|\mathbb{H} : \boldsymbol{\eta}\| = 0$*, respectively. However,* $\|\boldsymbol{\eta}_{\mathrm{tr}}\|_{\mathbb{H}} = 0$ *implies* $\|\boldsymbol{\eta}_{\mathrm{tr}}\|_{\mathbb{H}} < Y$*, in which case the NCP function reduces to* $\boldsymbol{G}_{\mathrm{p}} = c_{\mathrm{p}}\mathbb{H}^{+} : \Delta\mathbf{D}_{\mathrm{p}} = \mathbf{0}$*. Therefore, one directly obtains* $\Delta\mathbf{D}_{\mathrm{p}} = \mathbf{0}$ *and the evolution of the isotropic hardening variable is set to* $\alpha_{\mathrm{i},n+1} = \alpha_{\mathrm{i},n}$*.*

In Christensen [37] and Hager [90], a similar NCP function complemented by a scalar one for the evolution of α_{i} is analyzed for small strain kinematics and shown to be equivalent with the RMA, if linear kinematic hardening ($\Psi_{\mathrm{p}}(\alpha_{\mathrm{i}}, \boldsymbol{\alpha}_{\mathrm{k}}) = \Psi_{\mathrm{p,i}}(\alpha_{\mathrm{i}}) + 1/2 H_{\mathrm{k}}\|\boldsymbol{\alpha}_{\mathrm{k}}\|^2$, kinematic hardening modulus H_{k}) is assumed and the complementarity parameter c_{p} is chosen as $c_{\mathrm{p}} = 2\mu + 2/3 H_{\mathrm{k}}$ with the shear modulus μ. However, any modification of (3.17a) that does not alter its root yields an equally valid NCP function to the problem (3.5), (3.13) and (3.14). Based on ideas of Hager and Wohlmuth [91], Hüeber *et al.* [109], a shape parameter $s_{\mathrm{p}} \geq 0$ is introduced to add convexity to the NCP function (3.17a) by

$$\begin{aligned}\boldsymbol{G}_{\mathrm{p},s_{\mathrm{p}}} &= \left(\max\left(Y, \sqrt{\frac{3}{2}}\,\|\boldsymbol{\eta}_{\mathrm{tr}}\|_{\mathbb{H}}\right)\right)^{s_{\mathrm{p}}} \cdot \boldsymbol{G}_{\mathrm{p}} \\ &= \left(\max\left(Y, \sqrt{\frac{3}{2}}\,\|\boldsymbol{\eta}_{\mathrm{tr}}\|_{\mathbb{H}}\right)\right)^{s_{\mathrm{p}}} \cdot \left(\operatorname{dev}\boldsymbol{\eta} - \min\left(1, \frac{Y}{\sqrt{3/2}\,\|\boldsymbol{\eta}_{\mathrm{tr}}\|_{\mathbb{H}}}\right)\boldsymbol{\eta}_{\mathrm{tr}}\right)\quad.\end{aligned} \tag{3.23}$$

Note, that the $\max$-function therein is strictly greater than zero since $Y > 0$ and therefore the modification has no influence on the root of the NCP function and therefore its equivalence

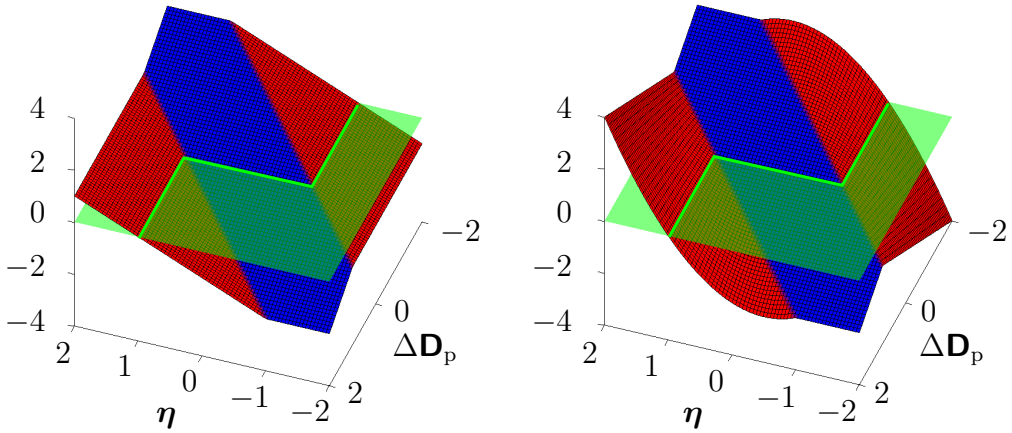

(a) $\boldsymbol{G}_{\mathrm{p},0}$. (b) $\boldsymbol{G}_{\mathrm{p},1}$.

Figure 3.1: Visualization of the NCP function (3.23) for a one-dimensional problem with $Y = 1$, $c_{\mathrm{p}} = 1$ and $s_{\mathrm{p}} \in \{0, 1\}$. The blue and red parts of the functions denote the elastic ($|\boldsymbol{\eta}_{\mathrm{tr}}| \leq Y$) and plastic branches ($|\boldsymbol{\eta}_{\mathrm{tr}}| > Y$), respectively. The transparent green plane indicates the zero-plane and a solid green line the root of the NCP function.

with the plastic inequality constraints. (3.17a) is recovered for $s_{\mathrm{p}} = 0$. For a one-dimensional plasticity problem, (3.23) is visualized in Figure 3.1 for different values of s_{p}. The root of both these NCP functions apparently reproduce the Kraush–Kuhn–Tucker conditions (3.5): either the absolute value of the effective stress $\boldsymbol{\eta}$ is lower than $Y = 1$ and the plastic flow $\Delta\mathbf{D}_{\mathrm{p}}$ is zero, or $|\boldsymbol{\eta}| = Y = 1$ and the plastic flow points in the same direction (same sign in the one-dimensional case) as the stress $\boldsymbol{\eta}$.

Remark 3.4. *The employed quadratic yield functions of von Mises and Hill according to* (3.13) *admittedly fit particularly well into this framework of NCP functions, since they can be represented by a single NCP function* (3.17a)*. Still, pressure sensitivity (see* (2.78)*) may easily be added to extend the methodology to the Drucker–Prager yield function. Also, multi-surface yield criteria such as the one by Tresca* (2.73) *or single crystal plasticity may be adopted by using multiple NCP functions for the different yield surfaces. Yield criteria in which the equivalent stress may not be represented as a quadratic (semi-) norm of the effective stress, on the contrary, pose greater difficulty in deriving an equivalent NCP function. A general methodology to derive such for arbitrary yield criteria is, to the best of the author's knowledge, still an open issue.*

3.3.2 Solution by a Semi-Smooth Newton Method

As the equivalence of the root of the NCP function with the plastic material constraints is established, it can be solved alongside the discrete structural and thermal balance equations (2.165) and (2.166), respectively. The presentation of the solution algorithm is, at this point, restricted to quasi-static processes (see Remark 2.6), the absence of plastic spin, i.e. $\Delta\mathbf{W}_{\mathrm{p}} = \mathbf{0}$ and $\Delta\mathbf{L}_{\mathrm{p}} = \Delta\mathbf{D}_{\mathrm{p}}$, rate-independent plasticity and isothermal processes. The extension to dynamic processes is straightforward by replacing the balance equations (2.165) and (2.166) in the following by (2.159) and (2.163). The extensions to plastic spin, visco-plasticity, and thermo-elasto-plasticity will be outlined in the subsequent Sections 3.4.1 - 3.4.3.

To solve the quasi-static discrete balance of linear momentum (2.165) with the constraints of elasto-plasticity, the plastic flow increment $\Delta\mathbf{L}_{\mathrm{p},q}$ at every quadrature point $q \in \mathcal{G}$ is introduced as additional unknowns with the same "dignity" as the unknown nodal displacements. The nonlinear system of equations to be solved in each time step for the displacements $\mathbf{d}_{n+1}$ and plastic deformations $\Delta\mathbf{L}_{\mathrm{p},n+1}$ then consists of

$$\boldsymbol{r}_{\mathrm{u}}(\mathbf{d}_{n+1}, \Delta\mathbf{L}_{\mathrm{p},n+1}) = \boldsymbol{F}_{\mathrm{u,int},n+1}(\mathbf{d}_{n+1}, \Delta\mathbf{L}_{\mathrm{p},n+1}) - \boldsymbol{F}_{\mathrm{u,ext},n+1} = \mathbf{0} \quad , \tag{3.24a}$$

$$\boldsymbol{G}_{\mathrm{p},s_{\mathrm{p}},q}(\mathbf{d}_{n+1}, \Delta\mathbf{L}_{\mathrm{p},q,n+1}) = \mathbf{0} \quad , \quad \forall q \in \mathcal{G} \quad , \tag{3.24b}$$

$$\operatorname{tr} \Delta\mathbf{L}_{\mathrm{p},q,n+1} = 0 \quad , \quad \forall q \in \mathcal{G} \quad , \tag{3.24c}$$

$$\Delta\mathbf{W}_{\mathrm{p},q,n+1} = \operatorname{skew} \Delta\mathbf{L}_{\mathrm{p},q,n+1} = \mathbf{0} \quad , \quad \forall q \in \mathcal{G} \quad . \tag{3.24d}$$

The evolution of the hardening variables is thereby expressed in terms of $\Delta\mathbf{D}_{\mathrm{p}}$ by (3.15b) and (3.16). In the following, the time step index $(\cdot)_{n+1}$ will be dropped for brevity of notation. Despite the non-smoothness of $\boldsymbol{G}_{\mathrm{p},s_{\mathrm{p}}}$ due to the involved norms and $\min$- and $\max$-functions, the set of equations (3.24) still qualifies for the use of non-smooth versions of Newton's method and quadratic convergence close to the solution may be expected, see Qi and Sun [178]. In every step i of the Newton scheme, the linearized system

$$\frac{\partial \boldsymbol{F}_{\mathrm{u,int}}(\mathbf{d}^i, \Delta\mathbf{L}_{\mathrm{p}}^i)}{\partial \mathbf{d}} \Delta\mathbf{d}^i + \frac{\partial \boldsymbol{F}_{\mathrm{u,int}}(\mathbf{d}^i, \Delta\mathbf{L}_{\mathrm{p}}^i)}{\partial \Delta\mathbf{L}_{\mathrm{p}}} \Delta\Delta\mathbf{L}_{\mathrm{p}}^i = -\boldsymbol{r}_{\mathrm{u}}(\mathbf{d}, \Delta\mathbf{L}_{\mathrm{p}}) \quad , \tag{3.25a}$$

$$\frac{\partial \boldsymbol{G}_{\mathrm{p},s_{\mathrm{p}},q}(\mathbf{d}^i, \Delta\mathbf{L}_{\mathrm{p}}^i)}{\partial \mathbf{d}} \Delta\mathbf{d}^i + \frac{\partial \boldsymbol{G}_{\mathrm{p},s_{\mathrm{p}},q}(\mathbf{d}^i, \Delta\mathbf{L}_{\mathrm{p},q}^i)}{\partial \Delta\mathbf{L}_{\mathrm{p},q}} \Delta\Delta\mathbf{L}_{\mathrm{p},q}^i = -\boldsymbol{G}_{\mathrm{p},s_{\mathrm{p}},q}(\mathbf{d}^i, \Delta\mathbf{L}_{\mathrm{p},q}^i) \quad , \quad \forall q \in \mathcal{G} \quad , \tag{3.25b}$$

$$\operatorname{tr} \Delta\mathbf{L}_{\mathrm{p},q}^i = 0 \quad , \quad \forall q \in \mathcal{G} \quad , \tag{3.25c}$$

$$\operatorname{skew} \Delta\mathbf{L}_{\mathrm{p},q}^i = \mathbf{0} \quad , \quad \forall q \in \mathcal{G} \tag{3.25d}$$

is solved for the increments $\Delta\mathbf{d}^i$ and $\Delta\Delta\mathbf{L}_{\mathrm{p}}^i$ and the displacements and plastic deformations are updated ($\mathbf{d}^{i+1} = \mathbf{d}^i + \Delta\mathbf{d}^i$, $\Delta\mathbf{L}_{\mathrm{p}}^{i+1} = \Delta\mathbf{L}_{\mathrm{p}}^i + \Delta\Delta\mathbf{L}_{\mathrm{p}}^i$, $i \leftarrow i+1$) until a convergence tolerance is met. The linear constraints (3.25c) and (3.25d) enforcing a symmetric, traceless plastic flow increment $\Delta\mathbf{L}_{\mathrm{p}}$ do not have to be treated explicitly but are ensured implicitly in the subsequently derived algorithm. With the plastic internal variables at each quadrature point being independent and the NCP function at one quadrature point only depending on the discrete displacements of the respective element, a Gauss point local formulation is sufficient. In the following, the resulting directional derivatives necessary at each quadrature point will be outlined. The subscript q will be omitted for ease of notation, keeping in mind that all quantities are evaluated at the Gauss point. To start with, the contribution $\boldsymbol{f}_{\mathrm{u,int}}$ of one quadrature point to the internal force vector $\boldsymbol{F}_{\mathrm{u,int}}$ emanating from (2.141) may be rewritten as

$$\boldsymbol{f}_{\mathrm{u,int}} = w \cdot (\boldsymbol{F}\boldsymbol{S}) : \nabla_{\boldsymbol{X}} \boldsymbol{N} \quad , \tag{3.26}$$

with the integration weight w composed of the weight of the quadrature point and the Jacobian of the isoparemetric element mapping (2.139) and the matrix of element ansatz functions $\boldsymbol{N}$. The

linearization of the internal force vector with respect to the discrete nodal displacements remains unaltered from a standard geometrically nonlinear finite element formulation and results in the tangential stiffness matrix contribution of a quadrature point:

$$\frac{1}{w}\frac{\partial \boldsymbol{f}_{\mathrm{u,int}}}{\partial \mathbf{d}} = (\boldsymbol{F}\nabla_{\boldsymbol{X}}\boldsymbol{N})^{\mathsf{T}} : \mathbb{C} : (\boldsymbol{F}\nabla_{\boldsymbol{X}}\boldsymbol{N}) + \boldsymbol{S} : \left((\nabla_{\boldsymbol{X}}\boldsymbol{N})^{\mathsf{T}} \cdot \nabla_{\boldsymbol{X}}\boldsymbol{N}\right) \quad , \tag{3.27}$$

with the material stiffness tensor $\mathbb{C} = 2^{\partial \boldsymbol{S}}/_{\partial \boldsymbol{C}}$. In the case of elasto-plasticity, this material stiffness tensor also depends on the current state of plastic deformation through equations (2.53) and (2.61). A derivation of $\mathbb{C}$ for arbitrary isotropic free energies Ψ_{e} multiplicative elasto-plastic kinematics is given in Appendix A. The linearization of the internal force vector with respect to the plastic flow increment yields

$$\frac{1}{w}\frac{\partial \boldsymbol{f}_{\mathrm{u,int}}}{\partial \Delta \mathbf{L}_{\mathrm{p}}} = (\boldsymbol{F}\nabla_{\boldsymbol{X}}\boldsymbol{N})^{\mathsf{T}} : \frac{\partial \boldsymbol{S}}{\partial \Delta \mathbf{L}_{\mathrm{p}}} \quad , \tag{3.28}$$

wherein the derivative of the second Piola–Kirchhoff stress follows from the multiplicative kinematics (2.53), the constitutive equation (2.61) and the evolution of the plastic deformation gradient (3.4). For elasically isotropic materials, this derivative is given in detail in Appendix A.

The derivatives of the NCP function (3.23) are more complicated and outlined below. To distinguish the two branches of the involved $\min$- and $\max$-functions, the set of quadrature points is split into elastic and plastic quadrature points $\mathcal{G}_{\mathrm{e}}$ and $\mathcal{G}_{\mathrm{p}}$, for which $\sqrt{3/2}\,\|\boldsymbol{\eta}_{\mathrm{tr}}\|_{\mathbb{H}} \leq Y$ and $\sqrt{3/2}\,\|\boldsymbol{\eta}_{\mathrm{tr}}\|_{\mathbb{H}} > Y$, respectively. In the special case of $\sqrt{3/2}\,\|\boldsymbol{\eta}_{\mathrm{tr}}\|_{\mathbb{H}} = Y$, the derivatives of either branch may be chosen or any other generalized derivative of the $\min$- and $\max$-functions. For the derivative of the NCP function with respect to the discrete displacements, one obtains

$$\frac{\partial \boldsymbol{G}_{\mathrm{p},s_{\mathrm{p}}}}{\partial \mathbf{d}} = \begin{cases} -s_{\mathrm{p}} c_{\mathrm{p}} \mathbb{H}^{+} : \Delta \mathbf{D}_{\mathrm{p}} Y^{s_{\mathrm{p}}-1} \otimes \frac{\partial Y}{\partial \mathbf{d}} & \text{if } q \in \mathcal{G}_{\mathrm{e}} \\ \left(\sqrt{\frac{3}{2}}\,\|\boldsymbol{\eta}_{\mathrm{tr}}\|_{\mathbb{H}}\right)^{s_{\mathrm{p}}} & \\ \quad \cdot \left\{ \left[\left(1 - \frac{Y}{\sqrt{3/2}\|\boldsymbol{\eta}_{\mathrm{tr}}\|_{\mathbb{H}}}\right) \mathbb{P}_{\mathrm{dev}} + \frac{\boldsymbol{\eta}_{s_{\mathrm{p}}} \otimes \mathbb{H} : \boldsymbol{\eta}_{\mathrm{tr}}}{\|\boldsymbol{\eta}_{\mathrm{tr}}\|_{\mathbb{H}}^2} \right] : \frac{2\partial \boldsymbol{\Sigma}}{\partial \boldsymbol{C}} : (\boldsymbol{F}\nabla_{\boldsymbol{X}}\boldsymbol{N}) \right. & \\ \qquad \left. - \frac{\boldsymbol{\eta}_{\mathrm{tr}}}{\|\boldsymbol{\eta}_{\mathrm{tr}}\|_{\mathbb{H}}} \otimes \frac{\partial Y}{\partial \mathbf{d}} \right\} & \text{if } q \in \mathcal{G}_{\mathrm{p}} \end{cases} \tag{3.29}$$

with

$$\boldsymbol{\eta}_{s_{\mathrm{p}}} = (1 - s_{\mathrm{p}}) \frac{Y}{\sqrt{3/2}\,\|\boldsymbol{\eta}_{\mathrm{tr}}\|_{\mathbb{H}}} \boldsymbol{\eta}_{\mathrm{tr}} + s_{\mathrm{p}} a_{\mathrm{p}} \boldsymbol{\eta} \quad . \tag{3.30}$$

The additional factor

$$a_{\mathrm{p}} = \min\left(1, \frac{Y}{\sqrt{3/2}\,\|\boldsymbol{\eta}\|_{\mathbb{H}}}\right) \tag{3.31}$$

is introduced in the spirit of Hager and Wohlmuth [91] to stabilize the Newton iteration within the pre-asymptotic range, whereas in the converged state a_{p} tends to one and the fully consistent Newton scheme is recovered. The derivative of the effective yield stress Y results trough

linearization of a time discrete evolution of the isotropic hardening parameter (3.15b) in

$$\frac{\partial Y}{\partial \mathbf{d}} = \begin{cases} \sqrt{\frac{2}{3}} \frac{\partial Y}{\partial \alpha_\mathrm{i}} \left[\frac{\Delta \mathbf{D}_\mathrm{p} : \mathbb{H} : \boldsymbol{\eta}}{\|\boldsymbol{\eta}\|_\mathbb{H} \|\mathbb{H} : \boldsymbol{\eta}\|^2} \mathbb{H} : \boldsymbol{\eta} + \frac{\|\boldsymbol{\eta}\|_\mathbb{H}}{\|\mathbb{H} : \boldsymbol{\eta}\|^2} \mathbb{H} : \Delta \mathbf{D}_\mathrm{p} \right. \\ \qquad \left. - 2 \frac{\|\boldsymbol{\eta}\|_\mathbb{H} \Delta \mathbf{D}_\mathrm{p} : \mathbb{H} : \boldsymbol{\eta}}{\|\mathbb{H} : \boldsymbol{\eta}\|^4} \mathbb{H} : \boldsymbol{\eta} : \mathbb{H} \right] : \frac{2 \partial \boldsymbol{\Sigma}}{\partial C} : (\boldsymbol{F} \nabla_{\boldsymbol{X}} \boldsymbol{N}) & \text{if } \Delta \mathbf{D}_\mathrm{p} : \mathbb{H} : \boldsymbol{\eta} > 0 \\ \mathbf{0} & \text{if } \Delta \mathbf{D}_\mathrm{p} : \mathbb{H} : \boldsymbol{\eta} \leq 0 \end{cases} , \tag{3.32}$$

with $\partial Y / \partial \alpha_\mathrm{i} = \partial^2 \Psi_\mathrm{p} / \partial \alpha_\mathrm{i}^2$ depending on the hardening potential Ψ_p. At this point, the advantage of the more complicated evolution of the isotropic hardening parameter in (3.15b) as compared to (3.15a) becomes obvious: Both variants result in a semi-smooth function for the equivalent yield stress, but (3.15b) additionally yields a zero derivative for elastic Gauss points (for which $\Delta \mathbf{D}_\mathrm{p} = \mathbf{0}$ holds). Consequently and foreclosing some of the following derivatives, the plastic complementarity function reduces to the trivial identity $\Delta \mathbf{D}^p = \mathbf{0}$, so that regular elasticity is recovered. This would not be the case if one used (3.15a) to describe the evolution of α_i.

Finally, the derivative of the NCP function with respect to the plastic flow increment $\Delta \mathbf{L}_\mathrm{p}$ results in

$$\frac{\partial \boldsymbol{G}_{\mathrm{p},s_\mathrm{p}}}{\partial \Delta \mathbf{L}_\mathrm{p}} = \begin{cases} -Y^{s_\mathrm{p}} \left(c_\mathrm{p} \mathbb{H}^+ + s_\mathrm{p} c_\mathrm{p} Y^{-1} \mathbb{H}^+ : \Delta \mathbf{D}_\mathrm{p} \otimes \frac{\partial Y}{\partial \Delta \mathbf{L}_\mathrm{p}} \right) & \text{if } q \in \mathcal{G}_\mathrm{e} \\ \left(\sqrt{3/2} \left\| \boldsymbol{\eta}_\mathrm{tr} \right\|_\mathbb{H} \right)^{s_\mathrm{p}} \left\{ \frac{\partial \boldsymbol{\eta}}{\partial \Delta \mathbf{L}_\mathrm{p}} - \frac{Y}{\sqrt{3/2} \|\boldsymbol{\eta}_\mathrm{tr}\|_\mathbb{H}} \boldsymbol{\eta}_\mathrm{tr} \frac{\partial Y}{\partial \Delta \mathbf{L}_\mathrm{p}} \right. & \\ \qquad \left. + \left[- \frac{Y}{\sqrt{3/2} \|\boldsymbol{\eta}_\mathrm{tr}\|_\mathbb{H}} \mathbb{P}_\mathrm{dev} + \frac{\boldsymbol{\eta}_{s_\mathrm{p}} \otimes \mathbb{H} : \boldsymbol{\eta}_\mathrm{tr}}{\|\boldsymbol{\eta}_\mathrm{tr}\|_\mathbb{H}^2} \right] : \frac{\partial \boldsymbol{\eta}_\mathrm{tr}}{\partial \Delta \mathbf{L}_\mathrm{p}} \right\} & \text{if } q \in \mathcal{G}_\mathrm{p} \end{cases} . \tag{3.33}$$

Herein, the derivatives of the effective stress and the effective trial stress are given by

$$\frac{\partial \boldsymbol{\eta}}{\partial \Delta \mathbf{L}_\mathrm{p}} = \frac{\partial \boldsymbol{\Sigma}}{\partial \Delta \mathbf{L}_\mathrm{p}} + \frac{\partial^2 \Psi_\mathrm{p}}{\partial \boldsymbol{\alpha}_\mathrm{k} \partial \boldsymbol{\alpha}_\mathrm{k}} \quad , \quad \frac{\partial \boldsymbol{\eta}_\mathrm{tr}}{\partial \Delta \mathbf{L}_\mathrm{p}} = \frac{\partial \boldsymbol{\eta}}{\partial \Delta \mathbf{L}_\mathrm{p}} + c_\mathrm{p} \mathbb{H}^+ \quad , \tag{3.34}$$

and the derivative of the effective yield stress as

$$\frac{\partial Y}{\partial \Delta \mathbf{L}_\mathrm{p}} = \begin{cases} \sqrt{\frac{2}{3}} \frac{\partial Y}{\partial \alpha_\mathrm{i}} \left[\left(\frac{\Delta \mathbf{D}_\mathrm{p} : \mathbb{H} : \boldsymbol{\eta}}{\|\boldsymbol{\eta}\|_\mathbb{H} \|\mathbb{H} : \boldsymbol{\eta}\|^2} \mathbb{H} : \boldsymbol{\eta} + \frac{\|\boldsymbol{\eta}\|_\mathbb{H}}{\|\mathbb{H} : \boldsymbol{\eta}\|^2} \mathbb{H} : \Delta \mathbf{D}_\mathrm{p} \right. \right. \\ \qquad \left. \left. - \frac{2 \|\boldsymbol{\eta}\|_\mathbb{H} \Delta \mathbf{D}_\mathrm{p} : \mathbb{H} : \boldsymbol{\eta}}{\|\mathbb{H} : \boldsymbol{\eta}\|^4} \mathbb{H} : \boldsymbol{\eta} : \mathbb{H} \right) : \frac{\partial \boldsymbol{\eta}}{\partial \Delta \mathbf{L}_\mathrm{p}} + \frac{\|\boldsymbol{\eta}\|_\mathbb{H}}{\|\mathbb{H} : \boldsymbol{\eta}\|^2} \mathbb{H} : \boldsymbol{\eta} \right] & \text{if } \Delta \mathbf{D}_\mathrm{p} : \mathbb{H} : \boldsymbol{\eta} > 0 \\ \mathbf{0} & \text{if } \Delta \mathbf{D}_\mathrm{p} : \mathbb{H} : \boldsymbol{\eta} \leq 0 \end{cases} . \tag{3.35}$$

As aforementioned, the plastic variables are discontinuous over the Gauss points, and hence only the plastic flow increment of the currently considered quadrature points enters the matrix blocks above. Consequently, the increment $\Delta \Delta \mathbf{L}_{\mathrm{p},q}$ of the plastic flow of each quadrature point $q \in \mathcal{G}$ in one step of the Newton iteration can be condensed from the global system of equations (3.25) on a local Gauss point level by

$$\Delta \Delta \mathbf{L}_{\mathrm{p},q} = - \left(\frac{\partial \boldsymbol{G}_{\mathrm{p},s_\mathrm{p},q}}{\partial \Delta \mathbf{L}_{\mathrm{p},q}} \right)^+ : \left(\boldsymbol{G}_{\mathrm{p},s_\mathrm{p},q} + \frac{\partial \boldsymbol{G}_{\mathrm{p},s_\mathrm{p},q}}{\partial \mathbf{d}} \Delta \mathbf{d} \right) . \tag{3.36}$$

The use of the pseudo-inverse $(\cdot)^+$ therein automatically guarantees (3.25c) and (3.25d) since the NCP function $\boldsymbol{G}_{\mathrm{p},s_\mathrm{p}}$ is symmetric and traceless by construction. Consequently, the linear

system to be solved at every quadrature point contains five remaining independent equations for the five components of the symmetric, traceless tensor $\Delta\Delta\mathbf{D}_{\mathrm{p},q}$. It should be point out, that in the case of linearized kinematics and linear kinematic hardening positive semi-definiteness of $\partial \boldsymbol{G}_{\mathrm{p},s_\mathrm{p},q} / \partial \Delta \mathbf{L}_{\mathrm{p},q}$ has been shown by Hager [90] to be ensured for $s_\mathrm{p} = 0, c_\mathrm{p} > 0$ and for $s_\mathrm{p} \in [0,1], c_\mathrm{p} \geq 2\mu + {}^2/_3 H_\mathrm{k}$ and a_p as in (3.31). Although this examination only considers infinitesimal deformations and a slightly different formulation with two complementarity functions, numerical experiments show that, for a sufficiently high complementarity parameter c_p, a solution to the local linear system for the five remaining unknowns exists. By inserting (3.36) in (3.25a), a reduced stiffness matrix and residual vector vector (indicated by a tilde) can be obtained as

$$\widetilde{\mathbf{K}}_{\mathrm{uu}} = \mathbf{K}_{\mathrm{uu}} - \sum_{q \in \mathcal{G}} \left[w_q \left(\frac{\partial \boldsymbol{f}_{\mathrm{u,int},q}}{\partial \Delta \mathbf{L}_{\mathrm{p},q}} \right) : \left(\frac{\partial \boldsymbol{G}_{\mathrm{p},s_\mathrm{p},q}}{\partial \Delta \mathbf{L}_{\mathrm{p},q}} \right)^{+} : \left(\frac{\partial \boldsymbol{G}_{\mathrm{p},s_\mathrm{p},q}}{\partial \mathbf{d}} \Delta \mathbf{d} \right) \right] \quad , \tag{3.37a}$$

$$\widetilde{\boldsymbol{r}}_{\mathrm{u}} = \boldsymbol{r}_{\mathrm{u}} - \sum_{q \in \mathcal{G}} \left[w_q \left(\frac{\partial \boldsymbol{f}_{\mathrm{u,int},q}}{\partial \Delta \mathbf{L}_{\mathrm{p},q}} \right) : \left(\frac{\partial \boldsymbol{G}_{\mathrm{p},s_\mathrm{p},q}}{\partial \Delta \mathbf{L}_{\mathrm{p},q}} \right)^{+} : \boldsymbol{G}_{\mathrm{p},s_\mathrm{p},q} \right] \quad . \tag{3.37b}$$

In practice, the full linearized system of equations (3.25) to be solved in each semi-smooth Newton step is never actually built. Instead, the discrete plastic flow increments are directly condensed at Gauss point level, thus eliminating the $\Delta \mathbf{L}_{\mathrm{p},q}$ from (3.25a) by using (3.37a) and (3.37b). After solving the remaining reduced system for the displacement increment $\Delta\mathbf{d}$, the plastic flow at each quadrature point can be recovered by (3.36).

3.3.3 Numerical Examples[1]

In this section, three representative numerical examples demonstrate the robustness of the proposed treatment of finite strain plasticity compared to the classical RMA. To avoid volumetric locking effects in the plastic region, $\mathbb{Q}_1$ hexahedral F-bar finite elements (see Section 2.8.1.1) are employed in all simulations. Convergence of the semi-smooth Newton method is checked in terms of the L^2-norm of the sub-residuals in (3.25a) and (3.25b) as well as the condensed residual in (3.37b) versus a convergence tolerance of 10^{-8}. In all simulations a simple explicit linear extrapolation predictor is used and equidistant load/displacement steps are applied.

In a first example, the influence of the algorithmic parameters involved in the plasticity formulation is investigated using the well-known example of a perforated strip. Second, the accuracy of our approach is demonstrated with the common finite deformation plasticity benchmark simulating the necking of a circular bar. Finally, a squeezed metal tube is analyzed to demonstrate the efficiency in the presence of kinematic hardening.

3.3.3.1 Perforated Strip

In this pseudo two-dimensional example, a strip with a circular hole is simulated. For both plane stress and plane strain conditions, this setting serves as a benchmark example for finite strain plasticity in the literature, e.g. in [76, 154, 155, 200, 204, 205]. A similar small strain setting has been used by Hager and Wohlmuth [91] to assess the influence of the parameters on the semi-smooth Newton method. Figure 3.2a illustrates the geometric setting; for obvious symmetry

[1] This section is adapted from the author's publication [192].

reasons and since isotropic plasticity is employed, only one quarter is simulated. The elastic material parameters are given by Young's modulus $E = 70$ and Poisson's ratio $\nu = 0.2$. To achieve the best possible comparison to the RMA, we assume a Hencky strain energy potential as commonly used in computational plasticity, e.g. in de Souza Neto *et al.* [57]. Von Mises plasticity is assumed with $y_0 = 0.243$ and linear isotropic hardening, i.e. $\Psi_{\mathrm{p}} = {}^1\!/_2 H_{\mathrm{i}} \alpha_{\mathrm{i}}^2$, with the linear hardening modulus $H_{\mathrm{i}} = 0.2$. The strip is stretched by a prescribed displacement of $u = 3$ using quasi-static time stepping, where different step sizes will be applied.

A plane strain setting is modeled with one F-bar hexahedral element in thickness direction and appropriate boundary conditions reducing the 3D problem to a 2D one. The following simulations are performed using a relatively coarse mesh consisting of 108 elements. Figure 3.2 shows the initial mesh and deformed configuration (with contour plots of the accumulated plastic strain α_{i}) at different time steps.

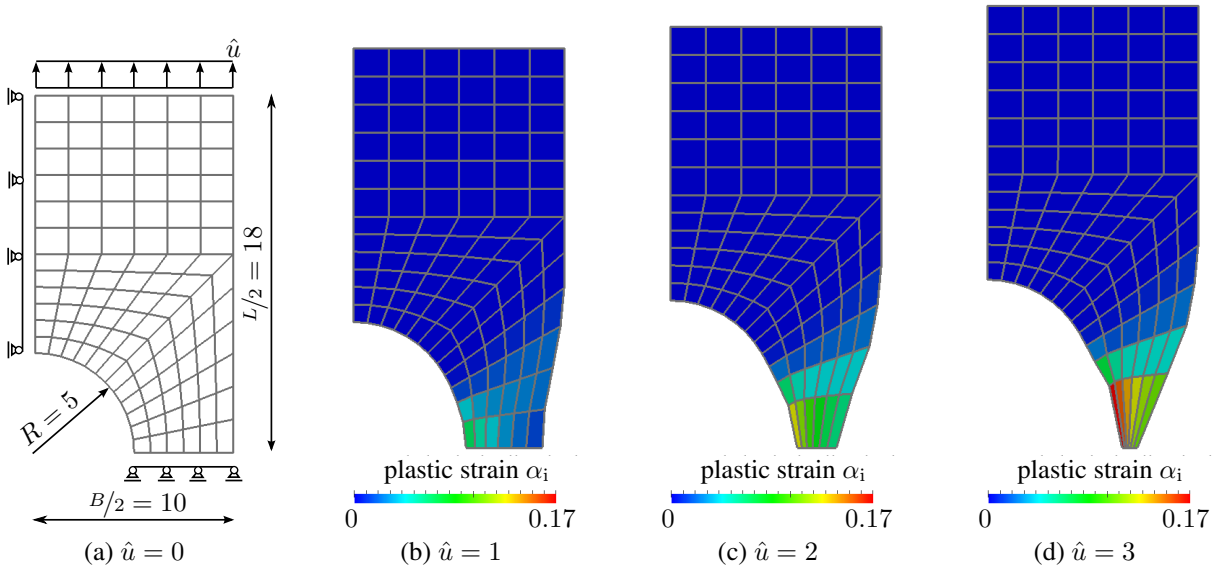

(a) $\hat{u} = 0$ (b) $\hat{u} = 1$ (c) $\hat{u} = 2$ (d) $\hat{u} = 3$

Figure 3.2: Perforated strip – Geometrical setting and deformed configuration at different displacement states with contour plots of the accumulated plastic strain α_{i}.

First, the influence of the shape parameter s_{p} defined in (3.23) on the convergence of the semi-smooth Newton method is investigated. Therefore, $c_{\mathrm{p}} = 2\mu$ is set and the damping factor a_{p} as defined in (3.31) is used. The total displacement is prescribed in 10, 20, 50 or 100 equal steps. Figure 3.3a displays the average number of nonlinear iterations per time step as a function of the shape parameter s_{p}. The lower and upper bounds of s_{p}, in between which convergence can be achieved, depend on the chosen step size. The fastest and most robust convergence behavior is obtained for $s_{\mathrm{p}} \approx 1$, whereas larger values of s_{p} result in a slight increase in the number of necessary iterations. These observations are in excellent agreement with the results in Hager and Wohlmuth [91]. A comparable simulation using the RMA, the same linear extrapolation predictor, and equidistant steps requires about 80 steps to achieve convergence of the nonlinear solver in every load step. For both methods the total number of necessary steps could, of course, be reduced if adaptive step size control was applied, since the first steps are the most critical with regard to convergence of the semi-smooth Newton scheme. Next, the step size is fixed at

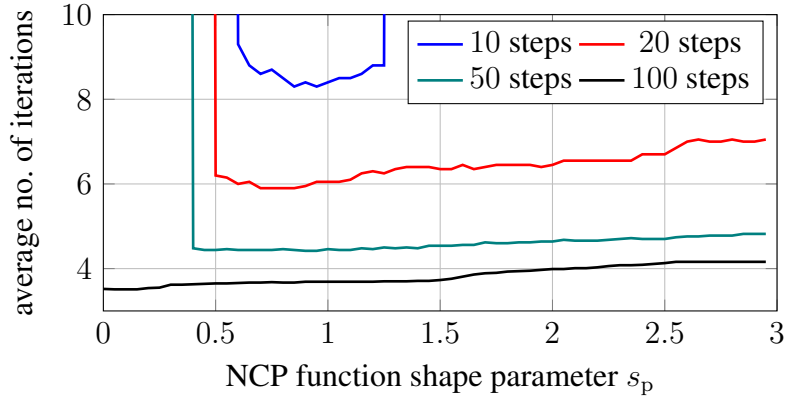

(a) Average no. of iterations for different step sizes over s_p.

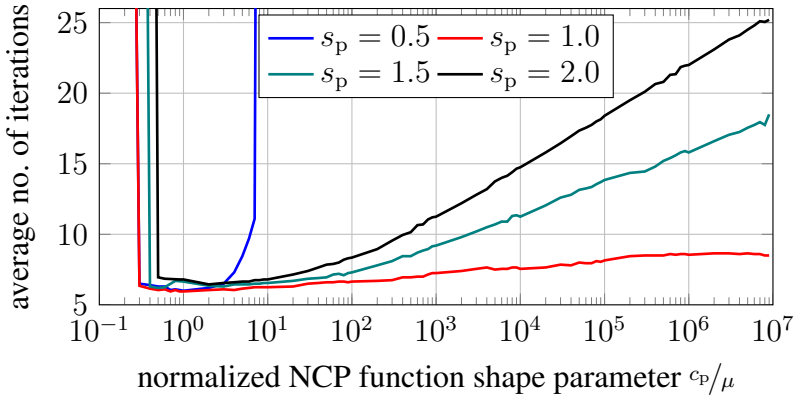

(b) Average no. of iterations for different values of s_p over c_p.

Figure 3.3: Perforated strip – Influence of the algorithmic parameters s_p and c_p for different time step sizes.

a total of 20 equal steps to analyze the influence of the plastic complementarity parameter c_p. Figure 3.3b shows the average number of iterations as a function of c_p normalized with the shear modulus μ for different values of s_p. In the present example, a lower bound emerges at about $c_\mathrm{p} \in [0.3\mu, 0.5\mu]$ depending on s_p. However, this bound is dependent on the step size and especially the hardening parameters of the material. In a similar example in Hager and Wohlmuth [91], the lower bound varied between 0.3 and 1.0 for different hardening parameters. A minimal number of iterations is achieved for $c_\mathrm{p} \in [2\mu, 4\mu]$, and the average number of required iterations increases at large values of c_p. But still, $s_\mathrm{p} > 0.5$ yields a robust scheme over a broad range of c_p. As one could expect from (3.23), the behavior of $s_\mathrm{p} = 1$ shows the least dependency on the complementarity parameter for large values of c_p.

In the previous results, the damping parameter a_p was set according to (3.31). This is crucial for the robustness of the overall system. A strict Newton method, i.e. setting $a_\mathrm{p} = 1$, instead of the quasi-Newton method using (3.31) would show similar robustness as setting $s_\mathrm{p} = 0$ in this example. The stabilizing effect of the parameter s_p can therefore only be exploited by an advantageous combination of the shape parameter s_p and the damping parameter a_p. Yet, this damping parameter tends to 1 quite quickly as is shown in Figure 3.4 for the minimal and mean values, so that a superlinear rate of convergence is always obtained asymptotically. Only for large

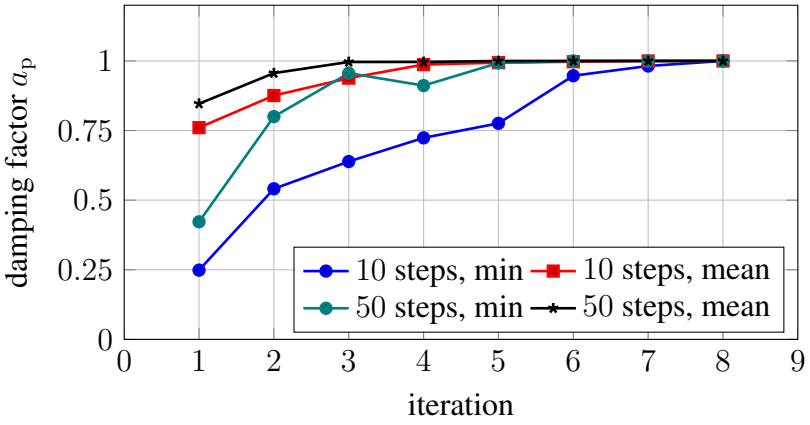

Figure 3.4: Perforated strip – Minimal and mean value of a_p over all quadrature points in the first of, respectively, 10 and 50 time steps.

step sizes locally smaller values of the damping parameter occur, thus resulting in the observed gain in robustness.

In conclusion, the choice of $s_\mathrm{p} = 1$, $c_\mathrm{p} = 2\mu$ and a_p as defined in (3.31) has proven to be the best choice in terms of robustness and efficiency. This observation not only holds for the illustrated academic example, but has also proven true in more complex examples, so that this set of algorithmic parameters will be used from now on.

3.3.3.2 Necking of a Circular Bar

The necking of a circular bar is by far the most common benchmark example for finite strain plasticity. It allows to assess the robustness and accuracy of plasticity formulations, nonlinear solution methods and finite element technology for nearly incompressible material [4, 26, 55–57, 64, 197–200]. Here, the necking of a tensile specimen with a radius of $6.413\,\mathrm{mm}$, a length of $53.334\,\mathrm{mm}$ and an elongation of $\hat{u}_\mathrm{max} = 7\,\mathrm{mm}$ is simulated. To trigger the necking phenomenon, a geometric imperfection of 1.8% is imposed in the mid-plane with a linear decrease of the radius. The elastic material behavior is described by a neo-Hookean hyperelastic material

$$\Psi_\mathrm{e} = \frac{c_1}{\beta}(I_3^{-\beta} - 1) + c_1(I_1 - 3) \quad , \quad c_1 = \frac{E}{4(1+\nu)} \quad , \quad \beta = \frac{\nu}{1-2\nu} \quad , \tag{3.38}$$

defined by the invariants (see (2.52)) of $\boldsymbol{C}_\mathrm{e}$ with the Young's modulus $E = 206.9\,\mathrm{GPa}$ and Poisson's ratio $\nu = 0.29$. Isotropic von Mises plasticity is assumed with $y_0 = 0.45$ and the nonlinear isotropic hardening potential

$$\Psi_\mathrm{p} = \frac{1}{2}H_\mathrm{i}\alpha_\mathrm{i}^2 + (y_\infty - y_0)\left(\alpha_\mathrm{i} + \frac{e^{-\delta\alpha_\mathrm{i}} - 1}{\delta}\right) \quad , \tag{3.39}$$

with the parameters $H_\mathrm{i} = 0.12924\,\mathrm{GPa}$, $y_\infty = 0.715\,\mathrm{GPa}$ and $\delta = 16.93$. The computational effort is reduced by exploiting the obvious symmetry, so that only one eighth of the bar is discretized with 960 first-order hexahedral F-bar finite elements and appropriate symmetry conditions (see Figure 3.5a). Figure 3.5b illustrates the von Mises equivalent stress distribution in the final deformation state. To quantitatively validate the results, load-displacement diagrams and

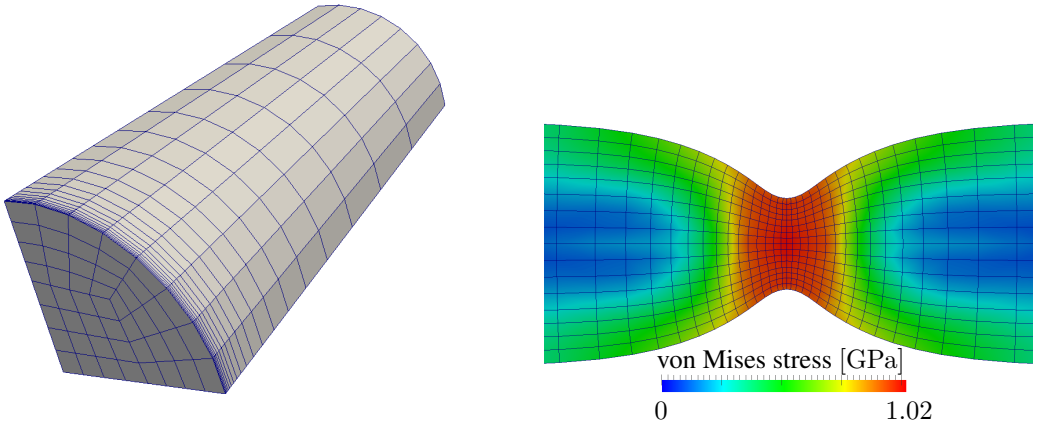

(a) initial mesh (b) deformed mesh

Figure 3.5: Necking of a circular bar – Initial mesh and final deformation state with a contour plot of the von Mises equivalent stress.

the evolution of the radius in the necking zone are commonly analyzed. Figure 3.6 compares these quantities for the RMA and the newly proposed algorithm based on NCP functions. For both characteristic measures, excellent agreement between the two methods is obtained,which is of course not surprising, since the same plastic constraints are enforced at each quadrature point. The essential difference of the proposed formulation rather lies in the nonlinear solution procedure than in the underlying physics to be solved.

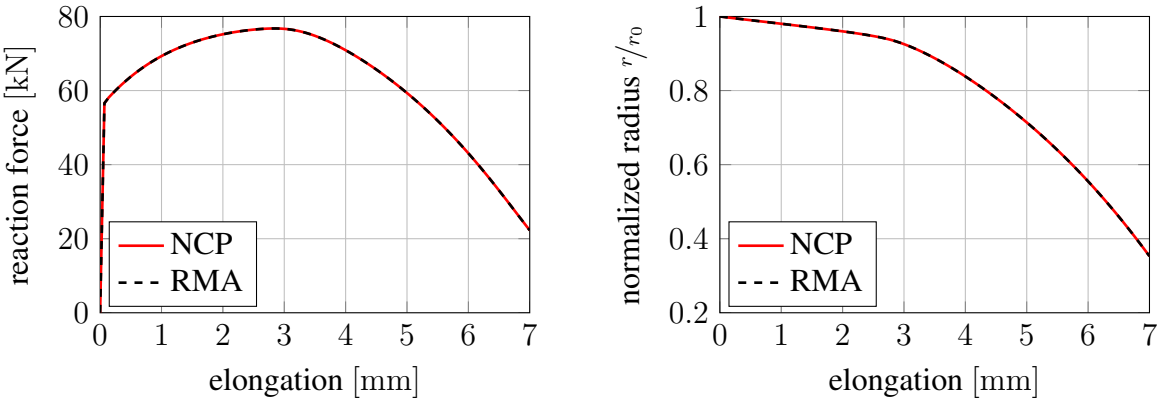

(a) Reaction force (b) Necking radius

Figure 3.6: Necking of a circular bar – Comparison of the evolution of the necking radius and force-displacement diagram between the plasticity algorithm presented in Section 3.3 and the classical RMA. The total displacement is applied in 100 equidistant steps.

As aforementioned, this example also serves as a benchmark for nonlinear solvers, since it poses severe difficulties to standard Newton methods. Different approaches to cope with these convergence problems are used in the literature, for instance line search [196, 198–200], increment cutting [57] or dynamic simulations with artificial viscosity [64]. However, the presented semi-smooth Newton approach allows for a computation in 42 equal load steps using the plain

(quasi-) Newton method without any measures for convergence acceleration. A comparable simulation using the same mesh and same predictor in combination with a classical RMA takes 62 equidistant steps to achieve convergence of the plain Newton scheme in every step. Figure 3.7 illustrates the decay in the L^2-norm of the reduced residual (3.37b) as well as different partial residuals in (3.25) at different stages: $u = 2.0$ corresponds to an almost uniform plastic deformation over the whole specimen, at $u = 3.5$ the localization of the plastic deformation begins (which is the most critical state), and at $u = 6.0$ plastic deformation is localized to the necking region. As expected, quadratic convergence is observed in the limit once the correct active set is found. Only at $u = 3.5$ the convergence of the norm of the structural residual stagnates at about 10^{-10} because some components are limited by numerical accuracy, so that no quadratic convergence can be observed.

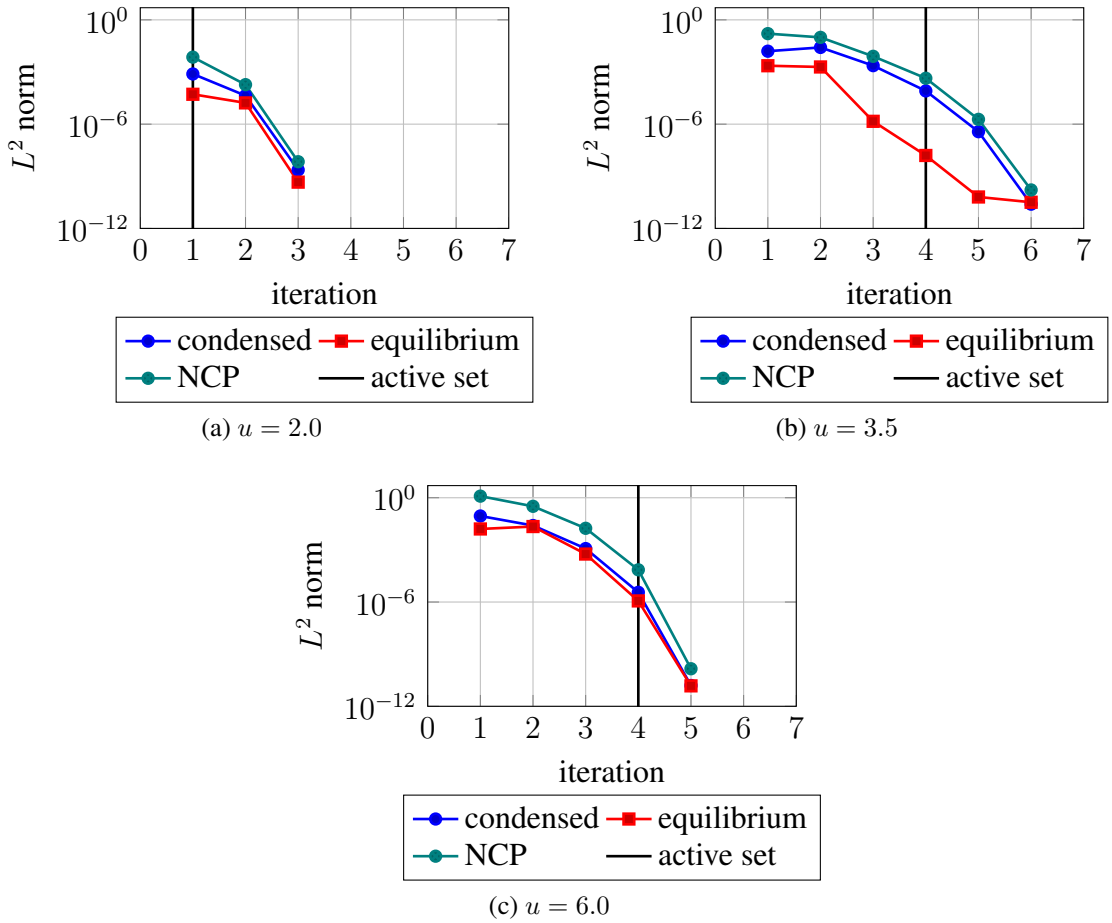

(a) $u = 2.0$

(b) $u = 3.5$

(c) $u = 6.0$

Figure 3.7: Necking of a circular bar – Exemplary convergence behavior of the semi-smooth Newton method in terms of the L^2-norm of the condensed residual (3.37b) ("condensed"), the balance of linear momentum (3.25a) ("equilibrium") and the NCP function (3.25b) ("NCP"). The vertical line "active set" indicates the iteration, in which the correct sets $\mathcal{G}_\mathrm{e}$ and $\mathcal{G}_\mathrm{p}$ are identified. The total displacement is applied in 42 equidistant steps.

3.3.3.3 Squeezed Elasto-Plastic Tube

This final example demonstrates the applicability not only to isotropic hardening (as used in all previous examples) but also includes kinematic hardening. Inspired by a similar example in [91], a cylindrical tube with an outer radius of 5, an inner radius of 4 and a length of 40 is squeezed in the middle by two rigid cylindrical tools of radius 5. Starting from an initially stress-free contact, the tools undergo a prescribed displacement of 3.0 in 40 equal steps. After that, the tools are removed within one step, the tube is rotated by 90 degrees about its axis and a second stroke is performed at the same speed. Again a neo-Hookean hyperelastic potential

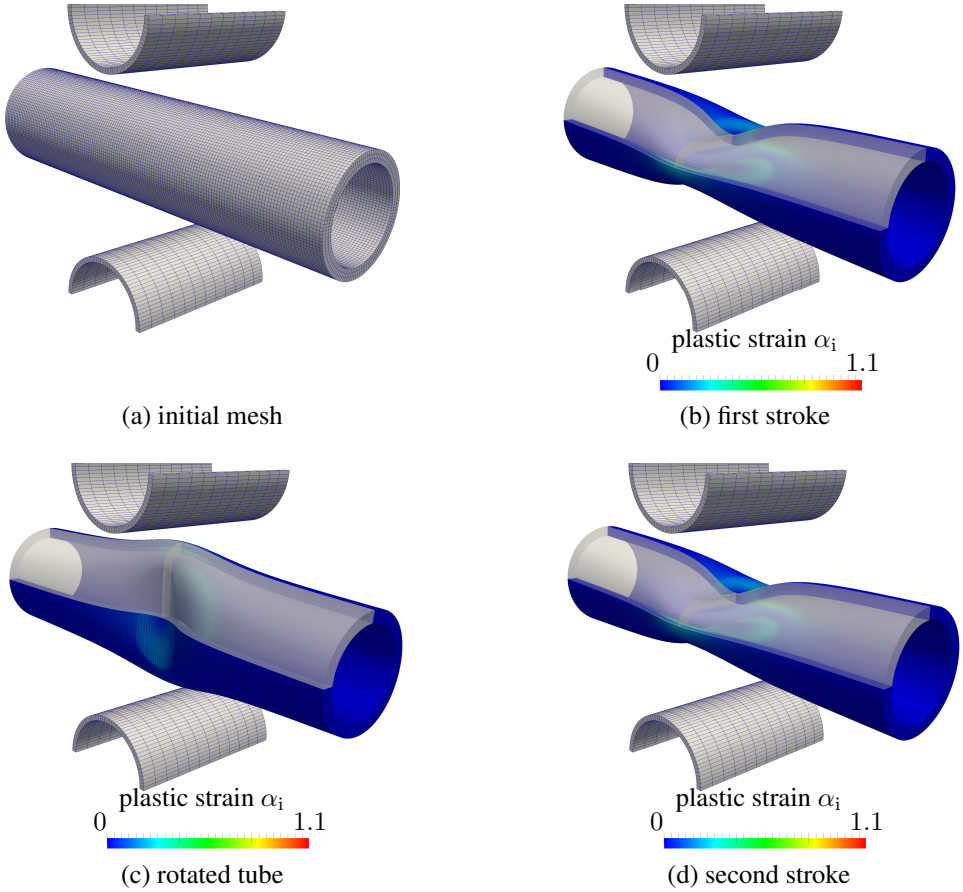

(a) initial mesh (b) first stroke (c) rotated tube (d) second stroke

Figure 3.8: Squeezed plastic tube – Initial mesh and deformed configurations at different stages with a contour plot of the accumulated plastic strain α_i in case of linear kinematic hardening.

(3.38) is used with $E = 206.9$ and $\nu = 0.29$. Moreover, von Mises plasticity is assumed with an initial yield stress $y_0 = 0.45$ in combination with either linear isotropic hardening $H_i = 0.1$ or linear kinematic hardening $H_k = 0.1$. At the contact interface, the tube surface is chosen as slave side and frictional contact according to Coulomb's law with a friction coefficient $\mu = 0.3$ is assumed.[1] To reduce the computational effort, only one eighth of the problem is discretized

[1]The exact numerical method to enforce the contact conditions is of no particular importance for the observations made in this example. For the results shown, a dual mortar method has been applied as derived in Chapter 4.

and appropriate symmetry conditions are applied. One eighth of the tube is meshed with approximately 6500 8-node hexahedral F-bar elements as shown in Figure 3.8a. Figures 3.8b–3.8d illustrate the deformation process in the case of kinematic hardening; the results for isotropic hardening are omitted here, since they look almost the same. A comparison of the total contact

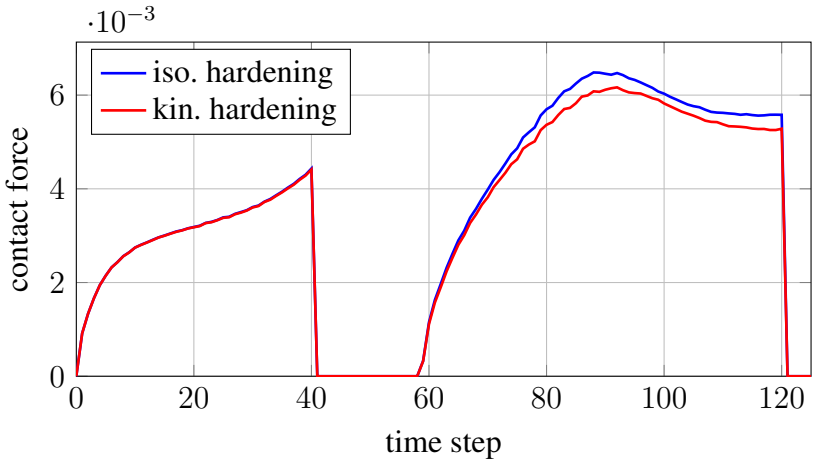

Figure 3.9: Squeezed plastic tube – Evolution of the total contact forces comparing linear isotropic and kinematic hardening material behavior.

force between the two settings using isotropic and kinematic hardening, respectively, is shown in Figure 3.9. While the first stroke yields very similar results in both cases due to the monotonic loading, the contact states differ significantly in the second stroke. As expected, the change in the direction of plastic deformation results in the material with kinematic hardening to behave softer during the second stroke.

3.4 Extensions to the Algorithm

In this section, several extensions to the basic methodology for the computational treatment of large deformation plasticity are presented. While the focus is set on numerical and algorithmic implications, inspiration for the extensions is taken from metal forming processes, especially sheet metal forming. One ingredient to sheet metal forming simulation has already been introduced by the use of an anisotropic yield function as sheet metal exhibits orthotropic behavior due to milling of sheets in production. The modeling of this anisotropic plastic material behavior will be further elaborated on in Section 3.4.1 by the introduction of plastic spin to the model. Next, high strain rates during metal forming may preclude the use of rate-insensitive yield functions considered so far. Instead, effects of visco-plasticity, coupling the apparent yield strength with the deformation rate, may be necessary and will be incorporated in Section 3.4.2. Finally, thermal effects are of interest in many forming applications, either by the heat produced by the plastic deformation, or by forming pre-heated parts to make use of temperature dependent plastic material behavior. Therefore, effects of thermo-elasto-plasticity will be considered in Section 3.4.3 within the computational framework developed above. Numerical examples accompany each of the developments to demonstrate their respective effects.

3.4.1 Anisotropic Plasticity with Plastic Spin

The plastic spin as introduced in Section 2.3.4.5 (see also Dafalias [47]) for Hill's yield criterion models the rotation of the axes of material orthotropy with respect to the macroscopic continuum. This rotation is determined by a constitutive equation on the skew-symmetric part $\boldsymbol{W}_\mathrm{p}$ of the plastic velocity gradient $\boldsymbol{L}_\mathrm{p}$, for instance (2.81). For plastic internal variables discretized in space and time as presented in Section 3.1 this yields the discrete evolution of the plastic spin (3.7). As published in Seitz *et al.* [192], this evolution equation can be encorporated in the system of nonlinear equations (3.24) by replacing (3.24d) with (3.7). As the NCP function (3.23) and (3.7) are, respectively, symmetric and skew-symmetric by construction and therefore orthogonal, conditions (3.24b) (i.e. solving for the root of the NCP function) and (3.7) (i.e. evolution of the plastic spin) may be combined as

$$\boldsymbol{H}_{\mathrm{p},s_\mathrm{p}} = \boldsymbol{G}_{\mathrm{p},s_\mathrm{p}} + \Delta\mathbf{W}_\mathrm{p} - \frac{\eta}{y_0}\left(\boldsymbol{\Sigma}\Delta\mathbf{D}_\mathrm{p} - \Delta\mathbf{D}_\mathrm{p}\boldsymbol{\Sigma}\right) = \mathbf{0} \quad . \tag{3.40}$$

The solution procedure by the semi-smooth Newton method presented in 3.3.2 can again be applied by simply replacing $\boldsymbol{G}_{\mathrm{p},s_\mathrm{p}}$ with $\boldsymbol{H}_{\mathrm{p},s_\mathrm{p}}$. Its derivatives with respect to the nodal displacements and plastic flow increment $\Delta\mathbf{L}_\mathrm{p}$ follow straightforwardly from (3.40) as

$$\frac{\partial \boldsymbol{H}_{\mathrm{p},s_\mathrm{p}}}{\partial \mathbf{d}} = \frac{\partial \boldsymbol{G}_{\mathrm{p},s_\mathrm{p}}}{\partial \mathbf{d}} - \frac{\eta}{y_0}\left(\left(\frac{2\partial\boldsymbol{\Sigma}}{\partial \boldsymbol{C}} : (\boldsymbol{F}\nabla_{\boldsymbol{X}}\boldsymbol{N})\right)^{\mathsf{T}}\Delta\mathbf{D}_\mathrm{p} - \Delta\mathbf{D}_\mathrm{p}\left(\frac{2\partial\boldsymbol{\Sigma}}{\partial \boldsymbol{C}} : (\boldsymbol{F}\nabla_{\boldsymbol{X}}\boldsymbol{N})\right)\right) \quad , \tag{3.41}$$

$$\frac{\partial \boldsymbol{H}_{\mathrm{p},s_\mathrm{p}}}{\partial \Delta\mathbf{L}_\mathrm{p}} = \frac{\partial \boldsymbol{G}_{\mathrm{p},s_\mathrm{p}}}{\partial \Delta\mathbf{L}_\mathrm{p}} + \mathbb{I}_\mathrm{sk} - \frac{\eta}{y_0}\left(\boldsymbol{\Sigma}\mathbb{I}_\mathrm{s} - \mathbb{I}_\mathrm{s}\boldsymbol{\Sigma} + \left(\frac{\partial\boldsymbol{\Sigma}}{\partial\Delta\mathbf{L}_\mathrm{p}}\right)^{\mathsf{T}}\Delta\mathbf{D}_\mathrm{p} - \Delta\mathbf{D}_\mathrm{p}\left(\frac{\partial\boldsymbol{\Sigma}}{\partial\Delta\mathbf{L}_\mathrm{p}}\right)\right) \quad . \tag{3.42}$$

When performing the condensation of the plastic flow increment $\Delta\mathbf{L}_\mathrm{p}$ by (3.36), now a system of eight unknowns for a non-symmetric, traceless second order tensor needs to be solved in comparison the the five unknowns in the absence of plastic spin. The condition of a traceless plastic flow (3.25c) is again satisfied automatically by the use of the pseudo-inverse in (3.36).

Numerical Example[1] A simple validation example is adopted from Ulz [222], where the same problem has been solved using the RMA, see also Miehe *et al.* [148], Papadopoulos and Lu [164] for a similar problem without plastic spin. The well-known benchmark example consists of a circular flange (oriented along the x_3-axis) with an inner radius of 200, an outer radius of 300 and a thickness of 10 which is supported on the lower surface. The inner surface is subjected to a displacement driven contraction of $\hat{u} = 50$. This setting can be interpreted as the loading condition of an outer ring in a deep-drawing process. Due to the plastic anisotropy, a so-called earing effect can be observed, i.e. the initially circular shape loses its rotational symmetry and a periodic shape evolves. The same orthotropic yield function as in [222] is used and the plastic spin parameter η controlling the evolution of the plastic spin is varied. The elastic response is governed by the neo-Hookean material (3.38) and a linear isotropic hardening law $\Psi_\mathrm{p} = {}^1\!/_2 H_\mathrm{i}\alpha_\mathrm{i}^2$ is employed, see Table 3.1 for the elastic and plastic material properties. Using the obvious symmetry, only one quarter of the flange is discretized with 10×20 eight-node hexahedral F-bar

[1] This example is taken from the author's publication Seitz *et al.* [192].

Table 3.1: Drawing of a circular flange – Material properties.

Young's modulus	E	210.0
Poisson's ratio	ν	0.3
Initial yield stress	y_0	0.275
Isotropic hardening modulus	H_i	0.1
Orthotropy factors	α_1	0.666666667
	$\alpha_2 = \alpha_3$	0.672790077
	$\alpha_7 = \alpha_9$	0.785052599
	α_8	1.012246821
Plastic spin parameter	η	$\{-500, -250, -100, 0\}$

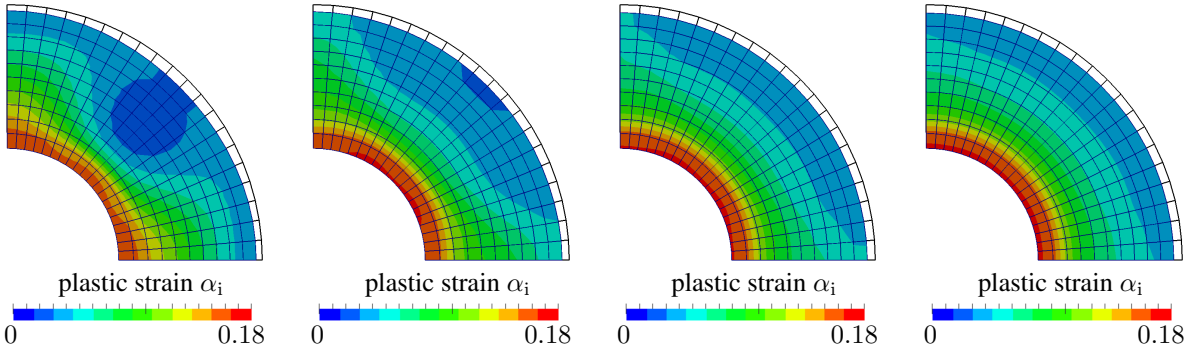

(a) $\eta = 0$ (b) $\eta = -100$ (c) $\eta = -250$ (d) $\eta = -500$

Figure 3.10: Drawing of a circular flange – Distribution of accumulated plastic strain for different values of the plastic spin parameter η at $u = 25$mm. The initial mesh is outlined by black lines in the background.

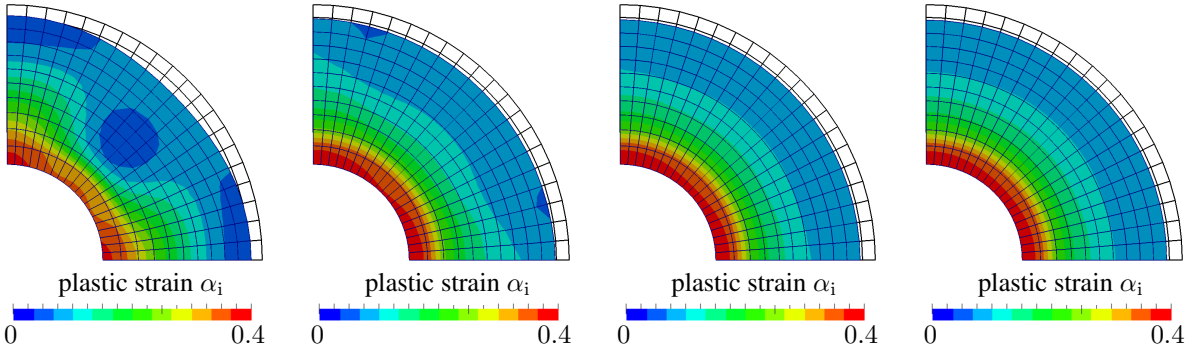

(a) $\eta = 0$ (b) $\eta = -100$ (c) $\eta = -250$ (d) $\eta = -500$

Figure 3.11: Drawing of a circular flange – Distribution of accumulated plastic strain for different values of the plastic spin parameter η at $u = 50$mm. The initial mesh is outlined by black lines in the background.

elements. Figures 3.10 and 3.11 depict the deformed configuration at different load stages for different values of η with the initial mesh being outlined in the background. In good agreement with the results of Ulz [222], the presence of plastic spin results in a more and more isotropic distribution of the accumulated plastic strain, the higher the absolute value of η becomes. At different polar positions the plastic triad rotates differently around the x_3-axis such that the plastic response to the radial stress assimilates. The rate at which this rotation takes place is controlled by the value of η. For $\eta = -500$, which is preferred in [222] with comparison to experimental data, hardly any earing can be observed at the final state $u = 50\text{mm}$. These results demonstrate, that the NCP function based approach to plasticity not only captures von Mises plasticity as in the previous examples, but also allows for an efficient computation of anisotropic Hill-type plasticity including plastic spin, which is especially important in the application to sheet metal forming.

3.4.2 Visco-Plasticity

Effects of visco-plasticity become increasingly important with higher strain rates. The presented algorithm for finite strain plasticity based on NCP functions can easily be extended to visco-plastic models based on dynamic yield surfaces as, for example, the model of Perić [166] introduced in Section 2.3.4.6. When approximating the plastic multiplier $\dot{\gamma}$ in (2.84) within the time interval $[t_n, t_{n+1}]$ by a finite difference of the isotropic hardening variable, i.e. $\dot{\gamma} \approx \frac{\alpha_{\mathrm{i},n+1} - \alpha_{\mathrm{i},n}}{\Delta t}$ the effective dynamic yield stress is obtained as

$$Y^{\mathrm{dyn}} = \left(1 + \mu \frac{\alpha_{\mathrm{i},n+1} - \alpha_{\mathrm{i},n}}{\Delta t}\right)^{\epsilon} \left(y_0 + \frac{\partial \Psi_{\mathrm{p}}}{\partial \alpha_{\mathrm{i}}}\right) \quad , \tag{3.43}$$

with the viscosity μ and the rate sensitivity ϵ. The only changes to be made to the method of Section 3.3 is to replace the effective yield stress Y by Y^{dyn} in (3.23) and consequently in all derived linearizations, particularly in (3.32) and (3.35).

Numerical Example To exemplify the effect of visco-plasticity, the necking of a circular bar introduced in Section 3.3.3.2 is revisited using the same discretization and material parameters. Figure 3.12 depicts the resulting force-displacement diagrams for different sets of visco-plastic material parameters (viscosity μ and rate sensitivity ϵ) each at varying loading rates $\dot{\hat{\boldsymbol{u}}}$. In the case of either $\mu \to 0$ or $\epsilon \to 0$ or $\dot{\hat{\boldsymbol{u}}} \to 0$, the rate-insensitive results of Figure 3.6a (black dashed line in Figure 3.12) are recovered. For high viscosities and especially rate sensitivities, the onset of necking, indicated by a decrease in force, is shifted towards larger elongations or precluded entirely. This behavior is in good agreement with results of a similar setup reported in de Souza Neto *et al.* [57].

3.4.3 Thermo-Plasticity[1]

Finally, the proposed plasticity algorithm based on NCP functions is extended to thermo-elasto-plasticity. The general concept of solving plasticity using NCP functions is now extended to a

[1] This example is taken from the author's publication Seitz *et al.* [194].

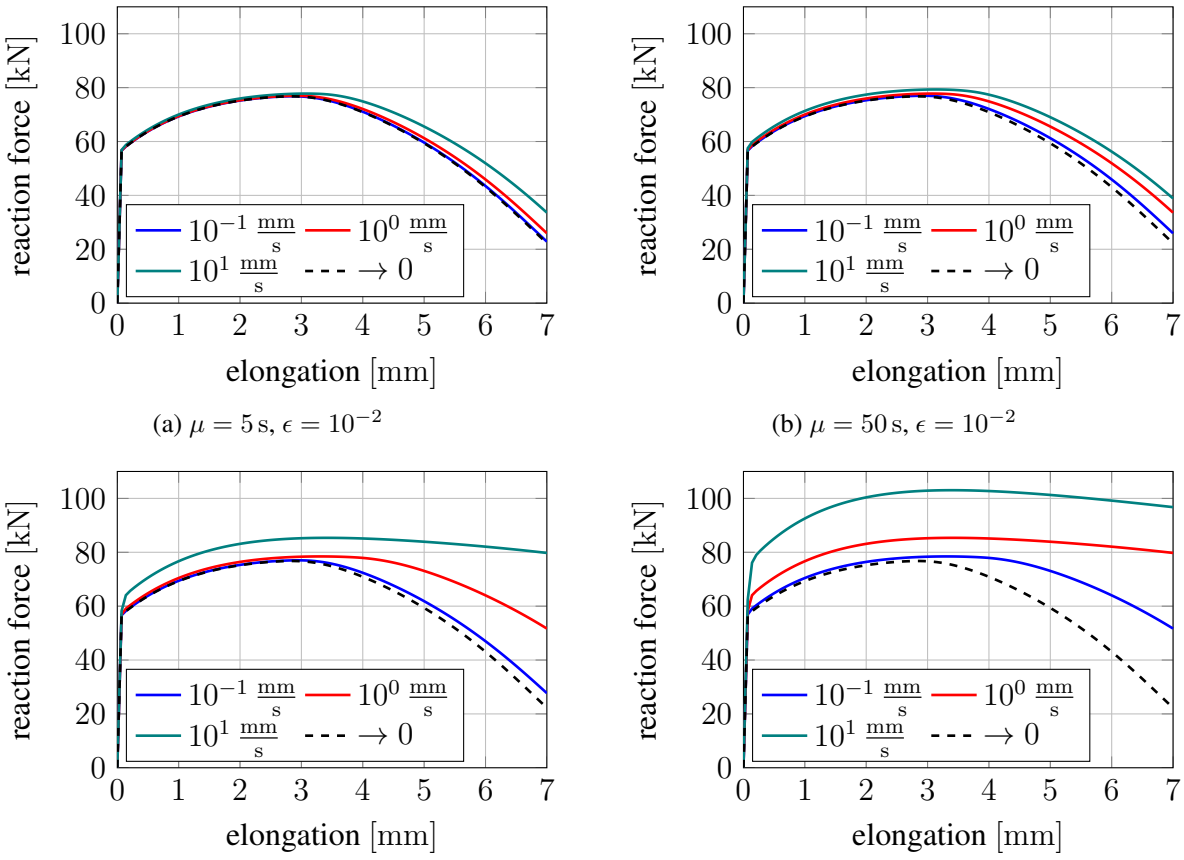

(a) $\mu = 5\,\text{s}$, $\epsilon = 10^{-2}$ (b) $\mu = 50\,\text{s}$, $\epsilon = 10^{-2}$

(c) $\mu = 5\,\text{s}$, $\epsilon = 10^{-1}$ (d) $\mu = 50\,\text{s}$, $\epsilon = 10^{-1}$

Figure 3.12: Elasto-visco-plastic necking of a circular bar – Force-displacement diagrams for different visco-plastic material parameters at prescribed loading velocities $\dot{\hat{\boldsymbol{u}}} = \{10^{-1}\ \frac{\text{mm}}{\text{s}}, 10^{0}\ \frac{\text{mm}}{\text{s}}, 10^{1}\ \frac{\text{mm}}{\text{s}}\}$ and the rate insensitive case of $\dot{\hat{\boldsymbol{u}}} \to 0$.

coupled thermomechanical system, which, in its discrete setting, is governed by the discrete balance of linear momentum (2.159) and heat conduction equation (2.163). Again, the discrete plastic flow increment $\Delta\mathbf{L}_\text{p}$ at each quadrature point is introduced as additional primary unknowns and the set of nonlinear equations is extended by (3.24b) - (3.24d). Applying a semi-smooth Newton method analogously to (3.25) yields the linearized system

$$\frac{\partial \boldsymbol{r}_\text{u}}{\partial \mathbf{d}}\Delta\mathbf{d} + \frac{\partial \boldsymbol{r}_\text{u}}{\partial \mathbf{T}}\Delta\mathbf{T} + \frac{\partial \boldsymbol{r}_\text{u}}{\partial \Delta\mathbf{L}_\text{p}}\Delta\Delta\mathbf{L}_\text{p} = -\boldsymbol{r}_\text{u} \ , \tag{3.44a}$$

$$\frac{\partial \boldsymbol{r}_T}{\partial \mathbf{d}}\Delta\mathbf{d} + \frac{\partial \boldsymbol{r}_T}{\partial \mathbf{T}}\Delta\mathbf{T} + \frac{\partial \boldsymbol{r}_T}{\partial \Delta\mathbf{L}_\text{p}}\Delta\Delta\mathbf{L}_\text{p} = -\boldsymbol{r}_T \ , \tag{3.44b}$$

$$\frac{\partial \boldsymbol{G}_{\text{p},s_\text{p},q}}{\partial \mathbf{d}}\Delta\mathbf{d} + \frac{\partial \boldsymbol{G}_{\text{p},s_\text{p},q}}{\partial \mathbf{T}}\Delta\mathbf{T} + \frac{\partial \boldsymbol{G}_{\text{p},s_\text{p},q}}{\partial \Delta\mathbf{L}_{\text{p},q}}\Delta\Delta\mathbf{L}_{\text{p},q} = -\boldsymbol{G}_{\text{p},s_\text{p},q}, \quad \forall q \in \mathcal{G} \ , \tag{3.44c}$$

$$\operatorname{tr}\Delta\mathbf{L}_{\text{p},q} = 0 \ , \qquad \forall q \in \mathcal{G} \ , \tag{3.44d}$$

$$\operatorname{skew}\Delta\mathbf{L}_{\text{p},q} = \mathbf{0} \ , \qquad \forall q \in \mathcal{G} \ , \tag{3.44e}$$

that has to be solved in each iteration step. Compared to the isothermal case, a temperature dependency of the stuctural residual $\boldsymbol{r}_{\mathrm{u}}$ is introduced by a temperature dependent stress derived from a temperature dependent elastic free energy $\Psi_{\mathrm{e}} = \Psi_{\mathrm{e}}(\boldsymbol{C}_{\mathrm{e}}, T)$. Conversely, the displacements enter the thermal residual via Fourier's law on finitely deforming bodies (see (2.48b)), thermo-elastic coupling and plastic work converted to heat (see third integral in (2.99)). Moreover, all involved stress measures may depend on the discrete displacements, temperatures, the plastic deformation history and the current plastic flow. In the NCP function, the additional temperature dependency may enter both in the stress $\boldsymbol{\eta}$ as well as the effective yield stress Y. The key arguments leading to the condensation of the plastic flow increments $\Delta\Delta\mathbf{L}_{\mathrm{p}}$ from the system (3.44) are the same as for the isothermal case in Section 3.3.2, namely the fact that (3.44c) only contains the discrete plastic increment $\Delta\mathbf{L}_{\mathrm{p},q}$ of one quadrature point q as well as the displacement and temperature degrees of freedom belonging to the element containing this quadrature point. Hence, (3.44c) can be solved for $\Delta\Delta\mathbf{L}_{\mathrm{p},q}$ at each quadrature point directly to obtain

$$\Delta\Delta\mathbf{L}_{\mathrm{p},q} = -\left(\frac{\partial \boldsymbol{G}_{\mathrm{p},s_{\mathrm{p}},q}}{\partial \Delta\mathbf{L}_{\mathrm{p},q}}\right)^{+} : \left(\boldsymbol{G}_{\mathrm{p},s_{\mathrm{p}},q} + \frac{\partial \boldsymbol{G}_{\mathrm{p},s_{\mathrm{p}},q}}{\partial \mathbf{d}}\Delta\mathbf{d} + \frac{\partial \boldsymbol{G}_{\mathrm{p},s_{\mathrm{p}},q}}{\partial \mathbf{T}}\Delta\mathbf{T}\right) \quad . \tag{3.45}$$

This condensation can in turn be inserted into (3.44a) and (3.44b) and results, analogously to (3.37), in condensed residuals and tangent matrices

$$\widetilde{\mathbf{K}}_{\{\mathrm{u,T}\}\mathrm{u}} = \mathbf{K}_{\{\mathrm{u,T}\}\mathrm{u}} - \sum_{q\in\mathcal{G}}\left[\left(\frac{\partial \boldsymbol{r}_{\{\mathrm{u,T}\}}}{\partial \Delta\mathbf{L}_{\mathrm{p}}}\right) : \left(\frac{\partial \boldsymbol{G}_{\mathrm{p},s_{\mathrm{p}},q}}{\partial \Delta\mathbf{L}_{\mathrm{p},q}}\right)^{+} : \left(\frac{\partial \boldsymbol{G}_{\mathrm{p},s_{\mathrm{p}},q}}{\partial \mathbf{d}}\Delta\mathbf{d}\right)\right] \quad , \tag{3.46a}$$

$$\widetilde{\mathbf{K}}_{\{\mathrm{u,T}\}\mathrm{T}} = \mathbf{K}_{\{\mathrm{u,T}\}\mathrm{T}} - \sum_{q\in\mathcal{G}}\left[\left(\frac{\partial \boldsymbol{r}_{\{\mathrm{u,T}\}}}{\partial \Delta\mathbf{L}_{\mathrm{p}}}\right) : \left(\frac{\partial \boldsymbol{G}_{\mathrm{p},s_{\mathrm{p}},q}}{\partial \Delta\mathbf{L}_{\mathrm{p},q}}\right)^{+} : \left(\frac{\partial \boldsymbol{G}_{\mathrm{p},s_{\mathrm{p}},q}}{\partial \mathbf{T}}\Delta\mathbf{T}\right)\right] \quad , \tag{3.46b}$$

$$\widetilde{\boldsymbol{r}}_{\{\mathrm{u,T}\}} = \boldsymbol{r}_{\{\mathrm{u,T}\}} - \sum_{q\in\mathcal{G}}\left[\left(\frac{\partial \boldsymbol{r}_{\{\mathrm{u,T}\}}}{\partial \Delta\mathbf{L}_{\mathrm{p}}}\right) : \left(\frac{\partial \boldsymbol{G}_{\mathrm{p},s_{\mathrm{p}},q}}{\partial \Delta\mathbf{L}_{\mathrm{p},q}}\right)^{+} : \boldsymbol{G}_{\mathrm{p},s_{\mathrm{p}},q}\right] \quad . \tag{3.46c}$$

The reduced linear system to be solved therefore consists of discrete displacement and temperature degrees of freedom only, such that it is of the same size as any monolithic thermo-structure-interaction problem (2.167).

Numerical Example The necking problem as introduced for isothermal finite deformation plasticity in Section 3.3.3.2 serves as a classical benchmark for thermo-plasticity as well, e.g. in Canajija and Brnić [27], Ibrahimbegovic and Chorfi [114], Simo and Miehe [201], Wriggers *et al.* [238]. In this thesis, further extension of the problem commonly analyzed using isotropic von Mises plasticity to anisotropic thermo-plasticity is presented. The geometrical setting is largely equivalent to the one described in Section 3.3.3.2 with the only difference being, that, in the isothermal case, a geometric imperfection is introduced to trigger the necking of the specimen. In the fully coupled thermomechanical setting, necking can be triggered without any geometrical imperfection merely by an inhomogeneous temperature distribution caused by convective heat transfer on the entire boundary of the specimen. The normal spatial heat flux is thereby defined as $q_{\mathrm{n}} = -h_{\mathrm{c}}(T - T_{\infty})$, where h_{c} denotes the coefficient of convection, T the temperature at the surface, and T_{∞} the temperature of the surrounding medium. Plastic anisotropy is

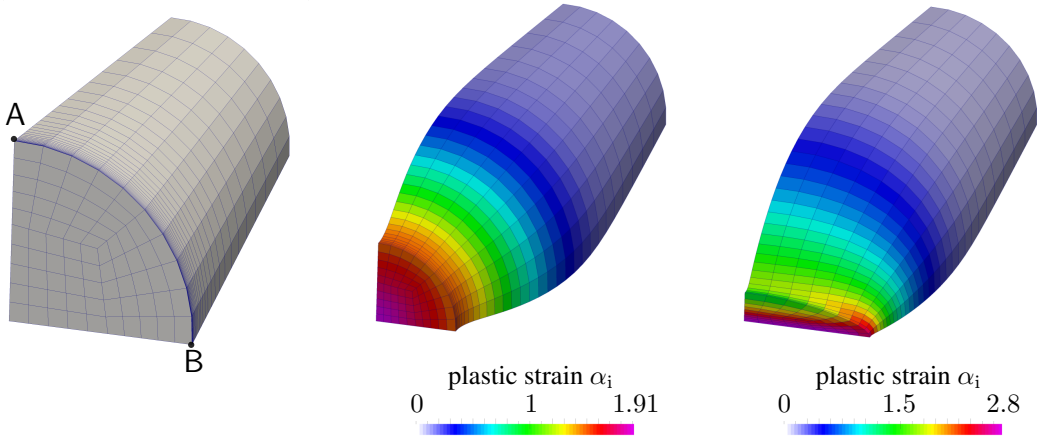

(a) initial mesh (b) final configuration, isotropic plasticity (c) final configuration, anisotropic plasticity

Figure 3.13: Thermally triggered necking of an anisotropic circular bar – Initial mesh and final deformed configuration colored by the accumulated plastic strain α_i.

introduced by reducing the normal yield stress in one transversal direction (direction from the central axis to point A in Figure 3.13a) by 17.5% (see y_{11} in Table 3.2). The isothermal elastic free energy (3.38) (denoted as $\Psi_{e,0}(I_1, I_2, I_3)$ in the following) is complemented by an additional term to account for thermal expansion

$$\Psi_e(I_1, I_2, I_3, T) = \Psi_{e,0}(I_1, I_2, I_3) - 6\alpha_T(T - T_0)\sqrt{I_3}\frac{\partial \Psi_{e,0}(3I_3^{1/3}, 3I_3^{2/3}, I_3)}{\partial I_3} \quad , \tag{3.47}$$

with the coefficient of thermal expansion α_T and a reference temperature T_0. The function $\Psi_{e,0}(3I_3^{1/3}, 3I_3^{2/3}, I_3)$ therein accounts for elastic stored energy associated to a purely volumetric deformation. This simple extension of linear thermal expansion to nonlinear hyperelasticity was proposed by Simo and Miehe [201] and is slightly generalized here to also accommodate for isothermal elastic free energies $\Psi_{e,0}$ in which the volumetric and deviatoric response do not decouple. The same nonlinear isotropic hardening potential (3.39) as in the isothermal case is used, however, the parameters in (3.39) are temperature dependent. This temperature dependency and all other material parameters are summarized in Table 3.2. To be able to accurately capture the effects of anisotropy, a slightly finer mesh (see Figure 3.13a) as compared to the isothermal case (see Figure 3.5a) is employed consisting of 2250 first-order hexahedral finite elements. Further, the anisotropic deformation involves a significant amount of shear (cf. Figure 3.13c), such that enhanced assumed strain (EAS) elements with nine additional strain modes, see e.g. Klinkel and Wagner [122], are employed. When the monolithic solution algorithm presented above is combined with enhanced strain elements, coupling effects of the additional strain modes with all other fields have to be considered carefully. The modes appear as additional (element-wise discontinuous) unknowns in the system (3.44), having common coupling terms with the discrete displacements $\mathbf{d}$, temperatures $\mathbf{T}$ and plastic deformation increments $\Delta\mathbf{L}_p$. The local condensation procedure in (3.46) then becomes a two-stage process: first, at Gauss-point level, the plastic deformation increment is eliminated, and secondly, the additional strain modes are condensed at element level. Figures 3.13b and 3.13c illustrate the final deformed stage and Figure 3.14a

Table 3.2: Thermally triggered necking of an anisotropic circular bar – Material parameters.

Young's modulus	E	$206.9\,\mathrm{GPa}$
Poisson's ratio	ν	0.29
Initial yield stress	$y_0(T)$	$(1-\omega_0(T-T_0))\cdot 0.45\,\mathrm{GPa}$
Anisotropy parameters	y_{11}	$y_{11}=\{0.825y_0, y_0\}$
	$y_{22}, y_{33}, y_{12}, y_{13}, y_{23}$	$y_{22}=y_{33}=y_{12}=y_{13}=y_{23}=y_0$
Linear hardening modulus	$H_\mathrm{i}(T)$	$(1-\omega_\mathrm{h}(T-T_0))\cdot 0.12924\,\mathrm{GPa}$
Saturation yield stress	$y_\infty(T)$	$(1-\omega_\mathrm{h}(T-T_0))\cdot 0.715\,\mathrm{GPa}$
Hardening exponent	δ	16.93
Density	ρ_0	$7.8\cdot 10^{-9}\,\frac{\mathrm{N\,s^2}}{\mathrm{mm^4}}$
Heat capacity	c_v	$3.588\,\frac{\mathrm{N}}{\mathrm{mm^2\,s^2\,K}}$
Heat conductivity	k_0	$45\,\frac{\mathrm{N}}{\mathrm{s\,K}}$
Expansion coefficient	α_T	$10^{-5}\,\frac{1}{\mathrm{K}}$
Yield stress softening	ω_0	$0.002\,\frac{1}{\mathrm{K}}$
Hardening softening	ω_h	$0.002\,\frac{1}{\mathrm{K}}$
Dissipation factor	χ	0.9
Initial temperature	T_0	$293\,\mathrm{K}$
Surrounding temperature	T_∞	$293\,\mathrm{K}$
Convection coefficient	h_c	$17.5\,\frac{\mathrm{N}}{\mathrm{mm\,s\,K}}$

the force-elongation curve for the isotropic and anisotropic thermomechanical necking problem. The isotropic case therein reproduces the results reported by Canajija and Brnić [27] accurately. In the first phase up to an elongation of approximately $3.5\,\mathrm{mm}$ the deformation is dominated by homogeneous plastic deformation in longitudinal direction, such that the reaction force is dominated by plastic hardening, and the influence of anisotropy is very low. Once the necking is initiated, the plastic deformation is anisotropic in the transversal plane of the specimen, thus resulting in an anisotropic deformation pattern, see Fig. 3.13c and 3.14b. The anisotropy in the temperature distribution in Figure 3.14c is less pronounced and the temperatures in points A and B follow the temperature evolution in the isotropic case.

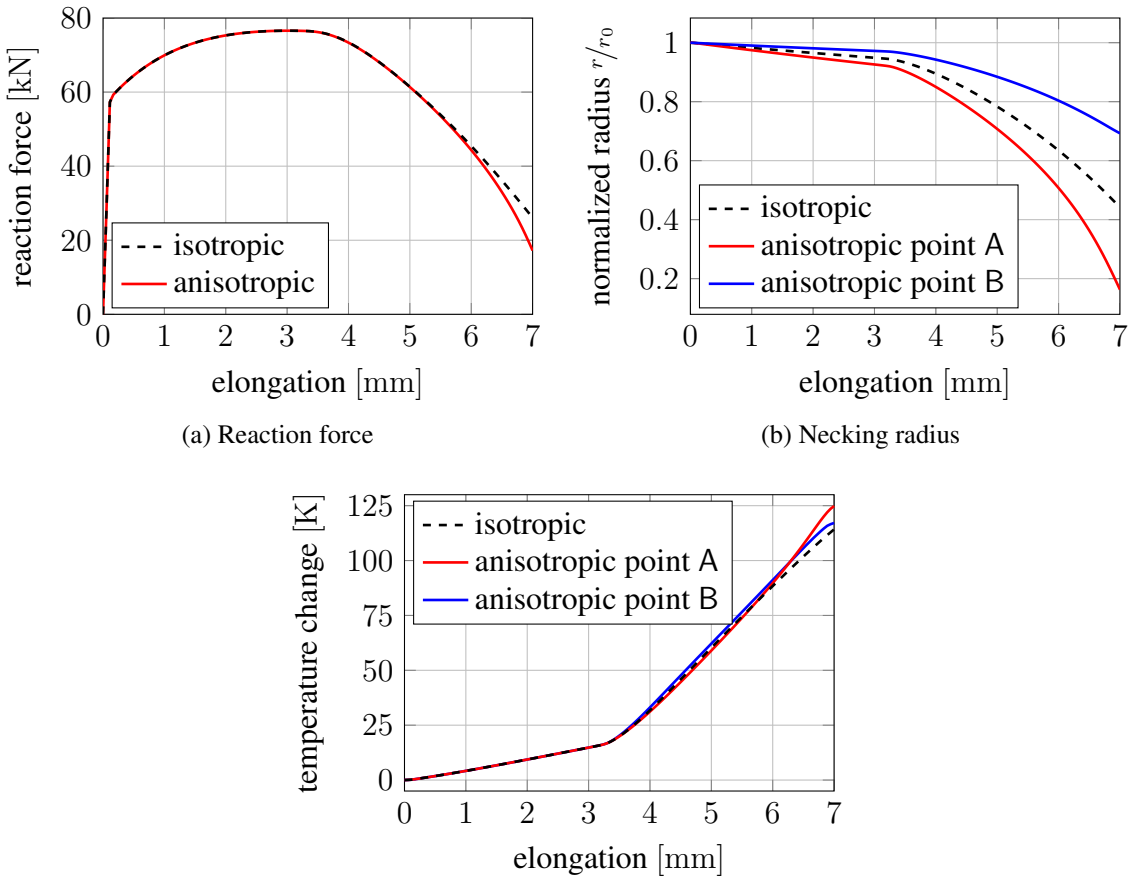

(a) Reaction force

(b) Necking radius

(c) Temperature

Figure 3.14: Thermally triggered necking of an anisotropic circular bar – Evolution of reaction force, necking radius and temperature in the necking zone for isotropic and anisotropic thermo-plasticity.

4 Mortar Methods for Contact Mechanics

This chapter is devoted to the development of mortar-based computational methods for isothermal and thermomechanical contact problems. Starting point is the continuum mechanical description of contact problems derived in Section 2.7, in particular the weak forms introduced in Section 2.7.4. Mortar methods are based on a mixed variational formulation introducing the boundary traction (or the heat flux for thermal problems) as an additional field of unknowns. The mathematical derivation of mortar methods for contact problems has become quite standard in the literature over recent years, such that it will only be sketched briefly in the following. A more detailed introduction may be found, for instance, in the theses by Hüeber [105], Popp [171] and the review article of Wohlmuth [235].

Section 4.1 introduces the concept mortar contact formulations for isothermal problems. A special focus therein is put on the discrete approximation space of the Lagrange multiplier. Meanwhile well-known in the literature are the so-called *standard* and *biorthogonal* (or *dual*) bases for finite elements recalled in Sections 4.1.1 and 4.1.2. Compared to the standard basis, dual bases have the advantage that the discrete Lagrange multiplier degrees of freedom can easily be eliminated from the global system of equations. Beyond those two well-known Lagrange multiplier bases, two novel schemes are developed within this thesis: First, Section 4.1.3 introduces a piece-wise constant Lagrange multiplier approximation for quadratic finite elements. This approach inherits the advantages of dual bases, including elimination of the discrete Lagrange multiplier and optimal convergence in contact problems, without the necessity of constructing a dual basis. Second, a biorthogonal NURBS basis is constructed in Section 4.1.4 for contact treatment in the framework of isogeometric analysis. Compared to classical finite elements, contact treatment by isogeometric analysis benefits from a smooth surface representation provided by the higher inter-element continuity of NURBS basis functions. Again, emphasis is put on achieving optimal convergence orders for contact problems. The performance of the developed methods is demonstrated by various numerical examples.

Finally, a thermomecanically coupled, fully nonlinear mortar finite element method is derived in Section 4.2. In the coupled thermomechanical mortar method, not only the contact traction, but also the contact heat flux is introduced as an unknown field to the mixed variational form. In the discrete setting, the use of biorthogonal or piece-wise constant Lagrange multiplier bases again allows for the condensation of the additional unknown Lagrange multiplier fields of traction and heat flux. Ultimately, a coupled system of equations consisting only of discrete displacement and temperature degrees of freedom needs to be solved. This renders the approach very efficient yet maintaining the variational foundation of the mortar method.

4.1 Mortar Methods for Isothermal Contact Problems

As aforementioned, the mortar finite element method is a mixed discretization scheme for which, in the isothermal case, the slave sided contact traction $\boldsymbol{t}_{\mathrm{c}}$ is introduced as an additional primary field, the *Lagrange multiplier*. For technical reasons it is convenient to actually take the *negative* slave-sided contact traction as the Lagrange multiplier field:

$$\boldsymbol{\lambda} = -\boldsymbol{t}_{\mathrm{c}} \quad . \tag{4.1}$$

To enforce the normal contact constraint (2.119) and Coulomb's law of friction (2.124) in tangential direction separately, the Lagrange multiplier $\boldsymbol{\lambda}$ is split into its normal and tangential components λ_{n} and $\boldsymbol{\lambda}_{\tau}$ by

$$\lambda_{\mathrm{n}} = \boldsymbol{n} \cdot \boldsymbol{\lambda} \quad , \tag{4.2a}$$

$$\boldsymbol{\lambda}_{\tau} = (\boldsymbol{I} - \boldsymbol{n} \otimes \boldsymbol{n})\boldsymbol{\lambda} \quad , \tag{4.2b}$$

in the style of (2.106). Accomodating the contact constraints, the Lagrange multiplier is chosen from the convex set

$$\boldsymbol{\mathcal{M}}(\boldsymbol{\lambda}) := \left\{ \boldsymbol{\omega} \in \boldsymbol{\mathcal{M}} \;\middle|\; \int_{\gamma_{\mathrm{c}}^{(1)}} \boldsymbol{\omega} \cdot \boldsymbol{v} \, \mathrm{d}\gamma \leq \int_{\gamma_{\mathrm{c}}^{(1)}} \mu \lambda_{\mathrm{n}} \|\boldsymbol{v}_{\tau}\| \, \mathrm{d}\gamma \, , \boldsymbol{v} \in \boldsymbol{\mathcal{W}} \text{ with } v_{\mathrm{n}} \leq 0 \right\} \quad , \tag{4.3}$$

wherein $\boldsymbol{\mathcal{W}}$ represents the trace space of $\boldsymbol{\mathcal{U}}_{\mathrm{u}}^{(1)}$ on $\Gamma_{\mathrm{c}}^{(1)}$ and $\boldsymbol{\mathcal{M}}$ its corresponding dual space. With this Lagrange multiplier space, the mixed variational form of the contact problem may be formulated as: Find $\boldsymbol{u} \in \boldsymbol{\mathcal{U}}_{\mathrm{u}}$ and $\boldsymbol{\lambda} \in \boldsymbol{\mathcal{M}}(\boldsymbol{\lambda})$, such that

$$\delta \mathcal{W}_{\mathrm{u}} + \int_{\gamma_{\mathrm{c}}^{(1)}} \boldsymbol{\lambda} \cdot [\![\delta \boldsymbol{u}]\!] \, \mathrm{d}\gamma = 0 \quad \forall \delta \boldsymbol{u} \in \boldsymbol{\mathcal{V}}_{\mathrm{u}} \quad , \tag{4.4}$$

$$\int_{\gamma_{\mathrm{c}}^{(1)}} (\delta \lambda_{\mathrm{n}} - \lambda_{\mathrm{n}}) g_{\mathrm{n}} \, \mathrm{d}\gamma - \int_{\gamma_{\mathrm{c}}^{(1)}} (\delta \boldsymbol{\lambda}_{\tau} - \boldsymbol{\lambda}_{\tau}) \cdot \boldsymbol{v}_{\tau} \, \mathrm{d}\gamma \geq 0 \quad \forall \delta \boldsymbol{\lambda} \in \boldsymbol{\mathcal{M}}(\boldsymbol{\lambda}) \quad . \tag{4.5}$$

The first line therein represents the discrete balance of linear momentum (2.132) replacing the contact traction with the Lagrange multiplier (4.1). The first integral in the second line is an equivalent reformulation of the normal contact constraints (2.119) in terms of a variational inequality and the second integral the equivalent variational inequality to Coulomb's law of friction (2.124). The technicalities of the proof of equivalence of the variational inequalities with (2.119) and (2.124) are of minor importance for this thesis and are therefore omitted. The interested reader is instead referred to, e.g., Curnier [42], Hüeber [105], Wohlmuth [235].

Spatial discretization To obtain the mortar finite element method, discretizations of both displacements as well as the Lagrange multiplier field $\boldsymbol{\lambda}$ are required. The discrete trial and test spaces for the displacement $\boldsymbol{\mathcal{U}}_{\mathrm{u}}$ and $\boldsymbol{\mathcal{V}}_{\mathrm{u}}$ are the same as derived in Section 2.8.1, i.e., (2.140) for classical finite elements and (2.157) in the case of isogeometric analysis. The Lagrange multiplier field on $\gamma_{\mathrm{c},h}^{(1)}$ is approximated by set $\mathcal{L}$ of still to be defined ansatz functions ϕ_i and discrete values $\boldsymbol{\lambda}_i$ similarly to (2.136) as

$$\boldsymbol{\lambda}(\boldsymbol{X}, t) \approx \boldsymbol{\lambda}_h(\boldsymbol{X}, t) = \sum_{i \in \mathcal{L}} \phi_i(\boldsymbol{X}) \boldsymbol{\lambda}_i(t) \quad , \tag{4.6}$$

resulting in the discrete space $\boldsymbol{\mathcal{M}}_h = [\mathrm{span}_{i\in\mathcal{L}}\{\phi_i\}]^{n_{\mathrm{dim}}}$. Different variants of how to choose the Lagrange multiplier basis functions ϕ_i will be discussed in detail in Sections 4.1.1 - 4.1.4. At this point, only inf-sup-stability of the pair of displacement and Lagrange multiplier basis shall be required, see e.g. Boffi *et al.* [18], Brivadis *et al.* [21], Wohlmuth [234][1]. The admissible discrete Lagrange multiplier space $\boldsymbol{\mathcal{M}}_h(\boldsymbol{\lambda}_h)$ derived therefrom by restricting the coefficients accordingly:

$$\boldsymbol{\mathcal{M}}_h(\boldsymbol{\lambda}_h) := \left\{ \boldsymbol{\omega}_h = \sum_{i\in\mathcal{L}} \phi_i \boldsymbol{\omega}_i \in \boldsymbol{\mathcal{M}}_h \;\middle|\; \omega_{i,\mathrm{n}} \geq 0 \,,\, \|\boldsymbol{\omega}_{i,\tau}\| \leq \mu\lambda_{i,\mathrm{n}} \right\} \quad . \tag{4.7}$$

Strictly speaking, putting the restrictions to positive normal values and bounded tangential values on the components rather than the interpolated function in the sense of (4.3) with $\boldsymbol{v} \in \boldsymbol{\mathcal{W}}_h$ is generally more restrictive. In the present case, it is only equivalent for the use of dual basis functions as derived in Sections 4.1.2 – 4.1.4, see Hüeber [105, Remark 2.5] for details. Spatially discretized, the contact contribution to weak form (4.4) is expressed as

$$\begin{aligned} \int_{\gamma_{\mathrm{c}}^{(1)}} \boldsymbol{\lambda} \cdot [\![\delta\boldsymbol{u}]\!] \,\mathrm{d}\gamma &\approx \int_{\gamma_{\mathrm{c},h}^{(1)}} \boldsymbol{\lambda}_h [\![\delta\boldsymbol{u}_h]\!] \,\mathrm{d}\gamma \\ &= \sum_{i\in\mathcal{L}} \sum_{j\in\mathcal{S}} \boldsymbol{\lambda}_i \left(\int_{\gamma_{\mathrm{c},h}^{(1)}} \phi_i \bar{N}_j^{(1)} \,\mathrm{d}\gamma \right) \delta\mathbf{d}_j^{(1)} \\ &\quad - \sum_{i\in\mathcal{L}} \sum_{k\in\mathcal{M}} \boldsymbol{\lambda}_i \left(\int_{\gamma_{\mathrm{c},h}^{(1)}} \phi_i \left(\bar{N}_k^{(2)} \circ \chi_{t,h} \right) \,\mathrm{d}\gamma \right) \delta\mathbf{d}_k^{(2)} \quad , \end{aligned} \tag{4.8}$$

with the sets $\mathcal{S}$ and $\mathcal{M}$ containing all nodes (or control points in IGA) on the slave and master contact boundary $\gamma_{\mathrm{c},h}^{(1)}$ and $\gamma_{\mathrm{c},h}^{(2)}$, respectively, and the $\bar{N}_j^{(i)} = N_j^{(i)}|_{\gamma_{\mathrm{c},h}^{(i)}}$ denotes the restriction of an ansatz function j to the contact boundary. Note that the present thesis only considers open knot vectors in IGA (cf. Section 2.8.1.2) and hence the discrete surfaces are described by the ansatz functions and coordinates of control points on the boundary only. When grouping the virtual displacements $\delta\mathbf{d} = [\delta\mathbf{d}_{\mathcal{N}}, \delta\mathbf{d}_{\mathcal{S}}, \delta\mathbf{d}_{\mathcal{M}}]^{\mathsf{T}}$ into the ones on the slave side $\delta\mathbf{d}_{\mathcal{S}}$, the master side $\delta\mathbf{d}_{\mathcal{M}}$ and all others $\delta\mathbf{d}_{\mathcal{N}}$ and combining all discrete Lagrange multiplier values in $\boldsymbol{\lambda}$, (4.8) can be abbreviated as

$$\int_{\gamma_{\mathrm{c},h}^{(1)}} \boldsymbol{\lambda}_h [\![\delta\boldsymbol{u}_h]\!] \,\mathrm{d}\gamma = \delta\mathbf{d}^{\mathsf{T}} \begin{bmatrix} \mathbf{0} \\ \mathbf{D}^{\mathsf{T}} \\ -\mathbf{M}^{\mathsf{T}} \end{bmatrix} \boldsymbol{\lambda} = \delta\mathbf{d}^{\mathsf{T}} \boldsymbol{F}_{\mathrm{u,c}}(\mathbf{d}, \boldsymbol{\lambda}) \quad , \tag{4.9}$$

with the discrete contact force $\boldsymbol{F}_{\mathrm{u,c}}$ and the well-known mortar matrices $\mathbf{D}$ and $\mathbf{M}$ consisting of blocks

$$\mathbf{D}[i,j] = \boldsymbol{I} \int_{\gamma_{\mathrm{c},h}^{(1)}} \phi_i \bar{N}_j^{(1)} \,\mathrm{d}\gamma \quad , \qquad i \in \mathcal{L},\ j \in \mathcal{S} \quad , \tag{4.10a}$$

$$\mathbf{M}[i,k] = \boldsymbol{I} \int_{\gamma_{\mathrm{c},h}^{(1)}} \phi_i \left(\bar{N}_k^{(2)} \circ \chi_{t,h} \right) \,\mathrm{d}\gamma \quad , \quad i \in \mathcal{L},\ k \in \mathcal{M} \quad . \tag{4.10b}$$

[1] Note that inf-sup-stability may not be sufficient for the mathematical analysis nonlinear problems, c.f. [136]. Exact mathematical analysis of nonlinear problems are, however, not the topic of this thesis such that details are omitted here.

A stable mortar method for contact problems requires [232, Assumption 1]:

$$\int_{\gamma_{\mathrm{c},h}^{(1)}} \phi_i \bar{N}_j^{(1)} \,\mathrm{d}\gamma \geq 0 \quad i \in \mathcal{L}, \;\; j \in \mathcal{S} \;\; . \tag{4.11}$$

Assuming frictionless contact for simplicity, this ensures that a positive Lagrange multiplier, i.e. a negative contact pressure p_{n}, yields by (4.9) discrete force separating the two contacting surfaces.

The matrix $\mathbf{D}$ contains the integration over a product of ansatz functions both defined on the slave mesh and thus could be integrated accurately by standard quadrature rules on slave elements. The matrix $\mathbf{M}$, on the other hand, includes the integration of a product two ansatz functions defined on the slave and the master sided mesh respectively. To maintain optimality of mortar methods, sufficiently accurate integration is of great importance. Various integration strategies have been proposed in the literature. The simplest and widely used one is termed *element-based* in Farah *et al.* [70] and consists of simply using higher order integration rules on slave elements, which, of course, cannot be exact as it disregards the master-sided mesh. An exact integration requires integration on an imprinted mesh constructed of both the slave and master side which is still rather simple to obtain in two-dimensional problems but becomes more intricate in 3D. Such an integration technique is commonly referred to *segmentation* and can be found, e.g., in Popp *et al.* [168, 169], Puso and Laursen [175, 176] for first order finite elements, Puso *et al.* [177] for second order finite elements, and Dittmann *et al.* [61], Hesch and Betsch [100], Seitz *et al.* [193] for isogeometric analysis. A comparison of element-based integration and segmentation in terms of accuracy and efficiency has been performed, e.g., by Farah *et al.* [70] for finite elements and Brivadis *et al.* [22] in the context of isogeometric analysis. Finally, Maday *et al.* [140] obtained accurate results integrating $\mathbf{D}$ and $\mathbf{M}$ using independent quadrature rules on the slave and master-sided mesh, respectively. This approach has been transferred and analyzed for isogeometric discretizations by Brivadis *et al.* [22].

In addition to the contact forces acting in the weak form of the balance of linear momentum (4.4) and are discretized by (4.9), the weak form of the contact constraints (4.5) have to be dealt with. In mortar methods for contact problems, they are commonly introduced for each discrete Lagrange multiplier independently. In normal direction, one obtains

$$\tilde{g}_{\mathrm{n},i} \geq 0 \;\; , \quad \lambda_{\mathrm{n},i} \geq 0 \;\; , \quad \lambda_{\mathrm{n},i} \tilde{g}_{\mathrm{n},i} = 0 \quad \forall i \in \mathcal{L} \;\; , \tag{4.12}$$

based on the so-called weighted gap

$$\tilde{g}_{\mathrm{n},i} = \int_{\gamma_{\mathrm{c},h}^{(1)}} \phi_i g_{\mathrm{n},h} \,\mathrm{d}\gamma \;\; , \tag{4.13}$$

with a discrete approximation $g_{\mathrm{n},h} \approx g_{\mathrm{n}}$ of the gap function (2.102). A minimum requirement to obtain a stable method is that the Lagrange multiplier ansatz functions have at least a positive mean value [232, Assumption 2]:

$$\int_{\gamma_{\mathrm{c},h}^{(1)}} \phi_i \,\mathrm{d}\gamma > 0 \quad \forall i \in \mathcal{L} \;\; . \tag{4.14}$$

This entails that a positive, constant gap $g_{\mathrm{n},h}$ over the support of ϕ_i yields a positive weighted gap value $\tilde{g}_{\mathrm{n},i}$. More desirable than merely positive mean values is non-negativity of ϕ_i, in which

case any strictly positive $g_{\mathrm{n},h}$ over the support of ϕ_i yields a positive weighted gap value $\tilde{g}_{\mathrm{n},i}$. If the ansatz functions ϕ_i, for some reason (e.g. dual basis, see Sections 4.1.2 and 4.1.4), cannot satisfy $\phi_i \geq 0$, Popp *et al.* [172] propose to use a Petrov–Galerkin-type approach to use different ansatz and test functions for $\boldsymbol{\lambda}$ and $\delta\boldsymbol{\lambda}$ in (4.4) and (4.5), respectively. The calculation of the mortar matrices (4.10) is then using the ansatz functions for $\boldsymbol{\lambda}_i$, which require (4.11) rather than (4.14), whereas in (4.13), ϕ_i is then replaced by the newly chosen test function for $\delta\boldsymbol{\lambda}_i$ which can be constructed to be non-negative.

Similarly, the constraints of Coulomb friction are enforced as

$$\phi_{\tau,h,i} := \|\boldsymbol{\lambda}_{\tau,i}\| - \mu\lambda_{\mathrm{n},i} \leq 0 \quad , \quad \tilde{\boldsymbol{v}}_{\tau,i} + \beta\boldsymbol{\lambda}_{\tau,i} = \boldsymbol{0} \quad , \quad \beta \geq 0 \quad , \quad \phi_{\tau,h,i}\beta = 0 \quad \forall i \in \mathcal{L} \ . \tag{4.15}$$

The weighted tangential velocity $\tilde{\boldsymbol{v}}_{\tau,i}$ associated with a Lagrange multiplier $\boldsymbol{\lambda}_i$ can either be derived analogously to (4.13) and the local tangential velocity (2.103), or, as introduced by Puso and Laursen [176], via a time derivative of the mortar matrices:

$$\tilde{\boldsymbol{v}}_{\tau,i} = -(\boldsymbol{I} - \boldsymbol{n}_i \otimes \boldsymbol{n}_i)\left(\sum_{j\in\mathcal{S}} \dot{\mathbf{D}}[i,j]\boldsymbol{x}_j^{(1)} - \sum_{k\in\mathcal{M}} \dot{\mathbf{M}}[i,k]\boldsymbol{x}_k^{(2)}\right) \quad , \tag{4.16}$$

which is frame indifferent for any discrete time derivative by construction and consistent for nodes in closed contact, see [176] for details. For all mortar methods including friction, (4.16) will be employed throughout this thesis.

Remark 4.1. *It should be noted that the decoupling of discrete constraints* (4.12) *and* (4.15) *only emanates consistently from the discretization of the variational inequality* (4.5)*, if the discrete Lagrange multiplier basis satisfies a biorthogonality condition as the ones derived in Sections 4.1.2 – 4.1.4, see Hüeber [105, Lemma 2.6]. For efficient implementations of mortar contact methods, however, the constraints are commonly still enforced on nodal values independently even if no dual basis for the Lagrange multiplier is employed, see e.g. [50, 51, 147, 176, 216, 217, 220, 245], which can be interpreted as a lumping technique. Only Blum* et al. *[17] enforce the constraints consistently with the variational inequality for standard Lagrange multiplier spaces.*

Temporal discretization Up to now, the contact terms have only been discretized in space but remain continuous in time. To encorporate contact forces in the time discrete balance of linear momentum, the contact force $\boldsymbol{F}_{\mathrm{u,c}}$ has to be included in the fully discrete equilibrium equation (2.159) for dynamic problems or (2.165) for quasi-static problems respectively. In the simpler case of quasi-static problems, this means including the contact forces at a given time step t_{n+1} to the equilibrium (2.165) to obtain

$$\boldsymbol{r}_{\mathrm{u}}(\mathbf{d}_{n+1}, \boldsymbol{\lambda}_{n+1}) = \boldsymbol{F}_{\mathrm{u,int}}(\mathbf{d}_{n+1}) - \boldsymbol{F}_{\mathrm{u,ext},n+1} + \boldsymbol{F}_{\mathrm{u,c}}(\mathbf{d}_{n+1}, \boldsymbol{\lambda}_{n+1}) = \boldsymbol{0} \ . \tag{4.17}$$

The discrete contact force $\boldsymbol{F}_{\mathrm{u,c}}$ therein depends nonlinearly on the displacements, since the projection and integration are performed in the displaced configuration, and linearly on the Lagrange multipliers $\boldsymbol{\lambda}_{n+1}$ via (4.9). For dynamic problems solved by the generalized-α method, see Section 2.8.2, the contact forces are applied at a generalized mid-point with the parameter $\alpha_{\mathrm{f,c}}$ resulting in the balance equation

$$\boldsymbol{r}_{\mathrm{u}}(\mathbf{d}_{n+1}, \boldsymbol{\lambda}_{n+1}) = \boldsymbol{M}_{\mathrm{u}}\mathbf{a}_{n+1-\alpha_{\mathrm{m,u}}} + \boldsymbol{F}_{\mathrm{u,int},n+1-\alpha_{\mathrm{f,u}}} - \boldsymbol{F}_{\mathrm{u,ext},n+1-\alpha_{\mathrm{f,u}}} + \boldsymbol{F}_{\mathrm{u,c},n+1-\alpha_{\mathrm{f,c}}} = \boldsymbol{0} \ , \tag{4.18}$$

whereby the discrete contact force at the interpolated mid-point is, as the inertia, internal and external forces, obtained by interpolation of time steps t_n and t_{n+1}, i.e. $\boldsymbol{F}_{\mathrm{u,c},n+1-\alpha_{\mathrm{f,c}}} = (1 - \alpha_{\mathrm{f,c}})\boldsymbol{F}_{\mathrm{u,c}}(\mathbf{d}_{n+1}, \boldsymbol{\lambda}_{n+1}) + \alpha_{\mathrm{f,c}}\boldsymbol{F}_{\mathrm{u,c}}(\mathbf{d}_n, \boldsymbol{\lambda}_n)$. Contact dynamics is inherently non-smooth in time, as, at the time of impact, an instantaneous deceleration of material points on the contacting surface occurs. In the time discrete setting of (4.18), this can result in oscillatory solutions of contact forces in highly dynamic impact problems. Several approaches to deal with this non-smoothness in time in the context of Newmark-type time integrators have been proposed in the literature, for instance by Deuflhard *et al.* [58], Hager *et al.* [89], Khenous *et al.* [119], Laursen and Chawla [132]. Krause and Walloth [124] provide a review and comparison of different modified Newmark-type time integrators for dynamic contact and impact problems. In this thesis, an approach originally proposed by Laursen and Love [133] for NTS contact algorithms is pursued. For simplicity of presentation, frictionless contact is assumed. [1]In a first step, a fully implicit treatment of the contact forces is chosen by setting $\alpha_{\mathrm{f,c}} = 0$, which guarantees that the discrete work in one time step $W_{\mathrm{c}} = (\mathbf{d}_{n+1} - \mathbf{d}_n) \cdot \boldsymbol{F}_{\mathrm{u,c}}$ becomes negative (i.e. dissipative) for Lagrange multipliers $\boldsymbol{\lambda}_i$ when the contact constraint is activated ($\tilde{g}_{\mathrm{n},i,n+1} = 0$) and zero if the contact constraint is deactivated ($\boldsymbol{\lambda}_i = \mathbf{0}$). Following an idea of Laursen and Love [133], the dissipated energy can be re-introduced into the system via a velocity update procedure. If, however, the contact force were discretized in time by a linear combination of two time steps, Lagrange multipliers leaving the active contact set would introduce energy to the discrete system, which one might not be able to compensate via the velocity update procedure.

Finally, also the relative tangential velocity (4.16) requires an appropriate time discretization. As in the case of plasticity, time in quasi-static frictional contact problems plays the role of a path variable. With a backward-Euler scheme, one obtains

$$\begin{aligned}\tilde{\boldsymbol{v}}_{\tau,i,n+1} &= \frac{\tilde{\boldsymbol{u}}_{\tau,\mathrm{rel},i,n+1}}{\Delta t} \\ &= -(\boldsymbol{I} - \boldsymbol{n}_{i,n+1} \otimes \boldsymbol{n}_{i,n+1}) \cdot \left(\sum_{j \in \mathcal{S}} \frac{\mathbf{D}_{n+1}[i,j] - \mathbf{D}_n[i,j]}{\Delta t} \boldsymbol{x}^{(1)}_{j,n+1} \right. \\ &\qquad \left. - \sum_{k \in \mathcal{M}} \frac{\mathbf{M}_{n+1}[i,k] - \mathbf{M}_n[i,k]}{\Delta t} \boldsymbol{x}^{(2)}_{k,n+1} \right) ,\end{aligned} \tag{4.19}$$

by means of which the contact constraints at t_{n+1} can be stated

$$\tilde{g}_{\mathrm{n},i,n+1} \geq 0 \ , \quad \lambda_{\mathrm{n},i,n+1} \geq 0 \ , \quad \lambda_{\mathrm{n},i,n+1}\tilde{g}_{\mathrm{n},i,n+1} = 0 \quad \forall i \in \mathcal{L} \ , \tag{4.20}$$

and

$$\begin{aligned}\phi_{\tau,h,i,n+1} := \|\boldsymbol{\lambda}_{\tau,i,n+1}\| - \mu\lambda_{\mathrm{n},i,n+1} &\leq 0 \ , \\ \tilde{\boldsymbol{u}}_{\tau,\mathrm{rel},i,n+1} + \beta\boldsymbol{\lambda}_{\tau,i,n+1} &= \mathbf{0} \ , \\ \beta &\geq 0 \ , \\ \phi_{\tau,h,i,n+1}\beta &= 0 \qquad \forall i \in \mathcal{L} \ ,\end{aligned} \tag{4.21}$$

in the time discrete setting.

[1]The remainder of this paragraph is adapted from the author's publication [194].

Reformulation of inequality constraints To this point, the mortar finite element discretization yields a nonlinear problem, that is, the balance of linear momentum (4.17) or (4.18), under the inequality constraints (4.20) and (4.21). Similar to the numerical algorithm for computational plasticity derived in Section 3, these inequality constraints are transferred to equivalent non-smooth equality constraints by means of nonlinear complementarity (NCP) functions. Hüeber and Wohlmuth [106] introduce the reformulation of the contact constraints in normal direction (4.20) in terms of the NCP function

$$G_{\mathrm{n},i} = \lambda_{\mathrm{n},i} - \max(0, \lambda_{\mathrm{n},i} - c_{\mathrm{n}}\tilde{g}_{\mathrm{n},i}) = 0 \quad \forall i \in \mathcal{L} \ , \tag{4.22}$$

where the subscript $(\cdot)_{n+1}$ is omitted for brevity. It can easily be verified that the root of (4.22) is equivalent to (4.20) for any complementarity parameter $c_{\mathrm{n}} > 0$, which is also apparent from the visualization of the NCP function in Figure 4.1. At the root (green line), either the weighted

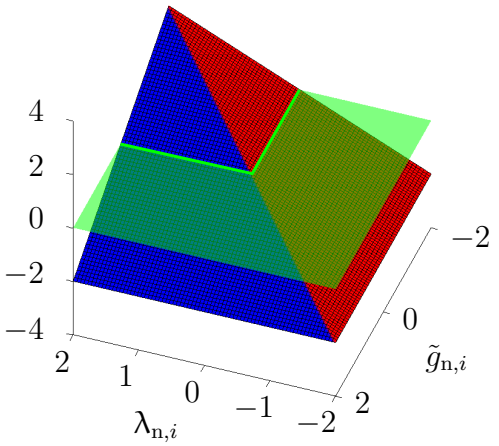

Figure 4.1: Visualization of the NCP function (4.22) for a one-dimensional problem with $c_{\mathrm{n}} = 1$. The blue and red parts of the functions denote the inactive ($\lambda_{\mathrm{n},i} - c_{\mathrm{n}}\tilde{g}_{\mathrm{n},i} \leq 0$) and active branches ($\lambda_{\mathrm{n},i} - c_{\mathrm{n}}\tilde{g}_{\mathrm{n},i} > 0$), respectively. The transparent green plane indicates the zero-plane and a solid green line the root of the NCP function.

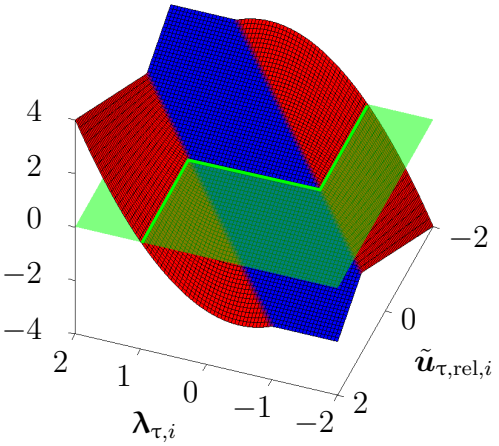

Figure 4.2: Visualization of the NCP function (4.23) for a one-dimensional problem with $\mu(\lambda_{\mathrm{n},i} - c_{\mathrm{n}}\tilde{g}_{\mathrm{n},i}) = 1$ and $c_\tau = 1$. The blue and red parts of the functions denote the stick ($\|\boldsymbol{\lambda}_{\tau,i} + c_\tau\tilde{\boldsymbol{u}}_{\tau,\mathrm{rel},i}\| \leq \mu(\lambda_{\mathrm{n},i} - c_{\mathrm{n}}\tilde{g}_{\mathrm{n},i})$) and slip branches ($\|\boldsymbol{\lambda}_{\tau,i} + c_\tau\tilde{\boldsymbol{u}}_{\tau,\mathrm{rel},i}\| > \mu(\lambda_{\mathrm{n},i} - c_{\mathrm{n}}\tilde{g}_{\mathrm{n},i})$), respectively. The transparent green plane indicates the zero-plane and a solid green line the root of the NCP function.

gap $\tilde{g}_{\mathrm{n},i}$ is positive and the and the normal Lagrange multiplier $\lambda_{\mathrm{n},i}$ is zero in the red zone, or the weighted $\tilde{g}_{\mathrm{n},i} = 0$ and $\lambda_{\mathrm{n},i} \geq 0$ in the blue zone. Meanwhile, the NCP function (4.22) has been widely used in computational contact mechanics based on mortar methods (see e.g. [39, 62, 80, 91, 95, 109, 168, 169, 235]) or other computational approaches, e.g. [34, 35, 173, 185].

The frictional constraints (4.21) bears great similarity to the ones of elasto-plasticity (see (3.5), (3.6)) and therefore a similar NCP function can be constructed as

$$\begin{aligned} \boldsymbol{G}_{\tau,i} = &\max\left(\mu(\lambda_{\mathrm{n},i} - c_{\mathrm{n}}\tilde{g}_{\mathrm{n},i}), \|\boldsymbol{\lambda}_{\tau,i} + c_\tau\tilde{\boldsymbol{u}}_{\tau,\mathrm{rel},i}\|\right) \\ &\cdot \left(\boldsymbol{\lambda}_{\tau,i} - \min\left(1, \frac{\mu(\lambda_{\mathrm{n},i} - c_{\mathrm{n}}\tilde{g}_{\mathrm{n},i})}{\|\boldsymbol{\lambda}_{\tau,i} + c_\tau\tilde{\boldsymbol{u}}_{\tau,\mathrm{rel},i}\|}\right)(\boldsymbol{\lambda}_{\tau,i} + c_\tau\tilde{\boldsymbol{u}}_{\tau,\mathrm{rel},i})\right) = \boldsymbol{0} \quad \forall i \in \mathcal{L} \ , \end{aligned} \tag{4.23}$$

with a complementarity parameter $c_\tau > 0$. As compared to the NCP function of elasto-plasticity (3.23), the analog to shape parameter s_p, i.e. an exponent to the $\max$-function, is directly set to 1 for frictional contact, since this has proven most robust in case of elasto-plasticity (cf. Section 3.3.3.1) and the study of Hager and Wohlmuth [91] for both elasto-plasticity and frictional contact at small strains. In the case of closed contact, i.e. $\lambda_{\mathrm{n},i} - c_\mathrm{n}\tilde{g}_{\mathrm{n},i} > 0$, it can easily be shown, that the root of $\boldsymbol{G}_{\tau,i}$ is equivalent to the inequality constraints (4.21). However, this does not necessarily hold for inactive contact $\lambda_{\mathrm{n},i} - c_\mathrm{n}\tilde{g}_{\mathrm{n},i} \leq 0$, in which case $\boldsymbol{G}_{\tau,i}$ is replaced by $\boldsymbol{\lambda}_{\tau,i} = \mathbf{0}$ as no contact traction, neither in normal nor in tangential direction, is permitted if there is no contact. A detailed discussion on this modification of the tangential NCP function in the case of inactive contact is given in Hüeber [105, Section 5.1.2.]. A more in-depth introduction to the NCP functions for frictional contact problems can be found in e.g. Gitterle [79], Gitterle *et al.* [80], Hager and Wohlmuth [91], Hüeber [105], Hüeber *et al.* [109], Wohlmuth [235].

Both in normal and tangential direction, the introcuded complementrity parameters c_n and c_τ have no effect on the solution (as the roots of the NCP functions are independent of c_n and c_τ). However, their choice can have significant effects on the convergence of the nonlinear solution scheme derived in the following. Since c_n and c_τ balance contact tractions λ_n and $\boldsymbol{\lambda}_\tau$ with the weighted geometric quantities $\tilde{g}_\mathrm{n}$ and $\tilde{\boldsymbol{u}}_{\tau,\mathrm{rel}}$, respectively, Hager and Wohlmuth [91] propose to scale c_n and c_τ with a material stiffness parameter, e.g. Young's modulus, and the inverse finite element mesh size. Numerical experiments on the influence of the compelementarity parameters on the convergence of the nonlinear solution procedure have been performed, among others, by Gitterle [79], Hager and Wohlmuth [91].

Semi-smooth Newton method With the NCP functions replacing the inequality constraints, the discretized system including frictional contact is given by a set of coupled nonlinear equations

$$\boldsymbol{r}_\mathrm{u} = \boldsymbol{M}_\mathrm{u}\mathbf{a}_{n+1-\alpha_{\mathrm{m,u}}} + \boldsymbol{F}_{\mathrm{u,int},n+1-\alpha_{\mathrm{f,u}}} - \boldsymbol{F}_{\mathrm{u,ext},n+1-\alpha_{\mathrm{f,u}}} + \boldsymbol{F}_{\mathrm{u,c},n+1-\alpha_{\mathrm{f,c}}} = \mathbf{0} \quad , \tag{4.24a}$$

$$G_{\mathrm{n},i} = 0 \quad \forall i \in \mathcal{L} \quad , \tag{4.24b}$$

$$\boldsymbol{G}_{\tau,i} = \mathbf{0} \quad \forall i \in \mathcal{L} \quad , \tag{4.24c}$$

which is amenable to a Newton-type scheme. Let $\boldsymbol{G}_{\mathrm{c},i} = \boldsymbol{n}_i G_{\mathrm{n},i} + \boldsymbol{G}_{\tau,i}$ denote the complete NCP function containing the contact constraints in both normal and tangential direction associated with a Lagrange multiplier $\boldsymbol{\lambda}_i$ and $\boldsymbol{G}_\mathrm{c}$ the combination of all $\boldsymbol{G}_{\mathrm{c},i}$ in one vector. The consistent linearization of (4.24) in a compact form then reads

$$\begin{bmatrix} \mathbf{K}_{\mathrm{uu},\mathcal{N}} & \mathbf{0} \\ \check{\mathbf{K}}_{\mathrm{uu},\mathcal{S}} & a_\mathrm{c}\mathbf{D}^\mathsf{T} \\ \check{\mathbf{K}}_{\mathrm{uu},\mathcal{M}} & -a_\mathrm{c}\mathbf{M}^\mathsf{T} \\ \mathbf{C}_\mathrm{u} & \mathbf{C}_{\boldsymbol{\lambda}} \end{bmatrix} \begin{bmatrix} \Delta\mathbf{d} \\ \Delta\boldsymbol{\lambda} \end{bmatrix} = - \begin{bmatrix} \boldsymbol{r}_{\mathrm{u},\mathcal{N}} \\ \boldsymbol{r}_{\mathrm{u},\mathcal{S}} \\ \boldsymbol{r}_{\mathrm{u},\mathcal{M}} \\ \boldsymbol{G}_\mathrm{c} \end{bmatrix} \tag{4.25}$$

with $a_\mathrm{c} = 1 - \alpha_{\mathrm{f,c}}$, and the derivatives of the NCP function $\mathbf{C}_\mathrm{u} = \frac{\partial \boldsymbol{G}_\mathrm{c}}{\partial \mathbf{d}}$ and $\mathbf{C}_{\boldsymbol{\lambda}} = \frac{\partial \boldsymbol{G}_\mathrm{c}}{\partial \boldsymbol{\lambda}}$. The check in $\check{\mathbf{K}}_{\mathrm{uu},\mathcal{S}}$ and $\check{\mathbf{K}}_{\mathrm{uu},\mathcal{M}}$ indicates that these stiffness blocks contain derivatives of the mortar matrices $\mathbf{D}$ and $\mathbf{M}$ in addition to the terms of a purely structural problem without contact. Within this thesis, the concrete derivations of $\mathbf{C}_\mathrm{u}$ and $\mathbf{C}_{\boldsymbol{\lambda}}$ are not elaborated on, as they are discussed extensively in Popp *et al.* [168, 169] for the frictionless case and Gitterle *et al.* [80] for terms related

to friction. Due to the non-smoothness of the NCP functions, a consistently linearized Newton scheme of (4.24) constitutes a semi-smooth Newton method, for which local quadratic convergence rates are proven in Qi and Sun [178]. Additionally, this semi-smooth Newton method including NCP functions actually constitutes a primal-dual active set strategy (PDASS) for the inequality constrained problem, as shown by Hintermüller *et al.* [103] in an abstract setting and Hüeber and Wohlmuth [106], Hüeber *et al.* [109] for frictionless and frictional contact problems, respectively.

Domain Decomposition as a simplified contact problem As mentioned in the beginning of this chapter, mortar methods originate in (non-overlapping) domain decomposition applications, sometimes termed *tied contact* or *mesh tying*, where an internal interface is introduced to a single physical domain. Splitting the computational domain Ω_0 along virtual interfaces into sub-domains $\Omega_0^{(i)}$ can be used beneficially to simplify mesh generation and allow for different mesh sizes in different sub-domains. In isogeometric analysis especially, composing the entire computational domain by sub-parts is crucial to analyze more complex geometries, cf. Figure 2.8. Within this thesis, mesh tying problems will be used to analyze mortar methods, and different Lagrange multiplier spaces in particular, on a simplified model problem before applying them to contact mechanics. Hence, the basic concept of mortar methods in mesh tying problems will be summarized briefly in the following; a more extensive introduction to mortar methods in nonlinear solid mechanics can be found, e.g., in Popp [171]. For simplicity, a decomposition of Ω_0 into two non-overlapping domains $\Omega_0^{(1)}$ and $\Omega_0^{(2)}$ with the common boundary

$$\overline{\Omega_0^{(1)}} \cap \overline{\Omega_0^{(2)}} \equiv \Gamma_\mathrm{c} \equiv \Gamma_\mathrm{c}^{(1)} \equiv \Gamma_\mathrm{c}^{(2)} \tag{4.26}$$

is considered only. As the interface Γ_c in mesh tying problems does not model a physical interface but is merely introduced to facilitate mesh generation, continuity of the solution across the interface has to be enforced, e.g., for displacements:

$$[\![\boldsymbol{u}]\!]_0 = \boldsymbol{0} \quad \text{on } \Gamma_\mathrm{c} \ . \tag{4.27}$$

with the jump operator $[\![(\cdot)]\!]_0 = (\cdot)^{(1)} - ((\cdot)^{(2)} \circ \chi_0)$ in reference configuration. In comparison to contact the contact constraints (2.119) and (2.124), the mesh tying constraint (4.27) is simpler in multiple regards. First, the constraints can be formulated directly in reference configuration, second, it does not distinguish between normal and tangential direction, and third, it is of equality nature rather than inequalities. A mixed variational form of the mesh tying problem is derived analogously to (4.4) and (4.5) by introducing a Lagrange multiplier field on Γ_c and reads: Find $\boldsymbol{u} \in \boldsymbol{\mathcal{U}}_\mathrm{u}$ and $\boldsymbol{\lambda} \in \boldsymbol{\mathcal{M}}$, such that

$$\delta \mathcal{W}_\mathrm{u} + \int_{\Gamma_\mathrm{c}} \boldsymbol{\lambda} \cdot [\![\delta \boldsymbol{u}]\!]_0 \, \mathrm{d}\Gamma = 0 \quad \forall \delta \boldsymbol{u} \in \boldsymbol{\mathcal{V}}_\mathrm{u} \ , \tag{4.28a}$$

$$\int_{\Gamma_\mathrm{c}} [\![\boldsymbol{u}]\!]_0 \cdot \delta \boldsymbol{\lambda} \, \mathrm{d}\Gamma = 0 \quad \forall \delta \boldsymbol{\lambda} \in \boldsymbol{\mathcal{M}} \ . \tag{4.28b}$$

The displacement field $\boldsymbol{u}$ is then discretized according to Section 2.8.1 and the Lagrange multiplier field according to (4.6). While the detailed derivation is being omitted, the resulting nonlinear system of equations is then again solved by Newton's method with the tangent system

$$\begin{bmatrix} \mathbf{K}_{\mathrm{uu},\mathcal{NN}} & \mathbf{K}_{\mathrm{uu},\mathcal{NS}} & \mathbf{K}_{\mathrm{uu},\mathcal{NM}} & \mathbf{0} \\ \mathbf{K}_{\mathrm{uu},\mathcal{SN}} & \mathbf{K}_{\mathrm{uu},\mathcal{SS}} & \mathbf{K}_{\mathrm{uu},\mathcal{SM}} & a_{\mathrm{c}}\mathbf{D}_0^{\mathsf{T}} \\ \mathbf{K}_{\mathrm{uu},\mathcal{MN}} & \mathbf{K}_{\mathrm{uu},\mathcal{MS}} & \mathbf{K}_{\mathrm{uu},\mathcal{MM}} & -a_{\mathrm{c}}\mathbf{M}_0^{\mathsf{T}} \\ \mathbf{0} & \mathbf{D}_0 & -\mathbf{M}_0 & \mathbf{0} \end{bmatrix} \begin{bmatrix} \Delta\mathbf{d}_{\mathcal{N}} \\ \Delta\mathbf{d}_{\mathcal{S}} \\ \Delta\mathbf{d}_{\mathcal{M}} \\ \Delta\boldsymbol{\lambda} \end{bmatrix} = - \begin{bmatrix} \boldsymbol{r}_{\mathrm{u},\mathcal{N}} \\ \boldsymbol{r}_{\mathrm{u},\mathcal{S}} \\ \boldsymbol{r}_{\mathrm{u},\mathcal{M}} \\ \mathbf{0} \end{bmatrix} \quad , \tag{4.29}$$

which is of saddle-point structure. The coupling matrices $\mathbf{D}_0$ and $\mathbf{M}_0$ are calculated according to (4.10) with the only difference being the integration on the boundary in reference configuration $\Gamma_{\mathrm{c},h}^{(1)}$ instead of the displaced boundary $\gamma_{\mathrm{c},h}^{(1)}$, as indicated by the subscript $(\cdot)_0$.

Notes on spatial convergence orders A crucial distinction of different mortar methods lies in the chosen discrete Lagrange multiplier space. This choice influences both the efficiency and accuracy of the resulting scheme. Efficiency improvements lie mostly in the construction of mortar coupling matrices $\mathbf{D}$ and $\mathbf{M}$ with a beneficial structure, such as a diagonal matrix $\mathbf{D}$ in dual mortar methods, see Section 4.1.2. In terms of accuracy, the achievable convergence orders with uniform mesh refinement depend on the polynomial reproduction order of both the discrete displacement and Lagrange multiplier field as well as the regularity of the solution. Since derivations of *a priori* error estimates and achievable convergence orders are beyond the scope of this thesis, only the relevant results are summarized briefly here. For a mathematical analysis, the reader is referred to the respective literature, e.g. Boffi *et al.* [18] for mixed finite elements in general, Bernardi *et al.* [14] for mortar methods Wohlmuth [234] for dual mortar methods for finite elements, Brivadis *et al.* [21] for isogeometric mortar methods, and Wohlmuth *et al.* [232] for dual mortar methods for contact problems based on classical finite elements. Consider a problem of linearized kinematics and let s denote the smoothness of the solution, i.e. $\boldsymbol{u} \in [H^{s+1}(\Omega_0)]^{n_{\mathrm{dim}}}$, p the polynomial order of $\boldsymbol{u}_h$, and q the polynomial approximation order of $\boldsymbol{\lambda}$ in the sense that for any $\lambda \in H^q(\Gamma_{\mathrm{c},h}^{(1)})$,

$$\inf_{\mu \in \mathcal{M}_h} \|\lambda - \mu\|_{L^2(\Gamma_{\mathrm{c},h}^{(1)})} \leq C h^q \|\lambda\|_{H^q(\Gamma_{\mathrm{c},h}^{(1)})} \quad , \tag{4.30}$$

with a generic constant C independent of h, see Brivadis *et al.* [21]. For example, a discrete space $\boldsymbol{\mathcal{M}}_h$ able to reproduce constants exactly yields $q = 1$. Roughly speaking, the expected convergence order under uniform mesh refinement is then given as

$$\|\boldsymbol{u}_h - \boldsymbol{u}\|_{H^1(\Omega_0)} \leq C h^k \quad , \text{ with } \quad k = \min(s, p, q + \frac{1}{2}) \quad , \tag{4.31}$$

and a generic constant C independent of h. Convergence of type (4.31) will be abbreviated as convergence of order $\mathcal{O}(h^k)$. In contact problems, the solution $\boldsymbol{u}$ is typically in $H^t(\Omega_0)$ with $t < 5/2$, such that *a priori* estimates (4.31) are limited to $\mathcal{O}(h^{3/2})$ already for quadratic approximations $p = 2$ with a Lagrange multiplier reproducing constants $q = 1$, see Wohlmuth *et al.* [232]. Restoring convergence orders $\mathcal{O}(h^p)$ requires either an enriched function space Graveleau *et al.* [83] or adaptive refinement, see e.g. the h-adaptive scheme of Rademacher [180], Rademacher and Frohne [181] and the rp-adaptive method by Franke [75]. The present thesis, however, considers uniform refinement exclusively.

In the following sections, different Lagrange multiplier spaces are discussed: Section 4.1.1 introduces the so-called standard mortar method most commonly used in the literature, and Section

4.1.2 recaps the dual mortar method for contact problems as derived by Hüeber and Wohlmuth [106], Hüeber *et al.* [109] and applied e.g. by Gitterle *et al.* [80], Popp *et al.* [168, 169] to finite deformation problems. As both these methods are fairly common in the literature, they are only introduced briefly and serve as a reference for the newly presented methods. Section 4.1.3 introduces a new piece-wise constant Lagrange multiplier approximation for second order finite elements, and Section 4.1.4 an isogeometric dual mortar method. For those newly derived methods, numerical examples of mesh tying and contact problems demonstrate optimal convergence orders for contact applications while sacrificing optimality for mesh tying applications.

4.1.1 Standard Lagrange Multipliers

The most common choice for the discrete Lagrange multiplier is to associate a discrete Lagrange multiplier $\boldsymbol{\lambda}_i$ with each node on the slave surface, i.e. $\mathcal{L} = \mathcal{S}$, and employ the same basis functions $\bar{N}_i^{(1)}$ for the interpolation of displacements on the slave boundary as well as the Lagrange multiplier to obtain the discrete Lagrange multiplier field

$$\boldsymbol{\lambda}_h(\boldsymbol{X}, t) = \sum_{i \in \mathcal{L}} \bar{N}_i^{(1)}(\boldsymbol{X}) \boldsymbol{\lambda}_i(t) \quad . \tag{4.32}$$

Obviously, the reproduction order (4.30) of the Lagrange multiplier interpolation is $q = p + 1$ for this choice, such that it does not have any negative effect on the convergence order according to (4.31).

For contact problems, however, additionally (4.11) and (4.14) have to be satisfied for stability reasons [232]. For first order finite elements, this is obviously guaranteed by the non-negativity of the ansatz functions $\bar{N}_i^{(1)}$. For $\mathbb{Q}_2$ element boundaries, i.e. facets of $\mathbb{Q}_2$,$\mathbb{T}_2$ and $\mathbb{P}_2$ elements in $n_{\mathrm{dim}} = 2$ dimensions and facets of $\mathbb{Q}_2$ hexahedrals in $n_{\mathrm{dim}} = 3$, (4.11) and (4.14), are also met when taking into account the fundamental requirements isoparametric mapping (2.139), see Section 2.8.1.1 and Hughes [111, Section 3.3]. However, for $\mathbb{T}_2$ and $\mathbb{P}_2$ element boundaries, i.e. facets of $\mathbb{T}_2$ and $\mathbb{P}_2$ elements in $n_{\mathrm{dim}} = 3$ dimensions, respectively, the ansatz functions for the corner nodes (cf. Figures 2.5e and 2.5f) do not have a positive mean value (4.14) on the reference element. To deal with this deficiency, Popp *et al.* [170] propose a basis transformation of the ansatz functions $\bar{N}_i^{(1)}$, to guarantee (4.11) and (4.14). Puso *et al.* [177] combines second order finite element approximations with a piece-wise linear Lagrange multiplier to ensure (4.14), which yields $q = p$ and therefore optimal convergence rates according to (4.31) can still be expected as demonstrated by numerical experiments in Popp *et al.* [170].

4.1.2 Biorthogonal Lagrange Multipliers for Finite Elments

Biorthogonal or dual Lagrange multiplier bases as introduced by Wohlmuth [233] for domain decomposition problems, aim at simplifying the coupling conditions by choosing the Lagrange multiplier ansatz functions ϕ_i such that $\mathbf{D}$ has a diagonal structure. To that end, it is again assumed that every node on the slave surface carries a discrete Lagrange multiplier value, i.e., $\mathcal{L} = \mathcal{S}$. A diagonal coupling matrix $\mathbf{D}$ according to (4.10a) is equivalent to

$$\int_{\gamma_{\mathrm{c},h}^{(1)}} \phi_i \bar{N}_j^{(1)} \, \mathrm{d}\gamma = \delta_{ij} c_i \quad , \tag{4.33}$$

with the Kronecker delta δ_{ij} and a constant $c_i > 0$ to ensure (4.11). Note that for contact problems, this biorthogonality has to hold as an integral over the displaced contact boundary $\gamma_{\mathrm{c},h}^{(1)}$, whereas in domain decomposition problems (4.28), it can be enforced on the $\Gamma_{\mathrm{c},h}^{(1)}$. Different methods to construct such dual bases exist. In the most simple one, where the dual basis functions have the same support as their primal counterparts, the dual basis fulfills a partition of unity and are constructed via element-wise linear combinations of the primal shape functions, see e.g. Flemisch and Wohlmuth [74], Lamichhane and Wohlmuth [129], Lamichhane *et al.* [130], Wohlmuth [234]. This can be achieved by enforcing the biorthogonality indepenently on each slave surface element $\tau_{\Gamma,h,k}^{(1)}$, i.e.

$$\int_{\tau_{\Gamma,h,k}^{(1)}} \phi_i \bar{N}_j^{(1)} \,\mathrm{d}\gamma = \delta_{ij} \int_{\tau_{\Gamma,h,k}^{(1)}} \bar{N}_i^{(1)} \,\mathrm{d}\gamma \quad , \tag{4.34}$$

and construct the dual basis functions ϕ_i as linear combinations of the primal ones $\bar{N}_j$:

$$\phi_i|_{\tau_{\Gamma,h,k}^{(1)}} = a_{ij}^{\tau_{\Gamma,h,k}^{(1)}} \bar{N}_j^{(1)}|_{\tau_{\Gamma,h,k}^{(1)}} \quad , \qquad \boldsymbol{A}_{\tau_{\Gamma,h,k}^{(1)}} = [a_{ij}^{\tau_{\Gamma,h,k}^{(1)}}] \in \Re^{n_{\mathrm{nod}}^{\tau_{\Gamma,h,k}^{(1)}} \times n_{\mathrm{nod}}^{\tau_{\Gamma,h,k}^{(1)}}} \quad , \tag{4.35}$$

where $n_{\mathrm{nod}}^{\tau_{\Gamma,h,k}^{(1)}}$ denotes the number of nodes associated with the slave surface element $\tau_{\Gamma,h,k}^{(1)}$ and the coefficient matrix for said element

$$\boldsymbol{A}_{\tau_{\Gamma,h,k}^{(1)}} = \boldsymbol{D}_{\tau_{\Gamma,h,k}^{(1)}} \boldsymbol{M}_{\tau_{\Gamma,h,k}^{(1)}}^{-1} \quad , \tag{4.36a}$$

$$\boldsymbol{D}_{\tau_{\Gamma,h,k}^{(1)}} = [d_{ij}^{\tau_{\Gamma,h,k}^{(1)}}] \,, \quad d_{ij}^{\tau_{\Gamma,h,k}^{(1)}} = \delta_{ij} \int_{\tau_{\Gamma,h,k}^{(1)}} \bar{N}_i^{(1)} \,\mathrm{d}\gamma \quad , \tag{4.36b}$$

$$\boldsymbol{M}_{\tau_{\Gamma,h,k}^{(1)}} = [m_{ij}^{\tau_{\Gamma,h,k}^{(1)}}] \,, \quad m_{ij}^{\tau_{\Gamma,h,k}^{(1)}} = \int_{\tau_{\Gamma,h,k}^{(1)}} \bar{N}_i^{(1)} \bar{N}_j^{(1)} \,\mathrm{d}\gamma \quad , \qquad i,j = 1,\ldots,n_{\mathrm{nod}}^{\tau_{\Gamma,h,k}^{(1)}} \,. \tag{4.36c}$$

To ensure biorthogonality in the displaced configuration, also the integration of the element matrices $\boldsymbol{D}_{\tau_{\Gamma,h,k}^{(1)}}$ and $\boldsymbol{M}_{\tau_{\Gamma,h,k}^{(1)}}$ has to be performed in the displaced state. A direct consequence of this construction of the biorthogonal basis functions is that if the primal basis functions $\bar{N}_i^{(1)}$ form a partition of unity so do the dual basis functions ϕ_i, and therefore their reproduction (4.30) yields at least $q = 1$. For higher order finite elements, Lamichhane and Wohlmuth [129] prove that a higher reproduction order of the presented dual basis can be obtained if the elements are constructed using Gauß–Lobatto nodes. For quadratic finite elements, this means locating the nodes on edges, faces and inside the element symmetrically, as it is the natural choice, cf. Figure 2.5. Finally, for the mean value of ϕ_i, one obtains as

$$\int_{\gamma_{\mathrm{c},h}^{(1)}} \phi_i \,\mathrm{d}\gamma = \int_{\gamma_{\mathrm{c},h}^{(1)}} \bar{N}_i^{(1)} \,\mathrm{d}\gamma \quad , \tag{4.37}$$

and hence (4.14) requires a positive mean value of $\bar{N}_i^{(1)}$. As already discussed in the context of standard mortar methods (cf. Section 4.1.1), this may not always be the case for higher order finite elements which necessitates a basis transformation as proposed by Popp *et al.* [170], Wohlmuth *et al.* [232].

The use of dual basis functions for the Lagrange multiplier brings two major advantages. For one, nodally decoupled constraints emanate consistently from the variational inequality (4.5) as discussed in Remark 4.1. Moreover, (4.34) directly results in a diagonal structure of the mortar matrix $\mathbf{D}$ in (4.10a) and so its inverse is cheaply obtained and sparse. This fact can be used to eliminate the discrete Lagrange multiplier increments $\Delta\boldsymbol{\lambda}$ from the linearized system of equations solved in each Newton step. For contact problems, solving the second line in (4.25) for the multiplier increment yields

$$\Delta\boldsymbol{\lambda} = -\frac{1}{a_\mathrm{c}}\mathbf{D}^{-\mathsf{T}}\left(\breve{\mathbf{K}}_{\mathrm{uu},\mathcal{S}}\Delta\mathbf{d} + \boldsymbol{r}_{\mathrm{u},\mathcal{S}}\right) \quad , \tag{4.38}$$

which can be used to eliminate $\Delta\boldsymbol{\lambda}$ from the remaining lines in (4.25) and results in the reduced linear system

$$\begin{bmatrix} \mathbf{K}_{\mathrm{uu},\mathcal{N}} \\ \breve{\mathbf{K}}_{\mathrm{uu},\mathcal{M}} + \mathbf{P}^{\mathsf{T}}\breve{\mathbf{K}}_{\mathrm{uu},\mathcal{S}} \\ \mathbf{C}_\mathrm{u} - \frac{1}{a_\mathrm{c}}\mathbf{C}_{\boldsymbol{\lambda}}\mathbf{D}^{-\mathsf{T}}\breve{\mathbf{K}}_{\mathrm{uu},\mathcal{S}} \end{bmatrix} \Delta\mathbf{d} = -\begin{bmatrix} \boldsymbol{r}_{\mathrm{u},\mathcal{N}} \\ \boldsymbol{r}_{\mathrm{u},\mathcal{M}} + \mathbf{P}^{\mathsf{T}}\boldsymbol{r}_{\mathrm{u},\mathcal{S}} \\ \boldsymbol{G}_\mathrm{c} - \mathbf{C}_{\boldsymbol{\lambda}}\frac{1}{a_\mathrm{c}}\mathbf{D}^{-\mathsf{T}}\boldsymbol{r}_{\mathrm{u},\mathcal{S}} \end{bmatrix} \quad , \tag{4.39}$$

with the mortar projection matrix $\mathbf{P} = \mathbf{D}^{-1}\mathbf{M}$. In contrast to (4.25), the condensed linear system (4.39) contains the discrete displacement unknowns $\Delta\mathbf{d}$ only and is positive definite, whereas (4.25) is of saddle-point structure. Having solved this reduced linear system, the Lagrange multiplier increment $\Delta\boldsymbol{\lambda}$ can be recovered using (4.38).

In mesh tying problems, dual Lagrange multipliers not only allow for the condensation of the discrete Lagrange multipliers, but also the displacement unknowns on the slave side of the interface. For that purpose, the second line of (4.29) is solved for the $\Delta\boldsymbol{\lambda}$ and the last line for $\Delta\mathbf{d}_\mathcal{S}$ to obtain

$$\Delta\boldsymbol{\lambda} = -\frac{1}{a_\mathrm{c}}\mathbf{D}_0^{-\mathsf{T}}\left(\mathbf{K}_{\mathrm{uu},\mathcal{SN}}\Delta\mathbf{d}_\mathcal{N} + \mathbf{K}_{\mathrm{uu},\mathcal{SS}}\Delta\mathbf{d}_\mathcal{S} + \mathbf{K}_{\mathrm{uu},\mathcal{SM}}\Delta\mathbf{d}_\mathcal{M} + \boldsymbol{r}_{\mathrm{u},\mathcal{S}}\right) \tag{4.40a}$$

$$\Delta\mathbf{d}_\mathcal{S} = \mathbf{P}_0\Delta\mathbf{d}_\mathcal{M} \quad , \tag{4.40b}$$

with the mortar projection matrix $\mathbf{P}_0 = \mathbf{D}_0^{-1}\mathbf{M}_0$. These expressions can then be used to eliminate $\Delta\boldsymbol{\lambda}$ and $\Delta\mathbf{d}_\mathcal{S}$ from (4.29). The condensed linear system to be solved then reads

$$\begin{bmatrix} \mathbf{K}_{\mathrm{uu},\mathcal{NN}} & \mathbf{K}_{\mathrm{uu},\mathcal{NM}} + \mathbf{K}_{\mathrm{uu},\mathcal{NS}}\mathbf{P}_0 \\ \mathbf{K}_{\mathrm{uu},\mathcal{MN}} + \mathbf{P}_0^{\mathsf{T}}\mathbf{K}_{\mathrm{uu},\mathcal{SN}} & \mathbf{K}_{\mathrm{uu},\mathcal{MM}} + \mathbf{P}_0^{\mathsf{T}}\mathbf{K}_{\mathrm{uu},\mathcal{SS}}\mathbf{P}_0 \end{bmatrix} \begin{bmatrix} \Delta\mathbf{d}_\mathcal{N} \\ \Delta\mathbf{d}_\mathcal{M} \end{bmatrix} = -\begin{bmatrix} \boldsymbol{r}_{\mathrm{u},\mathcal{N}} \\ \boldsymbol{r}_{\mathrm{u},\mathcal{M}} + \mathbf{P}_0^{\mathsf{T}}\boldsymbol{r}_{\mathrm{u},\mathcal{S}} \end{bmatrix} \quad . \tag{4.41}$$

Unlike (4.29), a saddle-point system containing Lagrange multipliers, this condensed linear system contains displacement degrees of freedom only and is positive definite. If, moreover, the original tangent matrix $\mathbf{K}_\mathrm{uu}$ is symmetric, so is the condensed system (4.41).

4.1.3 Piece-wise Constant Lagrange Multipliers for Quadratic Finite Elements

This section introduces an alternative Lagrange multiplier space, that allows for the condensation of the discrete Lagrange multiplier degrees of freedom and yields optimal convergence results

for contact problems under uniform mesh refinement without the necessity of constructing a biorthogonal basis. Thus, it combines all the advantages of standard and dual mortar methods.

In a first observation, (4.31) reveals, that a reproduction order $q = 1$ for the Lagrange multiplier is already sufficient to obtain convergence of order $\mathcal{O}(h^{3/2})$ in the H^1-norm, which, due to the lower regularity of the solution $\boldsymbol{u}$ is considered optimal for contact problems [232]. Arguably the simplest way to ensure reproduction order $q = 1$ is to use constant Lagrange multipliers on each slave element, resulting in a globally piece-wise constant approximation. Interestingly, this was one of the first segment-to-segment contact algorithms proposed by Simo *et al.* [207]. Therein, however, this piece-wise constant Lagrange multiplier is combined with first order finite elements which is not an inf-sup-stable pair [18]. Recently, Brivadis *et al.* [21] combined piece-wise constant Lagrange multipliers with quadratic splines in isogeometric analysis and proved stability for that pair. Without giving a formal proof, this stability should also apply to quadratic finite elements of $\mathbb{Q}_2$, since for regular meshes, the quadratic spline space is included in $\mathbb{Q}_2$, and numerical experiments confirm this stability.

4.1.3.1 The Lagrange Multiplier Space

To formalize the method, let $\Omega_0^{(1)}$ be meshed with $\mathbb{Q}_2$, $\mathbb{T}_2$ or $\mathbb{P}_2$ elements in two dimensions or $\mathbb{Q}_2$ elements in three dimensions. In the two dimensional case, $\tau_{\Gamma,h,i}^{(1)}$ then represents a three node quadratic line element with the Lagrange polynomial ansatz functions depicted in Figure 2.4b. It is observed that the ansatz functions $\bar{N}_i^{(1)}$ corresponding to the center node of the line at $\xi = 0$ (i.e. $N_3^{(\tau_h)}$ in Figure 2.4b) is only supported on one slave surface element and hence represents a bubble function on $\gamma_{\mathrm{c},h}^{(1)}$. In the three dimensional case, the same holds for the center node for $\mathbb{Q}_2$ surfaces (cf. Figure 2.5d) emanating as slave surface elements in a three dimensional problem with $\mathbb{Q}_2$ finite elements in the bulk discretization.

Instead of associating discrete Lagrange multiplier values with every node on the slave surface $\mathcal{S}$, now one discrete Lagrange multiplier value $\boldsymbol{\lambda}_i$ is set for every slave surface element $\tau_{\Gamma,h,i}^{(1)}$ and the discrete multiplier field is given by (4.6) with ansatz functions

$$\phi_i(\boldsymbol{X}) = \begin{cases} 1 & \text{if } \boldsymbol{X} \in \tau_{\Gamma,h,i}^{(1)} \\ 0 & \text{else} \end{cases} . \tag{4.42}$$

These ansatz functions obviously satisfy (4.14) and, for isoparametric finite elements (see Section 2.8.1.1 and Hughes [111, Section 3.3]), also (4.11).

Formally, the vector of nodal displacements on the slave surface can be split into the displacements of the boundary bubble functions $\mathbf{d}_{\mathcal{S}_\odot}$ and those of the skeleton $\mathbf{d}_{\mathcal{S}_\square}$. With this split of the displacement vector and the corresponding virutal displacements $\delta\mathbf{d}$, the linear system of a mortar contact problem with Lagrange multipliers (4.25) reads

$$\begin{bmatrix} \mathbf{K}_{\mathrm{uu},\mathcal{N}} & \mathbf{0} \\ \check{\mathbf{K}}_{\mathrm{uu},\mathcal{S}_\odot} & a_\mathrm{c}\mathbf{D}_\odot^\mathsf{T} \\ \check{\mathbf{K}}_{\mathrm{uu},\mathcal{S}_\square} & a_\mathrm{c}\mathbf{D}_\square^\mathsf{T} \\ \check{\mathbf{K}}_{\mathrm{uu},\mathcal{M}} & -a_\mathrm{c}\mathbf{M}^\mathsf{T} \\ \mathbf{C}_\mathrm{u} & \mathbf{C}_{\boldsymbol{\lambda}} \end{bmatrix} \begin{bmatrix} \Delta\mathbf{d} \\ \Delta\boldsymbol{\lambda} \end{bmatrix} = - \begin{bmatrix} \boldsymbol{r}_{\mathrm{u},\mathcal{N}} \\ \boldsymbol{r}_{\mathrm{u},\mathcal{S}_\odot} \\ \boldsymbol{r}_{\mathrm{u},\mathcal{S}_\square} \\ \boldsymbol{r}_{\mathrm{u},\mathcal{M}} \\ \boldsymbol{G}_\mathrm{c} \end{bmatrix} , \tag{4.43}$$

with the mortar matrices $\mathbf{D} = [\mathbf{D}_\odot, \mathbf{D}_\square]$ and $\mathbf{M}$ as defined in (4.10). Unlike the previous methods of Sections 4.1.1 and 4.1.2 which used $\mathcal{L} = \mathcal{S}$, the matrix $\mathbf{D}$ is now no longer square but rectangular. However, the combination of element-wise constant Lagrange multipliers (4.42) with the bubble functions corresponding to the nodes in $\mathcal{S}_\odot$ results in a diagonal structure of $\mathbf{D}_\odot$. Thus, the second line of 4.43 can be easily solved for the increments of the Lagrange multiplier

$$\Delta\boldsymbol{\lambda} = -\frac{1}{a_\mathrm{c}}\mathbf{D}_\odot^{-\mathsf{T}}\left(\breve{\mathbf{K}}_{\mathrm{uu},\mathcal{S}_\odot}\Delta\mathbf{d} + \boldsymbol{r}_{\mathrm{u},\mathcal{S}_\odot}\right) \quad , \tag{4.44}$$

similar to (4.38) in the case of dual Lagrange multipliers. This, in turn, can be used in the remaining lines of (4.43) to eliminate $\Delta\boldsymbol{\lambda}$ finally resulting in the condensed linear system

$$\begin{bmatrix} \mathbf{K}_{\mathrm{uu},\mathcal{N}} \\ \mathbf{K}_{\mathrm{uu},\mathcal{S}_\square} - \mathbf{P}_\square^{\mathsf{T}}\breve{\mathbf{K}}_{\mathrm{uu},\mathcal{S}_\odot} \\ \breve{\mathbf{K}}_{\mathrm{uu},\mathcal{M}} + \mathbf{P}_\mathcal{M}^{\mathsf{T}}\breve{\mathbf{K}}_{\mathrm{uu},\mathcal{S}_\odot} \\ \mathbf{C}_\mathrm{u} - \frac{1}{a_\mathrm{c}}\mathbf{C}_{\boldsymbol{\lambda}}\mathbf{D}_\odot^{-\mathsf{T}}\breve{\mathbf{K}}_{\mathrm{uu},\mathcal{S}_\odot} \end{bmatrix}\Delta\mathbf{d} = \begin{bmatrix} \boldsymbol{r}_{\mathrm{u},\mathcal{N}} \\ \boldsymbol{r}_{\mathrm{u},\mathcal{S}_\square} - \mathbf{P}_\square^{\mathsf{T}}\boldsymbol{r}_{\mathrm{u},\mathcal{S}_\odot} \\ \boldsymbol{r}_{\mathrm{u},\mathcal{M}} + \mathbf{P}_\mathcal{M}^{\mathsf{T}}\boldsymbol{r}_{\mathrm{u},\mathcal{S}_\odot} \\ \boldsymbol{G}_\mathrm{c} - \frac{1}{a_\mathrm{c}}\mathbf{C}_{\boldsymbol{\lambda}}\mathbf{D}_\odot^{-\mathsf{T}}\boldsymbol{r}_{\mathrm{u},\mathcal{S}_\odot} \end{bmatrix} \quad , \tag{4.45}$$

with the two matrices $\mathbf{P}_\square = \mathbf{D}_\odot^{-1}\mathbf{D}_\square$ and $\mathbf{P}_\mathcal{M} = \mathbf{D}_\odot^{-1}\mathbf{M}$. For mesh tying problems, of course not only the discrete Lagrange multipliers but also the displacement unknowns $\mathbf{d}_{\mathcal{S}_\odot}$ can be condensed from the global system of equations analogously to (4.41).

Remark 4.2. *The proposed element-wise constant Lagrange multiplier for quadratic finite elements can be extended further to higher approximation orders p, by taking piece-wise, element-discontinuous $(p-2)$-polynomials for the Lagrange multiplier. For instance in a two-dimensional problem with third order polynomials, every element on the slave side (i.e. a line) is discretized with third order Lagrange polynomials which contain two bubble functions that are only supported on the specific slave element. Now taking an element-wise discontinuous linear Lagrange multiplier yields block-diagonal matrix $\mathbf{D}_\odot$ consisting of 2×2-blocks for each element that is still cheap to invert. For any polynomial order $p \geq 2$, the Lagrange multiplier can therefore be chosen of reproduction order $q = p - 1$ and, according to* (4.31)*, convergence orders $\mathcal{O}(h^{p-1/2})$ can be achieved, given sufficient regularity of the solution. As contact problems, however, do not provide this regularity, higher order approximations are not pursued further at this point.*

4.1.3.2 Numerical Examples

To validate the approach of using element-wise constant Lagrange multipliers for quadratic finite elements, several numerical examples are presented in the following and results are compared to standard and dual mortar methods.

4.1.3.2.1 Mesh tying – Infinite Plate with a Circular Hole First, a two-dimensional mesh tying example, the well-known and wide-spread benchmark of an infinite plate with a circular hole, is studied for which an analytical solution exists, see e.g. Apostolatos *et al.* [6]. In the framework of linear elasticity applied for this example, the Cauchy stress $\boldsymbol{\sigma} = 2\mu\boldsymbol{\varepsilon} + \lambda\,\mathrm{tr}\,\boldsymbol{\varepsilon}\boldsymbol{I}$ depends linearly on the linearized strain $\boldsymbol{\varepsilon} = {}^1\!/_2(\nabla_{\boldsymbol{X}}\boldsymbol{u} + (\nabla_{\boldsymbol{X}}\boldsymbol{u})^{\mathsf{T}})$ via the Lamé parameters $\mu = \frac{E}{2(1+\nu)}$ and $\lambda = \frac{E\nu}{(1+\nu)(1-2\nu)}$. At an infinite distance from the hole, a constant traction $\boldsymbol{t}_\infty = [t_\infty, 0]^{\mathsf{T}}$ in x-direction is applied. For the numerical analysis, the geometry is cut and

the exact traction is applied as a boundary condition and, moreover, only one quarter is analyzed with appropriate symmetry conditions. The geometric setup as well as the material properties are given in Figure 4.3a. The domain is cut by the diagonal interface Γ_c into two sub-domains

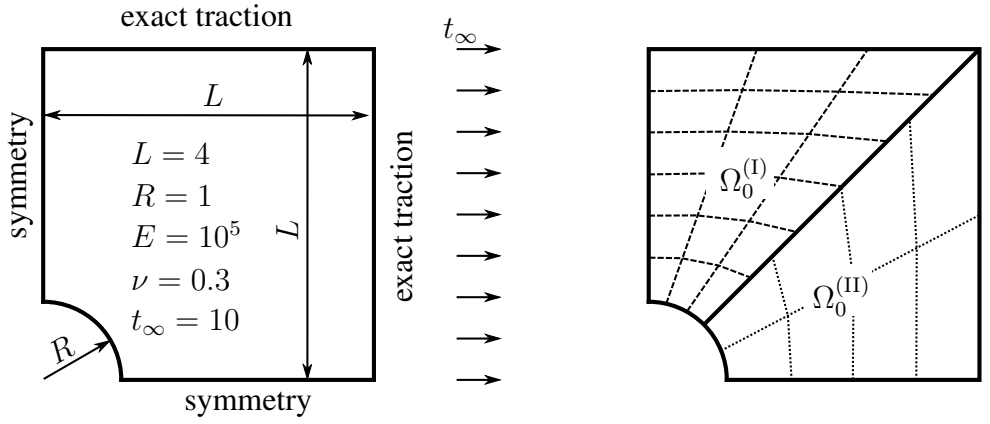

(a) Problem setup.

(b) Coarsest mesh, nomralized mesh size $\bar{h} = 1$.

Figure 4.3: Infinite plate with a circular hole – Geometry and material properties as well as coarsest mesh with a ratio 3 : 2.

$\Omega_0^{(\mathrm{I})}$ and $\Omega_0^{(\mathrm{II})}$, which, on the coarsest level are discretized with 3×6 and 2×4 quadratic $\mathbb{Q}_2$ finite elements, respectively. Starting from this mesh, uniform mesh refinement is performed and convergence is monitored in the energy norm

$$\|\boldsymbol{u} - \boldsymbol{u}_h\|_E = \sqrt{\sum_i \int_{\Omega_0^{(i)}} \boldsymbol{\sigma}(\boldsymbol{u} - \boldsymbol{u}_h) : \boldsymbol{\varepsilon}(\boldsymbol{u} - \boldsymbol{u}_h) \, \mathrm{d}\Omega} \ , \tag{4.46}$$

an equivalent norm to the H^1-norm, considered in (4.31). The convergence results are summarized in Figure 4.4 once choosing the finer mesh of $\Omega_0^{(\mathrm{I})}$ as the slave side (Figure 4.4a) and once choosing the coarser mesh of $\Omega_0^{(\mathrm{II})}$ as the slave side (Figure 4.4b). As a reference, the results of the standard and dual mortar methods of Sections 4.1.1 and 4.1.2 are included. Both these references exhibit optimal convergence orders $\mathcal{O}(h^2)$, as they provide the full reproduction order $q = p + 1$; the standard mortar method by nature and the dual mortar method since the nodes are chosen as Gauß–Lobatto nodes, putting the interior nodes of faces centered between the element corners which yields optimal convergence results according to Lamichhane and Wohlmuth [129]. Focusing on the piece-wise constant Lagrange multiplier interpolation, convergence of $\mathcal{O}(h^2)$ is observed if the slave side is chosen as the finer side (Figure 4.4a) with an error level sightly higher than for the standard or dual mortar method. The convergence order $\mathcal{O}(h^2)$ thereby exceeds the theoretical prediction of $\mathcal{O}(h^{3/2})$. In the case of a coarse slave side (Figure 4.4b), the convergence order of the piece-wise constant Lagrange multiplier deviates more significantly from the standard and dual mortar method and tends towards the predicted value $\mathcal{O}(h^{3/2})$ for fine meshes. For mesh tying problems, it is therefore advisable to choose the finer side as the slave side when working with piece-wise constant Lagrange multipliers.

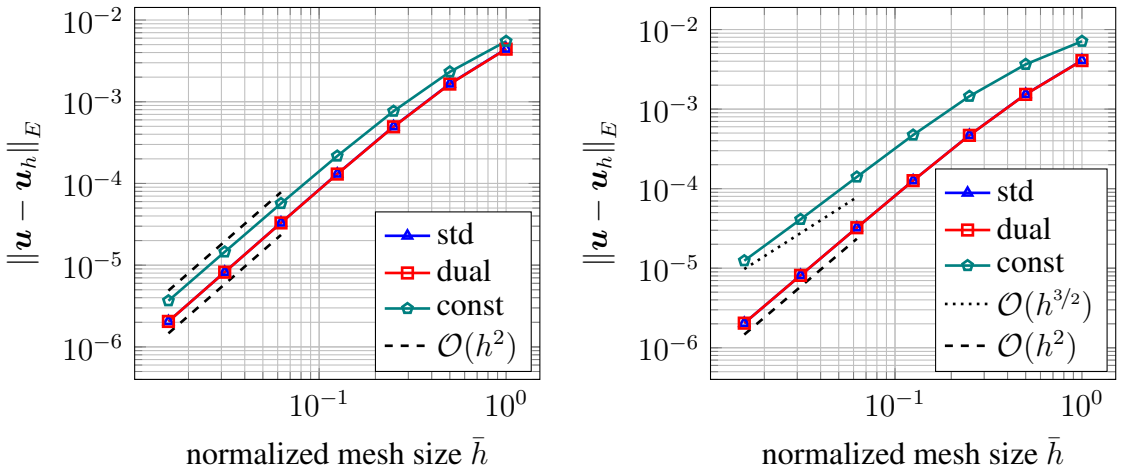

(a) Mesh ratio $s : m = 3 : 2$.

(b) Mesh ratio $s : m = 2 : 3$.

Figure 4.4: Infinite plate with a circular hole – Spatial convergence for $\mathbb{Q}_2$ finite elements standard ('std'), dual ('dual') or piece-wise constant ('const') Lagrange multipliers. For the mesh ratio $s : m = 3 : 2$, $\Omega_0^{(\mathrm{I})}$ is chosen the slave side, and for the mesh ratio $s : m = 2 : 3$, $\Omega_0^{(\mathrm{II})}$ is chosen the slave side (cf. Figure 4.3b).

4.1.3.2.2 Two-dimensional Contact – Convergence Study As observed in the previous example, the piece-wise constant Lagrange multiplier approximation ensures at least convergence orders $\mathcal{O}(h^{3/2})$ and hence are supposed to yield optimal convergence results for contact problems. To verify this expected behavior, the two-dimensional frictionless contact of a cylindrical arc with a rectangular block as defined in Figure 4.5a is investigated.

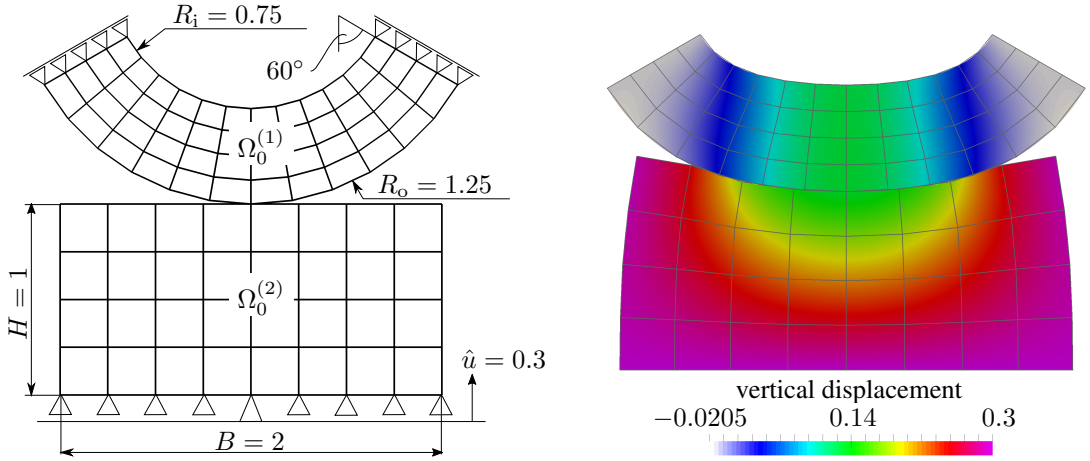

(a) Initial geometry, boundary conditions and exemplary mesh with $h = 2^{-2}$.

(b) Deformed mesh for $h = 2^{-2}$ and $\mathbb{Q}_2$ finite elements.

Figure 4.5: Two dimensional contact of a circular arc with a rectangle – Geometric setup, exemplary mesh and deformed configuration.

Both $\Omega_0^{(1)}$ and $\Omega_0^{(2)}$ are modeled with a neo–Hookean material (3.38) with $E^{(1)} = 5$, $E^{(2)} = 1$ and $\nu^{(1)} = \nu^{(2)} = 0.3$ under plane strain conditions. Owing to the obvious symmetry of

the problem, one half is solved with appropriate symmetry conditions. Despite the fact, that *a priori* estimates are only given for linearized kinematics, large deformations are applied by moving the lower edge of the rectangle upwards while keeping lateral motion unconstrained. The final, displaced configuration is depicted in Figure 4.5b. Obviously, no analytical solution exists for this finitely deforming contact problem, such that errors are computed versus a numeric reference solution obtained with using a very fine mesh of $h = 2^{-8}$ and $\mathbb{Q}_2$ finite elements with dual Lagrange multipliers. Figure 4.6 displays the obtained convergence results for $h \in$

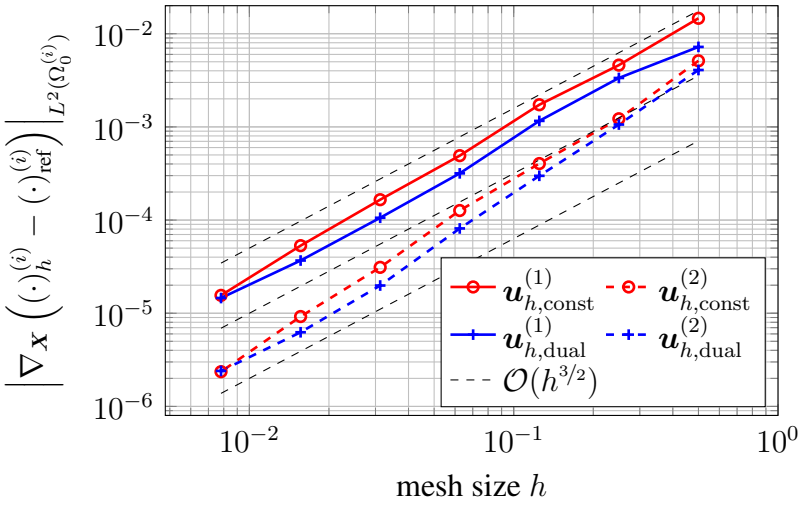

Figure 4.6: Two dimensional contact of a circular arc with a rectangle – Spatial convergence of the displacements of the slave and master body in the H^1 semi-norm using dual (denoted as 'dual') and piece-wise constant (denoted as 'const') Lagrange multipliers.

$\{2^{-1}, \dots, 2^{-7}\}$ measured in the H^1 semi-norm of the displacements within the two bodies. Both the proposed piece-wise constant Lagrange multiplier and the classical dual mortar method of Section 4.1.2 exhibit optimal convergence of $\mathcal{O}(h^{3/2})$; only the finest mesh deviates from the expected order for both methods, since the employed mesh of $h = 2^{-7}$ it is too close to the reference solution of $h = 2^{-8}$. Comparing the piece-wise constant Lagrange multiplier with the dual one, a slightly elevated error level is observed which can be attributed to the use of a smaller Lagrange multiplier space. However, this marginally increased error level comes at the benefit of not having to construct deformation dependent, biorthogonal basis functions.

To further exemplify the effect of the piece-wise constant Lagrange multiplier, the example is enhanced with Coulomb friction with a friction coefficient of $\mu = 0.25$ and the discrete approximation of the contact traction is investigated. Figure 4.7 displays the discrete representation of the contact traction (i.e. the Lagrange multiplier) over the x-coordinate (horizontal direction in Figure 4.5b) for two relatively coarse meshes as well as the fine reference solution. Note the transition between stick and slip at $|x| \approx 0.2$ in the reference solution. While the coarser mesh $h = 2^{-2}$ exhibits larger discrepancies in the normal contact pressure, the next refined mesh $h = 2^{-3}$ with 14 active Lagrange multipliers already yields a good approximation of the reference data. Naturally, the jump in the discrete Lagrange multiplier values across element edges reduces further with mesh refinement.

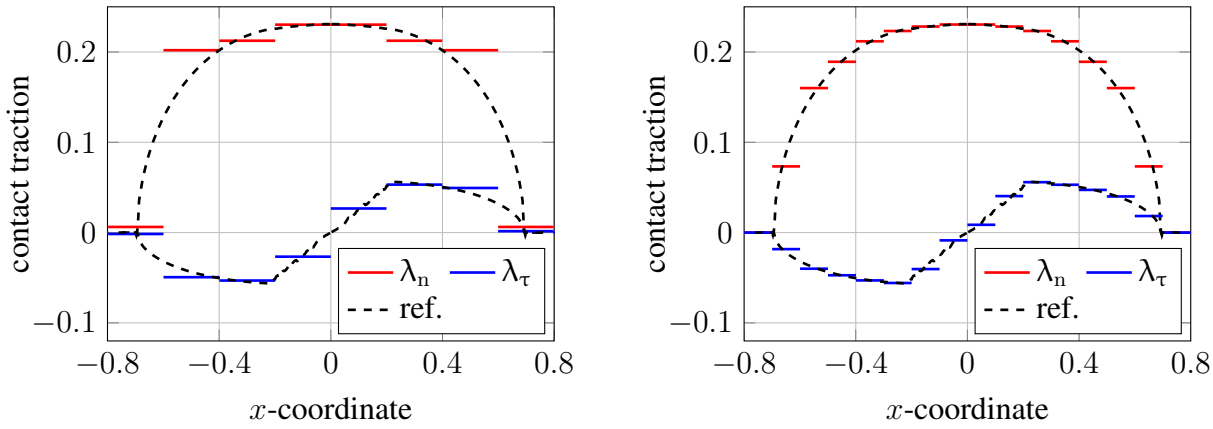

(a) $h = 2^{-2}$. (b) $h = 2^{-3}$.

Figure 4.7: Two dimensional contact of a circular arc with a rectangle – Discrete solution of the normal and tangential Lagrange multiplier compared to the reference solution obtained using dual Lagrange multipliers and $h = 2^{-7}$.

4.1.3.2.3 Three-dimensional Contact – Ironing Example Finally, the extension to three-dimensional contact problems is demonstrated by an example introduced in Popp *et al.* [169], Popp [171] for frictionless contact using first and second order finite elements and also analyzed by Gitterle [79] for frictional contact using first order finite elements. The quasi-static contact of a cylindrical shell $\Omega_0^{(2)}$ of internal radius 3, thickness 0.2 and height 5.2 with a cuboid $\Omega_0^{(1)}$ of size $9 \times 4 \times 3$ is analyzed. As shown in Figure 4.8a, the two bodies are discretized with $24 \times 5 \times 1$

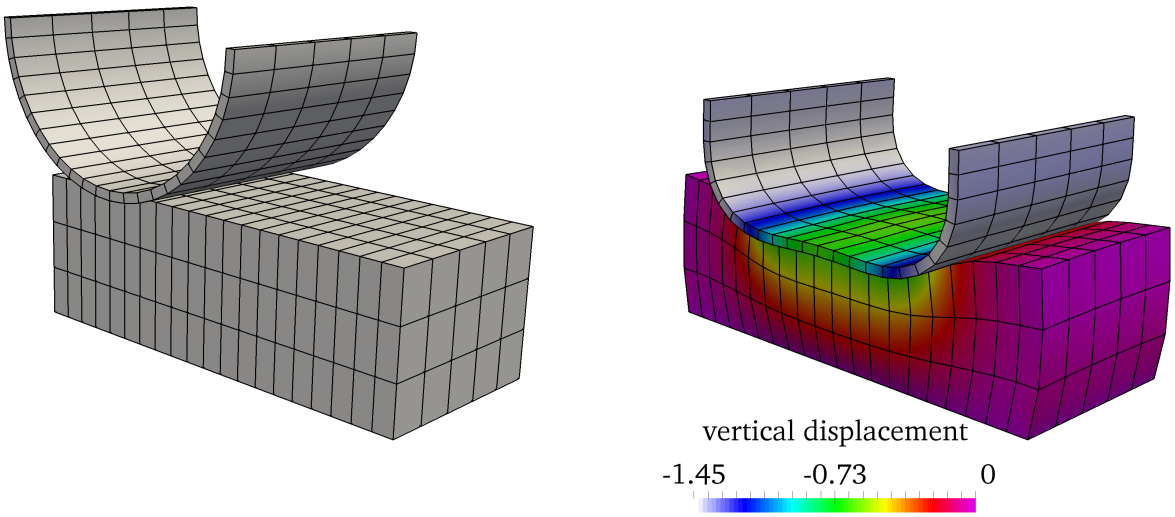

(a) Initial geometry and applied mesh. (b) Deformed configuration in step 85.

Figure 4.8: Three-dimensional ironing problem – Initial mesh and exemplary deformed configuration.

and $20 \times 5 \times 3$ quadratic $\mathbb{Q}_2$ finite elements respectively. As given in [169], both bodies are modeled with a neo–Hookean material (3.38) with $E^{(1)} = 1$, $E^{(2)} = 1000$ and $\nu^{(1)} = \nu^{(2)} = 0.3$. Within the first 20 time steps, a prescribed vertical displacement of 1.4 is applied to the top sur-

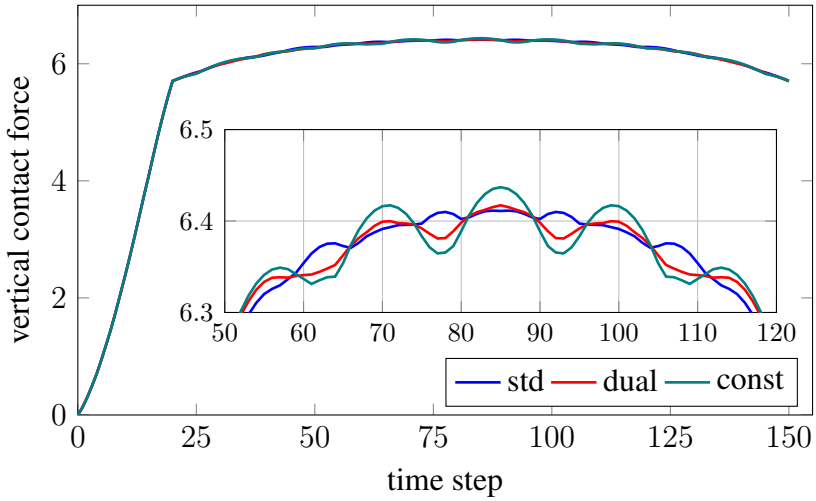

Figure 4.9: Three-dimensional ironing problem – Evolution of vertical contact force over time for the standard (denoted as 'std'), dual (denoted as 'dual') and piece-wise constant (denoted as 'const') Lagrange multipliers.

faces of the cylinder. Subsequently, a horizontal movement of 4 in direction of the longest edge of the cuboid is applied in 130 steps. Both motions are applied in equidistant increments. The cuboid is deliberately chosen as the slave body, such that the contact location moves relative to the Lagrange multiplier mesh. Figure 4.9 displays the vertical contact force over time for different Lagrange multiplier discretizations, namely the standard approach of Section 4.1.1, the dual mortar method of Section 4.1.2 and the newly proposed piece-wise constant Lagrange multiplier. Depending on the position of the contact patch relative to the Lagrange multiplier mesh, all methods exhibit marginal oscillations in the total contact force. For the piece-wise constant Lagrange multiplier, these oscillations are slightly larger compared to the other methods which can again be attributed to the smaller Lagrange multiplier space. Yet, the piece-wise constant Lagrange multiplier presents a competitive alternative to dual mortar methods since it allows for the same condensation of the Lagrange multiplier values without the necessity to construct deformation dependent biorthogonal basis functions.

4.1.4 Biorthogonal Lagrange Multipliers for Isogeometric Analysis[1]

In isogeometric analysis, the geometry and solution field are discretized using spline basis functions, most commonly NURBS as introduced in Section 2.8.1.2. In a two-dimensional example, the (slave) contact boundary and the displacement thereof may then, for instance, be discretized by the ansatz functions depicted in Figure 2.6. Mortar methods for isogeometric analysis can then be constructed similar to discretizations based on classical finite elements, e.g. using standard or dual basis functions as introduced in Sections 4.1.1 and 4.1.2, respectively. Brivadis *et al.* [21] mathematically analyzes the standard mortar method in the context of domain decomposition and additionally proposes the use of lower order spline spaces for the Lagrange multiplier. Applications of the standard mortar method to isogeometric contact problems are presented, e.g.,

[1] This section is adapted from the author's publication [193].

in De Lorenzis *et al.* [51], Kim and Youn [121]. This section now focuses on the extension of the biorthogonal basis introduced in Section 4.1.2 to isogeometric analysis.

4.1.4.1 The Lagrange Multiplier Space

Although splines, and NURBS in particular, are defined not on elements but on entire patches, a notion of elements can still be applied as discussed in Section 2.8.1.2. To summarize the definition of elements in the context of NURBS-based IGA, an element boundary is defined by a non-zero interval in the knot vector. On each element $(p+1)^d$ basis functions take non-zero values, with p being the polynomial order of the spline and d the number of parametric directions of the element. In this respect, NURBS discretizations bear great similarities to classical finite elements and consequently, the construction of dual basis functions as linear combinations of primal basis functions independently on each element, as outlined in Section 4.1.2, can be transferred to IGA. A discrete Lagrange multiplier is associated with every control point i on the slave side, i.e. $\mathcal{L} = \mathcal{S}$, and dual NURBS basis functions are constructed that satisfy the biorthogonality

$$\int_{\tau_{\Gamma,h,k}^{(1)}} \phi_i \bar{R}_j^{(1)} \,\mathrm{d}\gamma = \delta_{ij} \int_{\tau_{\Gamma,h,k}^{(1)}} \bar{R}_i^{(1)} \,\mathrm{d}\gamma \quad , \tag{4.47}$$

where $\bar{R}_i^{(1)} = R_i^{(1)}|_{\gamma_{\mathrm{c},h}^{(1)}}$ denotes the restriction of the NURBS function associated with control point i to the contact boundary. The dual NURBS basis functions ϕ_i are obtained via element-wise linear combinations of the primal basis functions by

$$\phi_i|_{\tau_{\Gamma,h,k}^{(1)}} = a_{ij}^{\tau_{\Gamma,h,k}^{(1)}} \bar{R}_j^{(1)}|_{\tau_{\Gamma,h,k}^{(1)}} \quad , \qquad \boldsymbol{A}_{\tau_{\Gamma,h,k}^{(1)}} = [a_{ij}^{\tau_{\Gamma,h,k}^{(1)}}] \in \Re^{n_{\mathrm{cp}}^{\tau_{\Gamma,h,k}^{(1)}} \times n_{\mathrm{cp}}^{\tau_{\Gamma,h,k}^{(1)}}} \quad , \tag{4.48}$$

with $n_{\mathrm{cp}}^{\tau_{\Gamma,h,k}^{(1)}}$ being the number of basis functions taking non-zero values on element $\tau_{\Gamma,h,k}^{(1)}$. Similar to (4.36), the coefficient matrix is obtained by

$$\boldsymbol{A}_{\tau_{\Gamma,h,k}^{(1)}} = \boldsymbol{D}_{\tau_{\Gamma,h,k}^{(1)}} \boldsymbol{M}_{\tau_{\Gamma,h,k}^{(1)}}^{-1} \quad , \tag{4.49a}$$

$$\boldsymbol{D}_{\tau_{\Gamma,h,k}^{(1)}} = [d_{ij}^{\tau_{\Gamma,h,k}^{(1)}}] \,, \quad d_{ij}^{\tau_{\Gamma,h,k}^{(1)}} = \delta_{ij} \int_{\tau_{\Gamma,h,k}^{(1)}} \bar{R}_i^{(1)} \,\mathrm{d}\gamma \quad , \tag{4.49b}$$

$$\boldsymbol{M}_{\tau_{\Gamma,h,k}^{(1)}} = [m_{ij}^{\tau_{\Gamma,h,k}^{(1)}}] \,, \quad m_{ij}^{\tau_{\Gamma,h,k}^{(1)}} = \int_{\tau_{\Gamma,h,k}^{(1)}} \bar{R}_i^{(1)} \bar{R}_j^{(1)} \,\mathrm{d}\gamma \quad , \qquad i,j = 1,\ldots,n_{\mathrm{cp}}^{\tau_{\Gamma,h,k}^{(1)}} \,. \tag{4.49c}$$

Figure 4.10 illustrates an exemplary set of NURBS basis functions and its corresponding dual basis.

Remark 4.3. *For simplicity of presentation, this thesis assumes that the discrete projection $\chi_{h,t}$, i.e. the discrete version of* (2.101)*, exists on the entire slave contact boundary $\gamma_{\mathrm{c},h}^{(1)}$. If this is not the case, the mortar coupling matrices* $\mathbf{D}$ *and* $\mathbf{M}$ *have to be evaluated only on the part of $\gamma_{\mathrm{c},h}^{(1)}$ for which a feasible projection exists, see Cichosz and Bischoff [39], Popp* et al. *[172] for a detailed discussion in the context of first order finite elements. Consequently, also the biorthogonality* (4.48) *has to be guaranteed not on the entire element $\tau_{\Gamma,h,k}^{(1)}$ but the part that has a feasible*

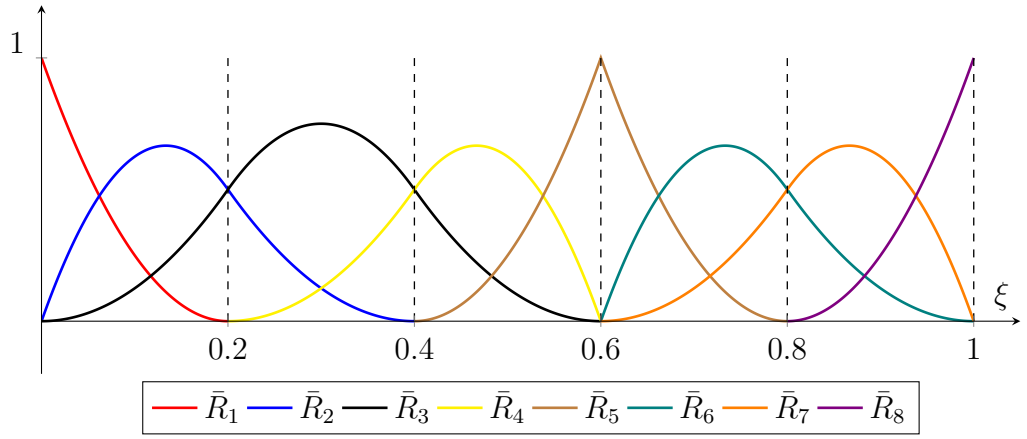

(a) Primal basis

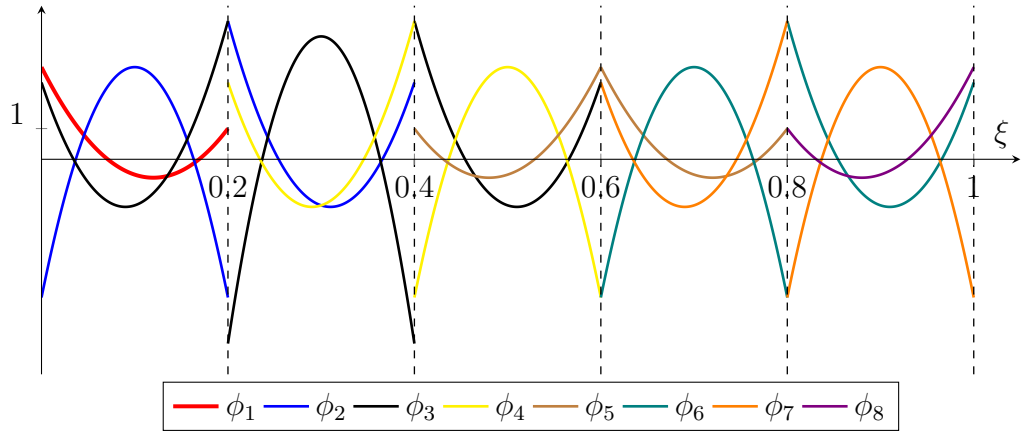

(b) Dual basis

Figure 4.10: Primal and dual B-spline basis functions of degree $p = 2$ on the uniform knot-vector $\Xi = \{0, 0, 0, \frac{1}{5}, \frac{2}{5}, \frac{3}{5}, \frac{3}{5}, \frac{4}{5}, 1, 1, 1\}$. Element boundaries are depicted by dashed lines. The primal basis is reproduced from Figure 2.6.

projection and therefore contributes to the integration of $\mathbf{D}$. *This is achieved by restricting the integrals in* (4.49) *accordingly. For first order finite elements discussed in [39, 172] and NURBS of arbitrary order, regularity of* $\boldsymbol{M}_{\tau_{\Gamma,h,k}^{(1)}}$ *in* (4.49) *is guaranteed by the non-negativity and linear independence of* $\bar{R}_i^{(1)}$. *Second order finite element ansatz functions are not non-negative and, as a consequence, existence of* $\boldsymbol{M}^{-1}_{\tau_{\Gamma,h,k}^{(1)}}$ *cannot be ensured ad hoc. Popp* et al. *[170], Wohlmuth* et al. *[232] introduce a basis transformation to cure this issue for second order finite elements. It is important to note, that no such transformation is necessary for any approximation order in the isogeometric setting.*

It should be pointed out that the dual basis functions generated by (4.48) only guarantee a partition of unity. Consequently, the *global* approximation order q in (4.30) is limited to one, independent of the *local* approximation, i.e. the polynomail degree of the primal NURBS basis. Since the dual NURBS do not possess the optimal reproduction order, optimal convergence rates in domain decomposition applications as proven in Brivadis *et al.* [21] cannot be guaranteed. For dual mortar methods based on Lagrange polynomials optimality can be recovered by

a transformation of the primal basis [129] or by extending the support of the dual basis functions [161]. An extension of the latter approach to NURBS basis functions has been proposed recently by Wunderlich *et al.* [242], Wunderlich [243]. Moreover, Dornisch *et al.* [66] develop approximate dual basis functions with enlarged support that exhibit optimal convergence orders in numerical examples and Zou *et al.* [254] locally refines the master-sided mesh to obtain optimal convergence if matching parametrizations of the slave and master surface are used. For contact problems of linearized kinematics, the solution is typically in $[H^t(\Omega_0^{(i)})]^{n_{\mathrm{dim}}}$ with $t < 5/2$, such that the *a priori* estimate (4.31) is already limited by the regularity of the solution. Even this simple construction of dual basis functions meets the requirements in [232] for optimal *a priori* estimates for the displacements in the H^1-norm of order $\mathcal{O}(h^{3/2})$. Namely, we have

- a partition of unity $\sum_{i\in\mathcal{L}} \phi_i = 1$ by construction; proof see e.g. [74],
- inf-sup stability, see e.g. [128, Remark 2.11],
- a positive mean value of the dual basis function (4.14) on each element $\tau_{\Gamma,h,k}^{(1)}$, since

$$\int_{\tau_{\Gamma,h,k}^{(1)}} \phi_i \,\mathrm{d}\gamma = \int_{\tau_{\Gamma,h,k}^{(1)}} \bar{R}_i \,\mathrm{d}\gamma > 0 \quad \forall i \in \mathcal{L} \tag{4.50}$$

  where the equality directly follows from (4.47) in conjunction with the element-wise construction (4.48), (4.49) together with the partition of unity property of the NURBS basis functions, and the inequality results from the non-negativity of NURBS.

- Finally, a non-negative integral of each dual basis function tested with a primal one

$$\int_{\gamma_{\mathrm{c},h}^{(1)}} \phi_i \bar{R}_j \,\mathrm{d}\gamma \geq 0 \;\; \forall i,j \in \mathcal{L} \;\; , \tag{4.51}$$

  which follows from (4.47) and the non-negativity of the NURBS basis functions $\bar{R}_j$.

These properties, together with a regularity assumption on the shape of the active contact zone gives the optimal a priori estimates [232] for the discrete contact problem. Therefore, the more intricate construction of dual NURBS basis functions with optimal reproduction properties of [66, 242, 243, 254] are not pursued further in this thesis.

4.1.4.2 Numerical Examples

In the following, the proposed isogeometric dual mortar method is investigated in three numerical examples and results are compared to standard isogeometric mortar methods as well as contact formulations based on Lagrange polynomials. In a first example, the isogeometric dual mortar method for domain decomposition is analyzed for linear elasticity. The problem of an infinite plate with a circular hole under tension is simulated to investigate the convergence order in a domain decomposition case and shows predicted reduced convergence order $\mathcal{O}(h^{3/2})$. The second example is a two-dimensional, small deformation, frictionless Hertzian type contact problem against a rigid obstacle. Both spatial convergence orders as well as contact stress representations are analyzed. Due to the switch-over from domain decomposition to unilateral

contact, the reduced regularity of the solution already limits the spatial convergence order. Thus, both standard and dual mortar methods now converge equally optimal at order $\mathcal{O}(h^{3/2})$. Finally, a three dimensional rotating ironing example is simulated to compare the isogeometric formulation to approximations based on Lagrange polynomials of first and second order. This last example incorporates both finite deformations and large frictional sliding.

4.1.4.2.1 Mesh tying – Infinite Plate with a Circular Hole The infinite plate with a circular hole is a common benchmark in (isogeometric) domain decomposition (mesh tying) applications and has been analyzed e.g. in [21, 40, 66, 254]. Here, the same geometric setup and material parameters as in Section 4.1.3.2.1 (cf. Figure 4.3a) is discretized with two different types of meshes; one with a straight interface (Figure 4.11a) whereby the NURBS at the interface reduce to B-splines (i.e. piece-wise polynomials), and one with a circular interface (Figure 4.11b) with an actual NURBS approximation of the interface. For the given geometry

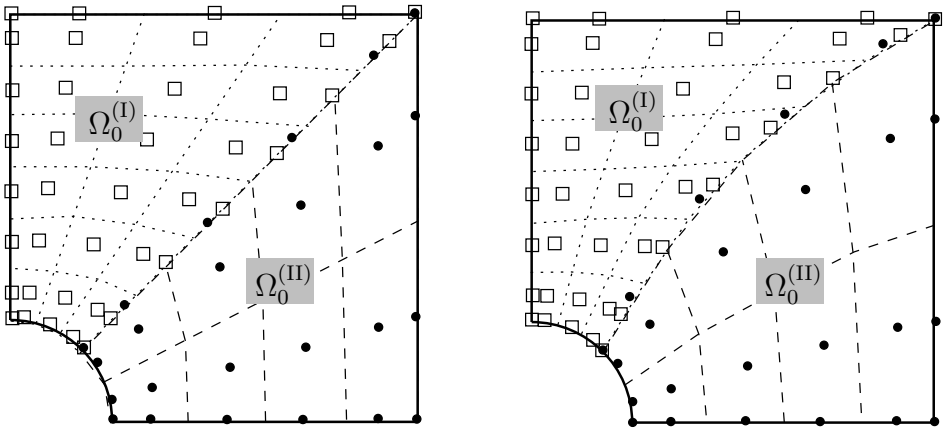

(a) Coarsest mesh, straight interface. (b) Coarsest mesh, curved interface.

Figure 4.11: Infinite plate with a circular hole - Coarsest mesh represented by the control points (dots and boxes) and mesh (dashed and dotted lines) for the two patches of second order NURBS.

a parametrization with a single NURBS patch is only possible using repeated control points as done in [40] which, however, results in a singular point in the inverse mapping at the repeated node. Instead, two patches are used here such that the mapping of the isogeometric surface and its inverse is well defined everywhere within the domain. After uniform knot insertion for both patches an element size ratio of $2:3$ at the interface is reached, see Figure 4.11 for the coarsest levels; this ratio is fixed in the following. Uniform refinement via knot insertion is analyzed for second and third order NURBS basis functions. Note that the two patches do not share any control points at the interface, but the coupling is enforced using the mortar method. Convergence of the approximated solution $\boldsymbol{u}_h$ towards the analytical solution $\boldsymbol{u}$ is assessed in terms of the energy norm (4.46) in which, given the smoothness of the analytical solution, $\mathcal{O}(h^p)$ is the optimal order, whereas for the presented dual Lagrange multiplier basis only $\mathcal{O}(h^{3/2})$ can be guaranteed theoretically for any $p \geq 2$. This is again due to the reduced approximation order of one of the dual Lagrange multiplier basis. Figures 4.12 and 4.13 compare the convergence behavior for standard and dual Lagrange multiplier shape functions for second and third order NURBS and different choices of the slave side for the straight and curved interface, respectively.

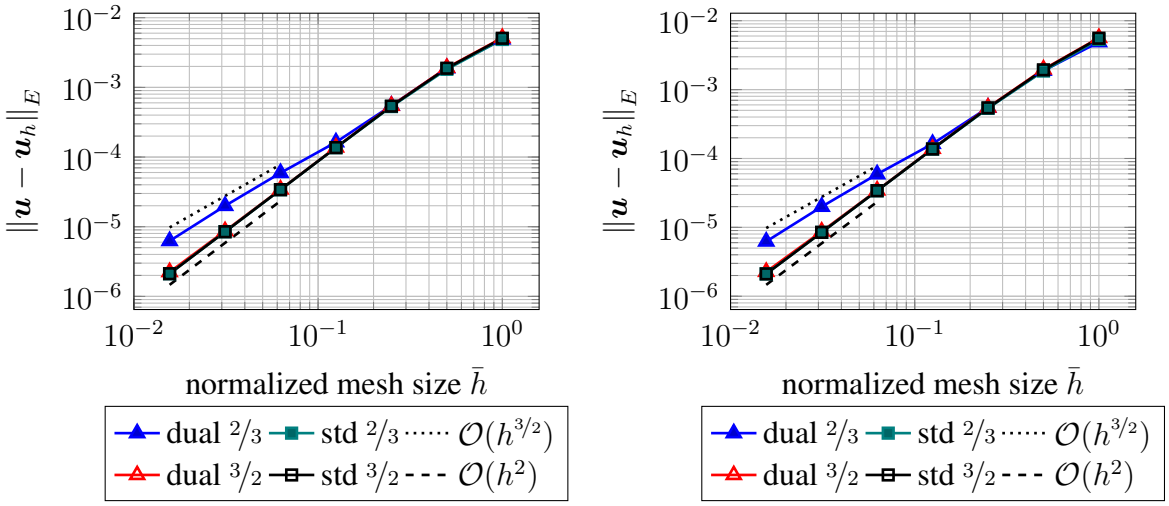

(a) Straight interface. (b) Curved interface.

Figure 4.12: Infinite plate with a circular hole – Spatial convergence for second order NURBS with standard ('std') or dual ('dual') Lagrange multipliers. Fractions indicate the slave to master mesh ratio, i.e., for a ratio of $^3/_2$, $\Omega_0^{(\mathrm{I})}$ is chosen the slave side, and for the mesh ratio $^2/_3$, $\Omega_0^{(\mathrm{II})}$ is chosen the slave side (cf. Figure 4.11).

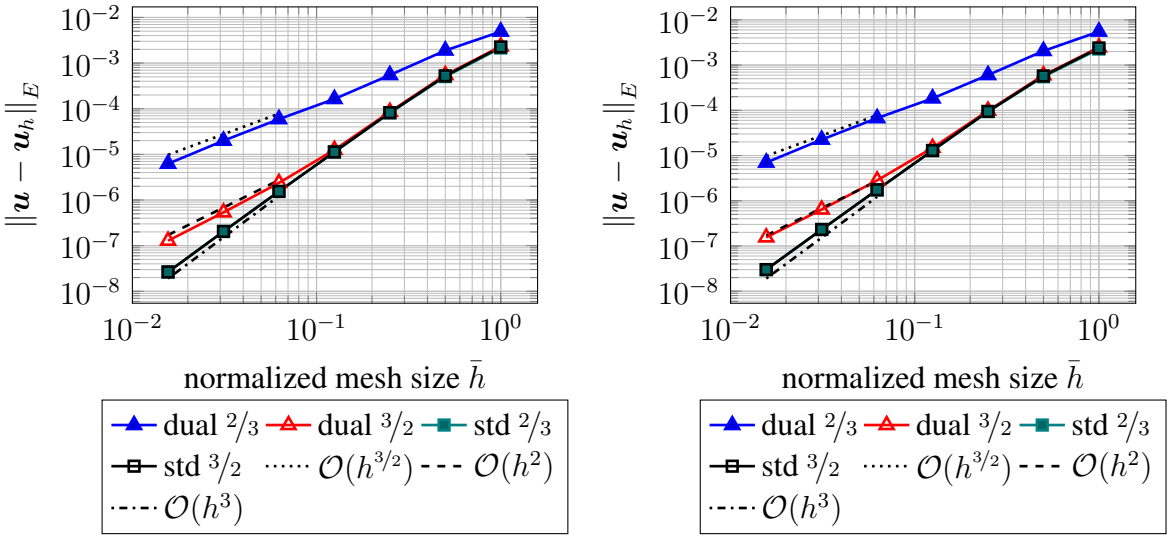

(a) Straight interface. (b) Curved interface.

Figure 4.13: Infinite plate with a circular hole – Spatial convergence for third order NURBS with standard ('std') or dual ('dual') Lagrange multipliers. Fractions indicate the slave to master mesh ratio, i.e., for a ratio of $^3/_2$, $\Omega_0^{(\mathrm{I})}$ is chosen the slave side, and for the mesh ratio $^2/_3$, $\Omega_0^{(\mathrm{II})}$ is chosen the slave side (cf. Figure 4.11).

As expected, a standard Lagrange multiplier method yields optimal convergence of order $\mathcal{O}(h^p)$ for both choices of the slave side. In the isogeometric dual mortar approach, on the other hand, the choice of the slave side has an influence on the convergence orders. If the coarser side is chosen as slave, the convergence order drops to the theoretically predicted $\mathcal{O}(h^{3/2})$, whereas if the finer side is chosen as slave, order $\mathcal{O}(h^2)$ convergence can be observed. This implies optimal behavior for second order NURBS (Figure 4.12) if the finer side is chosen as the slave side. For third order NURBS in Figure 4.13, on the other hand, even a finer slave side yields sub-optimal convergence results and choosing a coarse slave side significantly deteriorates the achievable convergence order. The gain of order $\mathcal{O}(h^{1/2})$ may be the result of super convergence effects, theoretical investigation of which are, however, beyond the scope of this thesis.

Next, the results above are compared to approximations based on Lagrange polynomials of first and second order. For the sake of brevity, the investigation is restricted to the more general case of a curved interface, since the results are qualitatively the same. Figure 4.14 displays the

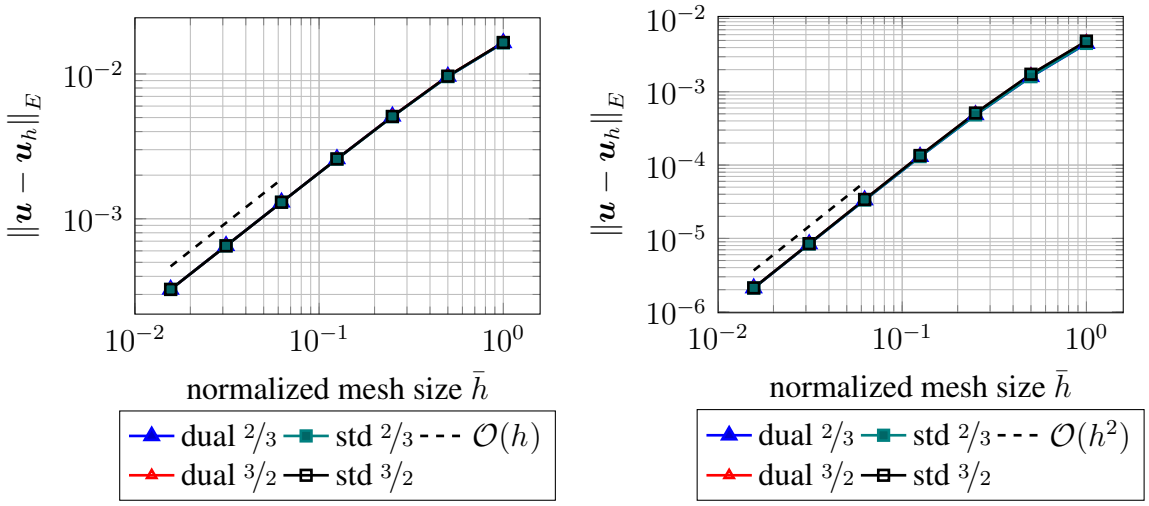

(a) $\mathbb{Q}_1$ finite elements.

(b) $\mathbb{Q}_2$ finite elements.

Figure 4.14: Infinite plate with a circular hole – Spatial convergence for $\mathbb{Q}_1$ and $\mathbb{Q}_2$ finite elements with standard ('std') or dual ('dual') Lagrange multipliers. Fractions indicate the slave to master mesh ratio, i.e., for a ratio of $^3/_2$, $\Omega_0^{(\mathrm{I})}$ is chosen the slave side, and for the mesh ratio $^2/_3$, $\Omega_0^{(\mathrm{II})}$ is chosen the slave side (cf. Figure 4.3b).

convergence behavior of first and second order finite elements with different approximations of the Lagrange multiplier. Here, *all* methods converge with the optimal order of $\mathcal{O}(h)$ and $\mathcal{O}(h^2)$, respectively, even the theoretically most critical one using second order dual basis functions with a coarser slave discretization. This is due to the fact that the used discretization with second order 9-node quadrilaterals always places the side-mid nodes and the central nodes equally spaced, i.e. at the locations of the Gauss–Lobatto points. Therefore, $\mathcal{O}(h^2)$ convergence can be expected, see Lamichhane and Wohlmuth [129]. For orders $p > 2$, equally spaced nodes do no longer correspond to Gauss–Lobatto points and convergence orders for the dual case may deteriorate. Such higher order Lagrange polynomial approximations are, however, beyond the scope of this thesis and the reader is referred to [129] for a detailed investigation of this topic.

Finally, a comparison of the convergence rates of different dual mortar interpolations in the most critical case, i.e. the curved interface with a coarse slave discretization and a dual Lagrange multiplier approximation, is drawn. Figure 4.15 compares the isogeometric results from 4.12b and 4.13b with the results using classical finite elements in Figure 4.14. Basically, two ways are

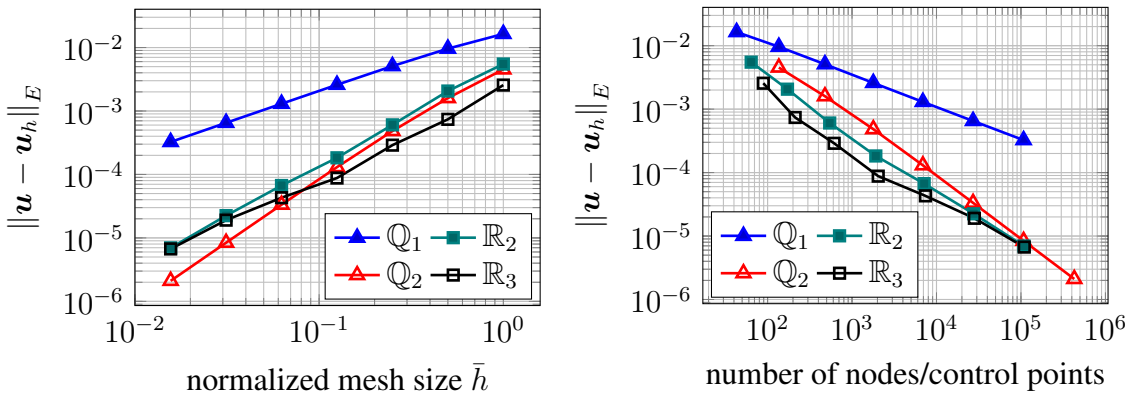

(a) Comparison by mesh size.

(b) Comparison by number of nodes or control points.

Figure 4.15: Infinite plate with a circular hole – Spatial convergence for first and second order finite elements ($\mathbb{Q}_1$ and $\mathbb{Q}_2$) as well as second and third order NURBS ($\mathbb{R}_2$ and $\mathbb{R}_3$) for the curved interface, a coarse slave discretization and dual Lagrange multipliers.

possible to compare finite elements and IGA, either by the element size (Figure 4.15a) or by the number of nodes, respectively control points (Figure 4.15b). Since IGA requires less control points per element, these two approaches yield different results. While the former compares the efficiency in terms of element evaluations, the latter rather focuses on the size of the resulting linear system to be solved. The complexity of solving this linear system is, however, not only determined by its size, but also the bandwidth, which is increasing with the polynomial order. Obviously, the first order approximation yields the largest errors and converges slowly. Comparing the second order methods $\mathbb{Q}_2$ and $\mathbb{R}_2$, one observes that when taking the element size as a reference the finite element version converges faster and yields lower errors from the beginning. However, taking the number of control variables as a reference, the isogeometric discretization $\mathbb{R}_2$ is more accurate than the finite element counterpart $\mathbb{Q}_2$, despite the reduced convergence order. Only if the already very fine mesh is further refined, the $\mathbb{Q}_2$ version would gain the advantage due to faster convergence. The third order NURBS version $\mathbb{R}_3$ gives the best results in coarse meshes and behaves similarly to the $\mathbb{R}_2$ case in the limit.

In summary, the presented simple element-wise construction of dual NURBS basis functions may yield a deterioration in the convergence orders for domain decomposition. Thanks to the higher accuracy per degree of freedom, however, the isogeometric dual mortar method is, despite sub-optimal convergence, competitive to classical finite elements using Lagrange polynomials. To obtain optimal convergence, more sophisticated methods of constructing the dual basis are necessary, e.g. dual shape functions with an extended support [66, 242, 243, 254]. Nonetheless, the presented method provides an easy and efficient way of coupling patches without increasing the global system size (compared to [21]) and gaining a localization of the coupling (compared to [65]).

4.1.4.2.2 Hertzian Contact Although the presented element-wise construction of dual shape functions yields sub-optimal convergence in domain decomposition applications, they may still be interesting for unilateral contact applications. In this case, the spatial convergence is usually limited by the reduced regularity of the solution, such that even the simple element-wise construction gives optimal convergence in finite element analysis [232]. Hence, in a second example, the spatial convergence properties of the isogeometric dual mortar contact algorithm is investigated in detail. Therefore, a two dimensional Hertzian-type contact of a cylindrical body (radius R) with a rigid planar surface under plane strain conditions is analyzed. To avoid singularities in the isogeometric mapping, a small inner radius (radius r) is introduce, see Figure 4.16 for the geometric setting, the material parameters and the coarsest mesh. The two horizontal upper boundaries undergo a prescribed vertical displacement. Meshes using second and third order NURBS basis functions are used as depicted in Figure 4.16 for the coarsest level, where different patches are marked with different shading. In this setup, half of the elements on the potential

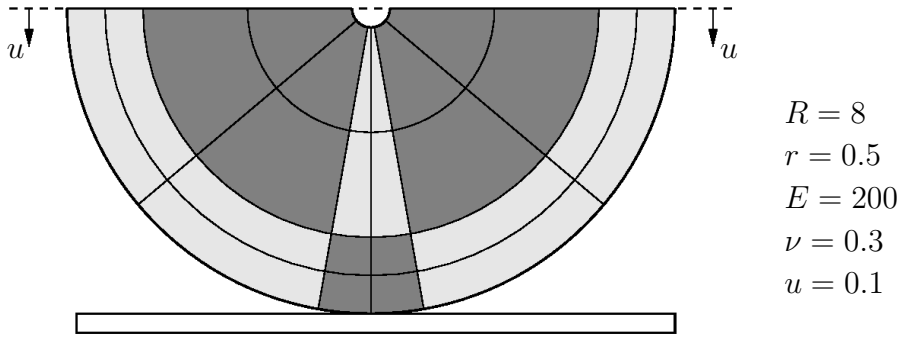

Figure 4.16: Hertzian contact – Problem setup and coarsest mesh with patches in different shading.

contact surface are located within one ninth of the circumferential length and C^{p-1} continuity is ensured over the entire active contact surface. In the convergence study, uniform mesh refinement via knot insertion is performed on each of the patches resulting in a constant local element aspect ratio. Although only relatively small deformations are to be expected, a fully nonlinear description of the continuum using nonlinear kinematics and a Saint–Venant–Kirchhoff material under plane strain condition is assumed. Figure 4.17 depicts the convergence behavior in terms of the energy norm. Since no analytical solution is available, the finest mesh of level 7 with standard third order NURBS is used as a numerical reference solution. In the limit, all methods converge with the expected order of $\mathcal{O}(h^{3/2})$ in the energy norm and also the absolute error values are quantitatively very similar. In the second order case ($p = 2$) the standard and dual mortar method yield the same error asymptotically, whereas for third order NURBS, a slightly elevated error of the dual mortar method as compared to the standard one can be observed. In view of Figure 4.17, the use of dual shape functions for the Lagrange multiplier instead of primal ones does not come at the expense of a reduced accuracy but yields equally accurate results while reducing the total system size to the number of displacement degrees of freedom only. In contrast to the domain decomposition case above, the convergence is now limited by the regularity of the solution, such that both standard and dual interpolations converge with the same order. The use of higher order NURBS, i.e. third order in Figure 4.17 or even higher seems questionable from this viewpoint, since no faster convergence is gained from the higher order interpolation.

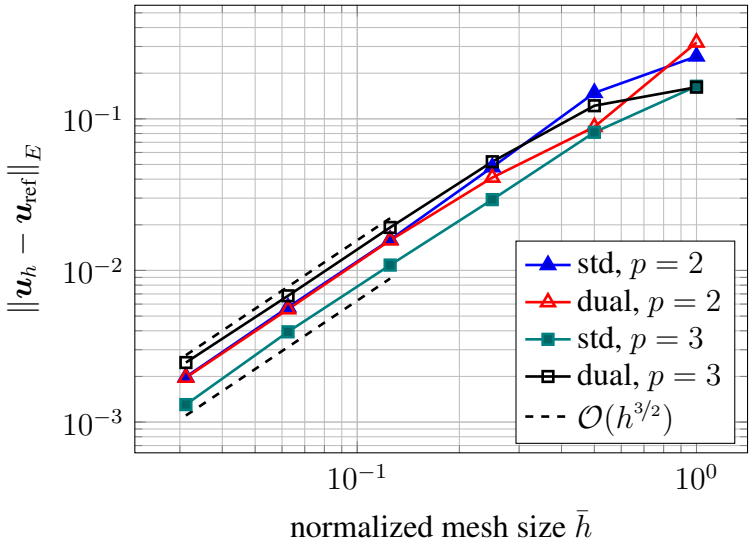

Figure 4.17: Hertzian contact – spatial convergence for standard (denoted as 'std') and dual (denoted as 'dual') mortar methods for second and third order NURBS.

In the context of isogeometric contact formulations, Hertzian-type contact settings are commonly used to assess the smoothness of the pressure distribution using different computational methods, see e.g. [50, 51, 53, 59, 121, 216]. Strictly speaking, the Lagrange multiplier in a variationally consistent contact formulation is not a point-wise defined function but an element of the dual space of the trace space. Thus, one cannot evaluate the Lagrange multiplier point-wise with respect to the space coordinates, but only as a linear functional. This observation motivates to associate a NURBS function $\tilde{\boldsymbol{\lambda}}_h$ with $\boldsymbol{\lambda}_h$ in (4.6) specified in terms of the non-negative basis functions $\bar{R}_i^{(1)}$ and the discrete control point values $\boldsymbol{\lambda}_{i,\text{dual}}$ already computed using the dual mortar method. More precisely, the definition

$$\tilde{\boldsymbol{\lambda}}_h = \sum_{i \in \mathcal{L}} \bar{R}_i \boldsymbol{\lambda}_{i,\text{dual}} \tag{4.52}$$

guarantees that $\tilde{\boldsymbol{\lambda}}_h$ is strongly non-negative. Moreover, due to (4.50), one finds that

$$\int_{\tau_{\Gamma,h,k}^{(1)}} \tilde{\boldsymbol{\lambda}}_h \, \mathrm{d}\gamma = \int_{\tau_{\Gamma,h,k}^{(1)}} \boldsymbol{\lambda}_h \, \mathrm{d}\gamma \quad . \tag{4.53}$$

Thus, both $\tilde{\boldsymbol{\lambda}}_h$ and $\boldsymbol{\lambda}_h$ impose the same mean contact pressure per face $\tau_{\Gamma,h,k}^{(1)}$ on the contact zone. Following Hüeber [105], it can be shown that the modified discrete Lagrange multiplier has the same convergence order and, moreover, in contrast to the standard low order finite element approach, a C^{p-1} continuous contact pressure is found. Figures 4.18-4.20 compare the pressure distributions for the meshes $\bar{h} =\in \{2^{-1}, 2^{-3}, 2^{-5}\}$ using second order NURBS with the standard Lagrange multiplier approach and the dual approach using either dual or standard shape functions for the pressure post-processing. Therein, red circles indicate the discrete control point values of the Lagrange multiplier. Since the given example does not exactly model a Hertzian contact problem (nonlinear kinematics vs. linear Hertzian theory, thick hollow cylinder vs. full circular disk, displacement control vs. point load), the contact pressure of the mesh $\bar{h} = 2^{-7}$ with

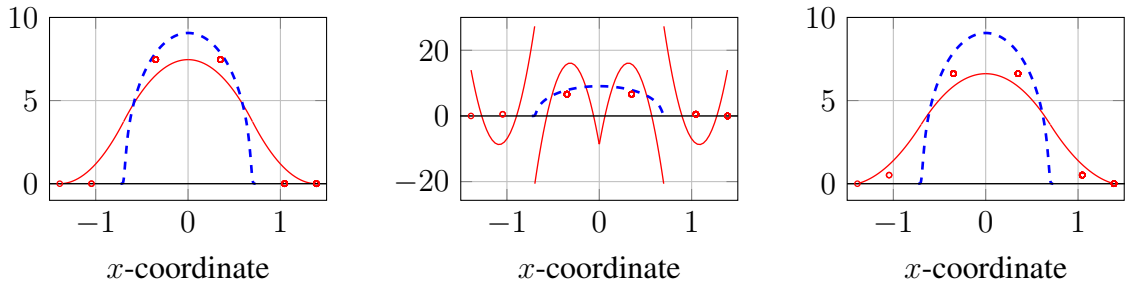

(a) Standard. (b) Dual. (c) Dual post-processed.

Figure 4.18: Hertzian contact – Contact pressure for $\bar{h} = 2^{-1}$ using different second order NURBS methods.

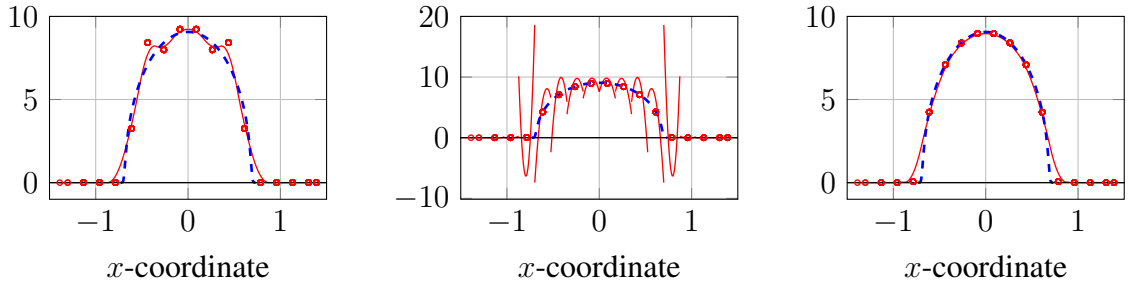

(a) Standard. (b) Dual. (c) Dual post-processed.

Figure 4.19: Hertzian contact – Contact pressure for $\bar{h} = 2^{-3}$ using different second order NURBS methods.

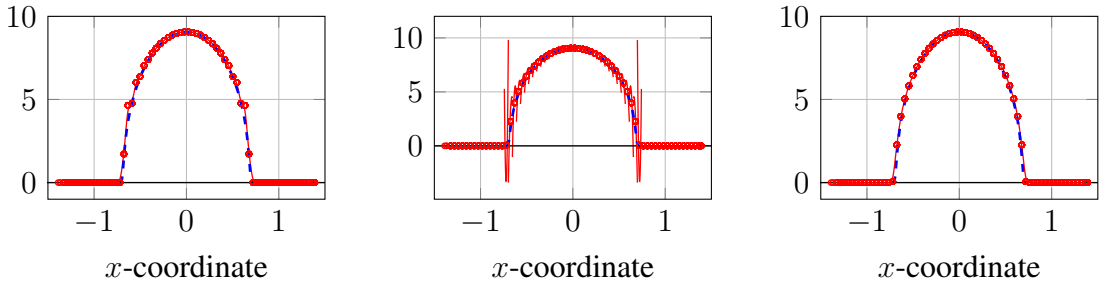

(a) Standard. (b) Dual. (c) Dual post-processed.

Figure 4.20: Hertzian contact – Contact pressure for $\bar{h} = 2^{-5}$ using different second order NURBS methods.

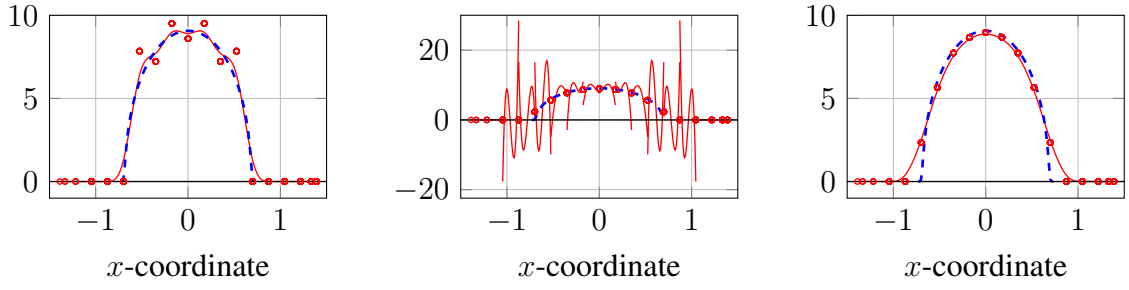

(a) Standard. (b) Dual. (c) Dual post-processed.

Figure 4.21: Hertzian contact – Contact pressure for $\bar{h} = 2^{-3}$ using different third order NURBS methods.

the post-processed dual NURBS approximation is depicted as a reference with dashed blue lines instead of the solution according to Hertzian theory. As expected, the visualization using dual shape functions results in a strongly oscillatory behavior due to the discontinuous and not even strictly non-negative nature of the dual shape functions. However, the post-processed contact traction for the dual Lagrange multiplier method yield even smoother and less oscillatory results than the standard case on the same mesh. Especially with the medium mesh (Fig. 4.19) the use of standard NURBS basis functions for the Lagrange multiplier yields oscillations in the contact stress; a similar behavior can also be observed in various IGA contact formulations, e.g. in De Lorenzis *et al.* [50, 51, 53], Temizer *et al.* [216]. Those oscillations vanish completely for the post-processed dual mortar method. This effect also transfers to higher order NURBS basis functions: Figure 4.21 depicts the contact stress distributions for third order NURBS and mesh $\bar{h} = 2^{-3}$. Again, the standard isogeometric mortar method shows some oscillations in the contact pressure whereas the dual mortar method yields a perfectly smooth result. Since the oscillations in the standard mortar method usually occur at the boundary of the active contact zone, they are suspected to be a result of the localized active set strategy. As mentioned in Remark 4.1, only the use of dual basis functions yields decoupled constraints in a consistent way. For standard mortar methods, the imbalance of coupled virtual work contributions for the control points in (4.4) and decoupled constraints may be responsible for the oscillations. This being only a suspicion at the current stage, the oscillations in standard mortar methods may require further study in the future.

Next, four different dual mortar methods are compared. Therefore, the NURBS approximation of mesh $\bar{h} = 2^{-3}$ from above is used and an approximation using the same number of elements, but based on first order Lagrange polynomials (denoted as $\mathbb{Q}_1$) is generated. Additionally, a second order Lagrange polynomial approximation is generated by keeping the number of nodes fixed and elevate the order to second order Lagrange polynomials (denoted as $\mathbb{Q}_2$). Figure 4.22 compares the obtained contact stress distribution from the four dual mortar methods. Figures 4.22c and 4.22d are reproduced from Figure 4.19c and 4.21c for illustrative purposes. One observes the usual behavior for higher order contact formulations: starting from the common ancestor $\mathbb{Q}_1/\mathbb{R}_1$ and a piece-wise linear approximation of the contact stress, order elevation for Lagrange polynomials ($\mathbb{Q}_2$) yields oscillations and locally negative contact traction. Order elevation using NURBS basis functions, on the other hand, gives smoother contact pressure distributions. This trend becomes even more pronounced, if the order is further increased, see e.g. [53]. Comparing the two isogeometric methods $\mathbb{R}_2$ and $\mathbb{R}_3$ in Figures 4.22c and 4.22d, it has to be noted that in the higher order case $\mathbb{R}_3$ the contact pressure distribution gets "smeared" over a larger region. This is a consequence of the inability of *smooth* NURBS basis functions to accurately represent the *non-smooth* contact pressure solution. Increasing the approximation order in the IGA case while keeping the inter-element continuity at a maximum aggravates this deficiency.

Finally, the adequate representation of frictional contact tractions should be investigated using this setup. To this end, the problem is enhanced with Coulomb friction with a friction coefficient $\mu = 0.75$. Figure 4.23 displays the solution of mesh $\bar{h} = 2^{-3}$ and the results are again compared to the solution of mesh $\bar{h} = 2^{-7}$ with the post-processed second order dual NURBS approximation. Obviously, none of the relatively coarse discretizations are able to fully capture the sharp kink in the frictional contact traction at the stick/slip transition. However, the observations already made for the normal contact pressure appear even more pronounced here. For the standard Lagrange multiplier approximation the oscillations in the normal contact pressure

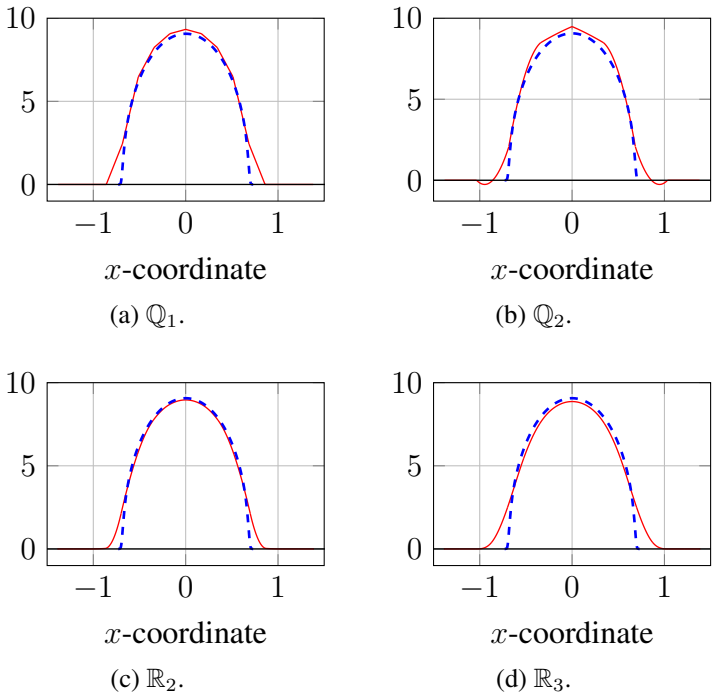

(a) $\mathbb{Q}_1$. (b) $\mathbb{Q}_2$.

(c) $\mathbb{R}_2$. (d) $\mathbb{R}_3$.

Figure 4.22: Hertzian contact – Post-processed contact pressure for $\bar{h} = 2^{-3}$ using different dual mortar methods.

also influence the frictional response, thus yielding oscillatory tangential tractions in the central region. The dual approximation seems to be oscillatory at first sight, but this is not the case since the discrete control point values are smoothly distributed. Quite in contrast, the oscillations in the standard approximation are actually completely removed in the post-processed dual solution where, a smooth distribution of both normal and tangential contact traction is obtained.

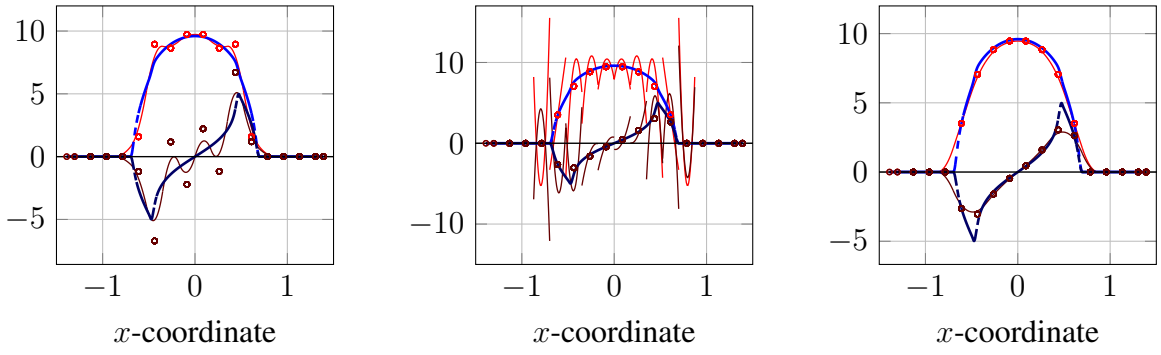

(a) Standard. (b) Dual. (c) Dual post-processed.

Figure 4.23: Hertzian contact – Computed pressure (red and blue lines) and frictional traction (dark red and dark blue lines) distributions for mesh $\bar{h} = 2^{-3}$ using different second order NURBS methods.

4.1.4.2.3 Three-dimensional Rotating Ironing This final example demonstrates the applicability of the presented isogeometric dual mortar method to large frictional sliding and

again compares the result to contact formulations based on Lagrange polynomials. Inspired by

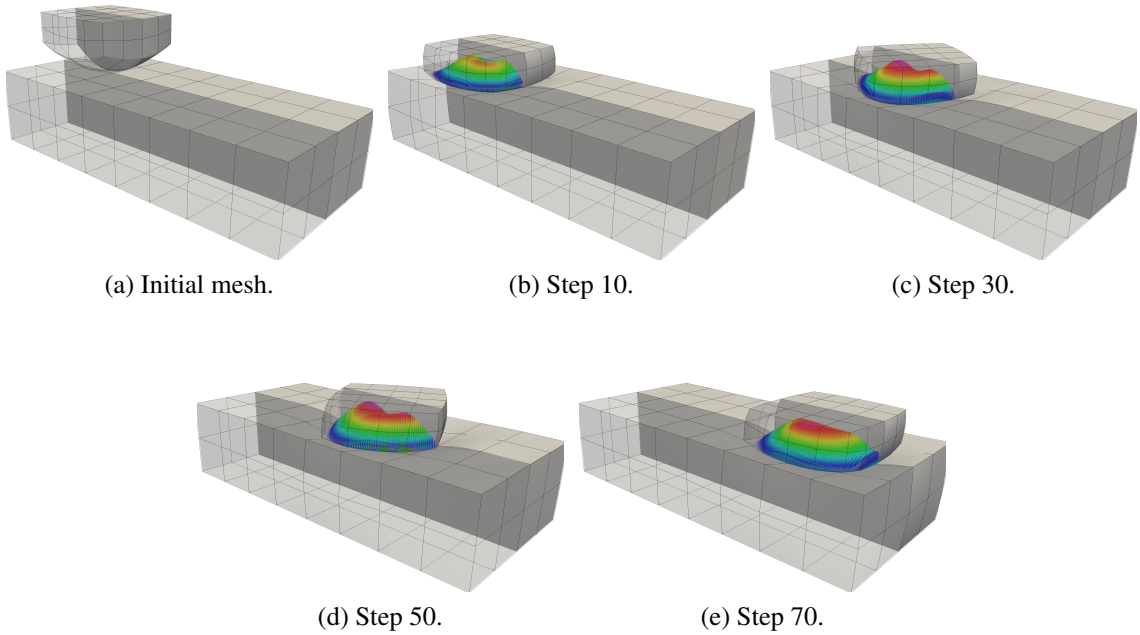

(a) Initial mesh. (b) Step 10. (c) Step 30.

(d) Step 50. (e) Step 70.

Figure 4.24: Rotating ironing – Initial mesh and deformed configurations displaying the post-processed normal contact pressure for the second order dual NURBS approximation.

De Lorenzis *et al.* [53], a rotating ironing example is chosen and enhanced with Coulomb friction (friction coefficient $\mu = 0.1$). An indentor $\Omega_0^{(1)}$ with an approximate size of $6 \times 6 \times 4$ with a curved contact surface is pressed onto an elastic cuboid $\Omega_0^{(2)}$ of size $10 \times 22 \times 5$. After 10 steps of this vertical movement, the indentor is slid over the cuboid while performing a rotation of 180 degrees around its vertical axis within 60 steps, see Figure 4.24 for an illustration of the initial mesh and different deformed stages. For both bodies, the same neo-Hookean hyperelastic material (3.38) with $E = 1$ and $\nu = 0.3$ is assumed. Starting from the common $\mathbb{Q}_1/\mathbb{R}_1$ discretization either eight first order finite elements are combined to one second order element $\mathbb{Q}_2$, i.e. keeping the number of nodes fixed, or keeping the number of elements fixed and elevating the NURBS order to $\mathbb{R}_2$ and $\mathbb{R}_3$ with C^{p-1} inter-element continuity, and slightly increasing the number of unknowns. Similar to De Lorenzis *et al.* [53], Temizer *et al.* [217], the total vertical and horizontal contact reaction forces during the sliding phase are analyzed in Figures 4.25 and 4.26. At first sight, the resulting normal contact force behaves quite smoothly for all discretization in Figure 4.25. Taking a closer look and magnifying the sliding phase, reveals that both the $\mathbb{Q}_1$ and $\mathbb{Q}_2$ schemes show some periodic oscillations. The isogeometric approaches $\mathbb{R}_2$ and $\mathbb{R}_3$, on the other hand, give much smoother results and for the third order case $\mathbb{R}_3$ hardly any oscillations can be observed. The oscillations become more pronounced, if the horizontal contact force due to frictional effects is analyzed as done in Figure 4.26. Here, even the second order NURBS solution $\mathbb{R}_2$ oscillates and only the $\mathbb{R}_3$ version gives reasonably smooth results for the friction force thanks to the smooth contact surface representation. Those investigations hold for both the standard and the dual Lagrange multiplier interpolations without any qualitative difference. In summary, the known advantages of isogeometric contact algorithms also transfer to the dual

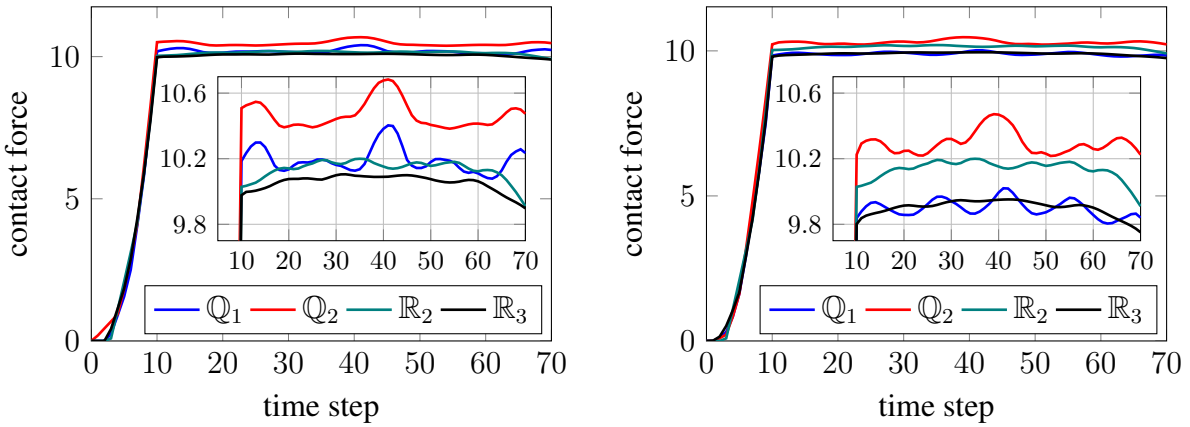

(a) Standard. (b) Dual.

Figure 4.25: Rotating ironing – Comparison of vertical contact forces for different approximation schemes.

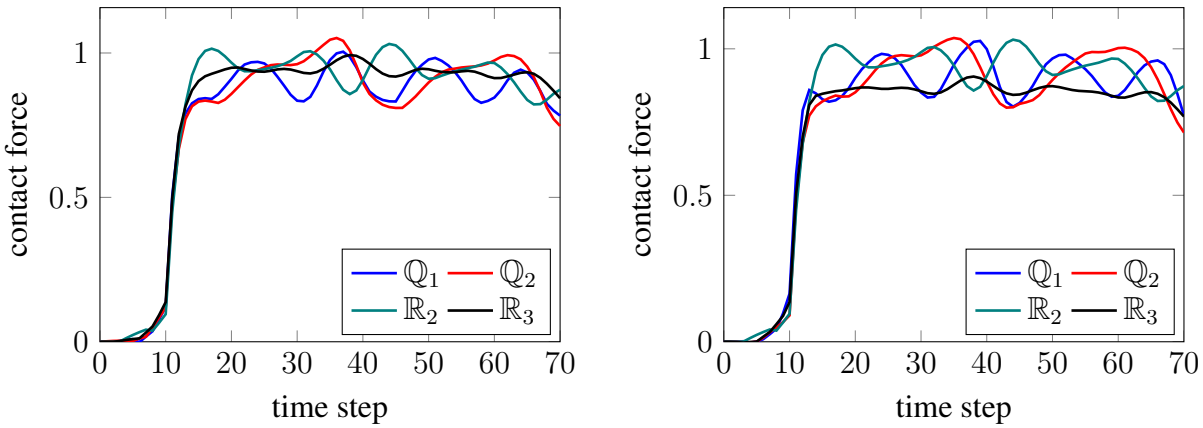

(a) Standard. (b) Dual.

Figure 4.26: Rotating ironing – Comparison of horizontal contact forces for different approximation schemes.

mortar approach: keeping the inter-element continuity at a maximum, higher order NURBS give smoother contact forces, whereas higher order Lagrange polynomial finite elements do not.

4.2 Mortar Methods for Thermomechanical Contact[1]

The mortar method for isothermal contact derived in the previous section is now to be extended to include thermal coupling effects consisting of heat conduction across the contact interface, frictional heating and a temperature dependent coefficient of friction. From the continuum mechanical perspective, the first two coupling effects are included in the contact interface heat fluxes (2.129), while the last one enters in Coulomb's law of friction (2.124) via the temperature dependent coefficient of friction (2.125). The thermomechanical coupling in the bulk continuum

[1] This section is adapted from the author's publication [194].

is not revisited here, but the reader is referred to Chapter 2 for the continuum mechanical description including finite element schemes for thermoelasticity, and Chapter 3 for the numerical treatment of thermo-elasto-plasticity.

4.2.1 Mortar Finite Element Discretization

To prepare the subsequent mortar finite element discretization of the thermomechanical contact problem, again a mixed formulation of the weak forms introduced in Section 2.7.4 has to be derived. As in the isothermal case of Section 4.1, a Lagrange multiplier field $\boldsymbol{\lambda}$ is introduced to enforce the mechanical contact constraints (2.119) and (2.124), and can be identified as the negative slave-sided contact traction, i.e. $\boldsymbol{\lambda} = -\boldsymbol{t}_{\mathrm{c}}^{(1)}$. In a similar fashion, a thermal Lagrange multiplier field λ_{T} is introduced to enforce the thermal constraint (2.129) and will be chosen as the slave side heat flux $\lambda_{\mathrm{T}} = q_{\mathrm{c}}^{(1)}$. The complete weak form of the coupled thermomechancial contact problem then reads: Find $\boldsymbol{u} \in \boldsymbol{\mathcal{U}}_{\mathrm{u}}$, $T \in \mathcal{U}_{\mathrm{T}}$, $\boldsymbol{\lambda} \in \boldsymbol{\mathcal{M}}(\boldsymbol{\lambda})$ and $\lambda_{\mathrm{T}} \in \mathcal{M}$, such that

$$\delta \mathcal{W}_{\mathrm{u}} + \int_{\gamma_{\mathrm{c}}^{(1)}} \boldsymbol{\lambda} \cdot [\![\delta \boldsymbol{u}]\!] \, \mathrm{d}\gamma = 0 \quad \forall \delta \boldsymbol{u} \in \boldsymbol{\mathcal{V}}_{\mathrm{u}} \ , \tag{4.54a}$$

$$\delta \mathcal{W}_{\mathrm{T}} + \int_{\gamma_{\mathrm{c}}^{(1)}} \lambda_{\mathrm{T}} [\![\delta T]\!] \, \mathrm{d}\gamma + \int_{\gamma_{\mathrm{c}}^{(1)}} \boldsymbol{\lambda} \cdot \boldsymbol{v}_{\tau} \left(\delta T^{(2)} \circ \chi_t \right) \, \mathrm{d}\gamma = 0 \quad \forall \delta T \in \mathcal{V}_{\mathrm{T}} \ , \tag{4.54b}$$

$$\int_{\gamma_{\mathrm{c}}^{(1)}} (\delta \lambda_{\mathrm{n}} - \lambda_{\mathrm{n}}) g_{\mathrm{n}} \, \mathrm{d}\gamma - \int_{\gamma_{\mathrm{c}}^{(1)}} (\delta \boldsymbol{\lambda}_{\tau} - \boldsymbol{\lambda}_{\tau}) \cdot \boldsymbol{v}_{\tau} \, \mathrm{d}\gamma \geq 0 \quad \forall \delta \boldsymbol{\lambda} \in \boldsymbol{\mathcal{M}}(\boldsymbol{\lambda}) \ , \tag{4.54c}$$

$$\int_{\gamma_{\mathrm{c}}^{(1)}} (\lambda_{\mathrm{T}} - \beta_{\mathrm{c}} \lambda_{\mathrm{n}} [\![T]\!] - \delta_{\mathrm{c}} \boldsymbol{\lambda} \cdot \boldsymbol{v}_{\tau}) \, \delta \lambda_{\mathrm{T}} \, \mathrm{d}\gamma = 0 \quad \forall \delta \lambda_{\mathrm{T}} \in \mathcal{M} \ . \tag{4.54d}$$

The first and second line represent the weak forms (2.132) and (2.134) replacing the slave sided contact traction and heat flux by the respective Lagrange multiplier. The third line reproduces the mechanical contact of no-penetration and Coulomb's law in form of a variational inequality as already introduced in (4.5) and finally the fourth line weakly enforces $\lambda_{\mathrm{T}} = q_{\mathrm{c}}^{(1)}$ with $q_{\mathrm{c}}^{(1)}$ as defined by (2.129a). Note that also for the thermal contact contributions, all integrals are written as slave-sided integrals only.

Within this thesis, the spatial discretization of displacements and temperatures is either done by classical finite elements (see Section 2.8.1.1) or NURBS in the case of isogeometric analysis (see Section 2.8.1.2). Since these discretizations do not require any special treatment for the thermomechanical mortar method, they are not recapitulated here. Also, the mechanical part of (4.54), i.e. the balance of linear momentum (4.54a) and the variational inequality (4.54c), remain virtually unaltered from the one treated in Section 4.1 and will not be discussed in detail in the following. The discrete contact forces entering the balance of linear momentum are again obtained via (4.9) and the inequality constraints are reformulated as nonlinear complementarity functions (4.22) and (4.23). The only noteworthy difference to the isothermal case is the temperature dependency of the coefficient of friction.

Focusing on the thermal contributions, the thermal Lagrange multiplier and its variation are discretized by discrete values $\lambda_{\mathrm{T},i}$ and $\delta\lambda_{\mathrm{T},i}$, and the same ansatz functions as used for the structural Lagrange multiplier $\boldsymbol{\lambda}$ in (4.6) resulting in the discrete field

$$\lambda_{\mathrm{T}} \approx \lambda_{\mathrm{T},h} = \sum_{i \in \mathcal{L}} \phi_i(\boldsymbol{X}) \lambda_{\mathrm{T},i}(t) \ , \quad \delta\lambda_{\mathrm{T}} \approx \delta\lambda_{\mathrm{T},h} = \sum_{i \in \mathcal{L}} \phi_i(\boldsymbol{X}) \delta\lambda_{\mathrm{T},i} \ . \tag{4.55}$$

The application of this discretization together with the approximation of displacements, temperatures and structural Lagrange multipliers (2.136) and (4.6) in the contact contribution to the weak heat conduction equation (4.54b) yields

$$\begin{aligned}
&\int_{\gamma_{\mathrm{c}}^{(1)}} \lambda_{\mathrm{T}} [\![\delta T]\!] \,\mathrm{d}\gamma + \int_{\gamma_{\mathrm{c}}^{(1)}} \boldsymbol{\lambda} \cdot \boldsymbol{v}_{\tau} \left(\delta T^{(2)} \circ \chi_t\right) \,\mathrm{d}\gamma \\
\approx &\int_{\gamma_{\mathrm{c},h}^{(1)}} \lambda_{\mathrm{T},h} [\![\delta T_h]\!] \,\mathrm{d}\gamma + \int_{\gamma_{\mathrm{c},h}^{(1)}} \boldsymbol{\lambda}_h \cdot \boldsymbol{v}_{\tau,h} \left({\delta T^{(2)}}_h \circ \chi_{t,h}\right) \,\mathrm{d}\gamma \\
= &\sum_{i\in\mathcal{L}} \sum_{j\in\mathcal{S}} \lambda_{\mathrm{T},i} \left(\int_{\gamma_{\mathrm{c},h}^{(1)}} \phi_i \bar{N}_j^{(1)} \,\mathrm{d}\gamma \right) \delta T_j^{(1)} \\
&- \sum_{i\in\mathcal{L}} \sum_{k\in\mathcal{M}} \lambda_{\mathrm{T},i} \left(\int_{\gamma_{\mathrm{c},h}^{(1)}} \phi_i \left(\bar{N}_k^{(2)} \circ \chi_{t,h} \right) \,\mathrm{d}\gamma \right) \delta T_k^{(2)} \\
&+ \sum_{i\in\mathcal{L}} \sum_{k\in\mathcal{M}} \boldsymbol{\lambda}_i \cdot \left(\int_{\gamma_{\mathrm{c},h}^{(1)}} \phi_i \boldsymbol{v}_{\tau,h} \left(\bar{N}_k^{(2)} \circ \chi_{t,h} \right) \,\mathrm{d}\gamma \right) \delta T_k^{(2)} \quad .
\end{aligned} \tag{4.56}$$

The first and second sum therein stem from the heat conduction over the contact interface and result in the similar coupling matrices $\mathbf{D}_{\mathrm{T}}$ and $\mathbf{M}_{\mathrm{T}}$ already introduced in the structural coupling (4.10). The only difference between the temperature coupling $\mathbf{D}_{\mathrm{T}}$ and $\mathbf{M}_{\mathrm{T}}$, and structural coupling $\mathbf{D}$ and $\mathbf{M}$ in (4.10) is in the size of the matrices: one entry per node for the thermal part and n_{dim} entries per node - one for each displacement degree of freedom - in the structural coupling. The last integral is the result of frictional dissipation at the contact interface and, in the stated form gives rise to some complications. First, an objective measure of relative tangential velocity $\boldsymbol{v}_{\tau,h}$ has to be used, e.g. a discrete version of (2.103). Moreover, it involves a triple integral over a product of three ansatz functions on the contact interface as $\boldsymbol{v}_{\tau,h}$ includes ansatz functions via (2.103) as well. This poses high demands on the quadrature accuracy at the contact interface, especially when going to higher order approximations using Lagrange polynomials or NURBS, see e.g. Dittmann *et al.* [61]. Following the work of Hüeber and Wohlmuth [107], an appropriate lumping technique in (4.56) is applied to reduce the computational cost by replacing the last summand by

$$\begin{aligned}
&\sum_{i\in\mathcal{L}} \sum_{k\in\mathcal{M}} \boldsymbol{\lambda}_i \cdot \left(\int_{\gamma_{\mathrm{c},h}^{(1)}} \phi_i \boldsymbol{v}_{\tau,h} \left(\bar{N}_k^{(2)} \circ \chi_{t,h} \right) \,\mathrm{d}\gamma \right) \delta T_k^{(2)} \\
\approx &\sum_{i\in\mathcal{L}} \sum_{k\in\mathcal{M}} \frac{\tilde{\boldsymbol{v}}_{\tau,i} \cdot \boldsymbol{\lambda}_i}{\int_{\gamma_{\mathrm{c},h}^{(1)}} \phi_i \,\mathrm{d}\gamma} \left(\int_{\gamma_{\mathrm{c},h}^{(1)}} \phi_i \left(\bar{N}_k^{(2)} \circ \chi_{t,h} \right) \,\mathrm{d}\gamma \right) \delta T_k^{(2)} \quad .
\end{aligned} \tag{4.57}$$

From a physical point of view, this means that instead of interpolating the contact Lagrange multiplier and the relative velocities separately, only the scalar product $\frac{\tilde{\boldsymbol{v}}_{\tau,i} \cdot \boldsymbol{\lambda}_i}{\int_{\gamma_{\mathrm{c},h}^{(1)}} \phi_i \,\mathrm{d}\gamma} = \mathcal{P}_{\mathrm{c},i}$ is interpolated, which represents the frictional dissipation power of a discrete Lagrange multiplier $\boldsymbol{\lambda}_i$ with the weighted relative tangential velocity $\tilde{\boldsymbol{v}}_{\tau,i}$ defined in (4.16). Numerically, (4.57) implies a lumping of the triple integrals, thus resulting in an integral over the product of two ansatz functions only. Equation (4.56) with the lumping (4.57) provide a spatial approximation of the contact-related terms in (4.54b) which is, however, still continuous in time.

An appropriate temporal discretization of the bulk terms by means of a generalized-α method or quasi-statics has been introduced in Section 2.8.2, so the focus here is on the contact terms only. The contact contribution to the discrete thermal equilibrium (2.163) is also interpolated at the generalized mid-point $\boldsymbol{F}_{\mathrm{T,c},n+\alpha_{\mathrm{f,T}}} = \alpha_{\mathrm{f,T}}\boldsymbol{F}_{\mathrm{T,c},n+1} + (1-\alpha_{\mathrm{f,T}})\boldsymbol{F}_{\mathrm{T,c},n}$, such that

$$\boldsymbol{r}_{\mathrm{T}} = \boldsymbol{M}_{\mathrm{T}}\dot{\mathbf{T}}_{n+\alpha_{\mathrm{m,T}}} + \boldsymbol{F}_{\mathrm{u,int},n+\alpha_{\mathrm{f,u}}} - \boldsymbol{F}_{\mathrm{u,ext},n+\alpha_{\mathrm{f,u}}} + \boldsymbol{F}_{\mathrm{T,c},n+\alpha_{\mathrm{f,T}}} = \mathbf{0} \quad , \tag{4.58}$$

with

$$\boldsymbol{F}_{\mathrm{T,c},n} = [\mathbf{0}, \mathbf{D}_{\mathrm{T}}, -\mathbf{M}_{\mathrm{T}}]^{\mathsf{T}}\boldsymbol{\lambda}_{\mathrm{T},n} + [\mathbf{0}, \mathbf{0}, \mathbf{M}_{\mathrm{T}}]^{\mathsf{T}}\boldsymbol{\mathcal{P}}_{\mathrm{c},n} \quad , \tag{4.59}$$

wherein the vector $\boldsymbol{\mathcal{P}}_{\mathrm{c},n}$ assembles the frictional power of all discrete Lagrange multipliers at time t_n. For clarity of notation, the discrete temperature variations $\delta\mathbf{T}$ have again been re-ordered as $\delta\mathbf{T} = [\delta\mathbf{T}_{\mathcal{N}}, \delta\mathbf{T}_{\mathcal{S}}, \delta\mathbf{T}_{\mathcal{M}}]^{\mathsf{T}}$ with $\delta\mathbf{T}_{\mathcal{S}}$, $\delta\mathbf{T}_{\mathcal{M}}$ and $\delta\mathbf{T}_{\mathcal{N}}$ containing all nodal values $\delta\mathsf{T}_i$ on the slave surface, the master surface and the remaining ones, respectively. Note that $\boldsymbol{F}_{\mathrm{T,c},n}$ is linear in the structural and thermal Lagrange multiplier but nonlinear in the discrete displacements due to the nonlinearity of the mortar matrices $\mathbf{D}_{\mathrm{T}}$ and $\mathbf{M}_{\mathrm{T}}$.

Lastly, the thermal interface constraint (4.54d) needs to be discretized. At this point, a slight deviation from a strict application of the spatial discretization to (4.54d) is introduced as already done in (4.57) to end up with a vector $\boldsymbol{G}_{\mathrm{T}}$ of nodal constraints and the discrete form

$$\begin{aligned}
\delta\boldsymbol{\lambda}_{\mathrm{T}} \cdot \boldsymbol{G}_{\mathrm{T}} = & \sum_{i\in\mathcal{L}} \delta\lambda_{\mathrm{T},i} \left(\int_{\gamma_{\mathrm{c},h}^{(1)}} \phi_i \, \mathrm{d}\gamma \right) \lambda_{\mathrm{T},i} \\
& - \sum_{i\in\mathcal{L}} \sum_{j\in\mathcal{S}} \delta\lambda_{\mathrm{T},i}\beta_{\mathrm{c}}\lambda_{\mathrm{n},i} \left(\int_{\gamma_{\mathrm{c},h}^{(1)}} \phi_i \bar{N}_j \, \mathrm{d}\gamma \right) \mathsf{T}_j^{(1)} \\
& + \sum_{i\in\mathcal{L}} \sum_{k\in\mathcal{M}} \delta\lambda_{\mathrm{T},i}\beta_{\mathrm{c}}\lambda_{\mathrm{n},i} \left(\int_{\gamma_{\mathrm{c},h}^{(1)}} \phi_i \left(\bar{N}^{(2)} \circ \chi_{t,h} \right) \, \mathrm{d}\gamma \right) \mathsf{T}_k^{(2)} \\
& - \sum_{i\in\mathcal{L}} \delta\lambda_{\mathrm{T},i} \left(\int_{\gamma_{\mathrm{c},h}^{(1)}} \phi_i \, \mathrm{d}\gamma \right) \mathcal{P}_{\mathrm{c},i} \\
= & 0 \qquad\qquad \forall \delta\lambda_{\mathrm{T},i} \in \Re \quad .
\end{aligned} \tag{4.60}$$

Thanks to the lumping procedure, especially for the first integral, the thermal interface condition decouples for the Lagrange multiplier $\mathcal{L}$, i.e. one can set $\lambda_{\mathrm{T},i}$ to zero for all inactive contact nodes. For the contact interface constraints, this decoupling can be achieved in a consistent manner using dual shape functions, such that only local, decoupled constraints have to be solved instead of an inequality constraint coupling all interface nodes, see Remark 4.1. To keep up this advantage in the coupled thermomechanical contact problem, the presented lumping is required, see Hüeber and Wohlmuth [107] for a more detailed discussion. It should be emphasized that for standard thermomechanical mortar methods, e.g. Dittmann *et al.* [61], a similar simplification is made implicitly by using a node-wise decoupled active set strategy, although strictly speaking the variational inequality does not not allow for such a decoupled treatment in that case as discussed in Blum *et al.* [17], Wohlmuth [235].

Remark 4.4. *To enforce the thermal interface constraints, it is not necessary to introduce the Lagrange multiplier field λ_{T}. An alternative formulation proposed e.g. in Dittmann* et al. *[61],*

Gitterle [79], Pantuso et al. *[163] directly substitutes the heat fluxes* $q_{\mathrm{c}}^{(i)}$ *according to* (2.129) *in the weak form of the heat conduction equation* (2.133)*. In the present syntax, the resulting thermal weak form would read*

$$\begin{aligned}\delta\mathcal{W}_{\mathrm{T}} &+ \int_{\gamma_{\mathrm{c}}^{(1)}} \left(\beta_{\mathrm{c}}\lambda_{\mathrm{n}}[\![T]\!] + \delta_{\mathrm{c}}\boldsymbol{\lambda}_{\tau}\cdot\boldsymbol{v}_{\tau}\right)\delta T^{(1)}\,\mathrm{d}\gamma \\ &+ \int_{\gamma_{\mathrm{c}}^{(1)}} \left(-\beta_{\mathrm{c}}\lambda_{\mathrm{n}}[\![T]\!] + (1-\delta_{\mathrm{c}})\boldsymbol{\lambda}_{\tau}\cdot\boldsymbol{v}_{\tau}\right)(\delta T^{(2)}\circ\chi_t)\,\mathrm{d}\gamma = 0 \quad \forall \delta T \in \mathcal{V}_{\mathrm{T}} \ ,\end{aligned} \tag{4.61}$$

in which only the displacement and temperature field as well as the structural Lagrange multiplier $\boldsymbol{\lambda}$ *need to be discretized. At first glance, this seems to be the more intuitive formulation as no additional thermal Lagrange multiplier field and corresponding weak form* (4.54d) *has to be introduced. In comparison to the weak constraint enforcement derived above, there is, however, a drawback to this method: it becomes ill-conditioned for large values of* β_{c}*, that is for a high thermal conductivity enforcing the two contacting surfaces to have the same temperature. In this case, the terms* $\beta_{\mathrm{c}}\lambda_{\mathrm{n}}[\![T]\!]$ *will dominate the remaining terms in the discretized weak form of* (4.61)*. The presented weak constraint enforcement* (4.54d)*, and its discrete counterpart* (4.60)*, on the other hand, reduce to a mesh tying type condition weakly enforcing continuity of temperatures across the contact interface and therefore remains well-conditioned in the limit* $\beta_{\mathrm{c}} \to \infty$*.*

4.2.2 Algebraic Representation

The fully coupled nonlinear system to be solved for each time step is comprised of the structural and thermal equilibrium (4.18) and (4.58), respectively, the contact NCP function $\boldsymbol{G}_{\mathrm{c},i} = \boldsymbol{n}_i G_{\mathrm{n},i} + \boldsymbol{G}_{\tau,i}$ composed by its normal and tangential components (4.22) and (4.23), and, finally, thermal contact interface condition (4.60). All in all, one obtains

$$\boldsymbol{r}_{\mathrm{u}}(\mathbf{d},\mathbf{T},\boldsymbol{\lambda}) = \mathbf{0} \ , \tag{4.62a}$$

$$\boldsymbol{r}_{\mathrm{T}}(\mathbf{d},\mathbf{T},\boldsymbol{\lambda},\boldsymbol{\lambda}_{\mathrm{T}}) = \mathbf{0} \ , \tag{4.62b}$$

$$\boldsymbol{G}_{\mathrm{c},i}(\mathbf{d},\mathbf{T},\boldsymbol{\lambda}) = \mathbf{0} \qquad \forall i \in \mathcal{L} \ , \tag{4.62c}$$

$$G_{\mathrm{T},i}(\mathbf{d},\mathbf{T},\boldsymbol{\lambda},\boldsymbol{\lambda}_{\mathrm{T}}) = 0 \qquad \forall i \in \mathcal{L} \ , \tag{4.62d}$$

which is to be solved for the discrete displacements and temperatures $\mathbf{d}$ and $\mathbf{T}$ as well as the Lagrange multipliers $\boldsymbol{\lambda}$ and $\boldsymbol{\lambda}_{\mathrm{T}}$. As in the isothermal case (cf. equation (4.24)), (4.62) is non-smooth due to the involved NCP functions, but still amenable to non-smooth versions of Newton's method. A consistent linearization with respect to all unknowns yields the tangent system

$$\begin{bmatrix} \mathbf{K}_{\mathrm{uu},\mathcal{N}} & \mathbf{K}_{\mathrm{uT},\mathcal{N}} & \mathbf{0} & \mathbf{0} \\ \breve{\mathbf{K}}_{\mathrm{uu},\mathcal{S}} & \mathbf{K}_{\mathrm{uT},\mathcal{S}} & a_{\mathrm{c}}\mathbf{D}^{\mathsf{T}} & \mathbf{0} \\ \breve{\mathbf{K}}_{\mathrm{uu},\mathcal{M}} & \mathbf{K}_{\mathrm{uT},\mathcal{M}} & -a_{\mathrm{c}}\mathbf{M}^{\mathsf{T}} & \mathbf{0} \\ \mathbf{K}_{\mathrm{Tu},\mathcal{N}} & \mathbf{K}_{\mathrm{TT},\mathcal{N}} & \mathbf{0} & \mathbf{0} \\ \breve{\mathbf{K}}_{\mathrm{Tu},\mathcal{S}} & \mathbf{K}_{\mathrm{TT},\mathcal{S}} & \mathbf{0} & \alpha_{\mathrm{f,T}}\mathbf{D}_{\mathrm{T}}^{\mathsf{T}} \\ \breve{\mathbf{K}}_{\mathrm{Tu},\mathcal{M}} & \mathbf{K}_{\mathrm{TT},\mathcal{M}} & \mathbf{V} & -\alpha_{\mathrm{f,T}}\mathbf{M}_{\mathrm{T}}^{\mathsf{T}} \\ \mathbf{C}_{\mathrm{u}} & \mathbf{C}_{\mathrm{T}} & \mathbf{C}_{\boldsymbol{\lambda}} & \mathbf{0} \\ \mathbf{E}_{\mathrm{u}} & \mathbf{E}_{\mathrm{T}} & \mathbf{E}_{\boldsymbol{\lambda}} & \mathbf{E}_{\boldsymbol{\lambda}_{\mathrm{T}}} \end{bmatrix} \begin{bmatrix} \Delta\mathbf{d} \\ \Delta\mathbf{T} \\ \Delta\boldsymbol{\lambda} \\ \Delta\boldsymbol{\lambda}_{\mathrm{T}} \end{bmatrix} = - \begin{bmatrix} \boldsymbol{r}_{\mathrm{u},\mathcal{N}} \\ \boldsymbol{r}_{\mathrm{u},\mathcal{S}} \\ \boldsymbol{r}_{\mathrm{u},\mathcal{M}} \\ \boldsymbol{r}_{\mathrm{T},\mathcal{N}} \\ \boldsymbol{r}_{\mathrm{T},\mathcal{S}} \\ \boldsymbol{r}_{\mathrm{T},\mathcal{M}} \\ \boldsymbol{G}_{\mathrm{c}} \\ \boldsymbol{G}_{\mathrm{T}} \end{bmatrix} \tag{4.63}$$

to be solved in every Newton step. Therein, $a_\mathrm{c} = 1 - \alpha_{\mathrm{f,c}}$ denotes the time integration factor for the contact forces, the matrix $\mathbf{V}$ follows differentiation of (4.56) with respect to the contact Lagrange multiplier $\boldsymbol{\lambda}$, and $\mathbf{E}_*$ represent the derivatives of $\boldsymbol{G}_\mathrm{T}$ with respect to the discrete unknowns. These matrix blocks are not specified in detail here, as their derivation follow straightforwardly from (4.60) and do not yield any further insight. The superposed check at the stiffness blocks $\mathbf{K}_{*\mathrm{u}}$ indicates that these blocks contain additional linearizations of the discrete coupling forces and heat fluxes with respect to the displacement unknowns. Finally, in the case of thermo-elasto-plastic materials, the stiffness blocks $\mathbf{K}_*$ and the residuals $\boldsymbol{r}_*$ contain the condensed plastic NCP functions of every quadrature point as derived in Section 3.4.3.

If dual basis functions as introduced in Section 4.1.2 for finite elements and Section 4.1.4 for NURBS are used for the Lagrange multipliers $\boldsymbol{\lambda}$ and λ_T, the mortar matrices $\mathbf{D}$ and $\mathbf{D}_\mathrm{T}$ are of square and diagonal shape. Hence, the Lagrange multiplier increments can be trivially condensed one after another: the second and fifth row of (4.63) can easily be solved for the increments $\Delta\boldsymbol{\lambda}$ and $\Delta\boldsymbol{\lambda}_\mathrm{T}$. The general procedure is similar to the one presented in Section 4.1.2, however, in the thermomechanically coupled system, expressions become more cumbersome such that an explicit presentation of the condensed system is omitted here. After inserting those values for the Lagrange multiplier increments in the other lines, the remaining linear system to be solved consists of displacement and temperature degrees of freedom only; in an abstract notation, it reads

$$\begin{bmatrix} \mathcal{K}_{\mathrm{uu}} & \mathcal{K}_{\mathrm{uT}} \\ \mathcal{K}_{\mathrm{Tu}} & \mathcal{K}_{\mathrm{TT}} \end{bmatrix} \begin{bmatrix} \Delta\mathbf{d} \\ \Delta\mathbf{T} \end{bmatrix} = - \begin{bmatrix} \not{r}_\mathrm{u} \\ \not{r}_\mathrm{T} \end{bmatrix} \quad . \tag{4.64}$$

Having solved this condensed system, the discrete Lagrange multiplier values can be recovered using the second and fifth row of (4.63). Obviously, a similar condensation can be performed for the piece-wise constant Lagrange multiplier interpolation introduced in Section 4.1.3.

4.2.3 Numerical Examples

In the following, several numerical examples are presented to demonstrate the wide range of applications covered with the methods presented. In a first step, consistency of the discrete method is demonstrated by a thermomechanical contact patch test. Next, optimal spatial convergence orders are demonstrated in a finite deformation two-body contact problem for first and second order finite elements as well as NURBS-based isogeometric analysis. Next, the incorporation of frictional dissipation is analyzed. After that, energy conservation is investigated in a dynamic thermomechanical contact setting. Finally, a fully coupled thermo-elasto-plastic contact simulation concludes this section.

4.2.3.1 Stationary Heat Conduction

In this first example, the pressure dependent heat conduction (i.e. the first term on the right hand sides of (2.129)) over a non-matching contact interface is verified. This setting has already been studied in Oancea and Laursen [159], Wriggers and Miehe [236] for node-to-segment contact formulations with a matching interface discretization and a similar setting in Zavarise *et al.* [249]. Contact between two elastic unit cubes is analyzed, where the lower surface of the lower cube is supported and kept at a fixed temperature of 20, while the upper surface of the upper block is subjected to an increasing Neumann load and has a fixed temperature of 40, see Figure

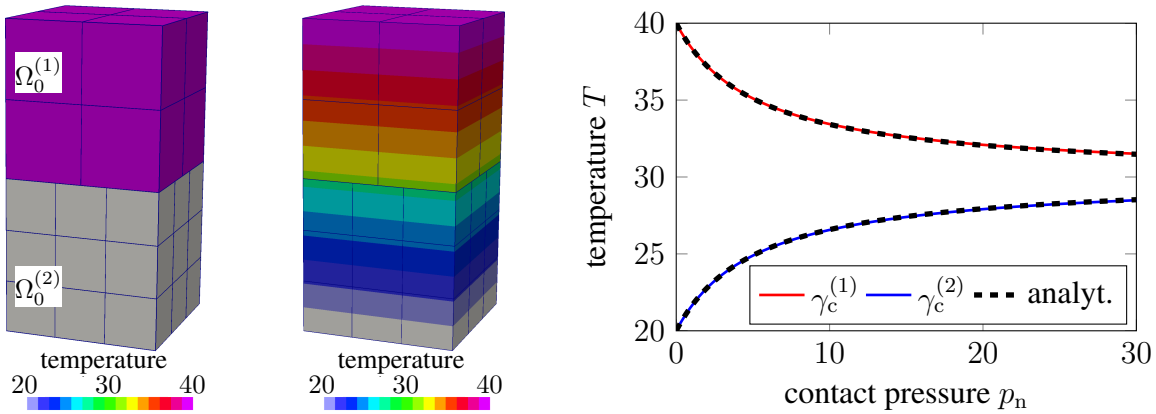

(a) $p_n = 0$. (b) $p_n = 30$. (c) Interface temperatures over p_n.

Figure 4.27: Thermomechanical contact patch test – Temperature distribution at different contact pressure and comparison with analytical solution.

4.27a. Both blocks are modeled with a Saint-Venant–Kirchhoff material with Young's modulus $E = 4000$, Poisson's ratio $\nu = 0$, a heat conductance of $k_0 = 52$ and no thermal expansion. For this setup, there exists an analytical solution for the steady state [236]. Figure 4.27b shows the resulting linear temperature distribution within each block. As can be expected for mortar methods, the contact patch test is passed to machine precision, i.e. a spatially constant contact pressure and contact heat flux can be transmitted exactly. Moreover, Figure 4.27c compares the interface temperatures depending on the normal contact pressure with the analytical solution, which is recovered perfectly. Notably, the results are independent of the choice of slave and master side and do not require a matching interface discretization as used in previous studies [159, 236].

4.2.3.2 Frictionless Two Body Contact: Convergence Study

To further study the accuracy of the presented method, spatial convergence is investigated in the following example. Thereto, the example introduced in Section 4.1.3.2.2 is extended to thermomechanics. Again, the contact of a cylindrical arc with a rectangular block is analyzed and, to include thermal coupling, the lower edge of the block is fixed at $\hat{T} = 0$ and the upper edges of the arc are fixed at $\hat{T} = 1$, see Figure 4.28a, for the exact geometric setup and boundary conditions. As in the isothermal setting of Section 4.1.3.2.2, both bodies are modeled with a neo-Hookean material law (3.38) with $E^{(1)} = 5$, $E^{(2)} = 1$ and $\nu^{(1)} = \nu^{(2)} = 0.2$. Further, thermal expansion according to (3.47) with the coefficent of thermal expansion $\alpha_\mathrm{T}^{(1)} = \alpha_\mathrm{T}^{(2)} = 0.01$ is included and thermal conductivities are set to $k_0^{(1)} = 1$ and $k_0^{(2)} = 5$. At the contact interface, frictionless contact is assumed with a contact heat conductivity $\beta_\mathrm{c} = 10^3$. The lower edge of the rectangular block is moved upwards quasi-statically to a total displacement of $\hat{u} = 0.3$; the final configuration and temperature distribution is illustrated in Figure 4.28b.

Figure 4.29 depicts the convergence behavior in the H^1 semi-norms of the discrete displacement and temperature fields within the two bodies $\Omega_0^{(1)}$ and $\Omega_0^{(2)}$ for mesh sizes of $h \in [2^{-7}, 2^{-1}]$. Different spatial discretizations and Lagrange multiplier methods derived in Sections 4.1.2 -

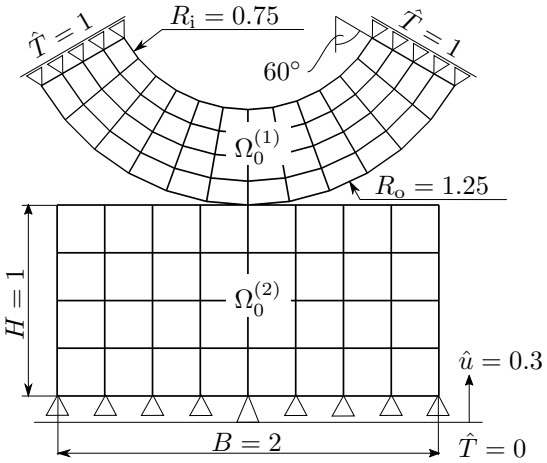

(a) Initial geometry, boundary conditions and exemplary mesh with $h = 2^{-2}$.

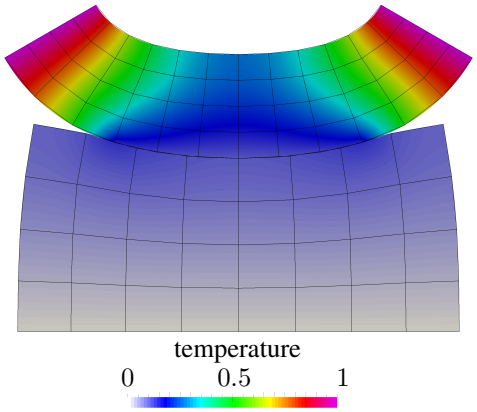

(b) Deformed mesh and temperature distribution for $h = 2^{-2}$ and $\mathbb{Q}_2$ finite elements.

Figure 4.28: Two dimensional contact of a circular arc with a rectangle – Geometric setup, exemplary mesh and deformed configuration.

4.1.4, namely

(a) first order $\mathbb{Q}_1$ finite elements with dual Lagrange multipliers (Figure 4.29a)

(b) second order $\mathbb{Q}_2$ finite elements with dual Lagrange multipliers (Figure 4.29b)

(c) second order $\mathbb{Q}_2$ finite elements with piece-wise constant Lagrange multipliers (Figure 4.29c)

(d) second order NURBS $\mathbb{R}_2$ with dual Lagrange multipliers (Figure 4.29d).

Since no analytical reference solution exists, errors are calculated versus a numerical reference solution obtained on a mesh of size $h = 2^{-8}$ with second order finite elements in combination with the dual Lagrange multiplier method. Before going into detail with the comparison of the different methods, it should be stressed that all variants converge with their respective optimal orders. In particular, the first order approximation in Figure 4.29a converges with $\mathcal{O}(h)$, whereas the second order approximations based on either finite elements or NURBS converge with order $\mathcal{O}(h^{3/2})$. In comparison of the two second order finite elements with either dual (Figure 4.29b) or piece-wise constant Lagrange multipliers (Figure 4.29c), the latter option yields slightly higher error values which confirms the findings of the isothermal case in Section 4.1.3.2.2. The loss in accuracy is, however, a small price to pay in view of the significantly simplified construction of the Lagrange multiplier basis. The second order NURBS approximation also converges with order $\mathcal{O}(h^{3/2})$, however, the absolute values are larger than for quadratic finite elements. Figure 4.30 gives a more detailed comparison of the second order NURBS discretization to the $\mathbb{Q}_2$ approximation both using dual Lagrange multipliers. The NURBS discretization yields larger errors compared to the $\mathbb{Q}_2$ approximations at the same mesh size (Figure 4.30a). This is not surprising, at the same mesh size h, the isogeometric approximation has a smaller function space. More specifically, the B-spline basis used for the discretization of $\Omega_0^{(2)}$ at a certain mesh size is included entirely in the corresponding $\mathbb{Q}_2$ discretization at the same mesh size. In addition the

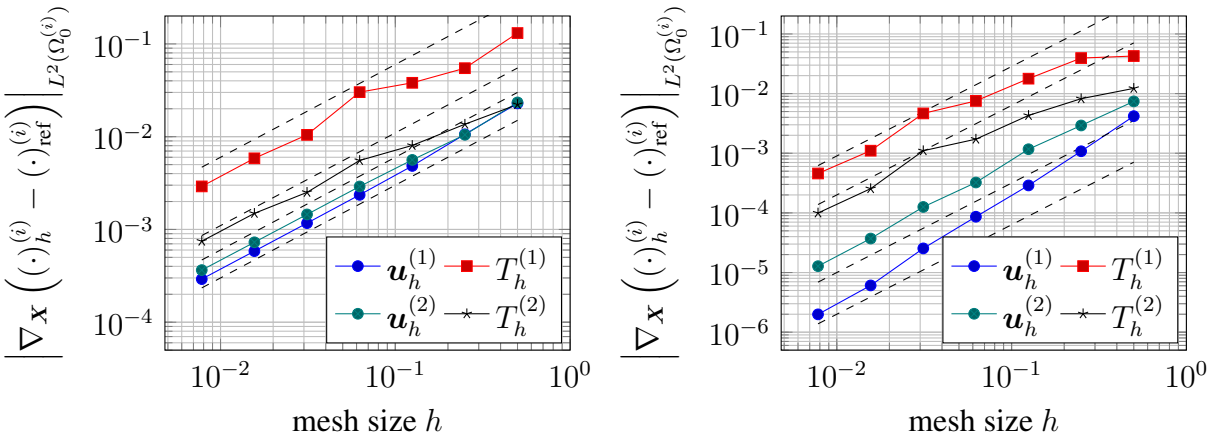

(a) $\mathbb{Q}_1$, dual Lagrange multiplier.

(b) $\mathbb{Q}_2$, dual Lagrange multiplier.

(c) $\mathbb{Q}_2$, piece-wise constant Lagrange multiplier.

(d) $\mathbb{R}_2$, dual Lagrange multiplier.

Figure 4.29: Two dimensional contact of a circular arc with a rectangle – Spatial convergence of different discretizations and Lagrange multiplier methods. Dashed lines indicate the optimal order of the respective method, that is $\mathcal{O}(h)$ in Figure 4.29a and $\mathcal{O}(h^{3/2})$ in Figures 4.29b - 4.29d.

$\mathbb{Q}_2$ approximation can represent kinks of the primal variables at element boundaries which $\mathbb{R}_2$ cannot. This, in turn, yields the lower errors of the $\mathbb{Q}_2$ approximation. If, however, the errors are analyzed with respect to the number of, respectively, nodes or control points, the isogeometric case is slightly more accurate in the displacement solution, whereas the error in the discrete temperature field is of similar accuracy as compared to finite elements (cf. Figure 4.30b).

4.2.3.3 Frictional Heating of a Rotating Ring

This short validation example is concerned with the effects of frictional heating. A rectangular block $\Omega_0^{(1)}$ of dimensions 100×25 is pressed onto a ring $\Omega_0^{(2)}$ with an inner radius $R_\mathrm{i} = 75$ and an outer radius of $R_\mathrm{o} = 100$. The top surface of the block is loaded with a constant vertical Neumann load of, in total, $F_\mathrm{n} = 150$. Moreover, this top surface is fixed in horizontal direction and kept planar at all time and the ring rotates at various angular velocities ω. Both

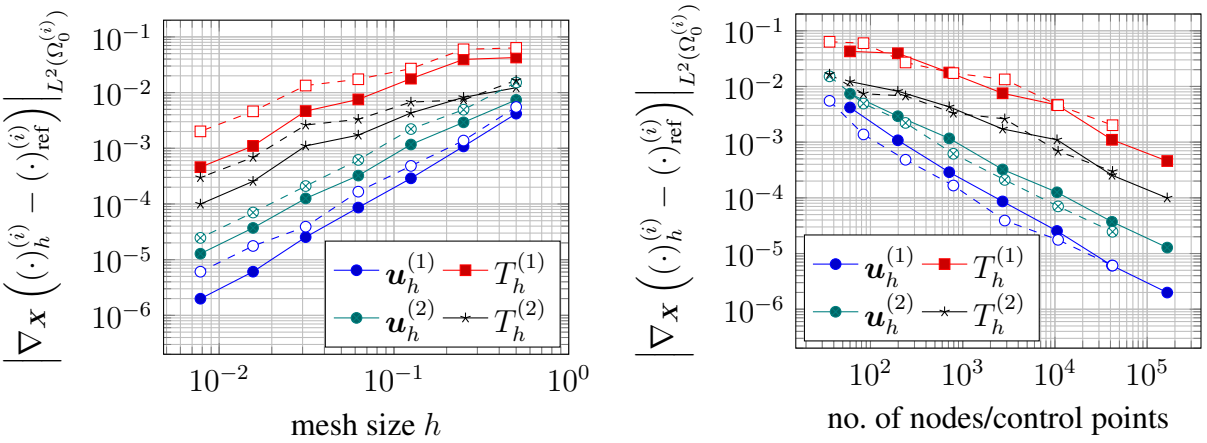

(a) Comparison by mesh size.

(b) Comparison by number of nodes or control points.

Figure 4.30: Two dimensional contact of a circular arc with a rectangle – Comparison of spatial convergence of second order finite elements (solid lines), and second order NURBS (dashed lines). For both approximations, dual Lagrange multipliers are employed.

bodies are modeled with a Saint-Venant–Kirchhoff masterial with Young's moduli $E_{\text{block}} = 2$ and $E_{\text{ring}} = 10$ and Poisson's ratios $\nu_{\text{block}} = \nu_{\text{ring}} = 0.25$ under plane strain conditions with a thickness of $z = 10$. The thermal material parameters are given by a specific heat capacity $c_{\text{v}} = 10^{-3}$ and thermal conductivity $k_0 = 6$. To keep the focus on the thermomechanical contact and avoid potential thermo-elastic dissipation effects, themal expansion is not accounted for in this example, i.e. $\alpha_{\text{T}} = 0$, and the structural response is assumed to be quasi-static. At the contact between the block and the ring, frictional contact is assumed with a temperature dependent coefficient of friction according to (2.125) with $\mu_0 = 0.2$, $T_0 = 293$ and $T_{\text{d}} = 493$. Further, heat conduction across the contact interface is precluded and the entire frictional power is converted to heat within the ring by setting the parameters $\beta_{\text{c}} = \delta_{\text{c}} = 0$. By doing so, and assuming an instantaneous heat conduction ($k_0 \to \infty$), or equivalently low rotational speeds $\omega \to 0$, an analytical solution for the temperature, or equivalently the thermal energy E_{thr}, of the ring can be derived:

$$E_{\text{Thr}} = \int_{\Omega_0^{(2)}} c_{\text{v}} T \,\mathrm{d}\Omega = \left(T_{\text{d}} - \frac{1}{\frac{1}{T_{\text{d}}-T_0} + \frac{\mu_0 F_{\text{n}} R_{\text{o}}}{(T_{\text{d}}-T_0)^2 c_{\text{v}} \pi z \left(R_{\text{o}}^2 - R_{\text{i}}^2\right)} \alpha(t)} \right) c_{\text{v}} \pi z \left(R_{\text{o}}^2 - R_{\text{i}}^2\right) \quad , \tag{4.65}$$

where $\alpha(t)$ is the rotation angle of the ring over time. Figure 4.31 displays the temperature distribution in the ring for different angular frequencies. Clearly, the higher the angular frequencies are, the more inhomogeneous the temperature distribution becomes; for the lowest shown frequency of $\omega = 10^{-1}$ an almost constant temperature across the entire ring is obtained. In Figure 4.32, the analytical solution is recovered for low angular frequencies, whereas higher frequencies show a discrepancy as the assumptions made for the analytical solution are not met. For all frequencies, the apparent coefficient of friction drops due to the increasing temperature, thus reducing the slope in the energy gain. Higher angular velocities result in locally higher temperatures in the contact zone (cf. Figure 4.31c) and therefore a lower friction coefficient, consequently reducing the increase in thermal energy. Ultimately, all energy curves in Figure

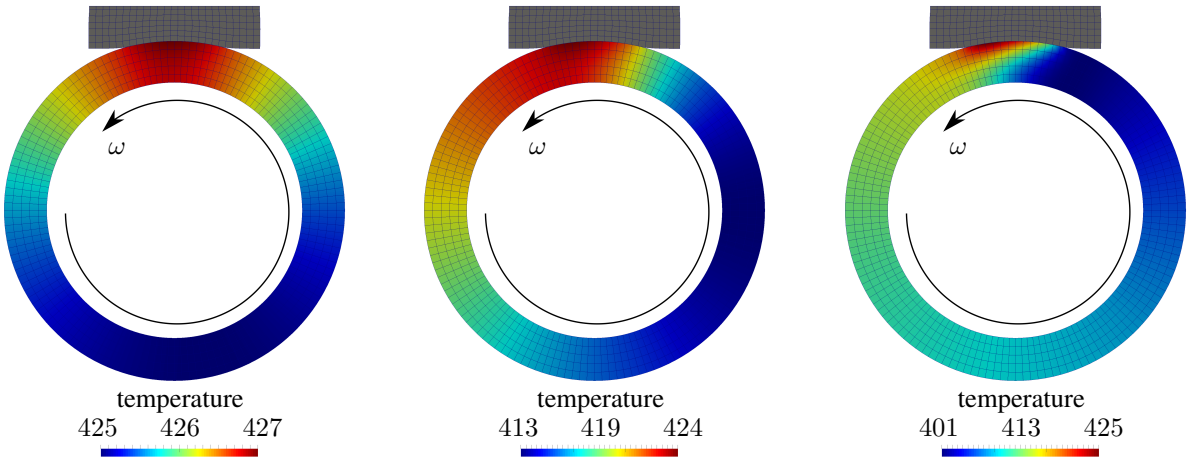

(a) $\omega = 10^{-1}$ (b) $\omega = 10^{0}$ (c) $\omega = 10^{1}$

Figure 4.31: Frictional heating of a rotating ring – Temperature distribution after three full rotation at different angular frequencies.

4.32 saturate at an energy, which corresponds to a homogeneous temperature T_d in the entire ring. Approaching this temperature, the friction coefficient tends to zero, thus precluding any further thermal energy being introduced via work of friction at the interface.

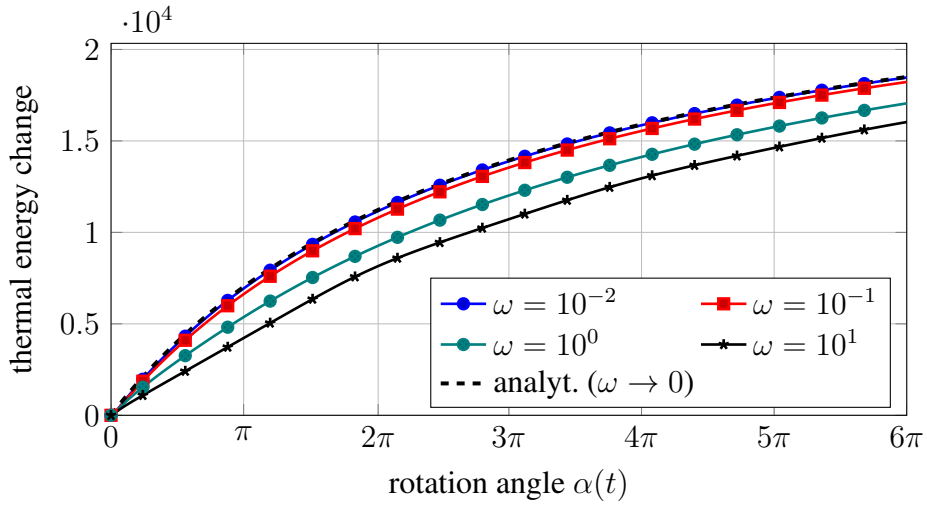

Figure 4.32: Frictional heating of a rotating ring – Change of thermal energy for different angular velocities ω compared to the analytical value for $\omega \to 0$.

4.2.3.4 Bouncing Ball

The next example considers contact dynamics and especially matters of energy conservation in the discrete system. A bouncing hollow sphere ($\Omega_0^{(1)}$, outer radius 4, inner radius 1) between two rigid plates ($\Omega_0^{(2)}$, dimensions $50 \times 1 \times 10$, distance 14) is simulated. The ball is modeled with a Saint-Venant–Kirchhoff material with Young's modulus $E = 12.5$ and Poisson's ratio

$\nu = 0.2$. The heat capacity and conductivity of the ball and the two plates are set to $c_{\mathrm{v,ball}} = 0.1$, $c_{\mathrm{v,plate}} = 1$, $k_{0,\mathrm{ball}} = 1$ and $k_{0,\mathrm{plate}} = 0.1$, respectively. Initially, the ball is given a velocity of $\sqrt{2}$ in a 45 degree angle towards the lower plate and a superimposed spin around an inclined axis. Initial temperatures are 1 in the ball and 0 in the plates. The coefficient of thermal expansion α_{T} is set to zero, such that no transfer from mechanical to thermal energy is possible and vice-versa. The ball is discretized with 3456 second order NURBS elements and the plates with 459 elements each. Figure 4.33 shows the deformation and temperature distribution at different time steps. During

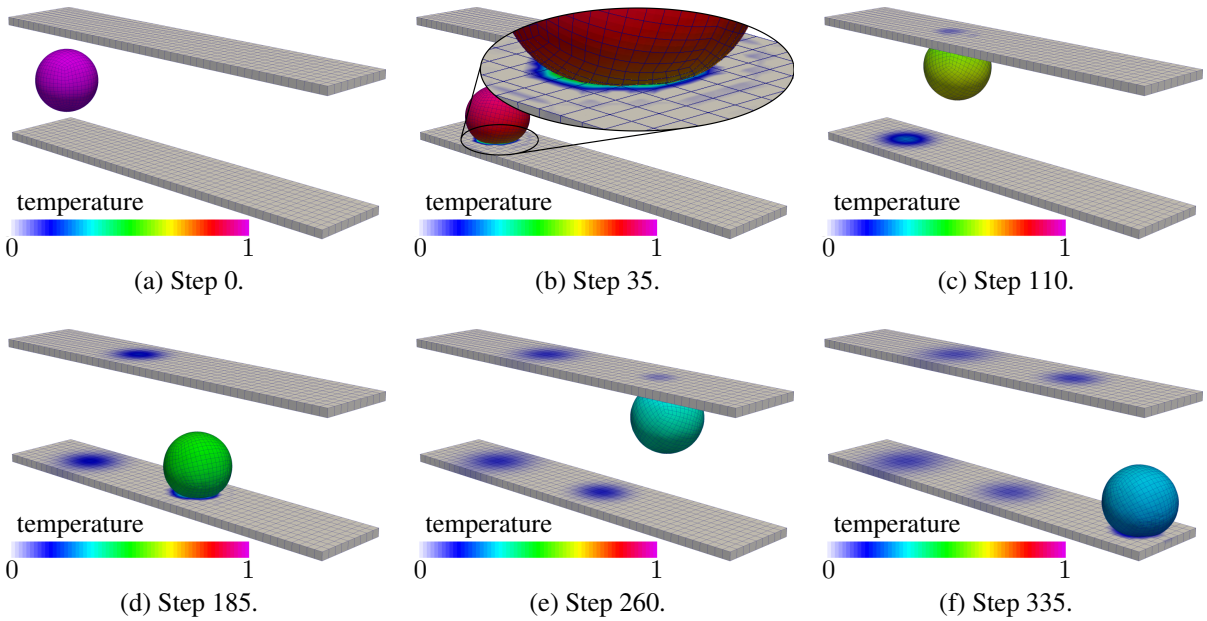

(a) Step 0. (b) Step 35. (c) Step 110.

(d) Step 185. (e) Step 260. (f) Step 335.

Figure 4.33: Bouncing ball – Temperature distribution and deformation state for $\rho_{\infty,\mathrm{u}} = \rho_{\infty,\mathrm{T}} = 0.9$ at different time steps.

the five contact events, heat is transferred from the ball to the plates and the ball cools down to a final temperature of approximately 0.25, meaning that 75% of the thermal energy in the system is transmitted through the contact interface. Owing to the relatively coarse discretization of the plates in combination with their low thermal conductivity, slight oscillations in the temperature distribution occur in the surroundings of the contact zone, see Figure 4.33b. This is due to the inability of the coarse discretization to correctly reproduce the steep gradients in the temperature field, an effect that vanishes for finer discretizations. Figure 4.34 shows the relative change in mechanical and thermal energy over time for different spectral radii of the generalized-α time integration schemes. As outlined in Remark 2.5, exact algorithmic energy conservation cannot be expected with the employed time integrator. For $\rho_\infty = 1$, a gain of about 8% in mechanical energy after the five contact events (see Figure 4.34a) is observed. Smaller values of ρ_∞ yield an energy dissipative, stable behavior. The thermal energy in Figure 4.34b, on the other hand, is conserved to a very high accuracy, especially considering the fact that a significant amount is transmitted through the contact interface.

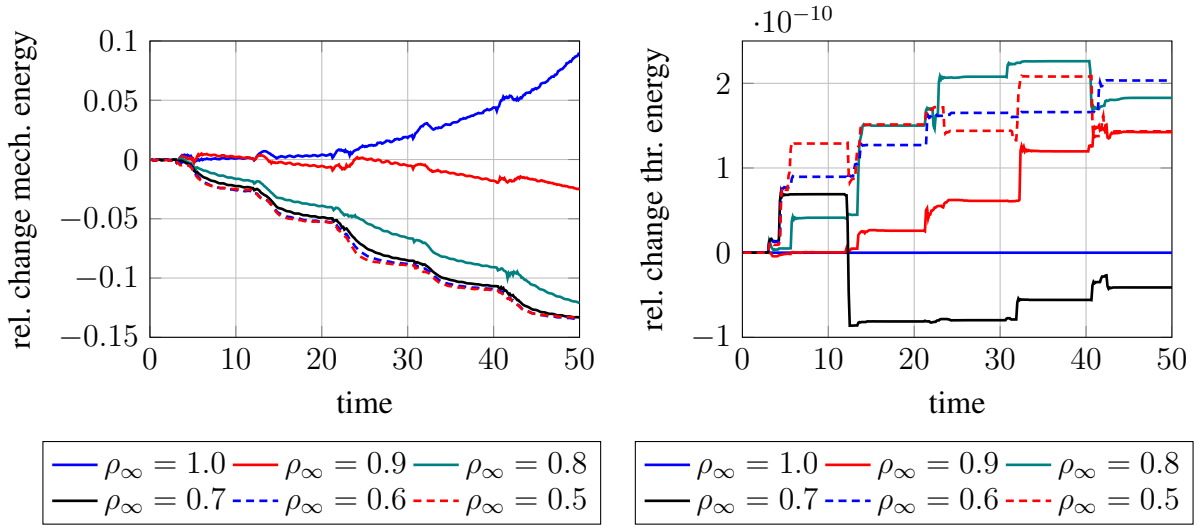

(a) Mechanical energy.

(b) Thermal energy.

Figure 4.34: Bouncing ball – Relative changes in mechanical and thermal energies for different time integration parameters $\rho_{\infty,\mathrm{u}} = \rho_{\infty,\mathrm{T}} = \rho_\infty$.

4.2.3.5 Squeezed Elasto-Plastic Tube

Finally, a fully coupled thermo-elasto-plastic contact example demonstrates the robustness of the developed thermomechanical contact algorithm and its compatibility with the computational method for thermoplasticity derived in Chapter 3. A squeezed metal tube $\Omega_0^{(1)}$ with an inner and outer radius of $4\,\mathrm{cm}$ and $5\,\mathrm{cm}$, respectively, and a length of $40\,\mathrm{cm}$ is analyzed. In the middle, the tube is squeezed by two rigid cylindrical tools $\Omega_0^{(2)}$ with an inner and outer radius of $4.5\,\mathrm{cm}$ and $5\,\mathrm{cm}$, respectively, and a length of $16\,\mathrm{cm}$. Figure 4.35 depicts the initial geometry and the employed mesh. Due to the symmetry of the problem, only one eighth of the entire model is discretized with about 20.000 first order F-bar finite elements (see Section 2.8.1.1 and de Souza Neto *et al.* [55]); all results are reflected for visualization purposes. The thermo-elasto-plastic material properties are set to the ones given in Table 3.2, with plastic isotropy,

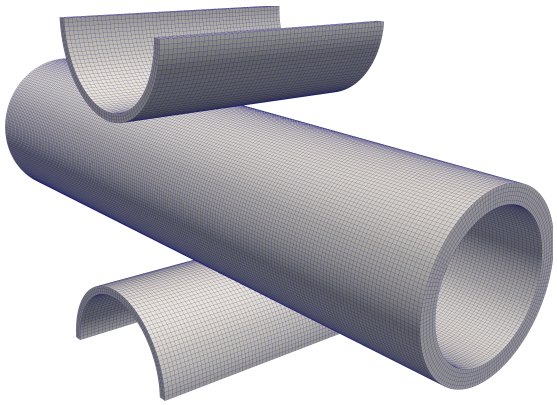

Figure 4.35: Squeezed elasto-plastic tube – Initial configuration and employed mesh.

i.e. $y_{11} = y_0$. Between the tools and the tube, frictional contact with a temperature dependent friction coefficient according to (2.125) is assumed with the initial coefficient of friction $\mu_0 = 0.25$, the reference temperature $T_0 = 293\,\mathrm{K}$ and the damage temperature $T_\mathrm{d} = 1793\,\mathrm{K}$. Heat conduction across the contact interface is allowed with $\beta_\mathrm{c} = 0.1\,\frac{\mathrm{W}}{\mathrm{N\,K}}$ and frictional dissipation is evenly distributed to the two sides by $\delta_\mathrm{c} = 0.5$. The tools are initially in stress free contact and perform a vertical displacement of $u(t) = (1-\cos(\frac{t}{1\,\mathrm{s}}\pi))\cdot 1.75\,\mathrm{cm}$ over time. Figure 4.36 illustrates the plastic strain and temperature distribution at different times. In the early de-

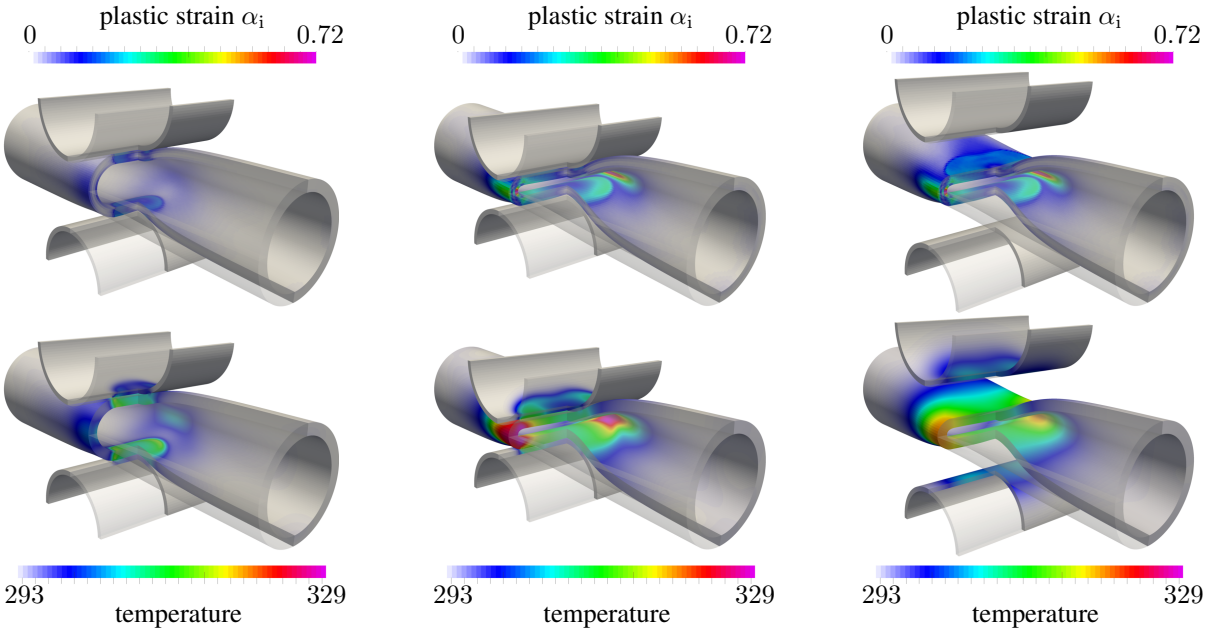

Figure 4.36: Squeezed elasto-plastic tube – Deformed configurations at different times including accumulated plastic strain and temperature distribution.

formation stages, plastic deformation and the heat generation induced thereby is mainly located directly beneath the contact zone (see Figure 4.36a), whereas later the main plastic deformation occurs at the side of the tube, where the highest temperatures are reached (see Figure 4.36b). After contact is released, thermal conduction tends to equilibrate the temperature inhomogeneity, see Figure 4.36c. The results of a coupled thermo-elasto-plastic analysis are compared with an isothermal simulation. Figure 4.37 displays the total contact forces for the two cases: initially, the temperature changes are low and the contact forces for both cases practically coincide. As the temperature increases, the coupled thermomechanical analysis softens and terminally yields contact forces about 4% lower than in the isothermal case, with a peak temperature change of $36\,\mathrm{K}$.

The presented monolithic scheme for thermo-elasto-plastic contact solves this problem within only 100 time steps with a constant step size of $\Delta t = 0.02\,\mathrm{s}$, of which the first 55 steps involve contact. Each of those time steps is solved with a standard Newton–Raphson scheme, which required an average of 9.9 iterations to converge to machine precision.To illustrate the efficient nonlinear solution procedure using Newton's method with a consistent linearization, Figure 4.38 displays the convergence behavior of different residual contributions in the time step of maximal

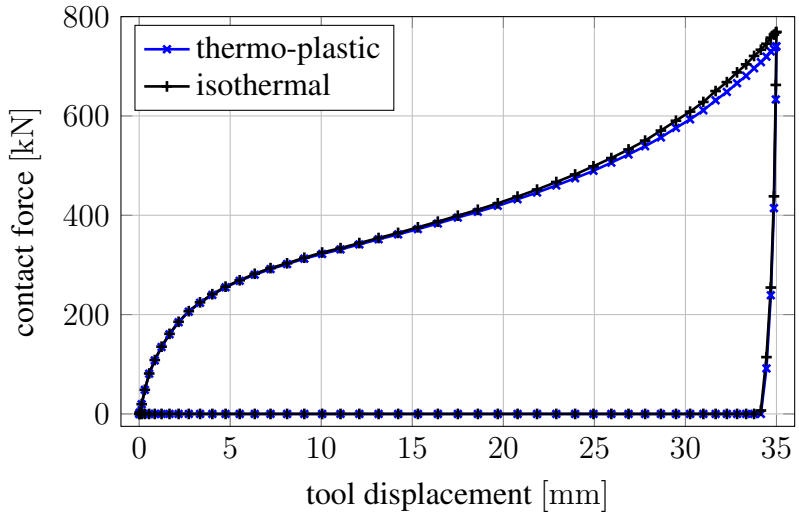

Figure 4.37: Squeezed elasto-plastic tube – Contact force over tool displacement for isothermal and coupled thermomechanical analysis.

tool velocity ($t = 0.5\,\mathrm{s}$). All residuals clearly exhibit a quadratic rate of convergence asymptotically, until they are at some point limited by machine precision. The residual of the NCP function for plasticity (3.44c), for instance, has been reduced by ten orders of magnitude within the first seven iterations and is then limited by numerical accuracy. In the final iteration steps, also the other residual contributions converge rapidly as expected.

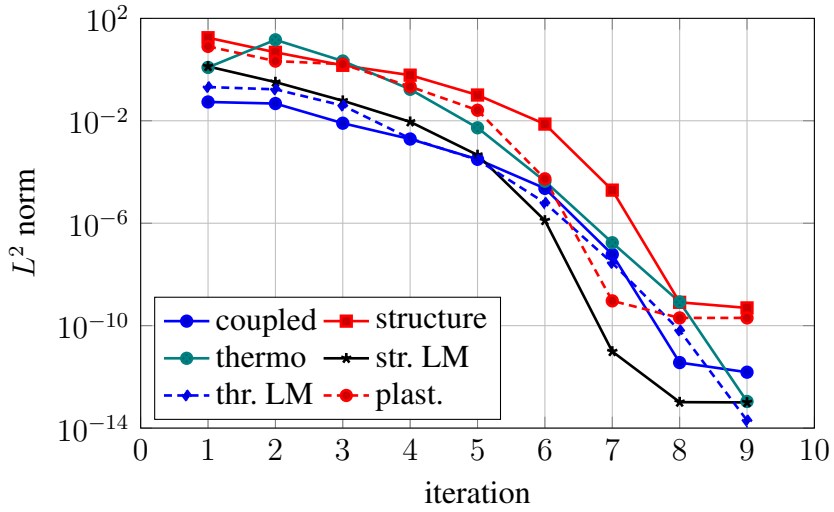

Figure 4.38: Squeezed elasto-plastic tube – Convergence of different residuals in Newton's method for $t = 0.5\,\mathrm{s}$. "coupled" shows the residual of (4.64), "structure" the residual (4.62a), "thermo" the residual (4.62b), "str. LM" the residual of (4.62c), "thr. LM" the residual (4.62d) and "plast." the residual (3.44c).

5 Nitsche Methods for Computational Contact Mechanics

In this chapter, a finite element method for thermo-elasto-plastic frictional contact based on Nitsche's method is derived. As for the mortar method derived in Chapter 4, the point of departure is the continuum mechanical description of the thermomechanical contact problem presented in Section 2.7, more specifically the weak forms in 2.7.4. In contrast to the mortar method, which is based on a mixed finite element method, Nitsche's method provides an alternative to impose boundary or interface constraints without the necessity to introduce any additional unknowns. Thereby, the consistent boundary integral in the derivation of the weak form remain unaltered and additional terms are added to weakly enforce the constraints. Stability of the numerical method is ensured by the presence of a consistent penalty term. In multi-field problems, e.g. thermomechanics, all coupling terms arise naturally by the respective inter-dependency of derived quantities, such as stresses, in the boundary integral. The apparent simplicity of Nitsche's method comes at the expense of the fact that the boundary traction computed from the underlying bulk discretization remains to be evaluated in the weak form. While this is rather simple to compute in linear problems, it adds significant complexity in nonlinear elasticity and elasto-plasticity.

The following derivation of Nitsche's method for contact problems starts with the isothermal case of finite deformation frictional contact in Section 5.1. Special focus is set on the nonlinearity resulting from finite deformation kinematics and nonlinear elasticity or even elasto-plasticity. Moreover, an accurate estimate for the required penalty parameter based on generlized eigenvalue problems is presented, which in the case of nonlinear material behavior needs to be updated to account for potential stiffening in the material. In Section 5.2, Nitsche's method is extended to thermomechanical contact problems. Two different methods to enforce the thermal interface conditions, i.e. heat flux across the contact interface and frictional heating, are presented.

It should be pointed out that the focus of this thesis is on nonlinear, coupled multi-field problems which, in general, precludes a thorough numerical analysis of well-posedness and optimal *a priori* error estimates. Nevertheless, convergence orders are investigated by numerical examples and optimal results are confirmed. Moreover, all methods derived for nonlinear problems in the following have been analyzed mathematically for simplified problems elsewhere; in particular, an analysis of Nitsche's method for isothermal small deformation frictionless contact can be found in Chouly *et al.* [35] and the penalty free variant in Burman *et al.* [25]. An extension to Tresca friction is investigated by Chouly [33]. The proposed Nitsche-type formulation for contact heat conduction is based on the original work by Juntunen and Stenberg [118], who provides numerical analysis for general boundary conditions on a Poisson problem. An extension to the genaral Navier boundary condition is presented by Winter *et al.* [231], who also perform mathematical analysis of a skew-symmetric variant on the Oseen equation. Finally, an adaptation

of the method of Juntunen and Stenberg [118] to interface rather than boundary conditions on linear elasticity problems is given by Annavarapu *et al.* [5].

5.1 Nitsche Methods for Isothermal Contact Problems

The starting point for the derivation of Nitsche's method for isothermal contact problems is the weak form (2.132). In its discretized form, it reads: Find $\boldsymbol{u}_h \in \boldsymbol{\mathcal{U}}_{\mathrm{u},h}$, such that

$$\delta\mathcal{W}_{\mathrm{u},h} - \int_{\gamma_{\mathrm{c},h}^{(1)}} \boldsymbol{t}_{\mathrm{c},h} \cdot [\![\delta\boldsymbol{u}_h]\!] \,\mathrm{d}\gamma = 0 \quad \forall \delta\boldsymbol{u}_h \in \boldsymbol{\mathcal{V}}_{\mathrm{u},h} \ . \tag{5.1}$$

Therein, $\delta\mathcal{W}_{\mathrm{u},h}$ (as defined in (2.141)) contains the contributions of intertia, internal and external forces. On the discrete contact boundary $\gamma_{\mathrm{c},h}^{(1)}$, the discrete contact traction $\boldsymbol{t}_{\mathrm{c},h} = \boldsymbol{t}_{\mathrm{c},h}^{(1)} = \boldsymbol{\sigma}_h^{(1)} \boldsymbol{n}_h^{(1)}$ of the slave side (see (2.104)) is computed from the approximate displacement field $\boldsymbol{u}_h^{(1)}$. In contrast to the mortar method of Chapter 4, where this traction is replaced by a discrete Lagrange multiplier field, it retains its original form of a boundary traction in Nitsche's method. In a first step towards a more general method, it is observed that, from (2.105),

$$\boldsymbol{t}_{\mathrm{c}} = \omega_{\mathrm{u}} \boldsymbol{t}_{\mathrm{c}}^{(1)} - (1-\omega_{\mathrm{u}}) \boldsymbol{t}_{\mathrm{c}}^{(2)} = \{\boldsymbol{t}_{\mathrm{c}}\}_{\omega_{\mathrm{u}}} \quad , \quad \omega_{\mathrm{u}} \in [0,1] \tag{5.2}$$

holds exactly in the continuous setting and approximately for the discrete solution. The operator $\{\cdot\}_{\omega}$ defined by (5.2) represents a weighted average of the traction derived from the slave and master side, respectively. The exact choice of the weighting ω_{u} will be discussed in detail in Section 5.1.2. The weighted average may be used in (5.1) to replace the contact traction yielding the discrete weak form: Find $\boldsymbol{u}_h \in \boldsymbol{\mathcal{U}}_{\mathrm{u},h}$, such that

$$\delta\mathcal{W}_{\mathrm{u},h} - \int_{\gamma_{\mathrm{c},h}^{(1)}} \{\boldsymbol{t}_{\mathrm{c},h}\}_{\omega_{\mathrm{u}}} \cdot [\![\delta\boldsymbol{u}_h]\!] \,\mathrm{d}\gamma = 0 \quad \forall \delta\boldsymbol{u}_h \in \boldsymbol{\mathcal{V}}_{\mathrm{u},h} \ , \tag{5.3}$$

wherein (5.1) can be recovered by $\omega_{\mathrm{u}} = 1$.

5.1.1 Weak Contact Constraint Enforcement

The weak form (5.3) represents a consistent approximation to the balance of linear momentum in the two contacting bodies. The additional contact constraints, i.e. the Hertz–Signiorini–Moreau conditions (2.119) in normal direction and Coulomb's law of friction (2.124) in tangential direction are still unaccounted for. Within this section, these inequality conditions are enforced on (5.3) weakly by means of different variations of Nitsche's method.

Normal contact constraints To include the Hertz–Signiorini–Moreau conditions (2.119) in the discretized weak form of the balance of linear momentum, the inequality constraints are reformulated in terms of non-smooth equality constraints. One possible reformulation has already been introduced as the NCP function in normal direction (4.22) as used in the mortar method of Chapter 4. In the context of Nitsche's method, a similar constraint function can be constructed

by replacing the negative Lagrange multiplier in normal direction $(-\lambda_{\mathrm{n},i})$ with the contact pressure p_n, the weighted gap $\tilde{g}_{\mathrm{n},i}$ with the local gap g_n and the complemetarity parameter c_n with a penalty parameter γ_n. One obtains

$$\{p_\mathrm{n}\}_{\omega_\mathrm{u}} = \left[\{p_\mathrm{n}\}_{\omega_\mathrm{u}} + \gamma_\mathrm{n} g_\mathrm{n}\right]_- \quad , \gamma_\mathrm{n} \geq 0 \quad , \tag{5.4}$$

where $[\cdot]_- = \min(0, \cdot)$ denotes the negative part of the argument. The penalty parameter therein is of order $\mathcal{O}(\frac{E}{h})$, where E represents the Young's modulus of one of the contacting materials and h the mesh size. The exact definition of the penalty parameter γ_n used will be the subject of Section 5.1.2. Since (5.4) holds if and only if the contact constraints (2.119) are met, these constraints can be enforced on (5.3) weakly by adding

$$\int_{\gamma_{\mathrm{c},h}^{(1)}} \left(\{p_{\mathrm{n},h}\}_{\omega_\mathrm{u}} - \left[\{p_{\mathrm{n},h}\}_{\omega_\mathrm{u}} + \gamma_\mathrm{n} g_{\mathrm{n},h}\right]_-\right) \left(\boldsymbol{n}_h \cdot [\![\delta \boldsymbol{u}_h]\!] - \frac{\theta_{\mathrm{u},1}}{\gamma_\mathrm{n}} \mathcal{D}\left\{p_{\mathrm{n},h}\right\}_{\omega_\mathrm{u}} [\delta \boldsymbol{u}_h]\right) \mathrm{d}\gamma \tag{5.5}$$

to (5.3). Therein, $\mathcal{D}y[x]$ denotes the directional derivative of y in direction of x and $\theta_{\mathrm{u},1} \in \{-1, 0, 1\}$ denotes a parameter. For linearized kinematics and $\omega_\mathrm{u} = 1$, this formulation is equivalent to the one presented by Chouly *et al.* [35], where the parameter $\theta_{\mathrm{u},1}$ is introduced to derive a symmetric variant ($\theta_{\mathrm{u},1} = 1$), a non-symmetric variant with fewer terms ($\theta_{\mathrm{u},1} = 0$) and a skew-symmetric variant ($\theta_{\mathrm{u},1} = -1$).

Recently, a more general formulation has been introduced by Burman *et al.* [25] in the context of the Signiorini problem, i.e., a Poisson problem with a boundary condition of type (2.119). Transferred to the present framework of nonlinear elasticity, it states that the inequality constraints (2.119) can also be cast in form of an equality condition as

$$\gamma_\mathrm{n} g_\mathrm{n} = \left[\{p_\mathrm{n}\}_{\omega_\mathrm{u}} + \gamma_\mathrm{n} g_\mathrm{n}\right]_+ \quad , \gamma_\mathrm{n} > 0 \quad , \tag{5.6}$$

with $[\cdot]_+ = \max(0, \cdot)$ denoting the positive part of the argument. Analogously to (5.5), the contact constraints can be in introduced in (5.3) weakly by adding

$$-\int_{\gamma_{\mathrm{c},h}^{(1)}} \left(\gamma_\mathrm{n} g_{\mathrm{n},h} - \left[\{p_{\mathrm{n},h}\}_{\omega_\mathrm{u}} + \gamma_\mathrm{n} g_{\mathrm{n},h}\right]_+\right) \left(\theta_{\mathrm{u},2} \boldsymbol{n}_h \cdot [\![\delta \boldsymbol{u}_h]\!] - \frac{\theta_{\mathrm{u},1}}{\gamma_\mathrm{n}} \mathcal{D}\left\{p_{\mathrm{n},h}\right\}_{\omega_\mathrm{u}} [\delta \boldsymbol{u}_h]\right) \mathrm{d}\gamma \quad , \tag{5.7}$$

with an additional parameter $\theta_{\mathrm{u},2} \in \{0, 1\}$. It can easily be verified that the classical version (5.5) of Chouly *et al.* [35] is recovered by (5.7) through fixing $\theta_{\mathrm{u},2} = 1$, such that further elaborations will be based on the more general case (5.7). When making the assumption of frictionless contact, the tangential stress $\boldsymbol{t}_\tau^{(i)}$ can be set to zero in the boundary integral of (5.3) and the resulting weak form including the contact constraints reads: Find $\boldsymbol{u}_h \in \boldsymbol{\mathcal{U}}_{\mathrm{u},h}$, such that

$$\begin{aligned} \delta \mathcal{W}_{\mathrm{u},h} &- \int_{\gamma_{\mathrm{c},h}^{(1)}} \{p_{\mathrm{n},h}\}_{\omega_\mathrm{u}} \boldsymbol{n}_h \cdot [\![\delta \boldsymbol{u}_h]\!] \, \mathrm{d}\gamma \\ &- \int_{\gamma_{\mathrm{c},h}^{(1)}} \left(\gamma_\mathrm{n} g_{\mathrm{n},h} - \left[\{p_{\mathrm{n},h}\}_{\omega_\mathrm{u}} + \gamma_\mathrm{n} g_{\mathrm{n},h}\right]_+\right) \\ &\qquad \cdot \left(\theta_{\mathrm{u},2} \boldsymbol{n}_h \cdot [\![\delta \boldsymbol{u}_h]\!] - \frac{\theta_{\mathrm{u},1}}{\gamma_\mathrm{n}} \mathcal{D}\left\{p_{\mathrm{n},h}\right\}_{\omega_\mathrm{u}} [\delta \boldsymbol{u}_h]\right) \mathrm{d}\gamma = 0 \quad \forall \delta \boldsymbol{u}_h \in \boldsymbol{\mathcal{V}}_{\mathrm{u},h} \quad . \end{aligned} \tag{5.8}$$

Tangential contact constraints For problems involving friction, a similar approach can be pursued to incorporate the contact constraints in tangential direction into the weak form (5.8). First, a time discrete form of the relative tangential velocity (2.103) is obtained by a simple backward-Euler method on the involved time derivatives (see e.g. Mlika *et al.* [152], Poulios and Renard [173]). For a time step $\Delta t = t_{n+1} - t_n$, this yields

$$\boldsymbol{v}_\tau(\boldsymbol{x}^{(1)}) \approx \frac{1}{\Delta t}\left(\boldsymbol{I} - \boldsymbol{n}_h \otimes \boldsymbol{n}_h\right)\left[\varphi_{t_n}^{(1)}(\boldsymbol{x}^{(1)}) - \varphi_{t_n}^{(2)}(\hat{\boldsymbol{x}}^{(2)}) - g_{\mathrm{n},h}\boldsymbol{n}_{h,n}\right] = \frac{\Delta \boldsymbol{u}_{\tau,h}(\boldsymbol{x}^{(1)})}{\Delta t} \quad , \tag{5.9}$$

wherein all quantities marked with a subscript $(\cdot)_n$ are evaluated at t_n and all others at t_{n+1}. Notably, the projection (2.101) to determine $\hat{\boldsymbol{x}}^{(2)}$ as the projection of $\boldsymbol{x}^{(1)}$ onto the master contact surface $\gamma_{\mathrm{c},h}^{(2)}$ is performed at t_{n+1}. Within one time step, the tangential slip distance is denoted as $\Delta \boldsymbol{u}_{\tau,h}$. The time discrete version of Coulomb's law of friction is then given by

$$\phi_\tau := \| \left\{\boldsymbol{t}_{\tau,h}\right\}_{\omega_\mathrm{u}} \| - \mu |p_{\mathrm{n},h}| \leq 0 \quad , \quad \Delta \boldsymbol{u}_{\tau,h} - \beta \left\{\boldsymbol{t}_{\tau,h}\right\}_{\omega_\mathrm{u}} = \boldsymbol{0} \quad , \quad \beta \geq 0 \quad , \quad \phi_\tau \beta = 0 \quad . \tag{5.10}$$

Inequality conditions of such type have already been transferred to equivalent equality constraints in the course of this thesis; once in the context of elasto-plasticity, see Chapter 3, and once in the context of mortar methods, see Chapter 4, which lead to the nonlinear complementarity functions (3.17a) and (4.23), respectively. For the present setting, (5.10) can be expressed equivalently as

$$\begin{aligned} \left\{\boldsymbol{t}_{\tau,h}\right\}_{\omega_\mathrm{u}} &= \min\left(1, \frac{-\mu\left[\left\{p_{\mathrm{n},h}\right\}_{\omega_\mathrm{u}} + \gamma_\mathrm{n} g_{\mathrm{n},h}\right]_-}{\| \left\{\boldsymbol{t}_{\tau,h}\right\}_{\omega_\mathrm{u}} + \gamma_\tau \Delta \boldsymbol{u}_{\tau,h} \|}\right)\left(\left\{\boldsymbol{t}_{\tau,h}\right\}_{\omega_\mathrm{u}} + \gamma_\tau \Delta \boldsymbol{u}_{\tau,h}\right) \\ &= P_{B(\bar{\mu})}\left(\left\{\boldsymbol{t}_{\tau,h}\right\}_{\omega_\mathrm{u}} + \gamma_\tau \Delta \boldsymbol{u}_{\tau,h}\right) \quad , \gamma_\tau > 0 \quad , \end{aligned} \tag{5.11}$$

wherein $\bar{\mu} = -\mu\left[\left\{p_{\mathrm{n},h}\right\}_{\omega_\mathrm{u}} + \gamma_\mathrm{n} g_{\mathrm{n},h}\right]_-$ represents the effective friction bound, $P_{B(r)}(\boldsymbol{z})$ denotes the orthogonal projection of $\boldsymbol{z}$ onto a ball (or disc) with radius r, and γ_τ is a penalty parameter potentially different from γ_n but also of order $\mathcal{O}(\frac{E}{h})$. Analogously to (5.7), the Coulomb's law of friction can be enforced consistently on the weak form (5.3) by adding

$$\int_{\gamma_{\mathrm{c},h}^{(1)}} \left(\left\{\boldsymbol{t}_{\tau,h}\right\}_{\omega_\mathrm{u}} - P_{B(\bar{\mu})}\left(\left\{\boldsymbol{t}_{\tau,h}\right\}_{\omega_\mathrm{u}} + \gamma_\tau \Delta \boldsymbol{u}_{\tau,h}\right)\right) \cdot \left(\theta_{\mathrm{u},2}[\![\delta \boldsymbol{u}_h]\!] - \frac{\theta_{\mathrm{u},1}}{\gamma_\tau}\mathcal{D}\left\{\boldsymbol{t}_{\tau,h}\right\}_{\omega_\mathrm{u}}[\delta \boldsymbol{u}_h]\right) \mathrm{d}\gamma \quad . \tag{5.12}$$

The complete weak form of a frictional contact problem finally comprises the structural balance (5.3), including the consistent boundary integral, the weak normal contact constraint (5.7) and the tangential constraint (5.12). In summary, it reads: Find $\boldsymbol{u}_h \in \boldsymbol{\mathcal{U}}_{\mathrm{u},h}$, such that

$$\begin{aligned} \delta \mathcal{W}_{\mathrm{u},h} &- \int_{\gamma_{\mathrm{c},h}^{(1)}} \left\{\boldsymbol{t}_{\mathrm{c},h}\right\}_{\omega_\mathrm{u}} \cdot [\![\delta \boldsymbol{u}_h]\!] \, \mathrm{d}\gamma \\ &- \int_{\gamma_{\mathrm{c},h}^{(1)}} \left(\gamma_\mathrm{n} g_{\mathrm{n},h} - \left[\left\{p_{\mathrm{n},h}\right\}_{\omega_\mathrm{u}} + \gamma_\mathrm{n} g_{\mathrm{n},h}\right]_+\right) \\ &\qquad \cdot \left(\theta_{\mathrm{u},2}\boldsymbol{n}_h \cdot [\![\delta \boldsymbol{u}_h]\!] - \frac{\theta_{\mathrm{u},1}}{\gamma_\mathrm{n}}\mathcal{D}\left\{p_{\mathrm{n},h}\right\}_{\omega_\mathrm{u}}[\delta \boldsymbol{u}_h]\right) \mathrm{d}\gamma \\ &+ \int_{\gamma_{\mathrm{c},h}^{(1)}} \left(\left\{\boldsymbol{t}_{\tau,h}\right\}_{\omega_\mathrm{u}} - P_{B(\bar{\mu})}\left(\left\{\boldsymbol{t}_{\tau,h}\right\}_{\omega_\mathrm{u}} + \gamma_\tau \Delta \boldsymbol{u}_{\tau,h}\right)\right) \\ &\qquad \cdot \left(\theta_{\mathrm{u},2}[\![\delta \boldsymbol{u}_h]\!] - \frac{\theta_{\mathrm{u},1}}{\gamma_\tau}\mathcal{D}\left\{\boldsymbol{t}_{\tau,h}\right\}_{\omega_\mathrm{u}}[\delta \boldsymbol{u}_h]\right) \mathrm{d}\gamma = 0 \quad \forall \delta \boldsymbol{u}_h \in \boldsymbol{\mathcal{V}}_{\mathrm{u},h} \quad . \end{aligned} \tag{5.13}$$

A family of Nitsche methods To illustrate the resulting family of Nitsche methods obtained by different combinations of $\theta_{\mathrm{u},1}$ and $\theta_{\mathrm{u},2}$, the contact boundary $\gamma_{\mathrm{c},h}^{(1)}$ is first decomposed in the regions of closed contact $\gamma_{\mathrm{c},h,0}^{(1)}$ and separation $\gamma_{\mathrm{c},h,+}^{(1)}$, such that

$$\left[\left\{p_{\mathrm{n},h}\right\}_{\omega_\mathrm{u}} + \gamma_\mathrm{n} g_{\mathrm{n},h}\right]_+ = \begin{cases} 0 & \text{on } \gamma_{\mathrm{c},h,0}^{(1)} \\ \left\{p_{\mathrm{n},h}\right\}_{\omega_\mathrm{u}} + \gamma_\mathrm{n} g_{\mathrm{n},h} & \text{on } \gamma_{\mathrm{c},h,+}^{(1)} \end{cases} . \tag{5.14}$$

The interface conditions to be applied on the two parts in normal direction are a homogeneous Neumann condition $\left\{p_{\mathrm{n},h}\right\}_{\omega_\mathrm{u}} = 0$ on $\gamma_{\mathrm{c},h,+}^{(1)}$ and a Dirichlet-type interface condition $g_{\mathrm{n},h} = 0$ on $\gamma_{\mathrm{c},h,0}$. For the treatment of frictional contact, the active contact zone is further split into stick and slip region $\gamma_{\mathrm{c},h,\tau_0}^{(1)}$ and $\gamma_{\mathrm{c},h,\tau_+}^{(1)}$, respectively. These regions are separated by the condition

$$\frac{-\mu\left[\left\{p_{\mathrm{n},h}\right\}_{\omega_\mathrm{u}} + \gamma_\mathrm{n} g_{\mathrm{n},h}\right]_-}{\left\| \left\{\boldsymbol{t}_{\tau,h}\right\}_{\omega_\mathrm{u}} + \gamma_\tau \Delta\boldsymbol{u}_{\tau,h}\right\|} \begin{cases} \geq 1 & \text{on } \gamma_{\mathrm{c},h,\tau_0}^{(1)} \\ < 1 & \text{on } \gamma_{\mathrm{c},h,\tau_+}^{(1)} \end{cases} . \tag{5.15}$$

The condition in the sticky region corresponds to the Dirichlet-type condition $\Delta\boldsymbol{u}_{\tau,h} = \boldsymbol{0}$ and in the slip region a Robin-type condition is applied.

To demonstrate how all these interface conditions are applied in the presented Nitsche methods, the weak form (5.13) is re-arranged as

$$\begin{aligned}
\delta\mathcal{W}_{\mathrm{u},h} + &\int_{\gamma_{\mathrm{c},h,+}^{(1)}} \left\{\boldsymbol{t}_{\mathrm{c},h}\right\}_{\omega_\mathrm{u}} \cdot \left((\theta_{\mathrm{u},2} - 1)[\![\delta\boldsymbol{u}_h]\!] - \boldsymbol{n}_h \frac{\theta_{\mathrm{u},1}}{\gamma_\mathrm{n}} \mathcal{D}\left\{p_{\mathrm{n},h}\right\}_{\omega_\mathrm{u}}[\delta\boldsymbol{u}_h] - \frac{\theta_{\mathrm{u},1}}{\gamma_\tau} \mathcal{D}\left\{\boldsymbol{t}_{\tau,h}\right\}_{\omega_\mathrm{u}}[\delta\boldsymbol{u}_h] \right) \mathrm{d}\gamma \\
&- \int_{\gamma_{\mathrm{c},h,0}^{(1)}} \left(\left\{p_{\mathrm{n},h}\right\}_{\omega_\mathrm{u}} + \theta_{\mathrm{u},2}\gamma_\mathrm{n} g_{\mathrm{n},h}\right) \boldsymbol{n}_h \cdot [\![\delta\boldsymbol{u}_h]\!] - \theta_{\mathrm{u},1} g_{\mathrm{n},h} \mathcal{D}\left\{p_{\mathrm{n},h}\right\}_{\omega_\mathrm{u}}[\delta\boldsymbol{u}_h] \,\mathrm{d}\gamma \\
&- \int_{\gamma_{\mathrm{c},h,\tau_0}^{(1)}} \left(\left\{\boldsymbol{t}_{\tau,h}\right\}_{\omega_\mathrm{u}} + \theta_{\mathrm{u},2}\gamma_\tau \Delta\boldsymbol{u}_{\tau,h}\right) \cdot [\![\delta\boldsymbol{u}_h]\!] - \theta_{\mathrm{u},1} \Delta\boldsymbol{u}_{\tau,h} \cdot \mathcal{D}\left\{\boldsymbol{t}_{\tau,h}\right\}_{\omega_\mathrm{u}}[\delta\boldsymbol{u}_h] \,\mathrm{d}\gamma \\
&- \int_{\gamma_{\mathrm{c},h,\tau_+}^{(1)}} \left((1-\theta_{\mathrm{u},2})\left\{\boldsymbol{t}_{\tau,h}\right\}_{\omega_\mathrm{u}} + \theta_{\mathrm{u},2} P_{B(\bar{\mu})}\left(\left\{\boldsymbol{t}_{\tau,h}\right\}_{\omega_\mathrm{u}} + \gamma_\tau \Delta\boldsymbol{u}_{\tau,h}\right)\right) \cdot [\![\delta\boldsymbol{u}_h]\!] \right. \\
&\qquad \left. + \theta_{\mathrm{u},1}\left(\left\{\boldsymbol{t}_{\tau,h}\right\}_{\omega_\mathrm{u}} - P_{B(\bar{\mu})}\left(\left\{\boldsymbol{t}_{\tau,h}\right\}_{\omega_\mathrm{u}} + \gamma_\tau \Delta\boldsymbol{u}_{\tau,h}\right)\right) \cdot \mathcal{D}\left\{\boldsymbol{t}_{\tau,h}\right\}_{\omega_\mathrm{u}}[\delta\boldsymbol{u}_h] \,\mathrm{d}\gamma \right. \\
&= 0 \quad \forall \delta\boldsymbol{u}_h \in \boldsymbol{\mathcal{V}}_{\mathrm{u},h} \ .
\end{aligned} \tag{5.16}$$

Note that this weak form is in fact continuous in the discrete displacements (at least for elasticity, see Section 5.1.3 for a discussion on elasto-plasticity) which may not be directly obvious in (5.16) but follows directly from the continuity of the $\min$ and $\max$ functions employed in (5.13).

In addition, one can observe from (2.102) and (2.103) that the directional derivatives of the normal gap $g_{\mathrm{n},h}$ and tangential velocity $\Delta\boldsymbol{u}_{\tau,h}$ in closed contact yield

$$\mathcal{D} g_{\mathrm{n},h}[\Delta\boldsymbol{u}_h] \approx -\boldsymbol{n}_h \cdot [\![\Delta\boldsymbol{u}_h]\!] \ , \tag{5.17a}$$

$$\mathcal{D}\Delta\boldsymbol{u}_{\tau,h}[\Delta\boldsymbol{u}_h] \approx -(\boldsymbol{I} - \boldsymbol{n}_h \otimes \boldsymbol{n}_h)[\![\Delta\boldsymbol{u}_h]\!] \ , \tag{5.17b}$$

meaning that $g_{\mathrm{n},h}$ and $\Delta\boldsymbol{u}_{\tau,h}$ represent the *negative* jump of the displacement field across the interface. A strict equality does not hold at this point due to the fact that in the discrete setting

the slave and master sided normals are only approximately equal and opposite, $\boldsymbol{n}_h^{(1)}(\boldsymbol{x}^{(1)}) \approx -\boldsymbol{n}_h^{(2)}(\hat{\boldsymbol{x}}^{(2)})$, even in closed contact $\gamma_{\mathrm{c},h,0}^{(1)}$. In conjunction with the projection strategy (2.101), this disparity in normal directions results in (5.17) holding only approximately as discussed in detail in Poulios and Renard [173].

The first class of Nitsche methods, the ones analyzed for linearized kinematics by Chouly [33], Chouly *et al.* [35], are recovered for $\theta_{\mathrm{u},2} = 1$, where (5.16) reduces to

$$
\begin{aligned}
\delta\mathcal{W}_{\mathrm{u},h} - &\int_{\gamma_{\mathrm{c},h,+}^{(1)}} \left\{\boldsymbol{t}_{\mathrm{c},h}\right\}_{\omega_{\mathrm{u}}} \cdot \left(\boldsymbol{n}_h \frac{\theta_{\mathrm{u},1}}{\gamma_{\mathrm{n}}} \mathcal{D}\left\{p_{\mathrm{n},h}\right\}_{\omega_{\mathrm{u}}} [\delta\boldsymbol{u}_h] + \frac{\theta_{\mathrm{u},1}}{\gamma_{\tau}} \mathcal{D}\left\{\boldsymbol{t}_{\tau,h}\right\}_{\omega_{\mathrm{u}}} [\delta\boldsymbol{u}_h] \right) \mathrm{d}\gamma \\
&- \int_{\gamma_{\mathrm{c},h,0}^{(1)}} \left(\left\{p_{\mathrm{n},h}\right\}_{\omega_{\mathrm{u}}} + \gamma_{\mathrm{n}} g_{\mathrm{n},h} \right) \boldsymbol{n}_h \cdot [\![\delta\boldsymbol{u}_h]\!] - \theta_{\mathrm{u},1} g_{\mathrm{n},h} \mathcal{D}\left\{p_{\mathrm{n},h}\right\}_{\omega_{\mathrm{u}}} [\delta\boldsymbol{u}_h] \, \mathrm{d}\gamma \\
&- \int_{\gamma_{\mathrm{c},h,\tau_0}^{(1)}} \left(\left\{\boldsymbol{t}_{\tau,h}\right\}_{\omega_{\mathrm{u}}} + \gamma_{\tau} \Delta\boldsymbol{u}_{\tau,h} \right) \cdot [\![\delta\boldsymbol{u}_h]\!] - \theta_{\mathrm{u},1} \Delta\boldsymbol{u}_{\tau,h} \cdot \mathcal{D}\left\{\boldsymbol{t}_{\tau,h}\right\}_{\omega_{\mathrm{u}}} [\delta\boldsymbol{u}_h] \, \mathrm{d}\gamma \\
&- \int_{\gamma_{\mathrm{c},h,\tau_+}^{(1)}} P_{B(\bar{\mu})} \left(\left\{\boldsymbol{t}_{\tau,h}\right\}_{\omega_{\mathrm{u}}} + \gamma_{\tau} \Delta\boldsymbol{u}_{\tau,h} \right) \cdot [\![\delta\boldsymbol{u}_h]\!] \\
&\qquad + \theta_{\mathrm{u},1} \left(\left\{\boldsymbol{t}_{\tau,h}\right\}_{\omega_{\mathrm{u}}} - P_{B(\bar{\mu})} \left(\left\{\boldsymbol{t}_{\tau,h}\right\}_{\omega_{\mathrm{u}}} + \gamma_{\tau} \Delta\boldsymbol{u}_{\tau,h} \right) \right) \cdot \mathcal{D}\left\{\boldsymbol{t}_{\tau,h}\right\}_{\omega_{\mathrm{u}}} [\delta\boldsymbol{u}_h] \, \mathrm{d}\gamma \\
=&0 \quad \forall \delta\boldsymbol{u}_h \in \boldsymbol{\mathcal{V}}_{\mathrm{u},h} \ .
\end{aligned}
\tag{5.18}
$$

In this case, $\theta_{\mathrm{u},1} = 1$ yields a symmetric Nitsche method. Summarizing the analysis in Chouly *et al.* [35], the homogeneous Neumann boundary condition in the inactive region is enforced by a symmetric penalty term (first integral in (5.18)), which, however, has a negative sign and does therefore not contribute to the stability of the method. In the active contact region $\gamma_{\mathrm{c},h,0}^{(1)}$, the Dirichlet-type condition $g_{\mathrm{n},h} = 0$ in normal direction is enforced by the classical symmetric Nitsche method (second line in (5.18)), as is the stick constraint of no relative tangential displacement (third line in (5.18)). Therein, the penalty terms $\int_{\gamma_{\mathrm{c},h,0}^{(1)}} \gamma_{\mathrm{n}} g_{\mathrm{n},h} \boldsymbol{n}_h \cdot [\![\delta\boldsymbol{u}_h]\!] \, \mathrm{d}\gamma$ and $\int_{\gamma_{\mathrm{c},h,\tau_0}^{(1)}} \gamma_{\tau} \Delta\boldsymbol{u}_{\tau,h} \cdot [\![\delta\boldsymbol{u}_h]\!] \, \mathrm{d}\gamma$ in normal and tangential directions, respectively, enter with a negative sign which, in view of (5.17), yields a positive, i.e. stabilizing, penalty term. Lastly, the Robin-type slip condition (fourth line in (5.18)) is constructed as the continuous extension of the stick case. Typical for the symmetric Nitsche method, the case of $\theta_{\mathrm{u},1} = \theta_{\mathrm{u},2} = 1$ requires a lower bound on γ_{n} and γ_{τ} to ensure stability. Conversely, setting $\theta_{\mathrm{u},1} = -1$ in (5.18) results in a skew-symmetric Nitsche method, where the penalty term on the homogeneous Neumann boundary (first integral in (5.18)) has a positive sign and is therefore stable, and the Dirichlet-type conditions are enforced with the well-known skew-symmetric Nitsche method [35]. This method is stable for any $\gamma_{\mathrm{n}}, \gamma_{\tau} > 0$. Finally, a non-symmetric Nitsche method is obtained by $\theta_{\mathrm{u},1} = 0$ in (5.18). This variant is particularly appealing in the case of nonlinear elasticity as it requires fewer terms. Specifically, all directional derivatives of the contact traction, $\mathcal{D}\left\{\boldsymbol{t}_{\mathrm{c},h}\right\}_{\omega_{\mathrm{u}}} [\delta\boldsymbol{u}_h]$, drop out of the equation. When solving the nonlinear, weak form (5.18) by a (generalized) Newton method, the linearization of this directional derivative requires the second derivative of the stress, a term commonly not present in nonlinear finite elements. Like the symmetric method, this non-symmetric variant exhibits a lower bound on the penalty parameters γ_{n} and γ_{τ} to ensure stability.

Finally, Burman *et al.* [25] propose a penalty free method which is obtained from (5.16) by setting $\theta_{\mathrm{u},1} = -1$ and $\theta_{\mathrm{u},2} = 0$. The weak form then reduces to

$$\begin{aligned}
\delta\mathcal{W}_{\mathrm{u},h} &+ \int_{\gamma^{(1)}_{\mathrm{c},h,+}} \left\{\boldsymbol{t}_{\mathrm{c},h}\right\}_{\omega_\mathrm{u}} \cdot \left(\boldsymbol{n}_h \frac{1}{\gamma_\mathrm{n}} \mathcal{D}\left\{p_{\mathrm{n},h}\right\}_{\omega_\mathrm{u}}[\delta\boldsymbol{u}_h] + \frac{1}{\gamma_\tau}\mathcal{D}\left\{\boldsymbol{t}_{\tau,h}\right\}_{\omega_\mathrm{u}}[\delta\boldsymbol{u}_h] \right) \mathrm{d}\gamma \\
&- \int_{\gamma^{(1)}_{\mathrm{c},h,0}} \left\{p_{\mathrm{n},h}\right\}_{\omega_\mathrm{u}} \boldsymbol{n}_h \cdot [\![\delta\boldsymbol{u}_h]\!] + g_{\mathrm{n},h}\mathcal{D}\left\{p_{\mathrm{n},h}\right\}_{\omega_\mathrm{u}}[\delta\boldsymbol{u}_h]\,\mathrm{d}\gamma \\
&- \int_{\gamma^{(1)}_{\mathrm{c},h,\tau_0}} \left\{\boldsymbol{t}_{\tau,h}\right\}_{\omega_\mathrm{u}} \cdot [\![\delta\boldsymbol{u}_h]\!] + \Delta\boldsymbol{u}_{\tau,h} \cdot \mathcal{D}\left\{\boldsymbol{t}_{\tau,h}\right\}_{\omega_\mathrm{u}}[\delta\boldsymbol{u}_h]\,\mathrm{d}\gamma \\
&- \int_{\gamma^{(1)}_{\mathrm{c},h,\tau_+}} \left\{\boldsymbol{t}_{\tau,h}\right\}_{\omega_\mathrm{u}} \cdot [\![\delta\boldsymbol{u}_h]\!] - \left(\left\{\boldsymbol{t}_{\tau,h}\right\}_{\omega_\mathrm{u}} - P_{B(\bar{\mu})}\left(\left\{\boldsymbol{t}_{\tau,h}\right\}_{\omega_\mathrm{u}} + \gamma_\tau\Delta\boldsymbol{u}_{\tau,h}\right)\right) \cdot \mathcal{D}\left\{\boldsymbol{t}_{\tau,h}\right\}_{\omega_\mathrm{u}}[\delta\boldsymbol{u}_h]\,\mathrm{d}\gamma \\
&= 0 \quad \forall \delta\boldsymbol{u}_h \in \boldsymbol{\mathcal{V}}_{\mathrm{u},h} \ .
\end{aligned} \tag{5.19}$$

In the first line, the homogeneous Neumann boundary condition on the inactive contact zone is enforced by a positive, symmetric penalty term. In the second and third line, the non-symmetric penalty free Nitsche method analyzed by Burman [23] is used to enforce the Dirichlet condition of closed contact in normal direction on $\gamma^{(1)}_{\mathrm{c},h,0}$ and the stick constraint in tangential direction on $\gamma^{(1)}_{\mathrm{c},h,\tau_0}$. Finally, the slip condition is obtained by a continuous extension of the stick branch. For the Signiorini problem and a nonconforming finite element method, Burman *et al.* [25] prove stability and optimal convergence orders of sufficiently low penalty parameters γ_n and γ_τ. Calling this method penalty free may be misleading as a penalty term is still present. The name rather originates from the fact that the constraint of closed contact $g_{\mathrm{n},h} = 0$ (and the stick constraint) are enforced by the penalty free Nitsche method.

5.1.2 Penalty Parameter Estimates and Harmonic Weights[1]

Besides the discussed parameters $\theta_{\mathrm{u},1}$ and $\theta_{\mathrm{u},2}$, the weak form (5.13) still contains the so-far unspecified weighting $\omega_\mathrm{u} \in [0,1]$ and penalty parameters γ_n and γ_τ. It is well-known that, to ensure coercivity, the penalty parameters need to scale with a material stiffness parameter (e.g. Young's modulus E) and the inverse mesh size, i.e. to be of the order $\mathcal{O}(\frac{E}{h})$ [35]. Moreover, the variants $\theta_{\mathrm{u},1} \in \{0,1\}$, $\theta_{\mathrm{u},2} = 1$ analyzed in [35] exhibit a lower bound on γ_n and γ_τ to ensure coercivity. At the same time, small penalty parameters are favorable, especially in nonlinear contact problems. This is due to the non-smoothness of the boundary integral (5.7), which, depending on the result of the involved $\min$-function, switches the penalty term on or off. For high penalty parameters, this nonlinearity can severely deteriorate the convergence behavior of a nonlinear solver for finding the equilibrium (e.g. Newton's method) or even lead to divergence.

For a first estimate of the penalty parameter, linearized kinematics based on the strain tensor $\boldsymbol{\varepsilon}(\boldsymbol{u}) = {}^1\!/_2(\nabla_{\boldsymbol{X}}\boldsymbol{u} + (\nabla_{\boldsymbol{X}}\boldsymbol{u})^\mathsf{T})$ and the linear elastic constitutive law $\boldsymbol{\sigma}(\boldsymbol{u}) = \mathbb{C} : \boldsymbol{\varepsilon}(\boldsymbol{u})$ with the constant, symmetric positive definite fourth order elasticity tensor $\mathbb{C}$ is assumed. Moreover, the discrete contact traction entering the weak form is taken from the slave side by setting $\omega_\mathrm{u} = 1$. Under these simplifying assumptions, Chouly *et al.* [35, Theorem 3.2] show that for $\theta_{\mathrm{u},1} \in$

[1] This section is adapted from the author's publication [195].

$\{0,1\}$, $\theta_{\mathrm{u},2}=1$ a spatially constant penalty parameter has to be chosen such that it satisfies

$$\gamma_{\{\mathrm{n},\tau\}} > C_{\mathrm{I,u}} \ , \tag{5.20}$$

where $C_{\mathrm{I,u}}$ in turn satisfies the trace inequality:

$$\int_{\Gamma_{\mathrm{c},h}^{(1)}} \|\boldsymbol{\sigma}(\boldsymbol{u}_h)\boldsymbol{N}\|^2 \,\mathrm{d}\Gamma \leq C_{\mathrm{I,u}} \int_{\Omega_{0,h}^{(1)}} \boldsymbol{\varepsilon}(\boldsymbol{u}_h) : \mathbb{C} : \boldsymbol{\varepsilon}(\boldsymbol{u}_h) \,\mathrm{d}\Omega \ , \quad \forall \boldsymbol{u}_h \in \boldsymbol{\mathcal{U}}_{\mathrm{u},h} \ , \tag{5.21}$$

with the unit normal $\boldsymbol{N}$ on $\Gamma_{\mathrm{c},h}^{(1)}$. The constant $C_{\mathrm{I,u}}$ is then obtained as the maximum eigenvalue $\lambda_{\max}$ of the associated eigenvalue problem [86]. Note that this eigenvalue problem contains all discrete degrees of freedom associated to elements $\tau_{h,k}^{(1)} \in \mathcal{T}_h^{(1)}$ intersecting the contact boundary $\Gamma_{\mathrm{c},h}^{(1)}$. To avoid solution of the large eigenvalue problem across the entire interface to compute $C_{\mathrm{I,u}}$ as proposed by Griebel and Schweitzer [86], local eigenvalue problems

$$\boldsymbol{A}\boldsymbol{v} = \lambda \boldsymbol{B}\boldsymbol{v} \ , \tag{5.22a}$$

with the Hessians $\boldsymbol{A}$ and $\boldsymbol{B}$ to the quadratic forms

$$A = \int_{\tau_{h,k}^{(1)} \cap \Gamma_{\mathrm{c},h}^{(1)}} \|\boldsymbol{\sigma}(\boldsymbol{u}_h)\boldsymbol{N}\|^2 \,\mathrm{d}\Gamma \ , \tag{5.22b}$$

$$B = \int_{\tau_{h,k}^{(1)}} \boldsymbol{\varepsilon}(\boldsymbol{u}_h) : \mathbb{C} : \boldsymbol{\varepsilon}(\boldsymbol{u}_h) \,\mathrm{d}\Omega \ , \tag{5.22c}$$

are solved in Hansbo [93] for every $\tau_{h,k}^{(1)} \in \mathcal{T}_h^{(1)}$ intersecting the contact boundary. From each eigenvalue problem, one obtains a local constant $C_{\mathrm{I,u}}^{\tau_{h,k}^{(1)}} = \lambda_{\max}^{\tau_{h,k}^{(1)}}$ as the maximum eigenvalue. Hansbo [93] suggests to choose a spatially constant penalty parameter $\gamma_{\{\mathrm{n},\tau\}} > \max_k C_{\mathrm{I,u}}^{\tau_{h,k}^{(1)}}$. More elaborate, Dolbow and Harari [63] show that stability can also be achieved by using piecewise constant penalty parameters

$$\gamma_{\{\mathrm{n},\tau\}}\big|_{\tau_{h,k}^{(1)} \cap \Gamma_{\mathrm{c},h}^{(1)}} = C_{\mathrm{I,u}}^{\tau_{h,k}^{(1)}} \, \gamma_{\{\mathrm{n},\tau\},0} \ , \tag{5.23}$$

satisfying (5.20) on each facet of the slave surface for given reference penalty parameters $\gamma_{\{\mathrm{n},\tau\},0} > 1$ independent of the mesh size and material parameters.

It is important to note that for problems of linear elasticity the eigenvalues λ of (5.22) can be determined to hold for any displacement state. This is due to the fact that A and B in (5.22b) and (5.22c) are quadratic in $\boldsymbol{u}_h$ and therefore the Hessians $\boldsymbol{A}$ and $\boldsymbol{B}$ in (5.22a) are constant. In problems of nonlinear elasticity, on the contrary, nonlinear strain measures are used and the stiffness of the material depends on the deformation state. In high compression cases, for instance, the material is expected to stiffen, tending to infinite stiffness for a compression to zero volume. Hence, to keep the penalty term to the order of the stiffness, the penalty parameters are required to increase in that case. A possible solution is to replace the eigenvalue problem (5.22) by a

deformation dependent analog the deformation dependent matrices

$$\boldsymbol{A} = \int_{\tau_{h,k}^{(1)} \cap \Gamma_{\mathrm{c},h}^{(1)}} \left((\boldsymbol{F} \otimes \boldsymbol{N}) : \mathbb{C} : \frac{\partial \boldsymbol{E}(\boldsymbol{u}_h)}{\partial \mathbf{d}} \right)^{\mathsf{T}} \cdot \left((\boldsymbol{F} \otimes \boldsymbol{N}) : \mathbb{C} : \frac{\partial \boldsymbol{E}(\boldsymbol{u}_h)}{\partial \mathbf{d}} \right) \mathrm{d}\Gamma \ , \tag{5.24a}$$

$$\boldsymbol{B} = \int_{\tau_{h,k}^{(1)}} \left(\frac{\partial \boldsymbol{E}(\boldsymbol{u}_h)}{\partial \mathbf{d}} \right)^{\mathsf{T}} : \mathbb{C} : \left(\frac{\partial \boldsymbol{E}(\boldsymbol{u}_h)}{\partial \mathbf{d}} \right) \mathrm{d}\Omega \ , \tag{5.24b}$$

and the nonlinear elasticity tensor $\mathbb{C} = \frac{\partial^2 \Psi}{\partial \boldsymbol{E} \partial \boldsymbol{E}}$. This present form is obtained from the inequality $\int_{\Gamma_{\mathrm{c},h}^{(1)}} \|(\boldsymbol{F}\boldsymbol{S})\boldsymbol{N}\|^2 \, \mathrm{d}\Gamma \leq C_{\mathrm{I,u}} \int_{\Omega_{0,h}} \Psi \, \mathrm{d}\Omega$ and linearizing the second Piola–Kirchhoff stress $\boldsymbol{S}$ only. Admittedly, this is a rather heuristic approximation as different linearized systems may be obtained, e.g. including the deformation gradient $\boldsymbol{F}$ therein. However, the presented form performed best in numerical examples (see Section 5.1.4.2) and will be used in the following. In the future, a combination with arguments of polyconvexity for the strain energy function [10] could yield more accurately tailored estimates for the penalty parameter in the nonlinear case.

A fixed one-sided weighting, i.e. $\omega_{\mathrm{u}} = 1$, can result in large penalty parameters from the strategy described above, especially if the body $\Omega_0^{(1)}$ has a much larger stiffness compared to $\Omega_0^{(2)}$. This can also negatively affect the accuracy of the discrete solution, see e.g. Annavarapu *et al.* [5]. For problems with a large contrast in material parameters, Burman and Zunino [24] introduce so-called harmonic weights. In the present case, the weight $\omega_{\mathrm{u}}^{\tau_{h,i}^{(1)} \tau_{h,j}^{(2)}}$ between a slave- and a master-sided element $\tau_{h,i}^{(1)}$ and $\tau_{h,j}^{(2)}$ is defined using their respective constants $C_{\mathrm{I,u}}^{\tau_{h,k}^{(i)}}$ obtained from the eigenvalue problems (5.22) or (5.24) as

$$\omega_{\mathrm{u}}^{\tau_{h,i}^{(1)} \tau_{h,j}^{(2)}} = \frac{C_{\mathrm{I,u}}^{\tau_{h,j}^{(2)}}}{C_{\mathrm{I,u}}^{\tau_{h,i}^{(1)}} + C_{\mathrm{I,u}}^{\tau_{h,j}^{(2)}}} \ . \tag{5.25}$$

This leads to a weighting that is discontinuous across boundaries of both slave- and master contact facets. Regarding the case where the master (resp. slave) side is much stiffer, than the slave (resp. master) side, or rigid in the limit case, i.e. $C_{\mathrm{I,u}}^{\tau_{h,i}^{(1)}} \ll C_{\mathrm{I,u}}^{\tau_{h,j}^{(2)}}$ (resp. $C_{\mathrm{I,u}}^{\tau_{h,i}^{(1)}} \gg C_{\mathrm{I,u}}^{\tau_{h,j}^{(2)}}$), (5.25) yields a one-sided weighting $\omega_{\mathrm{u}} = 1$ (resp. $\omega_{\mathrm{u}} = 0$). Hence, the weight is fully shifted to the softer side. Similar to Burman and Zunino [24], the penalty parameters in the common integration domain of $\tau_{h,i}^{(1)}$ and $\tau_{h,j}^{(2)}$ on $\gamma_{\mathrm{c},h}^{(1)}$ are then defined as

$$\gamma_{\{\mathrm{n},\tau\}}^{\tau_{h,i}^{(1)} \tau_{h,j}^{(2)}} = \left\{ C_{\mathrm{I,u}}^{\tau_{h,k}^{(i)}} \right\}_{\omega_{\mathrm{u}}} \gamma_{\{\mathrm{n},\tau\},0} \ . \tag{5.26}$$

Due to the discontinuity of the penalty term across both slave and master surface element edges, stability of the Nitsche method with $\theta_{\mathrm{u},1} \in \{0, 1\}$, $\theta_{\mathrm{u},2} = 1$ can, even for linearized kinematics, no longer be *guaranteed* for $\gamma_{\{\mathrm{n},\tau\},0} > 1$, but, by numerical evidence , $\gamma_{\{\mathrm{n},\tau\},0} > 1$ still appears to be sufficient.

Remark 5.1 (Nitsche methods with $\theta_{\mathrm{u},1} = -1$)**.** *The above investigations on the penalty parameter concerned the Nitsche methods of Chouly* et al. *[35] with $\theta_{\mathrm{u},1} \in \{0, 1\}$, $\theta_{\mathrm{u},2} = 1$. Beside*

those, two other options are of particular interest: First, $\theta_{\mathrm{u},1} = -1$, $\theta_{\mathrm{u},2} = 1$ *is shown in Chouly* et al. *[35] to be stable for any* $\gamma_{\{\mathrm{n},\tau\},0} > 0$. *Second, the so-called penalty free variant* $\theta_{\mathrm{u},1} = -1$, $\theta_{\mathrm{u},2} = 0$ *proposed by Burman [23] is proven stable for sufficiently low penalty parameters* $\gamma_{\{\mathrm{n},\tau\},0}$. *Although the proof in [23] considers the (scalar) Signiorini problem and nonconforming finite elements only, numerical experiments indicate that the result also transfers to contact problems.*

Remark 5.2 (unbiased formulation)**.** *If the weighting factor* ω_{u} *is defined independently of the chosen slave and master side (as is the case for harmonic weighting), the presented algorithm is almost unbiased, i.e. independent of the chosen slave side. The only influence of the slave and master choice is the integration domain and, more importantly, the definition of the contact normal* $\boldsymbol{n}$. *However, this influence of the contact normal is very limited, since in closed contact the discrete normals point in almost the same direction,* $\boldsymbol{n}_h^{(1)}(\boldsymbol{x}^{(1)}) \approx -\boldsymbol{n}_h^{(2)}(\hat{\boldsymbol{x}}^{(2)})$.

Remark 5.3 (numerical integration)**.** *Basically, two different integration strategies are common for computational contact mechanics: The simpler one suggests to generate integration points using standard quadrature rules for each element on the slave surface irrespective of the master-sided mesh, whereas the more accurate integration strategy first imprints the master-sided mesh on the slave side and then generates quadrature points on the polygonal intersection of one slave with one master element A detailed comparison of the two strategies to Nitsche-based contact algorithms is performed in Mlika [151]. In the case of harmonic weights* $\omega_{\mathrm{u}} \neq 1$, *the more accurate integration on the intersected slave and master mesh is strongly recommended. For classical finite elements, the integrand of the slave-side integral in* (5.13) *(or* (5.8) *in the frictionless case) then not only contains kinks at master element edges, but also jumps, since the traction vector* $\boldsymbol{t}_{\mathrm{c}}$ *is discontinuous across elements. Simply generating integration points on slave elements accurately integrates the possible discontinuities resulting from the slave-sided traction, but ignores potential discontinuities of the master sided traction. Therefore, if the master-side traction is involved, a large integration error is introduced that even deteriorates the convergence of Newton's method. In isogeometric analysis, on the contrary, the higher inter-element continuity of the basis functions yields a continuous stress approximation, however, accurate integration is still mandatory to achieve optimal convergence orders as demonstrated by Brivadis* et al. *[22] for mortar methods.*

5.1.3 Application to Elasto-Plasticity

The combination of the Nitsche-type contact formulation derived above with an elasto-plastic material introduces two major difficulties. These appear independently from the employed numerical treatment of elasto-plasticity in the bulk material whether it is the classical return mapping algorithm or the algorithm devised in Chapter 3.

The first difficulty is related to the directional derivative of the contact traction $\mathcal{D}\boldsymbol{t}_{\mathrm{c}}[\delta\boldsymbol{u}_h]$ in the weak form (5.13). As the derivative of a stress-like quantity, this directional derivative relates to the tangent stiffness of the material. In elasto-plasticity, however, the directional derivative $\mathcal{D}\boldsymbol{t}_{\mathrm{c}}[\delta\boldsymbol{u}_h]$, as material stiffness in general, is not continuous at the transition between elastic and plastic deformation. This discontinuity can be exemplified by means of the stress-strain (or macroscopic force-displacement) relationship depicted e.g. in Figure 3.6a. While the stress (or force in Figure 3.6a) is a continuous function of the strain (or elongation in Figure 3.6a), its

derivative is not. In the discrete weak form (5.13), the discontinuity of $\mathcal{D}\boldsymbol{t}_{\mathrm{c}}[\delta\boldsymbol{u}_h]$ renders the whole weak form a discontinuous function of the discrete unknown displacements. While the employed generalized Newton scheme does converge for non-smooth yet continuous problems [178], the same cannot be expected for a discontinuous residual. To this end, the only valid Nitsche-based contact formulation for elasto-plastic problems is the one with $\theta_{\mathrm{u},1} = 0$ and $\theta_{\mathrm{u},2} = 1$ in which no directional derivative of the contact traction occurs in the weak form.

The second difficulty in the combination of Nitsche's method and elasto-plastic materials lies in the evaluation of the contact traction $\boldsymbol{t}_{\mathrm{c}} = \boldsymbol{\sigma}\boldsymbol{n}$. In problems of elasticity, the contact traction depends on the current displacement state only such that it can be evaluated at any given point, e.g. an integration point on the contact surface $\gamma_{\mathrm{c},h}^{(1)}$. For elasto-plastic materials, on the other hand, the Cauchy stress $\boldsymbol{\sigma}$, and consequently the contact traction $\boldsymbol{t}_{\mathrm{c}}$, not only depends on the current displacement state but also on internal variables of state describing the plastic deformation history of the material. Classically, these internal variables of state are defined in the quadrature points of the bulk material (see Section 3.1) but not on the boundary of the domain. The numerical evaluation of the boundary integrals in (5.13), however, requires the evaluation of the contact traction at discrete integration points on the boundary. In principle there are three conceivable solutions to this problem:

1. The plastic deformation is tracked at all quadrature points on the potential contact surface. This approach is only practical for $\omega_{\mathrm{u}} = 1$ and an element based integration, since only then the set of surface quadrature points, on which $\boldsymbol{t}_{\mathrm{c}}$ needs to be evaluated, can be defined in advance and the plastic deformation can be tracked there.

2. When evaluating $\boldsymbol{t}_{\mathrm{c}}$, the plastic deformation history, i.e. all internal variables of state, are extrapolated from quadrature points in the bulk continuum to the contact boundary. With the displacement field and internal variables of state defined on the contact boundary, the Cauchy stress $\boldsymbol{\sigma}$ is determined such that the plastic material constraints are met. Several options to perform this extrapolation are imaginable, the simplest one consists of performing an extrapolation of each internal variable of state directly. A more complex option takes into account some physical properties of the internal variables of state. Particularly, the plastic deformation gradient $\boldsymbol{F}_{\mathrm{p}}$ usually has a determinant of one for pressure insensitive yield functions, which is not preserved by simply extrapolating Gauss-point values of $\boldsymbol{F}_{\mathrm{p}}$. Instead, Armero and Love [8] propose to extrapolate the exponential of the plastic deformation gradient rather than the deformation gradient itself and subsequently take the natural logarithm of the extrapolated value. This procedure actually preserves the condition $\det \boldsymbol{F}_{\mathrm{p}} \equiv 1$. Finally, the contact traction $\boldsymbol{t}_{\mathrm{c}} = \boldsymbol{\sigma}\boldsymbol{n}$ can be calculated.

3. The evaluation of the constitutive law and the extrapolation process described in the previous solution can also be reversed by first evaluating the (Cauchy) stress at the quadrature points of the bulk finite element and subsequently extrapolating the quadrature point values to the contact boundary. On the upside, this approach does not require any extrapolation of internal variables of state as the constitutive relation is, in any case, only evaluated at the quadrature points within an element. On the downside, the extrapolated stress state may not comply with the plastic material constraints even though the values at the bulk quadrature points do.

In summary, options 2 and 3 are more generally applicable than the first variant and both option 2 and 3 introduce some error in the extrapolation of either the the internal variables of state or the Cauchy stress. Throughout this thesis, only the third option will be considered.

5.1.4 Numerical Examples

To investigate the presented finite deformation contact discretization based on Nitsche's method, four numerical examples are presented in the following. In the first example, spatial convergence orders and benefits of the proposed harmonic weighting are demonstrated for a two-dimensional, frictionless contact problem. The second example underlines the necessity of an adaptive penalty parameter for highly nonlinear material behavior in a three dimensional setup. Third, the enforcement of frictional constraints is compared for various Nitsche methods in a two-dimensional ironing example. Finally, an elasto-plastic problem highlights the applicability of the derived methods to real-world applications.

5.1.4.1 Two-dimensional Frictionless Contact: Convergence Study

The first example considers the contact of a circular arc with a rectangular block and has already been analyzed in the context of isothermal and thermomechanical mortar methods in Sections 4.1.3.2.2 and 4.2.3.2, respectively. To recall, the exact geometric setting and deformed configuration is illustrated in Figure 5.1. Contact occurs due to a prescribed vertical displacement of $\hat{u} = 0.3$ of the lower edge of the rectangle. First, both bodies $\Omega_0^{(1)}$ and $\Omega_0^{(2)}$ are modeled with

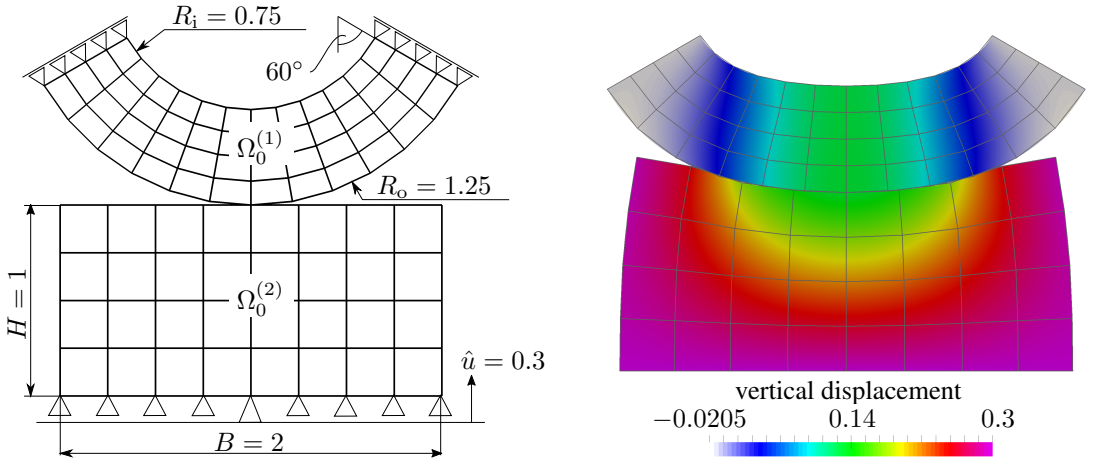

(a) Initial geometry, boundary conditions and exemplary mesh with $h = 2^{-2}$.

(b) Deformed mesh for $h = 2^{-2}$ and $\mathbb{Q}_2$ finite elements.

Figure 5.1: Two dimensional contact of a circular arc with a rectangle – Geometric setup, exemplary mesh and deformed configuration (reproduced from Figure 4.5 for illustration purposes).

a neo–Hookean material (3.38) with $E^{(1)} = 5$, $E^{(2)} = 1$ and $\nu^{(1)} = \nu^{(2)} = 0.3$ under plane strain conditions is considered and spatial convergence orders for different Nitsche methods are investigated. Due to the obvious lack of an analytical solution, the errors are calculated versus a numerical reference obtained with $\mathbb{Q}_2$ finite elements on an even finer mesh of $h = 2^{-8}$ and the mortar method of Chapter 4 with dual Lagrange multipliers. Figures 5.2 and 5.3 depict the

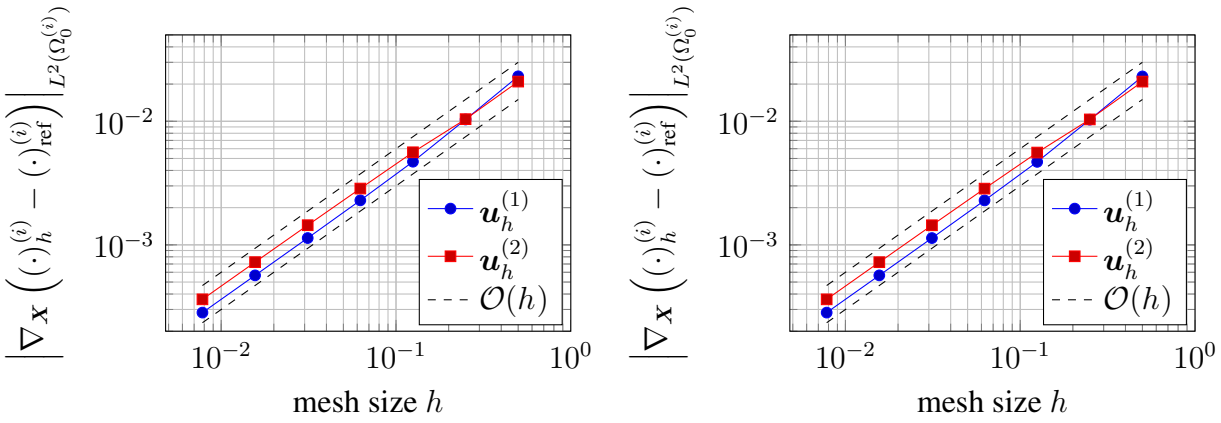

(a) $\theta_{\mathrm{u},1}=1$, $\theta_{\mathrm{u},2}=1$, $\gamma_{\mathrm{n},0}=2$.

(b) $\theta_{\mathrm{u},1}=0$, $\theta_{\mathrm{u},2}=1$, $\gamma_{\mathrm{n},0}=2$.

(c) $\theta_{\mathrm{u},1}=-1$, $\theta_{\mathrm{u},2}=1$, $\gamma_{\mathrm{n},0}=0.02$.

(d) $\theta_{\mathrm{u},1}=-1$, $\theta_{\mathrm{u},2}=0$, $\gamma_{\mathrm{n},0}=0.02$.

Figure 5.2: Two dimensional contact of a circular arc with a rectangle – Spatial convergence of the displacements of the slave and master body in the H^1 semi-norm using linear order $\mathbb{Q}_1$ finite elements and different Nitsche methods.

convergence behavior of the discrete displacement field obtained for first and second order finite elements, mesh sizes of $h \in \{2^{-7}, 2^{-6}, \ldots, 2^{-1}\}$, and different Nitsche methods. Specifically, the four distinct methods devised from (5.8) are analyzed:

(a) The symmetric Nitsche method of Chouly and Hild [34], Chouly *et al.* [35] is obtained by setting $\theta_{\mathrm{u},1}=1$ and $\theta_{\mathrm{u},2}=1$. This method requires a sufficiently large penalty parameter, which is ensured by setting $\gamma_{\mathrm{n},0}=2$.

(b) The non-symmetric Nitsche method with fewer terms analyzed in [35] is obtained by setting $\theta_{\mathrm{u},1}=0$ and $\theta_{\mathrm{u},2}=1$. This variant as well requires a sufficiently large penalty parameter, which is ensured by setting $\gamma_{\mathrm{n},0}=2$.

(c) The skew-symmetric variant of [35] obtained by setting $\theta_{\mathrm{u},1}=-1$ and $\theta_{\mathrm{u},2}=1$ is, in the linearized case, stable for any $\gamma_{\mathrm{n},0}>0$. To demonstrate this, a small value of $\gamma_{\mathrm{n},0}=0.02$ is chosen.

(d) The penalty free variant of Burman [23] emanates from (5.8) by setting $\theta_{\mathrm{u},1} = -1$ and $\theta_{\mathrm{u},2} = 0$. This variant requires a sufficiently small value of γ_{n} here set to $\gamma_{\mathrm{n},0} = 0.02$.

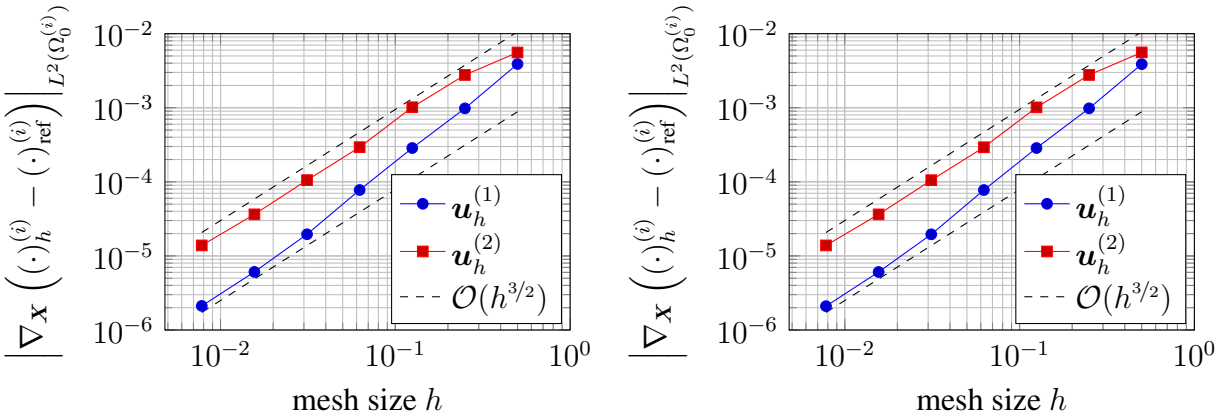

(a) $\theta_{\mathrm{u},1} = 1$, $\theta_{\mathrm{u},2} = 1$, $\gamma_{\mathrm{n},0} = 2$.

(b) $\theta_{\mathrm{u},1} = 0$, $\theta_{\mathrm{u},2} = 1$, $\gamma_{\mathrm{n},0} = 2$.

(c) $\theta_{\mathrm{u},1} = -1$, $\theta_{\mathrm{u},2} = 1$, $\gamma_{\mathrm{n},0} = 0.02$.

(d) $\theta_{\mathrm{u},1} = -1$, $\theta_{\mathrm{u},2} = 0$, $\gamma_{\mathrm{n},0} = 0.02$.

Figure 5.3: Two dimensional contact of a circular arc with a rectangle – Spatial convergence of the displacements of the slave and master body in the H^1 semi-norm using quadratic $\mathbb{Q}_2$ finite elements and different Nitsche methods.

The linear finite elements exhibit optimal convergence of order $\mathcal{O}(h)$ in Figure 5.2 for all methods. Also the absolute error values for all methods are virtually identical. The quadratic finite elements all converge with order $\mathcal{O}(h^{3/2})$ in Figure 5.3, which can be considered optimal for contact problems due to the reduced regularity of the solution [35, 232]. Comparing the various methods, some variation in the error appears for coarse meshes. In addition, the variants with $\theta_{\mathrm{u},1} = -1$ in Figures 5.3c and 5.3d yield marginally elevated absolute error values in the asymptotic region.

Next, the influence of the relative stiffness of the two contacting bodies is analyzed. To this end, Young's modulus of the master body $\Omega_0^{(2)}$ is fixed at $E^{(2)} = 1$ and the stiffness of the slave body is given values of $E^{(1)} \in \{1, 5, 20, 100\}$. The symmetric Nitsche method $\theta_{\mathrm{u},1} = \theta_{\mathrm{u},2} = 1$ and a $\mathbb{Q}_1$ finite element mesh of size $h = 2^{-3}$ is used. The lines in Figure 5.4 indicate the experimentally determined minimal penalty parameter γ_{n} to obtain a converged solution depending

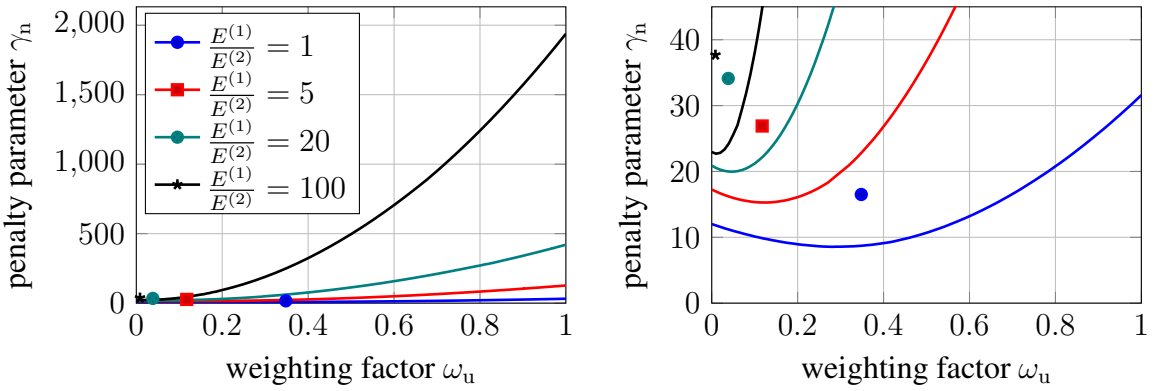

(a) Overall dependency.

(b) Zoom to low penalty parameters.

Figure 5.4: Two dimensional contact of a circular arc with a rectangle – Minimal required penalty parameter for $\mathbb{Q}_1$ finite elements and $h = 2^{-3}$ depending on the weighting ω_u for different material pairings. Lines indicate experimentally determined lower bounds and dots the estimate of Section 5.1.2 with $\gamma_{n,0} = 1$.

on the weighting factor ω_u. This minimum value to obtain convergence in the nonlinear solution procedure is a good indicator for the stability limit of the spatial discretization as unstable methods tend to diverge in nonlinear problems. Conversely, low penalty parameters are in general favorable since the penalty term is switched on and off depending on active or inactive contact. As a consequence, the nonlinearity of the discrete problem is reduced by low penalty parameters and the robustness of the nonlinear solution procedure is increased. Obviously, there exists a weighting $\omega_{u,min}$ at which the required penalty parameter takes a minimum value; location and value of this minimum depends on the material pairing. For equal stiffnesses of the two bodies ($\frac{E^{(1)}}{E^{(2)}} = 1$), varying the ω_u has only a limited effect on the required penalty parameter. Although both bodies have equal stiffness, the minimal penalty parameter is not obtained for a symmetric weight $\omega_u = 0.5$, since the location of the minimum not only depends on the stiffness but also the mesh size ratio. Hence, the minimum of the penalty parameter for equally stiff bodies is shifted towards the coarser mesh, that is $\Omega_0^{(2)}$ in this case and therefore $\omega_{u,min} < 0.5$. For problems with large material contrasts, choosing an appropriate weight ω_u can yield a significant reduction in the necessary penalty parameter. In the case of a stiffness ratio $\frac{E^{(1)}}{E^{(2)}} = 100$ depicted in Figure 5.4, the minimal penalty parameter is obtained by shifting the weight almost entirely to the softer side $\Omega_0^{(2)}$, i.e. $\omega_{u,min} \approx 0$. In comparison to a completely one-sided weighting or a fixed weight of $\omega_u = 0.5$ as used in Chouly *et al.* [36], Mlika *et al.* [152], the required penalty parameter reduces by approximately 99% and 95%, respectively.

For practical applications, the experimental determination of a sufficient penalty parameter by trial and error is infeasible and an automatically determined value is required. Such an automatic estimation of the penalty parameter has been presented in Section 5.1.2 based on element-wise generalized eigenvalue problems. The thereby obtained average weighting and penalty parameter

$$\bar{\omega_u} = \frac{\int_{\gamma_{c,h}^{(1)}} \omega_u \, d\gamma}{\int_{\gamma_{c,h}^{(1)}} d\gamma} \quad , \quad \bar{\gamma_n} = \frac{\int_{\gamma_{c,h}^{(1)}} \gamma_n \, d\gamma}{\int_{\gamma_{c,h}^{(1)}} d\gamma} \quad , \tag{5.27}$$

with a reference value of $\gamma_{\mathrm{n},0} = 1$ are depicted as dots in Figure 5.4 for the different material pairings. Note that due to the nonlinear material behavior and the adaption of the generalized eigenvalue problem, ω_{u} and γ_{n} are not constant across the interface; accordingly only average values can be depicted. The harmonic weighting shifts $\bar{\omega_{\mathrm{u}}}$ automatically to the softer side and only a slight increase in the necessary penalty term appears in Figure 5.4b for increasing stiffness of $\Omega_0^{(1)}$. Especially in cases of high material contrasts, a significant reduction in the required penalty parameter can be achieved. It has to be emphasized that this shift in the weighting factor and the adaptation of the penalty parameter depending on the stiffness ratio happens without any user interference. The only parameter determining γ_{n} is the reference value $\gamma_{\mathrm{n},0}$, which can easily be set in low single digits without risking an unstable discretization, even for the symmetric Nitsche method.

5.1.4.2 High Compression Test: Adaptive Penalty Scaling

To assess the adaptive estimate of the penalty by the generalized eigenvalue problem (5.24) with deformation dependent matrices, a problem of high compression is investigated. A unit cube is compressed by a rigid spherical shell of unit radius as illustrated in Figure 5.5a. The block is

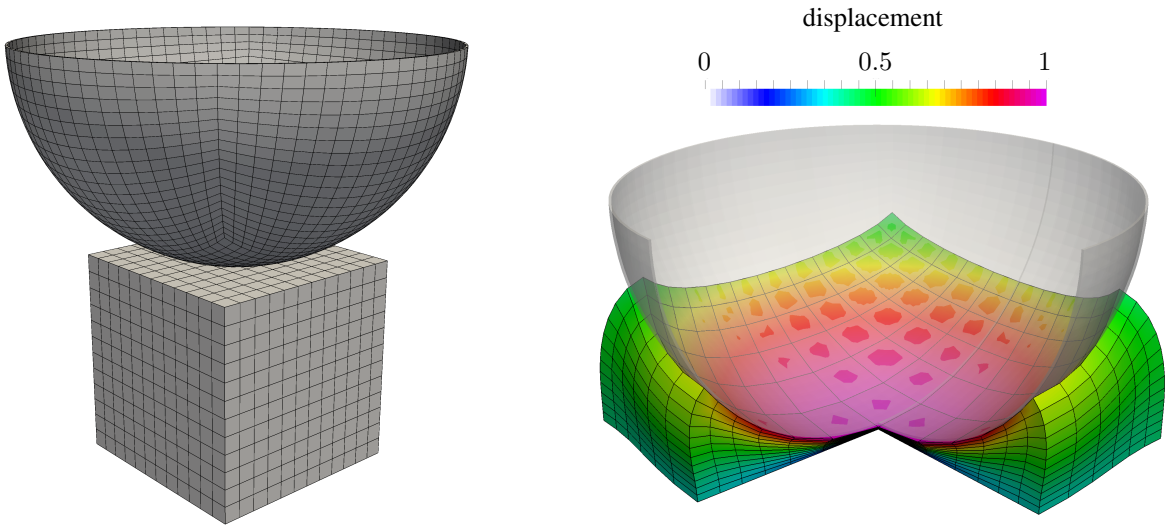

(a) Initial configuration.

(b) 98% compression.

Figure 5.5: High Compression Test – Initial configuration and deformed mesh at 98% compression.

modeled with a neo-Hookean material (3.38) with Young's modulus $E = 1$ and Poisson's ratio $\nu = 0.3$. For a vertical displacement of $\hat{u} = 1$ prescribed on the spherical shell, the material in the center of the cube would be compressed to zero volume. As such a compression to zero volume would require infinite (contact) force F_{c}, thus the effective stiffness of the cube tends to infinity as a compression of 100% is approached. Since in Nitsche's method the penalty parameter γ_{n} needs to scale with both the mesh size and the material stiffness, which exhibits significant changes in this example, an adaptive scaling of the penalty parameter is quintessential. Figure

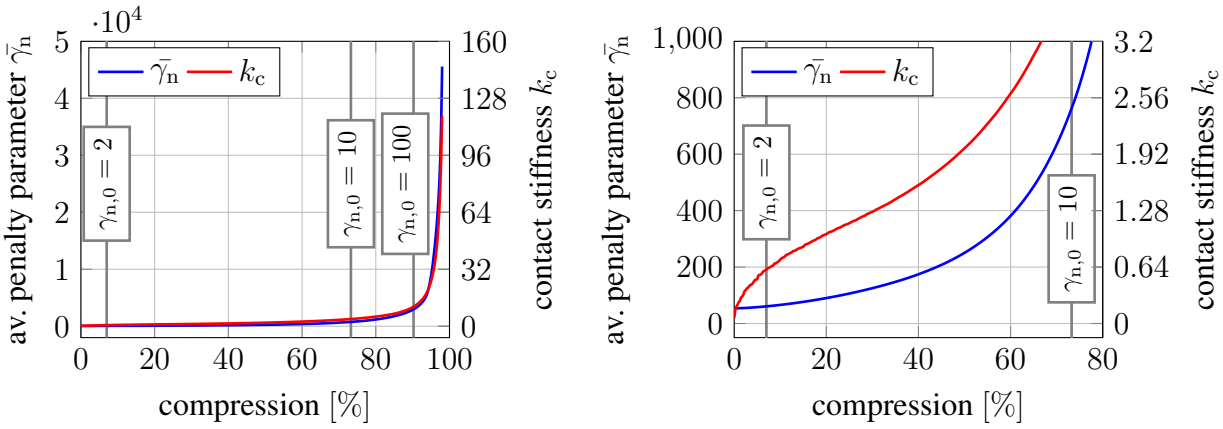

(a) Overall dependency.

(b) Zoom to low penalty parameters

Figure 5.6: High Compression Test – Evolution of system stiffness k_c and average penalty parameters $\bar{\gamma}_n$ ($\gamma_{n,0} = 2$) obtained by adaptive scaling over the compression of the block. Additional vertical lines indicate the maximum compression attainable using the linear estimate of the penalty parameter only.

5.6 depicts the evolution of the average penalty parameter $\bar{\gamma}_n$ (see (5.27)) employed during the compression of the block with a reference penalty parameter of $\gamma_{n,0} = 2$. As a reference, also the evolution of the overall system stiffness $k_c = \frac{dF_c}{d\hat{u}}$ is plotted. Both quantities show a very similar behavior and the adaptive penalty parameter closely follows the highly nonlinear stiffening effect at high compression. The additional gray vertical lines indicate the maximum compression upto which, for the symmetric Nitsche method, convergence of the nonlinear solution scheme can be achieved without nonlinear adaptation of the penalty parameter for different values of $\gamma_{n,0}$. Even for a large reference penalty parameter $\gamma_{n,0} = 100$, no solution can be obtained for the case of high compression $> 90\%$. With the nonlinear estimate of Section 5.1.2, on the other hand, a reference penalty parameter of $\gamma_{n,0} = 2$ is sufficient to obtain a stable solution for a compression up to 98%. As for the harmonic weighting analyzed in the previous section, it should be emphasized that also the adaptation of the penalty parameter does not require any user interference, but is obtained based on element-wise generalized eigenvalue problems (5.24) only.

5.1.4.3 Frictional Ironing

In this numerical example, frictional sliding and the stick-slip transition is studied for the different Nitsche-based methods derived in this chapter. A typical two-dimensional ironing example is investigated using an indentor $\Omega_0^{(1)}$ with a circular lower edge which is pressed into a rectangular foundation $\Omega_0^{(2)}$ and is dragged in its tangential direction. The exact geometric setting and the coarser of two investigated $\mathbb{Q}_1$ meshes is depicted in Figure 5.7a; the finer of the two meshes is obtained by one level of h-refinement. Both bodies are modeled with a neo-Hookean material (3.38) under plane strain conditions with Young's moduli $E^{(1)} = 10$ and $E^{(2)} = 1$ and Poisson's ratios $\nu^{(1)} = \nu^{(2)} = 0.32$, respectively. At the contact interface, Coulomb's law of friction is applied with a friction coefficient of $\mu = 0.3$. Within the first 20 time steps, the top edge of the indentor performs a prescribed vertical displacement of, in total, 0.5 and is then moved a distance of 2.5 horizontally within 100 equidistant steps. Three characteristic deformation stages are illustrated in Figures 5.7b - 5.7d. Four different methods are compared, namely

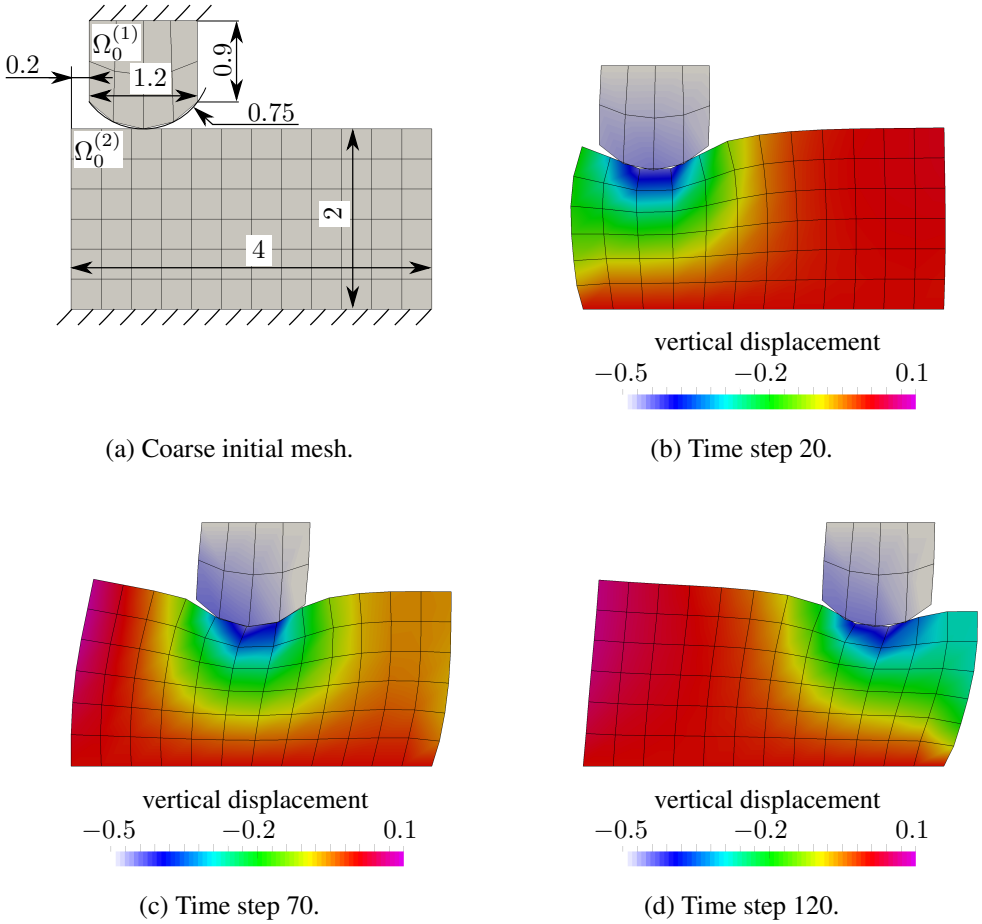

(a) Coarse initial mesh.

(b) Time step 20.

(c) Time step 70.

(d) Time step 120.

Figure 5.7: Frictional ironing – Geometric setup and representative deformation stages.

the symmetric method ($\theta_{\mathrm{u},1} = \theta_{\mathrm{u},2} = 1$) of Chouly *et al.* [35] with a sufficiently large penalty parameter $\gamma_{\{\mathrm{n},\tau\},0} = 2$, the skew-symmetric variant ($\theta_{\mathrm{u},1} = -1$, $\theta_{\mathrm{u},2} = 1$) of [35] with either the same penalty parameter as the symmetric variant or a low penalty parameter of $\gamma_{\{\mathrm{n},\tau\},0} = 0.02$ and finally the penalty-free variant ($\theta_{\mathrm{u},1} = -1$, $\theta_{\mathrm{u},2} = 0$) based on Burman *et al.* [25] with a sufficiently low penalty parameter of $\gamma_{\{\mathrm{n},\tau\},0} = 0.02$. Figure 5.8 depicts the vertical and horizontal contact forces, which approximately correspond to the normal and tangential components, respectively. Focusing on the vertical contact force on the coarse mesh (Figure 5.8a) first, slight oscillations can be observed, originating in the coarseness of the mesh and therefore rather poor smoothness of the boundary representation. For the variants with low penalty parameters, the weak form puts less emphasis on the exact, point-wise satisfaction of the kinematic constraint $g_{\mathrm{n}} \geq 0$ and hence exhibit less oscillations. For the penalty-free variant, hardly any oscillations can be observed, even on the coarse mesh. In horizontal direction, the variants with a penalty parameter of $\gamma_{\{\mathrm{n},\tau\},0} = 2$ accurately capture frictional sliding with a ratio between horizontal and vertical contact force of 0.304 (computed at time step 70, see Figure 5.7c) which is almost exactly the set friction coefficient of $\mu = 0.3$. For low penalty parameters, the tangential constraint is not enforced with sufficient accuracy, resulting in the horizontal contact force to be clearly underestimated. For the skew-symmetric variant of [35], the apparent coefficient of friction is

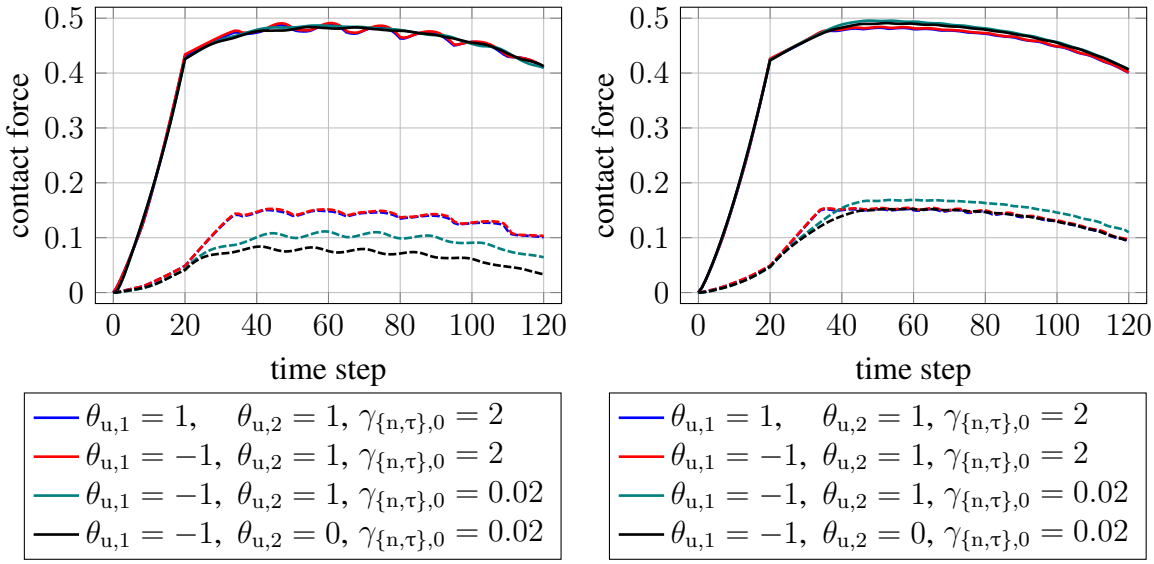

(a) Coarse mesh.

(b) Fine mesh.

Figure 5.8: Frictional ironing – Vertical (solid lines) and horizontal (dashed lines) contact forces for different meshes and methods.

only 0.221 and, even more significant, merely 0.165 for the penalty-free method. The underestimation of friction forces is, however, only a noticeable effect on relatively coarse meshes, as shown by the results after performing one step of h-refinement reported in Figure 5.8b. In vertical direction, the amplitude of the oscillations of the contact force has diminished noticeably while their frequency follows the mesh size and is therefore doubled. In tangential direction the accuracy of frictional forces increased also for the variants with low penalty parameters. Only the skew-symmetric variant with $\theta_{u,1} = -1$, $\theta_{u,2} = 1$ in combination with a low penalty parameter of $\gamma_{\{n,\tau\},0} = 0.02$ now slightly overestimates frictional forces, yielding a ratio of horizontal to vertical contact force of 0.342 whereas all other methods give values in the range of $[0.310, 0.317]$. It should be noted that, due to nonlinear geometric effects, the investigated ratio of horizontal to vertical contact force does not converge to to the coefficient of friction μ. The stick-slip transition in step 35, marked by a kink in the evolution of the horizontal contact force, is only well captured for sufficiently large penalty parameters, even on the finer mesh. Otherwise, the transition is "smeared" over several time steps. Nevertheless, also for low penalty parameters, the stick-slip transition becomes sharper for more refined meshes. In summary, this example demonstrates, that even if the penalty term is not necessary for stability for all methods, it still contributes to an accurate constraint enforcement on coarse meshes, especially in tangential direction.

5.1.4.4 Squeezed Elasto-Plastic Tube

Finally, a coupled elasto-plastic frictional contact problem is considered. The same setup has already been analyzed in the context of thermomechanical mortar contact formulations in Section 4.2.3.5. A metal tube (length $40\,\mathrm{cm}$, inner radius $4\,\mathrm{cm}$, outer radius $5\,\mathrm{cm}$) is deformed by two rigid cylindrical tools (outer radius $5\,\mathrm{cm}$), see Figure 5.9. The tools are subjected to a time

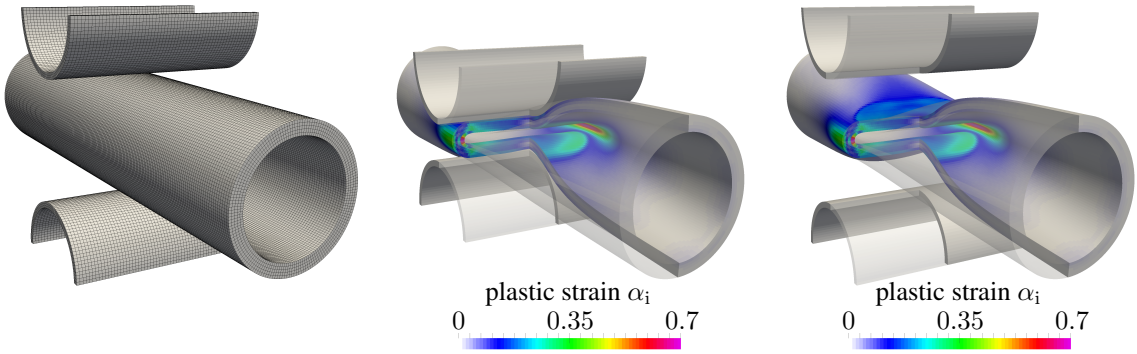

(a) Initial configuration. (b) $t = 1\,\mathrm{s}$. (c) $t = 2\,\mathrm{s}$.

Figure 5.9: Squeezed elasto-plastic tube – Initial configuration and representative deformed states colored by the accumulated plastic strain α_i.

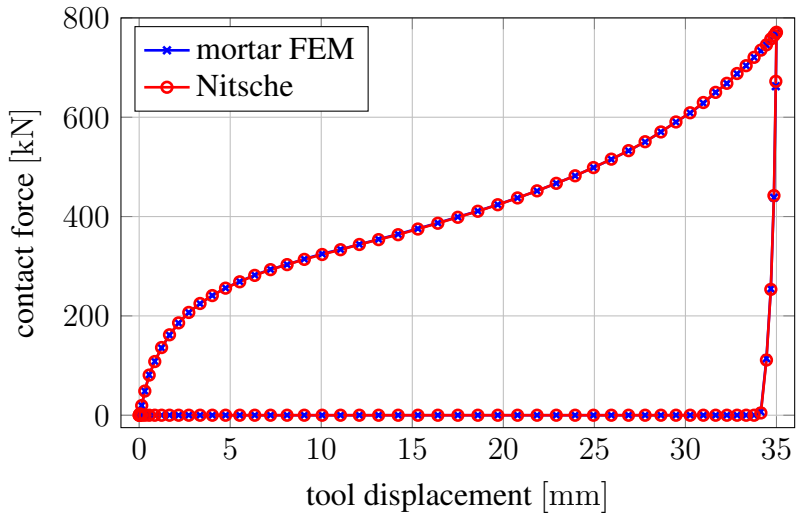

Figure 5.10: Squeezed elasto-plastic tube – Total contact force for dual mortar and Nitsche-based contact formulations.

dependent prescribed displacement of $u(t) = (1 - \cos(\frac{t}{1\,\mathrm{s}}\pi)) \cdot 1.75\,\mathrm{cm}$ applied in time steps $\Delta t = 0.02\,\mathrm{s}$. The elastic material response of the tube is modeled with a neo-Hookean material (3.38) with Young's modulus $E = 206.9\,\mathrm{GPa}$ and Poisson's ratio $\nu = 0.29$. Further, von Mises plasticity with an initial yield stress of $y_0 = 0.45\,\mathrm{GPa}$ and the nonlinear isotropic hardening potential (3.39) with $H_i = 0.12924\,\mathrm{GPa}$, $y_\infty = 0.715\,\mathrm{GPa}$ and $\delta = 16.93$ is assumed. Between the tube and the tools, frictional contact with a coefficient of friction $\mu = 0.25$ occurs. Making use of the apparent symmetry of the problem, only one eighth of the tube is meshed with 18000 elements. To avoid volumetric locking due to the volume preserving plastic flow, first order F-bar elements as discussed in Section 2.8.1.1 are employed and the plastic material constraints are imposed by the algorithm devised in Section 3. As discussed in Section 5.1.3, the only viable Nitsche method for elasto-plastic problems is the simple non-symmetric one with $\theta_{u,1} = 0$ and $\theta_{u,2} = 1$ which, in this example, has been used with a reference penalty parameter $\gamma_{\{n,\tau\},0} = 1$. Figure 5.10 compares the total contact force obtained with Nitsche's method with a reference so-

lution using the dual mortar method of Chapter 4. Both methods yield virtually identical results, hence it can be concluded that the extrapolation of stresses for elasto-plastic materials introduced in Section 5.1.3 represents a feasible approach to incorporate inelastic material behavior in Nitsche-type algorithms.

5.2 Nitsche Methods for Thermomechanical Contact Problems[1]

This section extends the isothermal Nitsche-based contact algorithm introduced in the previous section to coupled thermomechanics. As far as the weak form of the mechanical problem (5.13) is concerned, two minor modifications have to be accounted for as compared to the isothermal case. For one, the contact traction $\boldsymbol{t}_{\mathrm{c},h}$ (and its directional derivative $\mathcal{D}\boldsymbol{t}_{\tau,h}[\delta\boldsymbol{u}_h]$) are now temperature dependent. In the simplest case, thermal expansion is modeled via (3.47) or, more complex, coupled thermo-elasto-plasticity is included with potentially temperature dependent plastic material parameters as introduced in Section 3.4.3. The second temperature dependency in (5.13) stems from a temperature dependent coefficient of friction, in accordance with (2.125). Both additional temperature dependencies do not alter the characteristic of Nitsche's method for contact problems (5.13), and are therefore not discussed in detail here. It should, however, be noted that they require consistent linearization if, as is the case in this thesis, the coupled thermomechanical problem is to be solved within a monolithic Newton scheme (see Section 2.8.3).

Considering the thermal sub-problem, the point of origin for the subsequently devised methods is again the weak forms introduced in Section 2.7, in particular the weak form of the heat conduction equation (2.133) including contact heat fluxes (2.129). The two following sections introduce two different methods to consistently introduce these thermal heat fluxes to the weak form: First, a strong substitution method is discussed which, at first glance, captivates with its simplicity. However, it yields an ill-conditioned problem for large values of the thermal contact conductivity β_{c}. This drawback can be overcome by using the second option, a Nitsche-type formulation, which reduces to a classical Nitsche method for interface-continuity in the limit case $\beta_{\mathrm{c}} \to \infty$.

5.2.1 A Substitution Method for the Thermal Interface Condition

The probably most straight-forward way to account for contact heat conduction is to simply substitute the interface heat fluxes $q_{\mathrm{c}}^{(i)}$ in (2.133) (or its discrete counterpart, to be precise) by the expressions (2.129a) and (2.129b), respectively. This approach is known as the substitution method. Since the normal contact constraint is introduced via (5.4) (or (5.6)), the effective heat conductivity

$$\bar{\beta}_{\mathrm{c}} = -\beta_{\mathrm{c}} \left[\{p_{\mathrm{n}}\}_{\omega_{\mathrm{u}}} + \gamma_{\mathrm{n}} g_{\mathrm{n}} \right]_{-} \tag{5.28}$$

is introduced as a consistent substitute for $\beta_{\mathrm{c}}|p_{\mathrm{n}}|$. Similarly, the frictional power

$$\mathcal{P}_{\mathrm{c},h} = P_{B(\bar{\mu})} \left(\{\boldsymbol{t}_{\tau,h}\}_{\omega_{\mathrm{u}}} + \gamma_{\tau} \Delta\boldsymbol{u}_{\tau,h} \right) \cdot \boldsymbol{v}_{\tau,h} \tag{5.29}$$

[1] This section is adapted from the author's publication [195].

obtained utilizing relation (5.11) serves as a replacement for $\boldsymbol{t}_\tau \cdot \boldsymbol{v}_\tau$ in (2.129) in the continuous problem. With these surrogates, the heat fluxes $q_{\mathrm{c}}^{(i)}$ can be substituted in a discretized form of (2.133) yielding the weak form: Find $T_h \in \mathcal{U}_{\mathrm{T},h}$, such that

$$\begin{aligned} \delta\mathcal{W}_{\mathrm{T},h} + \int_{\gamma_{\mathrm{c},h}^{(1)}} \left(\bar{\beta}_{\mathrm{c}}[\![T_h]\!] - \delta_{\mathrm{c}}\mathcal{P}_{\mathrm{c},h}\right) \delta T_h^{(1)} \\ + \left(-\bar{\beta}_{\mathrm{c}}[\![T_h]\!] - (1-\delta_{\mathrm{c}})\mathcal{P}_{\mathrm{c},h}\right) \left(\delta T_h^{(2)} \circ \chi_{t,h}\right) \mathrm{d}\gamma = 0 \quad \forall \delta T_h \in \mathcal{V}_{\mathrm{T},h} \ . \end{aligned} \tag{5.30}$$

There is, however, a drawback to this method: The case of a very high thermal contact conductivity, i.e. $\bar{\beta}_{\mathrm{c}} \to \infty$, is no longer permitted, since for increasing $\bar{\beta}_{\mathrm{c}}$ the jump terms in (5.30) will increase linearly with $\bar{\beta}_{\mathrm{c}}$, dominating the weak form, and finally yield an ill-conditioned system.

5.2.2 Nitsche's Method for the Thermal Interface Condition

To overcome this drawback of the substitution method and to allow the case of $\bar{\beta}_{\mathrm{c}} \to \infty$, a Nitsche method for general boundary conditions has been introduced in Juntunen and Stenberg [118] and extended to interface conditions in Annavarapu *et al.* [5] with prescribed jumps in the primal variable (i.e. the temperature in the present case) and its derivative. This method is now applied to the Robin-type interface condition in equation (2.129). As its derivation does not yield any deep insight, only the resulting weak form of the thermal problem including the Nitsche terms is presented here. In addition, Appendix B briefly demonstrates that this weak form is actually consistent with the continuous problem. The weak form reads: Find $T_h \in \mathcal{U}_{\mathrm{T},h}$, such that

$$\begin{aligned} \delta\mathcal{W}_{\mathrm{T},h} &+ \int_{\gamma_{\mathrm{c},h}^{(1)}} \frac{\bar{\beta}_{\mathrm{c}}}{\bar{\beta}_{\mathrm{c}} + \gamma_{\mathrm{T}}} \left\{q_{\mathrm{c},h}(T_h)\right\}_{\omega_{\mathrm{T}}} [\![\delta T_h]\!] \, \mathrm{d}\gamma \\ &+ \int_{\gamma_{\mathrm{c},h}^{(1)}} \frac{\gamma_{\mathrm{T}}\bar{\beta}_{\mathrm{c}}}{\bar{\beta}_{\mathrm{c}} + \gamma_{\mathrm{T}}} [\![T_h]\!][\![\delta T_h]\!] \, \mathrm{d}\gamma \\ &- \theta_{\mathrm{T}} \int_{\gamma_{\mathrm{c},h}^{(1)}} \frac{1}{\bar{\beta}_{\mathrm{c}} + \gamma_{\mathrm{T}}} \left\{q_{\mathrm{c},h}(T_h)\right\}_{\omega_{\mathrm{T}}} \left\{q_{\mathrm{c},h}(\delta T_h)\right\}_{\omega_{\mathrm{T}}} \, \mathrm{d}\gamma \\ &+ \theta_{\mathrm{T}} \int_{\gamma_{\mathrm{c},h}^{(1)}} \frac{\bar{\beta}_{\mathrm{c}}}{\bar{\beta}_{\mathrm{c}} + \gamma_{\mathrm{T}}} [\![T_h]\!] \left\{q_{\mathrm{c},h}(\delta T_h)\right\}_{\omega_{\mathrm{T}}} \, \mathrm{d}\gamma \\ &- \int_{\gamma_{\mathrm{c},h}^{(1)}} \mathcal{P}_{\mathrm{c},h} \left(\delta_{\mathrm{c}}\delta T_h^{(1)} + (1-\delta_{\mathrm{c}})(\delta T_h^{(2)} \circ \chi_{t,h})\right) \, \mathrm{d}\gamma \\ &- \int_{\gamma_{\mathrm{c},h}^{(1)}} \frac{\bar{\beta}_{\mathrm{c}}}{\bar{\beta}_{\mathrm{c}} + \gamma_{\mathrm{T}}} (1 - \delta_{\mathrm{c}} - \omega_{\mathrm{T}}) \mathcal{P}_{\mathrm{c},h} [\![\delta T_h]\!] \, \mathrm{d}\gamma \\ &+ \theta_{\mathrm{T}} \int_{\gamma_{\mathrm{c},h}^{(1)}} \frac{1}{\bar{\beta}_{\mathrm{c}} + \gamma_{\mathrm{T}}} (1 - \delta_{\mathrm{c}} - \omega_{\mathrm{T}}) \mathcal{P}_{\mathrm{c},h} \left\{q_{\mathrm{c},h}(\delta T_h)\right\}_{\omega_{\mathrm{T}}} \, \mathrm{d}\gamma = 0 \quad \forall \delta T_h \in \mathcal{V}_{\mathrm{T},h} \ . \end{aligned} \tag{5.31}$$

Therein, $q_{\mathrm{c},h}^{(i)}(T_h) = -\frac{k_0^{(i)}}{\det \boldsymbol{F}^{(i)}} \nabla_{\boldsymbol{x}} T_h^{(i)} \cdot \boldsymbol{n}^{(i)}$ represents the surface (Cauchy-) heat flux computed from the discrete temperature field according to Fourier's law (2.48a) and Stokes' heat flux theorem (2.29); $q_{\mathrm{c},h}^{(i)}(\delta T_h)$ is defined analogously. Furthermore, $\omega_{\mathrm{T}} \in [0,1]$ is a weighting between

the slave and master sided heat flux and γ_{T} is a penalty parameter of order $\mathcal{O}(\frac{k_0}{h})$. The determination of ω_{T} and γ_{T} will be discussed in detail in Section 5.2.2.2. Finally, $\theta_{\mathrm{T}} \in \{-1, 0, 1\}$ allows the use of different variants of Nitsche's method, similar to the structural formulation in (5.13). For frictionless contact of one body $\Omega_0^{(1)}$ with a rigid surface of constant temperature, and when choosing $\omega_{\mathrm{T}} = 1$ and $\theta_{\mathrm{T}} = 1$, (5.31) reduces to the method originally presented by Juntunen and Stenberg [118]. Furthermore, setting $\omega_{\mathrm{T}} = 1 - \delta_{\mathrm{c}}$ and $\theta_{\mathrm{T}} = 1$ yields the method presented by Annavarapu *et al.* [5]. Depending on the parameter θ_{T} different variants are obtained similar to the structural problem: $\theta_{\mathrm{T}} = 1$ gives a symmetric method, $\theta_{\mathrm{T}} = 0$ has fewer terms and $\theta_{\mathrm{T}} = -1$ yields a coercive formulation for any $\gamma_{\mathrm{T}} > 0$, whereas the other variants have a lower bound for γ_{T} (see Winter *et al.* [231] for a proof of the same method applied to boundary conditions in the Oseen equation). The simple substitution approach (5.30) is recovered in the limit $\gamma_{\mathrm{T}} \to \infty$.

5.2.2.1 Limit Cases of Nitsche's Method

In contrast to the substitution method (5.30), the Nitsche method (5.31) also allows both limit cases $\beta_{\mathrm{c}} = 0$ and $\beta_{\mathrm{c}} \to \infty$, i.e. an adiabatic contact interface and perfect heat conduction across the contact interface. To illustrate this, the resulting weak forms of these limit cases are discussed in the following.

Adiabatic contact interface. For an adiabatic contact interface, $\beta_{\mathrm{c}} = 0$, no heat flux may occur across the contact interface but only source terms appear due to frictional dissipation. Inserting $\beta_{\mathrm{c}} = 0$ in (5.31) reduces to

$$\begin{aligned} \delta\mathcal{W}_{\mathrm{T},h} &- \theta_{\mathrm{T}} \int_{\gamma_{\mathrm{c},h}^{(1)}} \frac{1}{\gamma_{\mathrm{T}}} \left\{q_{\mathrm{c},h}(T_h)\right\}_{\omega_{\mathrm{T}}} \left\{q_{\mathrm{c},h}(\delta T_h)\right\}_{\omega_{\mathrm{T}}} \mathrm{d}\gamma \\ &- \int_{\gamma_{\mathrm{c},h}^{(1)}} \mathcal{P}_{\mathrm{c},h} \left(\delta_{\mathrm{c}} \delta T_h^{(1)} + (1-\delta_{\mathrm{c}})(\delta T_h^{(2)} \circ \chi_{t,h})\right) \mathrm{d}\gamma \\ &+ \theta_{\mathrm{T}} \int_{\gamma_{\mathrm{c},h}^{(1)}} \frac{1}{\gamma_{\mathrm{T}}} (1 - \delta_{\mathrm{c}} - \omega_{\mathrm{T}}) \mathcal{P}_{\mathrm{c},h} \left\{q_{\mathrm{c},h}(\delta T_h)\right\}_{\omega_{\mathrm{T}}} \mathrm{d}\gamma = 0 \quad \forall \delta T_h \in \mathcal{V}_{\mathrm{T},h} \ . \end{aligned} \tag{5.32}$$

In comparison to the substitution method, which is recovered for $\gamma_{\mathrm{T}} \to \infty$ (i.e. dropping the fist and third integral), an additional symmetric penalty-like term (first integral in (5.32)) remains along with the frictional heat source in the third line of (5.32). For $\theta_{\mathrm{T}} = -1$, this penalty term has a positive sign and therefore stability of the method is retained for $\gamma_{\mathrm{T}} > 0$. However, low values of $\gamma_{\mathrm{T}} \to 0$ results in an ill-conditioned system, since the first integral in (5.32) increases. For $\theta_{\mathrm{T}} = 1$, on the other hand, the negative sign of the penalty term requires γ_{T} to be sufficiently large to ensure stability.

Perfect contact heat conduction. The other limit case of $\beta_{\mathrm{c}} \to \infty$ corresponds to perfect heat conduction, i.e. the contacting surfaces have equal temperature at any point of closed contact. To illustrate the resulting method, the contact boundary is split into its active and inactive part $\gamma_{\mathrm{c},h,0}^{(1)}$ and $\gamma_{\mathrm{c},h,+}^{(1)}$ according to (5.14), such that

$$\bar{\beta}_{\mathrm{c}} = \begin{cases} 0 & \text{on } \gamma_{\mathrm{c},h,+}^{(1)} \\ \infty & \text{on } \gamma_{\mathrm{c},h,0}^{(1)} \end{cases} \ . \tag{5.33}$$

The weak form (5.31) then reduces to

$$\begin{aligned}
&\delta\mathcal{W}_{\mathrm{T},h} - \theta_{\mathrm{T}} \int_{\gamma_{\mathrm{c},h,+}^{(1)}} \frac{1}{\gamma_{\mathrm{T}}} \left\{q_{\mathrm{c},h}(T_h)\right\}_{\omega_{\mathrm{T}}} \left\{q_{\mathrm{c},h}(\delta T_h)\right\}_{\omega_{\mathrm{T}}} \mathrm{d}\gamma \\
&\quad + \int_{\gamma_{\mathrm{c},h,0}^{(1)}} \left\{q_{\mathrm{c},h}(T_h)\right\}_{\omega_{\mathrm{T}}} [\![\delta T_h]\!] \,\mathrm{d}\gamma \\
&\quad + \int_{\gamma_{\mathrm{c},h,0}^{(1)}} \gamma_{\mathrm{T}} [\![T_h]\!] [\![\delta T_h]\!] \,\mathrm{d}\gamma \\
&\quad + \theta_{\mathrm{T}} \int_{\gamma_{\mathrm{c},h,0}^{(1)}} [\![T_h]\!] \left\{q_{\mathrm{c},h}(\delta T_h)\right\}_{\omega_{\mathrm{T}}} \mathrm{d}\gamma \\
&\quad - \int_{\gamma_{\mathrm{c},h,0}^{(1)}} \mathcal{P}_{\mathrm{c},h} \left(\delta_{\mathrm{c}} \delta T_h^{(1)} + (1-\delta_{\mathrm{c}})(\delta T_h^{(2)} \circ \chi_{t,h})\right) \mathrm{d}\gamma \\
&\quad - \int_{\gamma_{\mathrm{c},h,0}^{(1)}} (1-\delta_{\mathrm{c}}-\omega_{\mathrm{T}}) \mathcal{P}_{\mathrm{c},h} [\![\delta T_h]\!] \,\mathrm{d}\gamma = 0 \quad \forall \delta T_h \in \mathcal{V}_{\mathrm{T},h} \ .
\end{aligned} \tag{5.34}$$

In the inactive contact zone (first integral in (5.34)), an additional penalty term, identical to the one in the adiabatic case (5.32), remains enforcing the homogeneous Neumann boundary condition. In the active contact zone, the second to fourth line in (5.34) enforce continuity of the temperature field across the contact interface via the classical symmetric ($\theta_{\mathrm{T}} = 1$) or skew-symmetric ($\theta_{\mathrm{T}} = -1$) Nitsche method. Finally, the fifth and sixth line act as source terms introducing frictional heating. Although the thermomechanical coupling and nonlinear kinematics preclude a thorough mathematical analysis, the typical stability results for Nitsche's method apply if the mechanical state was fixed. This implies that the symmetric variant $\theta_{\mathrm{T}} = 1$ is stable for a sufficiently large penalty parameter γ_{T}, whereas the skew-symmetric variant $\theta_{\mathrm{T}} = -1$ is stable for any $\gamma_{\mathrm{T}} > 0$.

5.2.2.2 Penalty Parameter Estimates and Harmonic Weights[1]

The required penalty parameter γ_{T} to ensure stability of the symmetric Nitsche method $\theta_{\mathrm{T}} = 1$ in (5.31) can, in analogy to the structural problem discussed in Section 5.1.2, be estimated by solving local generalized eigenvalue problems. To start with, a slave sided weighting of the contact heat flux, $\omega_{\mathrm{T}} = 1$, is considered. Under some simplifying assumptions such as Fourier's law of heat conduction (2.48), the absence of thermo-strucutural coupling and closed contact on the entire potential contact boundary $\gamma_{\mathrm{c},h}^{(1)}$, stability of the approximation (5.31) can be guaranteed if $\gamma_{\mathrm{T}} > 0$ and $\theta_{\mathrm{T}} = -1$ [231, Lemma 5.2] and, according to [118, Theorem 3.2], for $\theta_{\mathrm{T}} \neq -1$ with $\gamma_{\mathrm{T}} > C_{\mathrm{I,T}}$ where $C_{\mathrm{I,T}}$ satisfies the trace inequality

$$\int_{\gamma_{\mathrm{c},h}^{(1)}} \|\boldsymbol{q}^{(1)}(T_h) \cdot \boldsymbol{n}\|^2 \,\mathrm{d}\gamma \leq C_{\mathrm{I,T}} \int_{\Omega_{t,h}^{(1)}} \boldsymbol{q}^{(1)}(T_h) \cdot \nabla_{\boldsymbol{x}} T_h \,\mathrm{d}\Omega \ , \quad \forall T_h \in \mathcal{U}_{\mathrm{T},h} \ , \tag{5.35}$$

or equivalently in reference configuration

$$\int_{\Gamma_{\mathrm{c},h}^{(1)}} \|\boldsymbol{Q}^{(1)}(T_h) \cdot \boldsymbol{N}\|^2 \,\mathrm{d}\Gamma \leq C_{\mathrm{I,T}} \int_{\Omega_{0,h}^{(1)}} \boldsymbol{Q}^{(1)}(T_h) \cdot \nabla_{\boldsymbol{X}} T_h \,\mathrm{d}\Omega \ , \quad \forall T_h \in \mathcal{U}_{\mathrm{T},h} \ . \tag{5.36}$$

[1] This section is adapted from the author's publication [195].

Akin to the trace estimate of the structural problem in Section 5.1.2, local generalized eigenvalue problems

$$\boldsymbol{A}\boldsymbol{v} = \lambda \boldsymbol{B}\boldsymbol{v} \tag{5.37a}$$

with the Hessians $\boldsymbol{A}$ and $\boldsymbol{B}$ to

$$A = \int_{\tau_{h,k}^{(1)} \cap \Gamma_{\mathrm{c},h}^{(1)}} \| \boldsymbol{Q}^{(1)}(T_h) \cdot \boldsymbol{N} \|^2 \, \mathrm{d}\Gamma \ , \tag{5.37b}$$

$$B = \int_{\tau_{h,k}^{(1)}} \boldsymbol{Q}^{(1)}(T_h) \cdot \nabla_{\boldsymbol{X}} T_h \, \mathrm{d}\Omega \ , \tag{5.37c}$$

yield constants $C_{\mathrm{I,T}}^{\tau_{h,k}^{(1)}} = \lambda_{\max}^{\tau_{h,k}^{(1)}}$ for each element on the slave contact surface. Note that for Fourier's law of heat conduction (2.48), $\boldsymbol{Q}$ is linear in the temperatures but nonlinear in the structural displacements. Consequently, the constants $C_{\mathrm{I,T}}^{\tau_{h,k}^{(1)}}$ depend on the deformation state but not on the temperature. A sufficient penalty parameter to ensure stability for $\theta_{\mathrm{T}} \neq -1$ is given by a piece-wise constant function

$$\gamma_{\mathrm{T}}|_{\tau_{h,k}^{(1)} \cap \Gamma_{\mathrm{c},h}^{(1)}} = C_{\mathrm{I,T}}^{\tau_{h,k}^{(1)}} \, \gamma_{\mathrm{T},0} \quad , \quad , \tag{5.38}$$

with a reference value $\gamma_{\mathrm{T},0} > 1$.

Following up on the discussions of Section 5.1.2, (5.38) yields large penalty parameters in cases where the thermal conductivity of the slave side is much larger than that on the master side, i.e. $k_0^{(1)} \gg k_0^{(2)}$. To reduce the penalty parameter in such cases, harmonic weights are again introduced based on Burman and Zunino [24] and applied in a similar fashion as in Section 5.1.2. On the common integration domain of a slave sided element $\tau_{h,i}^{(1)}$ and a master sided element $\tau_{h,j}^{(2)}$, the weighting is defined according to

$$\omega_{\mathrm{T}}^{\tau_{h,i}^{(1)} \tau_{h,j}^{(2)}} = \frac{C_{\mathrm{I,T}}^{\tau_{h,j}^{(2)}}}{C_{\mathrm{I,T}}^{\tau_{h,i}^{(1)}} + C_{\mathrm{I,T}}^{\tau_{h,j}^{(2)}}} \ , \tag{5.39}$$

and the corresponding penalty parameter by

$$\gamma_{\mathrm{T}}^{\tau_{h,i}^{(1)} \tau_{h,j}^{(2)}} = \left\{ C_{\mathrm{I,T}}^{\tau_{h,k}^{(i)}} \right\}_{\omega_{\mathrm{T}}} \gamma_{\mathrm{T},0} \ . \tag{5.40}$$

In contrast to Annavarapu *et al.* [5], who set $\omega_{\mathrm{T}} = 1 - \delta_{\mathrm{c}}$, the proposed harmonic weighting (5.39) is determined independently of the interface parameter δ_{c} distributing the frictional heating to the two sides. Since δ_{c} is a physical parameter, it cannot be set freely as proposed in [5], where δ_{c} is adjusted to reduce the necessary penalty parameter. Instead, the weighting (5.39) is solely based on element shapes and the thermal conductivity. Additional terms are added in the sixth and seventh line of (5.31) as compared to [5] to allow $\omega_{\mathrm{T}} \neq 1 - \delta_{\mathrm{c}}$.

5.2.3 Numerical Examples

In this section, numerical examples of increasing complexity are presented. Starting with a thermomechanical patch test demonstrating the consistency of the method in Section 5.2.3.1, spatial convergence orders for thermo-elastic frictionless contact problems are investigated in 5.2.3.2. Next, effects of frictional heating are demonstrated in Section 5.2.3.3 and finally a fully coupled thermo-elasto-plastic problem is presented in Section 5.2.3.4. The distinctive features of stability and potential ill-conditioning of the presented methods will be highlighted.

5.2.3.1 Thermomechanical Contact Patch Test

As a first example, consistency of the presented methods is demonstrated by means of a contact patch test with heat conduction. The presented setting has already been analyzed using a node-to-segment penalty contact formulation in Oancea and Laursen [159], Wriggers and Miehe [236] and using a mortar method with dual Lagrange multipliers in Section 4.2.3.1. As illustrated in Figure 5.11a, two stacked unit cubes are simulated, where the lower surface of the lower cube is fixed in space with a uniform temperature of $T = 20$ and the upper surface of the upper cube is fixed at $T = 40$. The two blocks are compressed until a final value of the contact pressure of $p_\mathrm{n} = 30$ is reached. Both cubes are modeled with a Saint-Venant–Kirchhoff material model with a Young's modulus of $E = 4000$ and a Poisson's ratio $\nu = 0$ as well as a heat conductivity of $k_0 = 52$. Frictionless contact with a heat conductivity of $\beta_\mathrm{c} = 5$ is assumed. The final temperature distribution is depicted in Figure 5.11b, which perfectly reproduces the analytical solution as shown for the temperatures of the contact surfaces in Figure 5.11c. The analytical solution is

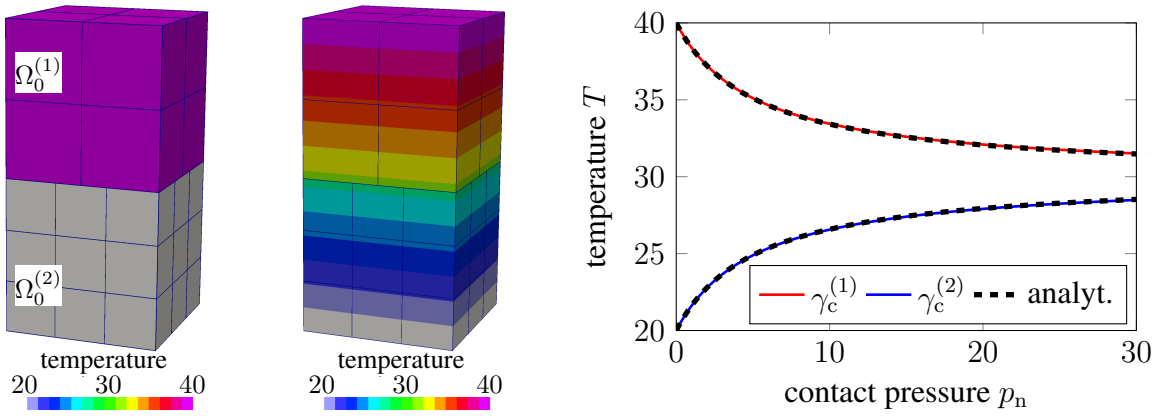

(a) $p_n = 0$ (b) $p_n = 30$ (c) interface temperatures over p_n

Figure 5.11: Thermomechanical contact patch test – Temperature distribution at different contact pressure and comparison with analytical solution.

a linear displacement field and a piece-wise linear temperature field with a jump at the contact interface [159, 236]. Since this solution can be represented exactly by a discretization with first order hexahedral elements, any consistent method will reproduce this analytical solution up to machine precision. This is also the case for all combinations of the methods presented in this chapter, i.e. for any choice of the slave and master side as well as any γ_n, $\theta_{\mathrm{u},1}$, $\theta_{\mathrm{u},2}$ and ω_u in (5.8), in combination with either the substitution method (5.30) or Nitsche's method (5.31) with

varying γ_{T}, θ_{T} and ω_{T}. For this setup, the methods are completely unbiased if harmonic weights are used, since the discrete normals point exactly in opposite directions, i.e. $\boldsymbol{n}^{(1)} = -\boldsymbol{n}^{(2)}$. As a result, the final system matrix is identical for either choice of the slave and master side. It is worth mentioning that the analytical solution is only reproduced exactly, if the numerical integration at the contact interface is exact. This in particular includes integration on the intersected slave- and master-side mesh as discussed in Remark 5.3. If integration points are defined on slave elements only, an integration error is introduced. The effect of this integration error on the contact patch test performance of an isothermal finite deformation Nitsche method is analyzed in Mlika *et al.* [152]. Due to the simplicity of the solution, even unstable approximations with penalty parameters that would otherwise be too low yield the correct results.

5.2.3.2 Convergence Study of Frictionless Thermo-Elastic Contact

The convergence behavior of the presented methods with mesh refinement is studied using the 2-dimensional, plane strain example already used in this thesis for the isothermal mortar method in Section 4.1.3.2.2 and the thermomechanical mortar method in Section 4.2.3.2. A rectangular block $\Omega_0^{(2)}$ is pressed against a circular arc $\Omega_0^{(1)}$ by a prescribed vertical displacement of $\hat{u} = 0.3$. Moreover, a prescribed temperature difference between the lower end of the block and the upper ends of the arc yields an inhomogeneous temperature distribution. The exact geometry and boundary conditions are given in Figure 5.12a. The elastic material behavior of both bodies is

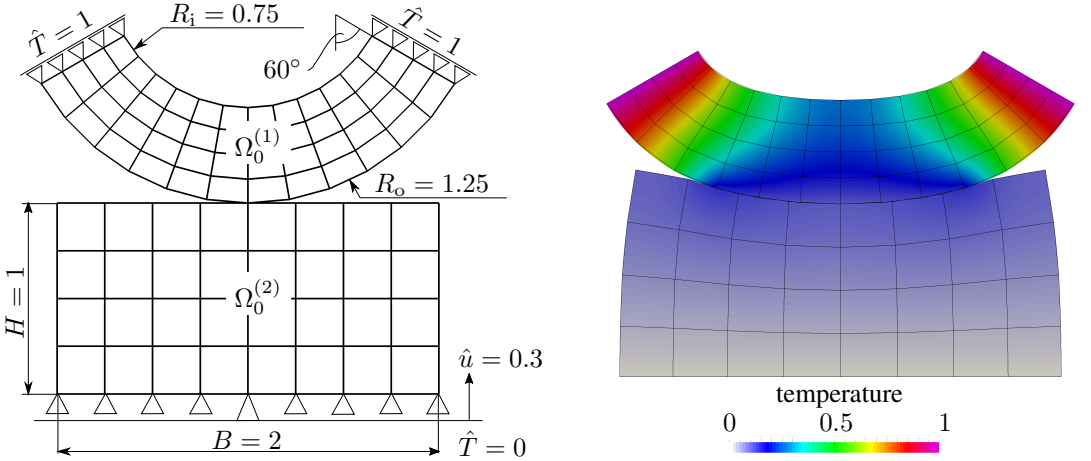

(a) Initial geometry, boundary conditions and exemplary mesh with $h = 2^{-2}$.

(b) Deformed mesh and temperature distribution for $h = 2^{-2}$ and $\mathbb{Q}_2$ finite elements.

Figure 5.12: Two dimensional contact of a circular arc with a rectangle – Geometric setup, exemplary mesh and deformed configuration. (Reproduced from Figure 4.28 for illustrative purposes.)

modeled by the neo-Hookean material law (3.38) and thermal expansion is included by means of (3.47). The material parameters are chosen as Young's moduli $E^{(1)} = 5$ and $E^{(2)} = 1$, Poisson's ratio $\nu^{(1)} = \nu^{(2)} = 0.2$, thermal conductivity $k_0^{(1)} = 1$ and $k_0^{(2)} = 5$, and the coefficient of thermal expansion $\alpha_{\mathrm{T}}^{(1)} = \alpha_{\mathrm{T}}^{(2)} = 0.01$. Note that for those material parameters, the harmonic weighting presented in Sections 5.1.2 and 5.2.2.2 yields different weightings for the structural and thermal part. Here, the weighting of the contact traction is shifted to the softer side, i.e. $\Omega_0^{(2)}$, whereas the weighting of the contact heat flux is shifted to the side with lower thermal conductivity, i.e. $\Omega_0^{(1)}$.

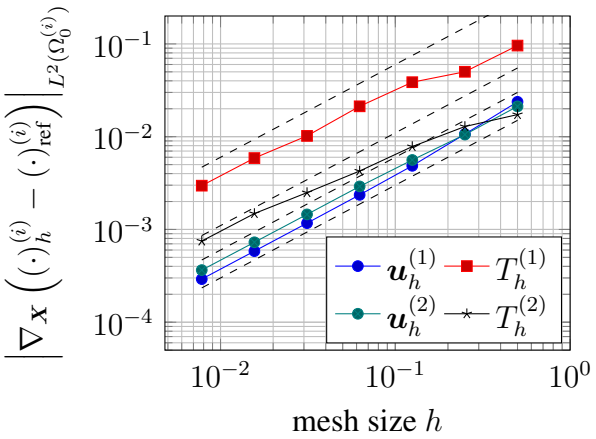

(a) $\theta_{\mathrm{u},1} = \theta_{\mathrm{u},2} = 1$, $\gamma_{\mathrm{n},0} = 2$, substitution.

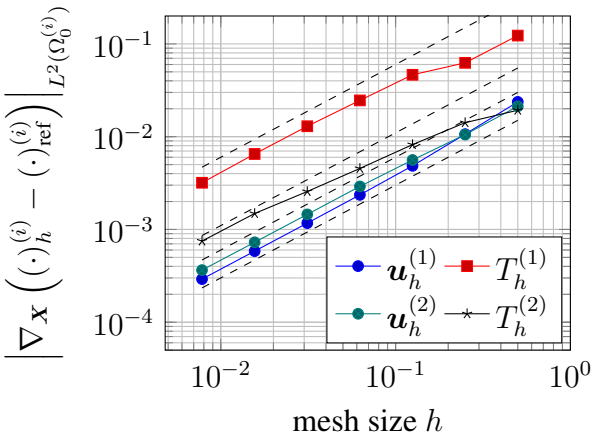

(b) $\theta_{\mathrm{u},1} = \theta_{\mathrm{u},2} = 1$, $\gamma_{\mathrm{n},0} = 2$, $\theta_{\mathrm{T}} = 1$, $\gamma_{\mathrm{T},0} = 2$.

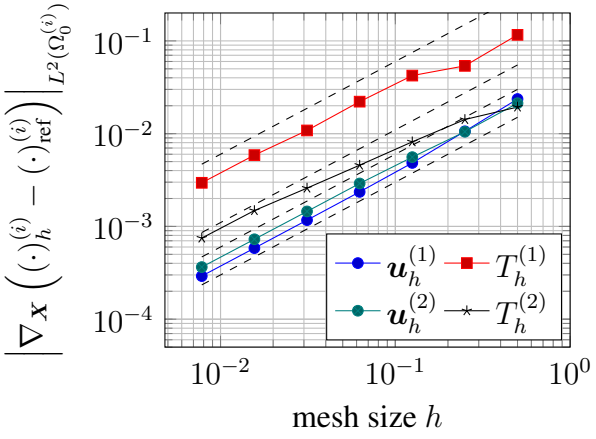

(c) $\theta_{\mathrm{u},1} = 0$, $\theta_{\mathrm{u},2} = 1$, $\gamma_{\mathrm{n},0} = 2$, $\theta_{\mathrm{T}} = 0$, $\gamma_{\mathrm{T},0} = 2$.

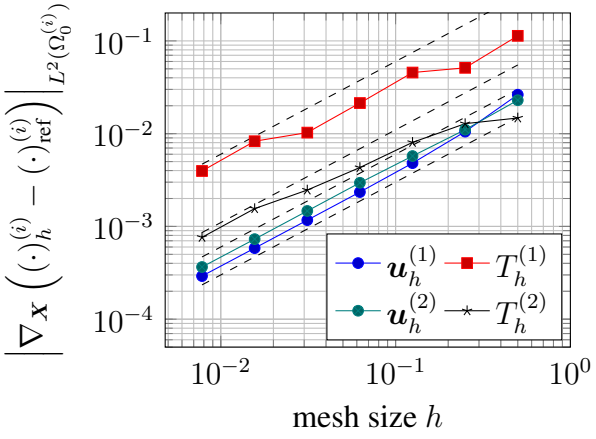

(d) $\theta_{\mathrm{u},1} = -1$, $\theta_{\mathrm{u},2} = 1$, $\gamma_{\mathrm{n},0} = 0.02$, $\theta_{\mathrm{T}} = -1$, $\gamma_{\mathrm{T},0} = 0.02$.

Figure 5.13: Convergence study of frictionless thermo-elastic contact – Convergence behavior of H^1 semi-norms of displacements and temperatures on the two sub-domains using $\mathbb{Q}_1$ finite elements and different variants of Nitsche's method for mechanical and thermal interface constraints. Dashed lines are of order $\mathcal{O}(h)$.

At the contact interface, frictionless contact is assumed and the heat transfer parameter is set to $\beta_{\mathrm{c}} = 10^3$.

In the following, the convergence behavior of the presented methods is investigated using linear $\mathbb{Q}_1$ and quadratic $\mathbb{Q}_2$ finite elements of mesh sizes $h \in \{2^{-7}, 2^{-6}, \ldots, 2^{-1}\}$. Since there is no analytical solution to this problem, the error norms are calculated with respect to a reference solution $\boldsymbol{u}_{\text{ref}}$ and T_{ref} that has been calculated with a very fine mesh ($h = 2^{-8}$), quadratic finite elements and the Lagrange multiplier method using dual basis functions for the Lagrange multiplier as introduced in Section 4.2. Owing to the symmetry of the problem, only one half is discretized with appropriate symmetry conditions and the result in Figure 5.12b is reflected for visualization purposes. Different combinations of the proposed methods are analyzed, namely

(a) the symmetric Nitsche method for the structural problem ($\theta_{\mathrm{u},1} = \theta_{\mathrm{u},2} = 1$, $\gamma_{\mathrm{n},0} = 2$) in combination with the substitution method for the contact heat flux (5.30),

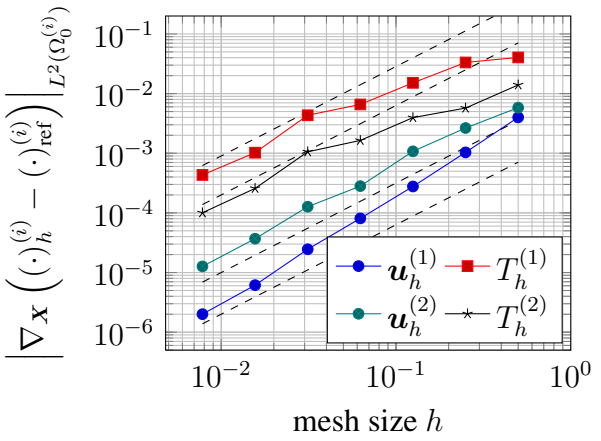

(a) $\theta_{\mathrm{u},1} = \theta_{\mathrm{u},2} = 1$, $\gamma_{\mathrm{n},0} = 2$, substitution.

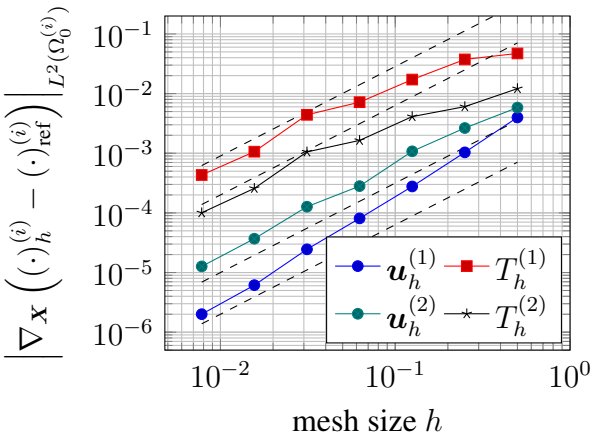

(b) $\theta_{\mathrm{u},1} = \theta_{\mathrm{u},2} = 1$, $\gamma_{\mathrm{n},0} = 2$, $\theta_{\mathrm{T}} = 1$, $\gamma_{\mathrm{T},0} = 2$.

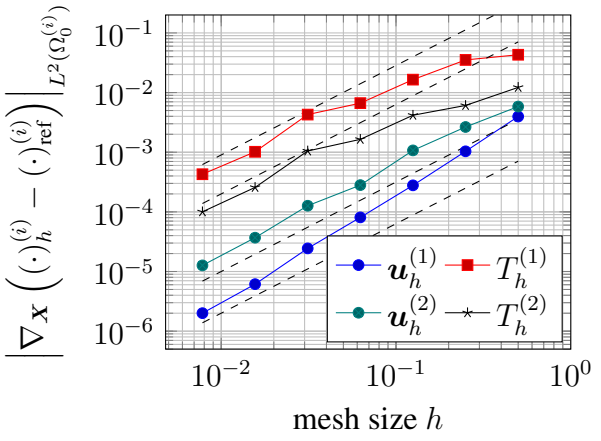

(c) $\theta_{\mathrm{u},1} = 0$, $\theta_{\mathrm{u},2} = 1$, $\gamma_{\mathrm{n},0} = 2$, $\theta_{\mathrm{T}} = 0$, $\gamma_{\mathrm{T},0} = 2$.

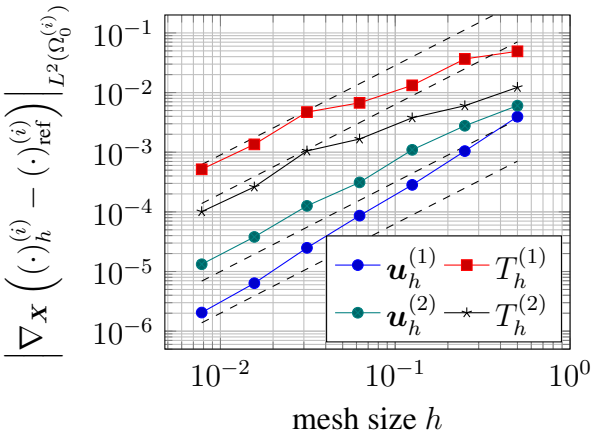

(d) $\theta_{\mathrm{u},1} = -1$, $\theta_{\mathrm{u},2} = 1$, $\gamma_{\mathrm{n},0} = 0.02$, $\theta_{\mathrm{T}} = -1$, $\gamma_{\mathrm{T},0} = 0.02$.

Figure 5.14: Convergence study of frictionless thermo-elastic contact – Convergence behavior of H^1 semi-norms of displacements and temperatures on the two sub-domains using $\mathbb{Q}_2$ finite elements and different variants of Nitsche's method for mechanical and thermal interface constraints. Dashed lines are of order $\mathcal{O}(h^{3/2})$.

(b) the symmetric Nitsche method for both the structural and thermal problem ($\theta_{\mathrm{u},1} = \theta_{\mathrm{u},2} = 1$, $\gamma_{\mathrm{n},0} = 2$ and $\theta_{\mathrm{T}} = 1$, $\gamma_{\mathrm{T},0} = 2$),

(c) the non-symmetric Nitsche method for both the structural and thermal problem ($\theta_{\mathrm{u},1} = 0$, $\theta_{\mathrm{u},2} = 1$, $\gamma_{\mathrm{n},0} = 2$ and $\theta_{\mathrm{T}} = 0$, $\gamma_{\mathrm{T},0} = 2$) and

(d) the skew-symmetric Nitsche method with a small penalty parameter for both the structural and thermal problem ($\theta_{\mathrm{u},1} = -1$, $\theta_{\mathrm{u},2} = 1$, $\gamma_{\mathrm{n},0} = 0.02$ and $\theta_{\mathrm{T}} = -1$, $\gamma_{\mathrm{T},0} = 0.02$).

Of course, other combinations are possible; in particular it is not necessary to use the same parameters for the structural and thermal interface problems. Figures 5.13 and 5.14 show the convergence behavior of the H^1 semi-norms of displacements and temperatures on the two sub-domains for first and second order finite elements, respectively, and dashed lines indicate the

expected orders. All combinations in Figure 5.13 show the optimal convergence order of $\mathcal{O}(h)$ with only slight variations between the different methods. For quadratic $\mathbb{Q}_2$ finite elements in Figure 5.14, convergence of order $\mathcal{O}(h^{3/2})$ is observed for all variables. As usual in computational contact mechanics, the convergence order of the discrete displacement field is, for second order finite elements and uniform refinement, no longer limited by the polynomial order of the finite element approximation but rather by the smoothness of the solution [35, 232]. Under these circumstances, the obtained order $\mathcal{O}(h^{3/2})$ in the H^1 semi-norm can be considered optimal for the displacement approximation $\boldsymbol{u}_h$. The reduced converge order of the temperature solution T_h is, most likely, a secondary effect of the limited convergence of $\boldsymbol{u}_h$ as the approximation of the contact pressure is derived from $\boldsymbol{u}_h$ and enters the thermal interface condition via (2.129).

Next, the possible ill-conditioning arising from the substitution method (5.30) and Nitsche's method (5.31) with high or low penalty parameters is investigated. Exemplarily, the mesh size $h = 2^{-3}$ with $\mathbb{Q}_1$ elements is used with fixed parameters for the structural problem $\theta_{\mathrm{u},1} = \theta_{\mathrm{u},2} = 1$ and $\gamma_{\mathrm{n},0} = 2$. Both the methods applied to enforce the contact heat conduction and the contact heat conductivity parameter β_{c} are varied. Note that by altering β_{c} the solution of the problem is altered: In the limit case $\beta_{\mathrm{c}} \to 0$ there is no heat flux across the interface, such that $\Omega_0^{(1)}$ and $\Omega_0^{(2)}$ will have homogeneous temperatures of 1 and 0, respectively. Conversely, for

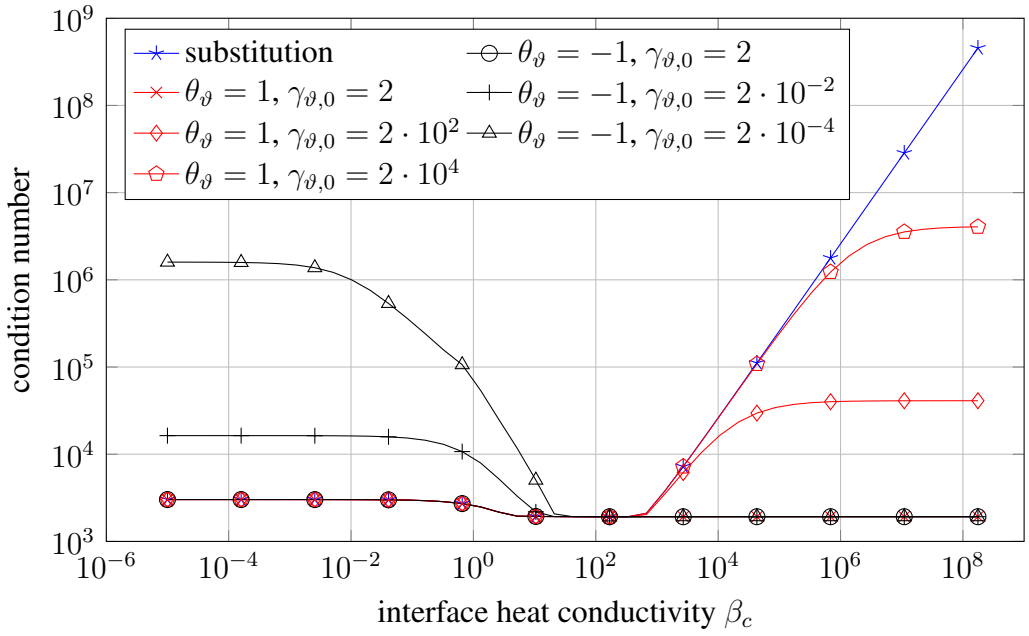

Figure 5.15: Convergence study of frictionless thermo-elastic contact – Condition numbers over β_{c} for $\theta_{\mathrm{u},1} = \theta_{\mathrm{u},2} = 1, \gamma_{\mathrm{n},0} = 2$ and different methods for the thermal interface condition.

$\beta_{\mathrm{c}} \to \infty$ both sides of the contact interface are forced to have the same temperature as there is no interface resistance to heat conduction. Figure 5.15 illustrates the condition number of the fully coupled tangent matrix in (2.167) including all Nitsche coupling terms of (5.8) and (5.30) or (5.31), respectively, at the final converged state for different methods for the thermal interface condition. First, one observes the expected linear increase in the condition number with β_{c} for the substitution method (5.30) as the absolute value of the boundary integral term $\bar{\beta}_{\mathrm{c}}[\![T_h]\!]$ increases, while the other integrals (5.30) remain unchanged and therefore $\bar{\beta}_{\mathrm{c}}[\![T_h]\!]$ dominates the condition

number starting at $\beta_c \approx 350$. This value, however, depends on the mesh and material parameters. Next, the influence of high penalty parameters is investigated by using the symmetric variant $\theta_T = 1$, see the red lines in Figure 5.15. The condition number remains constant for lower values of β_c, while higher values yield an increase of the condition number. This increase is expected for stabilized methods with increasing penalty parameter and in the present case only appears for larger values of β_c, since the penalty term (i.e. the integral in the second line of (5.31)) vanishes for low values of β_c. Still, in contrast to the substitution method, the condition number remains bounded for $\beta_c \to \infty$. Finally, the case of low penalty parameters is adressed using $\theta_T = -1$, since stability for low penalty parameters can only be ensured using the skew-symmetric variant of (5.31), see Winter *et al.* [231]. As expected, low values of β_c results in an increased condition number, as the integral in the third line of (5.31) increases for low values of γ_T ($\lim_{\beta_c \to 0} {}^{1}/_{(\bar{\beta}_c - \gamma_T)} = -{}^{1}/_{\gamma_T}$).

5.2.3.3 Frictional Heating of a Rotating Ring

To assess the effect of frictional heating, the example of a rotating ring introduced in Section 4.2.3.3 is revisited. To recall, a block $\Omega_0^{(1)}$ of dimension 100×25 is pressed onto a rotating ring $\Omega_0^{(2)}$ (outer radius 100, inner radius 75, angular velocity ω) with a resultant force $F_n = 150$. The block and ring are modeled with a Saint-Venant–Kirchhoff material with Young's moduli

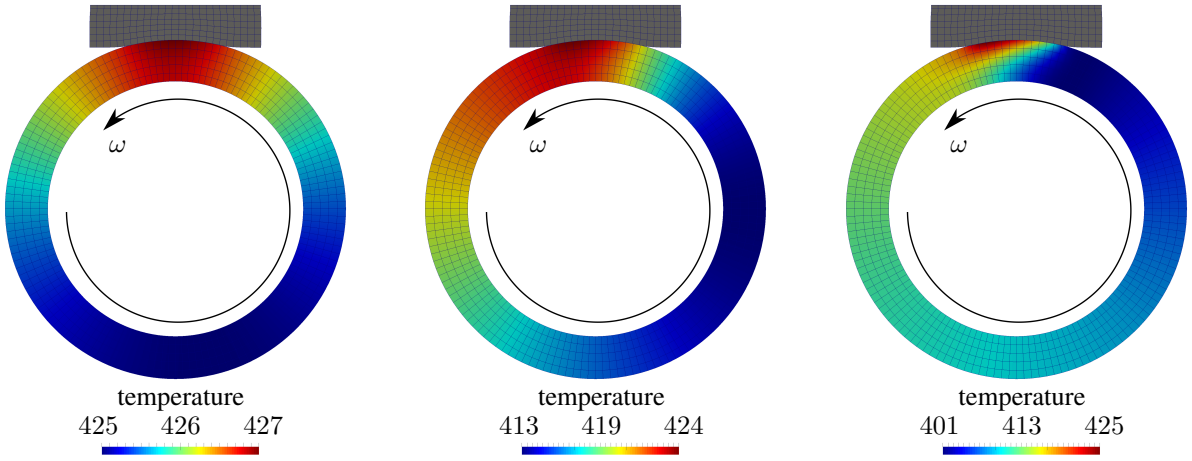

(a) $\omega = 10^{-1}$. (b) $\omega = 10^{0}$. (c) $\omega = 10^{1}$.

Figure 5.16: Frictional heating of a rotating ring – Temperature distribution after three full rotation at different angular frequencies. An arrow indicates the direction of rotation.

$E_{\text{block}} = 2$ and $E_{\text{ring}} = 10$ and Poisson's ratios $\nu_{\text{block}} = \nu_{\text{ring}} = 0.25$ under plane strain conditions with a thickness of 10. Furthermore, both bodies have a heat capacity of $c_v = 10^{-3}$ and thermal conductivity of $k_0 = 6$. At the contact interface, a temperature dependent coefficient of friction according to (2.125) with $\mu_0 = 0.2$, $T_0 = 293$ and $T_d = 493$ is applied. The heat transfer parameters at the interface are chosen as $\beta_c = \delta_c = 0$, thus excluding any heat conduction across the interface and restricting frictional heating to the ring only such that an analytical solution (4.65) can be obtained in the limit case of $\omega \to 0$. Three full rotations at different angular

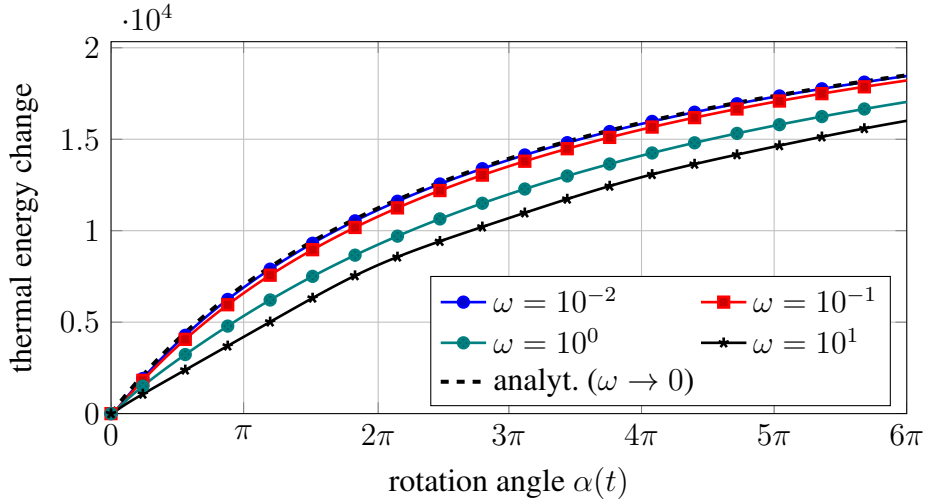

Figure 5.17: Frictional heating of a rotating ring – Change of thermal energy for different angular velocities ω compared to the analytical value for $\omega \to 0$.

velocities are simulated using in total 375 time steps. Figure 5.16 illustrates the final temperature distribution in the ring for different angular velocities. When comparing the change in thermal energy of the different angular velocities to the analytical solution in Figure 5.17, one observes a good agreement for the slowest angular velocity $\omega = 10^{-2}$ for which an almost homogeneous temperature distribution is observed. In addition, the results for larger angular velocities are in perfect agreement with the ones obtained by the thermomechanical mortar method depicted in Figure 4.32.

Finally, Table 5.1 compares the change in thermal energy for different parameters in the presented methods after three full rotations. To be able to actually draw a comparison to the analytical solution, an angular velocity of $\omega = 10^{-2}$ is used. In the presented setting, the skew-symmetric Nitsche method for the mechanical constraints yields the lowest error in the thermal energy, whereas the chosen method of thermal constraint enforcement (substitution or different Nitsche variants) has little effect on the result. As expected, the symmetric variant with an insufficient penalty parameters does not converge, since it does not result in a stable approximation.

Table 5.1: Frictional heating of a rotating ring – Comparison error in thermal energy change for different methods of constraint enforcement.

mechanical contact parameters	thermal contact parameters	energy error
$\theta_{\mathrm{u},1} = 1, \quad \theta_{\mathrm{u},2} = 1, \gamma_{\{\mathrm{n},\tau\},0} = 2$	substitution	0.283%
$\theta_{\mathrm{u},1} = 1, \quad \theta_{\mathrm{u},2} = 1, \gamma_{\{\mathrm{n},\tau\},0} = 2$	$\theta_{\mathrm{T}} = 1, \ \gamma_{\mathrm{T},0} = 2$	0.282%
$\theta_{\mathrm{u},1} = 1, \quad \theta_{\mathrm{u},2} = 1, \gamma_{\{\mathrm{n},\tau\},0} = 0.02$	$\theta_{\mathrm{T}} = 1, \ \gamma_{\mathrm{T},0} = 2$	no convergence
$\theta_{\mathrm{u},1} = -1, \ \theta_{\mathrm{u},2} = 1, \gamma_{\{\mathrm{n},\tau\},0} = 2$	substitution	0.281%
$\theta_{\mathrm{u},1} = -1, \ \theta_{\mathrm{u},2} = 1, \gamma_{\{\mathrm{n},\tau\},0} = 0.02$	substitution	0.267%
$\theta_{\mathrm{u},1} = -1, \ \theta_{\mathrm{u},2} = 1, \gamma_{\{\mathrm{n},\tau\},0} = 0.02$	$\theta_{\mathrm{T}} = -1, \ \gamma_{\mathrm{T},0} = 0.02$	0.268%

5.2.3.4 Squeezed Thermo-Elasto-Plastic Tube

The final example is again taken from the analysis of the thermomechanical mortar method derived in Chapter 4 involving finite thermo-elasto-plasticity. To recap Section 4.2.3.5, the setup illustrated in Figure 5.18a consists of a metal tube $\Omega_0^{(1)}$ with an inner and outer radius of $4\,\mathrm{cm}$ and $5\,\mathrm{cm}$, respectively, and a length of $40\,\mathrm{cm}$. At its center, the tube is squeezed between two rigid cylindrical tools $\Omega_0^{(2)}$ with an inner and outer of radius $4.5\,\mathrm{cm}$ and $5\,\mathrm{cm}$, and a length of $16\,\mathrm{cm}$. Exploiting the symmetry of the problem, only one eighth is discretized with 18000 elements in

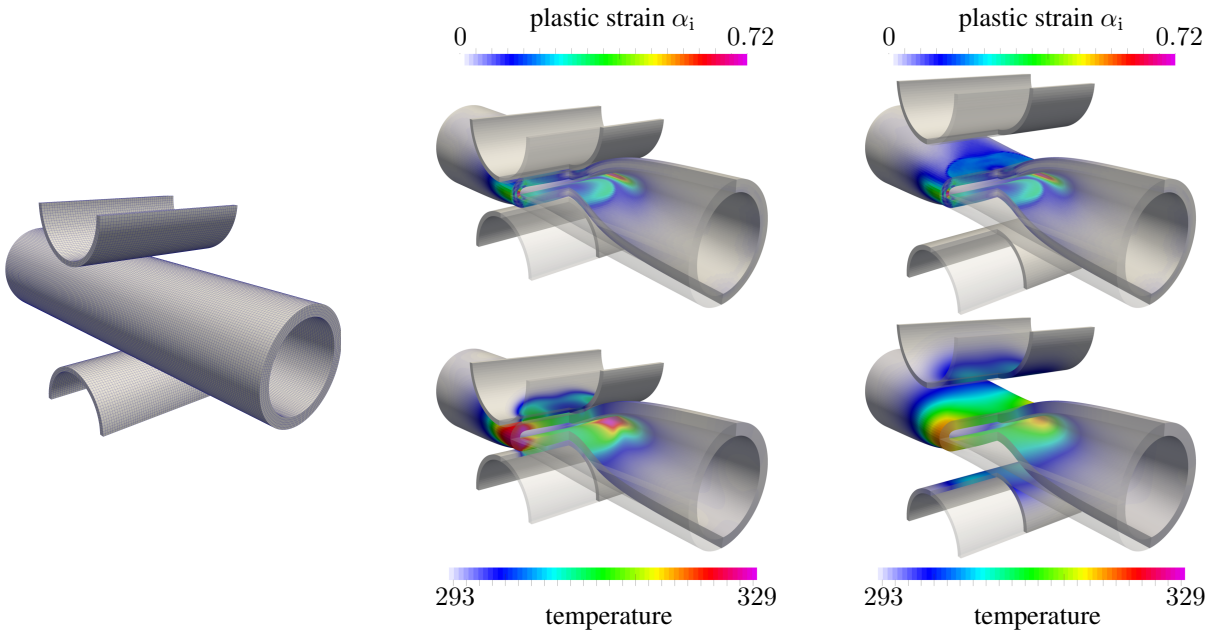

(a) Initial mesh. (b) $t = 1\,\mathrm{s}$. (c) $t = 2\,\mathrm{s}$.

Figure 5.18: Squeezed thermo-elasto-plastic tube – Initial mesh and displaced configurations at different times including accumulated plastic strain and temperature distribution.

the tube and 2700 elements in the tool. To overcome locking effects due to the incompressibility of plastic deformation, first order $\mathbb{Q}_1$ hexahedral elements with an F-bar technology as introduced in Section 2.8.1.1 are used. The tube is modeled with a thermo-elasto-plastic material law, which uses a neo-Hookean model (3.38) for the elastic part, thermal expansion according to (3.47) and isotropic von Mises plasticity with nonlinear hardening. All material parameters are summarized in Table 3.2 with $y_{11} = y_0$. From a numerical point of view, the plasticity algorithm developed in Chapter 3 is used, where the plastic inequality constraints are recast as non-smooth equality conditions at every quadrature point and additionally introduced unknowns are condensed at quadrature points. The tools start from an initially stress-free contact state and perform a prescribed motion of $u(t) = (1 - \cos(\frac{t}{1\,\mathrm{s}}\pi)) \cdot 1.75\,\mathrm{cm}$ in equidistant time steps $\Delta t \in \{0.01\,\mathrm{s}, 0.02\,\mathrm{s}\}$ as illustrated in Figures 5.18b and 5.18c for the time of maximum compression and the final time $t_{\text{end}} = 2\mathrm{s}$. At the contact interface, contact with a temperature dependent coefficient of friction according to (2.125) with $\mu_0 = 0.25$, $T_0 = 293\mathrm{K}$ and $T_\mathrm{d} = 1793\mathrm{K}$ is assumed. A heat flux of $\beta_\mathrm{c} = 0.1\,\frac{\mathrm{W}}{\mathrm{NK}}$ is permitted across the contact interface and both bodies are equally heated by frictional work by setting $\delta_\mathrm{c} = 0.5$. As outlined in Section 5.1.3, the non-smooth stress-strain

relation in elasto-plasticity exclusively permits the use of the non-symmetric Nitsche method $\theta_{\mathrm{u},1} = 0$ and $\theta_{\mathrm{u},2} = 1$ to enforce the mechanical contact constraints. Moreover, the fact that the tools are rigid results in a one-sided weighting of the stress at the interface, i.e. $\omega_{\mathrm{u}} = 1$. Contrary to the structural problem, the thermal interface formulation can be chosen freely from the proposed methods, including harmonic weights and $\theta_{\mathrm{T}} \neq 0$. Figure 5.19 depicts the total contact

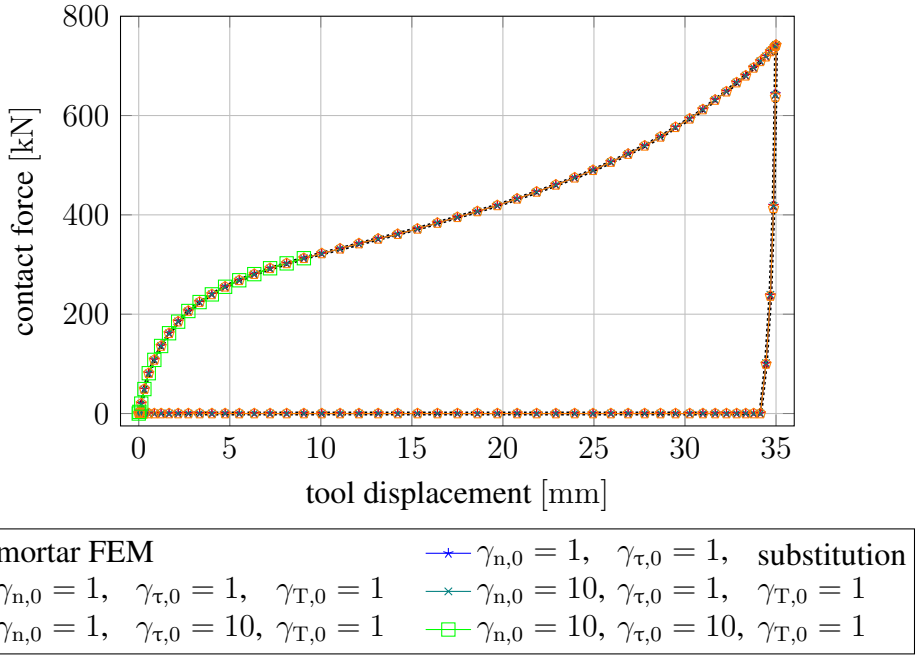

Figure 5.19: Squeezed thermo-elasto-plastic tube – Contact force over tool displacement for different mechanical contact penalty parameters and $\Delta t = 0.02\,\mathrm{s}$.

force over the tool displacement for different values of the contact penalty parameters and, as a reference, the solution using the dual mortar method of Chapter 4 (see Section 4.2.3.5). All variants accurately reproduce the results of the reference solution if convergence can be achieved. At the larger time step size $\Delta t = 0.02\,\mathrm{s}$ depicted in Figure 5.19, no convergence could be achieved in Newton's method for $\gamma_{\{\mathrm{n},\tau\},0} = 10$ at a tool displacement of $u \approx 8\,\mathrm{mm}$. Although different methods yield virtually indistinguishable results (if convergence can be achieved), they significantly differ in the number of nonlinear iterations required to achieve convergence. Table 5.2 summarizes average number of required iterations during Newton's method and potential line

Table 5.2: Squeezed thermo-elasto-plastic tube – Average number of Newton iterations (line search steps) per time step during $t \in [0, 1.1\,\mathrm{s}]$ for different methods and time step sizes.

mechanical contact parameters	thermal contact parameters	Newton iter. (+ls steps) $\Delta t = 0.01\,\mathrm{s}$	Newton iter. (+ls steps) $\Delta t = 0.02\,\mathrm{s}$
$\gamma_{\mathrm{n},0} = 1, \quad \gamma_{\tau,0} = 1$	substitution	6.06 (+0.05)	8.49 (+0.35)
$\gamma_{\mathrm{n},0} = 1, \quad \gamma_{\tau,0} = 1$	$\theta_{\mathrm{T}} = 1, \ \gamma_{\mathrm{T},0} = 1$	6.24 (+0.07)	8.69 (+0.33)
$\gamma_{\mathrm{n},0} = 10, \ \gamma_{\tau,0} = 1$	$\theta_{\mathrm{T}} = 1, \ \gamma_{\mathrm{T},0} = 1$	7.47 (+0.19)	9.98 (+0.87)
$\gamma_{\mathrm{n},0} = 1, \quad \gamma_{\tau,0} = 10$	$\theta_{\mathrm{T}} = 1, \ \gamma_{\mathrm{T},0} = 1$	9.47 (+2.90)	11.51 (+3.60)
$\gamma_{\mathrm{n},0} = 10, \ \gamma_{\tau,0} = 10$	$\theta_{\mathrm{T}} = 1, \ \gamma_{\mathrm{T},0} = 1$	10.58 (+3.15)	no convergence

search steps per time increment during $t \in [0, 1.1\,\mathrm{s}]$, that is, the time steps involving contact. Obviously, increasing penalty parameters yields stiffer nonlinear systems and therefore make it harder to achieve a converged solution. It is important to note, that the lack of convergence for $\gamma_{\{\mathrm{n},\tau\},0} = 10$ and the larger time step $\Delta t = 0.02\,\mathrm{s}$ is not due to an instability of the discretization but rather a divergence of Newton's method as shown by the fact that convergence for the same set of parameters can be achieved with a reduced time step.

Finally, to demonstrate the effect of the consistent linearization, the convergence behavior of Newton's method is given in Table 5.3 at the time of maximal tool speed, the larger time step and the more reasonable penalty parameters $\gamma_{\{\mathrm{n},\tau\},0} = 1$. A clear acceleration in convergence is observed as the solution is approached. Full quadratic convergence is not observed, since, given the severe nonlinearity of the problem, the region of quadratic convergence is very small and machine precision already limits the decay of the residuals. In particular, machine precision limits the structural residual $\|\boldsymbol{r}_\mathrm{u}\|$ to $5 \cdot 10^{-10}$ and the thermal residual $\|\boldsymbol{r}_\mathrm{T}\|$ to $2 \cdot 10^{-14}$, which corresponds to a decay of over 12 orders of magnitude compared to their respective initial values.

Table 5.3: Squeezed thermo-elasto-plastic tube – Convergence of the L^2 norms of the partial residuals in (2.167) at $t = 0.5\,\mathrm{s}$ for $\Delta t = 0.02\,\mathrm{s}$ and $\gamma_{\{\mathrm{n},\tau\},0} = 1$, $\theta_\mathrm{T} = 1$, $\gamma_{\mathrm{T},0} = 1$.

step	$\|\boldsymbol{r}_\mathrm{u}\|$	$\|\boldsymbol{r}_\mathrm{T}\|$
0	5.68e+02	3.46e-01
1	2.56e+01	2.99e-01
2	8.69e+00	1.80e-02
3	2.98e+00	4.68e-03
4	1.61e+00	3.65e-03
5	5.38e-01	2.65e-03
6	9.28e-02	4.22e-04
7	3.37e-04	2.27e-05
8	9.32e-07	1.20e-08
9	5.01e-10	4.78e-12

6 Summary and Outlook

This thesis dealt with innovative numerical methods for thermo-elasto-plastic contact problems at finite deformations by the finite element method. To this end, a new method for computational (thermo-) plasticity has been developed and new methods of computational contact mechanics based on mortar methods and Nitsche's method have been derived for isothermal and thermo-mechanical contact problems. Originally motivated by the analysis of metal forming processes, the developments have been kept as general as possible such that the method is to be open to any application of thermomechanical contact problems.

In a first step, a novel approach to computational plasticity at finite deformations has been developed. Its distinctive feature is the reformulation of the plastic material constraints of Hill's anisotropic yield criterion in terms of a non-smooth nonlinear complementarity (NCP) function. By solving the resulting equality constraint within the same semi-smooth Newton scheme as the balance of linear momentum, the plastic material constraints are guaranteed to hold at convergence. Unlike the commonly used return mapping algorithm (RMA) for elasto-plastic materials, however, a violation of the material constraints is permitted pre-asymptotically. Hence, it allows for an increased flexibility in the development of robust algorithms compared to the classical RMA. Numerical examples confirm the superior robustness of the proposed method. The derived semi-smooth Newton method has been extended to include various physical effects relevant to practical applications of metal forming: First, the anisotropic yield criterion is supplemented by an evolution of the plastic spin taking into account the relative rotation of the axes of anisotropy with respect to the macroscopic continuum. Second, effects of visco-plasticity at high strain rates have been included. Finally, a fully coupled algorithm for thermo-elasto-plastic problems has been derived, which solves not only for the discrete displacement field and the plastic deformation but also for the discrete temperature distribution. A consistently linearized, monolithic solution scheme ensures fast convergence even in strongly coupled problems. For future research, some issues have to be addressed, which all revolve around the construction of appropriate NCP functions. For one, the number of local unkowns may be reduced by a suitable re-parametrization of the yield function. A similar approach has been applied successfully in the context of variational constitutive update algorithms by Bleier and Mosler [16]. For another, the derivations presented in this thesis are restricted to Hill's orthotropic yield criterion that includes the widely used von Mises law as a special case. Therein, the equivalent stress is a quadratic (semi-) norm of the effective stress tensor which facilitates the construction of the NCP function. While extensions to other quadratic yield functions, such as the Tresca yield function or the ones employed in single crystals seems straightforward, the construction of appropriate NCP functions for arbitrary, non-quadratic yield functions remains open.

The second field of research in this thesis concerned mortar finite element methods for contact problems. In the isothermal setting, two new Lagrange multiplier spaces have been proposed, namely a piece-wise constant Lagrange multiplier for second order finite elements and an isogeometric dual mortar method. As commonly known for dual mortar methods, these spaces result in a localization of the coupling conditions and allow for an elimination of the discrete Lagrange multiplier. Both spaces have a reduced polynomial reproduction order as compared to the underlying displacement approximation limiting the achievable convergence orders in domain decomposition applications. Yet, they still provide optimal convergence orders (under uniform mesh refinement) for contact problems due to the reduced regularity of the solution. If, however, future applications include adaptive mesh refinement for contact problems, the point of reproduction orders needs to be revisited. In that case, the adaptive displacement approximation can provide higher order convergence but only if the Lagrange multiplier approximation provides a sufficient reproduction order. For domain decomposition applications, such optimal Lagrange multiplier spaces have been studied by Lamichhane and Wohlmuth [129], Oswald and Wohlmuth [161] for classical finite elements. Very recently, the idea of [161] has been extended to isogeometric analysis by Wunderlich *et al.* [242]. Concerning thermomechanical frictional contact, a new discretization approach based on dual mortar finite element methods has been derived. The model includes a pressure dependent heat conduction across the contact interface as well as frictional work converted to heat. An additional thermal Lagrange multiplier field has been introduced to enforce these effects. The use of dual basis functions again allows for an easy condensation of the additional Lagrange multiplier degrees of freedom, such that the resulting system consists of discrete displacements and temperatures only. Numerical examples showed optimal convergence orders and a broad applicability from contact dynamics to isogeometric analysis and coupled thermo-elasto-plastic problems.

Finally, various Nitsche-type methods for finite deformation contact mechanics have been developed. In particular, this includes the extension of the symmetric and non-symmetric methods of Chouly *et al.* [35] and the penalty free variant of Burman [23] to geometrically nonlinear frictional contact problems. One of the main challenges when applying Nitsche's method to nonlinear elasticity, or even elasto-plasticity, lies in the use of the boundary traction, which has been derived consistently with the employed nonlinear material. Furthermore, an accurate estimate of the necessary penalty parameter has been devised based on local eigenvalue problems. While for linear problems the lower bound of the penalty parameter can be determined in advance, nonlinear materials require an estimate adjusted to the current displacement. Therefore, an adaptive penalty parameter estimate has been developed and verified in highly nonlinear examples. It should be pointed out, that the presented nonlinear estimate is rather heuristic but performs well in numerical tests. Future research should focus on a mathematical analysis of Nitsche's method for problems of nonlinear elasticity based on arguments of poly-convexity [10]. In the course of such research, a more accurate lower bound for the necessary penalty term could emerge. Moreover, the solution of the local eigenvalue problems has been used to derive a harmonic weighting of the boundary traction which allows for a significant reduction in the penalty term for problems involving a large contrast in stiffness of the contacting bodies. Lastly, Nitsche's method has been extended to thermomechanical contact problems. The Robin-type condition of heat conduction (and frictional dissipation) can either be substituted directly into the weak form of the heat conduction equation or introduced weakly by employing a Nitsche-type approach. While being a rather simple formulation, the substitution method becomes ill-conditioned for

high thermal contact conductivities. The Nitsche-type method, on the other hand, involves more terms but remains well-conditioned over the entire range of physical parameters. Although nonlinear kinematics and thermomechanical coupling preclude strict mathematical analysis and optimal *a priori* estimates, numerical examples evidence the expected optimal convergence orders. Furthermore, extensions from thermo-elasticity to coupled thermo-elasto-plasticity have been demonstrated by a numerical example.

In summary, this work provides numerical methods for thermo-elasto-plastic contact problems at finite deformations based on mathematically sound and well analyzed discretizations. Taking a broader perspective, contact analysis in a thermomechanically coupled system investigated in this work can be seen as a prototype for contact interaction in a general multi-field problem. Therefore, as a closure to this thesis, an outlook to ongoing research on the numerical treatment of contact problems in two other multi-field applications is given. The first one deals with contact modeling inside all-solid-state batteries. In this post lithium-ion battery technology, not only the electrodes but also the electrolyte consists of a solid material. Consequently, contact interaction takes place between the different components. The greatest difficulty in the development of robust contact discretizations lies in the highly complex geometries and potential self-contact. This is due to the fact that a maximized interface area between electrode and electrolyte is beneficial for the battery performance which results in a porous, sponge-like micro-structure. Figure 6.1 depicts such a micro-structure of a cathode reconstructed from X-ray tomography by Ebner *et al.* [67]. During charging and discharging of the battery, transport of Lithium ions takes place. Fur-

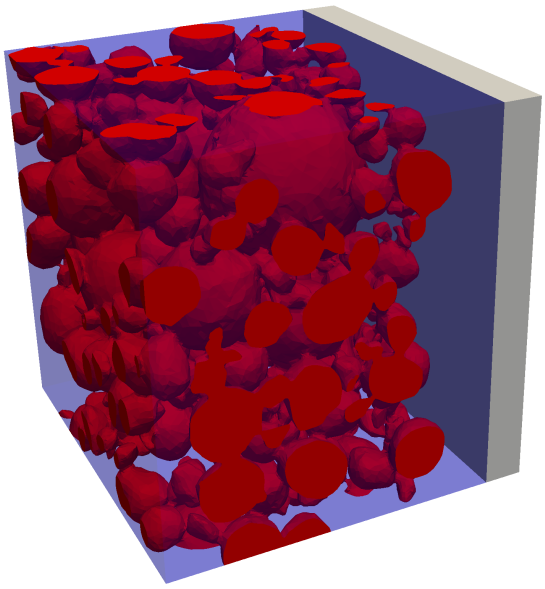

Figure 6.1: Micro-scale geometry of an all-solid-state battery with the cathode in red, the anode in gray and the electrolyte in blue.

ther, the intercalation of Lithium in the electrodes alters their mechanical properties and yields volumetric growth. Hence, the coupling of electro-chemistry and structural response bears great similarity to the problem of thermomechanical coupling investigated in this thesis. In the analogy to thermomechanics, the concentration of Lithium takes the place of the temperature distribution in a thermomechanical system as temperature also follows a diffusive transport, changes me-

chanical properties, and results in volumetric changes due to thermal expansion. Consequently, the numerical methods proposed for thermomechanical contact can readily be extended to electromechanical systems.

Conceptually, thermomechanical and electromechanical systems as volume-coupled multi-field problems form only one class of coupled problems. Another class consists of surface coupled problems such as fluid-structure interaction (FSI). A promising approach to handle contact scenarios in FSI applications is the use of non-boundary fitted discretizations for the fluid domain, as they allow for large motion of the structure or even topological changes. The cut finite element method provides such a discretization approach and the use of Nitsche's method allows for a stable imposition of the constraints of fluid-structure interaction. For details, the reader is referred to Schott [190] and the references therein. With the FSI condition enforced by Nitsche's method, it is advisable to also treat the contact interaction by Nitsche-type methods as derived in this work. This allows for a continuous transition between the two type of interface conditions: either FSI or contact between two solids. A detailed description of the combined formulation of fluid-structure-contact interaction is given in Ager *et al.* [2]. Without specifying any details, a first numerical example is illustrated in Figure 6.2 and models a simple pump consisting of two valves. The initial geometry and meshes for the fluid (light gray) and solid discretization (dark gray) are depicted in Figure 6.2a. Note that while a classical boundary fitted discretization is

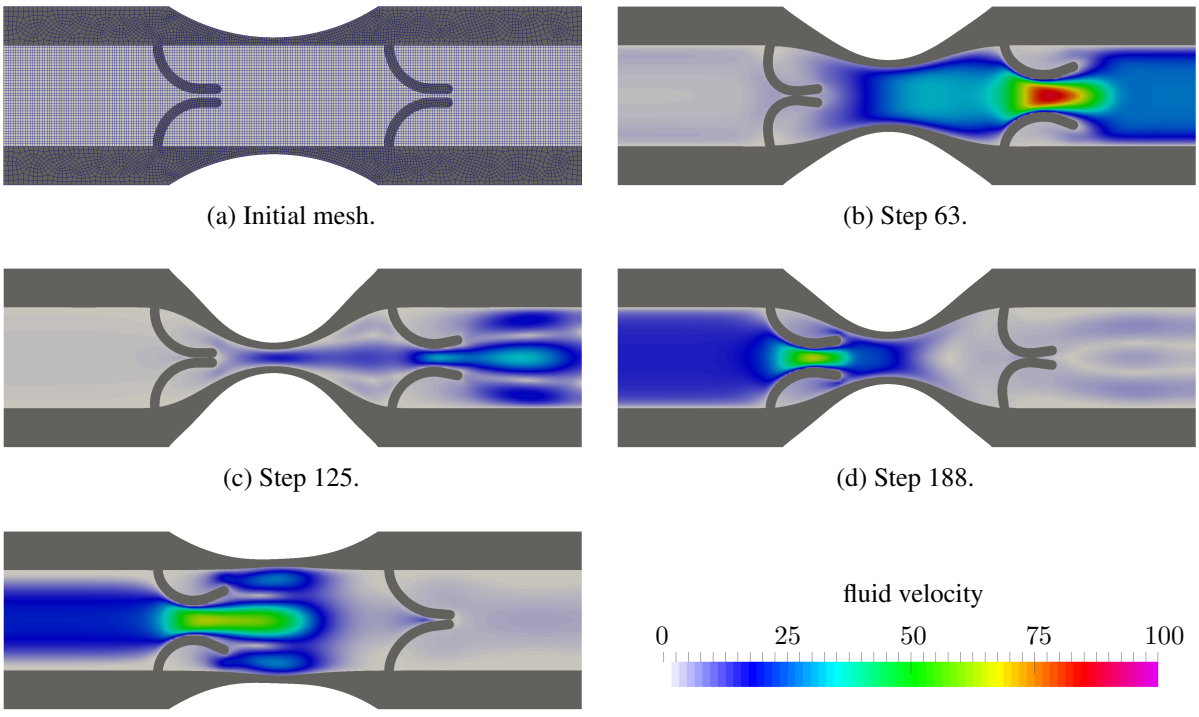

(a) Initial mesh.

(b) Step 63.

(c) Step 125.

(d) Step 188.

(e) Step 250.

Figure 6.2: Fluid structure contact interaction in a simplified pump: Initial mesh and deformed configurations at different time steps with contours of the fluid velocity magnitude.

applied for the solid, the fluid discretization is not fitted to the FSI interface but rather cut by the solid domain. In the center, the structure is compressed vertically by a harmonic Neumann

load with one period divided in 250 time steps. During compression (Figures 6.2b, 6.2c), the left valve closes and fluid is pushed out on the right hand side. As the load is removed (Figures 6.2d, 6.2e), the structure relaxes, the right valve closes and fluid is sucked in from the left. Figure 6.3

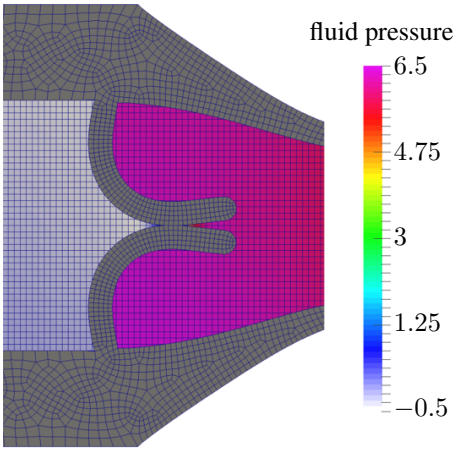

Figure 6.3: Fluid structure contact interaction in a simplified pump: Detail view to the left valve in Figure 6.2b with fluid pressure distribution.

provides a detailed view to the left valve in step 63 (cf. Figure 6.2b) and the corresponding fluid pressure distribution. It can again be seen, that the fluid discretization is cut by the structural mesh and the pressure jump between the two sides of the valve is captured sharply. In terms of contact mechanics, it is remarkable that the use of Nitsche's method as a consistent contact discretization yields accurate contact constraint enforcement and no residual penetration is to be seen.

In conclusion, the methods developed in this thesis not only cover computational analysis of thermomechanical contact problems but provide a basis for the treatment of contact constraints in multi-field problems in general.

A Hyperelasticity and some derivatives

In this appendix, some of the directional derivatives employed in Section 3.3.2 are particularized for the application of arbitrary isotropic hyperelastic materials. The linearizations follow from rather straight forward computations when inserting the multiplicative split of the deformation gradient (2.53) into the definition of the second Piola–Kirchhoff stress tensor $\mathbf{S}$ and the Mandel stress tensor $\boldsymbol{\Sigma}$. The notation generally follows the one in Holzapfel [104]. For an elastically isotropic material, $\Psi_\mathrm{e} = \Psi_\mathrm{e}(I_1, I_2, I_3)$ may be expressed in terms of the invariants

$$I_1 = \operatorname{tr} \boldsymbol{C}_\mathrm{e} \quad , \quad I_2 = \frac{1}{2}\left((\operatorname{tr} \boldsymbol{C}_\mathrm{e})^2 - \operatorname{tr}\left(\boldsymbol{C}_\mathrm{e}^2\right)\right) \quad , \quad I_3 = \det \boldsymbol{C}_\mathrm{e} \tag{A.1}$$

of the elastic right Cauchy–Green tensor $\boldsymbol{C}_\mathrm{e}$. The second Piola–Kirchhoff stress tensor can then be expressed as

$$\boldsymbol{S} = \gamma_1 \boldsymbol{C}_\mathrm{p}^{-1} + \gamma_2 \boldsymbol{C}_\mathrm{p}^{-1}\boldsymbol{C}\boldsymbol{C}_\mathrm{p}^{-1} + \gamma_3 \boldsymbol{C}^{-1} \quad , \tag{A.2}$$

with the coefficients

$$\gamma_1 = 2\left(\frac{\partial \Psi_\mathrm{e}}{\partial I_1} + I_1 \frac{\partial \Psi_\mathrm{e}}{\partial I_2}\right) \quad , \quad \gamma_2 = -2\frac{\partial \Psi_\mathrm{e}}{\partial I_2} \quad , \quad \gamma_3 = 2I_3 \frac{\partial \Psi_\mathrm{e}}{\partial I_3} \quad . \tag{A.3}$$

The derivative of the second Piola–Kirchhoff stress with respect to the right Cauchy–Green tensor as well as the inverse plastic deformation gradient follow by straightforward calculations as

$$\begin{aligned}
\mathbb{C} = 2\frac{\partial \boldsymbol{S}}{\partial \boldsymbol{C}} &= \delta_1 \boldsymbol{C}_\mathrm{p}^{-1} \otimes \boldsymbol{C}_\mathrm{p}^{-1} + \delta_2 \left(\boldsymbol{C}_\mathrm{p}^{-1} \otimes \boldsymbol{C}_\mathrm{p}^{-1}\boldsymbol{C}\boldsymbol{C}_\mathrm{p}^{-1} + \boldsymbol{C}_\mathrm{p}^{-1}\boldsymbol{C}\boldsymbol{C}_\mathrm{p}^{-1} \otimes \boldsymbol{C}_\mathrm{p}^{-1}\right) \\
&\quad + \delta_3 \left(\boldsymbol{C}_\mathrm{p}^{-1} \otimes \boldsymbol{C}^{-1} + \boldsymbol{C}^{-1} \otimes \boldsymbol{C}_\mathrm{p}^{-1}\right) + \delta_4 \boldsymbol{C}_\mathrm{p}^{-1}\boldsymbol{C}\boldsymbol{C}_\mathrm{p}^{-1} \otimes \boldsymbol{C}_\mathrm{p}^{-1}\boldsymbol{C}\boldsymbol{C}_\mathrm{p}^{-1} \\
&\quad + \delta_5 \left(\boldsymbol{C}_\mathrm{p}^{-1}\boldsymbol{C}\boldsymbol{C}_\mathrm{p}^{-1} \otimes \boldsymbol{C}^{-1} + \boldsymbol{C}^{-1} \otimes \boldsymbol{C}_\mathrm{p}^{-1}\boldsymbol{C}\boldsymbol{C}_\mathrm{p}^{-1}\right) + \delta_6 \boldsymbol{C}^{-1} \otimes \boldsymbol{C}^{-1} \\
&\quad + \delta_7 \boldsymbol{C}^{-1} \odot \boldsymbol{C}^{-1} + \delta_8 \boldsymbol{C}_\mathrm{p}^{-1} \odot \boldsymbol{C}_\mathrm{p}^{-1}
\end{aligned} \tag{A.4}$$

and

$$\begin{aligned}
\frac{\partial \boldsymbol{S}}{\partial \boldsymbol{F}_\mathrm{p}^{-1}} &= 2\gamma_1 \boldsymbol{I} \odot \boldsymbol{F}_\mathrm{p}^{-1} + 2\gamma_2 \left((\boldsymbol{I} \odot (\boldsymbol{F}_\mathrm{p}^{-1}\boldsymbol{C}_\mathrm{e}) + (\boldsymbol{C}_\mathrm{p}\boldsymbol{C}) \odot \boldsymbol{F}_\mathrm{p}^{-1}\right) \\
&\quad + \delta_1 \boldsymbol{C}_\mathrm{p}^{-1} \otimes \boldsymbol{C}\boldsymbol{F}_\mathrm{p}^{-1} + \delta_2 \left(\boldsymbol{C}_\mathrm{p}^{-1} \otimes \boldsymbol{C}\boldsymbol{F}_\mathrm{p}^{-1}\boldsymbol{C}_\mathrm{e} + \boldsymbol{C}_\mathrm{p}^{-1}\boldsymbol{C}\boldsymbol{C}_\mathrm{p}^{-1} \otimes \boldsymbol{C}\boldsymbol{F}_\mathrm{p}^{-1}\right) \\
&\quad + \delta_3 \left(\boldsymbol{C}_\mathrm{p}^{-1} \otimes \boldsymbol{C}\boldsymbol{F}_\mathrm{p}^{-1}\boldsymbol{C}_\mathrm{e}^{-1} + \boldsymbol{C}^{-1} \otimes \boldsymbol{C}\boldsymbol{F}_\mathrm{p}^{-1}\right) + \delta_4 \boldsymbol{C}_\mathrm{p}^{-1}\boldsymbol{C}\boldsymbol{C}_\mathrm{p}^{-1} \otimes \boldsymbol{C}\boldsymbol{F}_\mathrm{p}^{-1}\boldsymbol{C}_\mathrm{e} \\
&\quad + \delta_5 \left(\boldsymbol{C}_\mathrm{p}^{-1}\boldsymbol{C}\boldsymbol{C}_\mathrm{p}^{-1} \otimes \boldsymbol{C}\boldsymbol{F}_\mathrm{p}^{-1}\boldsymbol{C}_\mathrm{e}^{-1} + \boldsymbol{C}^{-1} \otimes \boldsymbol{C}\boldsymbol{F}_\mathrm{p}^{-1}\boldsymbol{C}_\mathrm{e}\right) + \delta_6 \boldsymbol{C}^{-1} \otimes \boldsymbol{C}\boldsymbol{F}_\mathrm{p}^{-1}\boldsymbol{C}_\mathrm{e}^{-1}
\end{aligned} \tag{A.5}$$

with the coefficients

$$\begin{aligned}
&\delta_1 = 4\left(\frac{\partial^2\Psi_\mathrm{e}}{\partial I_1\partial I_1} + 2I_1\frac{\partial^2\Psi_\mathrm{e}}{\partial I_1\partial I_2} + \frac{\partial\Psi_\mathrm{e}}{\partial I_2} + I_1^2\frac{\partial^2\Psi_\mathrm{e}}{\partial I_2\partial I_2}\right) \quad , \quad \delta_2 = -4\left(\frac{\partial^2\Psi_\mathrm{e}}{\partial I_1\partial I_2} + I_1\frac{\partial^2\Psi_\mathrm{e}}{\partial I_2\partial I_2}\right) \quad , \\
&\delta_3 = 4\left(I_3\frac{\partial^2\Psi_\mathrm{e}}{\partial I_1\partial I_3} + I_1I_3\frac{\partial^2\Psi_\mathrm{e}}{\partial I_2\partial I_3}\right) \quad , \quad \delta_4 = 4\frac{\partial^2\Psi_\mathrm{e}}{\partial I_2\partial I_2} \quad , \quad \delta_5 = -4\frac{\partial^2\Psi_\mathrm{e}}{\partial I_2\partial I_3} \quad , \\
&\delta_6 = 4\left(I_3\frac{\partial\Psi_\mathrm{e}}{\partial I_3} + I_3^2\frac{\partial^2\Psi_\mathrm{e}}{\partial I_3\partial I_3}\right) \quad , \quad \delta_7 = -4I_3\frac{\partial\Psi_\mathrm{e}}{\partial I_3} \quad , \delta_8 = -4\frac{\partial\Psi_\mathrm{e}}{\partial I_2} \quad .
\end{aligned} \tag{A.6}$$

Analogously, the Mandel stress $\boldsymbol{\Sigma}$ for an isotropic hyperelastic material can be computed as

$$\boldsymbol{\Sigma} = \gamma_1\boldsymbol{C}_\mathrm{e} + \gamma_2\boldsymbol{C}_\mathrm{e}^2 + \gamma_3\boldsymbol{I} \quad , \tag{A.7}$$

and its relevant directional derivatives as

$$\begin{aligned}
\frac{\partial\boldsymbol{\Sigma}}{\partial\boldsymbol{C}} = {}& \gamma_1\boldsymbol{F}_\mathrm{p}^{-\mathsf{T}}\odot\boldsymbol{F}_\mathrm{p}^{-\mathsf{T}} + \gamma_2\left(\boldsymbol{F}_\mathrm{p}^{-\mathsf{T}}\odot\left(\boldsymbol{C}_\mathrm{e}\boldsymbol{F}_\mathrm{p}^{-\mathsf{T}}\right) + \left(\boldsymbol{C}_\mathrm{e}\boldsymbol{F}_\mathrm{p}^{-\mathsf{T}}\right)\odot\boldsymbol{F}_\mathrm{p}^{-\mathsf{T}}\right) \\
&+ {}^1\!/_2\delta_1\boldsymbol{C}_\mathrm{e}\otimes\boldsymbol{C}_\mathrm{p}^{-1} + {}^1\!/_2\delta_2\left(\boldsymbol{C}_\mathrm{e}\otimes\boldsymbol{C}_\mathrm{p}^{-1}\boldsymbol{C}\boldsymbol{C}_\mathrm{p}^{-1} + \boldsymbol{C}_\mathrm{e}^2\otimes\boldsymbol{C}_\mathrm{p}^{-1}\right) \\
&+ {}^1\!/_2\delta_3\left(\boldsymbol{C}_\mathrm{e}\otimes\boldsymbol{C}^{-1} + \boldsymbol{I}\otimes\boldsymbol{C}_\mathrm{p}^{-1}\right) + {}^1\!/_2\delta_4\boldsymbol{C}_\mathrm{e}^2\otimes\boldsymbol{C}_\mathrm{p}^{-1}\boldsymbol{C}\boldsymbol{C}_\mathrm{p}^{-1} \\
&+ {}^1\!/_2\delta_5\left(\boldsymbol{C}_\mathrm{e}^2\otimes\boldsymbol{C}^{-1} + \boldsymbol{I}\otimes\boldsymbol{C}_\mathrm{p}^{-1}\boldsymbol{C}\boldsymbol{C}_\mathrm{p}^{-1}\right) + {}^1\!/_2\delta_6\boldsymbol{I}\otimes\boldsymbol{C}^{-1} \quad ,
\end{aligned} \tag{A.8}$$

and

$$\begin{aligned}
\frac{\partial\boldsymbol{\Sigma}}{\partial\boldsymbol{F}_\mathrm{p}^{-1}} = {}& 2\gamma_1\left(\boldsymbol{F}_\mathrm{p}^{-\mathsf{T}}\boldsymbol{C}\right)\odot\boldsymbol{I} + 2\gamma_2\left(\left(\boldsymbol{F}_\mathrm{p}^{-\mathsf{T}}\right)\odot\boldsymbol{C}_\mathrm{e} + \left(\boldsymbol{C}_\mathrm{e}\boldsymbol{F}_\mathrm{p}^{-\mathsf{T}}\boldsymbol{C}\right)\odot\boldsymbol{I}\right) + \delta_1\boldsymbol{C}_\mathrm{e}\otimes\boldsymbol{C}\boldsymbol{F}_\mathrm{p}^{-1} \\
&+ \delta_2\left(\boldsymbol{C}_\mathrm{e}\otimes\boldsymbol{C}\boldsymbol{F}_\mathrm{p}^{-1}\boldsymbol{C}_\mathrm{e} + \boldsymbol{C}_\mathrm{e}^2\otimes\boldsymbol{C}\boldsymbol{F}_\mathrm{p}^{-1}\right) + \delta_3\left(\boldsymbol{C}_\mathrm{e}\otimes\boldsymbol{C}\boldsymbol{F}_\mathrm{p}^{-1}\boldsymbol{C}_\mathrm{e}^{-1} + \boldsymbol{I}\otimes\boldsymbol{C}\boldsymbol{F}_\mathrm{p}^{-1}\right) \\
&+ \delta_4\boldsymbol{C}_\mathrm{e}^2\otimes\boldsymbol{C}\boldsymbol{F}_\mathrm{p}^{-1}\boldsymbol{C}_\mathrm{e} + \delta_5\left(\boldsymbol{C}_\mathrm{e}^2\otimes\boldsymbol{C}\boldsymbol{F}_\mathrm{p}^{-1}\boldsymbol{C}_\mathrm{e}^{-1} + \boldsymbol{I}\otimes\boldsymbol{C}\boldsymbol{F}_\mathrm{p}^{-1}\boldsymbol{C}_\mathrm{e}\right) + \delta_6\boldsymbol{I}\otimes\boldsymbol{C}\boldsymbol{F}_\mathrm{p}^{-1}\boldsymbol{C}_\mathrm{e}^{-1} \quad .
\end{aligned} \tag{A.9}$$

Finally, the directional derivative of the inverse plastic deformation gradient with respect to the plastic flow increment follows from the discrete evolution equation (3.4), i.e.

$$\frac{\partial\mathbf{F}_{\mathrm{p},n+1}^{-1}}{\partial\Delta\mathbf{L}_\mathrm{p}} = \mathbf{F}_{\mathrm{p},n}^{-1}\frac{\partial\exp(-\Delta\mathbf{L}_\mathrm{p})}{\partial\Delta\mathbf{L}_\mathrm{p}} \quad , \tag{A.10}$$

from which the derivative of the second Piola–Kirchhoff and Mandel stress with respect to the plastic flow increment $\Delta\mathbf{L}_\mathrm{p}$ follow as

$$\frac{\partial\boldsymbol{S}}{\partial\Delta\mathbf{L}_\mathrm{p}} = \frac{\partial\boldsymbol{S}}{\partial\boldsymbol{F}_\mathrm{p}^{-1}} : \frac{\partial\mathbf{F}_{\mathrm{p},n+1}^{-1}}{\partial\Delta\mathbf{L}_\mathrm{p}} \quad , \quad \frac{\partial\boldsymbol{\Sigma}}{\partial\Delta\mathbf{L}_\mathrm{p}} = \frac{\partial\boldsymbol{\Sigma}}{\partial\boldsymbol{F}_\mathrm{p}^{-1}} : \frac{\partial\mathbf{F}_{\mathrm{p},n+1}^{-1}}{\partial\Delta\mathbf{L}_\mathrm{p}} \quad . \tag{A.11}$$

B Consistency of the thermal weak form using Nitsche's method

To show the consistency of (5.31), i.e. equivalence of (the continuous form of) (5.31) with (2.133) in combination with (2.129), first observe that $\bar{\beta}_\mathrm{c}$ and $\mathcal{P}_\mathrm{c}$ are, due to (5.4) and (5.11), consistent substitutes for $\beta_\mathrm{c}|p_\mathrm{n}|$ and $\boldsymbol{t}_\tau \cdot \boldsymbol{v}_\tau$ in (2.129). Next, (2.129) provide the following equivalences for weighted heat fluxes:

$$\{q_\mathrm{c}(T)\}_{\omega_\mathrm{T}} = \{q_\mathrm{c}(T)\}_{(1-\delta_\mathrm{c})} + (1-\delta_\mathrm{c}-\omega_\mathrm{T})\boldsymbol{t}_\tau \cdot \boldsymbol{v}_\tau \ , \tag{B.1a}$$

$$\{q_\mathrm{c}(T)\}_{(1-\delta_\mathrm{c})} = \beta_\mathrm{c}|p_\mathrm{n}|[\![T]\!] \ , \tag{B.1b}$$

with which (5.31) can be re-written as

$$\begin{aligned}
&\delta\mathcal{W}_\mathrm{T} + \int_{\gamma_\mathrm{c}^{(1)}} \frac{\beta_\mathrm{c}|p_\mathrm{n}|}{\beta_\mathrm{c}|p_\mathrm{n}|+\gamma_\mathrm{T}} \{q_\mathrm{c}(T)\}_{(1-\delta_\mathrm{c})} [\![\delta T]\!] \,\mathrm{d}\gamma \\
&\quad + \int_{\gamma_\mathrm{c}^{(1)}} \frac{\gamma_\mathrm{T}\beta_\mathrm{c}|p_\mathrm{n}|}{\beta_\mathrm{c}|p_\mathrm{n}|+\gamma_\mathrm{T}} [\![T]\!][\![\delta T]\!] \,\mathrm{d}\gamma \\
&\quad - \theta_\mathrm{T} \int_{\gamma_\mathrm{c}^{(1)}} \frac{1}{\beta_\mathrm{c}|p_\mathrm{n}|+\gamma_\mathrm{T}} \{q_\mathrm{c}(T)\}_{(1-\delta_\mathrm{c})} \{q_\mathrm{c}(\delta T)\}_{\omega_\mathrm{T}} \,\mathrm{d}\gamma \\
&\quad + \theta_\mathrm{T} \int_{\gamma_\mathrm{c}^{(1)}} \frac{\beta_\mathrm{c}|p_\mathrm{n}|}{\beta_\mathrm{c}|p_\mathrm{n}|+\gamma_\mathrm{T}} [\![T]\!] \{q_\mathrm{c}(\delta T)\}_{\omega_\mathrm{T}} \,\mathrm{d}\gamma \\
&\quad - \int_{\gamma_\mathrm{c}^{(1)}} \boldsymbol{t}_\tau \cdot \boldsymbol{v}_\tau \left(\delta_\mathrm{c}\delta T^{(1)} + (1-\delta_\mathrm{c})(\delta T^{(2)} \circ \chi_t)\right) \mathrm{d}\gamma = 0 \quad \forall \delta T \in \mathcal{V}_\mathrm{T} \ .
\end{aligned} \tag{B.2}$$

Next, a closer look is taken at the third and fourth line containing all terms tested with $\{q_\mathrm{c}(\delta T)\}_{\omega_\mathrm{T}}$:

$$\begin{aligned}
&- \theta_\mathrm{T} \int_{\gamma_\mathrm{c}^{(1)}} \frac{1}{\beta_\mathrm{c}|p_\mathrm{n}|+\gamma_\mathrm{T}} \{q_\mathrm{c}(T)\}_{(1-\delta_\mathrm{c})} \{q_\mathrm{c}(\delta T)\}_{\omega_\mathrm{T}} \,\mathrm{d}\gamma \\
&+ \theta_\mathrm{T} \int_{\gamma_\mathrm{c}^{(1)}} \frac{\beta_\mathrm{c}|p_\mathrm{n}|}{\beta_\mathrm{c}|p_\mathrm{n}|+\gamma_\mathrm{T}} [\![T]\!] \{q_\mathrm{c}(\delta T)\}_{\omega_\mathrm{T}} \,\mathrm{d}\gamma \\
= &- \theta_\mathrm{T} \int_{\gamma_\mathrm{c}^{(1)}} \frac{1}{\beta_\mathrm{c}|p_\mathrm{n}|+\gamma_\mathrm{T}} \underbrace{\left(\{q_\mathrm{c}(T)\}_{(1-\delta_\mathrm{c})} - \beta_\mathrm{c}|p_\mathrm{n}|[\![T]\!]\right)}_{\overset{\text{eq. (B.1b)}}{=} 0} = 0 \ .
\end{aligned} \tag{B.3}$$

What remains from (B.2) is

$$
\begin{aligned}
&\delta\mathcal{W}_{\mathrm{T}} + \int_{\gamma_{\mathrm{c}}^{(1)}} \frac{\beta_{\mathrm{c}}|p_{\mathrm{n}}|}{\beta_{\mathrm{c}}|p_{\mathrm{n}}| + \gamma_{\mathrm{T}}} \left\{q_{\mathrm{c}}(T)\right\}_{(1-\delta_{\mathrm{c}})} [\![\delta T]\!] \,\mathrm{d}\gamma \\
&\quad + \int_{\gamma_{\mathrm{c}}^{(1)}} \frac{\gamma_{\mathrm{T}}\beta_{\mathrm{c}}|p_{\mathrm{n}}|}{\beta_{\mathrm{c}}|p_{\mathrm{n}}| + \gamma_{\mathrm{T}}} [\![T]\!][\![\delta T]\!] \,\mathrm{d}\gamma \\
&\quad - \int_{\gamma_{\mathrm{c}}^{(1)}} \boldsymbol{t}_{\tau} \cdot \boldsymbol{v}_{\tau} \left(\delta_{\mathrm{c}}\delta T^{(1)} + (1-\delta_{\mathrm{c}})(\delta T^{(2)} \circ \chi_t)\right) \,\mathrm{d}\gamma \\
=&\delta\mathcal{W}_{\mathrm{T}} + \int_{\gamma_{\mathrm{c}}^{(1)}} \left\{q_{\mathrm{c}}(T)\right\}_{(1-\delta_{\mathrm{c}})} [\![\delta T]\!] \,\mathrm{d}\gamma \\
&\quad - \int_{\gamma_{\mathrm{c}}^{(1)}} \frac{\gamma_{\mathrm{T}}}{\beta_{\mathrm{c}}|p_{\mathrm{n}}| + \gamma_{\mathrm{T}}} \underbrace{\left(\left\{q_{\mathrm{c}}(T)\right\}_{(1-\delta_{\mathrm{c}})} - \beta_{\mathrm{c}}|p_{\mathrm{n}}|[\![T]\!]\right)}_{\overset{\text{eq. (B.1b)}}{=} 0} [\![T]\!] \,\mathrm{d}\gamma \\
&\quad - \int_{\gamma_{\mathrm{c}}^{(1)}} \boldsymbol{t}_{\tau} \cdot \boldsymbol{v}_{\tau} \left(\delta_{\mathrm{c}}\delta T^{(1)} + (1-\delta_{\mathrm{c}})(\delta T^{(2)} \circ \chi_t)\right) \,\mathrm{d}\gamma \\
=&\delta\mathcal{W}_{\mathrm{T}} + \int_{\gamma_{\mathrm{c}}^{(1)}} \underbrace{(\beta_{\mathrm{c}}|p_{\mathrm{n}}| - \delta_{\mathrm{c}}\boldsymbol{t}_{\tau} \cdot \boldsymbol{v}_{\tau})}_{\overset{\text{eq. (2.129a)}}{=} q_{\mathrm{c}}^{(1)}} \delta T^{(1)} + \underbrace{(-\beta_{\mathrm{c}}|p_{\mathrm{n}}| - (1-\delta_{\mathrm{c}})\boldsymbol{t}_{\tau} \cdot \boldsymbol{v}_{\tau})}_{\overset{\text{eq. (2.129b)}}{=} q_{\mathrm{c}}^{(2)}} (\delta T^{(2)} \circ \chi_t) \,\mathrm{d}\gamma \\
=&\delta\mathcal{W}_{\mathrm{T}} + \int_{\gamma_{\mathrm{c}}^{(1)}} q_{\mathrm{c}}^{(1)}\delta T^{(1)} + q_{\mathrm{c}}^{(2)}(\delta T^{(2)} \circ \chi_t) \,\mathrm{d}\gamma = 0 \quad \forall \delta T \in \mathcal{V}_{\mathrm{T}} \quad ,
\end{aligned}
$$

which is indeed equivalent to (2.133).

Bibliography

[1] M. F. Adams, Parallel multigrid solvers for 3D unstructured finite element problems in large deformation elasticity and plasticity, *International Journal for Numerical Methods in Engineering* **48**, 1241–1262, 2000.

[2] C. Ager, A. Seitz, and W. A. Wall, A cut finite element method for non-linear fluid-structure-contact interaction based on Nitsche's method, *in preparation*, 2018.

[3] P. Alart and A. Curnier, A mixed formulation for frictional contact problems prone to Newton like solution methods, *Computer Methods in Applied Mechanics and Engineering* **92**, 353–375, 1991.

[4] F. M. Andrade Pires, E. A. de Souza Neto, and J. L. de la Cuesta Padilla, An assessment of the average nodal volume formulation for the analysis of nearly incompressible solids under finite strains, *International Journal for Numerical Methods in Biomedical Engineering* **20**, 569–583, 2004.

[5] C. Annavarapu, M. Hautefeuille, and J. E. Dolbow, A robust Nitsche's formulation for interface problems, *Computer Methods in Applied Mechanics and Engineering* **225**, 44–54, 2012.

[6] A. Apostolatos, R. Schmidt, R. Wüchner, and K.-U. Bletzinger, A Nitsche-type formulation and comparison of the most common domain decomposition methods in isogeometric analysis, *International Journal for Numerical Methods in Engineering* **97**, 473–504, 2014.

[7] F. Armero, Energy-dissipative momentum-conserving time-stepping algorithms for finite strain multiplicative plasticity, *Computer Methods in Applied Mechanics and Engineering* **195**, 4862–4889, 2006.

[8] F. Armero and E. Love, An arbitrary Lagrangian–Eulerian finite element method for finite strain plasticity, *International Journal for Numerical Methods in Engineering* **57**, 471–508, 2003.

[9] F. Auricchio, L. Beirão da Veiga, T. J. R. Hughes, A. Reali, and G. Sangalli, Isogeometric collocation methods, *Mathematical Models and Methods in Applied Sciences* **20**, 2075–2107, 2010.

[10] J. M. Ball, Convexity conditions and existence theorems in nonlinear elasticity, *Archive for Rational Mechanics and Analysis* **63**, 337–403, 1976.

[11] Y. Bazilevs, V. M. Calo, J. A. Cottrell, J. A. Evans, T. J. R. Hughes, S. Lipton, M. A. Scott, and T. W. Sederberg, Isogeometric analysis using T-splines, *Computer Methods in Applied Mechanics and Engineering* **199**, 229–263, 2010.

[12] F. Ben Belgacem, The Mortar finite element method with Lagrange multipliers, *Numerische Mathematik* **84**, 173–197, 1999.

[13] F. Ben Belgacem, P. Hild, and P. Laborde, The mortar finite element method for contact problems, *Mathematical and Computer Modelling* **28**, 263–271, 1998.

[14] C. Bernardi, Y. Maday, and A. T. Patera, A new nonconforming approach to domain decomposition: the mortar element method, In H. Brezis and J. Lions (eds.), *Nonlinear partial differential equations and their applications*, pages 13–51, Pitman/Wiley: London/New York, 1994.

[15] A. Bertram, *Elasticity and plasticity of large deformations*, Springer, 2005.

[16] N. Bleier and J. Mosler, Efficient variational constitutive updates by means of a novel parameterization of the flow rule, *International Journal for Numerical Methods in Engineering* **89**, 1120–1143, 2012.

[17] H. Blum, H. Frohne, J. Frohne, and A. Rademacher, Semi-smooth Newton methods for mixed FEM discretizations of higher-order for frictional, elasto-plastic two-body contact problems, *Computer Methods in Applied Mechanics and Engineering* **309**, 131–151, 2016.

[18] D. Boffi, F. Brezzi, and M. Fortin, *Mixed finite element methods and applications*, Volume 44, Springer, 2013.

[19] J. Bonet and R. D. Wood, *Nonlinear Continuum Mechanics for Finite Element Analysis*, Cambridge University Press, 2 Edition, 2008.

[20] F. A. Bräu, A. Seitz, R. C. Aydin, and C. J. Cyron, Homogenized constrained mixture models for anisotropic volumetric growth and remodeling, *Biomechanics and modeling in mechanobiology* **16**, 889–906, 2017.

[21] E. Brivadis, A. Buffa, B. Wohlmuth, and L. Wunderlich, Isogeometric mortar methods, *Computer Methods in Applied Mechanics and Engineering* **284**, 292–319, 2015.

[22] E. Brivadis, A. Buffa, B. Wohlmuth, and L. Wunderlich, The influence of quadrature errors on isogeometric mortar methods, *Lecture Notes in Computational Science and Engineering* **107**, 33–50, 2015.

[23] E. Burman, A penalty-free nonsymmetric Nitsche-type method for the weak imposition of boundary conditions, *SIAM Journal on Numerical Analysis* **50**, 1959–1981, 2012.

[24] E. Burman and P. Zunino, Numerical approximation of large contrast problems with the unfitted Nitsche method, In *Frontiers in Numerical Analysis-Durham 2010*, pages 227–282, Springer, 2011.

[25] E. Burman, P. Hansbo, and M. G. Larson, The penalty-free Nitsche method and nonconforming finite elements for the Signorini problem, *SIAM Journal on Numerical Analysis* **55**, 2523–2539, 2017.

[26] M. Á. Caminero, F. J. Montáns, and K.-J. Bathe, Modeling large strain anisotropic elasto-plasticity with logarithmic strain and stress measures, *Computers & Structures* **89**, 826–843, 2011.

[27] M. Canajija and J. Brnić, Associative coupled thermoplasticity at finite strain with temperature-dependent material parameters, *International Journal of Plasticity* **20**, 1851–1874, 2004.

[28] C. Carstensen, K. Hackl, and A. Mielke, Non-convex potentials and microstructures in finite-strain plasticity, In *Proceedings of the Royal Society of London A: Mathematical, Physical and Engineering Sciences*, Volume 458, pages 299–317. The Royal Society, 2002.

[29] F. J. Cavalieri and A. Cardona, An augmented Lagrangian technique combined with a mortar algorithm for modelling mechanical contact problems, *International Journal for Numerical Methods in Engineering* **93**, 420–442, 2013.

[30] J. L. Chaboche, A review of some plasticity and viscoplasticity constitutive theories, *International Journal of Plasticity* **24**, 1642–1693, 2008.

[31] F. Chouly, P. Hild, and Y. Renard, A Nitsche finite element method for dynamic contact: 1. Space semi-discretization and time-marching schemes, *ESAIM: Mathematical Modelling and Numerical Analysis* **49**, 481–502, 2015.

[32] F. Chouly, P. Hild, and Y. Renard, A Nitsche finite element method for dynamic contact: 2. Stability of the schemes and numerical experiments, *ESAIM: Mathematical Modelling and Numerical Analysis* **49**, 503–528, 2015.

[33] F. Chouly, An adaptation of Nitsche's method to the Tresca friction problem, *Journal of Mathematical Analysis and Applications* **411**, 329–339, 2014.

[34] F. Chouly and P. Hild, A Nitsche-based method for unilateral contact problems: numerical analysis, *SIAM Journal on Numerical Analysis* **51**, 1295–1307, 2013.

[35] F. Chouly, P. Hild, and Y. Renard, Symmetric and non-symmetric variants of Nitsche's method for contact problems in elasticity: theory and numerical experiments, *Mathematics of Computation* **84**, 1089–1112, 2015.

[36] F. Chouly, R. Mlika, and Y. Renard, An unbiased Nitsche's approximation of the frictional contact between two elastic structures, *Numerische Mathematik*, 2018.

[37] P. W. Christensen, A nonsmooth Newton method for elastoplastic problems, *Computer Methods in Applied Mechanics and Engineering* **191**, 1189–1219, 2002.

[38] J. Chung and G. M. Hulbert, A time integration algorithm for structural dynamics with improved numerical dissipation: The generalized-α method, *Journal of Applied Mechanics* **60**, 371–375, 1993.

[39] T. Cichosz and M. Bischoff, Consistent treatment of boundaries with mortar contact formulations using dual Lagrange multipliers, *Computer Methods in Applied Mechanics and Engineering* **200**, 1317–1332, 2011.

[40] J. A. Cottrell, T. J. R. Hughes, and Y. Bazilevs, *Isogeometric analysis: toward integration of CAD and FEA*, John Wiley & Sons, 2009.

[41] M. A. Crisfield, Re-visiting the contact patch test, *International Journal for Numerical Methods in Engineering* **48**, 435–449, 2000.

[42] A. Curnier, Unilateral contact, In *New developments in contact problems*, pages 1–54, Springer, 1999.

[43] A. Curnier, Q.-C. He, and A. Klarbring, Continuum mechanics modelling of large deformation contact with friction, In *Contact mechanics*, pages 145–158, Springer, 1995.

[44] C. J. Cyron and J. D. Humphrey, Growth and remodeling of load-bearing biological soft tissues, *Meccanica* **52**, 645–664, 2017.

[45] C. J. Cyron, R. C. Aydin, and J. D. Humphrey, A homogenized constrained mixture (and mechanical analog) model for growth and remodeling of soft tissue, *Biomechanics and modeling in mechanobiology* **15**, 1389–1403, 2016.

[46] Y. F. Dafalias, The Plastic Spin, *Journal of Applied Mechanics* **52**, 865–871, 1985.

[47] Y. F. Dafalias, Plastic spin: necessity or redundancy?, *International Journal of Plasticity* **14**, 909 – 931, 1998.

[48] C. Danowski, *Computational Modelling of Thermo-Structure Interaction with Application to Rocket Nozzles*, PhD thesis, Technische Universität München, 2014.

[49] C. Danowski, V. Gravemeier, L. Yoshihara, and W. A. Wall, A monolithic computational approach to thermo-structure interaction, *International Journal for Numerical Methods in Engineering* **95**, 1053–1078, 2013.

[50] L. De Lorenzis, I. Temizer, P. Wriggers, and G. Zavarise, A large deformation frictional contact formulation using NURBS-based isogeometric analysis, *International Journal for Numerical Methods in Engineering* **87**, 1278–1300, 2011.

[51] L. De Lorenzis, P. Wriggers, and G. Zavarise, A mortar formulation for 3D large deformation contact using NURBS-based isogeometric analysis and the augmented Lagrangian method, *Computational Mechanics* **49**, 1–20, 2012.

[52] L. De Lorenzis, J. A. Evans, T. J. R. Hughes, and A. Reali, Isogeometric collocation: Neumann boundary conditions and contact, *Computer Methods in Applied Mechanics and Engineering* **284**, 21–54, 2015.

[53] L. De Lorenzis, P. Wriggers, and T. J. R. Hughes, Isogeometric contact: a review, *GAMM-Mitteilungen* **37**, 85–123, 2014.

[54] C. A. De Saracibar, Numerical analysis of coupled thermomechanical frictional contact problems. Computational model and applications, *Archives of Computational Methods in Engineering* **5**, 243–301, 1998.

[55] E. A. de Souza Neto, D. Peric, M. Dutko, and D. R. J. Owen, Design of simple low order finite elements for large strain analysis of nearly incompressible solids, *International Journal of Solids and Structures* **33**, 3277 – 3296, 1996.

[56] E. A. de Souza Neto, F. M. Andrade Pires, and D. R. J. Owen, F-bar-based linear triangles and tetrahedra for finite strain analysis of nearly incompressible solids. Part I: formulation and benchmarking, *International Journal for Numerical Methods in Engineering* **62**, 353–383, 2005.

[57] E. A. de Souza Neto, D. Perić, and D. R. J. Owen, *Computational methods for plasticity: Theory and applications*, Wiley, Chichester, 2008.

[58] P. Deuflhard, R. Krause, and S. Ertel, A contact-stabilized Newmark method for dynamical contact problems, *International Journal for Numerical Methods in Engineering* **73**, 1274–1290, 2008.

[59] R. Dimitri, L. De Lorenzis, M. A. Scott, P. Wriggers, R. L. Taylor, and G. Zavarise, Isogeometric large deformation frictionless contact using T-splines, *Computer Methods in Applied Mechanics and Engineering* **269**, 394–414, 2014.

[60] R. Dimitri, Isogeometric treatment of large deformation contact and debonding problems with T-splines: a review, *Curved and Layered Structures* **2**, 2015.

[61] M. Dittmann, M. Franke, I. Temizer, and C. Hesch, Isogeometric Analysis and thermomechanical Mortar contact problems, *Computer Methods in Applied Mechanics and Engineering* **274**, 192–212, 2014.

[62] T. Doca, F. M. Andrade Pires, and J. M. A. Cesar de Sa, A frictional mortar contact approach for the analysis of large inelastic deformation problems, *International Journal of Solids and Structures* **51**, 1697–1715, 2014.

[63] J. Dolbow and I. Harari, An efficient finite element method for embedded interface problems, *International Journal for Numerical Methods in Engineering* **78**, 229–252, 2009.

[64] S. Doll, K. Schweizerhof, R. Hauptmann, and C. Freischläger, On volumetric locking of low-order solid and solid-shell elements for finite elastoviscoplastic deformations and selective reduced integration, *Engineering Computations* **17**, 874–902, 2000.

[65] W. Dornisch, G. Vitucci, and S. Klinkel, The weak substitution method–an application of the mortar method for patch coupling in NURBS-based isogeometric analysis, *International Journal for Numerical Methods in Engineering*, 2015.

[66] W. Dornisch, J. Stöckler, and R. Müller, Dual and approximate dual basis functions for B-splines and NURBS–Comparison and application for an efficient coupling of patches with the isogeometric mortar method, *Computer Methods in Applied Mechanics and Engineering* **316**, 449–496, 2017.

[67] M. Ebner, F. Geldmacher, F. Marone, M. Stampanoni, and V. Wood, X-ray tomography of porous, transition metal oxide based lithium ion battery electrodes, *Advanced Energy Materials* **3**, 845–850, 2013.

[68] N. El-Abbasi and K.-J. Bathe, Stability and patch test performance of contact discretizations and a new solution algorithm, *Computers & Structures* **79**, 1473–1486, 2001.

[69] E. Fancello, J. M. Vassoler, and L. Stainier, A variational constitutive update algorithm for a set of isotropic hyperelastic-viscoplastic material models, *Computer Methods in Applied Mechanics and Engineering* **197**, 4132–4148, 2008.

[70] P. Farah, A. Popp, and W. A. Wall, Segment-based vs. element-based integration for mortar methods in computational contact mechanics, *Computational Mechanics* **55**, 209–228, 2015.

[71] K. A. Fischer and P. Wriggers, Frictionless 2D contact formulations for finite deformations based on the mortar method, *Computational Mechanics* **36**, 226–244, 2005.

[72] K. A. Fischer and P. Wriggers, Mortar based frictional contact formulation for higher order interpolations using the moving friction cone, *Computer Methods in Applied Mechanics and Engineering* **195**, 5020–5036, 2006.

[73] N. A. Fleck and J. W. Hutchinson, Strain gradient plasticity, *Advances in Applied Mechanics* **33**, 296–361, 1997.

[74] B. Flemisch and B. Wohlmuth, Stable Lagrange multipliers for quadrilateral meshes of curved interfaces in 3D, *Computer Methods in Applied Mechanics and Engineering* **196**, 1589–1602, 2007.

[75] D. Franke, *Investigation of mechanical contact problems with high-order finite element methods*, PhD thesis, Technische Universität München, 2011.

[76] P. Fuschi, D. Perić, and D. R. J. Owen, Studies on generalized midpoint integration in rate-independent plasticitywith reference to plane stress J_2-flow theory, *Computers & Structures* **43**, 1117–1133, 1992.

[77] C. Geiger and C. Kanzow, *Theorie und Numerik restringierter Optimierungsaufgaben*, Springer-Verlag, 2013.

[78] C. Giannelli, B. Jüttler, S. K. Kleiss, A. Mantzaflaris, B. Simeon, and J. Špeh, THB-splines: An effective mathematical technology for adaptive refinement in geometric design and isogeometric analysis, *Computer Methods in Applied Mechanics and Engineering* **299**, 337–365, 2016.

[79] M. Gitterle, *A dual mortar formulation for finite deformation frictional contact problems including wear and thermal coupling*, PhD thesis, Technische Universität München, 2012.

[80] M. Gitterle, A. Popp, M. W. Gee, and W. A. Wall, Finite deformation frictional mortar contact using a semi-smooth Newton method with consistent linearization, *International Journal for Numerical Methods in Engineering* **84**, 543–571, 2010.

[81] R. Glüge and S. Bucci, Does convexity of yield surfaces in plasticity have a physical significance?, *Mathematics and Mechanics of Solids* **23**, 1364–1373, 2018.

[82] O. Gonzalez, Exact energy and momentum conserving algorithms for general models in nonlinear elasticity, *Computer Methods in Applied Mechanics and Engineering* **190**, 1763–1783, 2000.

[83] M. Graveleau, N. Chevaugeon, and N. Moës, The inequality level-set approach to handle contact: membrane case, *Advanced Modeling and Simulation in Engineering Sciences* **2**, 16, 2015.

[84] A. E. Green and P. M. Naghdi, A general theory of an elastic-plastic continuum, *Archive for Rational Mechanics and Analysis* **18**, 251–281, 1965.

[85] A. E. Green and R. S. Rivlin, Multipolar continuum mechanics, *Archive for Rational Mechanics and Analysis* **17**, 113–147, 1964.

[86] M. Griebel and M. A. Schweitzer, A particle-partition of unity method part V: boundary conditions, In *Geometric Analysis and Nonlinear Partial Differential Equations*, pages 519–542, Springer, 2003.

[87] A. Grillo, R. Prohl, and G. Wittum, A generalised algorithm for anelastic processes in elastoplasticity and biomechanics, *Mathematics and Mechanics of Solids* **22**, 502–527, 2017.

[88] M. Groß, *Higher-order accurate and energy-momentum consistent discretisation of dynamic finite deformation thermo-viscoelasticity*, PhD thesis, Universität Siegen, 2009.

[89] C. Hager, S. Hüeber, and B. Wohlmuth, A stable energy-conserving approach for frictional contact problems based on quadrature formulas, *International Journal for Numerical Methods in Engineering* **73**, 205–225, 2008.

[90] C. Hager, *Robust numerical algorithms for dynamic frictional contact problems with different time and space scales*, PhD thesis, Universität Stuttgart, 2010.

[91] C. Hager and B. Wohlmuth, Nonlinear complementarity functions for plasticity problems with frictional contact, *Computer Methods in Applied Mechanics and Engineering* **198**, 3411–3427, 2009.

[92] W. Han and B. D. Reddy, *Plasticity: Mathematical Theory and Numerical Analysis*, Springer Science & Business Media, 2012.

[93] P. Hansbo, Nitsche's method for interface problems in computational mechanics, *GAMM-Mitteilungen* **28**, 183–206, 2005.

[94] G. Hansen, A Jacobian-free Newton Krylov method for mortar-discretized thermomechanical contact problems, *Journal of Computational Physics* **230**, 6546–6562, 2011.

[95] S. Hartmann, S. Brunssen, E. Ramm, and B. Wohlmuth, Unilateral non-linear dynamic contact of thin-walled structures using a primal-dual active set strategy, *International Journal for Numerical Methods in Engineering* **70**, 883–912, 2007.

[96] M. A. Heroux, E. T. Phipps, A. G. Salinger, H. K. Thornquist, R. S. Tuminaro, J. M. Willenbring, A. Williams, K. S. Stanley, R. A. Bartlett, V. E. Howle, R. J. Hoekstra, J. J. Hu, T. G. Kolda, R. B. Lehoucq, K. R. Long, and R. P. Pawlowski, An overview of the Trilinos project, *ACM Transactions on Mathematical Software* **31**, 397–423, 2005.

[97] H. Hertz, Über die Berührung fester elastischer Körper, *Journal für die reine und angewandte Mathematik* **92**, 156–171, 1882.

[98] C. Hesch and P. Betsch, A mortar method for energy-momentum conserving schemes in frictionless dynamic contact problems, *International Journal for Numerical Methods in Engineering* **77**, 1468–1500, 2009.

[99] C. Hesch and P. Betsch, Energy-momentum consistent algorithms for dynamic thermomechanical problems - Application to mortar domain decomposition problems, *International Journal for Numerical Methods in Engineering* **86**, 1277–1302, 2011.

[100] C. Hesch and P. Betsch, Isogeometric analysis and domain decomposition methods, *Computer Methods in Applied Mechanics and Engineering* **213-216**, 104–112, 2012.

[101] P. Hild, Numerical implementation of two nonconforming finite element methods for unilateral contact, *Computer Methods in Applied Mechanics and Engineering* **184**, 99–123, 2000.

[102] R. Hill, A theory of the yielding and plastic flow of anisotropic metals, *Proceedings of the Royal Society of London A: Mathematical, Physical and Engineering Sciences* **193**, 281–297, 1948.

[103] M. Hintermüller, K. Ito, and K. Kunisch, The primal-dual active set strategy as a semismooth Newton method, *SIAM Journal on Optimization* **13**, 865–888, 2002.

[104] G. A. Holzapfel, *Nonlinear Solid Mechanics*, Wiley, Chichester, 2000.

[105] S. Hüeber, *Discretization techniques and efficient algorithms for contact problems*, PhD thesis, Universität Stuttgart, 2008.

[106] S. Hüeber and B. Wohlmuth, A primal-dual active set strategy for non-linear multibody contact problems, *Computer Methods in Applied Mechanics and Engineering* **194**, 3147–3166, 2005.

[107] S. Hüeber and B. Wohlmuth, Thermo-mechanical contact problems on non-matching meshes, *Computer Methods in Applied Mechanics and Engineering* **198**, 1338–1350, 2009.

[108] S. Hüeber, A. Matei, and B. Wohlmuth, Efficient Algorithms for Problems with Friction, *SIAM Journal on Scientific Computing* **29**, 70–92, 2007.

[109] S. Hüeber, G. Stadler, and B. Wohlmuth, A Primal-Dual Active Set Algorithm for Three-Dimensional Contact Problems with Coulomb Friction, *SIAM Journal on Scientific Computing* **30**, 572–596, 2008.

[110] T. J. R. Hughes, Generalization of selective integration procedures to anisotropic and nonlinear media, *International Journal for Numerical Methods in Engineering* **15**, 1413–1418, 1980.

[111] T. J. R. Hughes, *The Finite Element Method: Linear Static and Dynamic Finite Element Analysis*, Dover Publications, 2000.

[112] T. J. R. Hughes, J. A. Cottrell, and Y. Bazilevs, Isogeometric analysis: CAD, finite elements, NURBS, exact geometry and mesh refinement, *Computer Methods in Applied Mechanics and Engineering* **194**, 4135–4195, 2005.

[113] J. D. Humphrey and K. R. Rajagopal, A constrained mixture model for growth and remodeling of soft tissues, *Mathematical Models and Methods in Applied Sciences* **12**, 407–430, 2002.

[114] A. Ibrahimbegovic and L. Chorfi, Covariant principal axis formulation of associated coupled thermoplasticity at finite strains and its numerical implementation, *International Journal of Solids and Structures* **39**, 499–528, 2002.

[115] K. E. Jansen, C. H. Whiting, and G. M. Hulbert, A generalized-α method for integrating the filtered Navier–Stokes equations with a stabilized finite element method, *Computer Methods in Applied Mechanics and Engineering* **190**, 305–319, 2000.

[116] M. Jirásek and Z. P. Bažant, *Inelastic Analysis of Structures*, Wiley, 2002.

[117] L. Johansson and A. Klarbring, Thermoelastic frictional contact problems: modelling, finite element approximation and numerical realization, *Computer Methods in Applied Mechanics and Engineering* **105**, 181–210, 1993.

[118] M. Juntunen and R. Stenberg, Nitsche's method for general boundary conditions, *Mathematics of Computation* **78**, 1353–1374, 2009.

[119] H. B. Khenous, P. Laborde, and Y. Renard, Mass redistribution method for finite element contact problems in elastodynamics, *European Journal of Mechanics-A/Solids* **27**, 918–932, 2008.

[120] N. Kikuchi and J. T. Oden, *Contact Problems in Elasticity: A Study of Variational Inequalities and Finite Element Methods*, Volume 8, SIAM, 1988.

[121] J.-Y. Kim and S.-K. Youn, Isogeometric contact analysis using mortar method, *International Journal for Numerical Methods in Engineering* **89**, 1559–1581, 2012.

[122] S. Klinkel and W. Wagner, A geometrical non-linear brick element based on the EAS-method, *International Journal for Numerical Methods in Engineering* **40**, 4529–4545, 1997.

[123] K. Krabbenhoft, A. V. Lyamin, S. W. Sloan, and P. Wriggers, An interior-point algorithm for elastoplasticity, *International Journal for Numerical Methods in Engineering* **69**, 592–626, 2007.

[124] R. Krause and M. Walloth, Presentation and comparison of selected algorithms for dynamic contact based on the Newmark scheme, *Applied Numerical Mathematics* **62**, 1393–1410, 2012.

[125] R. Kruse, N. Nguyen-Thanh, L. De Lorenzis, and T. J. R. Hughes, Isogeometric collocation for large deformation elasticity and frictional contact problems, *Computer Methods in Applied Mechanics and Engineering* **296**, 73–112, 2015.

[126] D. Kuhl and M. A. Crisfield, Energy-conserving and decaying algorithms in non-linear structural dynamics, *International Journal for Numerical Methods in Engineering* **45**, 569–599, 1999.

[127] D. Kuhl and E. Ramm, Generalized energy–momentum method for non-linear adaptive shell dynamics, *Computer Methods in Applied Mechanics and Engineering* **178**, 343–366, 1999.

[128] B. P. Lamichhane, *Higher order mortar finite elements with dual Lagrange multiplier spaces and applications*, PhD thesis, Universiät Stuttgart, 2006.

[129] B. P. Lamichhane and B. Wohlmuth, Biorthogonal bases with local support and approximation properties, *Mathematics of Computation* **76**, 233–249, 2007.

[130] B. P. Lamichhane, R. P. Stevenson, and B. Wohlmuth, Higher Order Mortar Finite Element Methods in 3D with Dual Lagrange Multiplier Bases, *Numerische Mathematik* **102**, 93–121, 2005.

[131] T. A. Laursen, *Computational Contact and Impact Mechanics*, Springer-Verlag Berlin Heidelberg, New York, 2002.

[132] T. A. Laursen and V. Chawla, Design of energy conserving algorithms for frictionless dynamic contact problems, *International Journal for Numerical Methods in Engineering* **40**, 863–886, 1997.

[133] T. A. Laursen and G. R. Love, Improved implicit integrators for transient impact problems - geometric admissibility within the conserving framework, *International Journal for Numerical Methods in Engineering* **53**, 245–274, 2002.

[134] E. H. Lee, Finite-Strain Elastic-Plastic Theory with Application to Plane-Wave Analysis, *Journal of Applied Physics* **38**, 19, 1967.

[135] J. Lengiewicz, J. Korelc, and S. Stupkiewicz, Automation of finite element formulations for large deformation contact problems, *International Journal for Numerical Methods in Engineering* **85**, 1252–1279, 2011.

[136] J. C. López-Marcos and J. M. Sanz-Serna, A definition of stability for nonlinear problems, *Numerical treatment of differential equations* **104**, 216–226, 1988.

[137] J. Lu, Isogeometric contact analysis: Geometric basis and formulation for frictionless contact, *Computer Methods in Applied Mechanics and Engineering* **200**, 726–741, 2011.

[138] V. A. Lubarda, *Elastoplasticity theory*, CRC press, 2001.

[139] J. Lubliner, *Plasticity theory*, Courier Corporation, 2008.

[140] Y. Maday, F. Rapetti, and B. Wohlmuth, The influence of quadrature formulas in 2D and 3D mortar element methods, In *Recent Developments in Domain Decomposition Methods*, pages 203–221, Springer, 2002.

[141] J. Mandel, *Plasticité classique et viscoplasticité: Course held at the Department of Mechanics of Solids at Udine, September-October 1971*, Springer, Wien [etc.], 1972.

[142] J. Mandel, Equations constitutives et directeurs dans les milieux plastiques et viscoplastiques, *International Journal of Solids and Structures* **9**, 725–740, 1973.

[143] J. E. Marsden and T. J. R. Hughes, *Mathematical Foundations of Elasticity*, Courier Corporation, 1994.

[144] M. E. Matzen and M. Bischoff, A weighted point-based formulation for isogeometric contact, *Computer Methods in Applied Mechanics and Engineering* **308**, 73–95, 2016.

[145] M. E. Matzen, T. Cichosz, and M. Bischoff, A point to segment contact formulation for isogeometric, NURBS based finite elements, *Computer Methods in Applied Mechanics and Engineering* **255**, 27–39, 2013.

[146] G. A. Maugin, The saga of internal variables of state in continuum thermo-mechanics (1893-2013), *Mechanics Research Communications* **69**, 79–86, 2015.

[147] T. W. McDevitt and T. A. Laursen, A mortar-finite element formulation for frictional contact problems, *International Journal for Numerical Methods in Engineering* **48**, 1525–1547, 2000.

[148] C. Miehe, N. Apel, and M. Lambrecht, Anisotropic additive plasticity in the logarithmic strain space: modular kinematic formulation and implementation based on incremental minimization principles for standard materials, *Computer Methods in Applied Mechanics and Engineering* **191**, 5383–5425, 2002.

[149] C. Miehe, *Kanonische Modelle multiplikativer Elasto-Plastizität: thermodynamische Formulierung und numerische Implementation*, Institut für Baumechanik und Numerische Mechanik, Universität Hannover, 1993.

[150] R. v. Mises, Mechanik der festen Körper im plastisch- deformablen Zustand, *Nachrichten von der Gesellschaft der Wissenschaften zu Göttingen, Mathematisch-Physikalische Klasse* **1913**, 582–592, 1913.

[151] R. Mlika, *Nitsche method for frictional contact and self-contact: mathematical and numerical study*, PhD thesis, Institut national des sciences appliquées de Lyon, 2018.

[152] R. Mlika, Y. Renard, and F. Chouly, An unbiased Nitsche's formulation of large deformation frictional contact and self-contact, *Computer Methods in Applied Mechanics and Engineering* **325**, 265 – 288, 2017.

[153] J. J. Moreau, On unilateral constraints, friction and plasticity, In *New Variational Techniques in Mathematical Physics*, pages 171–322, Springer Berlin Heidelberg, 2011.

[154] J. Mosler, Variationally consistent modeling of finite strain plasticity theory with nonlinear kinematic hardening, *Computer Methods in Applied Mechanics and Engineering* **199**, 2753–2764, 2010.

[155] J. Mosler and O. Bruhns, On the implementation of rate-independent standard dissipative solids at finite strain – Variational constitutive updates, *Computer Methods in Applied Mechanics and Engineering* **199**, 417–429, 2010.

[156] J. J. Muñoz, Modelling unilateral frictionless contact using the null-space method and cubic B-Spline interpolation, *Computer Methods in Applied Mechanics and Engineering* **197**, 979–993, 2008.

[157] D. M. Neto, M. C. Oliveira, L. F. Menezes, and J. L. Alves, A contact smoothing method for arbitrary surface meshes using Nagata patches, *Computer Methods in Applied Mechanics and Engineering* **299**, 283–315, 2016.

[158] J. Nitsche, Über ein Variationsprinzip zur Lösung von Dirichlet-Problemen bei Verwendung von Teilräumen, die keinen Randbedingungen unterworfen sind, In *Abhandlungen aus dem mathematischen Seminar der Universität Hamburg*, Volume 36, pages 9–15. Springer, 1971.

[159] V. Oancea and T. Laursen, A finite element formulation of thermomechanical rate-dependent frictional sliding, *International Journal for Numerical Methods in Engineering* **40**, 4275–4311, 1997.

[160] M. Ortiz and L. Stainier, The variational formulation of viscoplastic constitutive updates, *Computer Methods in Applied Mechanics and Engineering* **171**, 419–444, 1999.

[161] P. Oswald and B. Wohlmuth, On polynomial reproduction of dual FE bases, In *Thirteenth International Conference on Domain Decomposition Methods*, pages 85–96, 2001.

[162] V. Padmanabhan and T. A. Laursen, A framework for development of surface smoothing procedures in large deformation frictional contact analysis, *Finite Elements in Analysis and Design* **37**, 173–198, 2001.

[163] D. Pantuso, K.-J. Bathe, and P. A. Bouzinov, A finite element procedure for the analysis of thermo-mechanical solids in contact, *Computers & Structures* **75**, 551–573, 2000.

[164] P. Papadopoulos and J. Lu, On the formulation and numerical solution of problems in anisotropic finite plasticity, *Computer Methods in Applied Mechanics and Engineering* **190**, 4889–4910, 2001.

[165] R. H. J. Peerlings, R. de Borst, W. A. M. Brekelmans, and J. H. P. de Vree, Gradient enhanced damage for quasi-brittle materials, *International Journal for Numerical Methods in Engineering* **39**, 3391–3403, 1996.

[166] D. Perić, On a class of constitutive equations in viscoplasticity: formulation and computational issues, *International Journal for Numerical Methods in Engineering* **36**, 1365–1393, 1993.

[167] L. Piegl and W. Tiller, *The NURBS book*, Springer Science & Business Media, 2012.

[168] A. Popp, M. W. Gee, and W. A. Wall, A finite deformation mortar contact formulation using a primal-dual active set strategy, *International Journal for Numerical Methods in Engineering* **79**, 1354–1391, 2009.

[169] A. Popp, M. Gitterle, M. W. Gee, and W. A. Wall, A dual mortar approach for 3D finite deformation contact with consistent linearization, *International Journal for Numerical Methods in Engineering* **83**, 1428–1465, 2010.

[170] A. Popp, B. Wohlmuth, M. W. Gee, and W. A. Wall, Dual Quadratic Mortar Finite Element Methods for 3D Finite Deformation Contact, *SIAM Journal on Scientific Computing*, B421–B446, 2012.

[171] A. Popp, *Mortar methods for computational contact mechanics and general interface problems*, PhD thesis, Technische Universität München, 2012.

[172] A. Popp, A. Seitz, M. W. Gee, and W. A. Wall, Improved robustness and consistency of 3D contact algorithms based on a dual mortar approach, *Computer Methods in Applied Mechanics and Engineering* **264**, 67–80, 2013.

[173] K. Poulios and Y. Renard, An unconstrained integral approximation of large sliding frictional contact between deformable solids, *Computers & Structures* **153**, 75–90, 2015.

[174] M. A. Puso and T. A. Laursen, A 3D contact smoothing method using Gregory patches, *International Journal for Numerical Methods in Engineering* **54**, 1161–1194, 2002.

[175] M. A. Puso and T. A. Laursen, A mortar segment-to-segment contact method for large deformation solid mechanics, *Computer Methods in Applied Mechanics and Engineering* **193**, 601–629, 2004.

[176] M. A. Puso and T. A. Laursen, A mortar segment-to-segment frictional contact method for large deformations, *Computer Methods in Applied Mechanics and Engineering* **193**, 4891–4913, 2004.

[177] M. A. Puso, T. A. Laursen, and J. Solberg, A segment-to-segment mortar contact method for quadratic elements and large deformations, *Computer Methods in Applied Mechanics and Engineering* **197**, 555–566, 2008.

[178] L. Qi and J. Sun, A nonsmooth version of Newton's method, *Mathematical Programming* **58**, 353–367, 1993.

[179] A. Quarteroni and A. Valli, *Numerical Approximation of Partial Differential Equations*, Springer, 2008.

[180] A. Rademacher, NCP Function–Based Dual Weighted Residual Error Estimators for Signorini's Problem, *SIAM Journal on Scientific Computing* **38**, A1743–A1769, 2016.

[181] A. Rademacher and H. Frohne, A posteriori error estimates for finite elements of higher-order for frictional, elasto-plastic two-body contact problem, In *Proceedings of the 7th GACM Colloquium on Computational Mechanics for Young Scientists from Academia and Industry*, pages 148–151. Universität Stuttgart, 2017.

[182] A. Reali and T. J. R. Hughes, An introduction to isogeometric collocation methods, In *Isogeometric Methods for Numerical Simulation*, pages 173–204, Springer, 2015.

[183] B. D. Reddy and J. B. Martin, Algorithms for the solution of internal variable problems in plasticity, *Computer Methods in Applied Mechanics and Engineering* **93**, 253–273, 1991.

[184] S. Reese and S. Govindjee, A theory of finite viscoelasticity and numerical aspects, *International Journal of Solids and Structures* **35**, 3455–3482, 1998.

[185] Y. Renard, Generalized Newton's methods for the approximation and resolution of frictional contact problems in elasticity, *Computer Methods in Applied Mechanics and Engineering* **256**, 38–55, 2013.

[186] M. Ristinmaa and N. S. Ottosen, Consequences of dynamic yield surface in viscoplasticity, *International Journal of Solids and Structures* **37**, 4601–4622, 2000.

[187] I. Romero, Thermodynamically consistent time-stepping algorithms for non-linear thermomechanical systems, *International Journal for Numerical Methods in Engineering* **79**, 706–732, 2009.

[188] R. A. Sauer and L. De Lorenzis, An unbiased computational contact formulation for 3D friction, *International Journal for Numerical Methods in Engineering* **101**, 251–280, 2015.

[189] R. Schmidt, R. Wüchner, and K.-U. Bletzinger, Isogeometric analysis of trimmed NURBS geometries, *Computer Methods in Applied Mechanics and Engineering* **241**, 93–111, 2012.

[190] B. Schott, *Stabilized cut finite element methods for complex interface coupled flow problems*, PhD thesis, Technische Universität München, 2017.

[191] K. Schweizerhof and A. Konyukhov, Covariant description for frictional contact problems, *Computational Mechanics* **35**, 190–213, 2005.

[192] A. Seitz, A. Popp, and W. A. Wall, A semi-smooth Newton method for orthotropic plasticity and frictional contact at finite strains, *Computer Methods in Applied Mechanics and Engineering* **285**, 228–254, 2015.

[193] A. Seitz, P. Farah, J. Kremheller, B. Wohlmuth, W. A. Wall, and A. Popp, Isogeometric dual mortar methods for computational contact mechanics, *Computer Methods in Applied Mechanics and Engineering* **301**, 259–280, 2016.

[194] A. Seitz, W. A. Wall, and A. Popp, A computational approach for thermo-elasto-plastic frictional contact based on a monolithic formulation using non-smooth nonlinear complementarity functions, *Advanced Modeling and Simulation in Engineering Sciences* **5**, 5, 2018.

[195] A. Seitz, W. A. Wall, and A. Popp, Nitsche's method for finite deformation thermomechanical contact problems, *Computational Mechanics*, accepted for publication, 2018.

[196] J. C. Simo, A framework for finite strain elastoplasticity based on maximum plastic dissipation and the multiplicative decomposition. Part II: Computational aspects, *Computer Methods in Applied Mechanics and Engineering* **68**, 1–31, 1988.

[197] J. C. Simo, A framework for finite strain elastoplasticity based on maximum plastic dissipation and the multiplicative decomposition: Part I. Continuum formulation, *Computer Methods in Applied Mechanics and Engineering* **66**, 199–219, 1988.

[198] J. C. Simo, Algorithms for static and dynamic multiplicative plasticity that preserve the classical return mapping schemes of the infinitesimal theory, *Computer Methods in Applied Mechanics and Engineering* **99**, 61–112, 1992.

[199] J. C. Simo and F. Armero, Geometrically non-linear enhanced strain mixed methods and the method of incompatible modes, *International Journal for Numerical Methods in Engineering* **33**, 1413–1449, 1992.

[200] J. C. Simo and T. J. R. Hughes, *Computational Inelasticity*, Springer-Verlag New York Inc., 2000.

[201] J. C. Simo and C. Miehe, Associative coupled thermoplasticity at finite strains: Formulation, numerical analysis and implementation, *Computer Methods in Applied Mechanics and Engineering* **98**, 41–104, 1992.

[202] J. C. Simo and M. S. Rifai, A class of mixed assumed strain methods and the method of incompatible modes, *International Journal for Numerical Methods in Engineering* **29**, 1595–1638, 1990.

[203] J. C. Simo and N. Tarnow, The discrete energy-momentum method. Conserving algorithms for nonlinear elastodynamics, *Zeitschrift für angewandte Mathematik und Physik* **43**, 757–792, 1992.

[204] J. C. Simo and R. L. Taylor, Consistent tangent operators for rate-independent elastoplasticity, *Computer Methods in Applied Mechanics and Engineering* **48**, 101–118, 1985.

[205] J. C. Simo and R. L. Taylor, A return mapping algorithm for plane stress elastoplasticity, *International Journal for Numerical Methods in Engineering* **22**, 649–670, 1986.

[206] J. C. Simo, R. L. Taylor, and K. S. Pister, Variational and projection methods for the volume constraint in finite deformation elasto-plasticity, *Computer Methods in Applied Mechanics and Engineering* **51**, 177–208, 1985.

[207] J. C. Simo, P. Wriggers, and R. L. Taylor, A perturbed Lagrangian formulation for the finite element solution of contact problems, *Computer Methods in Applied Mechanics and Engineering* **50**, 163–180, 1985.

[208] S. Sitzmann, K. Willner, and B. Wohlmuth, A dual Lagrange method for contact problems with regularized contact conditions, *International Journal for Numerical Methods in Engineering* **99**, 221–238, 2014.

[209] M. Stadler, G. A. Holzapfel, and J. Korelc, C^n continuous modelling of smooth contact surfaces using NURBS and application to 2D problems, *International Journal for Numerical Methods in Engineering* **57**, 2177–2203, 2003.

[210] L. Stainier and M. Ortiz, Study and validation of a variational theory of thermo-mechanical coupling in finite visco-plasticity, *International Journal of Solids and Structures* **47**, 705–715, 2010.

[211] G. Strang and G. Fix, *An Analysis of the Finite Element Method*, Wellesley-Cambridge Press, 2008.

[212] D. Sun and L. Qi, On NCP-functions, *Computational Optimization and Applications* **13**, 201–220, 1999.

[213] G. I. Taylor and M. A. Quinney, The latent energy remaining in a metal after cold working, *Proceedings of the Royal Society of London A: Mathematical, Physical and Engineering Sciences* **143**, 307–326, 1934.

[214] R. L. Taylor and P. Papadopoulos, On a patch test for contact problems in two dimensions, In P. Wriggers and W. Wagner (eds.), *Computational Methods in Nonlinear Mechanics*, Springer-Verlag Berlin Heidelberg, 1991.

[215] I. Temizer, Multiscale thermomechanical contact: computational homogenization with isogeometric analysis, *International Journal for Numerical Methods in Engineering* **97**, 582–607, 2014.

[216] I. Temizer, P. Wriggers, and T. J. R. Hughes, Contact treatment in isogeometric analysis with NURBS, *Computer Methods in Applied Mechanics and Engineering* **200**, 1100–1112, 2011.

[217] I. Temizer, P. Wriggers, and T. J. R. Hughes, Three-dimensional mortar-based frictional contact treatment in isogeometric analysis with NURBS, *Computer Methods in Applied Mechanics and Engineering* **209–212**, 115–128, 2012.

[218] R. A. Toupin, Theories of elasticity with couple-stress, *Archive for Rational Mechanics and Analysis* **17**, 85–112, 1964.

[219] H. Tresca, *Mémoires sur l'écoulement des corps solides*, Imprimerie impériale, 1869.

[220] M. Tur, F. Fuenmayor, and P. Wriggers, A mortar-based frictional contact formulation for large deformations using Lagrange multipliers, *Computer Methods in Applied Mechanics and Engineering* **198**, 2860–2873, 2009.

[221] M. Tur, E. Giner, F. J. Fuenmayor, and P. Wriggers, 2D contact smooth formulation based on the mortar method, *Computer Methods in Applied Mechanics and Engineering* **247-248**, 1–14, 2012.

[222] M. H. Ulz, A finite isoclinic elasto-plasticity model with orthotropic yield function and notion of plastic spin, *Computer Methods in Applied Mechanics and Engineering* **200**, 1822 – 1832, 2011.

[223] F. Verdugo and W. A. Wall, Unified computational framework for the efficient solution of n-field coupled problems with monolithic schemes, *Computer Methods in Applied Mechanics and Engineering* **310**, 335–366, 2016.

[224] A.-V. Vuong, C. Giannelli, B. Jüttler, and B. Simeon, A hierarchical approach to adaptive local refinement in isogeometric analysis, *Computer Methods in Applied Mechanics and Engineering* **200**, 3554–3567, 2011.

[225] W. A. Wall, C. Ager, M. Grill, M. Kronbichler, A. Popp, B. Schott, and A. Seitz, BACI: A multiphysics simulation environment, Technical report, Institute for Computational Mechanics, Technical University of Munich, 2018.

[226] J. L. Wegner and J. B. Haddow, *Elements of Continuum Mechanics and Thermodynamics*, Cambridge University Press, 2009.

[227] C. Wieners, Nonlinear solution methods for infinitesimal perfect plasticity, *ZAMM* **87**, 643–660, 2007.

[228] C. Wieners, Multigrid methods for Prandtl-Reuss plasticity, *Numerical Linear Algebra with Applications* **6**, 457–478, 1999.

[229] T. A. Wiesner, A. Popp, M. W. Gee, and W. A. Wall, Algebraic multigrid methods for dual mortar finite element formulations in contact mechanics, *International Journal for Numerical Methods in Engineering* **114**, 399–430, 2018.

[230] M. Wilkins, L. L. Laboratory, and B. L. R. L. University of California, *Calculation of elastic-plastic flow*, University of California Lawrence Radiation Laboratory, 1963.

[231] M. Winter, B. Schott, A. Massing, and W. A. Wall, A Nitsche cut finite element method for the Oseen problem with general Navier boundary conditions, *Computer Methods in Applied Mechanics and Engineering* **330**, 220–252, 2018.

[232] B. Wohlmuth, A. Popp, M. W. Gee, and W. A. Wall, An abstract framework for a priori estimates for contact problems in 3D with quadratic finite elements, *Computational Mechanics* **49**, 735–747, 2012.

[233] B. Wohlmuth, A mortar finite element method using dual spaces for the Lagrange multiplier, *SIAM Journal on Numerical Analysis* **38**, 989–1012, 2000.

[234] B. Wohlmuth, Discretization techniques based on domain decomposition, In *Discretization Methods and Iterative Solvers Based on Domain Decomposition*, pages 1–84, Springer, 2001.

[235] B. Wohlmuth, Variationally consistent discretization schemes and numerical algorithms for contact problems, *Acta Numerica* **20**, 569–734, 2011.

[236] P. Wriggers and C. Miehe, Contact constraints within coupled thermomechanical analysis - a finite element model, *Computer Methods in Applied Mechanics and Engineering* **113**, 301–319, 1994.

[237] P. Wriggers and G. Zavarise, A formulation for frictionless contact problems using a weak form introduced by Nitsche, *Computational Mechanics* **41**, 407–420, 2008.

[238] P. Wriggers, C. Miehe, M. Kleiber, and J. C. Simo, On the coupled thermomechanical treatment of necking problems via finite element methods, *International Journal for Numerical Methods in Engineering* **33**, 869–883, 1992.

[239] P. Wriggers, L. Krstulovic-Opara, and J. Korelc, Smooth C^1-interpolations for two-dimensional frictional contact problems, *International Journal for Numerical Methods in Engineering* **51**, 1469–1495, 2001.

[240] P. Wriggers, *Computational Contact Mechanics*, Springer-Verlag Berlin Heidelberg, 2006.

[241] P. Wriggers, *Nonlinear Finite Element Methods*, Springer Science & Business Media, 2008.

[242] L. Wunderlich, A. Seitz, M. D. Alaydın, B. Wohlmuth, and A. Popp, Biorthogonal splines for optimal weak patch-coupling in isogeometric analysis with applications to finite deformation elasticity, *Computer Methods in Applied Mechanics and Engineering* **346**, 197–215, 2019.

[243] L. M. Wunderlich, *Hybrid Finite Element Methods for Non-linear and Non-smooth Problems in Solid Mechanics*, PhD thesis, Technische Universität München, 2017.

[244] H. Xing and A. Makinouchi, Three dimensional finite element modeling of thermomechanical frictional contact between finite deformation bodies using R-minimum strategy, *Computer Methods in Applied Mechanics and Engineering* **191**, 4193–4214, 2002.

[245] B. Yang, T. A. Laursen, and X. Meng, Two dimensional mortar contact methods for large deformation frictional sliding, *International journal for numerical methods in engineering* **62**, 1183–1225, 2005.

[246] Q. Yang, L. Stainier, and M. Ortiz, A variational formulation of the coupled thermo-mechanical boundary-value problem for general dissipative solids, *Journal of the Mechanics and Physics of Solids* **54**, 401–424, 2006.

[247] R. Zaera, J. A. Rodríguez-Martínez, and D. Rittel, On the Taylor–Quinney coefficient in dynamically phase transforming materials. Application to 304 stainless steel, *International Journal of Plasticity* **40**, 185–201, 2013.

[248] G. Zavarise and L. De Lorenzis, A modified node-to-segment algorithm passing the contact patch test, *International Journal for Numerical Methods in Engineering* **79**, 379–416, 2009.

[249] G. Zavarise, P. Wriggers, E. Stein, and B. Schrefler, Real contact mechanisms and finite element formulation - a coupled thermomechanical approach, *International Journal for Numerical Methods in Engineering* **35**, 767–785, 1992.

[250] H. Zbib and E. Aifantis, On the concept of relative and plastic spins and its implications to large deformation theories. Part I: Hypoelasticity and vertex-type plasticity, *Acta Mechanica* **75**, 15–33, 1988.

[251] O. C. Zienkiewicz, R. L. Taylor, and J. M. Too, Reduced integration technique in general analysis of plates and shells, *International Journal for Numerical Methods in Engineering* **3**, 275–290, 1971.

[252] O. C. Zienkiewicz, R. L. Taylor, and D. A. Fox, *The Finite Element Method for Solid and Structural Mechanics*, Butterworth-Heinemann, 2013.

[253] O. C. Zienkiewicz, R. L. Taylor, and J. Z. Zhu, *The Finite Element Method: Its Basis and Fundamentals*, Butterworth-Heinemann, 2013.

[254] Z. Zou, M. Scott, M. Borden, D. Thomas, W. Dornisch, and E. Brivadis, Isogeometric bézier dual mortaring: Refineable higher-order spline dual bases and weakly continuous geometry, *Computer Methods in Applied Mechanics and Engineering* **333**, 497–534, 2018.

Verzeichnis der betreuten Studienarbeiten

Im Rahmen dieser Dissertation entstanden am Lehrstuhl für Numerische Mechanik (LNM) in den Jahren von 2013 bis 2018 unter wesentlicher wissenschaftlicher, fachlicher und inhaltlicher Anleitung des Autors die im Folgenden aufgeführten studentischen Arbeiten.

Studierende(r)	**Studienarbeit**
Caglar Gürbüz	*Implementation of a variational constitutive update algorithm for finite element analysis of plasticity at finite strain*, Masterarbeit, 2016
Michael Obermeyer	*Combination of finite element analysis and isogeometric analysis for contact mechanics with a smooth surface description*, Bachelorarbeit, 2016
Christopher Jelich	*Thermo-mechanical mortar contact formulation for non-matching volume and interface meshes*, Masterarbeit, 2016
Gašper Odar	*Finite element analysis of frictional contact using Nitsche's method*, Semesterarbeit, 2017
Mikhail Zverlov	*Implementation of a finite element method for thermo-plasticity with temperature dependent material parameters*, Semesterarbeit, 2017
Helmuth Stahleder	*Implementation of a mass redistribution method for dynamic finite element simulations of contact problems*, Masterarbeit, 2017
Xiao Yu	*Mortar Finite Elemente Methode mit stückweise konstanten Lagrange Multiplikatoren*, Bachelorarbeit, 2017
Mert Deniz Alaydın	*Isogeometric biorthogonal basis with optimal reproduction orders*, Masterarbeit, 2018